University of Southampton

Faculty of Engineering, Science and Mathematics

School of Ocean and Earth Sciences

Detection and Classification of Oil Spills in MODIS Satellite Imagery

by

Fahad A. M. Alawadi

Thesis is submitted for the degree of Doctor of Philosophy

April 2011

UNIVERSITY OF SOUTHAMPTON

ABSTRACT

FACULTY OF ENGINEERING, SCIENCE AND MATHEMATICS
SCHOOL OF OCEAN AND EARTH SCIENCES

Doctor of Philosophy

Detection and Classification of Oil Spills in MODIS Satellite Imagery

By Fahad Alawadi

Using satellite imagery to achieve an early and accurate identification of oil spills will contribute towards the reduction of their impact on the marine ecosystem. Satellite imagery provided by the synthetic aperture radar (SAR) sensors are widely used for this task over the multi-temporal and multi-band visible near infra-red (VNIR) sensors. This is due to the SAR imaging capabilities through clouds, dust storms, soot and at night times, which limit the capability of VNIR sensors. However, gaps in knowledge exist regarding whether satellite ocean-colour sensors are capable of identifying unreported oil spills as true positives and whether they are able to discriminate them from look-alikes with the least uncertainty, particularly in arid land regions characterised with nearly cloud-free conditions. It was therefore, the goal of this research to develop reliable and robust methodology for data processing and interpretation of oil spills observed by VNIR sensors.

The Moderate Resolution Imaging Spectroradiometer (MODIS) is a VNIR-type sensor that was selected for this project for a number of reasons: it is characterised with adequate multi-spectral features (36 spectral bands 0.405-14.385 μm) spread over three spatial resolutions (250, 500 and 1000 m); and its data is freely distributed in near-real-time. MODIS bio-geophysical products processed in this study such as sea surface temperature (SST4 and SST) and chlorophyll-a (Chlor-a) have also proven their usefulness in providing complementary data.

As a result of this investigation, two methods were proposed: The spectral contrast shift (SCS) and the surface algal bloom index (SABI).

The SCS identifies oil spills and classifies their thickness by using MODIS extreme (maximum and minimum) top-of-atmosphere radiance (TOA) values in the 250 m/pixel resolution bands: the red (λ_1=645 nm) and the NIR (λ_2 =859 nm) measured over a relatively small area selected to encompass part of an unknown class and part of the surrounding pure sea water. The method has produced consistent and highly sensitive results independent of sun-glint illuminations. Oil spills have SCS values lying within the range 0.02-0.04±0.002 varying by 0.01 corresponding to different thicknesses of oil. The SCS succeeded also in classifying surface floating blooms having SCS values greater than or equal to 0.20.

The SABI is a four-band relationship, which according to MODIS 500 m/pixel resolution, is made up of the difference between the TOA radiance responses in the NIR and the red bands (aggregated from the 250 m resolution group) to the sum of the TOA radiance responses in the blue (λ_3=469 nm) and green (λ_4=555 nm) bands. The SABI aims to discriminate biological floating species that may appear as an oil spill look-alike without the need to perform complex corrections for atmosphere and sun-glint effects. The SABI succeeded in classifying 95% of surface blooms that had values greater than or equal to a baseline value of -0.10. Oil spills, however, always appear at values lower than the surface bloom baseline value.

ACKNOWLEDGEMENTS

First and foremost, I would like to thank God Almighty for providing me with this PhD opportunity and for facilitating the companionship of people who have enabled me to complete it.

I would like to thank Professor Carl Amos, for his constant help and guidance throughout every stage of my PhD study. Also, special thanks to Professor Ian Robinson and Dr. Valborg Byfield for their invaluable guidance, encouragement and support.

I am deeply indebted to Dr. Peter Petrov for the tremendous help and support that he has given me - without his perseverance, persistence and sometimes heated discussions this PhD may not have even begun.

I am very appreciative to my dear wife - Ms. Noorah Riyadh, for her help with the editing. I would also like to mention a word of gratitude to the National Oceanography Centre (NOC) for allowing me the use of their facilities and library. Also, my friends Dr. Thamer Al-Rashidi, Mr. Ali Abdullah, Mr. Basheer Jassim and my brother Dr. Hesham Alawadi have provided invaluable support and encouragement -thank you.

I am grateful to H. E. Dr. Abdulrahman Al-Awadi, the executive secretary of the Regional Organization for the Protection of Marine Environment (ROPME), for granting me unlimited access to the organization's full resources including access to ROPME's MODIS data -either in near-real-time, through their satellite receiving station, or stored in their archive. A special word of thanks goes to Captain Abdulmunem Al-Janahi, the director of the Marine Emergency Mutual Aid Centre (MEMAC), a ROPME affiliate, whose contribution was crucial in providing *in situ* verification of analysed oil spills. Finally I would like to give special thanks to my parents for their support and encouragement throughout my study and to my family -for their patience especially during the many times I have said: “Not now... I need to finish my work!”

GRADUATE SCHOOL OF THE SOUTHAMPTON OCEANOGRAPHY

PhD dissertation by

Fahad A. M. Alawadi

has been produced under the supervision of the following persons;

Supervisor/s

Prof. Carl Amos

Prof. Ian Robinson

Dr. Valborg Byfield

Dr. Peter Petrov

DECLARATION OF AUTHORSHIP

I, Fahad A. M. Alawadi, declare that the thesis entitled “Detection and Classification of Oil Spills in MODIS satellite imagery” and the work presented in the thesis are both my own, and have been generated by me as the result of my own original research. I confirm that: this work was done wholly or mainly while in candidature for a research degree at this University; where any part of this thesis has previously been submitted for a degree or any other qualification at this University or any other institution, this has been clearly stated; where I have consulted the published work of others, this is always clearly attributed; where I have quoted from the work of others, the source is always given. With the exception of such quotations, this thesis is entirely my own work; I have acknowledged all main sources of help; where the thesis is based on work done by myself jointly with others and, I have made clear exactly what was done by others and what I have contributed myself.

THESIS CONTENT

LIST OF FIGURES

LIST OF TABLES

LIST OF ACRONYMS

°API	American Petroleum Institute
AISA	Airborne Imaging Spectro–radiometer for Applications
ASAR	Advanced Synthetic Aperture Radar
ASCAT	Advanced Scatterometer
AVHRR	Advanced Very High Resolution Radiometer
AVIRIS	Airborne Visible and IR Imaging Spectrometer
BB	Black-Body
BRDF	Bidirectional Reflectance Distribution Function
CC	Cubic Convolution
CCSDS	Consultative Committee for Space Data Systems
Chlor-a or Chlora	Chlorophyll-a concentration
COAMPS	Coupled Ocean–Atmospheric Mesoscale Prediction System
CZCS	Coastal Zone Colour Scanner
DB	Direct Broadcast
DRL	Direct Readout Laboratory
DVDs	Density Digital Video Discs
Ecal	Electronic calibration
ENVISAT	European Environmental Satellite
EOLi	The Earth Observation Link
EOS	Earth Observing System
EPTOMS	Earth Probe Total Ozone Mapping Spectrometer
ERS	European Remote Sensing satellite
ESA	European Space Agency

F_0	Solar irradiance.
FAI	MODIS Floating Algae Index
FCM	Fuzzy C–Means
FOV	Field-Of-View
GIS	Geographic Information System
GLCF	Global Land Cover Facility
GLCM	Gray Level Co–occurrence Matrix
GRETL	Gnu Regression Econometrics and Time–series Library
GSFC	NASA Goddard Space Flight Center's
HABs	Harmful Algal Blooms
HDF	Hierarchical Data Format
Hs	Maximum significant wave heights
I–RSA	Inner ROPME sea area
IERS	International Earth Rotation Service
IMO	International Maritime Organization
IOSW	Indian Ocean Surface Water
L1B	MODIS Level 1B
Landsat TM	Landsat Thematic Mapper
LIDAR	Light Detection and Ranging
LNA	Low–to–Noise–Amplifier
L_p	Atmospheric path radiance
LTO	Light Thickness Oil (sheen)
LUTs	Look–Up Tables
M–RSA	Middle ROPME sea area
MCI	Maximum Chlorophyll Index

MEMAC	Marine Emergency Mutual Aid Centre
MERIS	Medium Resolution Imaging Spectrometer
MISR	Multi–angle Imaging SpectroRadiometer
MODIS	Moderate Resolution Imaging Spectroradiometer
MRTSwath	MODIS Re–projection Tool Swath
MT	Metric Tonnes
MTO	Medium Thickness Oil
MV	Motor Vessel
MWR	Microwave Radiometer
NCEP	National Centres for Environmental Prediction
NDVI	Normalized Difference Vegetation Index
NOAA	National Oceanic and Atmospheric Administration
NORAD	North American Aerospace Defence Command
NRCS	Normalized radar cross section
NRT	Near–Real–Time
O–RSA	Outer ROPME sea area
OBPG	NASA Ocean Biology Processing Group
OISST	NOAA Optimum Interpolation SST
PC	Single Class
PDS	Production Data Set
QA	Quality Assurance
R/V	Research Vessel
RGB	Red–Green–Blue
rhos	Rayleigh-corrected reflectance
ROPME	Regional Organisation for the Protection of Marine Environment

RSA	ROPME Sea Area
RSB	Reflective Solar Bands
RSR	Relative Spectral Response
RT–STPS	Real–Time Software Telemetry Processing System
RVS	Response Versus Scan angle
SABI	Surface Algal Bloom Index
SAM	Spectral Angle Mapper
SAR	Synthetic Aperture Radar
SBUV/2	Solar Backscatter UltraViolet Version 2
SCS	Spectral Contrast Shift
SD	Solar Diffuser
SDS	Scientific Data Set
SDSM	Solar Diffuser Stability Monitor
SeaDAS	SeaWiFS Data Analysis System
SGP4	Simplified General Perturbations 4
SNR	Signal–to–Noise Ratio
SRCA	Spectro Radiometric Calibration Assembly
SST	Sea Surface Temperature
SVP	Space View Port
SWIR	Short–Wave Infra–Red
T	Direct transmittance of the atmosphere
t_0 (λ)	Atmospheric diffuse transmittance in the solar direction
TEB	Thermal emissive bands
TLE	Two–Line Element file
TOA	Top-of-the atmosphere

TOVS	Advanced Tiros-N Operational Vertical Sounder
$t_{oz}(\lambda)$	Ozone transmittance from surface to sensor and sun to surface
TW	Turbid Water
UAE	United Arab Emirates
UTC	Coordinated Universal Time
UTM	Universal Transverse Mercator
VNIR	Visible Near Infra–Red
VNIRT	Visible, Near Infra–Red, and Thermal Infra–Red
WO	Weathered Oil
ε	Emissivity
μ	Dynamic viscosity
ρ	Top–of–atmosphere reflectance
ρ_w	Water–leaving reflectance
ρ_{wn}	Normalized water–leaving reflectance
σ	Standard deviation
τ	Aerosol optical thickness
τa_{869}	Optical thickness at 869 nm

LIST OF PUBLICATIONS

- Alawadi, F., Amos, C., Byfield, V., et al., "The application of hyperspectral image techniques on MODIS data for the detection of oil spills in the RSA," Proceedings of SPIE Vol. 7110, 71100Q (2008).

- Alawadi, F., "New pattern recognition methods for identifying oil spills from satellite remote sensing data," Proceedings of SPIE Vol. 7110, 71100Q (2009).

- Alawadi, F., "Detection of surface algal blooms using the developed algorithm surface algal bloom index (SABI)," Proceedings of SPIE Vol. 7825-6 (2010).

- Alawadi, F., "Shape and Texture Recognition Methods of Oil Spills in Remote Sensing Data," Environmental Remote Sensing and Systems Analysis. CRC Press (The Taylor and Francis Group), (2012).

PROVISIONAL PATENTS

- "System and method for airborne/spaceborne oil spill Determining system," provisional US patent application, serial No: 12/611,312.

Chapter 1: Introduction

1.1 An overview

The effectiveness of satellite ocean–colour sensors in detecting oil spills has always been under dispute, mainly due to their limited imaging capabilities particularly during night time and/or in heavy cloud coverage. However, their ability to discriminate between oil spills and look–alikes in nearly cloud–free conditions and close to nadir positions remains to be investigated. This has prompted the need to develop reliable and robust new algorithms to address this issue and to assess their applicability and credibility on a global scale. Therefore, in order to conduct this research the Moderate Resolution Imaging Spectroradiometer (MODIS) sensor was selected. MODIS is characterised with a unique design properties that will facilitate the goals of such research, and include: a spectral resolution that covers the visible, near infra–red, and thermal infra–red spectrum; a maximum spatial resolution of 250 m close to nadir; a high temporal resolution[1] (1–2 days revisiting time) due to its availability on–board two satellites; a wide field–of–view; and its data is received freely in near real–time.

1.2 Background and need

Oil spill contamination that results from accidents or hostilities, is considered one of the most detrimental man–made disasters that impact the global marine ecosystem. The direct and indirect adverse effects caused by large oil spills on the natural flora and fauna, may need several years to achieve satisfactory ecological mitigation, particularly if the contamination persists in the water column and in coastal sediments (Hayes et al., 1992). This causes damage to the biodiversity of the aquatic habitat and degradation in its productivity, and consequently may possess a potential health risk by introducing toxicity into the human food chain. The resulting emergence of chronic diseases over the coming years is also a possible consequence (Hayes et al., 1992; Husain, 1995).

The causes of oil spills vary, and include chronic discharges, which originate from various human activities such as transportation, industries, refineries, wastes and natural seepage, as well as accidental spills (Literathy et al., 2002). Figure 1.1 illustrates the relative sources of oil pollution worldwide, sub–divided into major causes.

[1] Resolution will sometimes be used as a measure of spatial resolution measured in pixel's spacing on the Earth's surface or as a measurement with respect to time (revisit time).

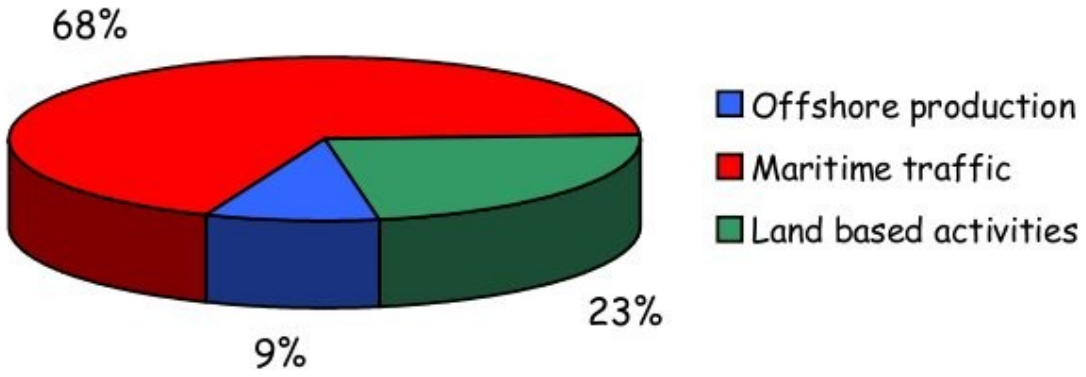

Figure 1.1. Average worldwide relative oil pollution input from 1990–1999 (Lentz et al., 2003).

The exploration for fossil fuel and its production, are expected to expand rapidly as new distribution systems and markets are developed (True, 1999). Such increasing demand for petroleum hydrocarbons has led to an increase in the probability of major spillages contaminating terrestrial and aquatic environments (Delille & Delille, 2000).

The most common method of oil spillage quantity distribution and assessment is by visual identification undertaken from helicopter or aircraft (Gillot et al., 1988). However, an oil spill detection system based on satellite images could be an effective early warning system, and possibly a deterrent to illegal dumping, as well as having a significant environmental impact (Kubat et al., 1998), particularly since the technology was first proved useful during the mid–1960s (Goodman, 1989). Currently, remote sensing sensors based on synthetic aperture radar (SAR) technology are generally considered to be the most popular method for oil spill detection, as they can image at night; and can penetrate clouds, dust storms and soot (Fiscella et al., 1994). Their main drawbacks include the high cost involved in acquiring the data; lack of availability on daily intervals due to prolonged revisiting times; and are limited by sea state (Liu et al., 2000). According to Fingas & Brown (1997), traditional satellite optical sensors (with coarse spatial resolution) have not been of much use for oil spill detection due to cloud cover interference and the lack of algorithms for data processing and interpretation. In such systems, whether based on visual documentation or sensors, the discrimination of real targets from false remains a major challenge, and their success has generally been limited to mapping predetermined oil spill locations (Fingas & Brown, 1997).

1.3 Rationale

In contrast to SAR, studies that have been reported in the literature covering the usage of visible near infra–red (VNIR) satellite imagery for oil spill detection remain scarce. There are not enough reliable methods that use VNIR data for this purpose, possibly due to the sporadic nature of high–resolution airborne photography and satellite imagery, and due to the difficulty in identifying slicks in visible imagery (Hu et al., 2009). Therefore, gaps in the knowledge still exist in relation to the ability of VNIR satellite sensors to discriminate between oil spills and look–alikes. Thus, a number of proposals were made to address these gaps in the knowledge. For example, because the visibility of multi–temporal and multi–band VNIR sensors is obscured by clouds, then choosing an arid land region characterised with cloud–free conditions to evaluate their performance has been recommended (Cosnefroy et al., 1996). Such regions will provide an ideal testing platform to assess the quality of oil spill detection, especially when their water bodies host an active petroleum industry, busy oil transportation systems and growing offshore exploration activities, thus increasing the probability of oil spill occurrence.

A suitable satellite sensor to carry out this research must include: adequate multi–spectral and multi–spatial resolution; minor temporal delays (i.e. shorter re–visiting times); and affordable data acquisition costs in order to maintain the flow of data. Fulfilling these criteria will provide a unique opportunity for the development of suitable algorithms capable of resolving the problems associated with discriminating and identifying oil spills from look–alikes in VNIR satellite sensors. Although such methods may be applicable but limited in reliability in cloudy regions, they may nevertheless pave the way for further development and insight into the design of future thematic multi–spectral satellite sensors.

1.4 The study area

The marine study area chosen to conduct this research is surrounded by the eight member states of the Regional Organisation for the Protection of Marine Environment (ROPME): Bahrain, Iran, Iraq, Kuwait, Oman, Qatar, Saudi Arabia and the United Arab Emirates (UAE). This area –which is also commonly known as the ROPME Sea Area (RSA) – is defined by the following geographic coordinates: 16°39' N, 53° 3' 30" E; 16° 00' N, 53° 25' E; 17°00'N, 56° 30' E; 20° 30' N, 60° 00' E; 25° 04' N, 61° 25' E (UNEP,

1983). It is a relatively small water body with a total area of about 240,000 km^2 (Linden et al., 1990), characterised with ~ 80% cloud–free conditions throughout the year. It is bound by the major oil–producing countries of the world; 49% of the world's oil production passes through the inner area of the RSA (I–RSA) (Al–Awadhi, 1999); it is subject to 1.79% of the world's total shipping activity; and 29% of the world's oil production comes from the member states of ROPME (MEMAC, 2008). The I–RSA sustains the world's 3rd largest concentration of active offshore drilling rigs (Glover, 2007). Because of the active increase in local exploration, exploitation, refining, routine handling and discharge of ballast–water, bilges and slop oil as well as natural seeps (Zarba et al., 1985), the RSA has become prone to frequent occurrences of oil spill incidents. The is clearly evident from latest statistics released by the Marine Emergency Mutual Aid Centre (MEMAC), a ROPME associate (Figure 1.2), showing the different oil spill incidents in the region during the period between 1988–2007.

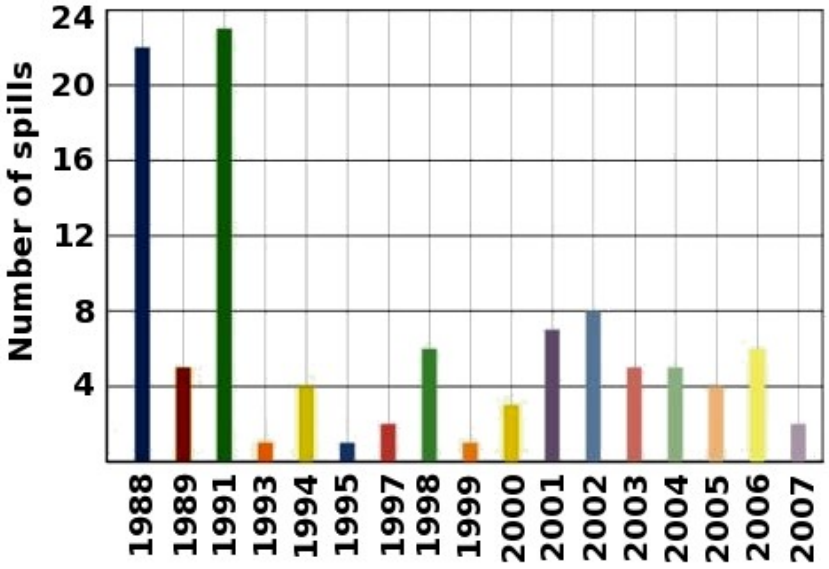

Figure 1.2. Number of spills in the RSA by year (MEMAC, 2008), with one peak in 1988 caused by the Iran–Iraq war and a second peak caused by the 1991 first Gulf War.

The influx of oil from tankers and offshore oil operations, are ranked as the leading source of pollution in the marine environment of the RSA (Figure 1.3). All this has, consequently, made the RSA a potential high risk area of oil spill occurrence, and thus making it a suitable target area for conducting a study on oil spill detection.

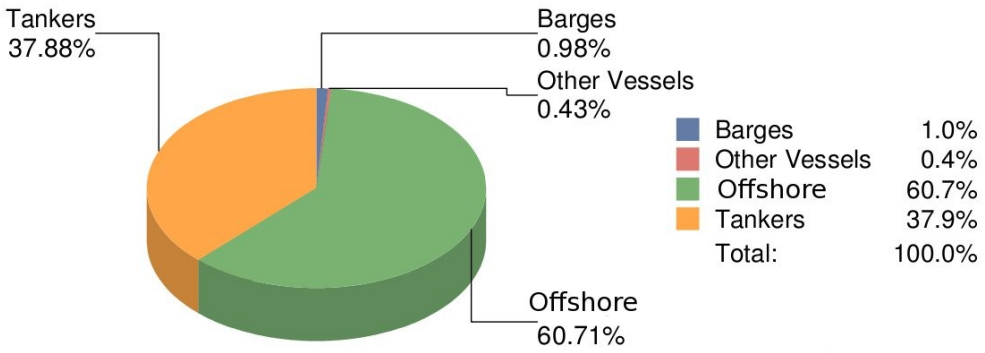

Figure 1.3. Major oil spill sources in the RSA between 1969–2009 (MEMAC, 2008).

1.4.1 Remote sensing of the 1991 oil spill in the RSA

In the RSA, a variety of satellite sensors have been employed to map pre–identified oil spills, as in the case of the 1991 Gulf War. The spill that resulted from this war was marked as one of the worst spills that ever occurred, in which four to six million gallons of crude oil were released from the Kuwaiti oil wells into the I–RSA, and 732 oil wells were set on fire (Abdali & Al-Yakoob, 1994). Figure 1.4 shows the extent of soot that resulted from the burning oil wells.

Figure 1.4. The black smoke plumes of more than 700 individual oil well fires. The soot is seen blowing to the south–west during 1991 (NASA Johnson Space Center, 1991).

Several research papers were produced corresponding to the type of sensor that was employed during and after the 1991 conflict. Astronauts aboard the Space Shuttle Atlantis photographed water features and coastal habitats in the Gulf during mission

STS–45 (24th March to 2nd April, 1992) (Ackleson et al., 1992), to assess the environmental impact of the oil. The astronauts collected 111 hand–held, colour photographs of the Gulf (seventy–two 70 mm photographs and thirty–nine 5 inch photographs) from an altitude of 296 km (160 n.mi.) (Ackleson et al., 1992).

Landsat Thematic Mapper (TM) was used by Al–Ghunaim et al. (1992) to delineate the oil spills using mid–infrared (1.55–2.35 μm) bands combined with the visible (0.45–0.6 μm) bands. Rand et al. (1992) found bands 6, 5, and 1 (10.40–12.50, 1.55–1.75, 0.45–0.52 μm) to be the most useful bands in classifying the oil spills out of Landsat TM bands. This is in contrast to the findings of Al–Hinai et al. (1993) who showed that a false RGB colour composite made up from Landsat TM bands 2, 4 and 7 (0.52–0.6, 0.76–0.9, 2.08–2.35 μm) produced the best classification results for the oil spill thickness.

Cross (1992) used the infrared channels on the National Oceanic and Atmospheric Administration (NOAA) Advanced Very High Resolution Radiometer (AVHRR) showed that the whole slick appears warmer than the sea at night and cooler by day. Whereas, Tseng & Chiu (1994) analysed the same data, and observed several "hot spots" in the vicinity of the centre of the larger oil spill regions, with apparent IR–skin temperatures of about 2–4 °C above the surrounding sea surface temperature (SST) during the daytime, embedded in a region with IR temperatures 1–3 °C below the surrounding SST. Kwarteng et al. (1997) studied the accumulation of oil lakes (shown in Figure 1.5) in the Kuwaiti desert using the Radarsat Synthetic Aperture Radar (SAR) data.

Figure 1.5. Oil lakes resulting from burning Kuwaiti oilfields in 1991 (NOAA Magazine Online, 2010).

1.5 The Moderate Resolution Imaging Spectroradiometer (MODIS)

The Moderate Resolution Imaging Spectroradiometer (MODIS) is an instrument that operates on both the Terra and Aqua spacecrafts and whose main role is to observe the change in the Earth's atmospheric, oceanic, and terrestrial processes (NASA, 2010). It has a viewing swath width of 2,330 km at nadir, and views the entire surface of the Earth every one to two days (NASA, 2010). It can measure top of the atmosphere (TOA) radiance in 36 spectral bands between 0.405 μm and 14.385 μm distributed over three spatial resolutions 250, 500 and 1000 m (NASA, 2010). Depending on the bands chosen, it is possible to derive high–level geophysical products called Level 2 (L2) products such as chlorophyll-a concentration (Chlor-a[*]) and sea surface temperature (SST) (Toller et al., 2003). The properties of all 36 spectral bands used in MODIS are shown in Table 1.1, including the highest resolution bands used in this research , as well as those used for the production of SST and Chlor-a (highlighted in red).

Table 1.1. MODIS spectral bands and their corresponding spatial resolutions (NASA, 2010).

Band[2]	Bandwidth[3]	Required SNR[4]	Band	Bandwidth	NE[delta]T(K)[5]
1	620 - 670	128	20	3.660 - 3.840	0.05
2	841 - 876	201	21	3.929 - 3.989	2
3	459 - 479	243	22	3.929 - 3.989	0.07
4	545 - 565	228	23	4.020 - 4.080	0.07
5	1230 - 1250	74	24	4.433 - 4.498	0.25
6	1628 - 1652	275	25	4.482 - 4.549	0.25
7	2105 - 2155	110	26	1.360 - 1.390	150 (SNR)
8	405 - 420	880	27	6.535 - 6.895	0.25
9	438 - 448	838	28	7.175 - 7.475	0.25
10	483 - 493	802	29	8.400 - 8.700	0.05
11	526 - 536	754	30	9.580 - 9.880	0.25
12	546 - 556	750	31	10.780 - 11.280	0.05
13	662 - 672	910	32	11.770 - 12.270	0.05
14	673 - 683	1087	33	13.185 - 13.485	0.25
15	743 - 753	586	34	13.485 - 13.785	0.25
16	862 - 877	516	35	13.785 - 14.085	0.25
17	890 - 920	167	36	14.085 - 14.385	0.35
18	931 - 941	57			
19	915 - 965	250			

[*] Chlorophyll-a can also be written as $Chlor_a$

[2] Bands 1-2 are in 250m/pixel, bands 3-5 are in 500m/pixel and remaining bands have a 1000m/pixel resolution

[3] Bands 1 to 19 are in nm; Bands 20 to 36 are in μm

[4] SNR = Signal-to-noise ratio

[5] NE(delta)T = Noise-equivalent temperature difference

1.6 Purpose of the project

MODIS, as any ocean–colour satellite sensor, was not intended in its original scientific design to detect oil spills. However, its properties make it a highly favourable candidate to do so. The frequent visiting space–time sampling windows gives it more operational credibility. Also important are its multi–spectral capabilities, its free data distribution in near–real–time (NRT) through its direct broadcast (DB) data mode, and having a consistent coverage of sun–glint allowing for the different contrast viewing of different surface floating films (layers), including oil.

Few of the scientific studies published so far, have illustrated how MODIS is capable of detecting different oil spill incidents at different water regions. Hu et al. (2003) demonstrated how it provided basic and critical assessments of a number of oil spills that occurred in Lake Maracaibo, Venezuela. Kostianoy et al. (2004) used MODIS data as part of an operational satellite system for monitoring oil spill pollution in the south–eastern Baltic Sea, where MODIS's high resolution VIS and IR images, in addition to its 1 km/pixel SST and Chlor-a data products were used to compare with the spills that have been detected in ASAR ENVISAT images: Their conclusion was that a synergy between the different satellites will improve the mechanisms to detect oil spills and also to predict their transport by currents. Chust & Sagarminaga (2006) compared MODIS oil spill observation quality to that of the Multi–angle Imaging SpectroRadiometer (MISR) – a multi–spectral sensor on–board the Terra satellite. MISR utilises nine cameras pointed at fixed angles, ranging from nadir to ±70.5°. Their conclusion was that MISR's cameras configuration provides it with a better capability for oil spill discrimination than MODIS–250 m single–view under sun–glint conditions. Nevertheless, the MODIS–250 m sensor remains valuable in complementing MISR's images because it provides daily images. Shi et al. (2007) demonstrated the possibility of automatically extracting oil spills viewed in MODIS data by using texture and feature methods such as the fuzzy C–means (FCM) cluster analysis algorithm. Hu et al. (2009) also studied the natural phenomenon of oil seepage in the NW Gulf of Mexico using MODIS imagery under different conditions of sun–glint. They concluded that the systematic application of such imagery may improve the estimation of global annual seepage rates.

Most of the studies that have discussed the role of MODIS in detecting oil spills, started with a pre–determined knowledge of oil spill events and locations, and have

focussed primarily on demonstrating its ability to map their spatial distribution and assess the oil's different spectral responses in relation to the water and position of sun–glint. However, none of the papers published so far have addressed the question of whether MODIS is able to identify large–sized suspected patches as true oil spills, and to discriminate them from look–alikes, even before reporting them as such by *in–situ* methods. It is, therefore, the purpose of this research to investigate the degree of accuracy at which a visible, near infra–red, and thermal infra–red (VNIRT) sensor such as MODIS is capable of identifying oil spills and discriminating them from look–alikes in almost cloudless regions, such as the RSA. The ROPME region has made it possible to conduct a thorough research using ocean colour tools for monitoring oil spills under different conditions of viewing geometry, climatology (e.g. degree of cloudiness and thickness of aerosols) and oceanography (e.g. wind speed/direction and the effect of sea surface temperatures). The study will also investigate the possibility of whether MODIS is able to identify relatively large oil spills from the surface patterns that they would appear with in its imagery generated from its (250 m/pixel) spatial resolution bands. The algorithms produced from this research may show that ocean–colour satellite sensors, such as MODIS, can extend their functionalities to carry out maritime early warning operations, aimed specifically at oil spill monitoring. These new proposed methods may also prove useful in introducing new applications to other existing satellite platforms or in the design of new generation sensors.

1.7 Limitations

MODIS as a multi–spectral optical sensor, can face a multitude of atmospheric and oceanographic phenomena that can resemble oil slicks and may lead to false positive sightings of oil spills (Solberg, 2005). Such false positives include natural biogenic oils, silt and suspended sediment, cloud shadows, jellyfish and mats of harmful algal blooms (HABs) (Pavia & Payton, 1983). Its moderate spatial resolution (maximum of 250 m/pixel at nadir) means that MODIS will face difficulties in detecting small–scale oil spills, thereby restricting the investigation to relatively large size oil spills.

Some of the suspected patches that were investigated and classified as oil spills, were not validated by ground truth due to inaccessibility of their locations.

1.8 Thesis overview

Satellite ocean-colour sensors were traditionally utilized in the surveillance and mapping of well-known locations of large, confirmed oil spills, during specific environmental conditions. However, the central science question is: to what extent can an optical ocean-colour sensor - such as MODIS – detect and classify unreported oil spills under the same environmental conditions. Answering this question will lead to the introduction of reliable new methodologies that can be studied in new detail which will ultimately promote their use in environmental impact assessment.

1.8.1 Aims and objectives

The aim of this thesis is to define a reliable multi or dual spectral relationship based on the VNIR bands offered by MODIS's highest spatial resolution channels, capable of discriminating oil spills in the RSA. These relations should have enough credibility for global usability and adequate stability against the different processes that affect the quality of imagery and the fate of oil in the environment.

More specifically, the objectives are: (a) to identify the optimal spectral bands available within MODIS that are most suitable to discriminate and classify oil present at the water surface; (b) to develop a spectral–based algorithm to discriminate oil spills from other look–alikes (true positive detection); (c) to develop a spectral–based algorithm to specifically discriminate surface floating algal blooms, the primary oil spill look–alike feature (true negative detection); and (d) to develop an algorithm to classify oil spills in terms of the spatial pattern they conform to at the water surface, in relation to oil viscosity; and the surrounding dynamics of wind and water forces.

1.8.2 Study methodology

The methodology will provide a systematic examination of an extensive MODIS time–series of over 7 years of archived MODIS data, available for the RSA. The data are stored on a variety of storage media such as digital magnetic tapes; external terabyte (1 terabyte is 10^{12} bytes) hard drives; and high density digital video discs (DVDs). Furthermore, NRT MODIS data were also processed and analysed as they are received by a satellite receiving station based at ROPME, Kuwait. The approach is to systematically analyse the highest resolution images available within the 500 m/pixel and 250 m/pixel band groups, that may contain either expected oil spill patches or

confirmed ones, as well as different categories of oil spill look–alikes. The research also accounts for the climatological and oceanographic conditions, including the effects introduced by the bidirectional reflectance distribution function (BRDF). The BRDF is a mathematical description of how reflectance varies for all possible combinations of illumination and viewing angles at a given wavelength (Schott et al., 1997).

Relevant standard MODIS products that may support this research, such as Chlorophyll-a concentration (Chlor-a), sea surface temperature (SST) and aerosol optical thickness at 869 nm (τ_a869) will also be investigated to either support the existence of an spill or negate it. The shape patterns made by oil spills due to lateral spreading at the water surface will also be investigated, in relation to: the size of the spill; the viscosity and duration of the oil in water; and physical parameters such as wind speed and sea state.

1.8.3 Thesis structure

This study, will be sub–divided into 8 chapters as follows: Chapter 1 will deliver a comprehensive introduction on the main theme of the thesis with a submission of a statement of the problem, its rationale and purpose. Chapter 2 will explore the extent of the current environmental and oceanographic characteristics of the study region, including its socio–economic attributes. This may contribute towards understanding the theme of the study, aid interpretation and the validation of its results. Chapter 3 will cover a review of the theoretical background on oil spill detection algorithms using ocean–colour data provided by remote sensing satellites. This will provide the necessary framework for the research area by highlighting the current developments in the field of "oil spill detection from space" and the related issues worthy of further analysis. Chapter 4 will detail the experimental procedures adopted in this thesis with an emphasis on MODIS's specifications and corresponding products. Chapter 5 will detail the theoretical basis for the introduction of a new spectral method postulated to classify different at–water–surface layers such as spills of different oil thicknesses and floating blooms. Chapter 6 will present a new spectral relationship proposed specifically to identify surface floating biological blooms –the prime oil spill look–alike species. This reversal strategy is based on eliminating the existence of an oil spill by appropriately identifying look–alike substances. Chapter 7 will summarize the results produced from this research and discuss the calibration tests that were carried out on pre–confirmed oil spill events that have been documented in the study area and elsewhere, to be followed

by an explanation of the validation tests that have been conducted to identify the oil spills that have occurred in the RSA. After that, an assessment of all algorithms' applicability and limitations, substantiated with a detailed discussion on their credibility, in view of their calibration and validation results. Chapter 8 will present the conclusions that have evolved from this research –described earlier, with an overall summary of its findings and recommend proposals for future studies.

Chapter 2: The study area

2.1 Definition of the ROPME Sea Area

In April 1978, eight governments comprising of Bahrain, Iran, Iraq, Kuwait, Oman, Qatar, Saudi Arabia and the United Arab Emirates (UAE) adopted the Kuwait Convention and Action Plan that led towards the creation of the Regional Organization for the Protection of the Marine Environment (ROPME) in 1979 (UNEP, 1983).

The ROPME Sea Area (RSA) is relatively small encompassing a total area of about 240,000 km^2 (Linden et al., 1990). It covers the coastal and marine waters of its member states defined as extending between the following latitudes and longitudes respectively: 16° 39´N, 53° 3´ 30´´E; 16° 00´N, 53° 25'E; 17° 00'N, 56° 30´E; 20° 30´N, 60° 00´E; 25° 04´N, 61° 25´E. On 1st August, 2008 the International Maritime Organization (IMO) declared the region to be a "Special Area" in which the discharge of wastes from ships is prohibited (Facey, 2008). The RSA can be divided into three parts (ROPME, 2003)[6]:

- The Inner RSA (I–RSA) is the area that starts from the northern coast to the Strait of Hormuz with a length of about 990 km; with a maximum width of about 338 km (Chao et al., 1992) and average depth of 36 m (Kaempf & Sadrinasab, 2006). Its water volume is variously estimated to be about 7,800 km^3 by Linden et al. (1990) and 8,630 km^3 by Reynolds (1993). It is surrounded by the Zagros mountains on the Iranian side and by low–lying land (Arabian Peninsula) on the Arabian side. To the northwest, the major freshwater inflow into the Gulf comes from the Shatt Al Arab, which is a combination of the Euphrates, the Tigris and the Karuan rivers (Purser & Seibold, 1973). The presence of a desert landmass on one side and mountains on the other increases the rate of water evaporation (2 m/yr (Privett, 1959)), which ensures that the exchange of water through the Strait of Hormuz remains quite active (Hunter, 1985) through a reverse estuarine circulation. Due to geostrophy, the dense bottom outflow is coupled with an inflow of Indian Ocean Surface Water (IOSW) (Sugden, 1963; Hunter, 1982) with an estimated exchange rate of 3–5 years to complete (Sheppard et al., 1992).

[6] This division was adopted by this thesis for ease of identification and not according to ROPME protocols.

- The Middle RSA (M–RSA) includes the Sea of Oman[7] and the east coast of the UAE. It is a deep basin with depths exceeding 2,500 m and has free access to the Arabian Sea and the Indian Ocean. The M–RSA provides an important link that allows the ambient oceanic waters to flow into the I–RSA and allows the warm saline waters to form a bottom layer that exits out of the I–RSA into the Sea of Oman. It extends from the Strait of Hormuz along the Iranian side, to Chah Bahar at the Pakistani border.
- The Outer RSA (O–RSA) extends from Ra's Al–Hadd to the southern border of Oman and exhibits a wide range of habitats ranging from the well–developed sandy shores of the large continental shelf, to the rocky highlands with the narrow continental shelf (Musandam peninsula). It is bound to the north by the relatively mountainous landmasses of Oman and Iran, and deepens rapidly to the south where no barriers separate it from the Arabian Sea and the rest of the Indian Ocean. Figure 2.1 shows a map of the three parts of the RSA.

Figure 2.1. The RSA is divided into three parts: the I–RSA to represent the inner Gulf area, M–RSA to represent the Sea of Oman area and the O–RSA to represent that part of the Arabian sea that starts from from Ra's Al–Hadd to the southern border of Oman.

The RSA region has witnessed three wars in 1980, 1991 and early 2003 each with their own devastating effects on the environment (ROPME, 2003). Following the

[7] The Gulf of Oman was renamed the Sea of Oman by the the Sultanate of Oman in January, 2010.

environmental crisis that resulted in the RSA from the 1991 conflict, several oceanographic observations were carried out to study its impact on the environment: (1) Cruise I: February–June, 1992 (2) Cruise I: January 15–24, 1993 (3) Cruise II: December 15–27, 1993 and (4) Cruise III: December 15–27, 1994 (Yoshida et al., 1998). The research vessel (R/V) Mt. Mitchell operated in 1992 by the U.S. National Oceanic and Atmospheric Administration (NOAA), was the first intensive expedition to investigate winter and summer hydrography of both the I–RSA and M–RSA regions. Recently, ROPME commissioned two R/V Ghods Cruises in the summer 2001 and winter 2004, the results which are yet to be published (ROPME, 2003).

2.2 Climatology

The I–RSA is located between latitudes 24–30° N (north of the Tropic of Cancer) where most of the Earth's deserts are located. It is sub–tropical, even though it is located within the large, arid, East Asian land mass, which means that its climate is more fiercely tropical in summer, and more temperate in winter, than most seas of equivalent latitude. In summer, air temperatures commonly reach 45–50 °C. While in winter, water and air temperatures can reach 3–13 °C (Walters Sr et al., 1990; Sheppard, 1993). This region marks the boundary between tropical circulations (Hadley Cell) and the synoptic weather systems of mid–latitudes, with descending dry air in these latitudes producing cloudless clear skies and arid conditions.

The local climate is influenced by orography; the Caucasus mountains of Iran; and the Hejaz mountains of the Arabian Peninsula together with the Tigris–Euphrates Valley, form a northwest southeast axis that strongly influences the tracks of extra–tropical storms to a southeast direction (Reynolds, 1993).

The yearly cycle in the O–RSA is normally divided into a northeast monsoon, characterized by moderate winds from the northeast during the late fall and winter, a southwest monsoon, characterized by strong winds from the southwest during the late spring and summer and fall and spring inter–monsoons (Tudhope et al., 1996). As Duing (1970) noted, the transition periods can vary from year to year and can occur at different times from region to region.

The major oil spills in the I–RSA tend to disappear surprisingly rapidly due to the advantage of high solar radiation that enhances photolysis, evaporation, solution and bacterial degradation on oil spills (Oostdam, 1980). According to Wheeler (1978),

evaporation in the I–RSA can reduce the surface slick volume of spilled light crude oil by up to 60%.

2.2.1 Wind patterns

In the summer, strong coastal wind patterns build up in the afternoons from 'sea breeze' effects, in which the hot land heats overlying air, which rises due to convection, bringing surface flows which sometimes reach tens of m/s. Land breezes can occur at night and, although less frequent, have powerful desiccating effects especially on the intertidal biota and coastal vegetation (Sheppard, 1993).

In the winter, winds usually remain below 5 m/s, although as in the summer, strong effects come from local winds rather than from the general broad pattern (Sheppard, 1993).

The most well–known, and notorious, weather phenomenon in the I–RSA is the "Shamal" (an Arabic word meaning north). It is a northwest wind that occurs year round (Perrone, 1979), and is related to the synoptic weather system that seldom exceeds 10 m/s (less than 5% frequency) but lasts for several days (Reynolds, 1993).

Winds in the area ahead of an approaching cold front blow from the southeast. These winds, called "Kaus" in Arabic, slowly increases in intensity as the front approaches. They may reach gale force before the passage of the front and the onset of the Shamal. Due to the channelling of the low–level air flow by the Zagros mountains of western Iran, the strongest of the southerly winds occur on the eastern seaboard (Reynolds, 1993).

The climate in the M–RSA is markedly different to the climate in the O–RSA. While the M–RSA is affected mainly by the extra–tropical weather systems from the northwest, the M–RSA is at the northern edge of the tropical weather systems of the O–RSA (Reynolds, 1993).

According to Fett et al. (1983) there are basically four seasons associated with the monsoonal flow patterns over the Middle East/O–RSA:

a. The southwest monsoon regime (June through September);
b. The fall transition period (October and November).
c. The northeast monsoon regime (December through March).
d. The spring transition period (April and May).

It should be realized that the periods of time shown for these seasons represent average conditions and the onset and duration of the seasons may vary considerably

from year to year. Figure 2.2 summarises these different monsoon seasons.

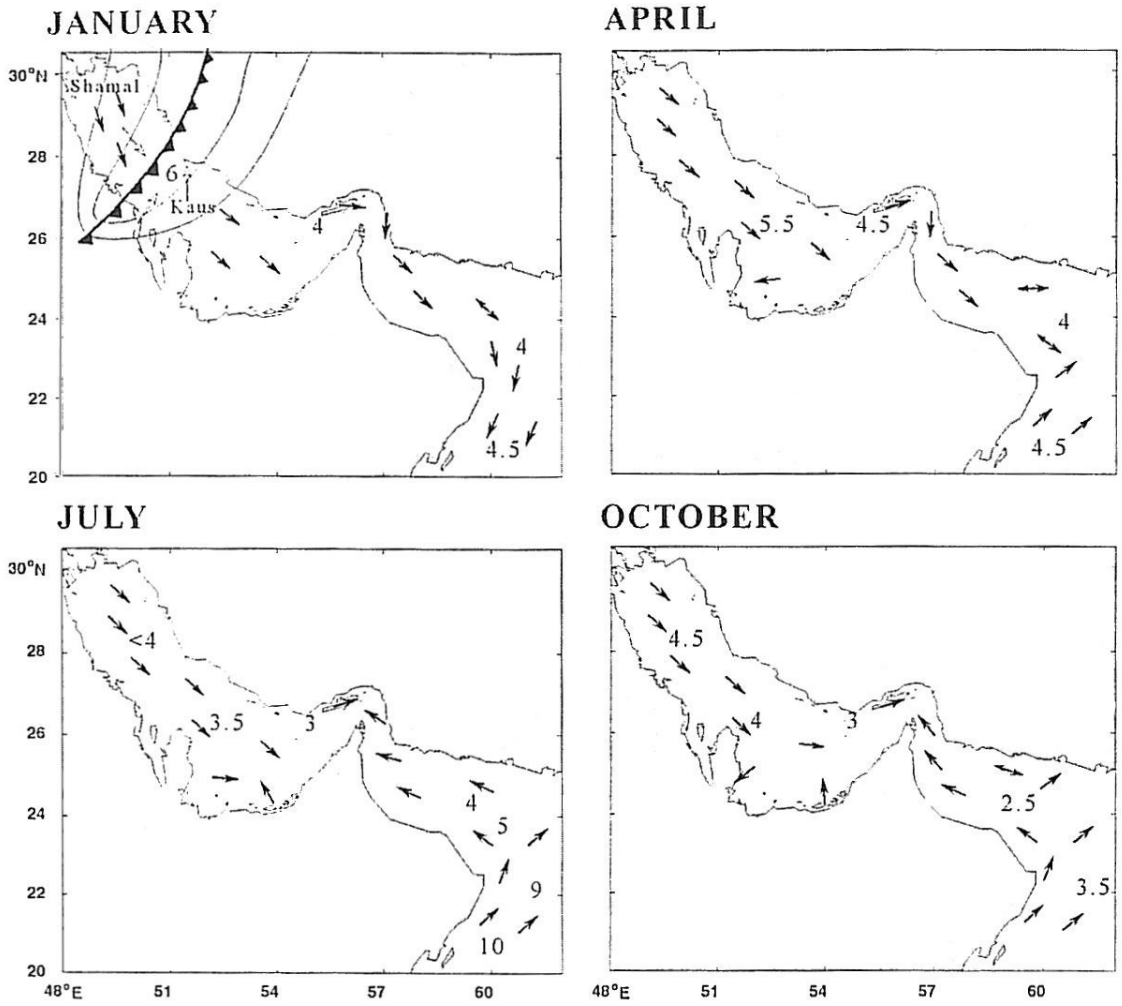

Figure 2.2. A schematic of typical wind patterns in the RSA during the year. The arrows indicate typical (mean) directions and the numbers show the mean wind speeds during the season. A synoptic pressure pattern and accompanying synoptic winds for a Shamal/Kaus wind event are overlaid over the mean pattern for the month of January (Reynolds, 2002a).

2.2.2 Dust

The I–RSA falls within a broad "dust belt" region, that lies in the northern hemisphere and extends from the eastern sub–tropical Atlantic eastwards to southwest Asia (2002). The major sources of contemporary mineral dust (suspension of minerals constituting the soil) are found to be the desert regions of the Northern Hemisphere, in the broad "dust belt" that extends from the eastern subtropical Atlantic eastwards through the Sahara Desert to Arabia and southwest Asia, with remarkably little large–scale dust suspension outside this region (Prospero et al., 2002). Estimates by ROPME (2003) suggest that the average monthly dust deposition at various sites in the

northwestern part of the region can range from 10 to 100 g/m^2.
However, a maximum deposition of 600 g/m^2 has been recorded in some areas, which are among the highest in the world (Linden et al., 1990). Dust storms passing over the northern part of the I–RSA are major sources of marine sediments, as in the month of July alone, they can deposit up to 1000 g/m^2 of sediment in the I–RSA (ROPME, 2003). Other aerosol types also dominate the atmospheric aerosol load in this region (Basart et al., 2009) and they include maritime aerosols which are those found over the oceans; fine polluted aerosols mainly originating from urban and industrial activities; contributions from burning biomass, as well as fine mode pollution particle sources from petroleum extraction and processing facilities which are located on islands, offshore platforms and coastal regions (Basart et al., 2009). The long–range transport of these dust particles usually takes place at higher altitudes (above 1500 m), whereas, urban–industrial and maritime aerosols concentrate at lower altitudes (Basart et al., 2009).

Figure 2.3A shows the 56-h forecast of dust mass load (the vertical integral of concentration) and surface wind vectors from the 9-km grid for 08:00 UTC 26th March, 2003. Figure 2.3B shows the observed surface winds and dust storm observations at 06:00 UTC 26th March, 2003 with an overlay of a 6-h forecasts of sea level pressure and surface temperature produced by the U.S. Navy's Coupled Ocean–Atmospheric Mesoscale Prediction System (COAMPS). Figure 2.3B shows the true colour image of MODIS Terra at 07:45 UTC 26th March, 2003 shows the dust covering most of Iraq and the northern Arabian Peninsula approaching the I–RSA. Figure 2.3C shows the same MODIS Terra images using a false colour composite proposed by Miller (2003) to demonstrate the capability of MODIS at distinguishing airborne dust from the surface and other atmospheric features, by replacing the red channel of the true colour composite with a multi–spectral term derived from seven channels from the visible, short–wave and thermal infra–red spectrum.

The start of dust storms over the land areas surrounding the I–RSA are largely influenced by diurnal changes of wind speed. During the summer Shamal, wind speeds are generally light at night and free from convectional eddies due to a strong low–level inversion. As the inversion disappears one to two hours after sunrise, turbulence increases rapidly, and surface winds exceed the critical dust–raising speed of about 16 knots (Hubert et al., 1983). It is widely believed that the land war activities that emerged during the 1991 Gulf War caused the land's gravel and compacted sand surface to break

up, which is behind the increase in the frequency of dust storms and the deposition of sand in populated coastal zone areas of the I–RSA (WCMC, 1991). The M–RSA will occasionally experience dust and haze from local sources, but these are usually limited to the period immediately preceding the onset of the southwest monsoon in the area (Hubert et al., 1983).

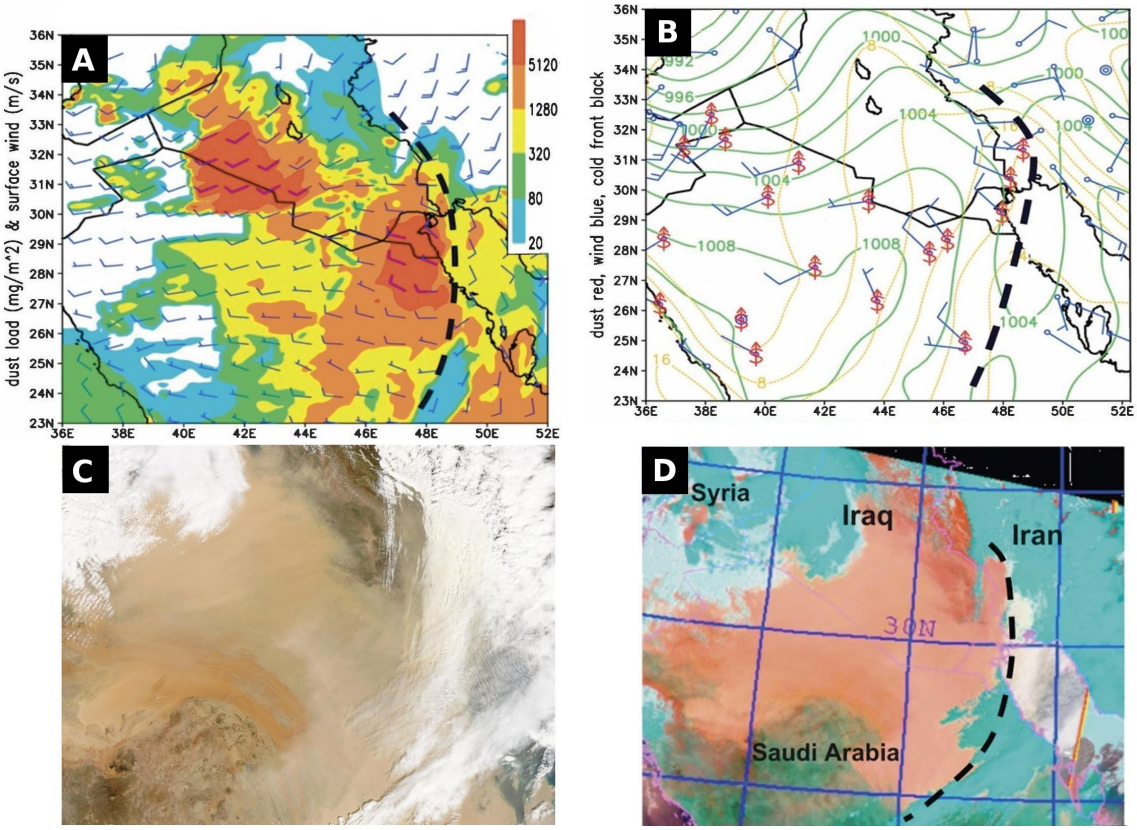

Figure 2.3. **(A)** COAMPS 56-h forecasts of dust mass load (vertically integrated, mg/m^2) and surface wind (full tick=10 m/s) on the 9-km grid valid at 08:00 UTC 26th March 2003. **(B)** A true colour image of MODIS Terra at 07:45 UTC 26th March shows the dust covering most of Iraq and the northern Arabian Peninsula approaching the I–RSA. **(C)** Weather map of observed surface wind (blue, full tick 10 m/s), dust observation (red symbols), and cold front (heavy black dashed line) for 06:00 UTC 26th March 2003. Simulated sea level pressure (green contours) and surface temperature (yellow contours) are also added to show synoptic forcing. **(D)** MODIS Terra image using a false RGB colour composite proposed by Miller (2003) to highlight the dust plumes in pink (Liu et al., 2007).

The O–RSA is bounded on three sides by arid and semi–arid land areas that are acknowledged sources of desert dust and dust clouds, particularly areas to the north of the Arabian Sea, the Middle East, Iran, and Pakistan (Pye, 1991). Figure 2.4 shows the main regional surface wind fields over the RSA.

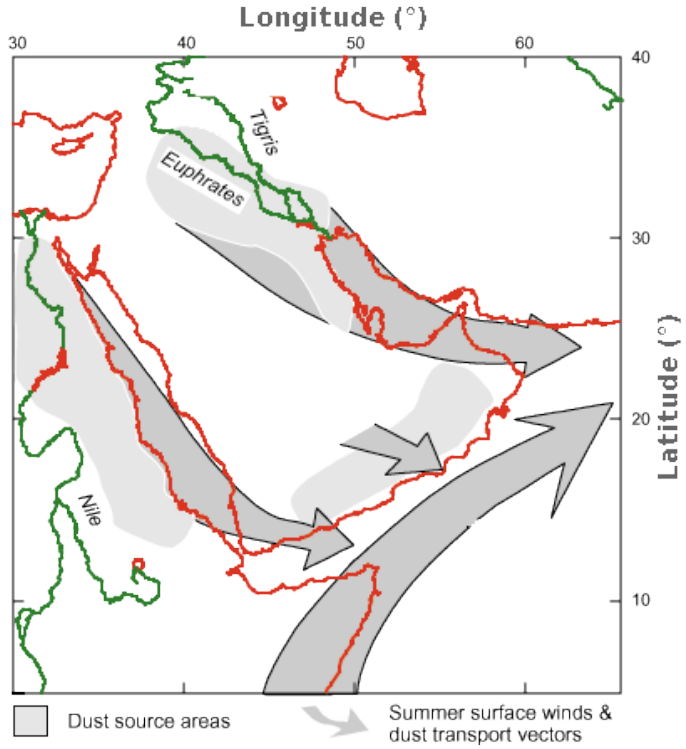

Figure 2.4. Mean atmospheric circulation of the regional surface wind field is shown, including the northwesterly "Shamal" winds including the dust transport vectors (Cullen et al., 2000).

2.2.3 Cloud and Precipitation

The I–RSA is characterized as extremely arid with approximately 80% cloud–free conditions (Alawadi et al., 2008). The region lies at the edge of two global weather systems, the Asian and the North Africa weather systems, whose fluctuations cause varied and severe environmental conditions: the summers are hotter and the winters colder than most sub–tropical zones (Sheppard et al., 1992).

The majority of rainfall events occur during winter months (October–April) from cloud bands that migrate from the eastern coast of Africa, or from the frontal systems that originate in the Mediterranean when the Siberian high pressure shrinks north–eastwards by late winter, or may be due to the southward advance of active westerly troughs over the southwestern part of the Arabian Peninsula (Bento, 2009).

Rainfall can also occur during the summer months due to: clouds drifting in from the Indian monsoon over the O–RSA; afternoon convective clouds due to orographic effects; and, in rare cases due to the Inter Tropical Convergence Zone shifting northward over the UAE and causing overcast weather and thunderstorm activity. Interestingly, data shows that the rainfall in the area might be closely linked with the

Pacific Decadal Oscillation, or ENSO El Ninõ and La Ninã events (Sheppard et al., 1992).

In the O–RSA area rainfall results from a combination of the general weather situation (e.g. monsoons, tropical cyclones and extra–tropical depressions) and the topography of the land. At present, when the air is sufficiently moist, rain falls when the air rises as it meets the mountain ranges in Iran, Oman or the UAE (Hassan & Gerges, 1994). This type of rain is expected to continue and its amount to increase. The average precipitation in the RSA over a period of 17 years has been calculated at about 78 mm/yr (ROPME, 2003).

2.3 Oceanography

2.3.1 Sea surface temperature

The I–RSA averaged sea surface temperature and salinity attains a robust, steady seasonal cycle within 4–5 years of simulation time and onward (Facey, 2008). Figure 2.5 shows the 4 km/pixel resolution monthly (2010) averaged SST composites (Ocean Level-3 products) produced from MODIS Aqua data over the RSA. The Figure confirms the oscillatory nature of the SST yearly distribution period and is an indicator for the heat exchange mechanism between the I–RSA and O–RSA.

In I–RSA the shallowness of the area accentuates the seasonal differences of SST with temperatures as cold as 13 °C and colder occurring at the head of the area in February and nearing 35 °C at the height of the long summer. The temperature difference between summer and winter is greatest (greater than 20 °C) in the north–western part and least (less than 11 °C) at Hormuz (Hassan & Gerges, 1994). Because there is no sill separating I–RSA from the M–RSA, the waters of the I–RSA is characterised with seasonal temperatures and high salinity forms. Due to the long summer in the I–RSA, the warm, high salinity pulse prevails over the cold, high salinity pulse in the intermediate water that reaches the M–RSA (Hassan & Gerges, 1994).

In the M–RSA water temperatures are moderate compared to the I–RSA and is not affected by the monsoons to the same extent. Typical winter surface water temperatures fall to 22–23 °C (minimum recorded of 12 °C in February), while summer temperature is characterized by a highly fluctuating regime caused by the rise and fall of a shallow, but strong thermocline (Bento, 2009).

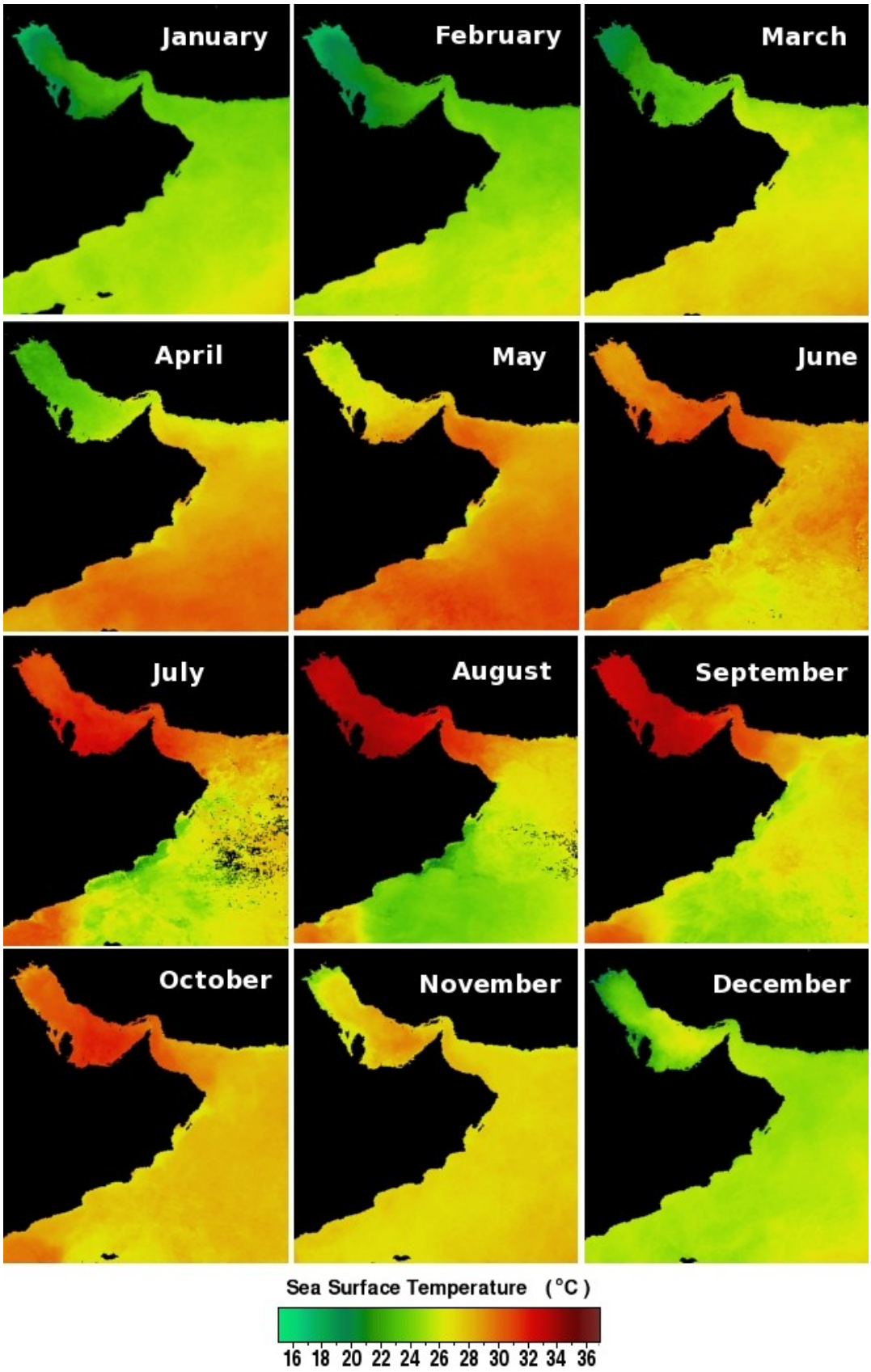

Figure 2.5. The monthly (2010) averaged day SST composites (Ocean Level-3) produced from MODIS Aqua data over the RSA in 4 km/pixel resolution (NASA OBPG, 2010).

Summer water temperatures range between 23–31 °C (maximum recorded of 35 °C in August –with water along the Arabian coast being generally warmer than along the Iranian coast) (Hassan & Gerges, 1994; Rezai et al., 2004). The cool water influences in the M–RSA are less constant, although occasional upwellings occur and can replace surface waters very rapidly so that falls of up to 10 °C over one or two days may occur. Such upwellings have significant impact on the marine ecology, and hereby areas of reef development are few (Randall & Hoover, 1995).

In the O–RSA, the seasonally reversing winds induced by the monsoon create a strong upwelling which causes the remarkable, low sea temperatures off southeast Arabian Peninsula in the hottest summer months (Sheppard et al., 1992). With the onset of the summer monsoon the temperature rises to around 28 °C in May but as upwelling takes hold the temperature in the upwelled areas drops to below 22 °C near the coast in August. The low temperature near the coast continues until the upwelling weakens and in November it is again around 26 °C in the whole area starting a new cycle.

2.3.2 Biological productivity

The O–RSA is one of the most biologically productive ocean regions (Madhupratap et al., 1996). Field data shows that upwelling is a dominant mechanism which triggers plankton blooms and results in extremely high productivity during the southwest monsoon from June to September; during the northeast monsoon from October to January and is higher than during the pre–monsoon from February to May (Qasim, 1982). Figure 2.6 shows the 4 km/pixel resolution monthly (2010) averaged Chlor-a composites (Ocean Level-3) produced from MODIS Aqua data over the RSA.

The rate of phytoplankton cell division is controlled by nutrient availability rather than light, while light inhibition of photosynthesis near the surface is negligible (Banse, 1987). The depths to which algae grow suggest that the euphotic zone extends to a depth of 20 m in the southern part of the I–RSA on the Arabian side, and is as deep as 30 m in the clear water portions of the axis (Purser & Seibold, 1973). Both the I–RSA and M–RSA have a high phytoplankton biodiversity due to the presence of 38 potentially bloom–forming, or harmful algal taxa, that have been reported (Rao & Al-Yamani, 1998). It is known that increasing human population and demand for resources and development is one of the main reasons for the rise in the distribution and size of harmful algal blooms and dead zones (Anderson, 1997).

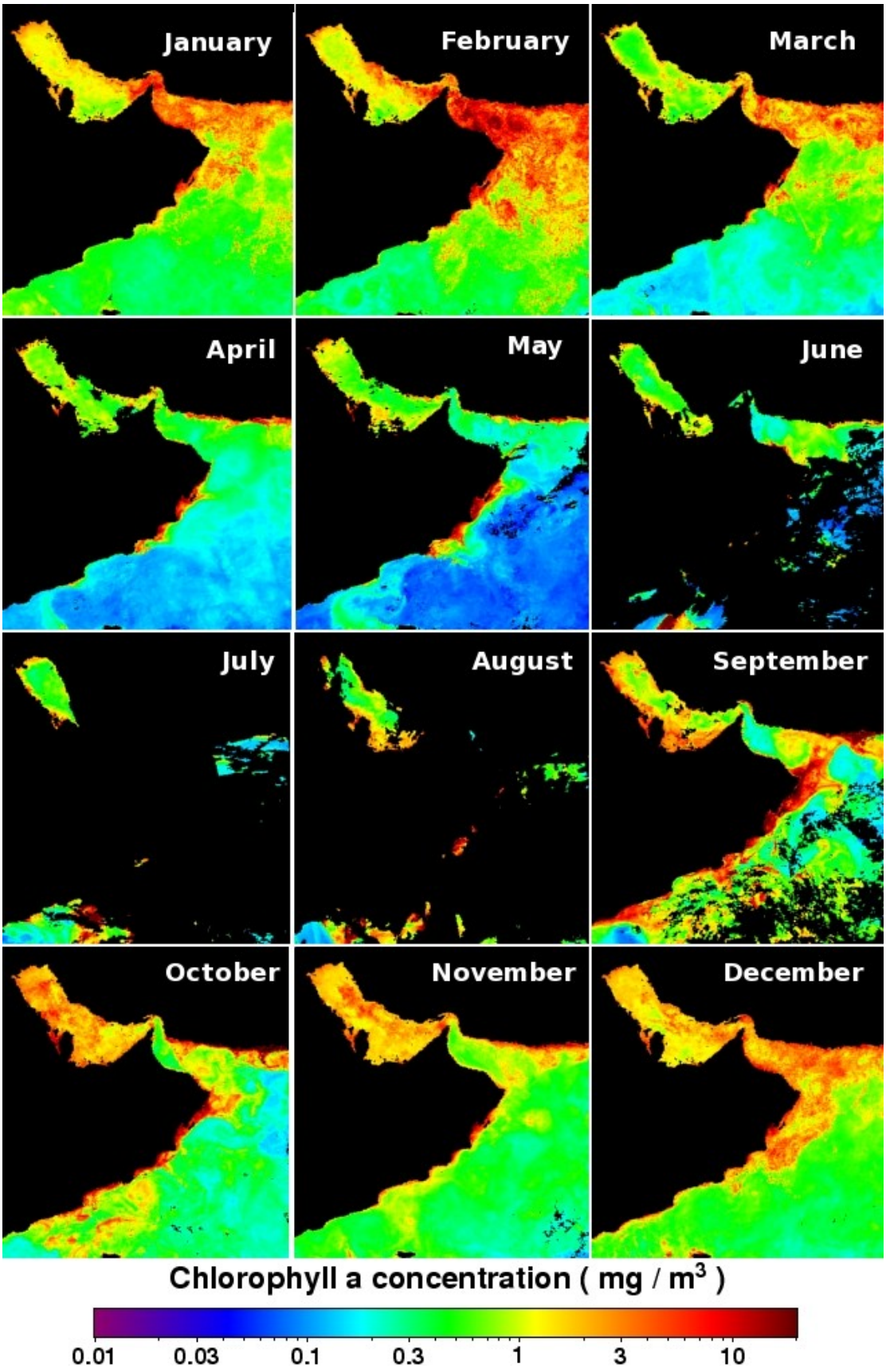

Figure 2.6. The monthly (2010) averaged Chlor-a composites (Ocean Level-3) produced from MODIS Aqua data over the RSA in 4 km/pixel resolution (NASA OBPG, 2010).

In the shallow coral reef areas of the Omani coast, algae tend to be filamentous greens and small browns which grow as an "algal lawn" (Sheppard et al., 1992). Algal communities in most of these areas are seasonal and are correlated with water temperatures, where the I–RSA is coldest in winter and the O–RSA is coldest during the summer upwelling. The study conducted by Goddard & Jupp (2001) has revealed the occurrence of 232 taxa in the Omani waters. In the Iranian coastal waters, seaweed beds can also be found along the part of their shores (ROPME, 2003).

Measurements of nutrients indicated that the surface nutrient content in the M–RSA and O–RSA is much higher than in the I–RSA (ROPME, 2003), where a recent estimate made during the ROPME Ghods Cruise in summer 2001, has shown that phytoplankton ranges are between 0.11 to 1.46 μg/l at the surface waters of the I–RSA (ROPME, 2003).

Soon after the 1991 Gulf War oil spill, intensive cyanobacterial growth on the oil surface was observed (Sorkhoh et al., 1992). This process was proposed to be a first step towards natural bioremediation (Radwan et al., 1999), but partial oil elimination was also attributed to the combined effects of physico–chemical weathering and microbial degradation (Sauer et al., 1998).

Surface floating blooms can sometimes be mistakenly sighted as oil spills such as the "red tide"[8] event that occurred in Kuwait on 19th May, 2000. The observed massive blooms of the blue–green alga *Trichodesmium erythraeum* consisted of strands and lattice–like structures at the surface, which coalesced into extensive floating mats (Rao et al., 2003). The algal aggregates varied from a thin sheen to ~ 2 cm thick; the thick layers included foamy oily complexes with heterogeneous strands, lattices, or rope–like structures in hues of green, blue, pink, red, orange, brown, and grey (Rao et al., 2003).

2.3.3 Sea currents

Waves and currents are the most important means of sediment transport (including surface films such as oil spills) in the shallow basin areas of the I–RSA (Purser & Seibold, 1973). Evaporation (Sugden, 1963; Hunter, 1986) estimated by Privitt (1959) to be 144 cm/yr and wind (Wright, 1974; Hughes & Hunter, 1979) are the major driving forces for circulation in the I–RSA.

[8] The term "red tide" is a common description for an algal bloom, though not all discoloured waters associated with algal blooms are red.

The I–RSA exhibits a reverse estuarine circulation in which, due to geostrophy, the dense bottom outflow follows the coastline of UAE (Figure 2.7A). As for the M–RSA, it is renowned for its complicated flow pattern consisting of several eddies (Böhm et al., 1999). The circulation in the coastal region off Oman is driven mainly by local winds and there is no remotely–driven western boundary current of this area (Figure 2.7B and 2.7C).

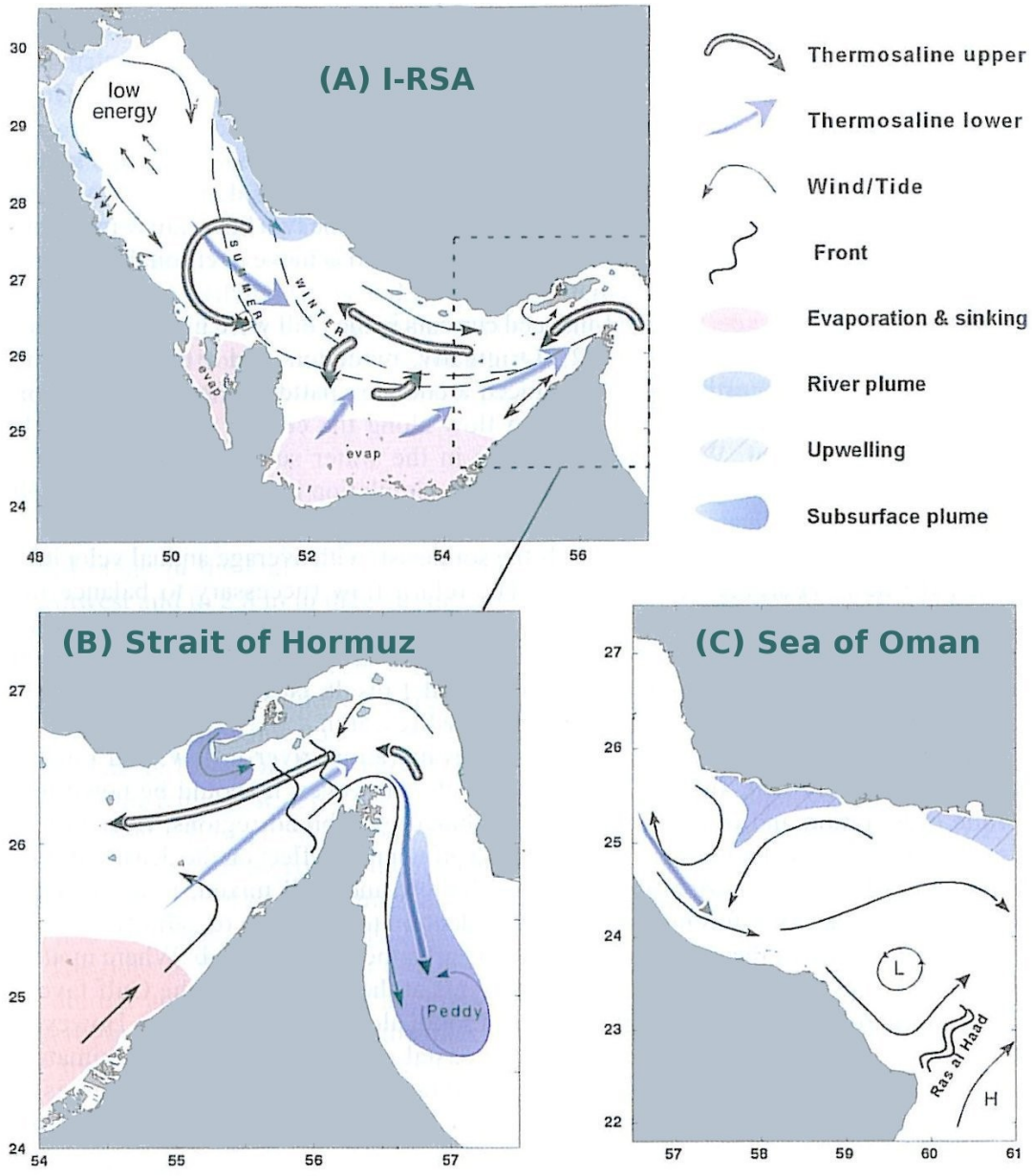

Figure 2.7. The major oceanographic vector processes in the **(A)** I–RSA, **(B)** Strait of Hormuz and **(C)** Sea of Oman (Reynolds, 2002b).

During the northeast monsoon (November–February), the winds blow from the northeast and have maximum wind stress magnitudes of about 2 dyn/cm^2 (Shetye et al.,

1994).

The inflow from the Indian Ocean Surface Water (IOSW) follows the Iranian coastline (Sugden, 1963) in a counter clockwise movement driven by density currents (Emery, 1956; Sheppard et al., 1992).

The circulation pattern in O–RSA consists of several eddies and meanders, with a pronounced anticyclonic (clockwise) eddy around 24° N, 64° E (Figure 2.8). In general, eddies appear to have appreciable deep vertical extension (Qasim, 1982) attributed to the influence of bottom topography, which is marked by depressions and rises (Das et al., 1980). Dynamics and thermodynamics of the surface layer of the O–RSA are dominated by the monsoon–related annual cycle of air–sea momentum and heat fluxes. The surface currents in the open–sea region of this layer can be largely accounted for by Ekman drift, and the thermal field is formed by local heat fluxes (Shetye et al., 1994). Figure 2.9 displays the overall general current circulation pattern in the M–RSA and O–RSA and its exchanges with the I–RSA through the Strait of Hormuz.

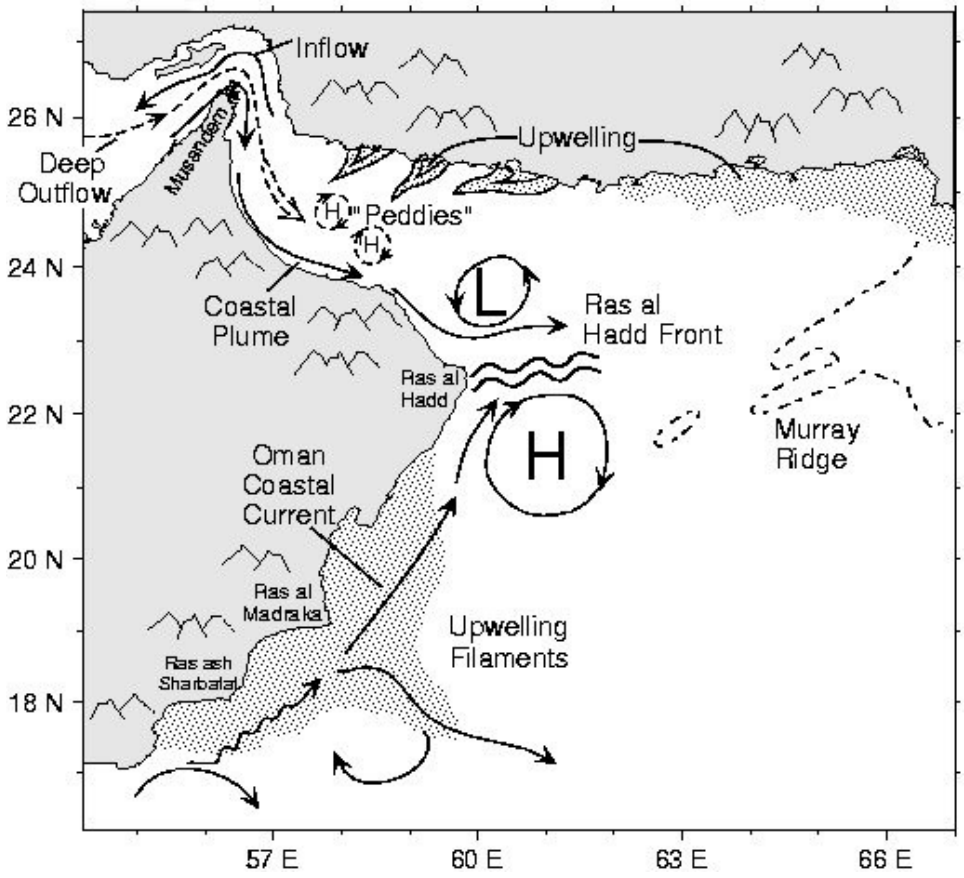

Figure 2.8. Schematic diagram of oceanic circulation in the M–RSA and O–RSA during the southwest monsoon. H=high pressure, L=low pressure, Peddies=The smaller anti–cyclonic eddies (Peddy, Persian Gulf eddy). Courtesy of the Rosenstiel School of Marine and Atmospheric Science, University of Miami.

The Figures 2.9, 2.10, 2.11 and 2.12 show the summer, autumn, winter and spring seasons respectively averaged over 5×5 grid cells (~ 400 km^2) for the surface and bottom current velocities overlaying the water density in the inner and middle part of the RSA.

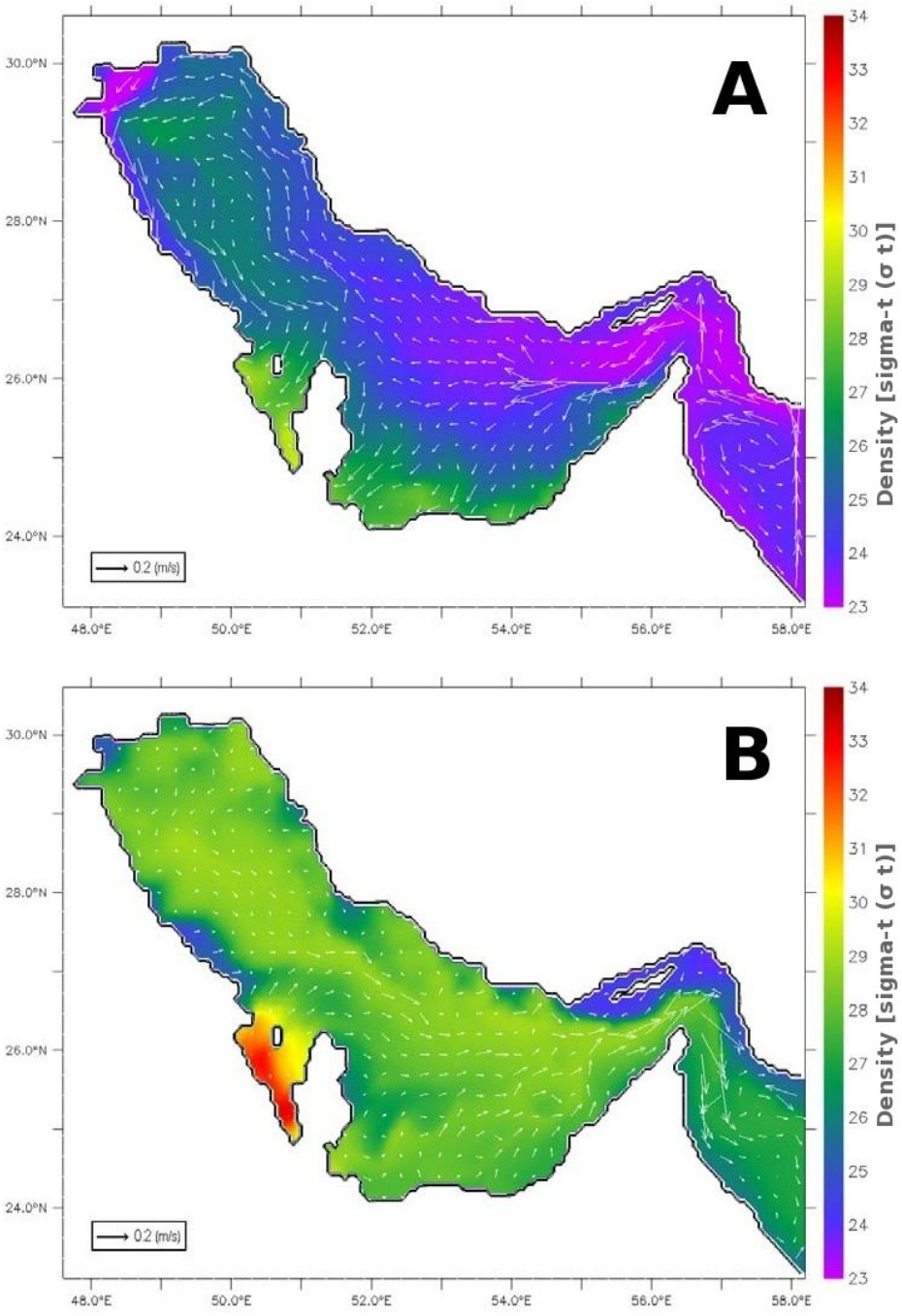

Figure 2.9. Lateral distributions of surface flow vectors (arrows, m/s) over density (colours, sigma-t units) averaged over the summer months (June–August) **(A)** at the surface and **(B)** near the bottom. Flow vectors are averaged over 5×5 grid cells (~ 400 km^2) for visualisation purposes (Kaempf & Sadrinasab, 2006).

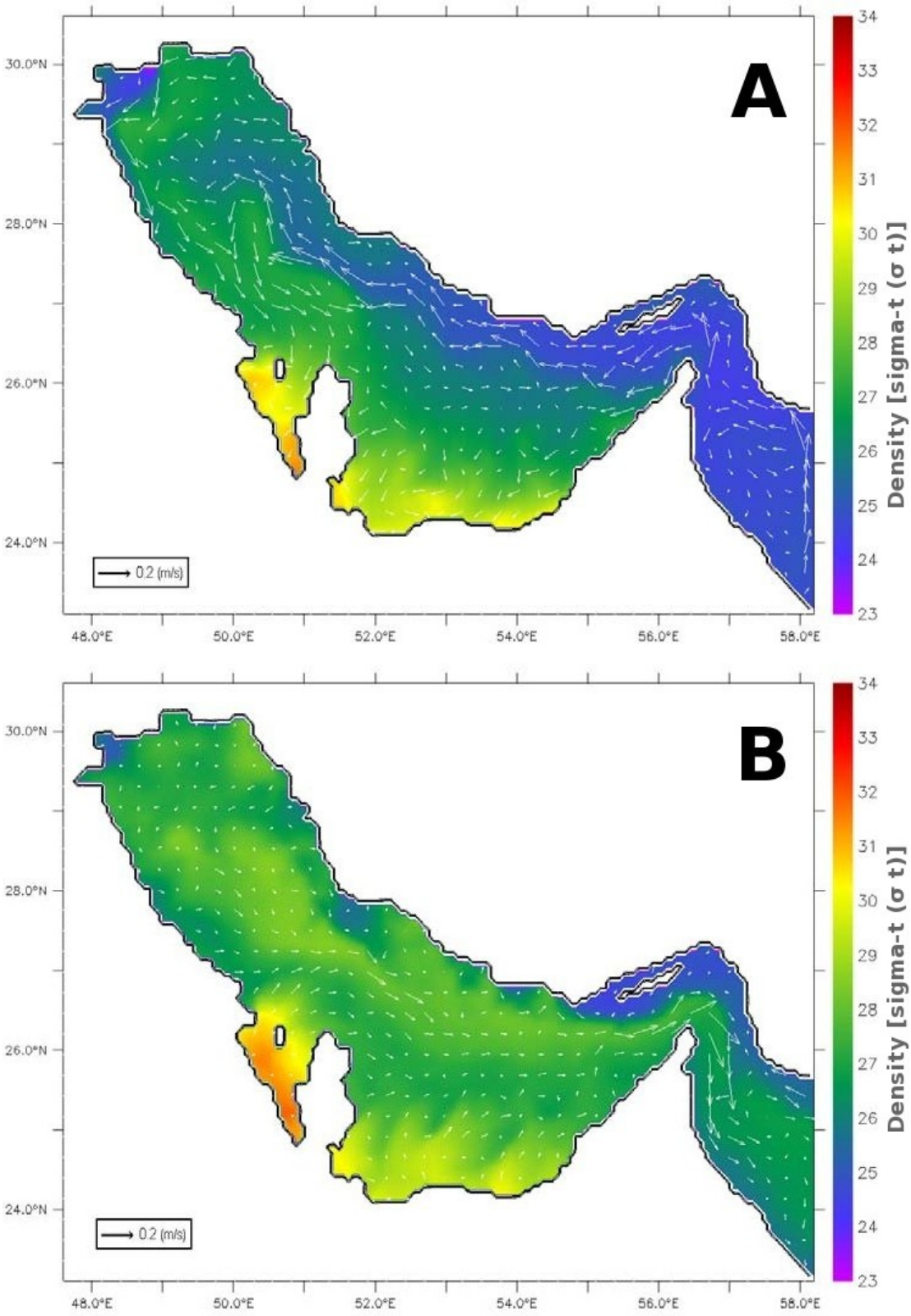

Figure 2.10. Lateral distributions of surface flow vectors (arrows, m/s) over density (colours, sigma-t units) averaged over the autumn months (September–November) **(A)** at the surface and **(B)** near the bottom. Flow vectors are averaged over 5×5 grid cells (~ 400 km^2) for visualisation purposes (Kaempf & Sadrinasab, 2006).

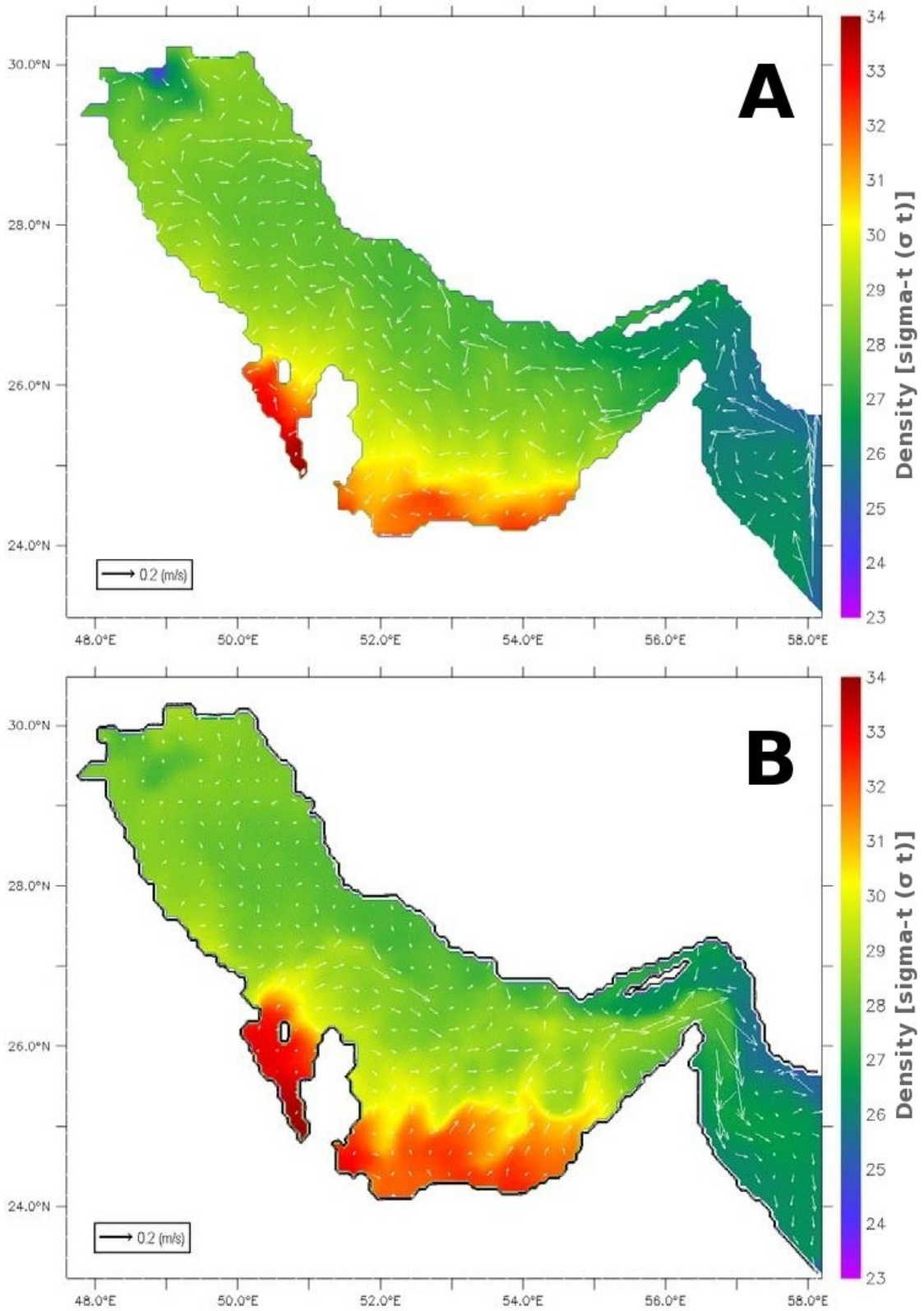

Figure 2.11. Lateral distributions of surface flow vectors (arrows, m/s) over density (colours, sigma-t units) averaged over the winter months (December–February) **(A)** at the surface and **(B)** near the bottom. Flow vectors are averaged over 5×5 grid cells (~ 400 km^2) for visualisation purposes (Kaempf & Sadrinasab, 2006).

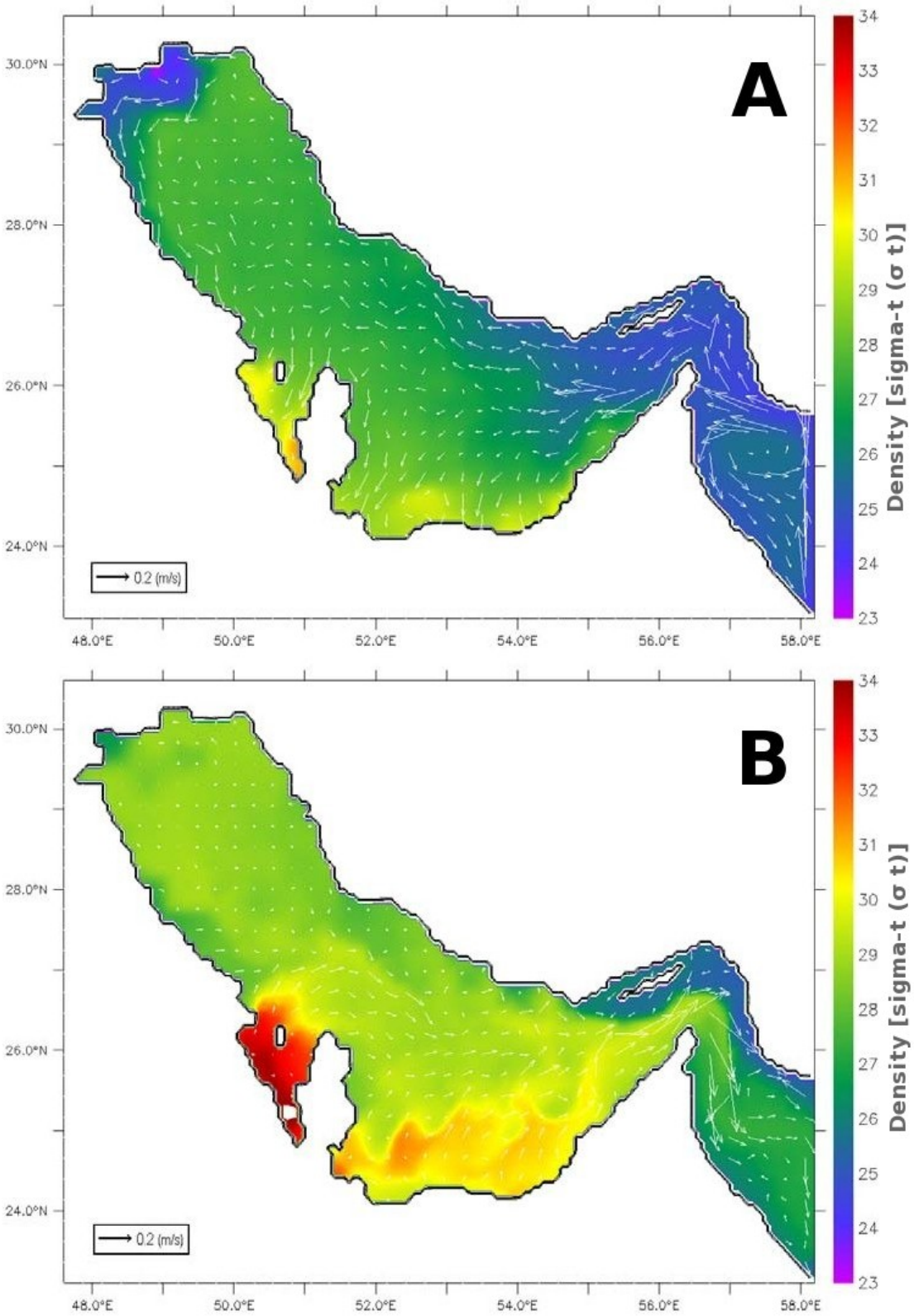

Figure 2.12. Lateral distributions of surface flow vectors (arrows, m/s) over density (colours, sigma-t units) averaged over the spring months (March–May) **(A)** at the surface and **(B)** near the bottom. Flow vectors are averaged over 5×5 grid cells (~ 400 km^2) for visualisation purposes (Kaempf & Sadrinasab, 2006).

The figures were produced using the eddy–resolving, three–dimensional numerical model "Coupled Hydro–dynamical Ecological model for Regional Shelf seas-COHERENS". The model's output agreed with observations that spans over 73 years from 1923 to 1996 (Kaempf & Sadrinasab, 2006). The effects of winds and of currents driven by density counteract each other along the northeast shores of the I–RSA in winter, causing oil slicks to maintain position. Along the southwest shores, by contrast, dispersal of slicks is enhanced by currents and winds moving in the same direction (Oostdam, 1980).

2.3.4 Sea waves

Rakha et al. (2007) have used a third–generation wind driven wave model WAM (Group, 1988) to model the wind waves in the I–RSA over a period of 12 years (from 1st January, 1993 till 31st December, 2004). Figures 2.13A and 2.13B provide a contour plot for the maximum significant wave heights (H_s) and mean periods (T_m) respectively over the same period.

There has been some study of internal waves in the O–RSA and the M–RSA through the use of European remote sensing satellite (ERS) SAR imagery (Small & Martin, 2002). The imagery shows evidence of fine–scale internal wave signatures along the continental shelf around the entire region propagating towards the Musandam Peninsula in Oman from the shelf–edge on the eastern edge of the M–RSA. The signatures had the classic appearance of rank ordered non–linear waves that depress the pycnocline. The images also suggest a tidal generation mechanism, yielding a phase speed estimate from 0.5 m/s near the coast to 0.7 m/s on the shelf. Figure 2.14 shows a wave rose plot generated also for location (A) shown earlier in Figure 2.13.

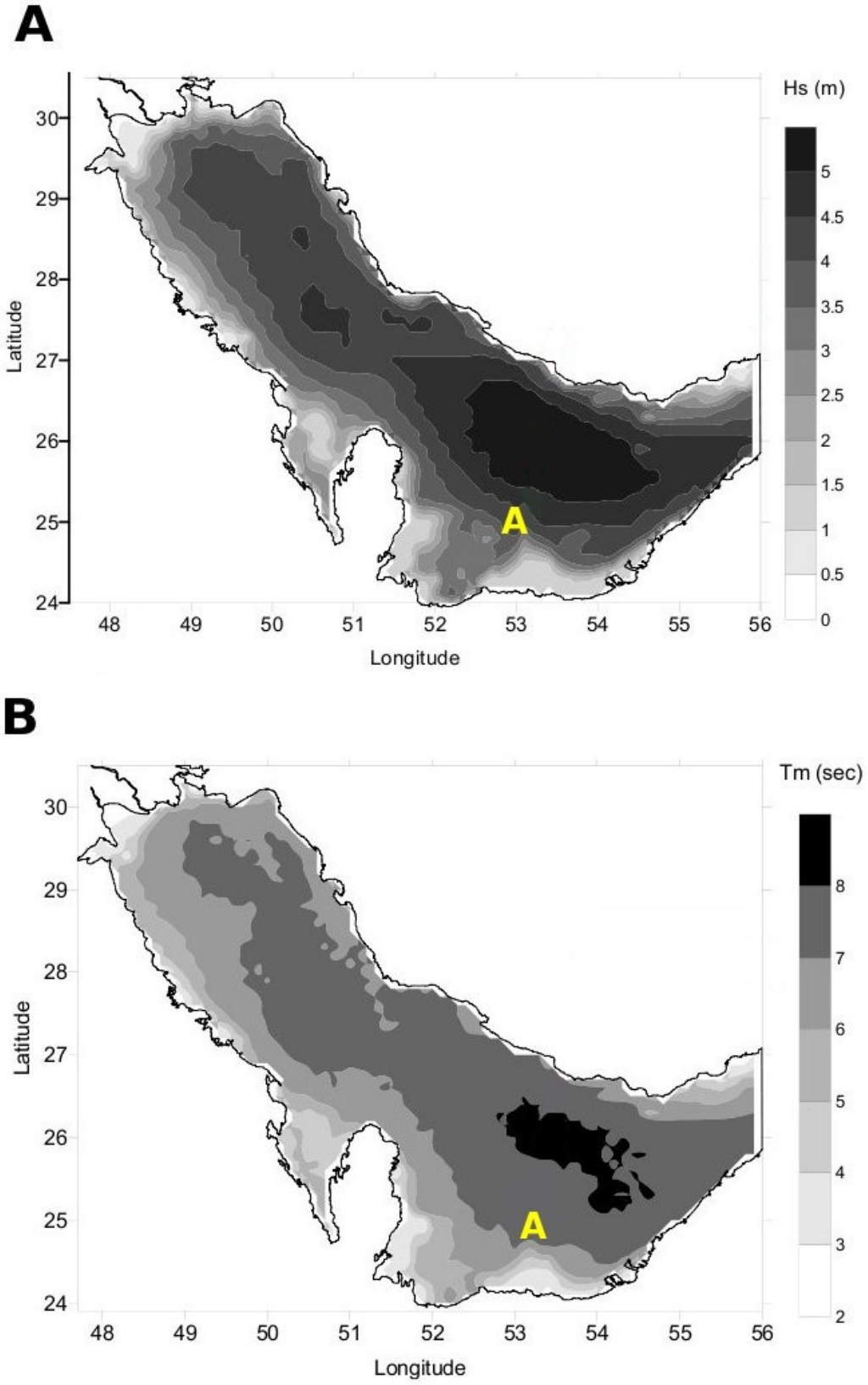

Figure 2.13. Wind and wave data for the I–RSA over a duration of 12 years (from 1st January, 1993 till 31st December, 2004) showing **(A)** Maximum Significant Wave Heights (Hs/m) and **(B)** Maximum Mean Wave Periods (Tm/sec) (Rakha et al., 2007).

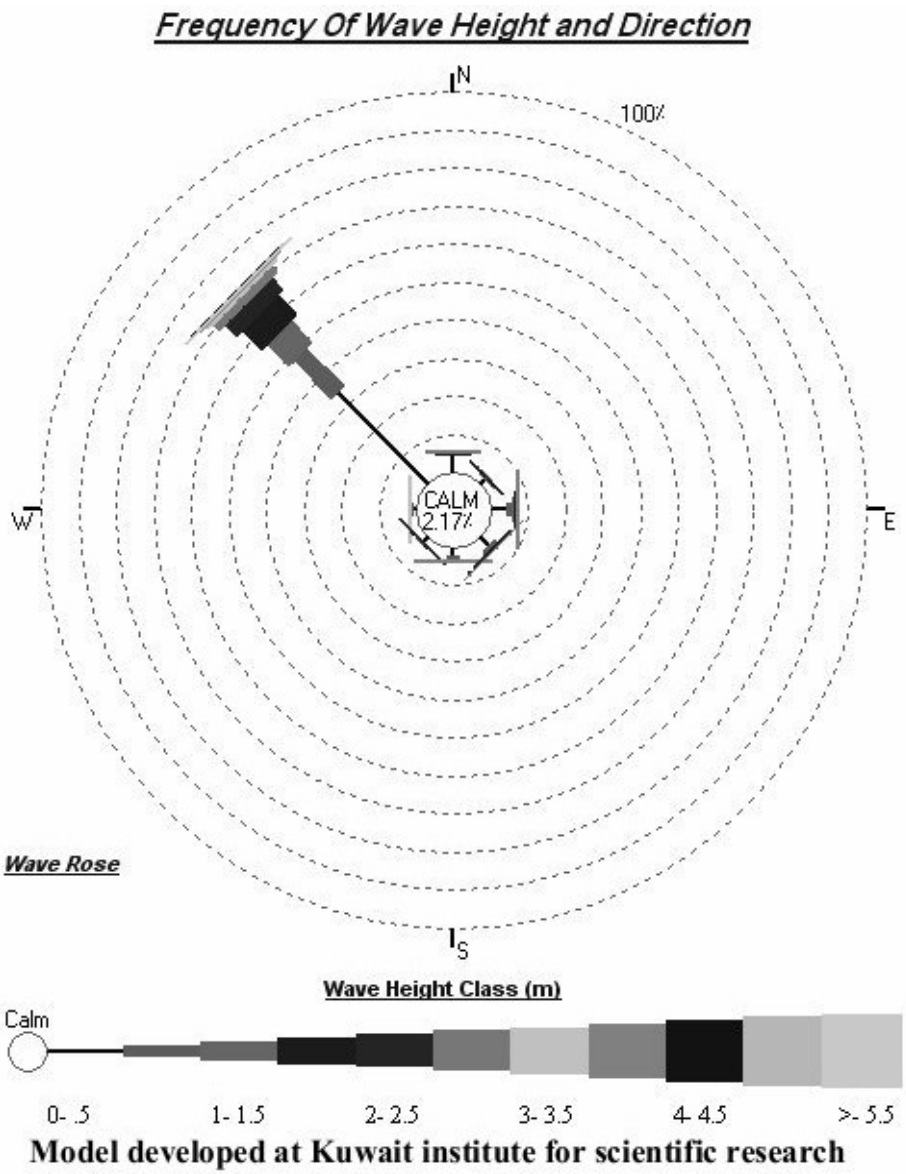

Figure 2.14. A wave rose plot generated for location A shown earlier in Figure 2.8 (Rakha et al., 2007).

2.3.5 Tidal patterns

Tides are important for stirring and mixing waters vertically and on a horizontal scale of 10 km, but they do not make an important contribution to the residual circulation of the RSA (Reynolds, 1993). The tides inside the I–RSA are complex standing waves and the dominant pattern varies from being primarily semi–diurnal to diurnal (Reynolds, 1993). They co–oscillate with those in the narrow Strait of Hormuz, which opens into the deep M–RSA (Figure 2.15).

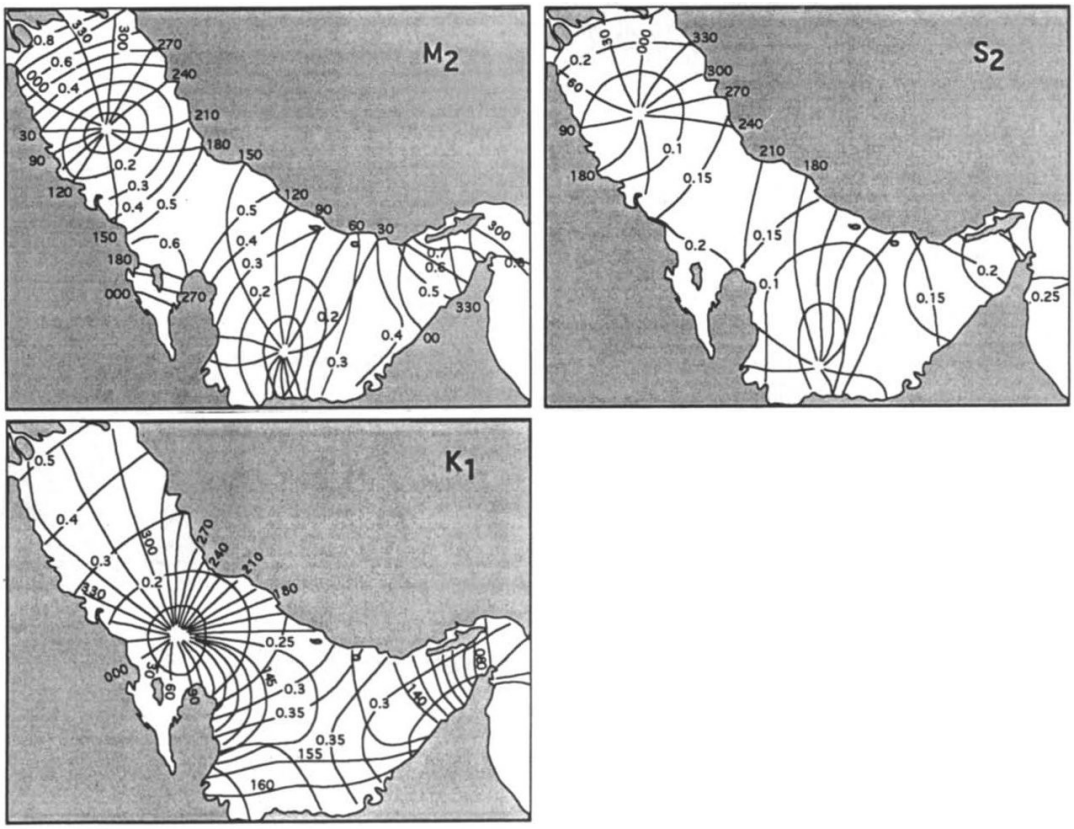

Figure 2.15. The M_2, S_2, and K_1 tidal constituents in the I–RSA (Lardner et al., 1982). Tide heights are shown in metres.

The major semi–diurnal and diurnal tidal constituents (M_2, O_1, S_2 and K_1) are prescribed as constant values (Table 2.1) along the eastern open–ocean boundary (Lardner et al., 1982). The tidal range in the I–RSA varies from about 1 m (during neap tides) to 4 m (during spring tides) in the north of the RSA (Rakha et al., 2007).

Table 2.1. Tidal amplitudes and phases prescribed at the eastern boundary (Kaempf & Sadrinasab, 2006).

Tidal Constituent	Period (h)	Amplitude (m)	Phase (°)
Principal lunar semi–diurnal (M_2)	12.42	1.10	214.98
Principal lunar diurnal (O_1)	25.82	0.63	192.20
Principal solar semi–diurnal (S_2)	12.00	0.44	248.90
Lunisolar diurnal (K_1)	23.93	0.34	289.30

There are two amphidromic points around which the tidal range is zero and tidal waves rotate (Linden et al., 1990). One is off the northern Saudi Arabian coast and the second off the UAE coast (Linden et al., 1990). Figure 2.16 summarizes these tidal processes.

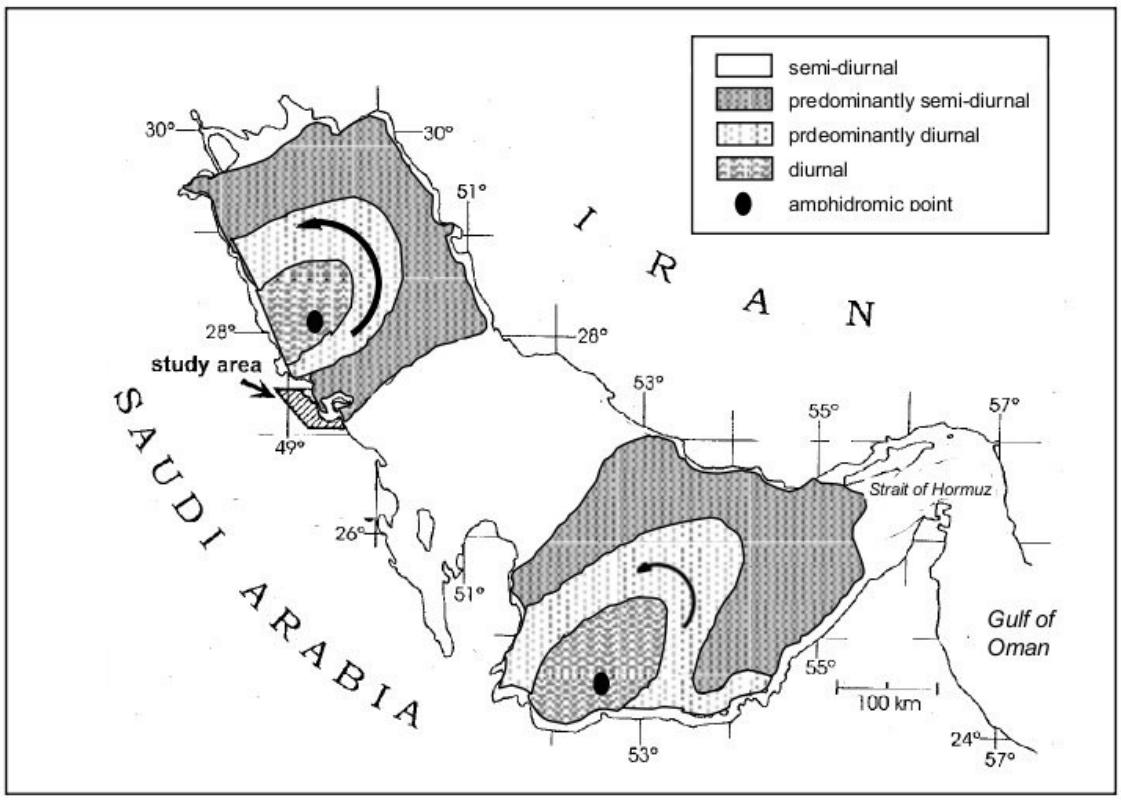

Figure 2.16. Tides in the I–RSA. Note the two amphiodromic points around which the tidal wave rotates and where tidal amplitude is zero (the general circulation of the water is anticlockwise due to the Coriolis effect) (Jones, 1986).

Tidal hydrodynamic simulations by Najafi, (1997) predict tidal flows of 0.9 m/s near the Strait of Hormuz and at the head of the I–RSA, and 0.3–0.6 m/s elsewhere in the I–RSA. Mean spring tide range is approximately 1.5 m, whilst the neap tidal range is about 0.8 m (Jones et al., 1994). Additional changes in tidal levels are caused by the influence of wind, where the strong onshore winds in shallow near–shore areas may push tidal waters up to 50 cm higher than normal (Arbeit & Barth, 2002). The tides in the M–RSA co–oscillate with those in the O–RSA (Reynolds, 1993). Tidal current averages longer than a day have negligible residual energy, and as a result, basin–scale advection from tides is not considered by oil trajectory models or general circulation models (Reynolds, 1993).

2.3.6 Salinity

The salinity in the northern I–RSA ranges from 40 to 41 psu, but can sometimes exceed 50 psu due to the high rates of evaporation (Al-Yamani et al., 2004) and the reduction in fresh water discharge from the Euphrates and Tigris rivers. This reduction

is caused primarily by the southeastern Anatolia Development project (GAP) in Turkey (Al-Yamani et al., 2007), where a total of 22 dams and 19 power plants have impounded 1.22×10^{11} m^3 of water mainly for agricultural purposes (El-Fadel et al., 2002).

High–salinity water flows out of the I–RSA and spreads at 200–350 m depth eventually exiting the Strait of Hormuz into the M–RSA (Hunter, 1986). Replacement water flows in through the Strait of Hormuz at the surface levels, passing inwards along the Iranian coast before reaching the Arabian coasts in a broadly anti–clockwise flow as shown in Figure 2.17 (Rochford, 1964).

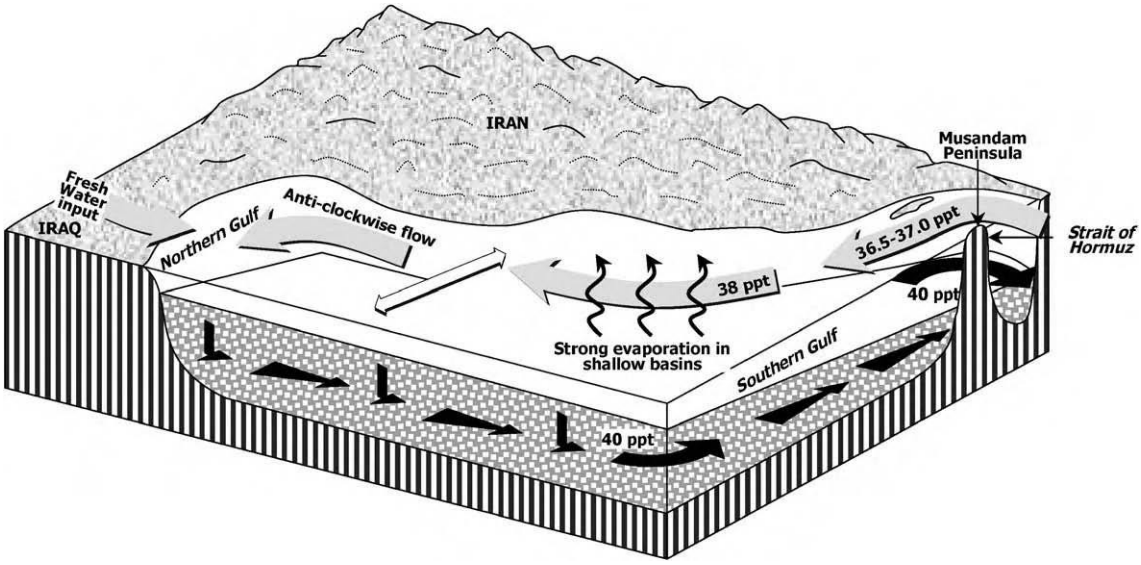

Figure 2.17. Counter–clockwise circulation patterns of the M–RSA that are driven by density currents. Salinity in the I–RSA is slightly higher than the O–RSA. Light arrows indicate incoming surface water from the M–RSA, and dark arrows indicate a denser deeper water flow (Sheppard et al., 1992).

Maps of surface salinity (Figure 2.18) show that salinity less than 37 psu spreads westward into the I–RSA from January–February into March–April. In May–June most contours spread 20–40 km further northwestward into the I–RSA (Swift & Bower, 2003). Low–salt water remains within the Iranian half of the I–RSA despite a wide–spread, well–developed thermocline at this time. By July–August, however, water with salinity less than 38.0 psu retracts almost 100 km southeastward along the coast and covers an area smaller than it does in January–February (Swift & Bower, 2003). Surface salinity values greater than 40 psu have disappeared, and the distribution of values is more uniform than for other months. The apparent uniformity in surface salinity in July–August (Figure 2.18) could result from mixing water from high and low salinity sources (Swift & Bower, 2003).

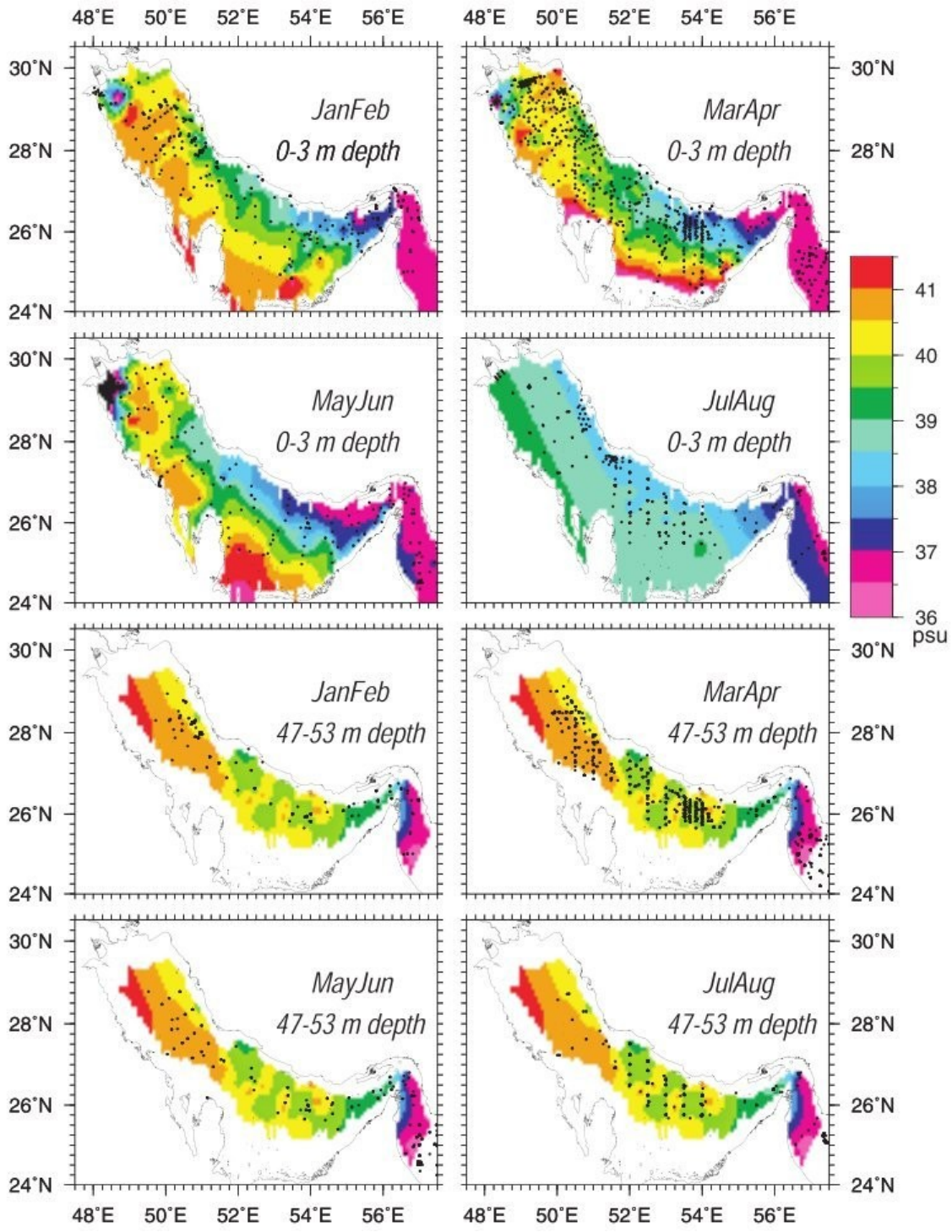

Figure 2.18. Surface salinity maps (top four panels) show that modified Indian Ocean Surface Water (IOSW) progressively moves farther up the I–RSA from January to June. This data suggest that surface water with salinity less than 38 psu then retreats ~100 km eastward toward the Strait of Hormuz in July. Since the seasonal thermocline develops in May–June, this retreat is unrelated to summer warming. Salinity distribution of I–RSA Deep Water at 50 m depth (bottom four panels) shows comparatively little seasonal change (Swift & Bower, 2003).

The uniformity could also result from the lower offshore flow of high–salinity water along the southern coast as peak winds decrease and the number of severe northwest Shamal wind events decreases in July and from the slower spreading of Indian Ocean Surface Water (IOSW) through the Strait of Hormuz. The maps of salinity at 50 m depth (Figure 2.18), indicate that the salinity of most of the water at this depth does not change significantly between May–June and July–August. Introduction of a new summer water mass from off the coasts flanking the Strait of Hormuz is unlikely because the higher temperatures are typically accompanied by normal or lower salinity, whereas high salinities, as well as high temperatures, are common in bays and on the shallow banks of the I–RSA in the summer (Sugden, 1963).

2.3.7 Bathymetry

The bathymetry of the RSA varies considerably over its three different parts as shown in Figure 2.19. The I–RSA is a sedimentary basin, shaped to a great extent by a Tertiary fold system which causes its deepest depression to run along its northern side (Sheppard, 1993). The I–RSA is asymmetric, its northwest southeast axis separates a stable and very gradually–sloping Arabian shoreline on one side from a geologically unstable and steeper Asian or Iranian shoreline (Purser & Seibold, 1973). This has resulted in the deepest region being closest to the Iranian coast. No part of the I–RSA has a continental shelf edge and there are no large or abrupt changes in bathymetry, except at the entrance to the M–RSA in the east (Sheppard, 1993).

Today the I–RSA is a basin which is relatively shallow sea with a depth ranging between 10–100 m which means almost all parts of it lie within the photic zone (Jones, 1985). However, off the eastern shore of Iran depths of greater than 100 m are found. The average depth is approximately 36 m, and the region between Kuwait and Qatar is shallower still (Reynolds, 1993). This shallow bathymetry affects the wave growth and propagation due to bottom friction (Hubert et al., 1983). There is no sill in the Strait of Hormuz; the trough simply deepens to more than 100 m through the Strait and drops quickly to more than 2 km within 200 km outside the Strait (Reynolds, 1993).

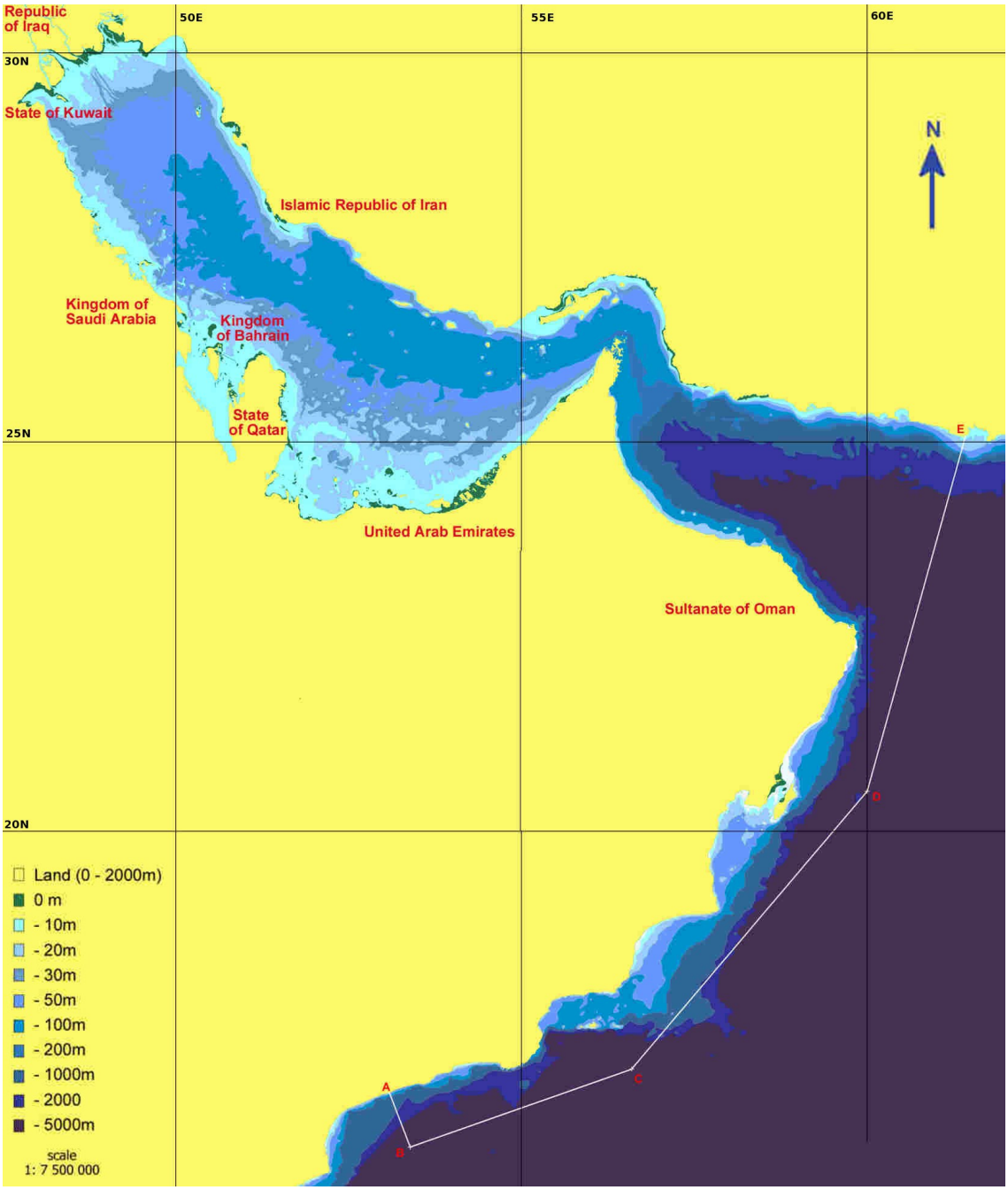

Figure 2.19. The bathymetry map of the RSA (constructed with modification from admiralty charts) (Courtesy of ROPME).

2.4 Socio–economic characteristics

The region has witnessed rapid socio–economic transformation since the 1970's with an unprecedented growth of urbanization, mass immigration and industrialization along the coast. The discovery of oil in the I–RSA during the 1930's and 1940's was principally responsible for its immense economic wealth and its strategic importance,

resulting in the region being viewed as an important military, economic and political region in the world, so much so that three major battles have erupted as a result during the past three decades. This anthropogenic growth has tended to outstrip the carrying capacity of the area, leading to tremendous environmental impact on its waters.

2.4.1 Shipping activity

The RSA has become one of the busiest waterways in the world, with an estimated annual passage of 20,000 to 30,000 tanker passages through the Strait of Hormuz and is significantly increasing (Linden et al., 1990). To the extent that the Fujairah port (Figure 2.20) alone in the UAE has been ranked the third bunkering port in the world after Rotterdam and Singapore, supplying on average of more than 1.8×10^{12} tons of fuel oil per month, having (in 2008 alone) discharged and loaded a total of 24 million tons of oil (Abed & Hellyer, 2001; Government of Fujairah, 2008).

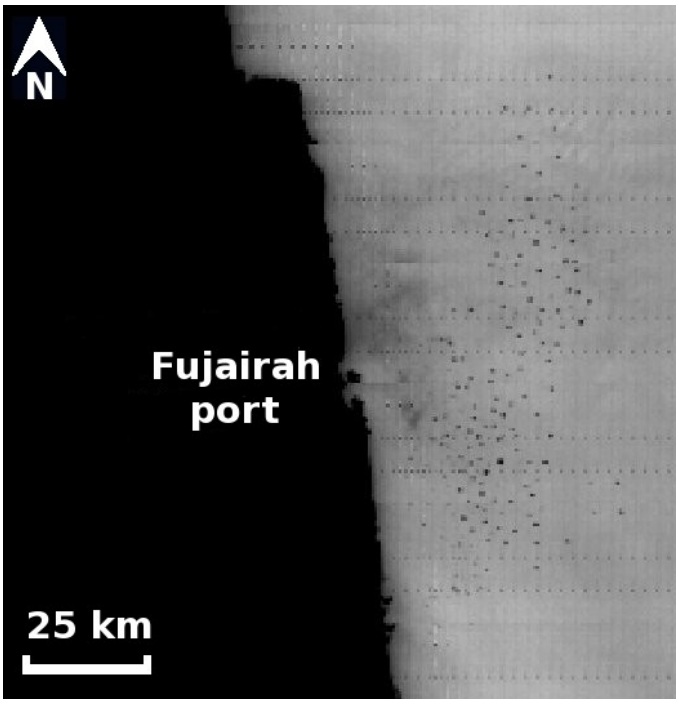

Figure 2.20. Hundreds of scattered tankers (represented by black dots) waiting opposite the Fujairah port, UAE observed in MODIS Terra on 11th October, 2010 at 07:14 UTC. The image was produced using a transformation of the 250 m/pixel NIR band (λ_2=859) and applied histogram stretching to enhance visibility. The centre position of the image is located at N25° 21' 19" E56° 21' 47".

Approximately 88% of all the petroleum exported from the I–RSA transits through the Strait of Hormuz (Figure 2.21), bound to Asia, Western Europe and the United States (Rodrigue, 2004).

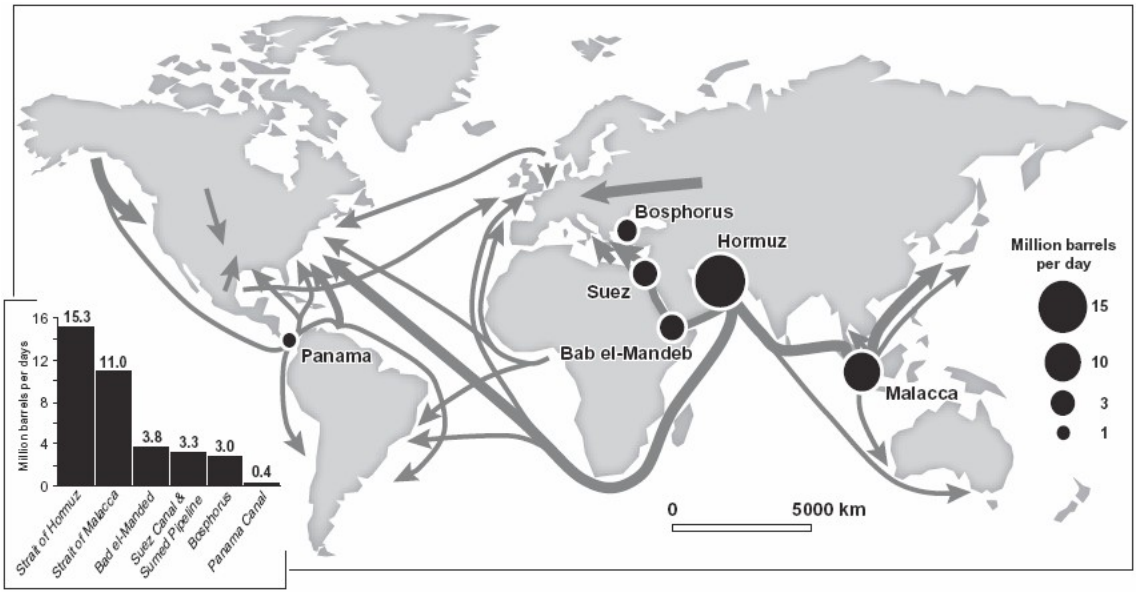

Figure 2.21. Oil flows, major choke–points and oil transited at major strategic locations, 2003 (Rodrigue, 2004).

2.4.2 Offshore oilfields

According to BP (2009) up until the year 2008, 60% of global oil reserves and 41% of gas reserves were located within the RSA member states, with the largest number of offshore oilfields located in Saudi Arabia, Iran and the UAE (ROPME, 2003). Figure 2.22 outlines the location of major land–based oil wells including offshore oilfields.

2.5 Pollution

Because the RSA is one of the busiest and most important oil transportation routes in the world, Golob and Bruss (1984) have estimated that oil pollution in the I–RSA is 47 times the average estimated amount for a marine environment of a similar surface area. Its ecosystem is facing a variety of stresses due to a multitude of marine pollution sources such as accidental and deliberate dumping from ships; land–based sources; exploration and exploitation of the seabed; and from other human activities, such as dredging and land reclamation (Facey, 2008).

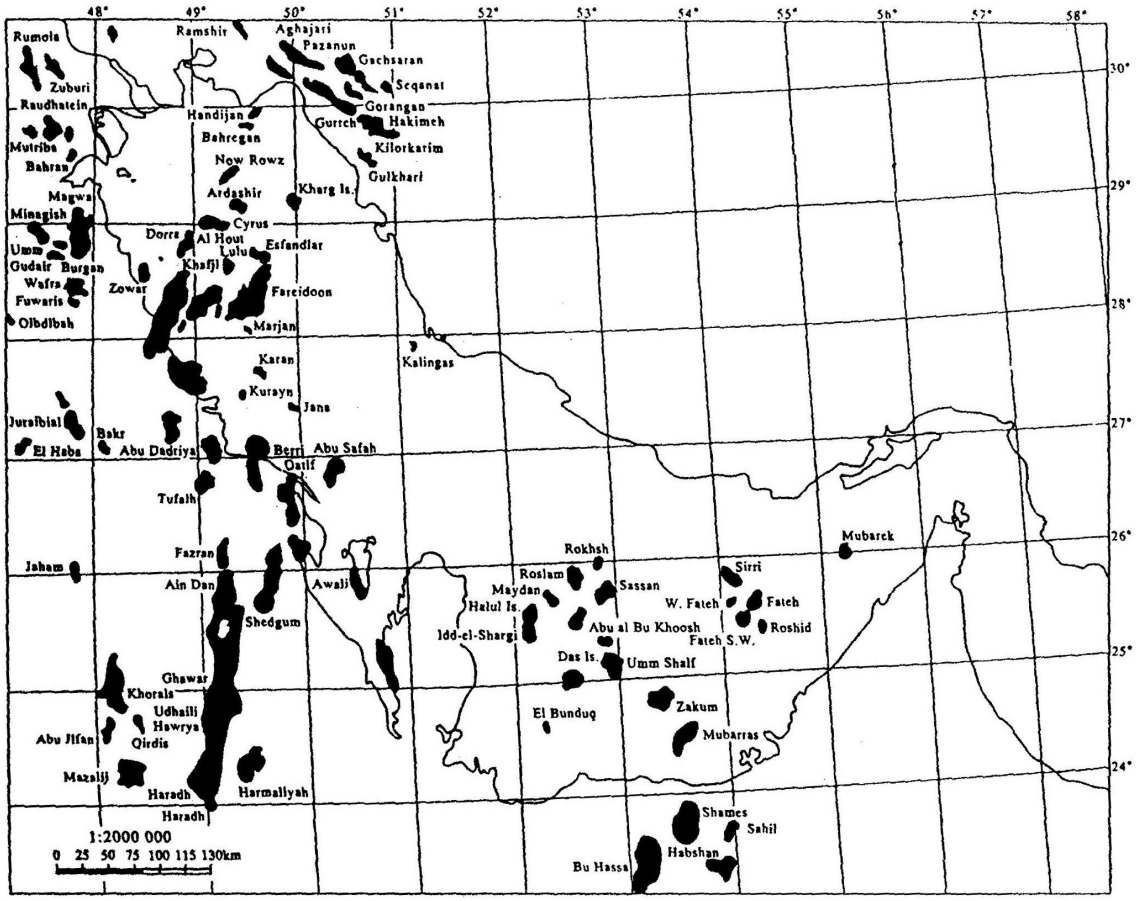

Figure 2.22. The location map of the major land–based and offshore oilfields in the I–RSA (Beydoun, 1991).

2.5.1 Ballast water

The intentional or accidental release of ballast water carried in ships has also been recognised as one of the main factors for the trans–location of non–indigenous (invasive) marine species around the world (Figure 2.23). According to ROPME (2003), invasive marine species constitute a new form of threat to the marine environment, in which such species can destroy rare native species by preying on them, competing with them for shelter, food or both, introducing harmful germs and parasites, and finally changing the normal function of the affected marine ecosystem.

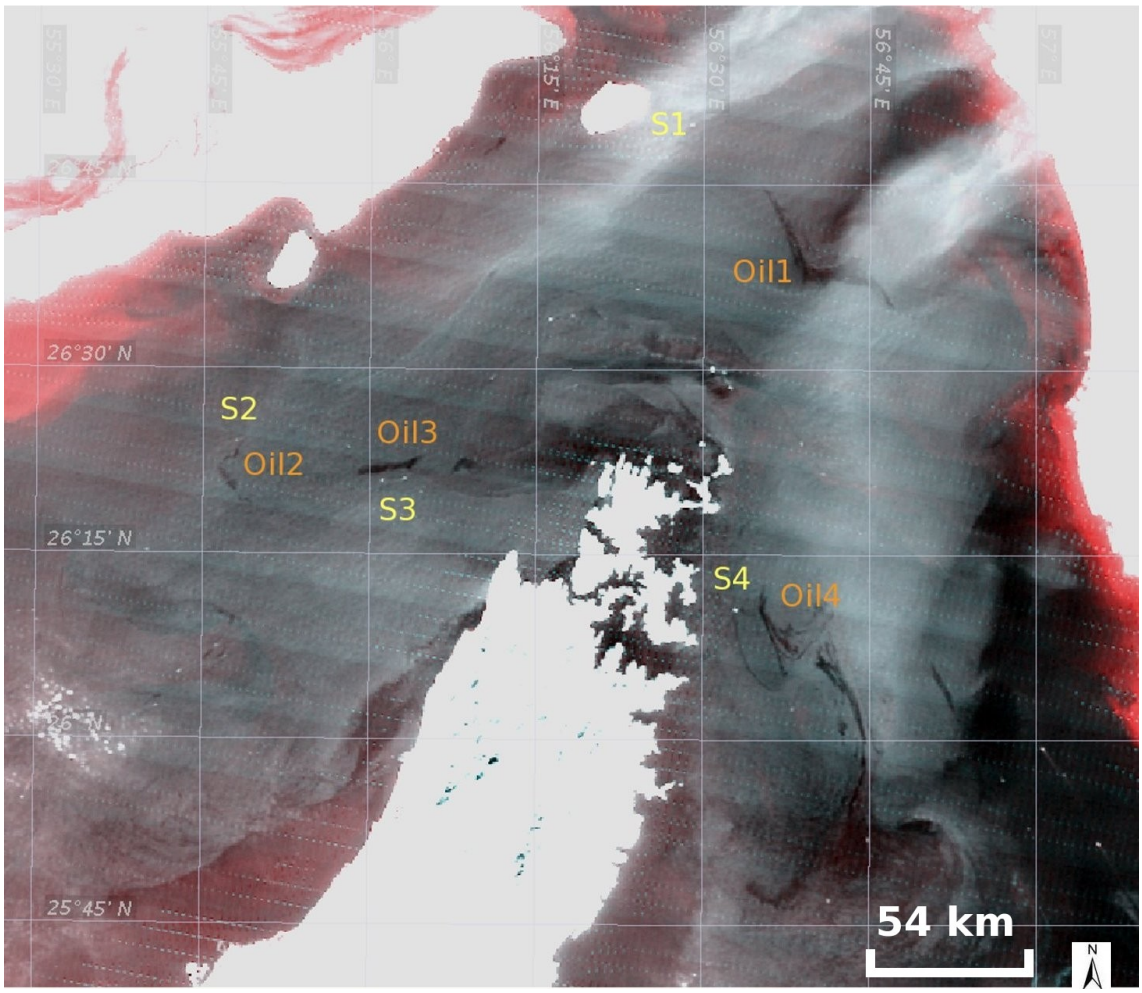

Figure 2.23. Scattered elongated dark tracks of ballast–polluted sea water (denoted as Oil) close to the tankers that may have caused them (denoted as S and appear as bright white points). The data is visible in MODIS Terra image on 15th February, 2010 at 07:02 UTC. The image is a 250 m/pixel resolution false RGB colour image composite corresponding to bands λ_2=859, λ_1=645 and λ_1=645 nm respectively, over the Strait of Hormuz area (Courtesy of ROPME).

2.5.2 Thermal pollution

Thermal pollution is also a major problem due to effluents of high temperature (up to 9 ºC higher than the ambient seawater temperature) because elevated temperatures affect the water density, viscosity and the solubility of gases (dissolved oxygen in particular). Such effects cause thermal stress that might result in eco–toxicological and respiration effects often fatal for the organisms and may affect population and ecosystem dynamics (Khordagui, 2002; Ibrahim, 2004).

2.5.3 Altering water salinity levels

A 3% salinity increase on the average climatology is expected from the large–scale desalination plants and power stations located along the coastline of the RSA (ROPME, 2003). The largest number of desalination plants can be found in the I–RSA with a total seawater desalination capacity of approximately 11 million m^3/day (Figure 2.24) which means a little less than half (45%) of the worldwide daily production (Lattemann & Höpner, 2008).

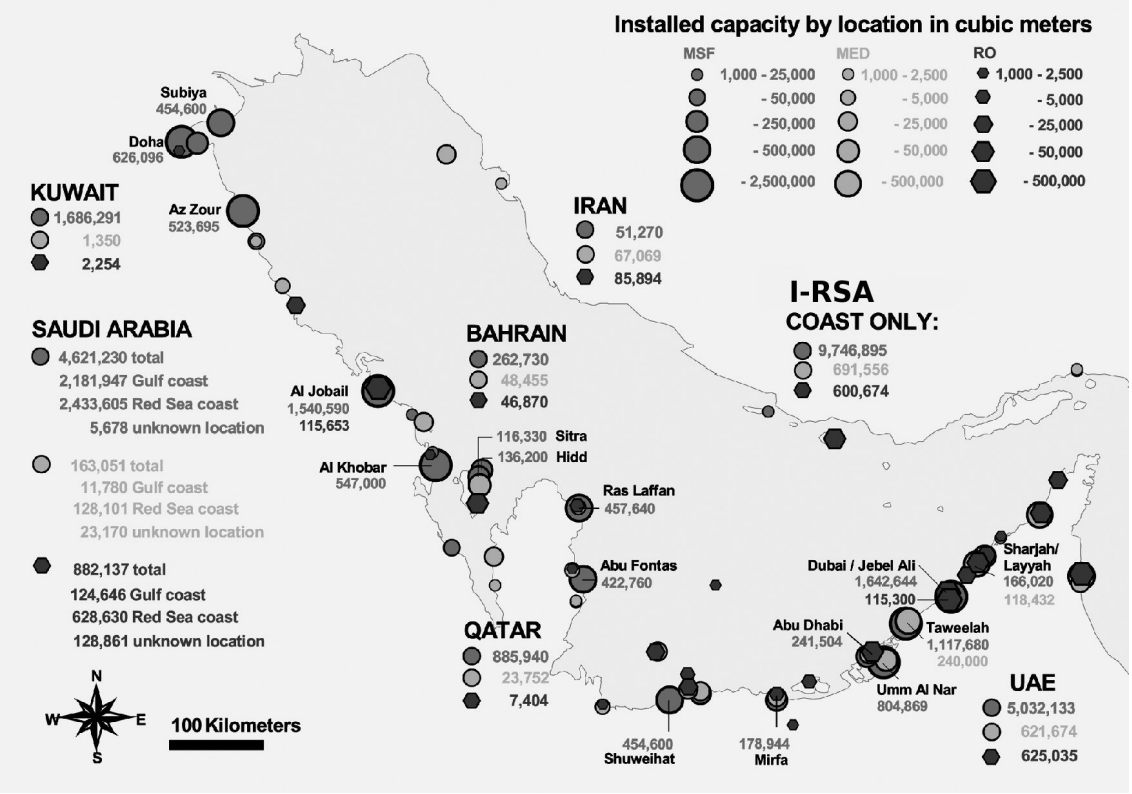

Figure 2.24. Seawater desalination capacity based on IDA (2006) of multi–stage flash (MSF), multi–effect distillation (MED) and the reverse osmosis (RO) plants in the I–RSA. Included all plants that are presumed online or in construction, with capacities greater than 1000 m^3/day. (Lattemann & Höpner, 2008).

Although as a whole, the effect of the discharged water on the I–RSA is probably minor, the long–term effects in the near–shore shallow areas may be considerable (Ali & Riley, 1986).

2.5.4 Air pollution

Air pollution is another major contributor to the overall pollution into the RSA originating from industrialized centres including oil refineries and wells (Figure 2.25);

petrochemical and fertilizer plants; asphalt plants and motor traffic (Baker & Dicks, 1982).

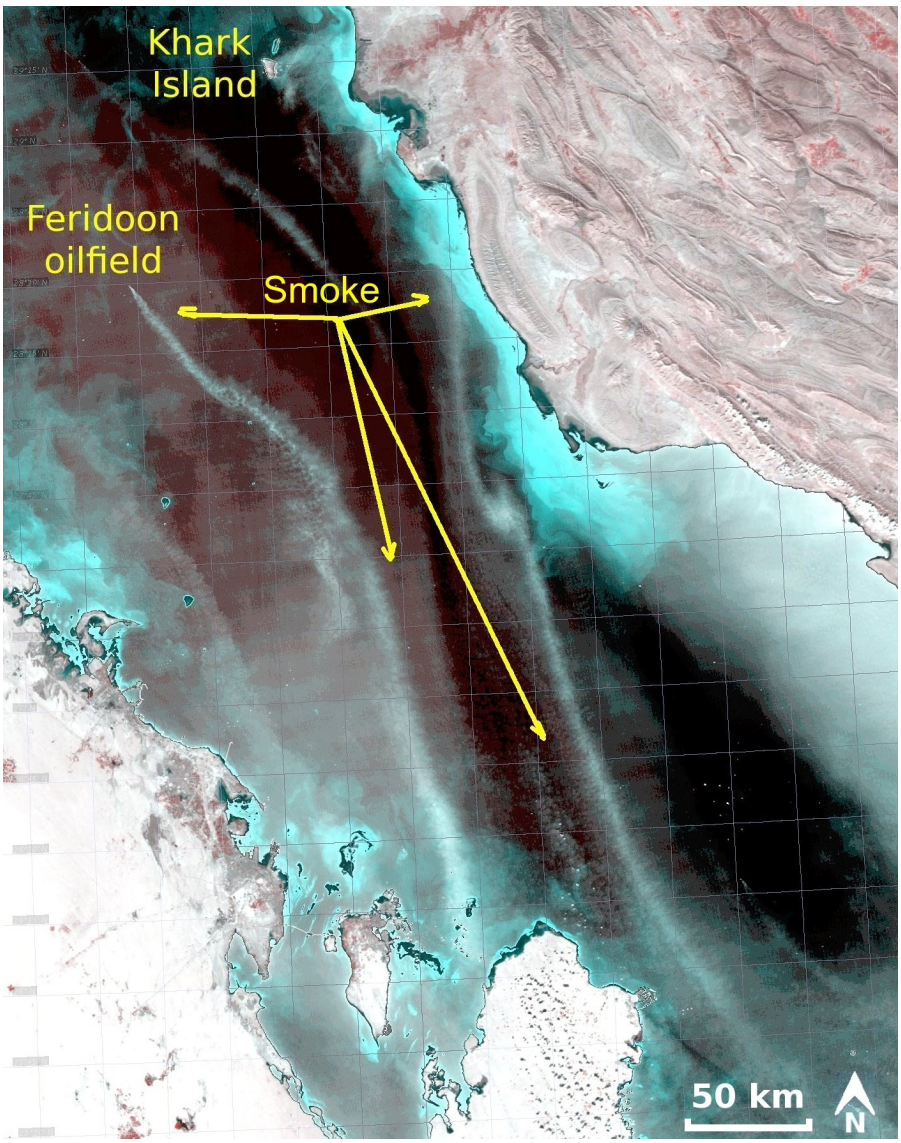

Figure 2.25. Long plumes of smoke from oilfields in Khark Island and Feridoon in Iran reaching Bahrain and Qatar across the I–RSA visible in MODIS Aqua on 15th October, 2010 at 10:02 UTC. The image is a 250 m/pixel resolution false RGB colour image corresponding to bands λ_2=859, λ_1=645 and λ_1=645 nm respectively (Courtesy of ROPME).

2.5.5 Dredging

Activities such as dredging, coastal reclamation, and infilling can greatly influence the total suspended matter in the marine habitat. Besides the increased turbidity and the associated drop of photosynthesis and primary production, the increased suspended matter may have other significant ecological impacts including loss of habitats, damage

to spawning grounds of fish species and seagrass beds, and disturbance of the benthos community that usually represents a major food source for several fish species (Elshorbagy, 2005).

Partially treated or untreated sewage discharged from urban and rural areas into the coastal and marine environment of the RSA is another source of pollution (ROPME, 2003).

2.5.6 War–related pollution

War–related pollution outcomes had a significant impact on the environment of the RSA both directly and indirectly. For example, following the 1991conflict, major concern was raised worldwide when around 500 million barrels of oil (~ 66 billion kg) were released or ignited (Readman et al., 1996). According to Clark Jr & Symons (1993) 740 wells were burning for 250 days sending enormous soot clouds into the air and approximately 6–11 million barrels of crude oil were directly released into the I–RSA (Price & Sheppard, 1991). Such amounts clearly made it the largest oil spill in history exceeding the largest previous 1979 Ixtoc spill in the Gulf of Mexico in which 500,000 tons were released, and the Nowruz spill 1983 during the Iran–Iraq war which saw the release of around 250,000 tons (Arbeit & Barth, 2002). A comparison to such oil spills as Exxon Valdez which lost 33,000 tons and oiled more than 1700 km of shoreline indicates that the extent of oiled shoreline from the Gulf War could have been far greater (Figure 2.26) (Owens & Teal, 1990). Ground operation activities that took place in the conflict, including preparatory exercises, were estimated to have consumed about 7 billion gallons of fuel and air operations used more than 600 million gallons of jet fuel during the crisis (Sadiq & McCain, 1993). Sengupta et al. (1993) concluded that in spite of the huge volume of oil released during the war, very little found its way out of the I–RSA into the O–RSA. It is reasonable to conclude therefore that the epuration mechanisms of the I–RSA are rapid.

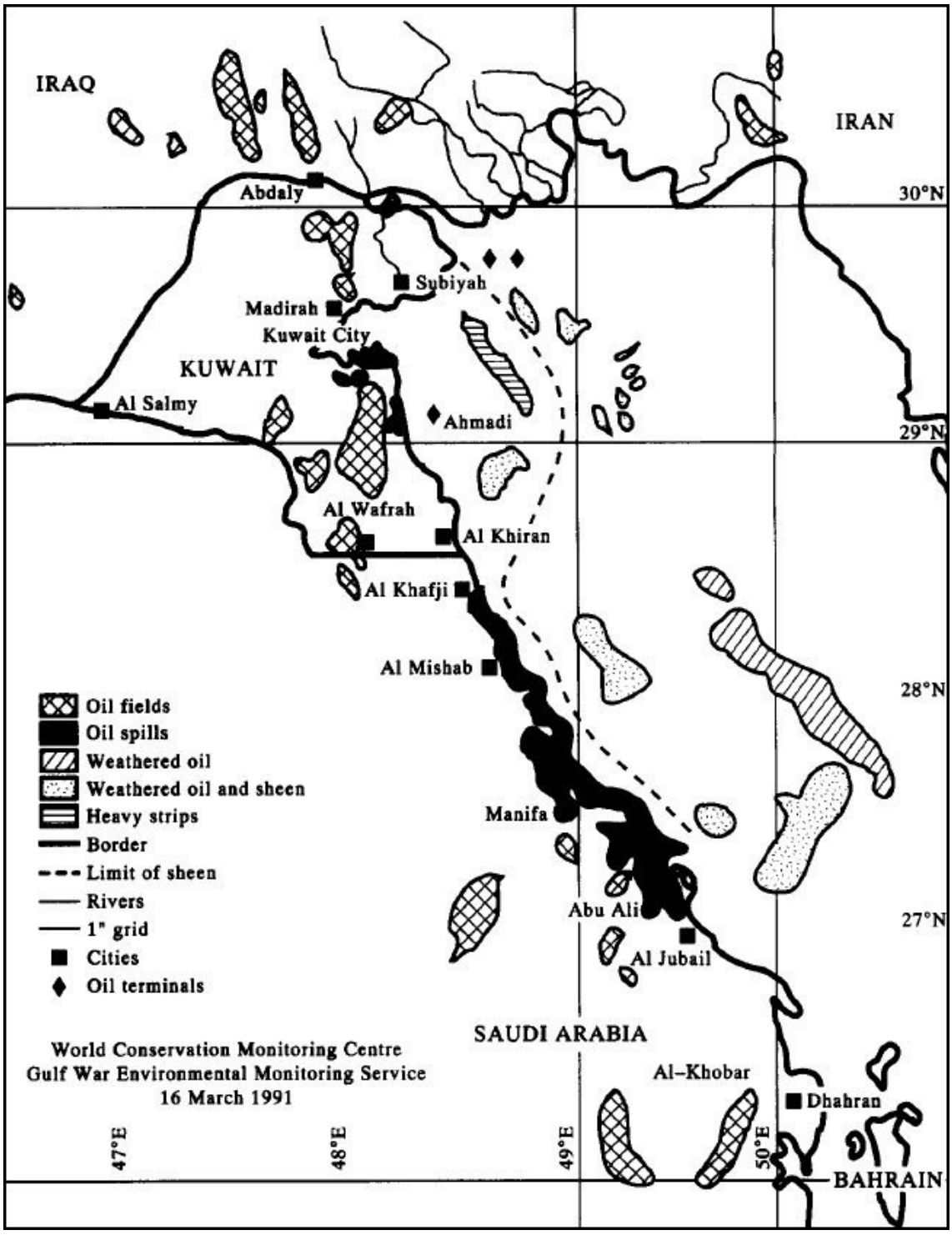

Figure 2.26. The extent of oil pollution on the shorelines of the I–RSA that resulted from 1991 Gulf War oil spills on 12th March, 1991 (WCMC, 1991).

Chapter 3: The remote sensing of oil spills

3.1 The physical characteristics of oil

The chemical composition of oils is such that they are usually characterized by a set of physical properties that distinguishes different types (Payne, 1994). The specific gravity or relative density of oil is the density relative to pure (fresh) water – it determines whether oil will float or sink. Most oils have a specific gravity below 1 and are lighter than sea water (ITOPF, 1986).

The American Petroleum Institute (°API) gravity scale is commonly used to describe the specific gravity of crude oils and petroleum products, and is calculated as follows:

$$^{\circ} API = \frac{141.5}{s.g.60/60F} - 131.5 \tag{3.1}$$

where s.g.60/60F is the specific gravity of the oil at 60 °F (15.6 °C) relative to the water at the same temperature (ITOPF, 1986). For example, a high °API (low specific gravity) tends to be of low viscosity and therefore contains a high proportion of volatile components. Oil dynamic viscosity (μ) is a temperature–dependent property defined as its resistance to flow or the ratio of shear stress to shear rate (Koleske, 1995). Due to this, petroleum fluids are generally complex fluids, that normally require simulation models to predict their dynamics. In general terms, oils become more viscous (i.e. flow less readily) as their temperature falls, some more than others depending on their composition (ITOPF, 1986). Viscosity is usually measured in centipoises, where 1cP = 0.001 kg/ms being the viscosity of water at 20 °C. The kinematic viscosity (υ) is measured in centistoke (cSt) where 1 cSt = 1 mm^2/s which is the kinematic viscosity of water at 20 °C and is defined as:

$$\upsilon = \frac{\mu}{\rho} \tag{3.2}$$

where ρ is density. There are several viscosity–temperature equations, some of which are purely empirical, whereas others are derived from theoretical models, but the most accurate is the one shown in Equation 3.3 (Zhang, 2000):

$$\mu = a\, e^{\frac{b}{T_A - c}} \tag{3.3}$$

where a, b, c are constants and T_A is the absolute temperature (K). Figures 3.1 and 3.2 show typical changes in kinematic viscosity in relation to changes in time and temperature respectively.

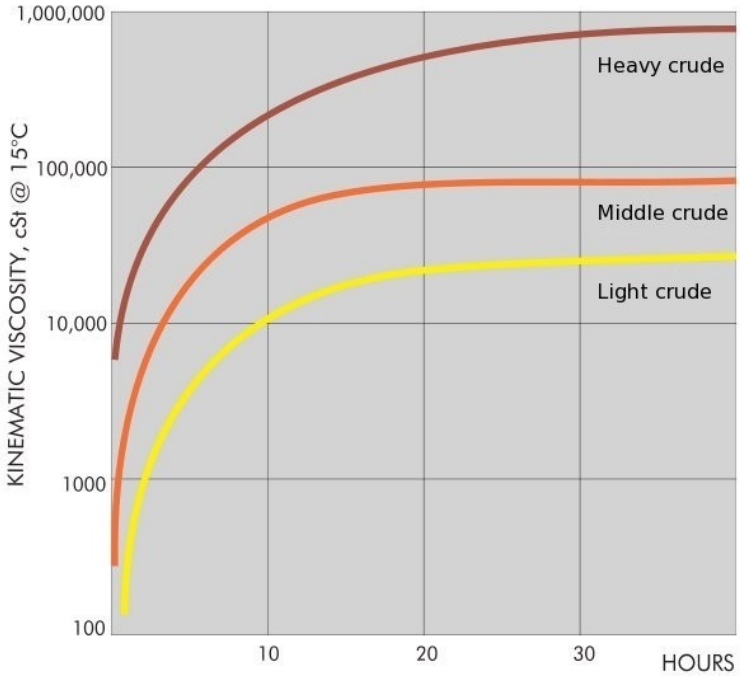

Figure 3.1. Typical rates of viscosity increase in moderate to rough seas. The viscosity of the very light group oils never exceeds 100 cSt and it is therefore not shown (ITOPF, 1986).

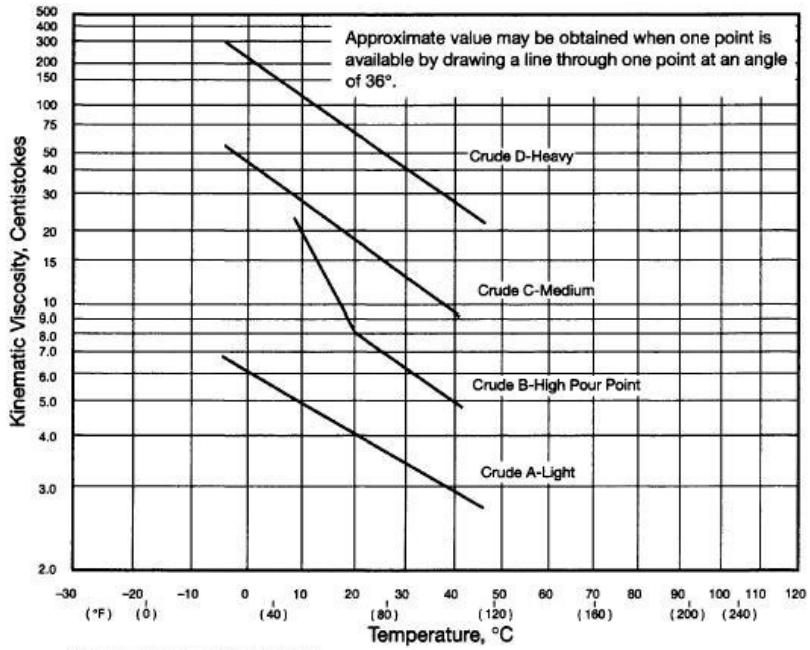

Figure 3.2. Viscosity–temperature graph for crude oils (ASTM D 341, 2007).

Generally less viscous oils such as lighter refined "fuel oils" will spread at a higher rate than heavy "crude oils", but in high temperature waters oil viscosity will decrease, hence becoming more susceptible to spread than in cold waters (Tsukihara, 1995). The "pour point" of an oil is defined as the lowest temperature at which an oil will flow. Therefore, when hydrocarbons are spilled at sea, they will remain liquid at temperatures above their pour point. The pour point is a function of the wax and asphaltene content of the oil (ITOPF, 1986). In addition to the chemical classification, crude oils are often divided into very light, light, medium and heavy on the basis of their °API gravity measurements (Killops & Killops, 1993). Table 3.1 shows the main characteristics of each oil group.

Table 3.1. The characteristics of different categories of crude oil (Michel, 1992).

Very light **(Jet Fuels, Gasoline)**	**Light** **(Diesel, No. 2 Fuel Oil, Light Crudes)**	**Medium** **(Most Crude Oils)**	**Heavy** **(Heavy Crude Oils, No. 6 Fuel Oil, Bunker C)**
Highly volatile (should all evaporate within 1–2 days). High concentrations of toxic (soluble) compounds. Result: Localized, severe impacts to water column and intertidal areas. No dispersion necessary. No clean–up necessary.	Moderately volatile; will leave residue (up to one–third of spill amount) after a few days. Moderate concentrations of toxic (soluble) compounds, especially distilled products. Has potential for sub–tidal impacts (dissolution, mixing, absorption onto suspended sediments). No dispersion necessary. Clean–up can be very effective.	About one–third will evaporate within 24 hours. Maximum water–soluble fraction 10–100 ppm. Oil contamination of intertidal areas can be severe and long–term. Oil impacts to waterfowl and fur–bearing mammals can be severe. Chemical dispersion is an option within 1–2 days. Clean–up most effective if conducted quickly.	Heavy oils with little or no evaporation or dissolution. Water–soluble fraction is less than 10 ppm. Heavy contamination of intertidal areas likely. Severe impacts to waterfowl and fur–bearing mammals (coating and ingestion). Long–term contamination of sediments possible. Weathers very slowly. Chemical dispersion seldom effective. Shoreline clean–up difficult under all conditions.

3.2 Fate of oil spills on water

3.2.1 Dynamics of oil spills

A number of mathematical models have been suggested since the early sixties to explain the spreading and transport mechanism of oil slicks in water. According to Cekirge et al. (1995) these models may be classified – with respect to their stages of evolution– as first, second, and third generation models. First–generation models are

essentially transport models with limited fate analysis. Although they are still used, their reliability is questionable. Second–generation oil spill models consist of limited two–dimensional hydrodynamic and fate analysis. Third generation models, or the comprehensive oil spill models, consists of a set of algorithms to simulate the fate and transport of oil in three dimensions, including the processes of advection, diffusion, surface spreading, vertical mechanical dispersion, evaporation, emulsification, and stranding. The fundamental principle upon which the pollutant fate and transport models are based on the law of conservation of mass, where the rate of change of mass concentration can be mathematically represented by the advection–diffusion equation proposed by Sverdrup et al. (1942) shown in Equation (3.4):

$$\frac{\partial \rho}{\partial t} = -U \nabla \rho + \nabla (K_h \nabla \rho) + Ø \tag{3.4}$$

where ρ is the density of the pollutant, U is the net advective velocity of the surrounding medium, K_h is the combined effects of dispersion and physical spreading (turbulent or diffusion tensor), and Ø represents the amount of oil which is added to the slick from a venting source such as a discharge from a ship or a drilling platform, as well as the amount taken away by weathering and grounding processes. The term ($-U\nabla\rho$) represents the advection of the slick from the wind and tidal currents, whereas the term $\nabla(Kh\nabla\rho)$ indicates how much of the slick spreads and disperses over time. Therefore, Equation 3.4 can be re–written in the format:

$$oil\ transport\ at\ water \equiv advection + (dispersion / spreading) + (source / sink) \tag{3.5}$$

Spreading in the open ocean was investigated by Fannelop & Waldman (1972) taking into consideration the effects of wind, waves, and currents. Whereas, Fay (1969); Fay and Hoult (1971); and Buckmaster (1973) have proposed a three stage model to explain the various forces that influence this behaviour in calm sea water conditions:

- The spill's gravitational forces – caused by the sizeable thickness of the slick at its early phase, will control the spreading of the oil across the surface, during which inertia will act as the main retarding force;
- in the second phase of this evolution, the spill's inertial force due to its weight will become negligible and instead it is dominated by a decelerating force attributed to the viscous drag on the bottom of the slick; and
- in its third and final phase, when the slick has become sufficiently thin, the inter–facial (surface tension) forces will dominate to further its spread. Spreading will continue, at least as long as the surface and inter–facial tensions

are unchanged by the change in the oil's physical, chemical and biological properties, collectively called weathering (see section 3.2.2).

If L is the diameter of the slick as it changes in time t; Δ is the difference between the water and oil densities ($\rho_w - \rho_o$); g is the gravitational acceleration; V is volume of the slick; ν is the kinematic viscosity; and σ is the spreading coefficient. Then it is possible to summarise the three stages postulated for the spreading mechanism, with an estimate for the duration for each stage as it is shown in Figure 3.3.

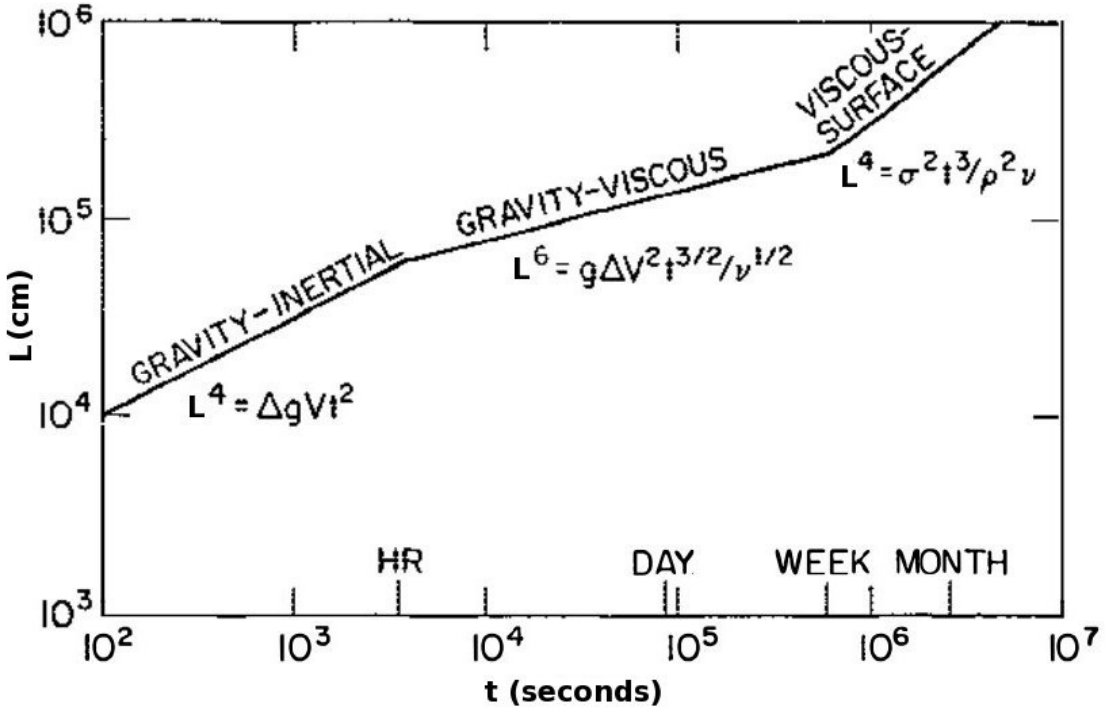

Figure 3.3. The three main stages of oil spill spreading in calm waters (Hoult, 1972).

According to Hoult (1972), the spread of an oil slick may be approximately caused by convection due to winds and currents; and the tendency of the oil to spread in calm water. The surface water drift due to wind may be estimated from the wind velocity (U_{wind}) at some height (usually 10 m) above the water surface using the shear stress:

$$\frac{1}{2}\rho_{air} C_{air} U_{wind}^2 \approx \frac{1}{2}\rho_{water} C_{water} U_{water}^2 \tag{3.6}$$

where ρ is the density; C is the drag coefficient and U is the velocity. Hoult (1972), as a rough approximation, assumed that the turbulent shear–stress law at the water interface is the same for both the air and the water, to give ($C_{air} \approx C_{water}$) leading to:

$$U_{water} = [\frac{\rho_{air}}{\rho_{water}}]^{\frac{1}{2}} U_{wind} \approx 0.03 U_{wind} \quad (3.7)$$

This result is known to be consistent with both laboratory studies (Hidy & Plate, 1966; O'Brien, 1971) over a range of 10^4 of Reynolds numbers based on water depth, wind speed, kinematic viscosity of the water, and field observations (Hughes, 1956; Smith, 1968). Spreading and advection of oil are also strongly influenced by the release conditions. Therefore, in deep underwater release conditions, such as the case of well–head blowout , the oil may be accompanied by gas, which forms gas hydrates in contact with the water (Hackett et al., 2006), similar to the cause of the Deepwater Horizon oil spill in the Gulf of Mexico. Some oil spill model systems include special initialization modules for deep sources (Johansen, 1998) .

Reliable prediction of an oil slick movement clearly depends upon the availability of accurate wind and current data and sometimes acquiring such data is difficult, particularly in near–shore regions where the currents are more difficult to predict and often poorly understood due to complex dynamics (ITOPF, 1986).

3.2.2 Weathering of oil

Weathering is a complex process where oil will typically undergo different degrees and multiple stages of evolution (Boyd et al., 2001). The degree of weathering will depend on a number of factors such as oil viscosity, wave condition and water temperature (Tsukihara, 1995). Weathering comprises the following processes:

1. evaporation – the volatile components of oil evaporate. Evaporation from an oil spill is influenced by the composition of the oil; air and sea temperatures; spill area; wind speed; solar radiation; and slick thickness (Al-Rabeh et al., 1989). Evaporation is lower for heavy fuels, whereas in products like petrol, kerosene and other light fuel fractions at 20 °C, approximately 50% will evaporate in the first 7 to 8 minutes and disappear almost completely after 24 hours (Cedre, 2006);
2. dissolution – some components of the oil will dissolve in the surrounding water. Less than 0.1% (very heavy oil) to 2% (gasoline) of the spilled oil volume dissolves into the water column, and it is often more toxic to the environment (NOAA, 2002);
3. natural dispersion – is the uptake of oil droplets of diminishing size into the water until they are no longer part of the oil. The percentage of natural

dispersion is essentially related to the nature of the oil and the sea state (Cedre, 2006);

4. emulsification – is the uptake of water into the oil (often reaches 50–80%) forming an emulsion varying in colour from dark brown to orange, and hence the common description "mousse" (NOAA, 2002). This phenomenon increases the apparent volume of the pollutant, reduces the spreading rate (by forming thick patches) and eventually increasing the apparent density of the pollutant until it is almost equal to that of seawater (Cedre, 2006);
5. photo–oxidation – is when sunlight (ultraviolet and near–ultraviolet areas of the spectrum), in the presence of oxygen, transforms hydrocarbons through photo–oxygenation (increasing the oxygen content of a hydrocarbon component) into new by–products (Mielke, 1990). Although the toxicity of photo–oxidation products is a concern because they are more water–soluble and reactive, the rates of photo–oxidation of liquid or solid fractions of the oil are too slow to significantly affect the mass balance of a spill within the first few months (Jordan & Payne, 1980);
6. adsorption/sedimentation – heavier oils or oil fractions, are sticky and tend to adhere to particles in the water column (adsorption) and on the sea floor (sedimentation) and will incorporate the oil within sediments (Boyd et al., 2001). It usually occurs with medium and heavy–weight oil components that do not dissolve into the surrounding water. The wave action can roll up small amounts of partially degraded oil into tar balls which vary in size from a millimetre to centimetres across and weighing several kilograms (Floodgate, 1995). Sedimentation can be considered an important mechanism for the removal of heavy fuel oil from the water column following some spills (Concawe, 1998); and;
7. biodegradation – is the process by which hydrocarbon–degrading organisms such as bacteria, fungi, and yeasts break down petroleum hydrocarbons ultimately into carbon dioxide and water (Yender et al., 2002). Figure 3.4 summarises these processes with an estimated duration for each.

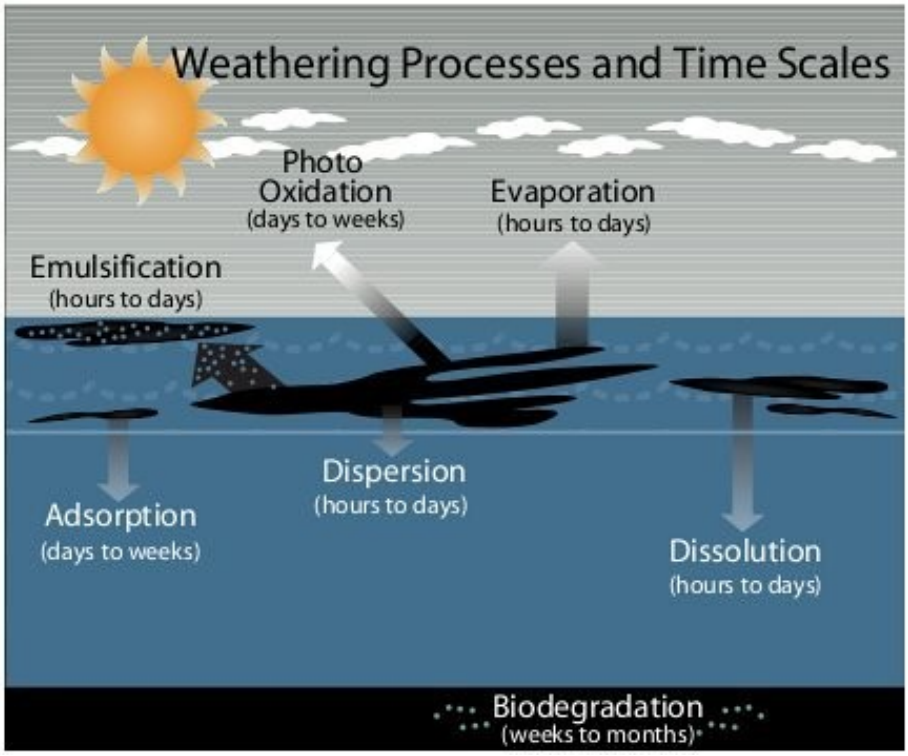

Figure 3.4. The different weathering processes that act on an oil spill at sea with an estimated time scale for each process (NOAA, 2002).

3.2.3 Thermal contrast of oil in water

The detection of oil films at the water surface depends on the difference of emissivity (ε) between that of water (~0.99) over oil (~0.97) (Stringer et al., 1992). The temperature variation between the two, however, is dependent upon several varying environmental factors that affect the temperature of the oil during the course of observation. These factors include the properties of the oil itself; its degree of emulsification; the air and sea temperatures; intensity of incident light; and the thickness of the oil (Goodman, 1989; Lunel et al., 1997). Generally, thick oil will appear warmer than water during the day due to thermal isolation from the underlying water and high absorption of solar radiation, which is then re-emitted as thermal energy mainly in the thermal infra-red (IR) region (8-14 μm) (Hurford, 1989; Samberg, 2005). At night, the reverse behaviour is observed: heat loss in oil is faster than in water and therefore, thick oil will appears cooler than the water (Samberg, 2005). As for thin oil or sheen, they will not have a noticeable temperature difference from their surrounding water (Fingas & Brown, 1997). The exact thickness at which these temperature transitions occur are not known, but evidence indicates that the transition between the hot and cold layers lie

between 50 and 150 µm and the minimum detectable layer is between 20 and 70 µm (Fingas et al., 1998).

In contrast to the observations made by others, Cross (1992) found from his studies of the thermal responses in AVHRR datasets over the Kuwaiti coastal oil slicks recorded in 1991, that the slick was warmer than the sea at night and cooler by day. Salisbury et al. (1993), however, concluded that reflectance in the thermal region is not a useful tool for determining relative oil slick thickness. The conclusions were reached when the thermal IR spectrum of oil slicks was measured for five different crude oil samples with a wide range of °API gravities and compositions. After a brief outgassing phase, the spectrum were similar for all oil slicks and little–affected by thickness, extended exposure to air or sunlight, and even by emulsification with seawater.

According to Fingas & Brown (1997), the reason why IR devices can not detect emulsions under most circumstances, is probably because they typically contain 70% water and thus do not show a significant temperature difference.

3.2.4 Wind and sea currents

The field experiments conducted by Cox and Munk (1954) show that the addition of an oil slick with thickness of order 1 µm causes a reduction of the surface slopes of waves from their clean water values by a factor of 2 or 3, and the disappearance of waves with lengths less than about 0.3m. The ambient conditions like wind speed, sea state, and currents work collectively to transport the oil on the water surface (Scholz et al., 1999). When both wind–driven currents (U_{wind}) and tidal currents ($U_{current}$) are present, it is supposed that the two vector velocities simply add and the centre of mass of the oil is thus supposed to move according to the following Equation:

$$\dot{\boldsymbol{X}} = \vec{U}_{current} + 0.035\,\vec{U}_{wind} \tag{3.8}$$

where $\dot{\mathbf{x}}$ is the resulting velocity of the oil from its centre of mass (Hoult, 1972). Figure 3.5 depicts this effect at different current and wind velocities. The fixed drift factor of 3% does not completely describe the velocity distribution of the entire slick, where parts of the slick may move faster than 3% and other parts may move slower (Lehr & Simecek-Beatty, 2000). Observations of actual oil experiments indicate that the wind drift can range from 1% to 6% (Smith, 1974; Stolzenbach et al., 1977).

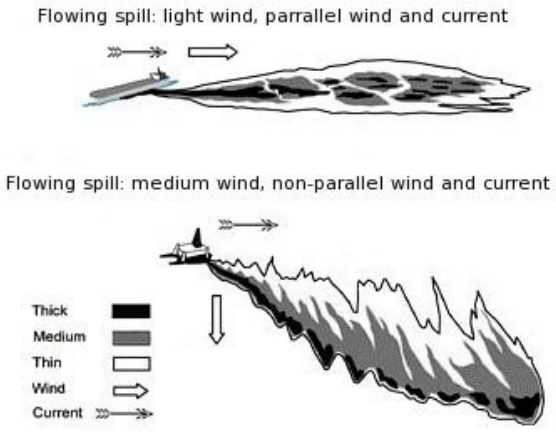

Figure 3.5. The drift direction of an oil spill corresponding to different wind direction (Cedre, 2006).

Elliot et al. (1986) proposed that different speeds within a slick are a result of sub–surface oil droplets and shear in the near surface current. They hypothesize that oil droplets in the water column move at a slower speed than droplets at the surface because they are transported only by the surface current and turbulence. While the surface droplets move faster due to an additional wind drift factor, which may explain the relatively greater thickness of the downwind leading edge of spills at relatively strong wind speeds. Figure 3.6 depicts this effect at different current and wind speeds.

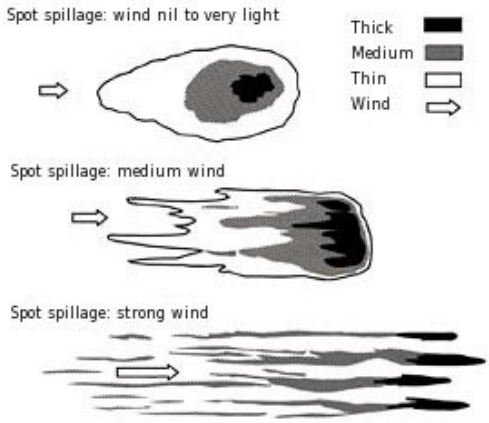

Figure 3.6. Different wind speeds change the slicks shapes (Cedre, 2006).

Less viscous oils, such as lighter refined “fuel oils” will generally tend to spread at a higher rate than the heavy “crude oils”, where the mixing energy of sea waves plays a substantial role in the emulsification of the oil making it more viscous than the original oil, and often referred to as “chocolate mousse” (Król et al., 2006). However, high frequency conditions; short term wind patterns; and turbulent surface currents will

greatly enhance the rate of spread and ultimately the break up of the slick in a process called “shear diffusion” (Elliott, 1986; Spaulding, 1988).

Winds also generate Langmuir circulations (Langmuir, 1938), which are defined as windrows or roll vortices organized in a counter–rotating secondary circulations embedded in the mean flow, that result from instabilities in the convective marine boundary layer (Brown, 1980). The Langmuir circulations (see Figure 3.7A) will act on the spill to break it into streaks after a period of time from the beginning of the spill, along the direction of the wind as it is shown in Figure 3.7B.

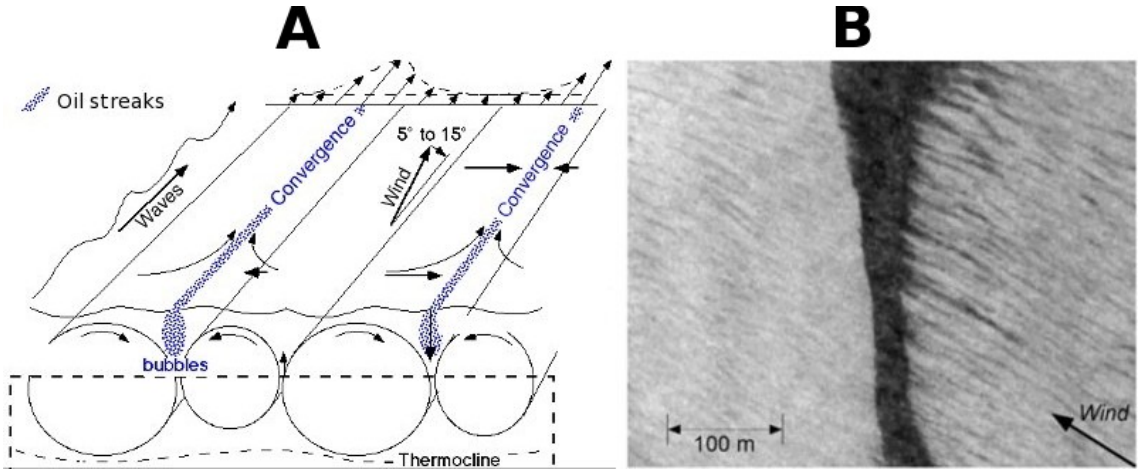

Figure 3.7. **(A)** a schematic showing the how Langmuir cells are formed (Smith, 2002) and an **(B)** IR image showing a slick with a smooth downwind edge and prominent windrows on its upwind side (Marmorino et al., 2008).

3.3 Optical characteristics of oil spills

3.3.1 Absorption and Reflectance

Optical absorption in crude oil increases strongly with decreasing optical wavelength and depends only on the molecular properties of oil and not on droplet size (Król et al., 2006). At the visible and near infra–red (NIR) wavelengths, the refractive index of oil (n_{oil}) is higher than that of seawater ($n_{sw} \approx 1.3$) (Byfield, 1998). In the ultra–violet (UV) bands, crude oils n_{oil} lie in the range 1.57–1.67 and are 1.48–1.52 in the visible part of the spectrum (Osadchy et al., 1994). The greater refractive index of oil relative to sea–water gives rise to greater surface reflection from an oil sheen than from clear water (Byfield, 1998). Figure 3.8 summarizes the inter–relationship between reflectance and absorption of an oil spill to unpolluted sea waters.

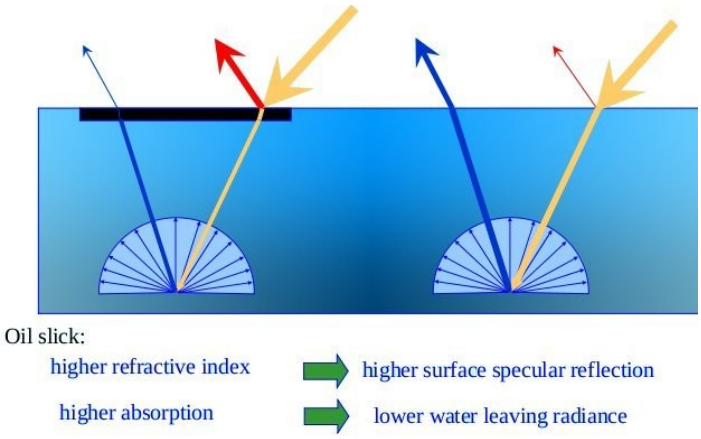

Figure 3.8. The inter–relationship between reflectance and absorption of an oil spill to unpolluted sea waters (Bulgarelli & Tarchi, 2006).

The reflectance measurements of four different oil types at different relative thickness compared to water are shown in Figure 3.9.

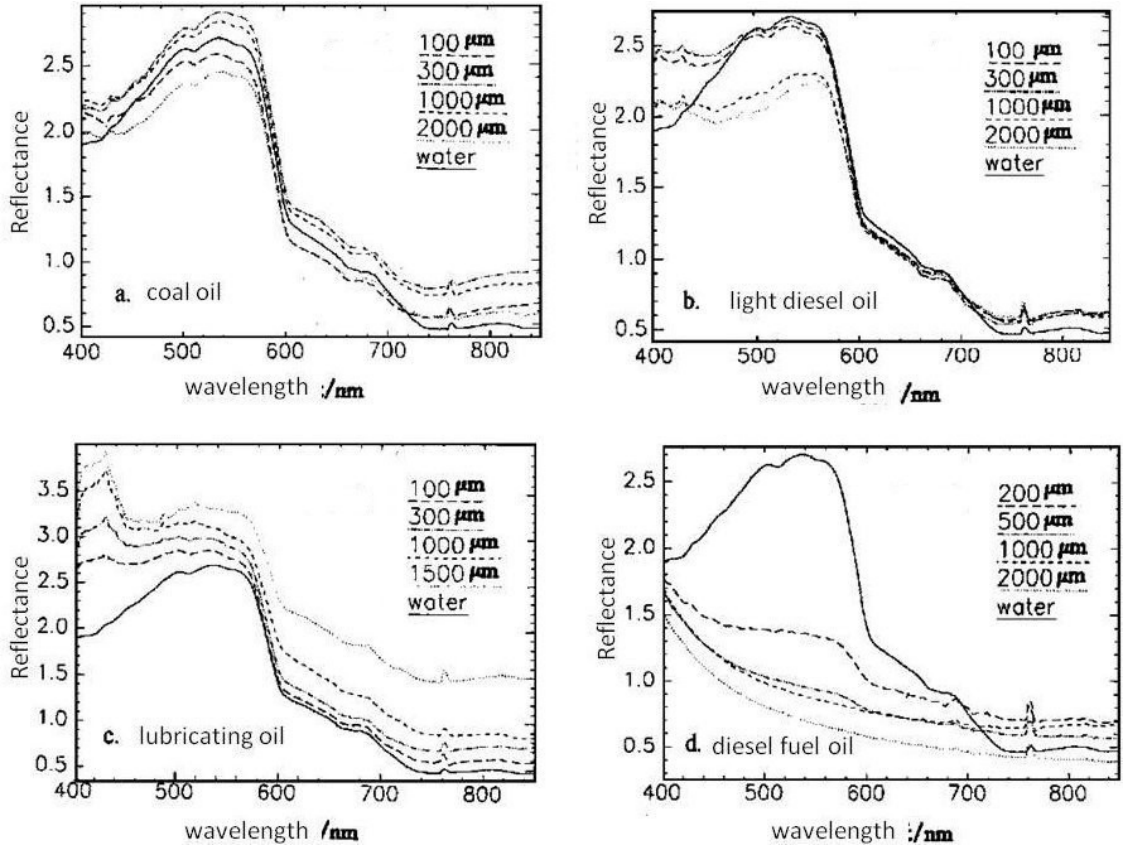

Figure 3.9. Spectral characteristics of four different oil types at different thickness (Dongzhi & Peifu, 2000; Zhang, 2000).

This confirms that increasing oil thickness decreases reflectance rapidly over clear water across the visible spectrum (Karpouzli & Malthus, 2007).

3.3.2 Optical contrast

In optical data imagery, oil spills appear either dark (negative contrast) or bright (positive contrast) depending on the angle of observation relative to the position of the sun glint (Elliott, 1986; Otremba & Piskozub, 2001). The key factors that appear to determine the degree of contrast of an oil spill in MODIS are: the optical properties of the oil; the film's thickness; the coefficients of light absorption and scattering of sea water; the overhead light conditions; sea surface state and depth; the type of sea bottom; the angle of illumination; and the angle of observation (Otremba, 1999; Otremba & Król, 2001). Simulation studies by Otremba and Piskozub (2001) have shown that when the look direction of the satellite sensor deviates from the direction of direct sunlight reflection, the rough water surface (i.e. with short waves) will appear brighter due to higher scattering from its surface than a smooth water surface dampened by oil, and thus, oil films will appear with negative (darker) contrast than water. This contrast, however, will become positive (brighter) when the look direction of the satellite sensor is close to the direction of sun's specular reflection (sun glint) caused a by a flat water surface, in which case, it will be the oil–dampened water surface (Otremba & Piskozub, 2001; Chust & Sagarminaga, 2006). Figure 3.10 shows the variations found in oil contrast as a function of angle of observation at different light incidence angles and wind speeds.

3.3.3 Oil fluorescence

Oil fluorescence can be induced by light excitation at UV to blue wavelengths (Karpicz et al., 2005). The spectral fluorescence properties of various oils when excited by laser pulses may be used to distinguish different oil types (Law, 1981). Figure 3.11 shows an example of this phenomena. Airborne fluorescence lidars can be used either during the day or night operations, provided that the atmosphere is reasonably clear (Jha et al., 2008). The excitation wavelength for the laser is typically chosen as 308 or 355 nm (Grüner et al., 1991).

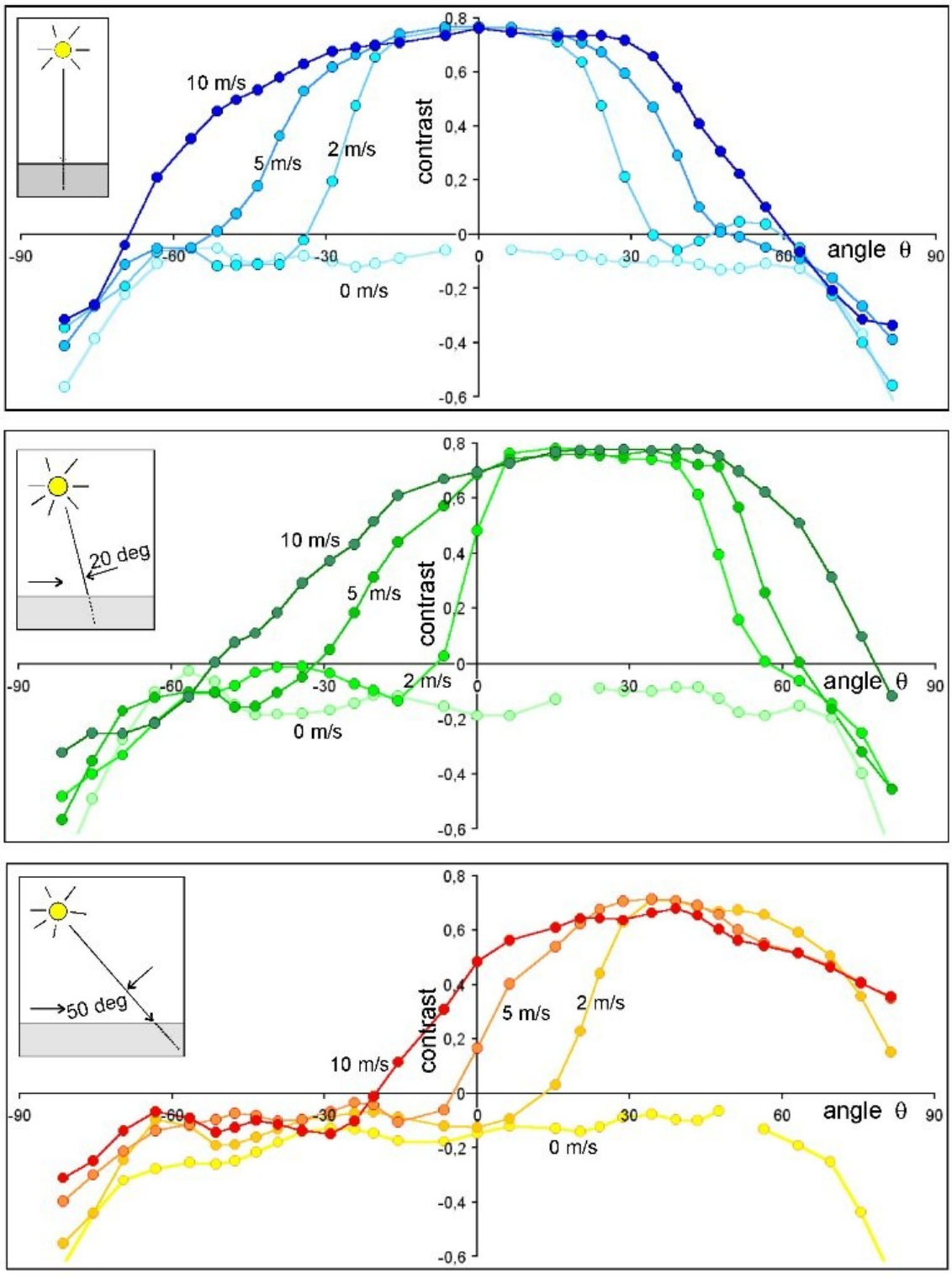

Figure 3.10. Contrast of an oil film as a function of angle of observation at various light incidence angles and at various wind speeds (Otremba & Piskozub, 2001).

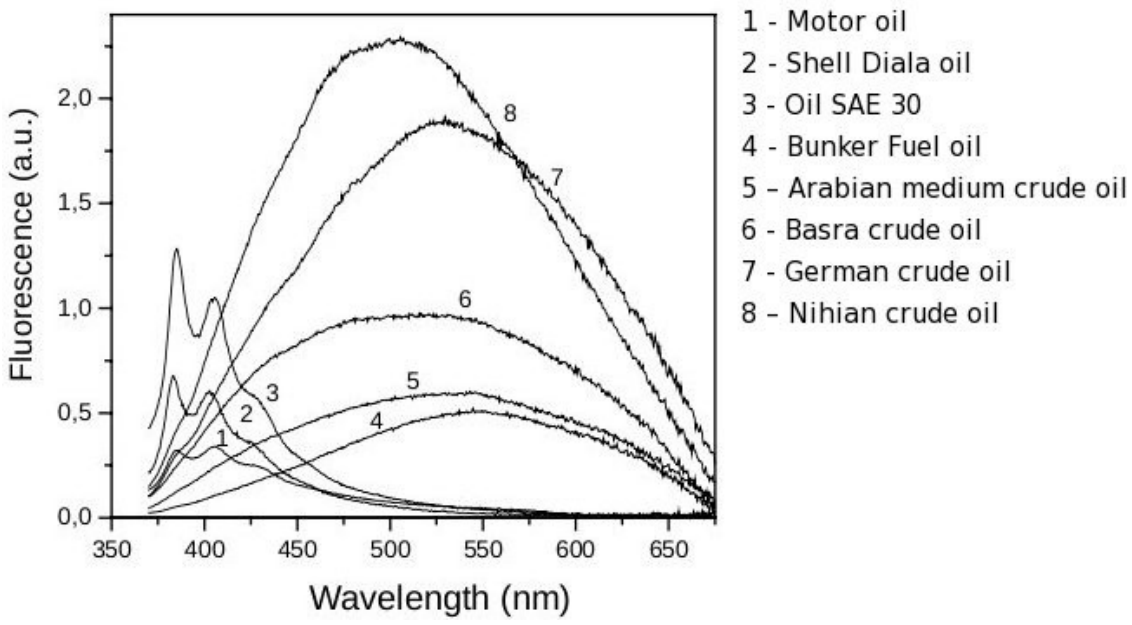

Figure 3.11. The fluorescence emission spectra of some oils excited at 355 nm (Karpicz et al., 2005).

3.4 Sensors used for oil spill detection

Synthetic Aperture Radar (SAR) sensors remain the most preferred spaceborne devices to be used for the detection of oil spills (Brekke & Solberg, 2005). Because SAR are active sensors that uses the microwave radar bands, it enables them to perform day or night imaging and regardless of the prevailing cloud cover – properties which are absent in other space–borne imaging techniques (eg. optical or thermal IR; Condley, 1991). Passive hyperspectral or multispectral optical sensors, encompassing the visible, near and middle infra–red wavelength regions, have nevertheless proven their success in detecting oil spills under certain meteorological conditions (Karpouzli & Malthus, 2007). It would appear, however, that no satellite systems suitable for the detection of oil spills in the UV wavelength range are currently available (Karpouzli & Malthus, 2007).

3.4.1 Oil spill detection using the SAR sensors

Real aperture radars (RAR's) as well as SAR's usually operate at incident angles (the angle between nadir[9] and the look direction of the antenna) that range between 20° and 70° (Valenzuela, 1978). It is at such incidence angles that radar back–scattering can be described by Bragg's scattering theory (Crombie, 1955), where radar microwaves are in

[9]Normal to the sea surface pointed down.

resonance with ocean waves of similar scale (Bragg waves), and can therefore be related to the radar wavelength as such (Figure 3.12A):

$$sin\theta = \frac{\lambda_r}{2\lambda_w} \tag{3.9}$$

where λ_w and λ_r are the ocean and radar wavelengths respectively, and θ is the incidence angle (Valenzuela, 1978). For wind speeds that lie between a range of 2–3 m/s and 12–15 m/s, the capillary and short gravity waves[10] will be called "Bragg waves" and thus obey the "Bragg resonance condition" (Hühnerfuss et al., 1978), and the SAR wavelengths should relatively match the size of surface waves. For example, a range of SAR incident angles between 20° to 26°, will have Bragg waves at the following common SAR frequencies: X–band (3 cm), 3.9 ± 0.5 cm; for C–band (5.5 cm), 7 ± 1 cm; and L–band (23 cm), 30 ± 4 cm (Holt, 2004). High density surface films such as oil, will appear as dark patches in the SAR images (Figure 3.12B) due to a dampening effect of water roughness, and hence the reduction of Bragg's backscattering coefficient (Guinard, 1971).

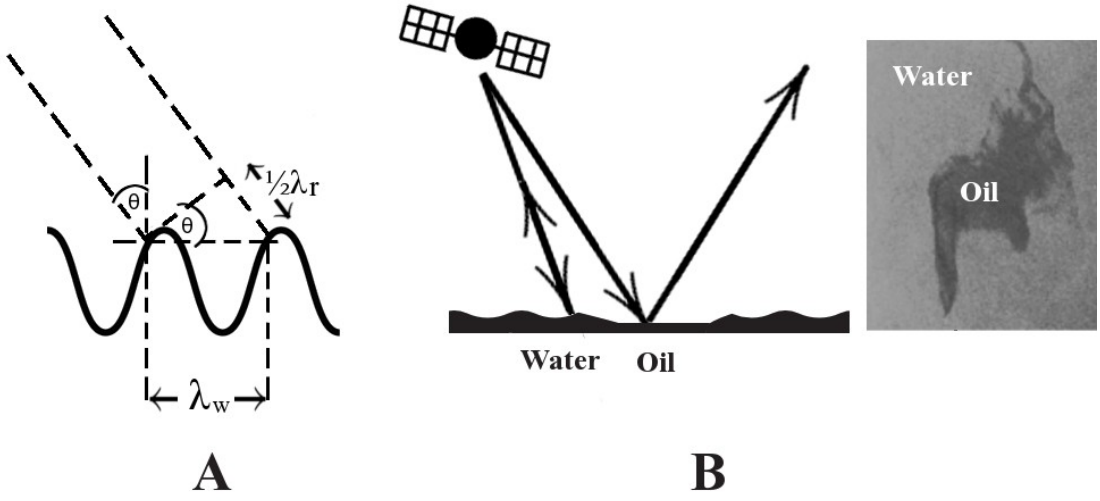

Figure 3.12. Bragg scattering waves in relation to **(A)** the sensor waves and **(B)** the SAR scattering mechanisms of an oil slick.

There is also an upper threshold of wind speed beyond which the water surface becomes so rough (diffused surface) that the oil film will be broken up by the breaking waves – depending on oil type and age, and therefore undetectable by radar (Demin et al., 1985;

[10] A wave occurring at the interface between two fluids, such as the interface between air and water on oceans will be called a capillary wave, if the principal restoring force is controlled by surface tension or called gravity waves, if the restoring force is gravity.

Brekke & Solberg, 2005). According to Solberg (2005), the general framework for the allocation of dark patches (oil spills and look–alikes) in a SAR image can be summarized in the following three steps (Figure 3.13): isolation of dark spots in the image, through an appropriate adaptive threshold and segmentation processing; the extraction and analysis of the main dark features and finally the classification of extracted features as either oil slicks or look–alikes, based on prior probability confidence values.

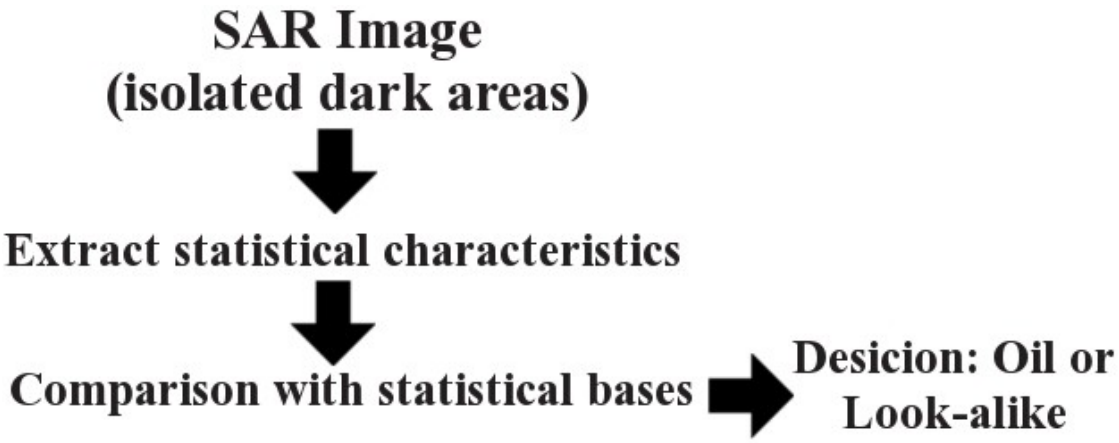

Figure 3.13. The three-step procedure for discriminating oil from look-alikes in a SAR image.

The most common methods used on a SAR data for the extraction of dark features as oil spills are summarized in Table 3.2.

The polarimetric properties for both transmission and reception of the SAR signal off an oil spill have been investigated from the results acquired during two spaceborne imaging radar–C/X band SAR (SIR–C/X–SAR) missions on–board the space shuttle Endeavour in 1994. The results have revealed that multi–frequency and multi–polarization SAR imagery is also able to detect oceanic surface films including oil (Gade et al., 1998a).

3.4.2 Oil spill detection using optical sensors

Satellite–based, optical passive sensors are not generally used for the detection of marine oil slicks, unlike radar sensors (Brekke & Solberg, 2005) which are capable of performing night–time imaging, penetrating clouds, dust storms and soot (Fiscella et al., 1994). According to Fingas & Brown (1997), there are several problems associated with

Table 3.2. The most common methods used in oil spill feature extraction processing (Brekke & Solberg, 2005).

#	Feature
1	Slick area (A)
2	Slick perimeter (P)
3	P/A
4	Slick complexity
5	Spreading (low for long thin slicks, high for circular shape)
6	Slick width
7	First invariant planar moment
8	Dispersion of slick pixels from longitudinal axis
9	Object/dark area standard deviation
10	Background/outside dark area standard deviation
11	Max contrast (between object and background)
12	Mean contrast (between object and background)
13	Max border gradient
14	Mean border gradient
15	Gradient standard deviation
16	Local area contrast ratio
17	Power-to-mean ratio of the slick
18	Homogeneity of surroundings
19	Average NRCS inside dark area
20	Average NRCS in limited area outside dark area
21	Gradient of the NRCS across the dark area perimeter
22	Ratio #9 to #10
23	Ratio #19 to #9
24	Ratio #20 to #10
25	Ratio #23 to #24
26	Ratio #19 to #20
27	Distance to a point source
28	Number of detected spots in the scene
29	Number of neighbouring spots

relying on optical satellites for oil spill remote sensing. The first is the timing and frequency of overpasses and the absolute need for clear skies to perform optical work. Radar systems are generally characterised by higher spatial resolution than optical sensors (Fingas & Brown, 1997), although, few high resolution optical sensors do exist, such as Landsat ETM+, SPOT and IKONOS, but are limited in spatial coverage, costly and unavailable on a daily basis (Hu et al., 2003).

3.4.2.1 Hyper–spectral sensors

Hyper–spectral sensors unlike multi–spectral sensors can record over 200 selected wavelengths over a broad, continuous range of the visible–NIR spectrum, as in the case of the Airborne Imaging Spectro–radiometer for Applications (AISA) and the Airborne

Visible and IR Imaging Spectrometer (AVIRIS) (Salem & Kafatos, 2001). The narrow spectral bands of hyperspectral sensors (typically 0.01 to 0.02 μm) are sensitive to the detection of distinct absorption and reflection responses unique to each substance, and exploiting the spectral signatures of different oil types (Salem & Kafatos, 2001) Figure 3.14 shows the spectral characteristics of the Arabian crude oil at different thickness, including that of water.

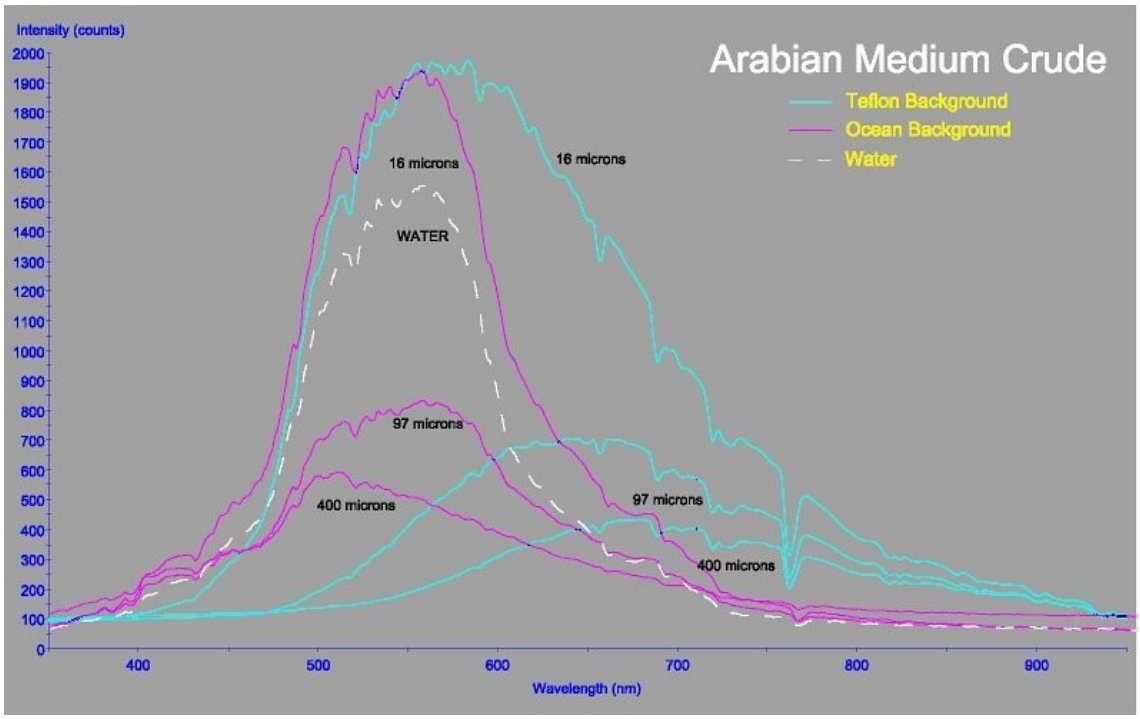

Figure 3.14. Spectrometer measurements of Arabian medium crude films of several thicknesses over an evenly different reflecting background (Svejkovsky & Muskat, 2006).

3.4.2.2 Infra–Red (IR) sensors

IR sensors are relatively cheap remote sensing technologies which can be used to detect oil spills, and are thus widely used for oil spill surveillance (Brown & Fingas, 2005). They are unable to detect emulsions of oil in water, as emulsions contain 70% of water, and thermal properties of emulsion are similar to the water background (Fingas & Brown, 1997).

Relative thickness estimates can be made using the peak to NIR radiance ratio, without extensive processing or detailed knowledge of background conditions (Byfield, 1998). Thermal radiation from sea weeds and the shoreline appear similar to the radiation arising from oil which may lead to false positive results. Figure 3.15 shows the passive microwave radiometer (MWR) image of water polluted by oil in direct

comparison with IR and UV images. The MWR shows the areas of higher thickness, as opposed to the IR and especially the UV, which also indicate the spatial extent of the thin oil film (Trieschmann et al., 2001).

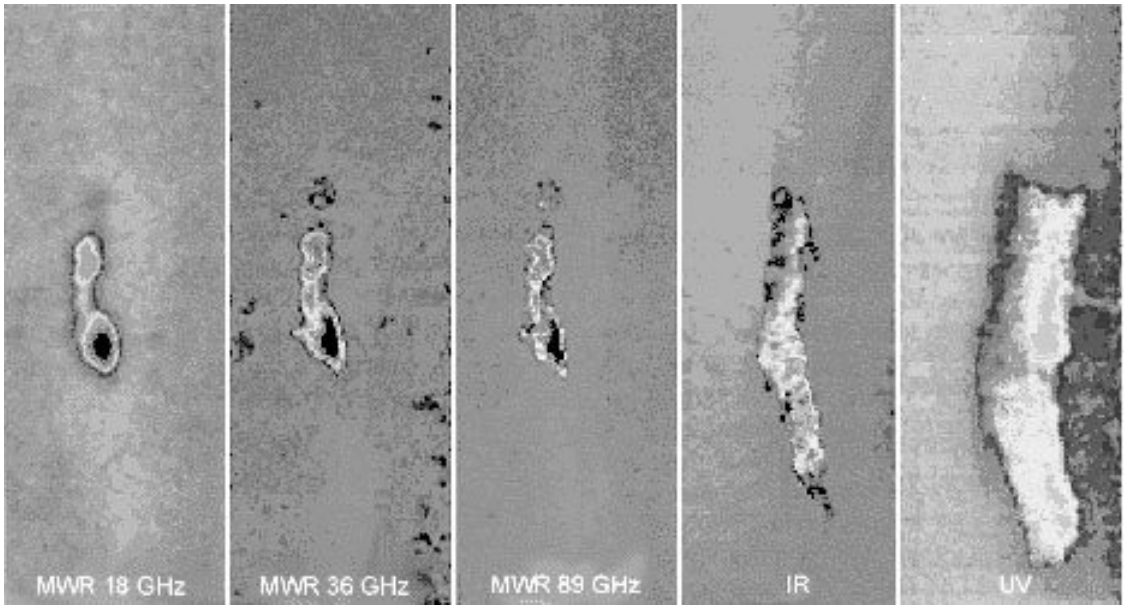

Figure 3.15. Airborne measurement examples of crude oil (~ 5m^3) with maximum layer thickness 1.8 mm (Trieschmann et al., 2001).

3.4.2.3 Effect of sun glint (glitter)

Sun glint or glitter is the specular reflection of sunlight from the facets of the rough water surface that are suitably tilted, which spread out the image of the sun from a disk to a speckly column (Cox & Munk, 1954; Su et al., 2002). If the sea surface was absolutely calm, a single mirror–like reflection of the sun would be centred at the horizontal specular point (Cox & Munk, 1956). However, the sea surface is almost always rough due to wind, which will scatter the direct solar beam into a range of angles, hence, the rougher the sea, the wider the range (Su et al., 2002). Cox & Munk (1956) have derived the sun glint radiance L_g as such:

$$L_g = E_s . p(z_x, z_y) \frac{\rho(\hat{\omega})}{\cos^4(\beta)\cos(\theta)} \tag{3.10}$$

where E_s is the solar irradiance at the sea surface; $p(z_x, z_y)$ is the probability distribution function (Equation 3.11) of slopes (the slope defines the partial derivatives with respect to x and y of surface elevation, z); $\rho(\omega)$ is the Fresnel reflection coefficient of the water surface; β is the surface tilt angle off the horizontal; and θ is the sensor (viewing) angle from zenith.

$$p(z_x, z_y) = \frac{1}{\pi\sigma^2} \exp\left[-\frac{z_x^2, z_y^2}{\sigma^2}\right] \tag{3.11}$$

Figure 3.16 summarizes the optical geometry for a glint configuration. The probability distribution function of the slopes (slope pdf) can be approximated as Gaussian with the mean square slope σ^2 as width parameters (Cox & Munk, 1956):

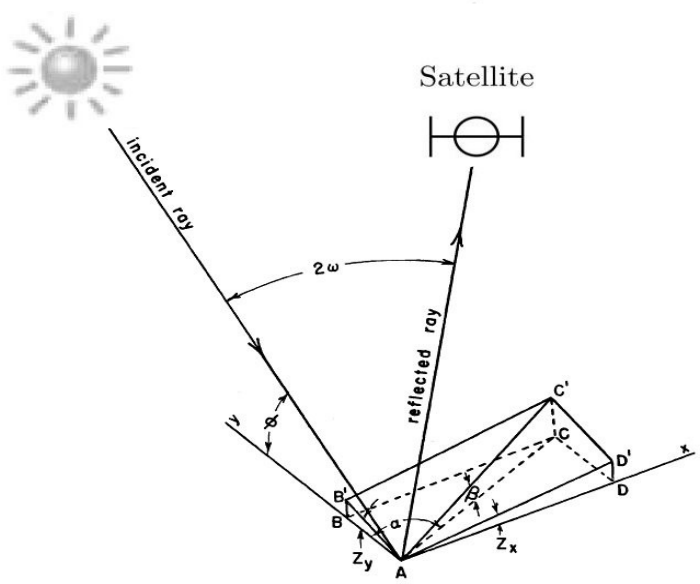

Figure 3.16. The coordinate system of a glint geometry is centred at the sea surface, with the z–axis vertically upward (not shown) and the y–axis drawn horizontally toward the sun. The incident ray is reflected at A to be viewed at the satellite. Points A B C D define a horizontal plane through A and A B' C' D' define a plane tangent to the sea surface. The tilt, β is measured in the direction AC of steepest ascent, and this direction makes an angle α clockwise from the sun (Cox & Munk, 1956).

Cox & Munk (1956) have also shown an empirical relationship between wind speed W in m/s and σ such that:

$$\sigma^2 = 0.003 + 5.12 \times 10^{-3} W \pm 0.004 \tag{3.12}$$

Melsheimer & Keong (2001) have provided an interpretation for the formation of a glint in relation to Equations 3.10, 3.11 and 3.12: For a given scene geometry, i.e., sensor's viewing direction and the sun's position in the sky, we can calculate the tilt angle β that would be needed for specular reflection of sunlight to the sensor. Thus, the result will be a sun glint radiance as a function of the surface roughness (mean square slope) for the given scene. Simple analysis shows that L_g as in Equation 3.10 has a maximum at $\sigma^2(W)=\tan^2 \beta$. Therefore, just calculating β from the scene geometry gives an idea of the shape or the sun glint radiance curve. The presence of glitter in an image

has often been considered to represent a serious cause for data loss (Chust & Sagarminaga, 2006) because the component of sensor–received radiance due to glint light can be much greater than the water–leaving radiance from sub–surface features (Kay et al., 2009). In this situation, retrieval of information such as chlorophyll content, benthic features or bathymetry requires both high measurement sensitivity and a robust algorithm that can mask the effect of glint (Kay et al., 2009). Conversely, the acquisition of imagery containing areas dominated by sun glitter can, in certain circumstances, be of considerable value (Khattak et al., 1991; MacDonald et al., 1993). This is the case of surface wind speed (Cox & Munk, 1954), oceanic internal waves (Matthews, 2005), shallow water bottom topography (Hennings et al., 1994) and river plume frontal boundaries (Matthews et al., 1997). Furthermore, water surfaces affected by sun glitter often manifest brightness reversal between two different views, in which relatively bright features at one angle appear dark in the other view. Such a region of brightness reversal can be indicative of a locally rough or smooth surface texture (Matthews, 2005), this may be found, for example, in the surroundings of internal waves or ship wakes. For the two sets of images examined, three domains of oil radiometric response as a function of view angle have been identified: 1) at angles unaffected by sun glitter, slicks were not identified or appeared slightly darker than adjacent unpolluted areas; 2) at angles affected by sun glitter, but moderately near to the specular direction, slicks appeared darker because they reflect the incoming solar radiation off their mirror–like surface away from the sensor; and 3) at the specular angle, or very near to, the slicks appeared brighter (Chust & Sagarminaga, 2006).

3.4.2.4 Atmospheric effect

Depending on wavelength, anything from 80% to 100% of the top of the atmosphere (TOA) radiance received at the satellite sensor, directed at the ocean surface outside the sun glint pattern, originates in atmospheric Rayleigh (air molecules) and aerosol scattering (Gordon et al., 1983; Kirk, 1994). The TOA radiance received by the satellite, $L_s(\lambda)$ or reflectance, $\rho_s(\lambda)$ are related:

$$\rho_s(\lambda,\theta)=\frac{\pi L_s(\lambda)}{F_0\cos\theta} \tag{3.13}$$

where F_0 is the extraterrestrial mean solar irradiance – which is wavelength dependent, and θ is the solar zenith angle – the angle between the line from the pixel under examination to the sun and the local vertical.

In order to relate the derived water–leaving reflectance (ρ_w) to the inherent optical properties of the ocean such as chlorophyll-a concentration (Chlor-a) or water absorption and scattering coefficients, one would need to normalize ρ_w to produce the normalized water–leaving reflectance (ρ_{wn}) which is approximately the reflectance that would exit the ocean in the absence of the atmosphere and with the sun at the zenith (Gordon & Clark, 1981):

$$\rho_{wn}(\lambda,\theta)=\frac{\rho_w(\lambda,\theta)}{t_0(\lambda)} \tag{3.14}$$

where, $t_0(\lambda)$ is the atmospheric diffuse transmittance in the solar direction.

Optical sensors will receive several different light pathways in the atmosphere (explained in Figure 3.17) that can be divided into several components, each of which is responding to a physical process in the atmosphere or in the ocean.

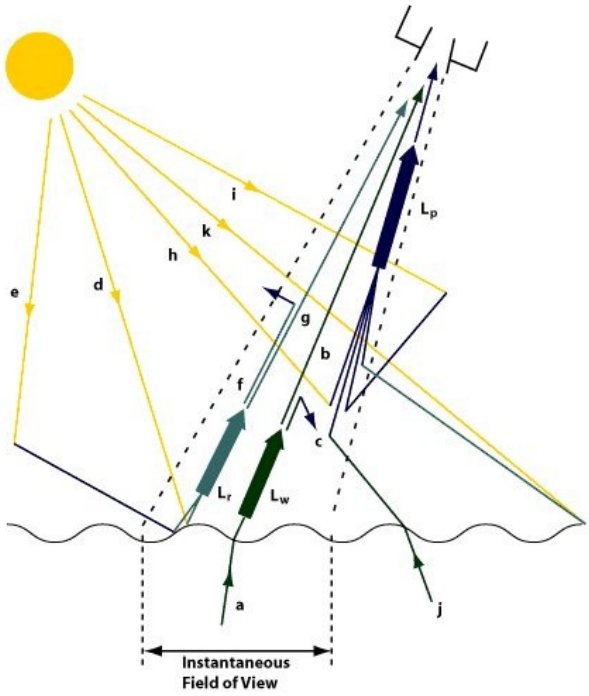

Figure 3.17. Optical pathways between the sea and the sensor: **(a)** The light path of the water–leaving radiance; **(b)** shows the attenuation of the water–leaving radiance; **(c)** scattering of the water–leaving radiance out of the sensor's field of view (FOV); **(d)** sun glint (reflection from the water surface); **(e)** sky glint (scattered light reflecting from the surface); **(f)** scattering of reflected light out of the sensor's FOV; **(g)** reflected light is also attenuated towards the sensor; **(h)** scattered light from the sun which is directed toward the sensor; **(i)** light which has already been scattered by the atmosphere which is then scattered toward the sensor; **(j)** water–leaving radiance originating out of the sensor FOV, but scattered toward the sensor; **(k)** surface reflection out of the sensor FOV which is then scattered toward the sensor. (Robinson & Mitchelson, 1983).

If L_s is the radiance received by the sensor, then it is made up of :

$$L_S = L_p + TL_w + TL_r \tag{3.15}$$

where L_p is the atmospheric path radiance which includes multiple scattering by air molecules (Rayleigh); atmospheric aerosols, and the interaction between Rayleigh and aerosol scattering; T is that proportion of the surface–leaving radiance which is not scattered out of the FOV and is called the direct transmittance of the atmosphere; L_w is the total water–leaving radiance (associated with radiance upwelling from beneath and transmitted through the sea surface); and L_r is the radiance above the sea surface due to all surface reflection effects within the FOV (Robinson & Mitchelson, 1983).

The atmospheric and ocean surface effects must be removed before ocean radiance signals may be analysed for the purpose of understanding the ocean biosphere. This step in the processing of satellite ocean colour imagery is referred to as the atmospheric correction procedure (Siegel et al., 2000). However, this step may not be necessary if the goal of processing is only to map the extent of an event instead of producing a biophysical parameter (Smith, 1968). Although several atmospheric correction methods do exist, the one used in MODIS data processing is generally referred to as the black/dark pixel assumption (Siegel et al., 2000). This method assumes that ocean water (case I waters) is optically black ($\rho_{NIR}=0$), that it has a zero water–leaving radiance at the NIR (Gordon & Clark, 1981). This assumption fails for highly productive (eutrophic) waters (Siegel et al., 2000) or turbid (case II waters) waters (Gould Jr. et al., 1999), due to significant backscatter contributions in the NIR leading towards an over–estimation of the atmospheric correction.

3.4.2.5 Effect of optical pathways

Imaging quality via an optical sensor can be either distorted or totally obscured by the atmospheric path–radiance. The direct transmittance of the atmosphere (T) discussed earlier in Equation 3.15 can be defined (in reference to Figure 3.18) as:

$$T(\lambda, z, \theta) = \exp\left(-\frac{\int_{z1}^{z2} k(\lambda, z)\, dz}{\cos(\theta)}\right) = \exp\left(\frac{-\tau(\lambda, z)}{\cos(\theta)}\right) \tag{3.16}$$

where k is the attenuation coefficient and τ is a dimensionless quantity termed the aerosol optical thickness.

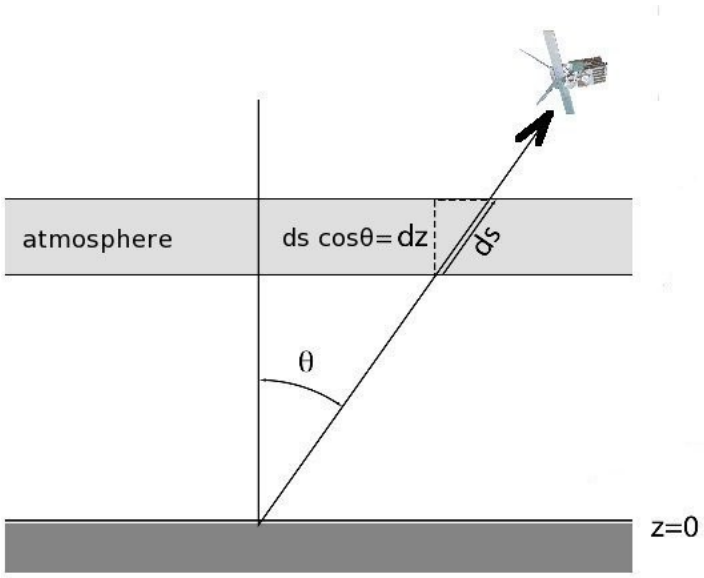

Figure 3.18. Definition sketch of the atmospheric path length (Robinson, 2004).

This imaging limitation can be highly exaggerated whilst observing objects at large off–nadir angles (large θ) or over an aerosol–dense region, causing both the incident and the reflected wave to suffer from signal attenuation caused by molecular and aerosol absorption and scattering effects. The path radiance will depend on the strength of the illumination and the density of scattering particles in the field of view. It will be a decreasing function of wavelength, because shorter waves are scattered more than long waves. Because of this trend, it can often be ignored in the NIR unless the haze is very thick or where some particles are as large as 1 μm. The attenuation due to the atmospheric path–radiances can also be minimized by confining the observation to the areas that are close to nadir (that is shortening the path radiance by reducing the zenith angle).

3.4.3 Oil spill imagery under the SAR and optical sensors

As it has been discussed earlier, oil spills will always appear as dark shape features in the SAR data and its contrast will be independent of the position of the sun to the position of the sensor. In optical data, however, spills can sometimes appear with either dark (negative) or bright (positive) contrast depending not only on the relation between the sensor–target–sun geometry, but also on the spectral band used. It is feasible, therefore, under such circumstances to apply the same shape and texture methods outlined in this study for oil spill detection to perform sampling on the SAR and optical data. The SAR has an active viewing geometry that is always in side–looking

configuration, while optical sensors are independent of look direction. Figure 3.19 shows this viewing geometry difference between the two sensors and its impact on the contrast of the spill, including the effect of sun glint on the contrast of oil spills in the case of optical sensors.

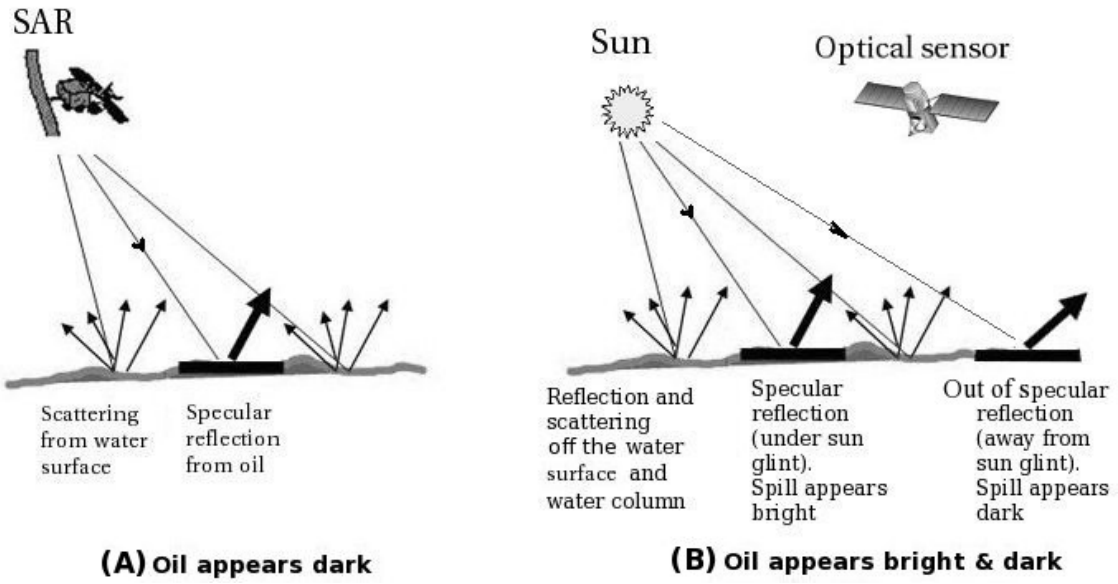

Figure 3.19. An observation comparison between the **(A)** SAR and **(B)** optical sensors of an oil spill in moderate sea state roughness (Data provided by the European Space Agency, 2010).

3.4.4 Oil spill look–alikes

The phenomena of oil spill look–alikes observed in satellite imagery that may lead to false positive interpretation of oil slicks is attributed to either meteorological or oceanographic features (Clemente-Colón & Yan, 2000; Solberg, 2005). This phenomena is common to both satellite sensor types (the SAR and the optical) such as low surface winds; surfactants; upwelling; and algal mat formations. Other look–alikes are sensor–specific such as clouds and/or their shadows as in the case of an optical sensor. Whereas in the case of SAR, oil spill look–alikes can include rain effects, sea ice or grease ice, and suspended sediment. Here is a brief description of each look–alike type discussed earlier:

1. “Low surface winds” are smooth water surface areas caused by low wind speeds (lower than 3 m/s, Trivero et al., 1998), and therefore, causing a specular reflection off the water's “mirror–like” surface away from the sensor, yielding a dark appearance of the observed target (Cox & Munk, 1954). This smoothing mechanism at the water surface can be caused by a variety of factors, such as

atmospheric gravity waves and boundary–layer rolls that affect the local wind conditions, producing distinctive quasi–periodic dark (low wind speed) and bright (high wind speed) patterns (Clemente-Colón & Yan, 2000). Areas of wind shadowing by coastal topography or man–made obstacles can also induce the same low wind speed effect (Espedal, 1999);

2. surfactants, as a whole, are perhaps the most popularly recognized oceanographic low back–scatter features imaged by SAR and optical sensors. These substances can be divided into two major categories: biogenic and minerogenic. Natural biogenic slicks are produced by plankton and fish substances normally released into the environment (Dietz & Lafond, 1950). Natural mineral slicks are the result of ocean–bottom oil seeps (Alpers & Hühnerfuss, 1989; Gade et al., 1998b);
3. upwelling occurs when a divergent surface flow, commonly driven by the wind, is compensated by an onshore deeper flow that brings colder and nutrient–rich water to the surface (Clemente-Colón & Yan, 2000). Temperature differences in the air–sea boundary layer over upwelling regions, can affect the efficiency of Bragg wave generation and will, therefore, have a direct effect on the observed backscatter (Friehe et al., 1991). The increased stability produced by lower sea surface temperature results in lower wind stress and a decrease in available Bragg scattering waves, producing an overall decrease in normalized radar cross section (NRCS). The lower temperature of the upwelled waters is also responsible for an increase in the viscosity of the air–sea boundary layer. This, in turn, affects the damping and initiation of Bragg waves (Zheng et al., 1997);
4. rain may produce low–backscatter signatures in SAR imagery through two distinct processes. First, atmospheric attenuation due to volume scattering will tend to decrease the total NRCS observed over an area under rain. Second, depending on the wind speed and Bragg wave scale, raindrop impact on the sea surface may tend to dampen the Bragg waves in the impacted region (Melshelmer et al., 1996; Clemente-Colón & Yan, 2000);
5. sea ice can also dampen ocean surface waves. In particular, grease ice (composed of small millimeter–sized frazil crystals that form when seawater begins to freeze) (Clemente-Colón & Yan, 2000);
6. suspended matter (sediments) in estuarine plumes may also contribute to locally decrease the sea surface roughness, and may potentially look like typical oil

spills in signature in SAR data. For this reason, the use of ocean colour (visible data) can bring useful information to resolve ambiguous targets (Cedre, 2007);

7. floating algae are non–planktonic species most of which perform photosynthesis. They are commonly classified into two groups: macro–algae, such as seaweed and micro–algae, such as filamentous cyanobacteria. They are also divided into three groups based on their photosynthetic pigments: Phaeophyta (the browns), Rhodophyta (the reds) and Chlorophyta (the greens), but can also appear in various other colour combinations (yellow or silvery grey). They are capable of regulating their buoyancy to modulate their photosynthetic activity to adapt to the changing lighting levels and to protect themselves from excessive radiation (Franklin & Forster, 1997). Therefore, they can be located in the top layer of water to access more light from the photic region or at the water surface instead of being uniformly mixed in the water column (Paerl & Ustach, 1982; Sellner, 1997). Texturally, surface blooms are often characterized by their thick extensive mats or scum that look like oil slicks or slightly foamy pollution; and
8. cloud shadows (for optical sensors only) can sometimes be mis–classified as oil spills, because clouds obscure the sun irradiance from reaching the water surface, which leads to a signal reduction in the upwelling radiance and causes them to superficially appear dark as oil (Pavia & Payton, 1983).

A multi–spectral optical sensor has an advantage over the SAR sensor (except in cloudy and night conditions) for retrieving the spectral properties for some of the observed biological targets that float at the water surface (algal blooms) and can achieve better discrimination (Brekke & Solberg, 2005). Prior knowledge of local conditions, for example surface winds, currents and vessel traffic, can also play a role in improving the accuracy of detection and the reduction of false positives (Karathanassi et al., 2006).

3.4.5 MODIS: an example of an optical sensor

The Moderate Resolution Imaging Spectroradiometer (MODIS) is an example of a multi–spectral sensor on–board two satellites whose main role is to observe the changes in the Earth's atmospheric, oceanic, and terrestrial processes. The instrument has a scan mirror with coverage of $\pm 55^{\circ}$ from nadir that results in a cross track swath of 2330 km and an along track swath of 10 km at nadir, and views the entire surface of the Earth every one or two days (Visible Earth, 2010). It is dedicated to perform measurements

from TOA radiance in 36 spectral bands (Table 3.3, shown earlier in Table 1.1) in the solar to thermal infra-red spectrum region from 0.415 to 14.235 µm covering three spatial resolutions -- 250m, 500m, and 1000m (Salomonson et al., 1989).

Table 3.3. MODIS spectral bands with their corresponding spatial resolution (NASA, 2010).

Band[11]	Bandwidth[12]	Required SNR[13]	Band	Bandwidth	NE[delta]T(K)[14]
1	620 - 670	128	20	3.660 - 3.840	0.05
2	841 - 876	201	21	3.929 - 3.989	2
3	459 - 479	243	22	3.929 - 3.989	0.07
4	545 - 565	228	23	4.020 - 4.080	0.07
5	1230 - 1250	74	24	4.433 - 4.498	0.25
6	1628 - 1652	275	25	4.482 - 4.549	0.25
7	2105 - 2155	110	26	1.360 - 1.390	150 (SNR)
8	405 - 420	880	27	6.535 - 6.895	0.25
9	438 - 448	838	28	7.175 - 7.475	0.25
10	483 - 493	802	29	8.400 - 8.700	0.05
11	526 - 536	754	30	9.580 - 9.880	0.25
12	546 - 556	750	31	10.780 - 11.280	0.05
13	662 - 672	910	32	11.770 - 12.270	0.05
14	673 - 683	1087	33	13.185 - 13.485	0.25
15	743 - 753	586	34	13.485 - 13.785	0.25
16	862 - 877	516	35	13.785 - 14.085	0.25
17	890 - 920	167	36	14.085 - 14.385	0.35
18	931 - 941	57			
19	915 - 965	250			

MODIS has demonstrated its capability of detecting relatively large oil spills (~ 2000 pixels, at its maximum 250 m/pixel spatial resolution), particularly in regions that are characterised with ~ 80% cloud–free conditions like, for example, the ROPME Sea Area (RSA). Because MODIS is installed on–board two satellites (Terra and Aqua), its temporal resolution becomes relatively high (two passes per day about 1.5–2 hours apart) that enables it to detect the evolution of oil spills. Both Terra and Aqua platforms have a direct broadcast X–band downlink that allows its data to be received in real–time by sites having the proper reception stations (NASA, 2010). MODIS's high signal-to-noise ratio (SNR) and high stability for having narrower spectral bands improves its accuracy for the production of science data algorithms such as chlorophyll-a concentration and sea surface temperature (Esaias et al., 1998). Table 3.4 shows a summary of MODIS's technical specifications.

[11] Bands 1-2 are in 250m/pixel, bands 3-5 are in 500m/pixel and remaining bands are in 1000m/pixel resolutions

[12] Bands 1 to 19 are in nm; Bands 20 to 36 are in µm

[13] SNR = Signal-to-noise ratio

[14] NE(delta)T = Noise-equivalent temperature difference

Table 3.4 Technical specifications of MODIS (Visible Earth, 2010).

Orbit	705 km, 10:30 a.m. descending node (Terra) or 1:30 p.m. ascending node (Aqua), sun–synchronous, near–polar, circular
Scan rate	20.3 rpm, cross track
Swath	2330 km (cross track) by 10 km (along track at nadir)
Telescope	17.78 cm diam. off–axis, afocal (collimated), with intermediate field stop
Data Rate	10.6 Mbps (peak daytime); 6.1 Mbps (orbital average)
Quantization	12 bits
Design life	6 years

3.4.6 Oil spill detection using MODIS

Hu et al. (2003) investigated the usage of MODIS in delineating historical oil spill incidents in and around Lake Maracaibo in Venezuela. The negative–contrasted spills (dark relative to surrounding waters) were visible even when significant sun glint contamination was present. They dismissed them being attributed to phytoplankton blooms, firstly by using prior knowledge of the environment since the patterns did not fall within the seasonal bloom period; and secondly, because their spectral characteristics did not match that of algal blooms. They also pointed out that the degree of turbidity underneath and around the oil spill plays a role in deriving accurate results in such empirical approaches. They concluded their findings by stating that there is no good reason to downplay the potential of optical satellite sensors for the detection of oil spill events and highlighted the need to develop good empirical algorithms to derive oil film thickness supported by *in–situ* measurements. Shi et al. (2007) used a fuzzy C–means (FCM) cluster algorithm with a texture feature analysis to delineate an oil spill in MODIS imagery. They estimated the degree of disorganization in the pixels' direction by applying a mathematical process based on the Gray Level Co–occurrence Matrix (GLCM) in pixels. In doing so, they have managed to delineate the oil spill area, as well as the shoreline regions, because oil like the shorelines exhibit the most rapid changes in pixel values, in relation to the moderately uniform water background. They concluded that their method was effective when the implementation is localised only on the spill and not performed on the image as a whole, since other parts of the image may have similar reflectance as the oil spill, such as high sediment loads. Their research also found no distinct temperature variations between the spill and its surrounding water. Shaban et al. (2007) studied the spills in MODIS data that resulted from the bombing of

oil tanks at Jiyeh power station in Lebanon and showed that they were clearly delineated in the images. Chuanmin Hu et al., (2009) used MODIS imagery to estimate the surface area of natural oil slicks in the NW Gulf of Mexico. In some images the spills have shown both negative and positive slick contrasts. The negative contrast can be explained as a reduction in glint due to dampening of the surface roughness, while the positive contrast results from higher specular reflection within the oil film patch.

In all of the aforementioned papers, it is clear that MODIS data was only utilized to describe and delineate an already documented and identified oil spills, and none of them have demonstrated or argued whether it is possible to identify, using solely MODIS data, a suspected target as an oil spill. It is therefore the purpose of this research to develop new reliable methodologies whereby it becomes possible to detect unreported oil spills visible in MODIS images and discriminate them from look–alikes.

Chapter 4: Experimental procedure

4.1 Data sources

The MODIS data used in this study were acquired from three main sources: those received in near–real–time (NRT) by MODIS's satellite station installed at ROPME, Kuwait; the second source was from ROPME's archived library of MODIS that stores data from 2003; and lastly, that which was directly downloaded from the NASA ocean colour website[15], which was mainly used to compensate for the unavailability of NRT data or to acquire data covering regions other than the RSA (the selected area of study).

Microwave radar data were also used as supporting data for oil spill incidents observed in MODIS images. Radar data were acquired from the Advanced Synthetic Aperture Radar (ASAR) operating at C–band on-board the European Environmental Satellite (ENVISAT) launched in 2002. A registration with ESA under the category–1 proposal was sought to acquire different ASAR data modes (see Table 4.1).

Table 4.1. ASAR data modes were made available under the category–1 proposal registration (Desnos et al., 2007).

Product id	Name	Resolution (m)
ASA_GM1_1P	ASAR Global Monitoring Mode Image	1000
ASA_WSM_1P	ASAR Wide Swath Medium Resolution Image	150
ASA_APM_1P	ASAR Alternating Polarization medium resolution image with either HH or VV polarisation modes	30
ASA_IMM_1P	ASAR image mode medium resolution image	150

Data from the Medium Resolution Imaging Spectrometer (MERIS) sensor on-board the ENVISAT satellite were also used. MERIS is an optical sensor like MODIS, but operates at a ground spatial resolution of 300[16] m, in 15 spectral bands. MERIS undertakes global coverage of the Earth in 3 days and has a swath that covers a width of 1150 km.

Data from the thematic mapper (TM) sensor on–board the Landsat–4 satellite were also used in this project (Table 4.2). The data were downloaded from the Global Land

[15] Website: http://oceancolor.gsfc.nasa.gov/cgi/browse.pl?sen=am

[16] The original pixel size is 260 by 290 m in nadir and increases towards the edge of the swath, but the full resolution (FR) data are spatially integrated to an equal grid with a pixel a size of 300 by 300 m (North et al., 2009).

Cover Facility (GLCF)[17].

Table 4.2. The spectral characteristics of Landsat–4 (TM) bands.

Band Number	Bandwidth (μm)	Resolution (m)
1	0.45–0.52	30
2	0.52–0.60	30
3	0.63–0.69	30
4	0.76–0.90	30
5	1.55–1.75	30
6	10.4–12.5	120
7	2.08–2.35	30

The high–resolution data (Table 4.3) provided by the optical imaging Earth observation satellite SPOT 5[18] were also used .

Table 4.3. The spectral characteristics of SPOT 5 bands.

Band Number	Bandwidth (μm)	Resolution (m)
1	0.50–0.59	20
2	0.61 – 0.68	20
3	0.78 – 0.89	20

Ocean surface wind vectors at 10 m above sea level were acquired at 25 km/pixel resolution using the observation data from NASA/JPL's SeaWinds Scatterometer[19] on-board the QuikSCAT satellite which was launched in 1999. QuikSCAT's nominal mission, however, ended on 23rd November, 2009, hence data became unavailable after that date. It has, nevertheless, remained a useful source for retrieving historical data. To compensate for the loss in wind vector data, a 50 km resolution surface wind dataset was used from the European Advanced Scatterometer (ASCAT)[20] system aboard the EUMETSAT METOP satellite launched in 2006.

Data pertaining to the characteristics and properties of oil involved in the detected spills were used from the website of Emergencies Science and Technology (a division

[17] http://glcf.umiacs.umd.edu

[18] Website: http://www.spotimage.com

[19] Websit: http://www.ssmi.com/qscat/scatterometer_data_daily.html

[20] Website: http://manati.orbit.nesdis.noaa.gov/datasets/ASCATData.php

of Environment Canada) (ESTC) Oil Properties Database[21] – provided that the identity of the oil was determined and its properties were available online. The location and names of the major offshore oilfields distributed across the RSA were retrieved from a geographic information system (GIS) map provided by Garmin Mapsource (version 6.13.7).

4.2 MODIS receiving station

The MODIS receiving station (Figure 4.1) was established by the Regional Organisation for the Protection of Marine Environment (ROPME) in 2003. The station receives two daily and two nightly passes from the Terra and Aqua satellites at 1° footprint in order to cover the whole of the ROPME Sea Area (RSA).

Figure 4.1. ROPME's MODIS antenna system in Kuwait.

4.3 Calibration of MODIS data

Various on-board calibration procedures are performed regularly on the MODIS sensor in both Terra and Aqua satellites. In addition, global *in situ* data are also being collected and updated to complement MODIS data and its algorithms. After which, code look–up tables (LUTs) are updated accordingly and made available for the MODIS global user group to download and implement in their processing algorithms.

[21] Website: http://www.etc-cte.ec.gc.ca/databases/OilProperties/oil_prop_e.html

The uncertainties involved in the estimates of MODIS biological or geophysical data products are contingent on the uncertainties of their model input parameters including those results arising from the calibration procedures. NASA, however, have set an accuracy requirement for water–leaving radiance to be within ±5% with regard to ocean colour products (Hooker et al., 1992). The following is a summary of the calibration processes that regularly take place within MODIS.

4.3.1 On-board calibration

MODIS has four on-board calibrators: the Solar Diffuser (SD) with two levels of irradiance; the Solar Diffuser Stability Monitor (SDSM), which compares the SD irradiance levels to direct solar view levels; the Spectro Radiometric Calibration Assembly (SRCA); and the ambient or heated Black-body (BB). In addition to these calibrators, MODIS has two electronic calibration (Ecal) processes for the different detector types to perform checks on the linearity of the on-board electronics (Hatten et al., 1999). A space view (SV) port measures deep space (cold space) to provide the sensor with a response of zero input source that is used also for lunar calibration when the moon is in the field of view (Guenther et al., 1995).

The SD/SDSM system is used to calibrate the SD bi–directional reflectance distribution function (BRDF) of the MODIS reflective bands (1 – 19 and 26). Changes are measured by comparing the SD/SDSM reference pre–launch calibration data to the data collected on–orbit (Hatten et al., 1999).

The SRCA operates in three different modes to calibrate the MODIS lens system. It provides radiometric calibration for the reflective bands. It also provides spectral characterization of the reflective bands by determining the centre wavelengths through the use of a diffraction grating. Additionally, the SRCA monitors spatial characterization of all detectors by determining the along–scan and along–track spatial co–registration (Hatten et al., 1999).

The black–body serves as the first of two calibration targets for the thermal bands. It can be viewed at ambient temperatures, approximately 270 K, or its temperature can be increased and stabilized at any level up to 315 K. Both sides of the MODIS rotating scan mirror are utilized to view the black–body, so calibration is expected to be mirror–side independent (Hatten et al., 1999). The second thermal calibration target, is a view of space that applies to bands 20–25 and 27–36. The two black–body measurements, together with the measurement from the space view (SV), are used as reference points

for the determination of the radiometric calibration of the thermal bands in each scan (Hatten et al., 1999). It can also be used to obtain the zero offset for the detectors in the reflected solar portion of the spectrum (Guenther et al., 1995).

Specific tables can be up–loaded to the orbit instrument. These tables contain values such as detector gains and offsets that may be changed in orbit. This data can include operating code as well as any one of 20 look–up tables (Hatten et al., 1999).

Some LUTs were derived from pre–launch calibration and characterization, such as the relative spectral response (RSR); the temperature correction coefficients; and the corresponding reference temperatures. Other LUT's are derived from on-orbit measurements and updated as needed, such as the RSB response versus scan angle (RVS) and SD calibration coefficients (Xiong et al., 2005). To maintain quality assurance of the processed NRT data during this study, LUT were continuously updated from the NASA ocean colour group website, whenever new files were made available.

4.3.2 Spacecraft (S/C) manoeuvres

Satellite orbit manoeuvres are mainly drag make–up manoeuvres designed to counteract the effects of atmospheric drag, and occasionally, inclination adjustment manoeuvres, that are performed every 2 to 3 months from launch to maintain the satellite repeat cycle (Wolfe et al., 2002). Although MODIS will occasionally view the moon through the Space View Port (SVP) while the spacecraft is in its normal orientation, the roll manoeuvre permits the moon to be viewed and used as a calibration source for long term stability and cross–calibration of MODIS. This event will nominally occur up to 7 times/year, with a duration of approximately 15 minutes (Hatten et al., 1999). Depending on the timing of these manoeuvres, the NRT reception of passes in the RSA is occasionally interrupted.

4.3.3 Code–related calibrations

The MODIS Level 1B (L1B) code look–up tables (LUTs) are organized into three calibration groups: one for the thermal emissive bands (TEB), another for the reflective solar bands (RSB), and a third for quality assurance (QA). Each individual LUT is implemented in the appropriate Hierarchical Data Format (HDF) file format as either a global attribute or a Scientific Data Set (SDS) (Xiong et al., 2005). The HDF – Earth Observing System (HDF–EOS) is the standard format used to store data collected from EOS satellites, in a versatile data model that can assist users in the storage and

manipulation of scientific data across diverse operating systems and machines (Fortner, 1998). It is this format that is used throughout this study.

4.4 MODIS data formats

MODIS data are received immediately in direct broadcast (DB) mode. The data are made up of raw (not synchronized) telemetry packets (typical day pass size is ~ 1614 MB and a typical night pass size is ~ 1200 MB). After which the data are decoded and time–ordered into the Consultative Committee for Space Data Systems[22] (CCSDS) format, with all the communication artefacts (e.g. synchronization frames, communication headers and duplicate packets) removed to create a compatible Level 0 (L0) file or the Production Data Set (PDS) format (typical day pass size is ~ 980 MB and a typical night pass size is ~ 280 MB), after adding additional construction records and file name conventions (Strabala et al., 2003; PML, 2010). Then, the Level 1A code organizes the L0 file into a set of small portions of scanned data or granules (typical L1A day pass size is ~ 1364 MB and a typical night pass size is ~ 485 MB), each of which contain approximately 5 minutes of MODIS data (Toller et al., 2003) containing the digitized counts for the 36 MODIS channels; the raw instrument engineering and spacecraft ancillary data; quality indicators to indicate missing or bad pixels; and the instrument's working mode. Visible, short–wave infra–red (SWIR), and near infra–red (NIR) measurements are made during daytime only at 250, 500, and 100 m resolutions, while the data received from the thermal infra–red (TIR) are measured during both the day and night portions, but at 1000 m resolutions only.

A MODIS geolocation file (GEO) (typical file size is ~ 152 MB) is produced using the attitude and ephemeris (satellite position) data files, which are embedded in Terra's data stream. The attitude and ephemeris data files in the Aqua satellite, however, are processed separately after receiving its L0 file. This is so because Aqua's position is not encoded in its L0 file as is the case with Terra (Strabala et al., 2003). The MODIS GEO file defines the geodetic latitude and longitude (WGS–84), sensor and solar geometry, slant range, and terrain height of the sensed MODIS 1km observations, that are subsequently used to spatially re–sample and temporally composite MODIS products into georeferenced grids (Wolfe et al., 2002). The positions of the 1 km bands are registered to within 73 m, the 500 m bands to 67 m, and the 250 m bands to 5 m (Wolfe et al., 2002).

[22] http://public.ccsds.org/default.aspx

Level 1B (L1B) processing is then applied to L1A data to produce the calibrated top–of–atmosphere (TOA) radiance data in three separate files (for day passes only) corresponding to the three distinct spatial resolutions of 250 m (size ~ 698 MB), 500 m (size ~ 671 MB) and 1 km (size is ~ 838 MB). During night passes however, the 1 km file that includes the TIR radiances (size is ~ 370 MB), is the only file that is produced. Each of the L1B files contains the associated uncertainty indices; the meta–data that include a wide variety of ancillary and quality assurance (QA) flags; and the geolocation data covering the latitude and longitude of a subset of pixels for the centre of each of the 1 km pixels, if interpolation is to be implemented (Toller et al., 2003). The calibration accuracy requirements at the typical scene radiance are ±2% for the RSB reflectance factors and ±5% for the RSB radiance product. For the TEB radiance product, the requirements are ±1% except ±0.75% for band λ_{20}=3.75 μm, ±10% for band λ_{21}=0.50 μm (a fire detection low gain band), and ±0.5% for bands λ_{31}=11.03 and λ_{32}=12.02 μm (for sea surface temperature) (Xiong & Barnes, 2006).

True and false red–green–blue (RGB) spectral colour images are generated at different spatial resolutions by combining their respective spectral bands from the corresponding HDF L1B files. If the images are to be geographically referenced (a swath–to–grid conversion) in order to produce geotiff files, a universal transverse mercator (UTM) projection is used as well as the cubic convolution (CC) interpolation method for re–sampling. The RGB colour composites that are used in the production of geotiffs are: the 500 m/pixel resolution natural colour composite corresponding to bands λ_1=645 (aggregated from the 250 m resolution band group), λ_4=555 and λ_3=469 nm respectively; and the 250 m/pixel resolution false RGB colour composite corresponding to bands λ_2=859, λ_1=645 and λ_1= 645 nm respectively. The 500 m resolution geotiff file is produced for the full swath (size ~ 400 MB). Whereas, the corresponding 250 m resolution file is sub–divided into three separate geotiff files to reduce the overall size (~ 1800 MB), such that the full RSA or most of it is included in one of its subsets (size ~ 530 MB).

Whenever geo–referencing is performed, a correction is applied to overcome the MODIS bow–tie effect shown in Figure 4.2. This effect is caused by the double–sided scan mirror that sweeps out a 110° Earth field of view in each scan (scan angles of ± 55°). Effectively moving the instrument's ten spatial elements over a swath of the Earth 10 km wide at nadir and, thus, the scan width increases to 20 km (Nishihama et al., 1997). Therefore, the adjacent scans begin to overlap away from nadir with a 10%

overlap occurring at scan angles of 24° , making the pixels of an image become bigger near the edge than the ones in the middle (Wolfe et al., 2002).

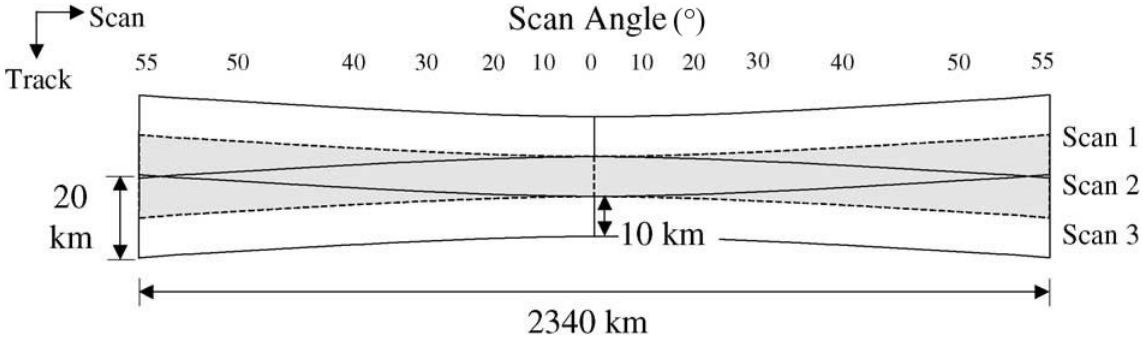

Figure 4.2. Ground projection of three consecutive MODIS scans showing the scan geometry and the ‘‘bow–tie’’ effect (along–track dimension exaggerated). The area sensed by Scan 2 is highlighted (grey), showing the overlap between it and the two adjacent scans (Wolfe et al., 2002).

The Level2 (L2) products are then processed from the L1B after applying atmospheric correction. The main data contents of the L2 products are geophysical values (such as sea surface temperature) for each pixel, including flags indicating any algorithm failures or warning conditions that occurred during processing each pixel (OceanColor, 2010). The different stages of processing used in thesis are shown in Figure 4.3 together with the level of data produced in each stage.

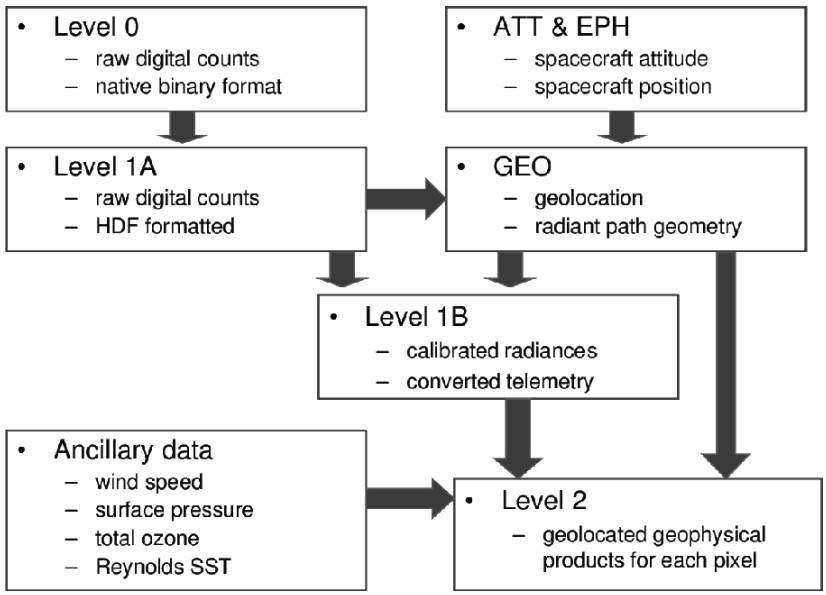

Figure 4.3. The production flow of the different MODIS data levels (Franz, 2007).

4.5 MODIS L2 products

Several L2 products were processed (see Section 4.9) to serve the purpose of this research, by first applying an atmospheric correction operation to remove the effects of the atmosphere and to retrieve the water–leaving radiance data. The following section will describe the main L2 products used in this project and the parameters associated with them.

4.5.1 Top–of–atmosphere reflectance (ρ)

MODIS L1B files contains the calibrated top–of–atmosphere (TOA) radiance data (L_t), which quantify the solar power reflected from the surface of the atmosphere and received by the sensor at a certain angle of view. Reflectance on the other hand is the percentage of light incident on a surface that is then reflected by that material which is independent of solar illumination, unlike water leaving radiance (Otremba & Piskozub, 2001). Theoretical studies have shown that reflectance may be related to the inherent optical properties of the water column (the backscattering and absorption coefficients, e.g. Gordon et al. 1988b) and represents the link between *in situ* ocean optical properties and satellite–derivable quantities (Garver et al., 1994). Reflectance is given by following relationship:

$$\rho_t(\lambda) = \frac{\pi L_t(\lambda)}{F_0(\lambda)\cos\theta} \tag{4.1}$$

where L_t is the calibrated TOA radiance; F_0 is the extra–terrestrial mean solar irradiance; and θ is the solar zenith angle.

4.5.2 Aerosol optical thickness or depth (τ)

The spectral dependence on the aerosol optical thickness (τ) is used to define aerosols' size distribution (King et al., 1978). Aerosols are formed by two main processes: a primary source which includes the dispersion of material from the Earth's surface (such as soil dust, sea salt particles, biomass burning, industrial debris), and a secondary source resulting from atmospheric chemical reactions, condensation, or coagulation processes (Mészáros, 1981).

The TOA reflectance received at a sensor ρ(λ) can be divided into the following components:

- $\rho_{path}(\lambda)$ which is the atmospheric path reflectance that includes multiple scattering caused by gas molecules (Rayleigh), the atmospheric aerosols, and the

interaction between Rayleigh and aerosol scattering;

- $\rho_g(\lambda)$ which is the contribution arising from specular reflection of direct sunlight from the sea surface (sun–glint);
- $\rho_{wc}(\lambda)$ which is the contribution arising from sunlight and skylight reflecting from individual whitecaps at the sea surface; and,
- $\rho_w(\lambda)$ which is the desired water–leaving reflectance, which are collectively expressed as such (Gordon & Voss, 1999):

$$\rho_t(\lambda) = \rho_{path}(\lambda) + t(\lambda)\rho_g(\lambda) + T(\lambda)\rho_{wc}(\lambda) + T(\lambda)\rho_w(\lambda) \tag{4.2}$$

where t and T are the direct and diffuse transmittance of the atmosphere respectively. When the value of $\rho_g(\lambda)$ is large, the imagery becomes virtually useless and it would need to be discarded or masked to remove the severely affected pixels. To relate the derived water–leaving reflectance to the inherent optical properties of the ocean, all geometric influences on $\rho_w(\lambda)$ must be eliminated. This is done by normalizing the water–leaving reflectance $\rho_{nw}(\lambda)$ defined as:

$$\rho_{nw}(\lambda) = \frac{\rho_w(\lambda)}{T(\lambda)} \tag{4.3}$$

In general, ρ_{path} can be decomposed into several components:

$$\rho_{path}(\lambda) = \rho_r(\lambda) + \rho_a(\lambda) + \rho_{ra}(\lambda) \tag{4.4}$$

where

- ρ_r is the reflectance resulting from multiple Rayleigh scattering in the absence of aerosols;
- ρ_a is the reflectance resulting from multiple scattering by aerosols in the absence of the atmospheric molecules; and,
- ρ_{ra} is the interaction term between molecular and aerosol scattering (Deschamps et al., 1983; Antoine & Morel, 1998).

The term ρ_{ra} is assumed zero in a single scattering case, in which photons are only scattered once, and it can be ignored as long as the amount of multiple scattering is a minimum, i.e., at small Rayleigh and aerosol optical thickness (Gordon et al., 1988a). According to the single scattering approximation, the single scattering aerosol reflectance ρ_{as} is approximated by Gordon & Voss (1999):

$$\rho_{as}(\lambda) \approx \frac{\tau(\lambda)\omega_0 P(\Theta, \lambda)}{4\cos(\theta)\cos(\theta_v)} \tag{4.5}$$

where θ, θ_v are the respective solar and viewing zenith angles; ω_0 and $P(\Theta)$ are the single scattering albedo (which is the probability that a photon will be scattered when it interacts with the atmosphere), and the phase function of scatterers and absorbers in the atmosphere respectively. The wavelength dependence of τ can also be approximately given by:

$$\tau(\lambda) \approx \beta\lambda^{-\alpha} \tag{4.6}$$

where β is the extinction coefficient at 1 μm and α is the aerosol Ångstrom coefficient (Hulst, 1981; Gregg & Carder, 1990). This formula is valid for all wavelengths only if the particle size distribution fits a Junge power law function (Junge, 1963; Hess et al., 1998). From Equation 4.6, the following expression may be derived:

$$\frac{\tau(\lambda_i)}{\tau(\lambda_j)} \approx \left(\frac{\lambda_j}{\lambda_i}\right)^{\alpha} \tag{4.7}$$

Gordon & Wang (1994a, 1994b) have defined the atmospheric correction parameter $\varepsilon(\lambda_i,\lambda_j)$ as a function of ρ_{as}:

$$\varepsilon(\lambda_i, \lambda_j) \approx \frac{\rho_{as}(\lambda_i)}{\rho_{as}(\lambda_j)} \tag{4.8}$$

Physically, $\varepsilon(\lambda_i, \lambda_j)$ represents the relative strengths of the aerosol scattering and absorption, which is largely independent of the power of the illumination incident upon the aerosol particles, viewing geometry, and the concentration of aerosol particles present. It is therefore, assumed constant everywhere in an image in which the aerosol type does not change from one position to another (Carder et al., 2002).

For large, iron–rich, desert dust particles (as in the RSA), the ratio of aerosol reflectance at 550 nm and 670 nm, $\varepsilon(550, 670)$, has been shown using the coastal zone colour scanner (CZCS) data to decrease to 0.94 and below (Carder et al., 1991) during strong dust events, whereas typical values of 1.0–1.5 are found for smaller, non–iron–bearing aerosols. In such cases, where aerosol reflectance is lower in the blue than in the green or red, strong absorption is likely to be present (Carder et al., 2002). Using Equations 4.5 and 4.8 to link $\varepsilon(\lambda_i,\lambda_j)$ to τ and λ:

$$\varepsilon(\lambda_s, \lambda_l) = \frac{\tau(\lambda_s)\omega_0(\lambda_s)P(\Theta, \lambda_s)}{\tau(\lambda_l)\omega_0(\lambda_l)P(\Theta, \lambda_l)} = \frac{\omega_0(\lambda_s)P(\Theta, \lambda_s)}{\omega_0(\lambda_l)P(\Theta, \lambda_l)}\left(\frac{\lambda_l}{\lambda_s}\right)^{\alpha} \tag{4.9}$$

where the subscript s and l stand for short and long NIR bands respectively which, in the case of MODIS, correspond to (λ_{15}=748 nm) and (λ_{16}=869 nm) respectively (Gordon & Voss, 1999).

According to the black pixel assumption, in clear open ocean waters (except in the glint region), the water–leaving reflectance (ρ_w) is generally taken to be negligibly small in the NIR bands ($\lambda > 650$ nm), and therefore all radiance in these bands will result from scattering within the atmosphere (Siegel et al., 2000). Therefore, combining Equations 4.2, and 4.5 at $\rho_w(\lambda_{NIR}=0)$ will yield:

$$\rho_t(\lambda) = \rho_r(\lambda) + \rho_{as}(\lambda) + T(\lambda)\rho_{wc}(\lambda) \tag{4.10}$$

The parameters $\rho_{as}(748)$ and $\rho_{as}(869)$ can be evaluated using Equation 4.5. $\rho_r(\lambda)$, $T(\lambda)$ and $\rho_{wc}(\lambda)$ were computed from LUTs and ancillary data to provide estimates of surface atmospheric pressure and surface wind speeds. $\varepsilon(748, 869)$ can then be computed from Equation 4.9, after which a suitable LUT created from 12 different aerosol models at a variety of sun–view geometries and aerosol loadings can be selected (Shettle & Fenn, 1979). These models were updated and modified by measurements collected from a network of sun/sky radiometers globally distributed to perform such measurements (Holben et al., 1998), and from which the values α and τ were estimated. The quantities determined from $\varepsilon(748, 869)$, were then extrapolated into the visible to obtain $\varepsilon(\lambda, 869)$; and hence $\rho_{as}(\lambda)$ to evaluate $\rho_w(\lambda)$ from Equation 4.2.

NASA Ocean Biology Processing Group (OBPG) adopts the iterative method developed by Siegel et al., (2000) to correct for non–negligible water reflectance in the NIR arising from moderate to high phytoplankton abundances (chlorophyll concentrations greater than 3 mg/m^3). This iteration scheme is employed in the ocean colour processing algorithms used for MODIS (Stumpf et al., 2003), which entails an initial guess for Chlor-a to acquire an estimate for the $\rho_{nw}(\lambda_{NIR})$. $\rho_{nw}(\lambda_{NIR})$ is then removed from the reflectance (Equation 4.2) to apply the atmospheric correction method described earlier to retrieve a new Chlor-a value. This process is repeated until a converged Chlor-a value is obtained. This NIR correction procedure can be summarized schematically as follows:

$$\underbrace{Chlor\text{-}a_0}_{intitial} \xrightarrow{atmospheric\ correction} \underbrace{\rho_{nw}(\lambda_{NIR})\ \ and\ \ Chlor\text{-}a \rightarrow repeat}_{iterations} \tag{4.11}$$

The iterations are stopped once the final Chlor-a retrieval is within 20% of the last iterate (Siegel et al., 2000). If the first iterated Chlor-a value is less than 0.3 mg/m^3, the iterations are terminated (Siegel et al., 2000). Figure 4.4 summarizes these procedures implemented in performing the atmospheric correction operation in a flowchart format.

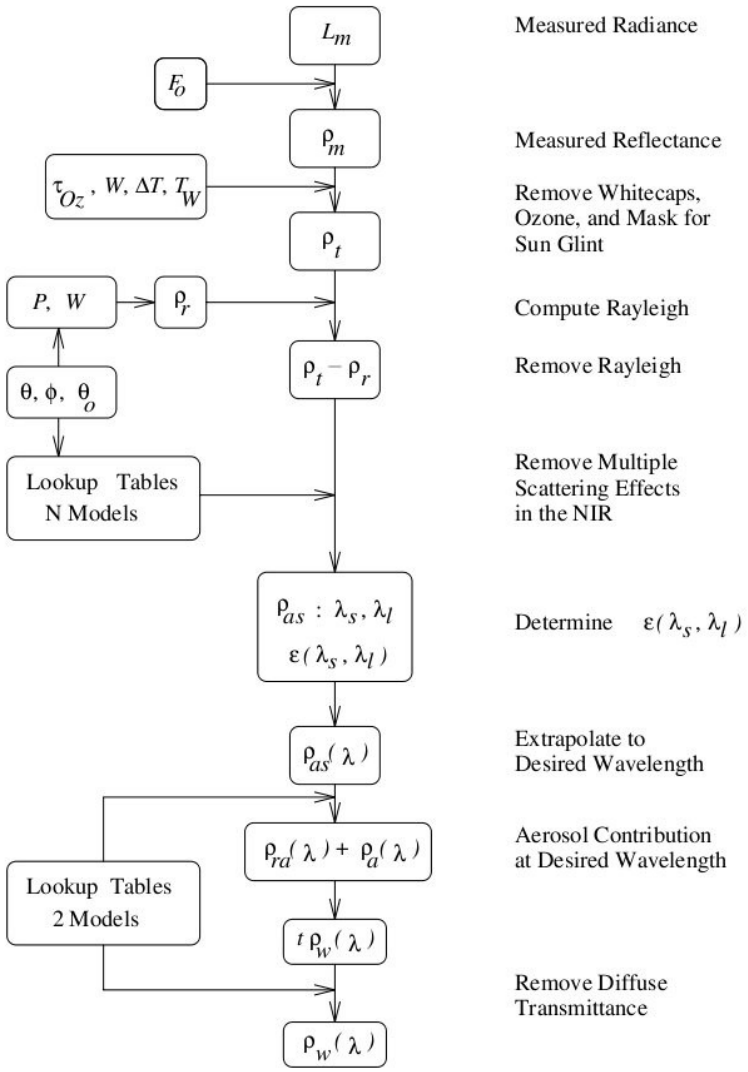

Figure 4.4. Annotated flowchart of the atmospheric correction procedure (Gordon & Voss, 1999).

4.5.3 Chlorophyll-a concentration (Chlor-a)

Variations in ocean colour are related to the concentration of phytoplankton in surface ocean waters. The standard MODIS Chlorophyll-a concentration (Chlor-a) product can be used as an indicator of plankton biomass, or to trace oceanographic currents, jets, and plumes (Carder et al., 2003).

Equations 4.12 and 4.13 show the general theoretical basis for a Chlor-a algorithm:

$$\log(Chlor_a) = c_0 + c_1 R + c_2 R^2 + c_3 R^3 + c_4 R^4 \qquad (4.12)$$

where c_0, c_1, c_2, c_3 and c_4 are empirically derived constants; and R at 1 km/pixel resolution is defined as:

$$10^R = \frac{max(\rho_{rs}(443), \rho_{rs}(488))}{\rho_{rs}(551)} \tag{4.13}$$

where the max (ρ_{rs} (443), ρ_{rs} (488)) is a shorthand representation, meaning the maximum of the two indicated waveband values; and ρ_{rs} is the remote sensing reflectance, defined as:

$$\rho_{rs} = \frac{L_{nw}(\lambda)}{F_0(\lambda)} \tag{4.14}$$

where F_0 is the extraterrestrial mean solar irradiance; and L_{nw} is the normalized water–leaving radiance, defined as the radiance that would be measured exiting a flat surface of the ocean with the sun at zenith (directly overhead) at no atmospheric interference (Gordon & Clark, 1981).

$$L_{nw}(\lambda) = \frac{L_w(\lambda)}{t(\lambda)\cos(\theta)} \tag{4.15}$$

where Lw is the water–leaving radiance; t is the atmospheric diffuse transmittance in the solar direction; and θ is the solar zenith angle.

At 1 km/pixel resolution, the MODIS Chlor-a algorithm is defined as:

$$\log(Chlor_a) = 0.283 - 2.753\mathrm{R} + 1.457\mathrm{R}^2 + 0.6591.457R^3 - 1.403\mathrm{R}^4 \tag{4.16}$$

Whereas at 500 m/pixel resolution, the MODIS Chlor-a algorithm is defined as:

$$\log(Chlor_a) = 0.1464 - 1.7953\mathrm{R} + 0.9718\mathrm{R}^2 - 0.8319\mathrm{R}^3 - 0.8073\mathrm{R}^4 \tag{4.17}$$

where R at 500 m/pixel resolution is defined as:

$$10^R = \frac{\rho_{rs}(469)}{\rho_{rs}(555)} \tag{4.18}$$

The ρ_{rs} in both Chlor-a algorithms must yield a positive value in order to produce a valid Chlor-a pixel value, otherwise a failed Chlor-a flag will be set instead at that particular pixel (Robinson et al., 2000). This failure can be caused by the presence of absorbing aerosols that cannot be detected by the atmospheric correction process (Werdell et al., 2007), causing an overestimation of the atmospheric contribution in all bands with increasing severity at shorter wavelengths, leading towards severe errors, if not total failure in the Chlor-a detection (Wang, 2000). When the Chlor-a value of a pixel is less than a minimum value of 0.001 mg/m^3 or greater than a maximum value of 100 mg/m^3, then a warning flag will be set instead (Robinson et al., 2000).

4.5.4 Sea surface temperature (SST)

The sea surface temperature (SST) or skin temperature is the water surface temperature at a depth of about 10 μm, which is different than the bulk temperature measured in the uppermost few metres of the ocean (Robinson, 2004). The SST variable characterises the emission and controls the IR brightness temperature[23] observed from space (OceanColor, 2010). Observable differences that exist between the bulk and radiation temperatures is caused either by the air–sea interaction that modifies the relationship between these two variables (Robinson et al., 1984) or it is caused by the diurnal heating conditions at low wind speed (Stramma et al., 1986).

Two SST products are generated from MODIS data at 1 km/pixel resolution. The first non–linear SST (Equation 4.19) calculated from the far IR bands at 11 and 12 μm, near the maximum emission for a 300 K black–body (an approximation for the average Earth temperature) (Brown & Minnett, 1999):

$$SST = a + bT_{31} + c(T_{31} - T_{32})T_{oisst} + d(T_{31} - T_{32})(sec(\theta) - 1) \quad (4.19)$$

where T_{31} and T_{32} are the brightness temperatures measured in bands (λ_{31}=11 μm) and (λ_{32}=12 μm) respectively; T_{oisst} is a first guess SST taken from a NOAA optimum interpolation SST (OISST); θ is the satellite zenith angle; and a, b, c and d are platform (Terra or Aqua) dependent coefficients (Brown & Minnett, 1999).

The second linear SST relationship (Equation 4.20) is calculated from the mid–IR bands channels, where the influence of column water vapour is minimal on the sensed radiances (Brown & Minnett, 1999):

$$SST4 = a + bT_{20} + cT_{23} \quad (4.20)$$

where T_{20} and T_{23} are the brightness temperatures measured in bands (λ_{20}=3.75 μm) and (λ_{23}=4.05 μm) respectively; and a, b and c are platform (Terra or Aqua) dependent coefficients (Brown & Minnett, 1999). The main disadvantage of SST4 is that the sun–glitter pattern can render a large fraction of the daytime swath unusable for its determination, which restricts its use to night–time, or to those parts of the daytime swath where the risk of glint contamination can be confidently discounted (Brown & Minnett, 1999).

[23] Equivalent black-body temperature determined using the Planck function .

4.6 MODIS L2 masks

A number of L2 masks were used in the processing operation to filter out features such as clouds, land and sun–glint in order to improve visualization and to test the quality of these masks for calibration purposes. The MODIS land/water mask is a static global 1 km resolution file, generated originally in 1993 based on the World Vector Shoreline (WVS) database, and was modified to include inland waterways, based on the World Data Bank (WDB) (OBPG, 2010a).

4.6.1 MODIS cloud mask

The MODIS cloud mask provides an estimate of whether a given MODIS field of view (FOV) is cloud free. It is a global Level 2 product generated daily at 1 km and 250 m spatial resolutions (Ackerman et al., 1998). Clouds are generally characterized by their higher reflectance and lower temperature than the underlying earth surface. However, many surface conditions reduce cloud–surface contrast in certain spectral regions, (e.g. bright clouds over snow and ice). Cloud types such as thin cirrus, low level stratus at night, and small cumulus clouds typically have low contrast with the underlying background (Ackerman et al., 1998).

Many of the single pixel tests rely on radiance (temperature) thresholds in the thermal infrared (IR) and reflectance thresholds in other bands. These thresholds are not constant but vary with surface emissivity, with atmospheric moisture and aerosol content, and MODIS viewing angle (MODIS Cloud Mask Team, et al., 2006). They are assigned four numerical levels of confidence flags assigned to each single pixel test based on a set of thresholds: 0.99 (confidence of clear), 0.95, 0.66 and less than 0.66. The individual confidence flags are then combined to produce the final cloud mask flag for the output file (MODIS Cloud Mask Team, et al., 2006). The uncertainty inherent in a threshold test is caused by instrument noise, inadequate characterization of the radiative properties of the earth surface, and variations in the atmospheric emission and scattering.

Visual inspection is an important first step in validating any cloud mask algorithm. More quantitative validation can be attained through direct pixel by pixel comparison

with collocated ground or instrument platform based observations, such as light detection and ranging (LIDAR) systems (MODIS Cloud Mask Team, et al., 2006).

4.6.2 Sun–glint/glitter mask

The term sun–glint or glitter indicates is the specular reflection of direct sunlight off the sea surface. Wang & Bailey (2000) have defined the normalized sun–glint radiance:

$$L_{GN}(\emptyset, \vec{W}) = \frac{L_g(\lambda)}{F_0(\lambda)t(\lambda)} \tag{4.21}$$

where the term ø represents viewing geometry, W is the wind vector, $F_0(\lambda)$ is the extraterrestrial solar irradiance (adjusted for the Earth–sun distance variations) and $t(\lambda)$ is the atmospheric direct transmittance. The sun–glint zone is normally masked, whilst analysing the water–leaving radiance. Pixels having L_{GN} values greater than or equal to 0.005 are masked, and therefore no further processing is necessary for retrieving ocean and atmospheric products (McClain et al., 1995).

4.7 Data prerequisite for processing

Several important ancillary input data sets are needed for the production of Levels 1 and 2: meteorological, ozone and the first SST guess (used in Equation 4.19). Such data can be retrieved either from near–real time (NRT) sources or from the climatology file already available from the OBPG. For the purpose of this research, during the NRT reception of MODIS data, the climatology file was used in the production of L2 data.

The NRT meteorological (MET) data were provided by the National Centres for Environmental Prediction (NCEP), which were available from the OBPG site and have already been quality–controlled and can be directly used into the processing (OBPG, 2010b).

The ancillary ozone data component of the atmosphere at a given time affects the atmospheric signal measured by a satellite and, therefore, its concentration needs to be taken into account and removed from the atmospheric signal. The ozone data sources are: Earth Probe Total Ozone Mapping Spectrometer (EPTOMS)[24], the primary source of ozone data, where the dataset consists of daily global maps of total column ozone over sunlit portions of the globe. It measures backscattered UV radiances in the 310–

[24] http://jwocky.gsfc.nasa.gov/eptoms/ep.html

380 nm region (OBPG, 2010b). Total Ozone Analysis from SBUV[25] and TOVS[26] (TOAST[27]) as a back–up source of ozone data.

The NOAA Optimum Interpolation Sea Surface Temperature (OISST)[28] file was used as input for the MODIS non–linear SST algorithm (Equation 4.19).

The "utcpole.dat" is the earth motion file that contains a record of the Earth's variable and slowing rotation with respect to Coordinated Universal Time (UTC); whereas the leapsec.dat file contains a record of the leap seconds that were designated by the International Earth Rotation Service (IERS) (D. Noerdlinger, 2010). Theses two additional ancillary files that are downloaded from the OBPG site every week are needed to maintain the accuracy of the generated geolocation (GEO) file that holds the pixels' earth location.

A Two–Line Element file (TLE), is a set of orbital elements that describe the orbit of earth satellites used to compute the precise position and velocity of the satellite using a mathematical model called the Simplified General Perturbations 4 (SGP4) (Hoots & Roehrich, 1988). The TLE file is sometimes referred to as the NORAD two–line file due to its format, which was specified by the North American Aerospace Defence Command (NORAD). The TLE was updated on a daily basis to guarantee the correct start and end times of passes and to accurately track the satellite's position as it passed over the station. Tracking the satellites was also possible, even when the TLE file is up to two days old. However, using TLE files older than two days may either cause a deterioration in the acquisition signal or total loss, particularly at high elevation passes.

4.8 Missing data

The near–real–time (NRT) data that was used in this research was occasionally interrupted either due to complete loss of reception or data was obscured by clouds,

[25] Solar Backscatter UltraViolet Version 2 (SBUV/2).

[26] Advanced Tiros-N Operational Vertical Sounder (TOVS).

[27] http://www.osdpd.noaa.gov/ml/air/toast.html

[28] http://www.esrl.noaa.gov/psd/data/gridded/data.noaa.oisst.v2.html

thick dust storms and sun–glint, in which case, it becomes virtually impossible to conduct any image interpretation or analysis of the marine area The disruption in data flow is caused by a number of factors: satellite performing a routine drag or inclination manoeuvres at the time of capture; failure of the station's instruments such as the failure of the low–to–noise–amplifier (LNA) or GPS unit. Hardware and software failures were sometimes experienced on-board the satellites.

An old TLE file (i.e. more than 2 to 3 days old) can cause the signal to deteriorate due to misalignment between the satellite track and the antenna. This can cause the appearance of gaps within the image (that is, loss of data frames), particularly at the nadir positions. In such circumstances, it was sometimes possible to retrieve the data a day later by directly downloading them from the OBPG website[29].

4.9 Processing software and tools

Different software packages were used to perform different processing tasks and analysis during this research. A Linux operating system was installed and used because most of the software packages were linux-based systems.

Ingesting raw telemetry data to produce the L0 file, was executed using the Java application real–time software telemetry processing system (RT–STPS, version 4.1). The ground–based attitude determination science processing algorithm (GBAD) was used on the L0 or PDS file to create the ephemeris and attitude files, for the Aqua satellite only. Both the RT–STPS and GBAD scripts were freely downloaded from the NASA Goddard Space Flight Center's (GSFC) Direct Readout Laboratory (DRL)[30].

For the day swaths, a low resolution natural RGB colour image was produced from the L0 file using the software tool “eoslzx–free”, that was originally downloaded from Dundee Satellite Systems[31]. This natural RGB colour combination corresponded to bands λ_1=645, λ_4=555 and λ_3=469 nm respectively. Whereas for the night swaths, a false RGB colour composite was produced instead corresponding to bands λ_{20}=3.75, λ_{22}=3.959 and λ_{29}=8.55 μm respectively. These low resolution images were generated to provide a rapid assessment of the data quality in terms of showing any missing data or cloud and/or dust coverage over the RSA.

[29] http://oceancolor.gsfc.nasa.gov/cgi/browse.pl?sen=am

[30] http://directreadout.sci.gsfc.nasa.gov/index.cfm?section=downloads&page=technology

[31] http://www.sat.dundee.ac.uk/~arb/eoslzx-free/

The MODISL1DB is a MODIS Level–1 Direct Broadcast (DB) command–line driven software, used for processing the MODIS Aqua and Terra L0 data files to produce the L1A and L1B data files. The MODISL1DB was provided by the OBPG, together with the SeaWiFS Data Analysis System (SeaDAS, version 6.0). SeaDAS was mainly used to produce the MODIS L2 data products and its associate cloud, land, and sun–glint masks; and also to display and analyse all MODIS data levels.

To produce the different geotiff file formats at different RGB colour composites, the MODIS re–projection tool swath (MRTSwath, version 2.1) was utilized[32].

The Basic ENVISAT Toolbox for (A)ATSR and MERIS (BEAM, version 4.8)[33] is an open–source java–based toolbox that was mainly used to view the geotiff, L1B and L2 MODIS files, by using one of BEAM's main components VISAT. VISAT is a desktop application developed for the visualization, analysing and processing of earth observation (EO) data. It was mainly used for performing spectral mixing, mathematical calculations; and histogram stretching. ENVI, a product of ITT Visual Information Solutions (ITT VIS), was occasionally used for the visualization digital imagery, though not as extensively as VISAT. The raster capabilities of Photoshop were utilized while investigating the shape properties of oil spills and their look–alikes, by applying its various edge enhancement filters. For statistical analysis, the Gnu Regression Econometrics and Time–series Library (GRETL, version 1.9.2)[34] was used. The Earth Observation Link (EOLi) is the European Space Agency's (ESA) java–based client that was used to browse, preview and order ASAR data.

4.10 Data processing procedures

The scheduling of passes over the RSA was carried out at about 04:00 UTC[35] each day starting with a download of the Two–Line Element file (TLE). The TLE file includes the orbital elements that describe the designated orbit of Terra and Aqua satellites. Accordingly, four nadir passes were selected (that is a day and night pass for each of the two satellites), covering most of or all of RSA. To maintain the accuracy of the generated geolocation (GEO) file, the two ancillary files utcpole.dat and leapsec.dat, were updated on weekly intervals. After which, the following process was automated

[32] https://lpdaac.usgs.gov/lpdaac/tools/modis_reprojection_tool_swath

[33] http://www.brockmann-consult.de/cms/web/beam/welcome

[34] http://gretl.sourceforge.net/

[35] Coordinated Universal Time

using a custom–written script: sending the telemetry data to the antenna motion controller; processing all MODIS levels to L2; and generating the false and natural geotiff RGB colour composites. Table 4.4 outlines the automated tasks and packages that were used together with their sources.

Table 4.4. The automated processing tasks with the packages used and their sources.

Data level	**Software & packages used**	**Source of packages**
Raw telemetry data to L0	RT–STPS	NASA Goddard Space Flight Centre's (GSFC) Direct Readout Laboratory (DRL)
L0 to L1A, GEO, L1B and L2	MODISL1DB and SeaDAS	OBPG

The antenna system and its associate hardware configuration used for its control and the processing of data are shown in Figure 4.5.

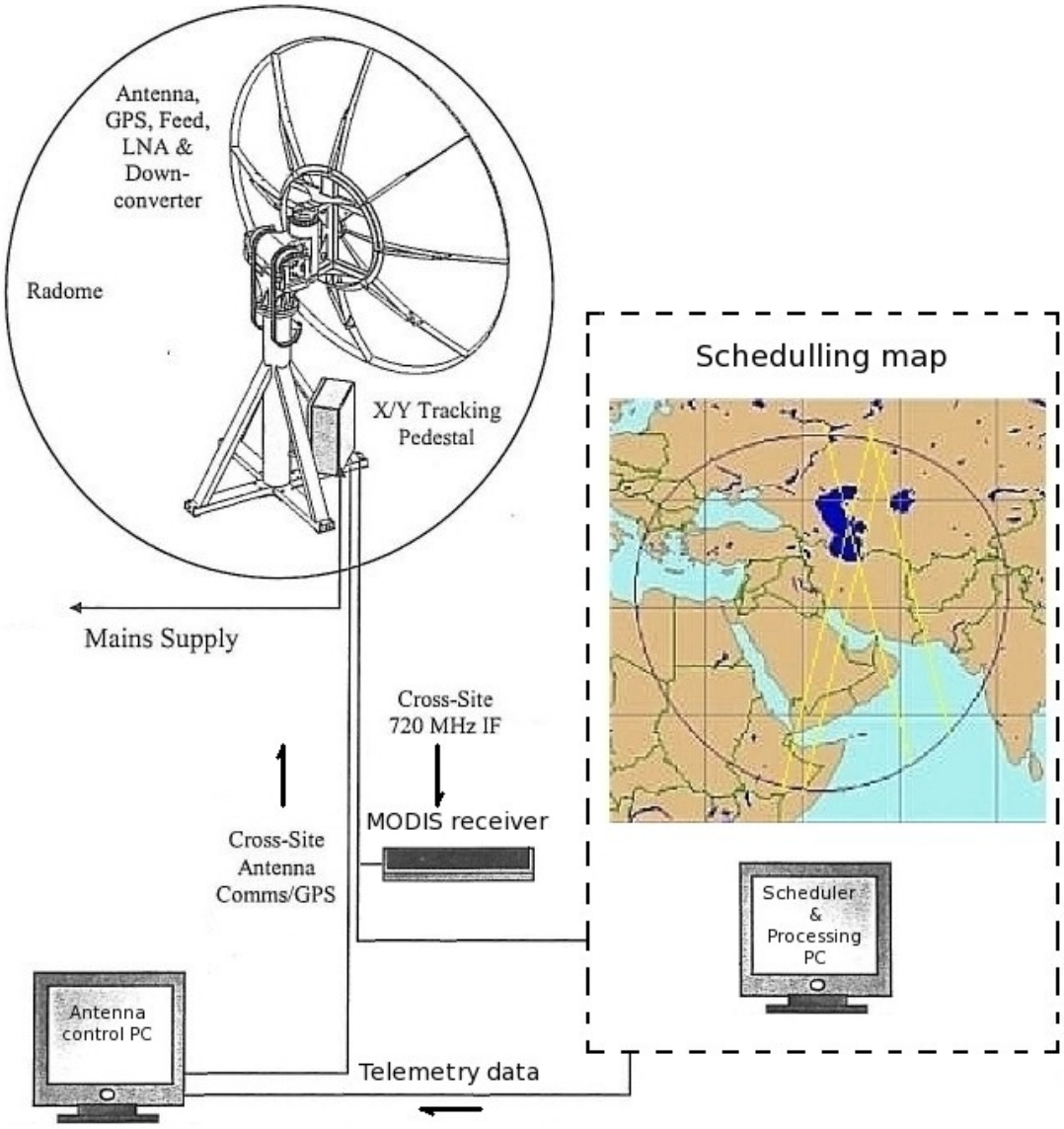

Figure 4.5.The hardware configuration for the MODIS antenna.

The 250 m/pixel resolution false RGB colour composite geotiff file corresponding to bands λ_2=859, λ_1=645 and λ_1=645 nm respectively is transferred to a remote server by ftp for manual analysis through a visual investigation during off–site periods. This file was chosen over other products to carry out the preliminary image processing for three reasons; firstly it is geo–referenced (pixel location is identified in terms of latitude and longitude); it is of maximum spatial resolution; and the RGB colour composite will

immediately highlight all surface–water features including oil spills and their look–alike patterns such as surface floating blooms. In this RGB colour combination, the water–surface blooms will appear reddish due to the "red edge" effect (the greatest reflectance slope between the maximum absorption in the red, due to photosynthetic pigments, and the maximum reflection in the IR) (Tucker, 1979; Jackson et al., 1983). BEAM is then used to analyse the two–band geotiff file, by producing a new grey scale image created using the NIR band (L_2=859 nm) according to the formula shown in Equation 4.22:

$$\frac{1}{(L_2)^2} \tag{4.22}$$

The reason for performing this step was to invert the data contrast in order to improve the visual discrimination efficiency in detecting surface water features such as oil platforms, algal mats, clouds and oil spills from the generally dark water appearance in single-band images of the whole RSA (covering ~ 240,000 km^2). Once a suspected patch is discovered, further spectral analysis was conducted, the details of which will be discussed in the following chapters. Additional L2 data such as Chlor-a concentration and SST were also investigated manually to see whether any relationship exists between the suspected spill and the biophysical/geophysical data. For spatially–large oil spills (in the order of 100's km), the SST4 data (Equation 4.20) of the previous night pass were also analysed to see whether any temperature difference between the spill and the water can be detected. This analysis is based on the presumption that the spill may have started a day earlier.

A GIS map was also used to identify the nearest oil production facilities to the suspected spills, such as offshore oil platforms.

An oil spill detected in MODIS Aqua on 19th June, 2010 at 09:03 UTC is shown under different RGB colour composites including the transformation in Equation 4.6 as demonstrated in Figure 4.6.

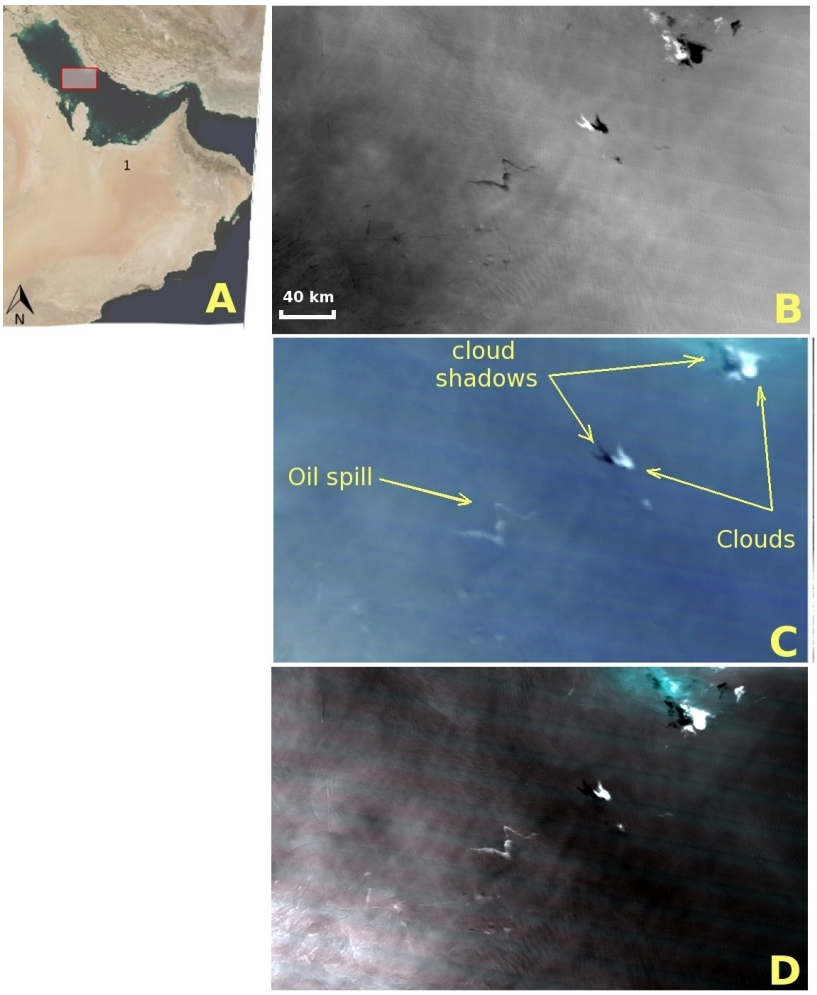

Figure 4.6. **(A)** The swath of MODIS Aqua on 19th June, 2010 at 09:03 UTC under which an oil spill was observed within the sun–glint. **(B)** An image of the spill produced using the transformation shown in Equation 4.6, in which the spill's negative contrast has been reversed to a positive one; **(C)** the natural 500 m/pixel resolution RGB colour composite corresponding to bands λ_1=645 (aggregated from the 250 m resolution band group), λ_4=555 and λ_3=469 nm respectively. Clouds and their shadows are visible; and **(D)** the 500 m/pixel resolution false RGB colour composite corresponding to bands (λ_2=859, λ_1=645 and λ_1= 645 nm respectively (λ_2 and λ_1 were oversampled from the 250 m/resolution bands) (Courtesy of ROPME). The image is centred at the position N27° 00' 57" E51° 03' 40".

In terms of validation, *in situ* verification of oil spills remains the main source for validation. Visual inspection of spills was usually conducted by the local environmental authorities that belong to the countries where the spill was located. This is carried out in liaison with the Marine Emergency Mutual Aid Centre (MEMAC)[36] – the Bahrain–based ROPME associate organization, whose role is to combat pollution caused by oil and other harmful substances in case of marine emergencies in the region. The

[36] http://www.memac-rsa.org/

verification task is normally undertaken by an aerial surveillance or boat dispatches. An alternative indirect method was also used for validation which involved comparing the spill's appearance in MODIS image with the corresponding image of ASAR data, whenever the ASAR data are available. In which case, it becomes possible to trace the evolution of the spill in both MODIS and ASAR images, due to the time difference between them.

Figure 4.7 summarizes the whole processing procedure starting from scheduling of the passes through to the validation process.

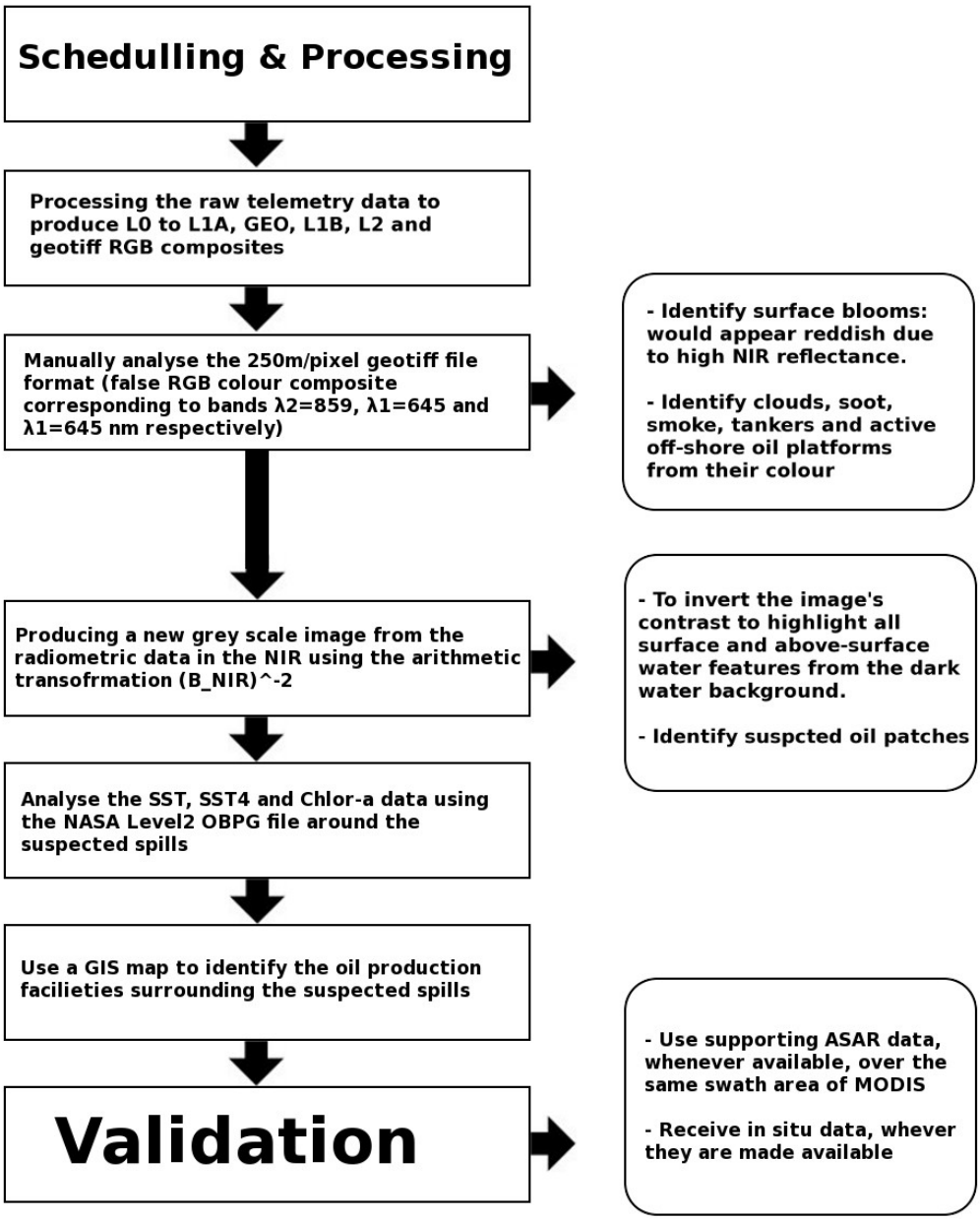

Figure 4.7. The scheduling and processing procedures carried out during this research.

Chapter 5: The spectral contrast shift (SCS)

5.1 Introduction

Oil spills exhibit different spectral properties to the surrounding waters when viewed by multi–spectral or hyper–spectral optical sensors. The Moderate Resolution Imaging Spectroradiometer (MODIS) sensor, for example, will respond to oil spills depending on: the spectral band used; the properties of the oil such as refractive index and thickness; surrounding water conditions; and the orientation of sea surface in relation to the sun–sensor configuration.

The spectral contrast shift (SCS) is a new robust spectral–based relationship that has been hypothesized in this thesis to identify oil spills on water, by comparing the spectral properties of spill edges to the adjacent pure sea water. This empirical method, uses the extreme (the maximum and minimum) apparent radiance values of MODIS 250 m/pixel spatial resolution channels.

The calibration of the SCS algorithm was performed using several confirmed oil spill incidents observed by MODIS in the RSA and elsewhere. A detailed review of this calibration procedure and its outcome will be presented in this chapter, in addition to the validation analysis carried out. The validation process identified oil spills in near–real–time settings, which were later verified by *in situ* observations. Geographic information system (GIS) data covering the location details of possible sources of oil spills such as offshore oil platforms and daily tanker routes were also combined with the experimental results in order to improve the accuracy of the verification methods. A statistical analysis was conducted on the results, to assess the general applicability of the method and to evaluate its sensitivity against the varying background conditions such as sun–glint and atmospheric aerosols. Finally, an index table was derived from the output values of the SCS algorithm to define different classes of oil spill thickness (light sheen, medium and thick) as well as floating algae and turbid water (or weathered oil). The ability of the SCS to discriminate between oil spills and look–alikes, such as surface floating algae, reflects the broad scope of its application. MODIS standard bio–geophysical products such as Chlor-a and sea SST were also processed and used as input information to support the interpretation of oil spill existence. Furthermore, ENVISAT ASAR imagery were also acquired (whenever possible) as complementary

data to the existing MODIS data. Throughout this analysis, the calibrated top–of–atmosphere (TOA) radiance data were used as input in the SCS algorithm which will be referred to in this thesis as "radiance". Unless otherwise stated, the images used in this chapter were not geometrically–corrected in order to ensure that the analysis is performed on data in its raw format and not have it modified by the pixel interpolation caused by the geo–referencing operation. Therefore, the spatial scales and geographic markings shown on the images should be viewed as approximations.

5.2 Defining the SCS algorithm

The SCS classifier is based on finding differences between two pure classes (one of which should be clear water) present in a pre–selected sampling area, where a class is defined by a ratio between its two extreme radiance values of MODIS's 250 m/pixel resolution channels (red and NIR).

$$SCS = \left| \frac{[L_{NIR}]_{max}}{[L_R]_{max}} - \frac{[L_{NIR}]_{min}}{[L_R]_{min}} \right| \tag{5.1}$$

The classification concept introduced by the SCS shares similar properties with two other classical classification methods: the Parallelepiped method (Figure 5.1A) and the spectral angle mapper (SAM) (Figure 5.1B).

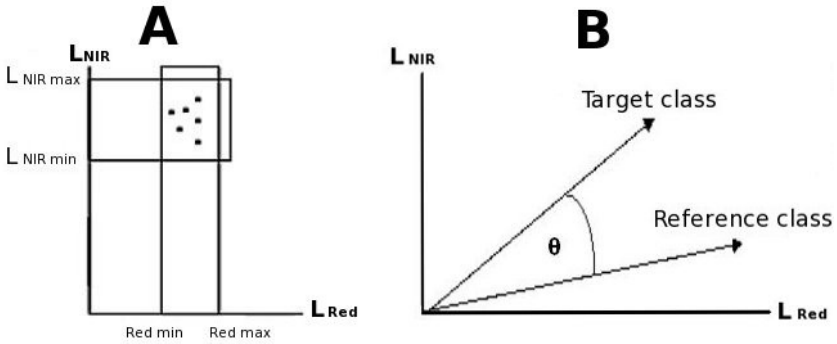

Figure 5.1. The spectral contrast shift classifier is analogous to two classical classification methods: **(A)** the Parallelepiped method and **(B)** the spectral angle mapper (SAM).

The Parallelepiped classification method uses the low and high thresholds (that is, the extreme values as the SCS classifier) of each class signature to determine whether a pixel lies within a class or not (Richards & Jia, 1993). Whereas, the SAM method measures the spectral similarity between classes by calculating the angle between the

reference and target spectra, treating them as vectors in an n–dimensional space, where small angles between two spectra indicate high similarity and large angles indicate low similarity (Kruse et al., 1993). The SCS algorithm is similar to the SAM method, in that its insensitive to illumination because it relies on differences between the directions of each class vector (their gradients) independently from their lengths (their intensity of illumination). But unlike the SAM method which relies on finding *similarities* between an unknown target class to a well–defined reference class, the SCS method discriminates between water–surface objects (including oil) by measuring their spectral *differences* from the reference class (sea-water) in two bands.

The sampling area needed to conduct the SCS analysis is selected based on the following criteria: the area should be spatially small in order to minimize the mixing of classes and include end members of two pure classes, one of which should be unpolluted sea water as a reference class and to ensure that both classes experience the same conditions of illumination and atmospheric effects. In the event where it is not feasible to select a single area encompassing two pure class members, two separate but close areas can be selected instead, provided that the viewing geometry experienced by the end members of sea water and oil are similar relative to the sun.

5.2.1 An example of application

Two confirmed oil spill were observed by MODIS Aqua at different times were used to illustrate how to apply the SCS method over them. The first spill occurred on 2nd June, 2010 at 09:57 UTC with a negative contrast for falling outside the sun–glint area. The second oil spill occurred on 16th July, 2008 at 09:44 UTC involving a thicker oil than the first spill and with negative contrast for falling within the sun–glint area. Both spills occurred inside the RSA near Al Jubail industrial city in Saudi Arabia and their MODIS swaths are shown in Figures 5.2A and 5.2A' respectively. A 250 m/pixel resolution false RGB colour composite images corresponding to bands λ_2=859, λ_1=645 and λ_1=645 nm respectively were generated for each spill as shown in Figures 5.2B and 5.2B' respectively. Both spills were also observed by ENVISAT ASAR (C–band, HH polarization, 1 km/pixel resolution) on 2nd June, 2010 at 18:42 UTC and on 16th July, 2008 at 06:32 UTC as shown in Figures 5.2C and 5.2C' respectively.

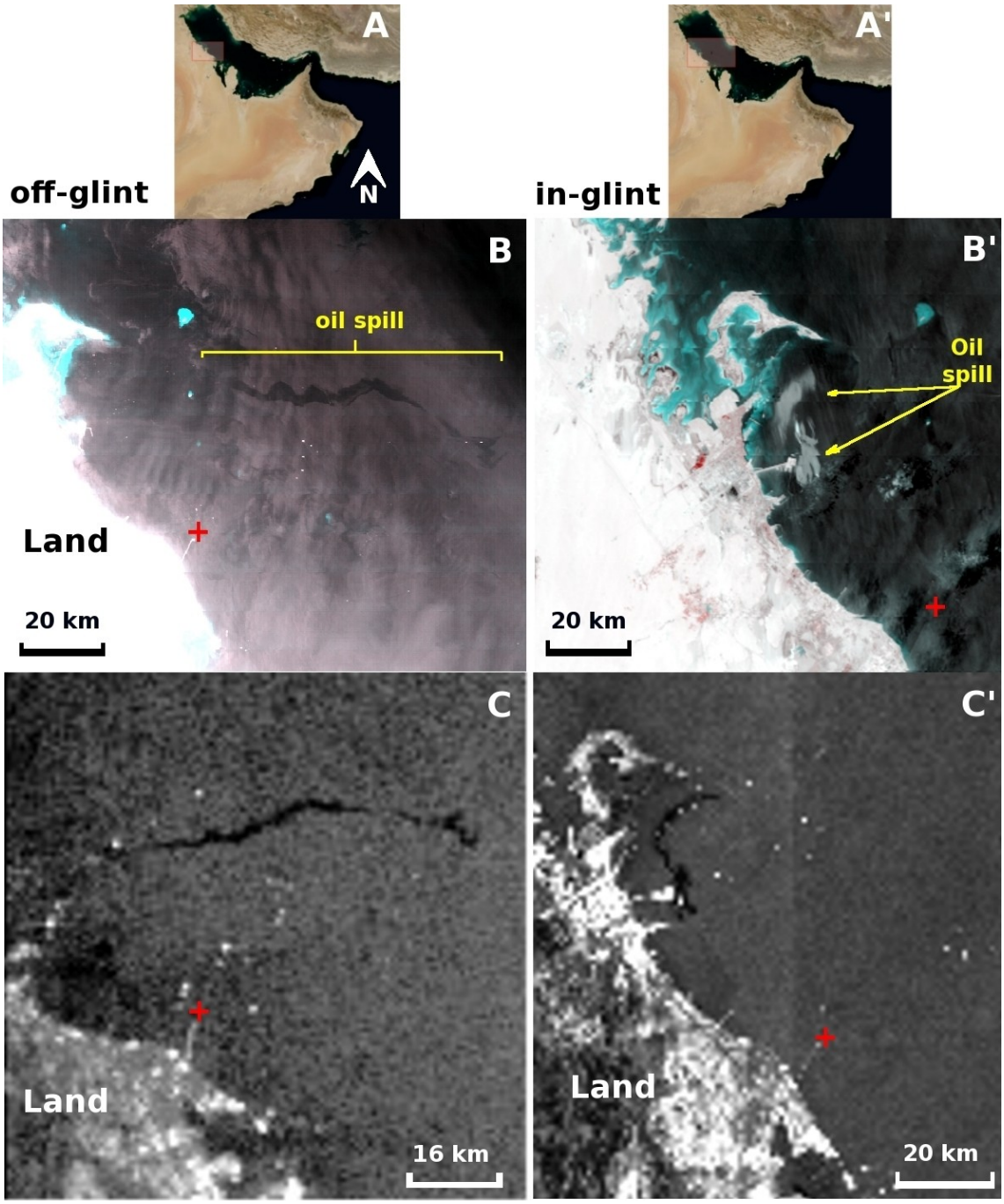

Figure 5.2. **(A)** and **(A')** show the location map of two MODIS Aqua swaths in which oil spills were detected on 2nd June, 2010 at 09:57 UTC and on 16th July, 2008 at 09:44 UTC respectively. **(B)** and **(B')** show the spills (A) and (A') respectively in a 250 m/pixel resolution false RGB colour composite corresponding to bands λ_2=859, λ_1=645 and λ_1=645 nm respectively. **(C)** and **(C')** show the spills (A) and (A') in ENVISAT ASAR images (C–band, HH polarization, 1 km/pixel resolution) at 18:42 UTC and 06:32 UTC respectively. The red + marking is positioned at N26° 53' 34" E50° 03' 42".

The spills will always appear dark in the ASAR images in relation to sea water, unlike their appearance in MODIS which can be brighter than sea water depending on

illumination geometry. The average wind speed recorded by the Advanced ASCAT instrument 10 m above sea level was ~ 5 m/s at the time of detection of both spills.

Grey–scale images of both spills were produced using the 250 m/pixel single NIR band (λ_2=859 nm) as shown in Figures 5.3A and 5.3B for each spill respectively. Sampling areas with N number of pixels inclusive of two classes (part of the oil and part of the unpolluted sea water) were selected over the images based on visual inspection. Figures 5.3C and 5.3D show a zoomed-in images of these areas and points at which spectral plots were made.

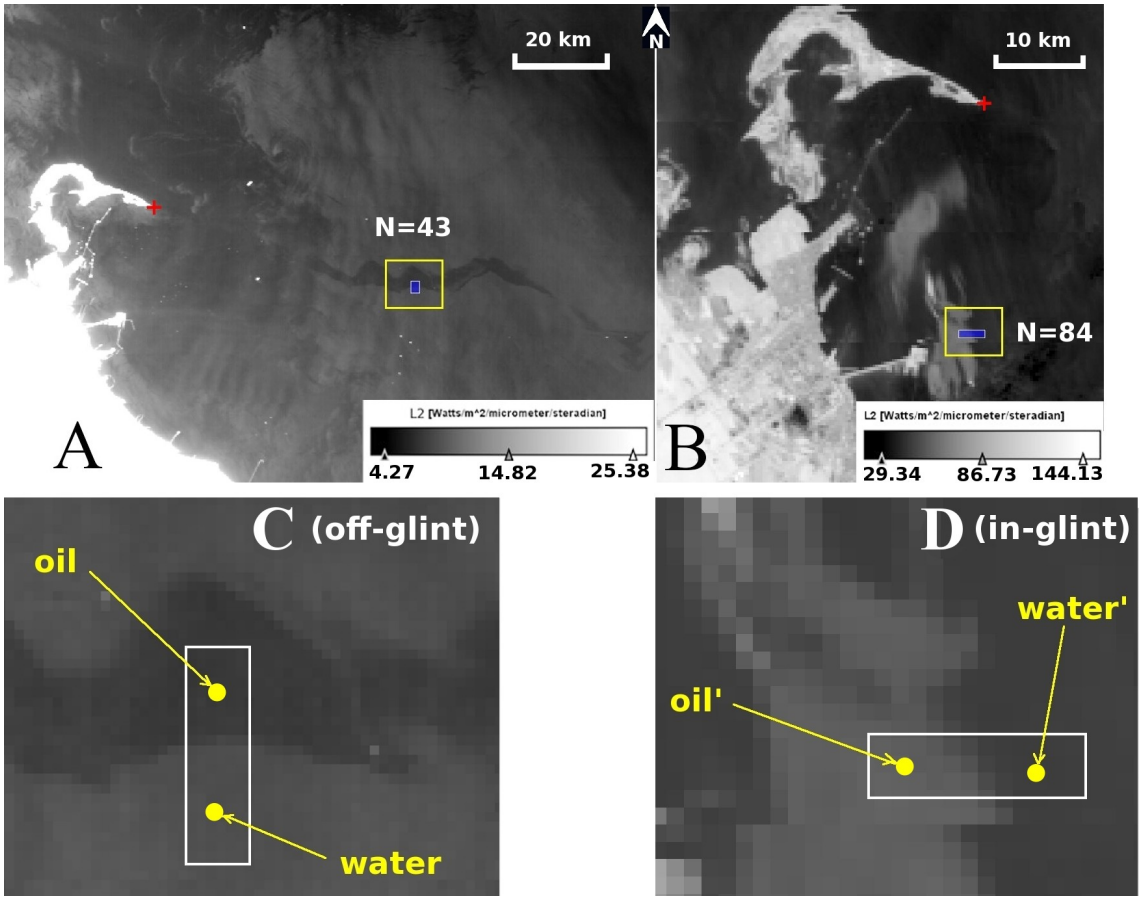

Figure 5.3. Two oil spill images each created from the radiance values in the NIR band (λ_2=859 nm) detected in MODIS Aqua on: **(A)** 2nd June, 2010 at 09:57 UTC and on **(B)** 16th July, 2008 at 09:44 UTC. Sampling areas (N number of pixels) selected over each image to include two classes: parts of the oil and water. A zoomed–in images of each area are shown respectively on (C) with N=43, R2= 0.95 and (D) with N=84, R2=0.99.. The red + marking is positioned at N27° 17' 58.3" E49° 42' 2".

The classification results over these sampling areas are summarized in Table 5.1. Based on these results, an interpolation was made to predict other possible classes that the SCS classifier may produce (Table 5.2) in response to different thickness of oil and surface

floating blooms. The validity of this classification table will be further examined during the next calibration and validation sections.

Table 5.1. The extreme values of radiance in L_1 (at λ_1=645 nm) and L_2 (at λ_2=859 nm) from the sampling areas selected over each part of the spill shown in Figures 5.4A and 5.4B and their corresponding SCS values. The standard deviation value measures the spread in L_1 and L_2.

Radiance ($W/m^2/sr/\mu m$)	**Negative contrast oil spill (darker, less thick) Aqua 2nd June, 2010**		**Positive contrast oil spill (brighter, more thick) Aqua 16th July, 2008**	
	$Oil_{Min.}$	**$Water_{Max.}$**	**$Water_{Min.}$**	**$Oil_{Max.}$**
L_2	7.34±0.54	8.86±0.54	38.89±8.0	63.3±8.0
L_1	19.3±0.75	21.42±0.75	65.06±11	99.71±11
SCS	0.033		0.037	

Table 5.2. A classification table interpolated from the results shown in Table 5.1.

Absolute SCS range	**Class name and description**
0.0-0.014	PC (Single class)
0.015-0.024	LTO (Light thickness oil, sheen)
0.025-0.034	MTO (Medium thickness oil)
0.035-0.045	Oil (Thick oil)
0.045-0.054	TW (Turbid water) or WO (weathered oil)
0.055-0.14	U (undetermined classification)

The reason why turbid water (TW) and weathered oil (WO) were predicted to share the same classification value is because according to Byfield ((1998), suspended oil mixtures such as weathered or dispersed oil can scatter light in a similar manner to other suspended particles, and thus increase the water–leaving radiance in the red and NIR bands. The undetermined classification (U) is probably closely correlated to higher sedimentation in water than the TW classification, but was nevertheless left as undetermined since it is not possible to quantify its distinction from the TW classification at this stage of the research.

Scatter plots for the areas shown earlier in Figures 5.3C and 5.3D appear in Figures in 5.4A (N=43 pixels, R^2=0.95) and 5.4B (N=84 pixels, R^2=0.99) respectively, in which the radiometric responses in the NIR (λ_2=859 nm) were plotted against those corresponding values in the red band (λ_1=645 nm). Spectral plots of two points of oil and water selected from the sampling areas shown earlier in Figures 5.3C and 5.3D are shown in Figures in 5.4C and 5.4D respectively.

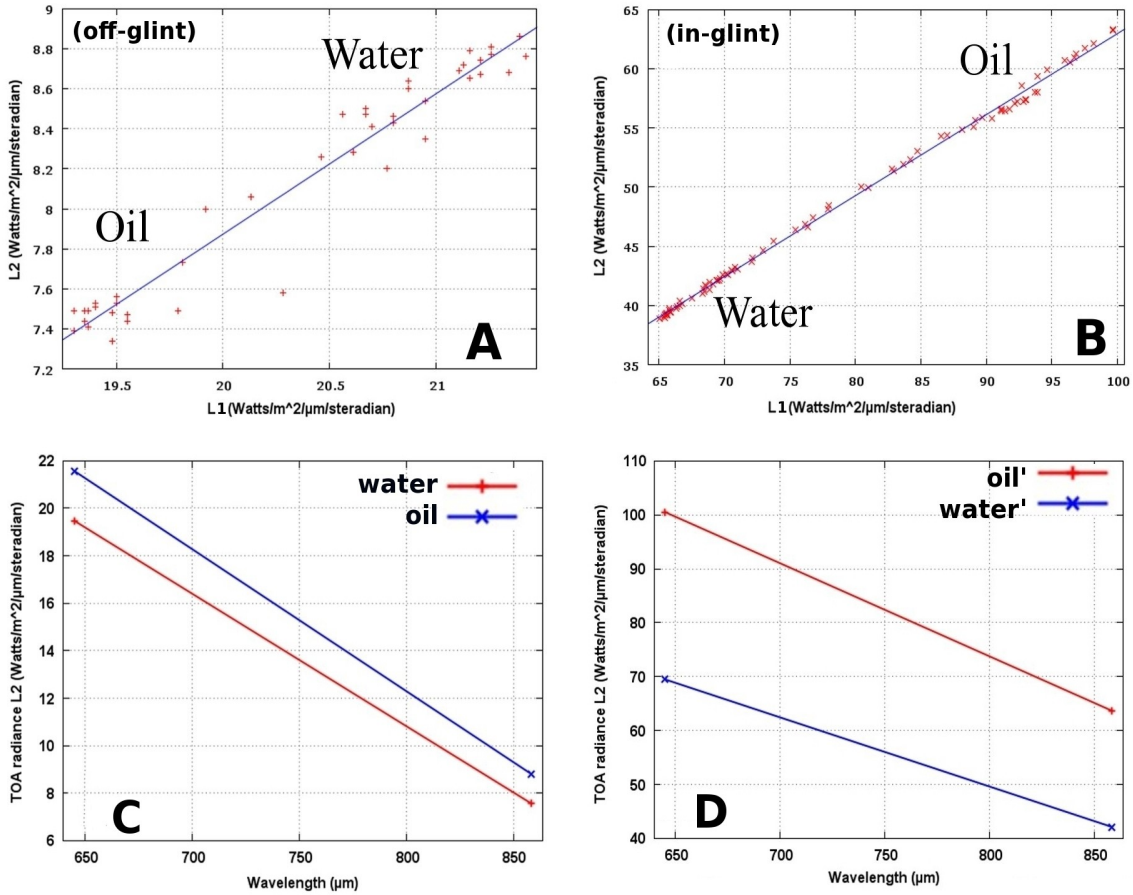

Figure 5.4. Scatter plots of radiance values in the NIR (λ_2=859 nm) versus those corresponding values in the red (λ_1=645 nm) band for the sampling areas that lie **(A)** outside the sun–glint and **(B)** within the sun–glint shown in Figures 5.3C and 5.3D respectively. Spectral plots at the 250 m/pixel band group (λ_1=645 nm and λ_2=859 nm) for the two points of oil and water selected from Figures **(C)** 5.3C (off-glint area) and **(D)** 5.3D (in-glint area). The straight lines in the spectral plots were added for demonstration purposes.

These scatter plots reveal less spread between the clusters of oil and water under the sun–glint case than it is in the out of sun–glint case, which suggests the purity of the oil and water classes. The plots also demonstrate a positive correlation between the radiance response in the red and NIR bands, but transpose their contrasts accordingly depending on the degree of illumination that each experiences. In other words, oil will

exhibit the same negative (dark) or positive (bright) contrast in relation to water in each separate band. Thus, making it possible to re–write Equation 5.1 as:

$$SCS = \frac{[L_{NIR}]_{WATERmax}}{[L_R]_{WATERmax}} - \frac{[L_{NIR}]_{OILmin}}{[L_R]_{OILmin}} \; (for\ a\ negative\ oil\ spill\ contrast) \tag{5.2}$$

$$SCS = \frac{[L_{NIR}]_{OILmax}}{[L_R]_{OILmax}} - \frac{[L_{NIR}]_{WATERmin}}{[L_R]_{WATERmin}} \; (for\ a\ positive\ oil\ spill\ contrast) \tag{5.3}$$

The relationship between MODIS's red and NIR bands in relation to oil and surrounding sea water under different illumination conditions can be schematically demonstrated in the spectral space plots shown in Figure 5.5.

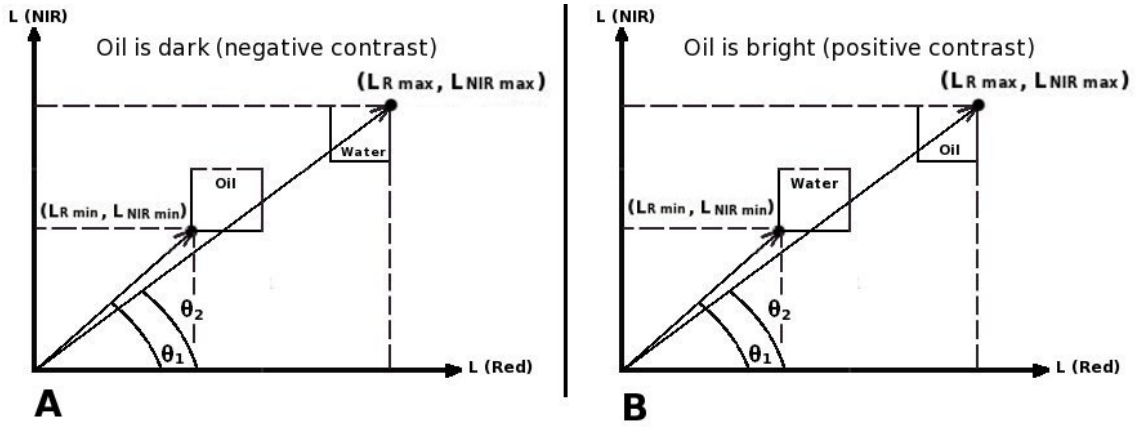

Figure 5.5. A spectral space plots (radiance in NIR against radiance in the red) for a **(A)** negative contrast oil spill and a **(B)** positive contrast oil spill. The SCS method can be interpreted as a spectral angle made between clear water and a suspected class (θ_1–θ_2). Illumination is represented by the vector's length.

The spectral vectors are defined as the extreme radiance response values (that is, the minimum and maximum values) in the red and NIR bands for each class. Therefore, with reference to Figure 5.5 if a class is to be represented by its extreme radiance values, then the gradient (slope) for each class vector ($\tan\theta_1$ and $\tan\theta_2$) can be represented respectively as:

$$tan(\theta_1) = \frac{[L_{NIR}]_{min}}{[L_R]_{min}} \tag{5.4}$$

$$tan(\theta_2) = \frac{[L_{NIR}]_{max}}{[L_R]_{max}} \tag{5.5}$$

where L_R and L_{NIR} are the radiance values in the red (λ_1=645 nm) and NIR (λ_2=859 nm) channels respectively of the MODIS 250 m/pixel spatial resolution band group. The sub–notations max and min stand for the maximum and minimum radiance values respectively. With reference to Equations 5.3 and 5.2, the SCS can be re-written as:

$$SCS = \left| tan(\theta_2) - tan(\theta_1) \right| \tag{5.6}$$

which can be interpreted as a classification that measures how the contrast of at water-surface bodies changes or shifts (independently from the geometry of illumination) in relation to a reference class (represented by adjacent clear sea-water) by using their maximum and minimum radiance responses in the red and NIR bands.

The fact that the SCS classifier takes advantage of the radiometric response in the red and NIR bands in discriminating between oil and water agrees with the findings presented in early studies about the usefulness of the NIR and the red bands for performing this. Salem et al. (2002) for example, have found that floating oil on water causes sharp absorption centred around 0.68 μm and is associated with a second peak at around 0.71 μm. Results by Rong-Rong Li et al. (2003), Miller & McKee (2004) and Mati Kahru et al. (2004) asserted the usefulness of MODIS 250 m resolution red and NIR bands in acting as high–resolution proxies for turbidity, which can then be related to concentrations of suspended matter or other scattering sources. Chust & Sagarminaga (2006) studied oil slicks detected in images from the Multiangle Imaging SpectroRadiometer (MISR) sensor on–board the Terra satellite, and concluded also that among the four visible and near infra–red (VNIR) bands at nadir, the NIR (λ_4=867 nm) is the best band for discriminating oil slicks, followed in most cases, by the red band (λ_3=672 nm).

5.3 The calibration of the SCS over oil spills in the RSA

The method proposed herein has been tested on more than 30 pre–confirmed oil spill incidents in the RSA and elsewhere (see Appendix A for such examples), out of which two confirmed oil spill incidents were chosen to perform further calibration. The first spill was observed by MODIS Terra on 21st October, 2007 at 07:02 UTC (outside a sun–glint region) and appeared with a negative contrast. The second spill was observed by MODIS Aqua 25th May, 2005 at 09:16 UTC (under a sun–glint area) with a positive contrast. The spectral transformation shown in the previous chapter (Equation 4.22) was first used to improve the visual discrimination between the predominant dark water from surface features. Colour stretching was occasionally performed in order to achieve further contrast enhancement.

5.3.1 Terra on 21st October, 2007

A reported oil spill opposite the waters of Dubai, UAE was observed in MODIS Terra on 21st October, 2007 at 07:02 UTC and whose swath is shown in Figure 5.6A (inset). The average wind speed estimated by the QuikSCAT Satellite 10 m above sea level was ~ 6±2 m/s around the spill's area. The spill appears in 250 m/pixel resolution false RGB colour composite corresponding to bands λ_2=859, λ_1=645 and λ_1=645 nm respectively (shown in Figure 5.6A) and in a 500 m/pixel resolution natural RGB colour composite corresponding to bands λ_1=645 (aggregated from the 250 m/pixel band group), λ_4=555 and λ_3=469 nm respectively (shown in Figure 5.6B).

The SCS classifier was applied to the reported oil spill, including to visible suspected patterns scattered nearby. The classified patterns were numbered on an image (shown in Figure 5.7) produced using the radiometric transformation, for which Table 5.3 display the results. The MODIS SST4 (3.959–4.050 μm), SST (11–12 μm) and Chlor-a maps are shown in Figures 5.8A, 5.8B and 5.8C respectively, were processed to investigate the possibility of delineating the oil spill(s) in them.

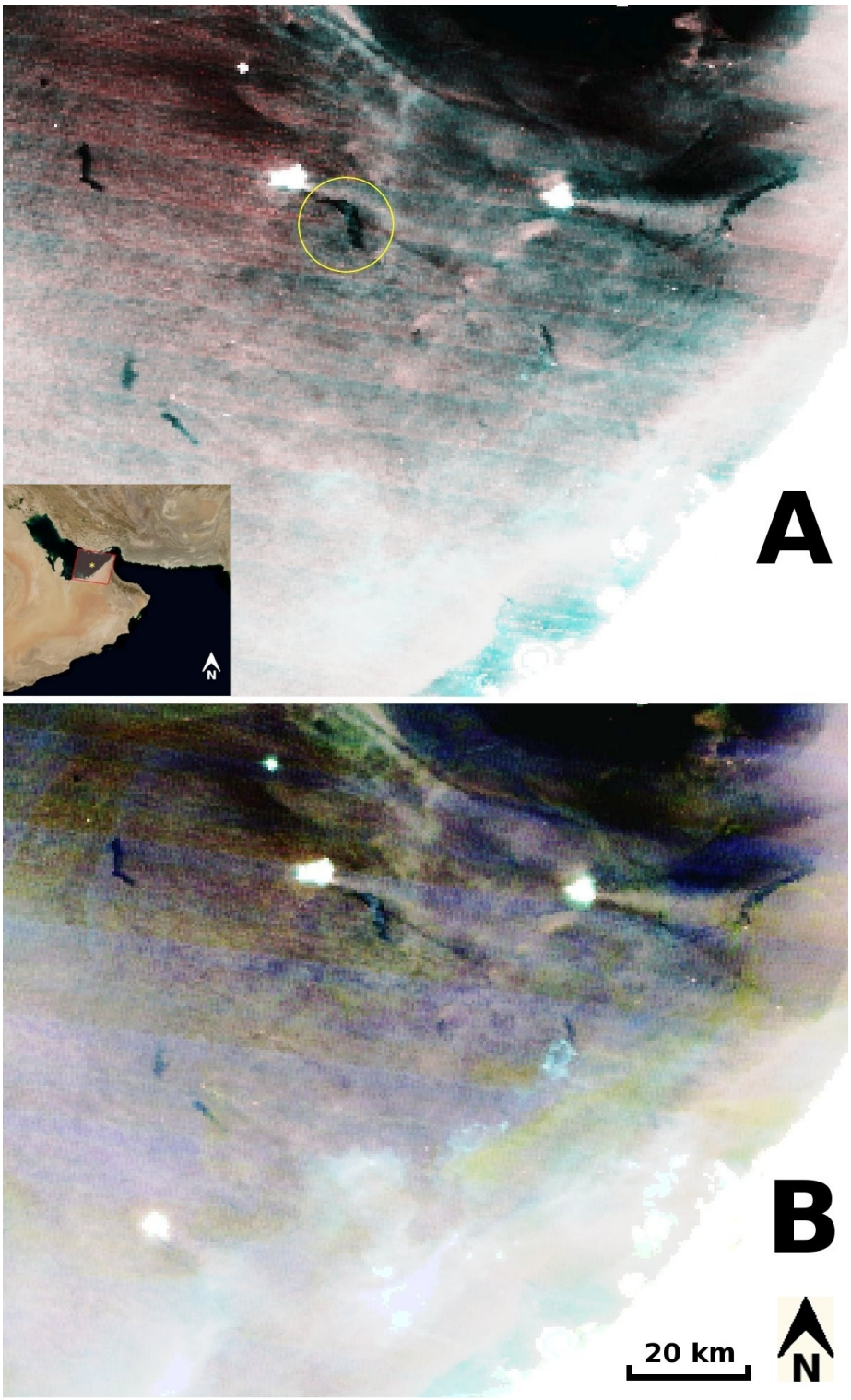

Figure 5.6. An oil spill observed in MODIS Terra on 21st October, 2007 at 07:02 UTC. The spill appears in **(A)** circled in a 250 m/pixel resolution false RGB colour composite corresponding to bands λ_2=859, λ_1=645 and λ_1=645 nm respectively. The swath of Terra is shown inset. **(B)** a 500 m/pixel resolution natural RGB colour composite corresponding to bands λ_1=645 (aggregated from the 250 m/pixel band group), λ_4=555 and λ_3=469 nm respectively. Unreported dark patches (possibly oil spills) also visible in both images.

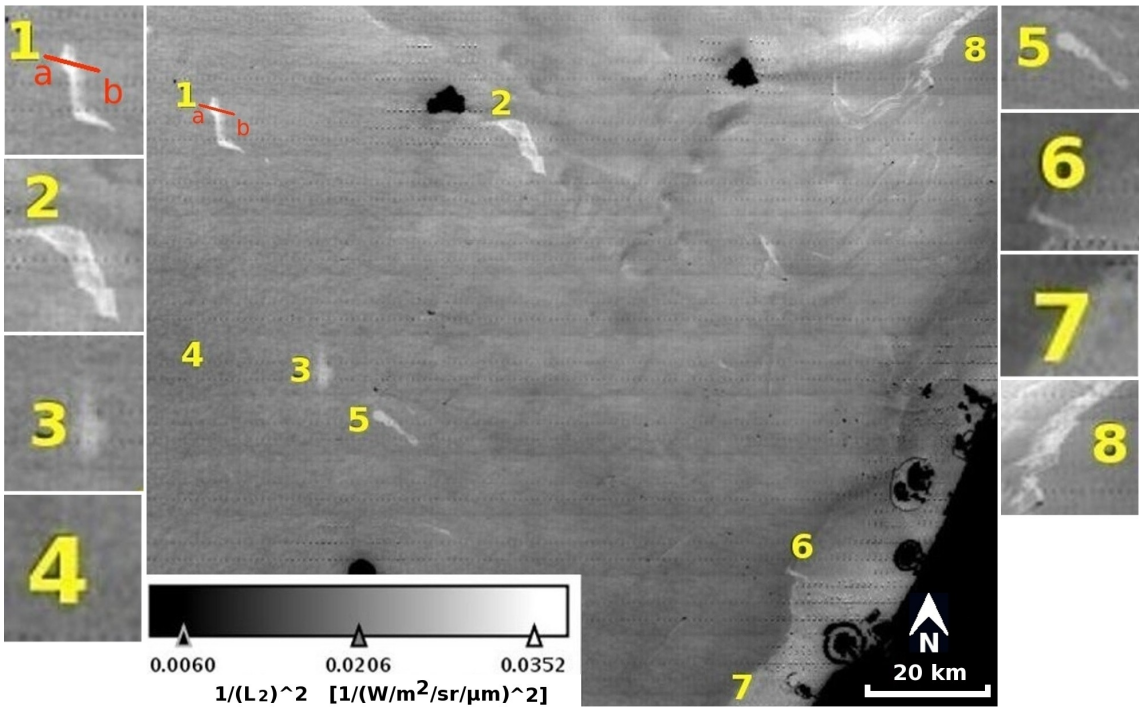

Figure 5.7. The SCS classifier was applied to the reported oil spill (marked 2) and nearby suspected spills observed in MODIS Terra on 21st October, 2007 at 07:02 UTC. The image was produced using the radiometric transformation, where land, islands and ships appear black. A line was drawn across a suspicious spill (marked 1) from a to b whose transects over SST4 and Chlor-a are shown in Figure 5.9. Some points were selected and shown as zoomed–in thumbnails on both sides.

Table 5.3. The output SCS classification carried out on the numbered patterns displayed on Figure 5.7. LTO=light thickness oil, MTO=medium thickness oil, Oil=thick oil, TW=turbid water, WO=weathered oil and PC=pure class.

Area No.	L_2 (W/m²/sr/µm)		L_1 (W/m²/sr/µm)		N pixels	Absolute (SCS)	Classification
	Min.	Max.	Min.	Max.			
1	5.38	6.65	15.41	17.49	25	0.031	MTO
2	5.43	6.57	15.86	17.41	48	0.035	Oil
3	6.09	6.98	16.8	18.06	32	0.024	LTO
4	6.45	7.18	17.33	18.8	272	0.010	PC (Water)
5	5.93	7.28	16.75	18.51	22	0.039	Oil
6	6.56	8.00	18.33	20.29	18	0.036	Oil
7	6.57	8.11	18.33	20.06	80	0.046	TW or WO
8	5.94	6.77	16.46	17.7	80	0.022	LTO

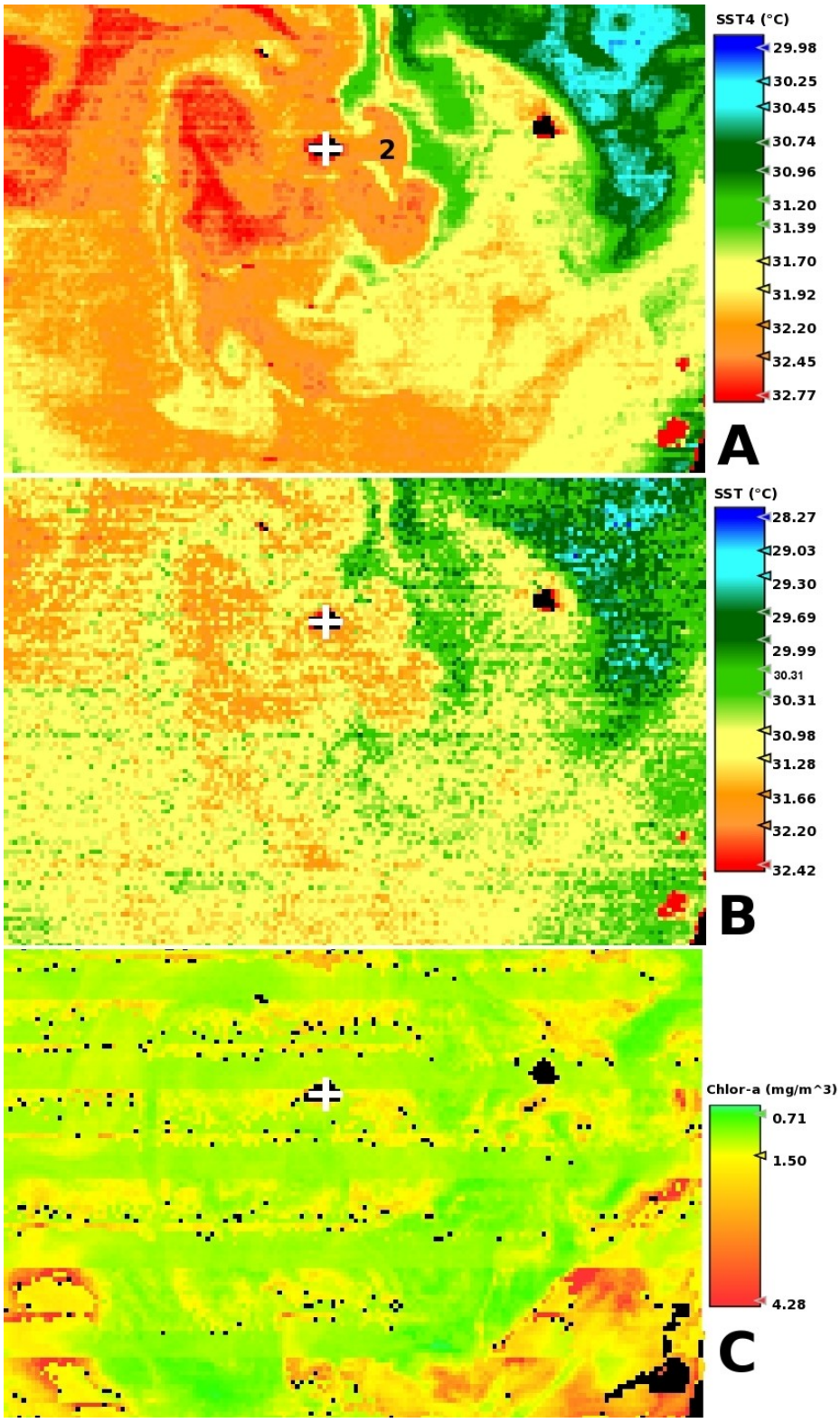

Figure 5.8. The appearance of a reported oil spill (numbered 2 on Figure 5.7) observed in MODIS Terra on 21st October, 2007 at 07:02 UTC in **(A)** SST4, where the spill (numbered 2) is well delineated due to solar interference reflected off its surface, in **(B)** SST (no temperature gradient between the spill and water), and in **(C)** Chlor-a (the spill is hardly visible). White + mark is positioned at N25° 54' 39.12" E54° 31' 34.65".

The SST4 temperature product is valid only during night observations to avoid solar interference during the day. Therefore, SST4 (Figure 5.8A) day readings should be seen as relative values and not absolute thermal readings. In this map, the reported oil pattern was well delineated by an apparent temperature reduction of ~ 1°C in relation to the surrounding waters. In the SST temperature map (Figure 5.8B), however, oil showed no significant thermal differences from its surrounding waters . The reported oil spill and other suspected patterns were hardly visible in the Chlor-a map product shown in Figure 5.8C, which would otherwise classify them as sub–surface blooms of chlorophyll. In the same time, the patterns were not masked-off as invalid Chlor-a data, which is probably attributed to the optical properties of the oil allowed the water–leaving radiances in the blue and green bands to be processed by the Chlor-a algorithm as valid Chlor-a data.

Furthermore, such pattern could not have been attributed to surface blooms since the 250 m/pixel resolution false RGB colour composite corresponding to bands λ_2=859, λ_1=645 and λ_1=645 nm respectively (Figure 5.6A) did not show delineate the observed patches in a reddish colour as would surface floating blooms. Because in this colour composite the surface floating blooms would appear reddish due to the “red–edge” phenomena (that is, high reflectance in the NIR coupled with higher absorption in the red) caused by embedded chlorophyll pigments. The dark appearance of oil in this colour composite, as well as in the natural colour composite (Figure 5.6B) is primarily caused by the reflectance of the VNIR bands off the wave–dampened water surface (due to oil) away from the sensor.

A zoomed–in image of a line crossing the spill (marked 1 on Figure 5.7) is shown in Figure 5.9A. The Chlor-a and SST4 transects are shown in Figure 5.9B, where they reveal a reduction of about 40% and 35% in SST4 and Chlor-a respectively over the spill area compared to surrounding waters.

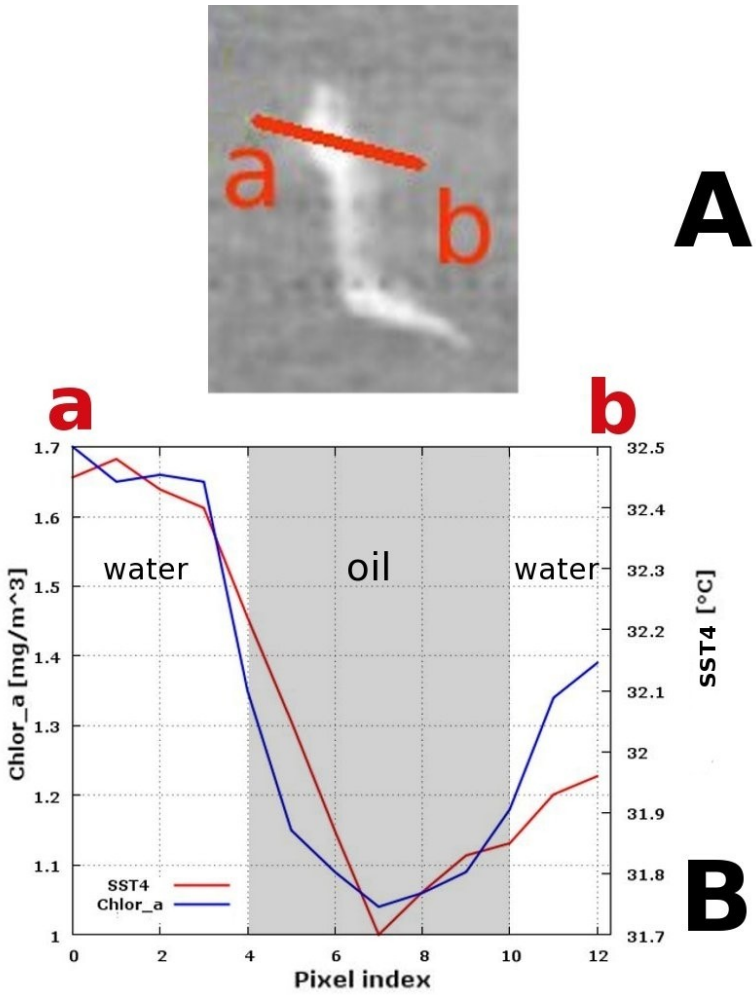

Figure 5.9. **(A)** shows a zoomed–in image of a suspected patch classified as medium thickness oil by the SCS (marked 1) on Figure 5.7, where a line was drawn across it (a–b). **(B)** shows the Chlor-a and SST4 transect responses respectively.

5.3.2 Aqua on 25th May, 2005

An oil spill occurred when the motor vessel (MV) Astro Lupus collided with RoRo MV Safari in the Sea of Oman[37] on 23rd May, 2005 where 620 metric tonnes (MT) of Iranian light crude oil leaked into the sea. Figures 5.10A 5.10B show the location map of the reported oil spill and how it looks as large dark trails in an ENVISAT ASAR image (C–band, VV polarization, 150 m/pixel resolution) acquired on 22nd May, 2005 18:16 UTC respectively. The average wind speed estimated by the QuikSCAT satellite 10 m above sea level was ~ 4±2 m/s near the spill's area. The spill was visible in MODIS Aqua on 25th May, 2005 at 09:16 UTC (two days after reporting it) near the sun–glint area. Figure 5.11A shows the spill area (circled) and its surroundings in the

[37] The Gulf of Oman was re–named the Sea of Oman by the the Sultanate of Oman in January 2010.

250 m/pixel resolution false RGB colour composite corresponding to bands λ_2=859, λ_1=645 and λ_1=645 nm respectively. Figure 5.11B shows the spill in a 500 m/pixel spatial resolution natural RGB colour composite corresponding to bands λ_1=645 (aggregated from the 250 m/pixel band group), λ_4=555 and λ_3=469 nm respectively.

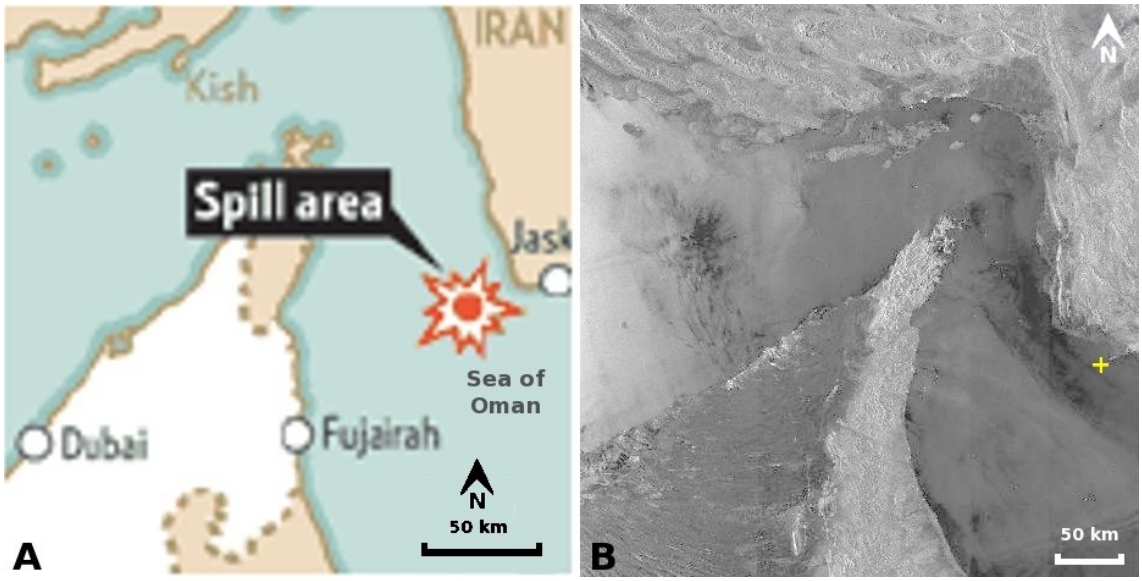

Figure 5.10. An oil spill occurred when the motor vessel (MV) Astro Lupus was reported to have collided with RoRo MV Safari in the Sea of Oman on 23rd May, 2005 where 620 MT of Iranian crude oil leaked into the sea in of Oman located **(A)** as shown in the map and in **(B)** ENVISAT ASAR (C–band, VV polarization, 150 m/pixel) image showing the spill as large dark streaks on 22nd May, 2005 at 18:16 UTC. The + marking is positioned at N25° 37' 48.5" E57° 45' 27.5".

The spill in the false RGB colour composite (shown in Figure 5.11A) does not appear reddish in colour as does land vegetation (due to the red–edge) effect. Therefore, the observed pattern cannot be attributed to surface–floating algae, since it lacks the reddish colour that surface algae would normally present in RGB false colour composites. In both RGB colour composites, the spills appear brighter than sea water due to them falling within the sun–glint area, since all water–surface patterns appear brighter (positive contrast) ±30° around the solar zenith (Kaufman & Tanré, 1998) than those patterns falling outside the sun–glint area.

An image of the spill (Figure 5.12) was processed using the radiometric transformation, over which various numbered points were added showing the sampling areas of the SCS classifier (shown on the sides of Figure 5.12) as zoomed–in thumbnail images). These sampling points correspond to the reported spill and to nearby suspected patches. The results of this classification are summarized in Table 5.4.

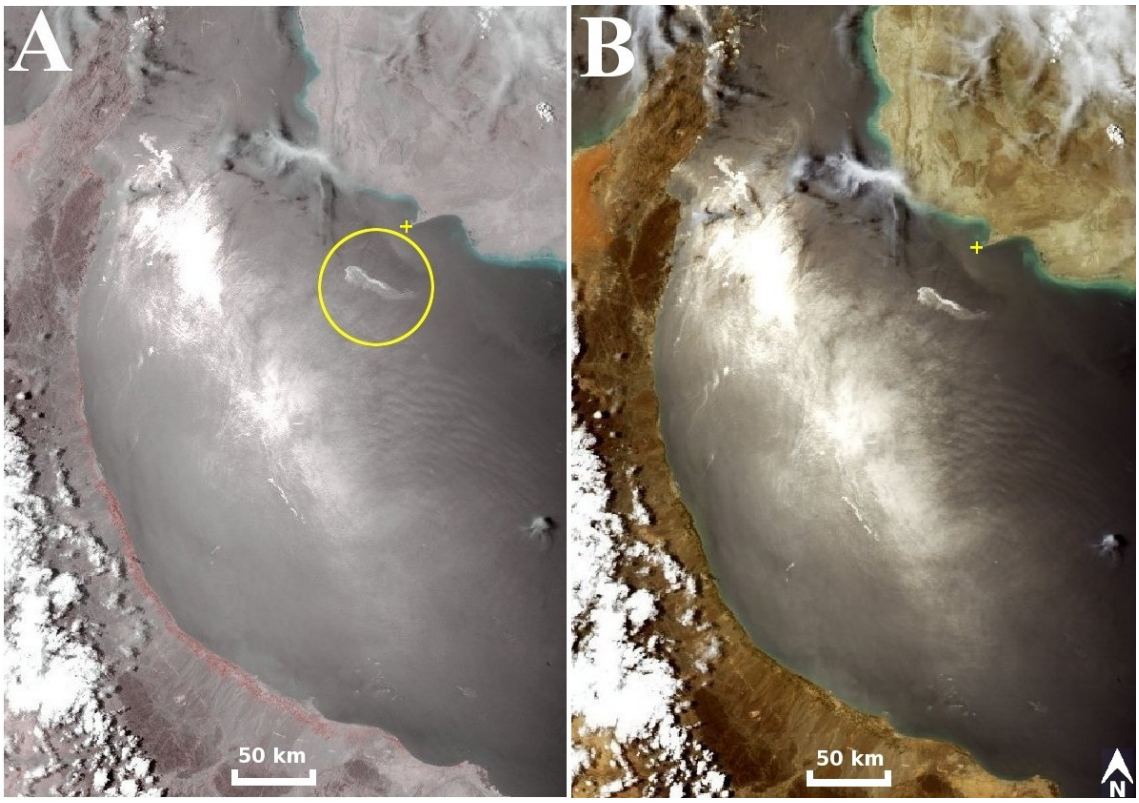

Figure 5.11. MODIS Aqua image on 25th May, 2005 at 09:16 UTC over an oil spill (circled) reported two days earlier shown in **(A)** a 250 m/pixel resolution false RGB colour composite corresponding to bands λ_2=859, λ_1=645 and λ_1=645 nm respectively, and **(B)** a 500 m/pixel resolution natural RGB colour composite corresponding to bands λ_1=645 (aggregated from the 250 m/pixel band group), λ_4=555 and λ_3=469 nm respectively. Other suspected patterns are also visible in both images. The + marking is positioned at N25° 37' 48.5" E57° 45' 27.5".

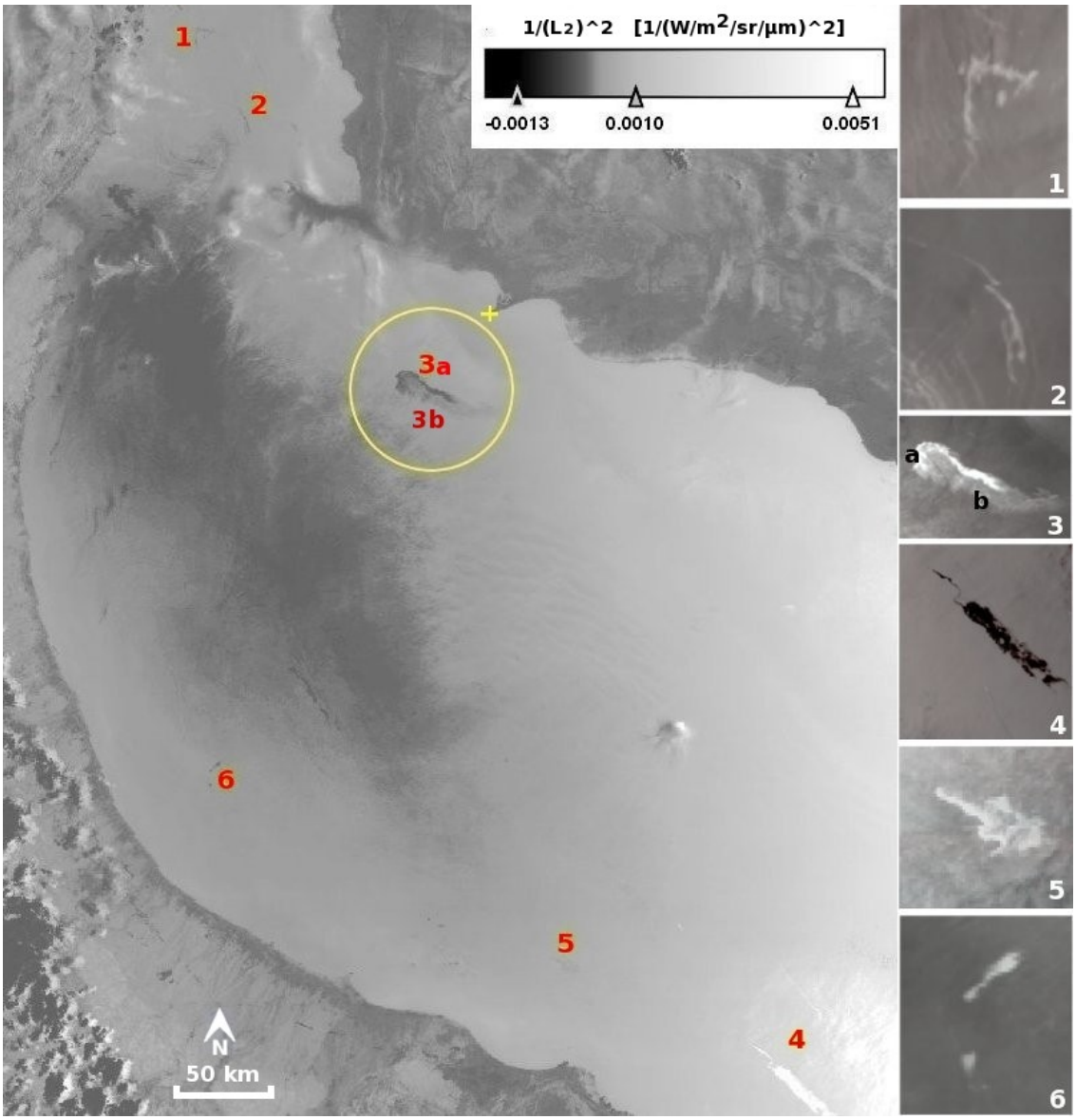

Figure 5.12. The oil spill viewed in MODIS Aqua on 25th May, 2005 at 09:16 UTC. The image was produced using the radiometric transformation. The areas where the SCS method was applied are marked, including the reported oil spill (circled). Zoomed–in images of the numbered test sites (created from the image shown in Figure 5.11A) are shown opposite. The + marking is positioned at N25° 37' 48.5" E57° 45' 27.5".

Table 5.4. The output SCS classification carried out on the numbered sampling areas displayed on Figure 5.12. MTO=medium thickness oil, Oil=thick oil, and TW=turbid water, WO=weathered oil, PC=pure class and U=undetermined.

Area No.	L_2 (W/m^2/sr/µm)		L_1 (W/m^2/sr/µm)		N pixels	SCS	Classification
	Min.	Max.	Min.	Max.			
1	50.94	78.49	78.81	114.69	121	0.038	Oil
2	51.79	80.60	79.78	118.97	100	0.028	MTO
3a	49.63	151.94	78.55	277.44	31	0.084	U
3b	46.74	72.08	74.19	112.22	242	0.012	PC
4	12.35	20.84	26.87	38.67	12	0.079	U
5	37.09	59.80	61.70	93.59	96	0.038	Oil
6	54.90	100.69	87.51	153.57	154	0.028	MTO

Although the Chlor-a product could not be produced due to interference from sun–glint over the area of interest, the SST and SST4 temperature maps were processed for the oil spill incident and are shown in Figures 5.13A and 5.13B respectively. The temperature readings in the SST4 map are not reliable due to masking of thermal emissivity caused by severe sun–glint; but as a direct result of this, the different texture features on the spill's surface area became well delineated. These distinctive shapes may correspond to different weathering conditions to which the spill had been exposed or may simply correspond to different thicknesses of oil. For example, in Table 5.4 points 3a (SCS=0.084, classified as undetermined) and 3b (SCS=0.012, pure class probably water) corresponding respectively to high and low solar reflectances on SST4 (Figure 5.13B). The SST4 is, therefore, useful in highlighting the different contrasts of objects appearing at the water–surface (including oil spills) when there is enough sun–glint over the scene. The SST map (Figure 5.13A), however, did not reveal any significant temperature differences between the oil spill and its surrounding sea water.

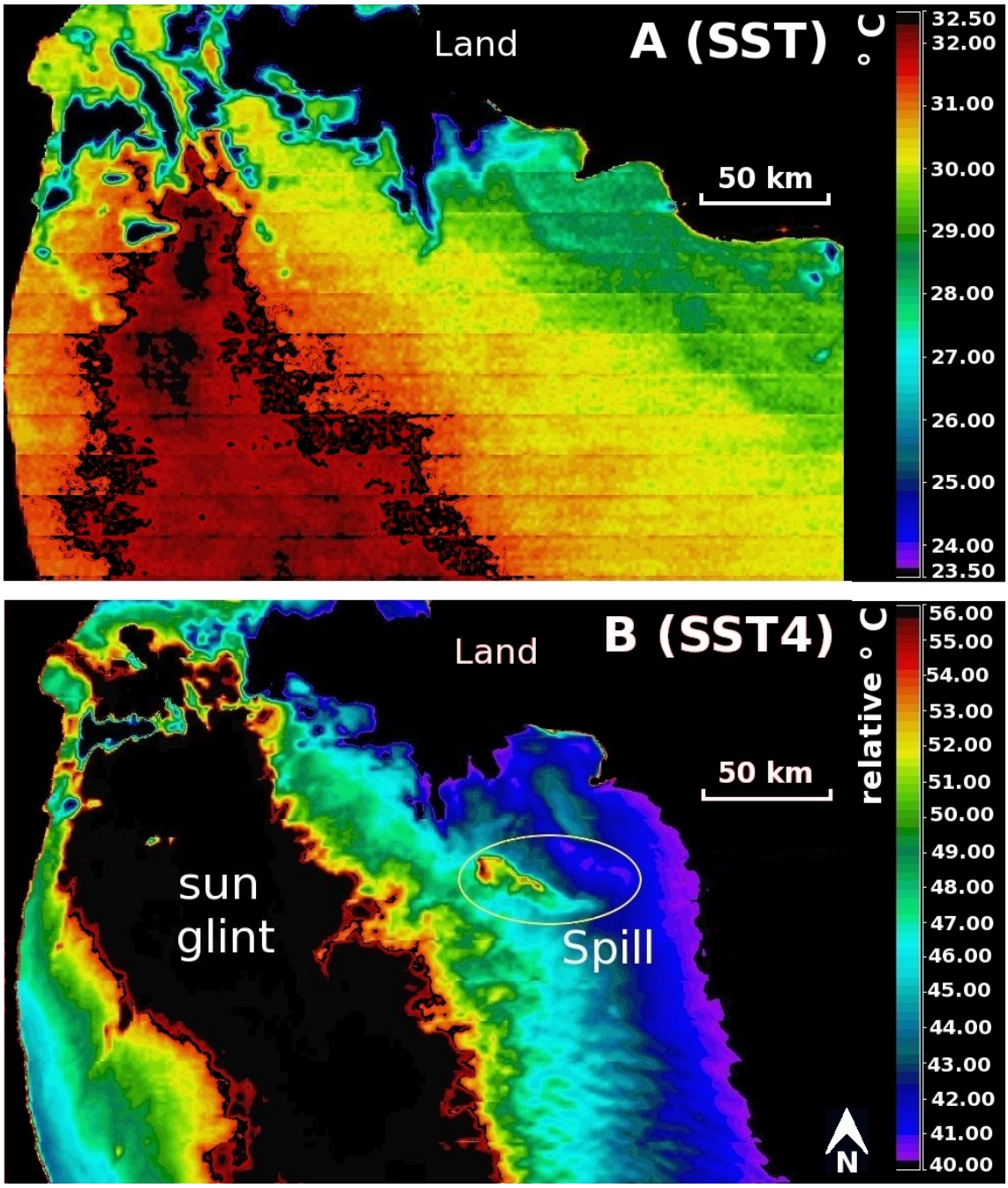

Figure 5.13. The SST (11–12 μm) and SST4 (3.96–4.05 μm) MODIS Aqua temperature maps processed over the spill study area observed on 25th May, 2005 at 09:16 UTC and shown in Figure 5.12.

5.4 The calibration of the SCS over oil spills out of the RSA

The calibration of the SCS algorithm was carried out on pre–confirmed oil spill incidents outside the RSA: (1) Beirut, Lebanon (Shaban et al., 2007); (2) Gulf of Cagliari, Sardinia–Italy (Dessì et al., 2008); and (3) the Deepwater Horizon oil spill in the Gulf of Mexico; and (4) Lake Maracaibo, Venezuela (Hu et al., 2003). Figure 5.14

shows a map over which the corresponding MODIS swaths in which the spills were observed are shown.

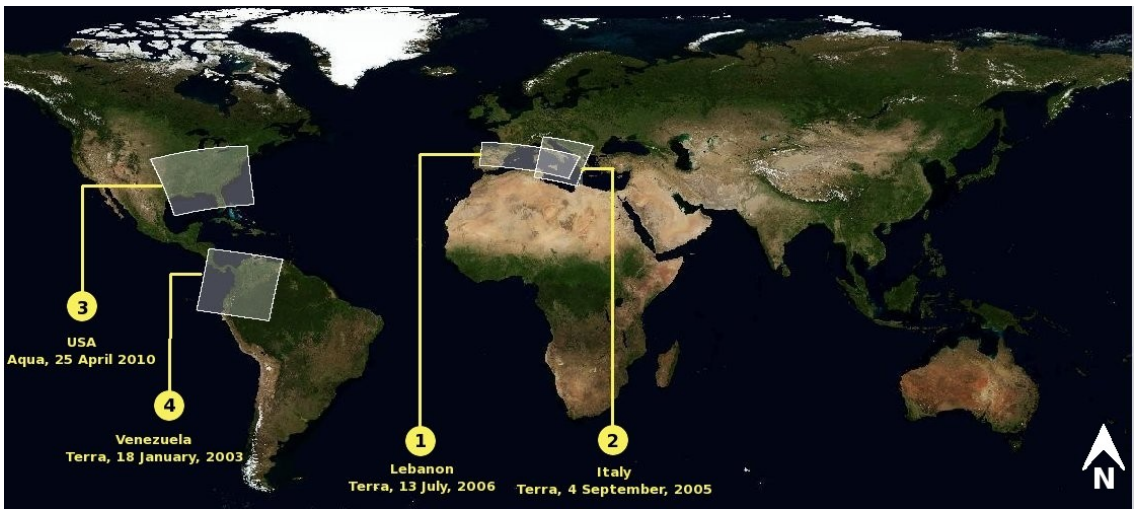

Figure 5.14. MODIS swaths of confirmed oil spill incidents that occurred outside the RSA over which the SCS algorithm was calibrated: **(1)** Beirut, Lebanon (Shaban et al., 2007); **(2)** Gulf of Cagliari, Sardinia–Italy (Dessì et al., 2008); (**3)** Deepwater Horizon, Gulf of Mexico; and **(4)** Lake Maracaibo, Venezuela (Hu et al., 2003).

5.4.1 Lebanon– 1st August, 2006

On 13th July, 2006, the Israeli army bombed oil tanks at Jiyeh power station, Lebanon causing the release of several million gallons of heavy fuel–oil (~15000 tons) into the seawater, covering an area of about 3000 km^2 (Shaban et al., 2007). The average wind speed estimated by the QuikSCAT Satellite 10 m above sea level was ~ 6±2 m/s at the time of imaging. The map shown in Figure 5.15A highlights the distribution of spills along the Lebanese coast. The spills were visible in MODIS Terra on 1st August, 2006 at 08:32 UTC, where Figure 5.15B shows them in a 500 m/pixel spatial resolution natural RGB colour composite image corresponding to bands λ_1=645 (aggregated from the 250 m/pixel band group), λ_4=555 and λ_3=469 nm respectively. The spills in Figure 5.15B appear as greyish and/or whitish in colour (that is brighter than water) because they lie directly under the sun–glint zone.

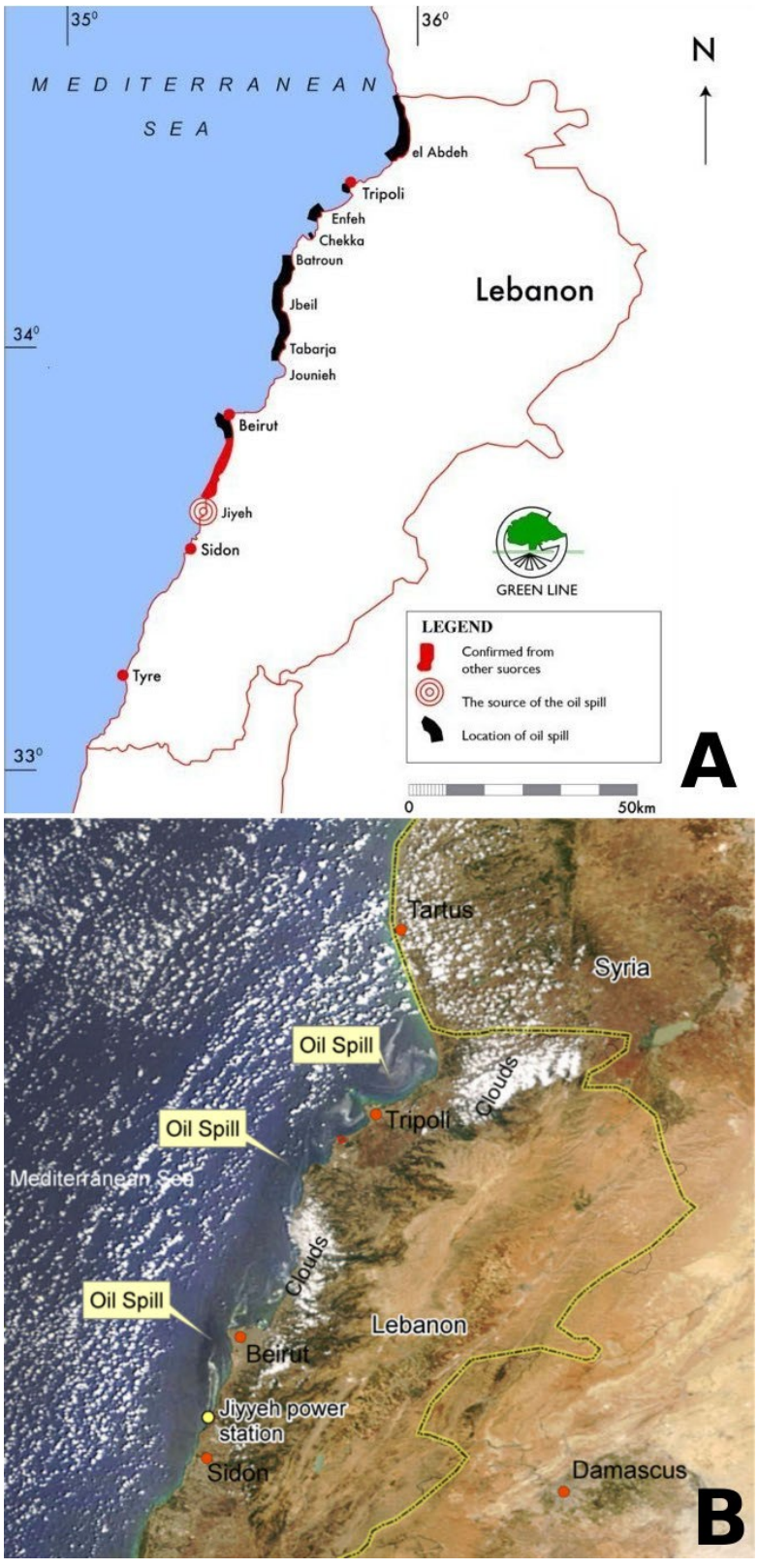

Figure 5.15. **(A)** shows a map highlighting the distribution of the oil spills along the Lebanese coast. **(B)** The MODIS Terra 500 m/pixel resolution natural RGB colour composite image corresponding to bands λ_1=645 (aggregated from the band group), λ_4=555 and λ_3=469 nm respectively (courtesy of the German remote sensing data centre, DLR).

The spills were also visible in a 250 m/pixel resolution MODIS Terra image processed using the radiometric transformation (Figure 5.16A) and in a 500 m/pixel resolution MODIS SST4 image map (interpolated from the 1 km/pixel resolution thermal bands) shown in Figure 5.16B. In the SST4 image map (Figure 5.16B), both the thick oil and sheen are clearly visible due to high sun–glint reflectance off their different surfaces (temperature units are relative due to sun–glint masking of thermal absolute readings). The Chlor-a map was irretrievable over the spill area due to prevailing sun–glint.

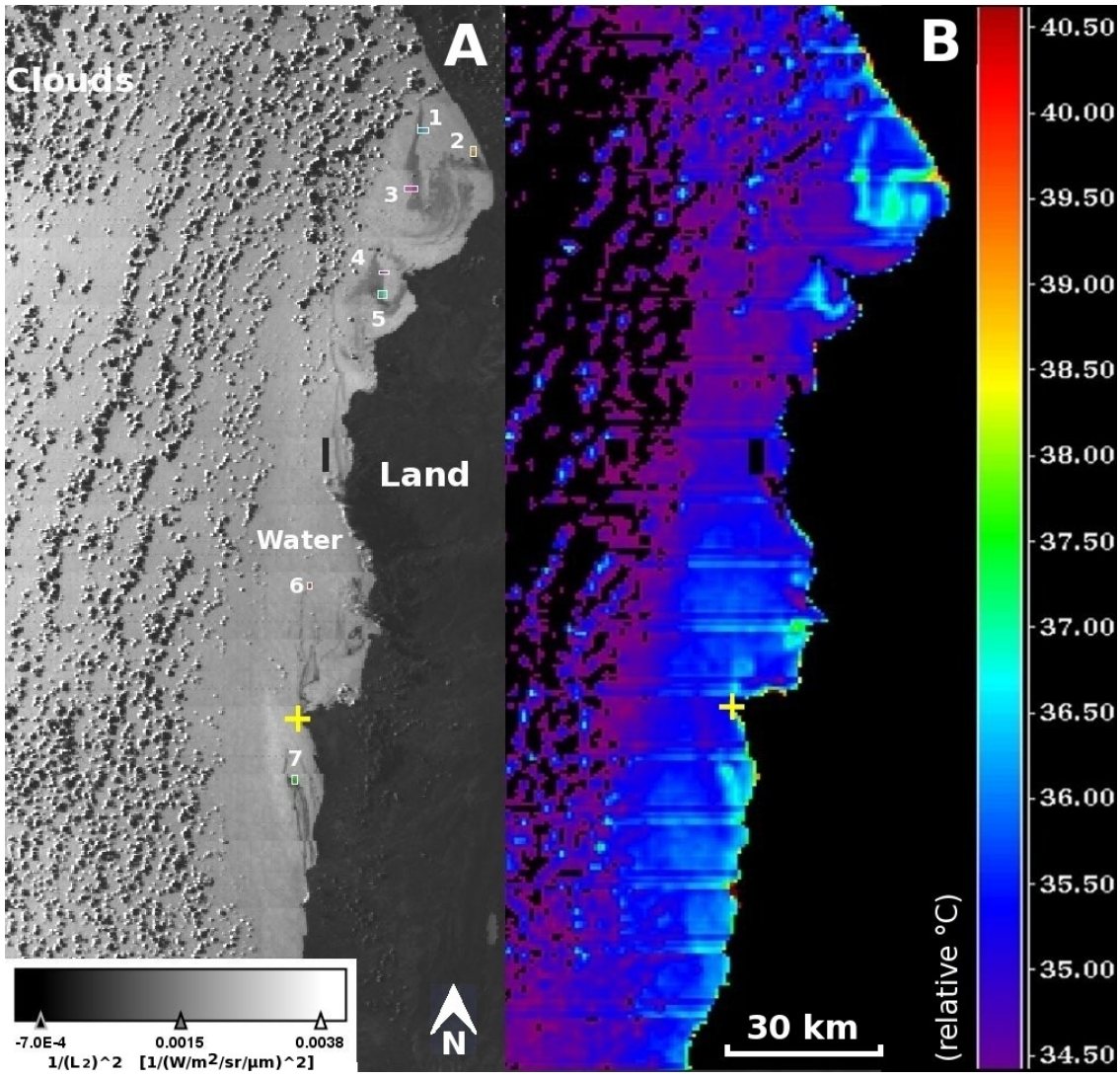

Figure 5.16. The oil spill in Lebanon as it appears in MODIS Terra viewed on 1st August, 2006 at 08:32 UTC as it appears on **(A)** an image processed according to the radiometric transformation, over which the SCS sampling areas are shown with their associate numbers; the results are shown in Table 5.5. **(B)** The MODIS Terra SST4 (3.95–4.05 µm) map processed over the same area shown in A. The oil–accumulated areas are clearly visible due to high solar reflectance off their surfaces. The + mark is positioned at N33° 54' 30.6" E35° 27' 22.3".

The numbered oil spill sampling areas shown in Figure 5.16A were subject to the SCS classifier and the results are summarized in Table 5.5.

Table 5.5. The SCS classification carried out over the sampling areas displayed in Figure 5.16. Oil=thick oil, LTO=light thickness oil and U=undetermined.

Area No.	L2 (W/m2/sr/µm)		L1 (W/m2/sr/µm)		N pixels	SCS	Classification
	Min.	Max.	Min.	Max.			
1	22.53	33.74	38.62	56.17	21	0.017	LTO
2	23.15	46.39	40.72	73.09	24	0.066	U
3	21.1	29.74	36.65	49.69	32	0.023	LTO
4	20.54	27.25	36.34	45.36	10	0.036	Oil
5	20.24	34.31	35.94	57.40	20	0.035	Oil
6	21.53	25.31	37.2	42.40	10	0.018	LTO
7	21.72	41.87	37.57	64.70	14	0.069	U

5.4.2 Gulf of Cagliari, Sardinia, Italy– 4th September, 2005

An extensive oil spill was reported on 4th September, 2005 around the south–eastern coast of the Gulf of Cagliari in Sardinia, Italy (Figure 5.17A) (Dessì et al., 2008). The average wind speed estimated by the QuikSCAT Satellite 10 m above sea level was ~ 4±2 m/s within the vicinity of the spill. The spill was visible in MODIS Terra on the same date at 10:25 UTC as is shown in a 250 m/pixel resolution false RGB colour composite corresponding to bands λ_2=859, λ_1=645 and λ_1=645 nm respectively (Figure 5.17B). The main reported spill (marked 1 on Figure 5.17B) appears with a negative contrast (dark) compared to water. Other scattered dark patterns are also visible nearby due to their position out of the sun-glint (marked 2 on Figure 5.17B), and were also selected to perform the SCS classification on. Figure 5.17C shows a zoomed-in image of the main spill (marked 1 in Figure 5.17B) created using the radiometric transformation (marked as S). Although, the suspected spill analysed by the SCS classifier (marked 2 in Figure 5.17B) was not independently proven to be an oil spill, its shape nevertheless, strongly indicate that it is one due to its typical "feathered" shape which is caused by the relatively narrow areas of thick oil moving downwind leading edge, surrounded by oil sheen trailing off in the upwind direction (Byfield, 1998).

According to the results presented in Table 5.6, the SCS classification carried out on the patch (marked 2 in Figure 5.17B) agreed with this shape interpretation of the feathered oil spill. The thick downwind leading edge (marked 2 in Figure 5.18B) of the spill was classified as oil by the SCS classifier (SCS=0.040). Whereas the trailing-off sheen layer in the upwind direction was classified as close to water (SCS equal to 0.012 and 0.005 at points marked 1 and 3 respectively in Figure 5.18B).

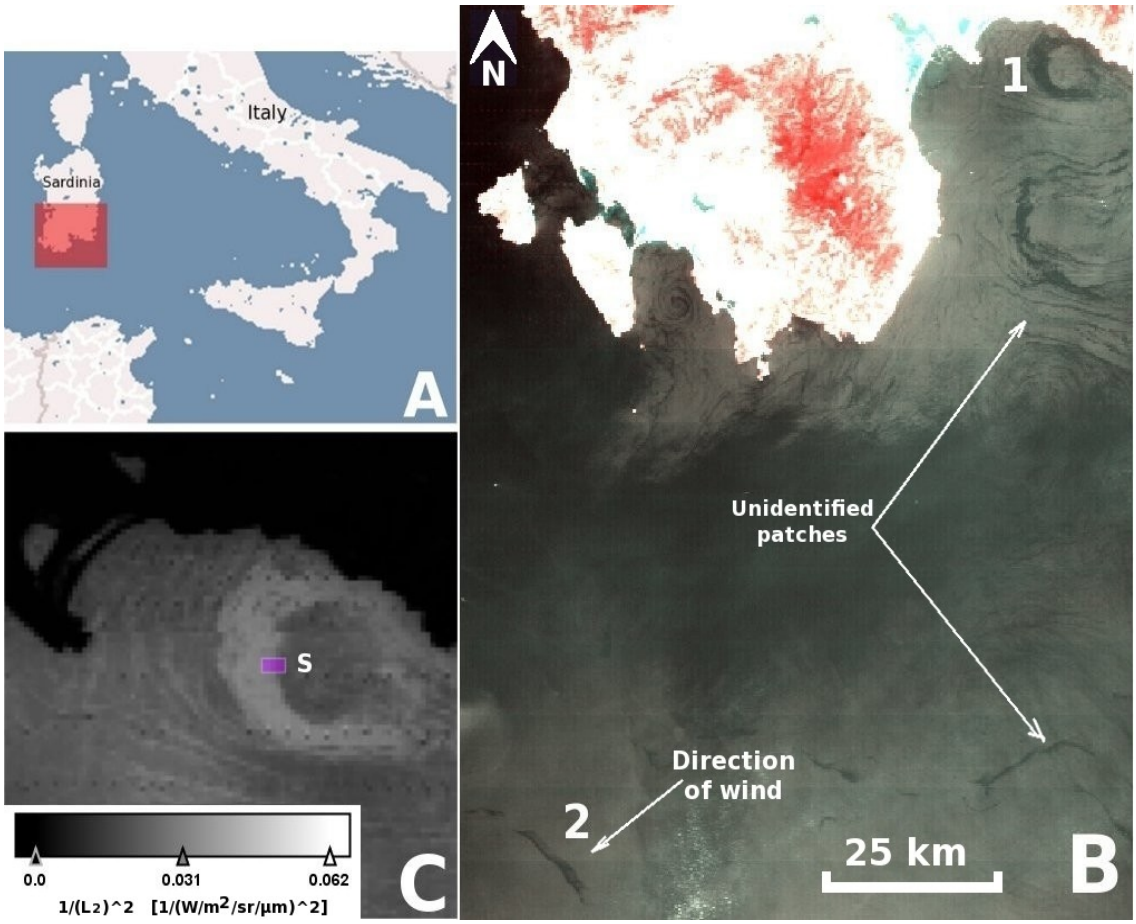

Figure 5.17. **(A)** An oil spill reported on 4th September, 2005 around the south-eastern coast of the Gulf of Cagliari (Sardinia-Italy). **(B)** The spill and its surroundings in the MODIS Terra 250 m/pixel resolution false RGB colour composite corresponding to bands λ_2=859, λ_1=645 and λ_1=645 nm respectively. Marked on it are the two points (1 and 2) where the SCS was applied. The image is centred at N38° 46' 37.8" E8° 38' 25" **(C)** A zoomed-in image of the main spill (marked 1) in B created using the radiometric transformation.. The SCS sampling area is also shown (marked as S) and highlighted in Figure 5.18.

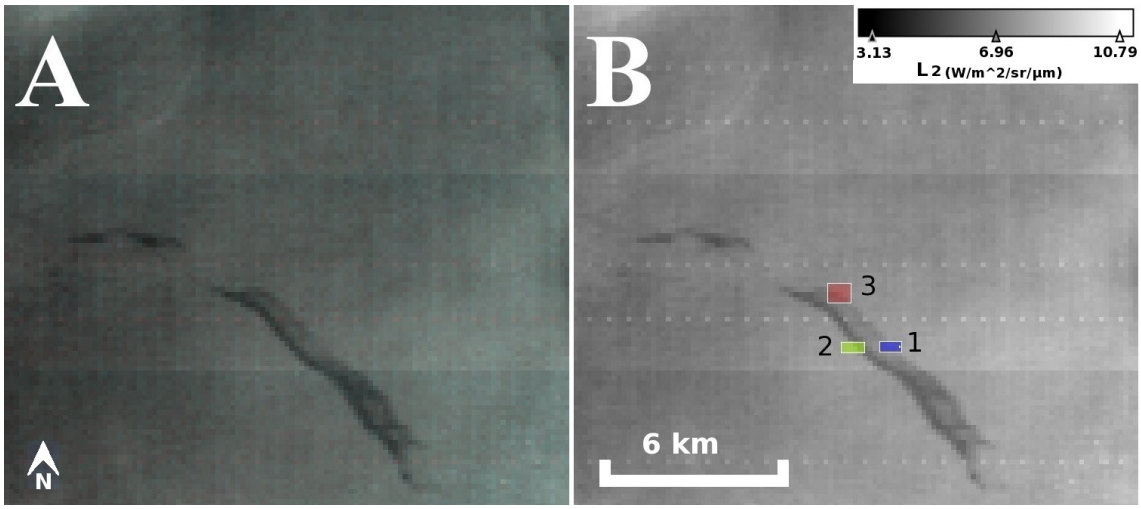

Figure 5.18. The suspected spill (marked 2) on Figure 5.17. **(A)** A 250 m/pixel resolution false RGB colour composite corresponding to bands λ_2=859, λ_1=645 and λ_1=645 nm respectively. **(B)** The suspected spill in a single NIR band radiance image (λ_2=859 nm) over which the SCS sampling areas are shown. The classifications results are summarized in Table 5.6.

Table 5.6. The output SCS classification carried out on the numbered areas displayed in Figures 5.17 and 5.18. Oil=thick oil, PC=pure class and U=undetermined.

Area No.	L_2 (W/m²/sr/µm)		L_1 (W/m²/sr/µm)		N pixels	SCS	Classification
	Min.	Max.	Min.	Max.			
S	6.44	9.42	17.73	21.31	15	0.078	U
1	7.53	7.94	18.42	18.86	8	0.012	PC (water or oil)
2	6.33	7.83	17.02	19.02	8	0.040	Oil
3	6.52	7.35	16.00	18.26	11	0.005	PC (water or oil)

5.4.3 Gulf of Mexico (Deepwater Horizon oil spill)– 25th April, 2010

On 20th April, 2010 approximately 4.9 million barrels of "sweet" (light) crude oil leaked from the Deepwater Horizon offshore oilfield in the Gulf of Mexico (see Appendix B to view the spill under different satellite sensors), 4000 feet below the water surface (Norse & Amos, 2010). Figure 5.19A shows a schematic map of the oil spill on 25th April, 2010 at 10:55 UTC, while Figure 5.19B shows the spill as it appears in MODIS Aqua on the same date but at 18:55 UTC. The MODIS image is a 250 m/pixel spatial resolution natural RGB colour composite image corresponding to bands λ_1=645, λ_4=555 and λ_3=469 nm respectively (λ_4 and λ_3 were oversampled from the 500 m/pixel band group), where the spill appears brighter than water because of its position

within the sun-glint. According to NOAA (2010), the estimated wind speed and sea state for that day was 15–20 knots (7.7–10.3 m/s) and 4–6 foot (1.2–1.8 m) respectively.

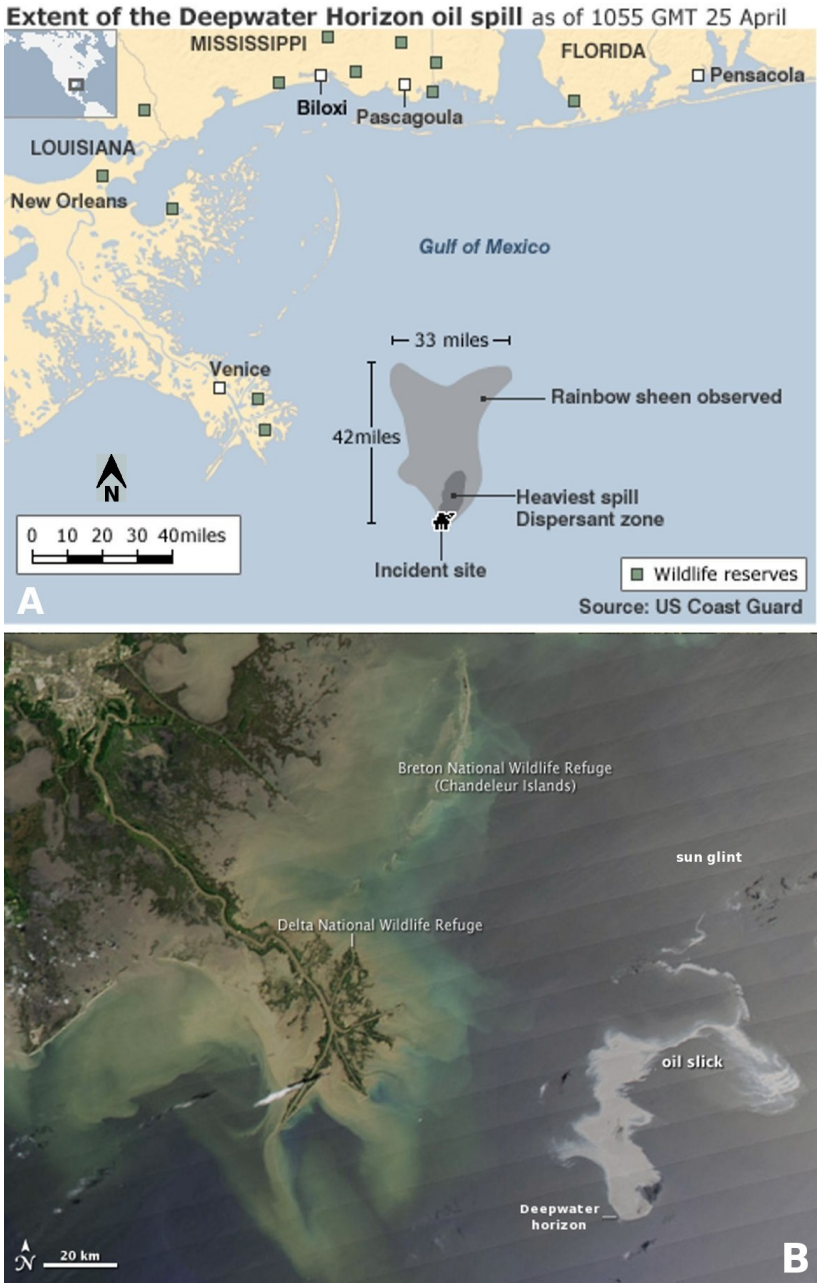

Figure 5.19. The Deep Horizon (positioned at N28° 44.20′ W88° 23.23′) oil spill in the Gulf of Mexico on 25th April 2010 in **(A)** schematic diagram at 10:55 UTC and **(B)** A MODIS Aqua image at 18:55 UTC in a natural 250 m/pixel spatial resolution RGB colour composite image corresponding to bands λ_1=645, λ_4=555 and λ_3=469 nm respectively (λ_4 and λ_3 were oversampled from the 500 m/pixel band group). The spill appears brighter than water because of its position under the sun-glint.

The different concentration layers of oil appear in the MODIS Terra 500 m/pixel resolution (interpolated from the 1 km/pixel resolution thermal bands) SST4 map

(Figure 5.20A). Figure 5.20B shows the 250 m/pixel resolution single NIR band radiance image from (λ_2=859 nm), over which a transect of almost equal-sized sampling areas were selected across different parts of the spill and sea water to test the performance of the SCS classifier. The classification results are shown in Table 5.7.

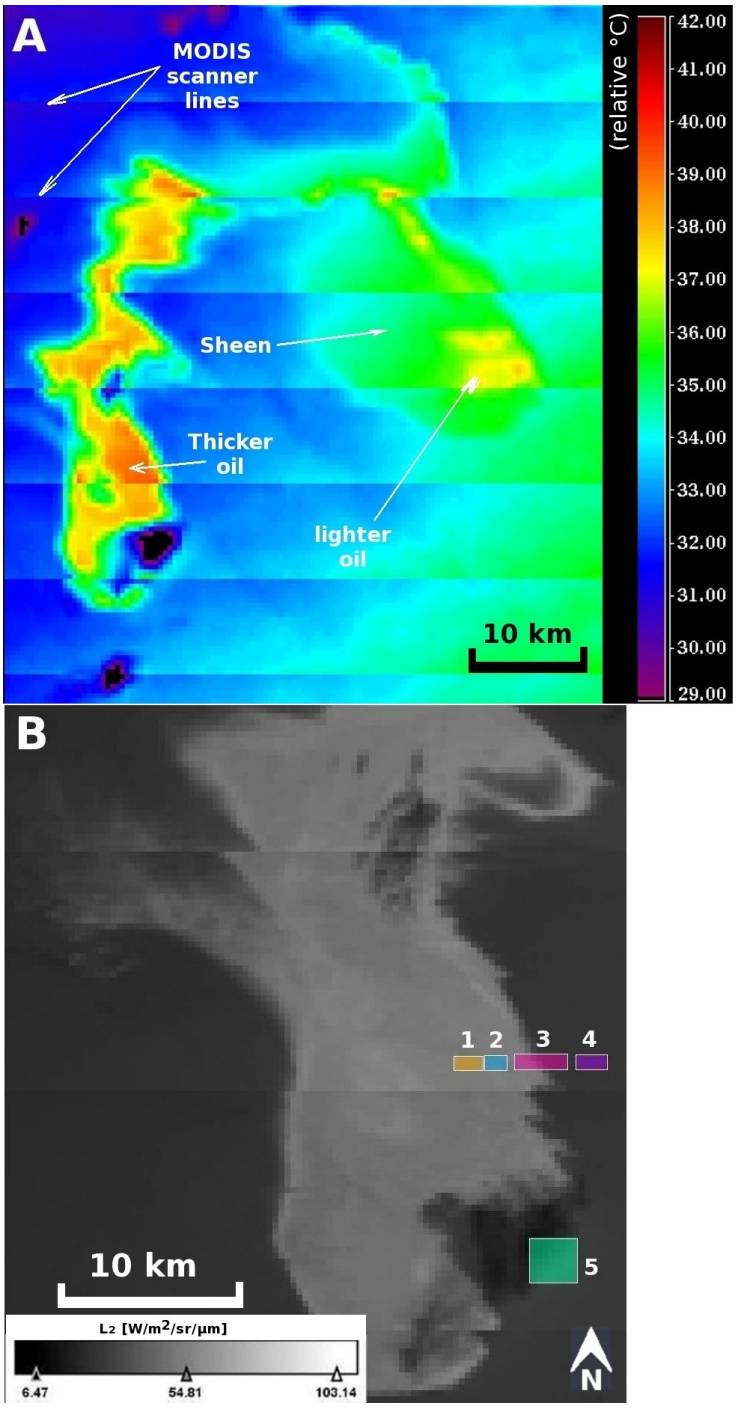

Figure 5.20. The Deep Horizon oil spill in the Gulf of Mexico observed in MODIS Aqua on 25th April 2010 at 18:55 UTC as it appears in **(A)** SST4 image processed at 500 m/pixel resolution interpolated from the 1 km/pixel resolution thermal bands; and in **(B)** a grey-scale image produced from the radiance single NIR band (λ_2=859 nm) at 250 m/pixel resolution.

Table 5.7. The SCS output results for the numbered sampling areas shown in Figure 5.20B. TW=turbid water, WO=weathered oil, U=undetermined and PC=pure class.

Area No.	L_2 (W/m^2/sr/µm)		L_1 (W/m^2/sr/µm)		absolute (SCS)	Classification
	Min.	Max.	Min.	Max.		
1	51.45	53.32	80.76	83.41	0.002	PC (oil)
2	52.73	54.10	80.99	82.86	0.002	PC (oil)
3	26.46	53.45	44.82	83.51	0.049	WO or TW
4	26.28	26.85	44.59	45.42	0.002	PC (water)
5	12.52	30.63	25.01	50.38	0.11	U

The output SCS classification value given for sampling area number 5 (Figure 5.20B) is undetermined (SCS=0.11). Therefore, further *in situ* information is required in order to provide valid interpretation for this result, which is currently unavailable. The area, nevertheless, does display distinct spectral features than the water and oil as is shown in Figures 5.20A and 5.20B respectively. This matches with the different classification results shown in Table 5.7.

To examine the spectral features of area number 5 of the spill in relation to other classes, a line (a to b) was drawn over a 500 m/pixel resolution single NIR band radiance image (λ_2=859 nm) as is shown in Figure 5.21A. After which the transect was plotted in Figure 5.21B revealing a reflectance peak across all bands over the mirror-like oil surface in the sun-glint region, except at the area examined whose reflectance is even lower than the surrounding sea water. This is probably caused by the presence of an invisible sub-surface layer of weathered oil coupled with a sheltering mechanism introduced by the unique boundary conditions of the surrounding thicker oil at this region. It is, therefore, possible that both phenomena have modulated the sea roughness to reflect off its surface all incoming solar illumination away from the sensor and thus appear darker than the surroundings.

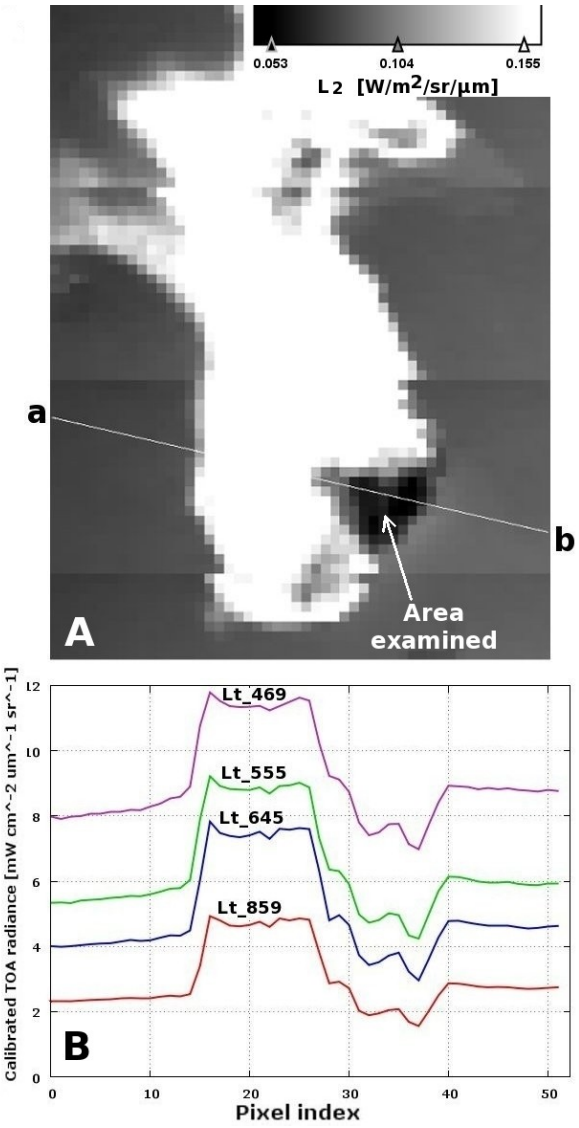

Figure 5.21. A transect line drawn (a to b) across different parts of the Gulf of Mexico oil spill including water from a to b **(A)** over a 500 m/pixel resolution MODIS Aqua image, produced from the single NIR band (λ_2=859 nm) of the Deepwater Horizon oil spill and **(B)** The radiance transect of (A) across all of the 500 m/pixel spectral group.

In order to assess the impact of sampling area size on the output of the SCS classifier, a 250 m/pixel resolution single NIR band (λ_2=859 nm) radiance image was produced (Figure 5.22A), over which different-sized sampling areas were selected over part of the spill. The output SCS values (summarized in Table 5.8) were plotted against the corresponding number of pixels (N) for each selected sampling area (Figure 5.22B).

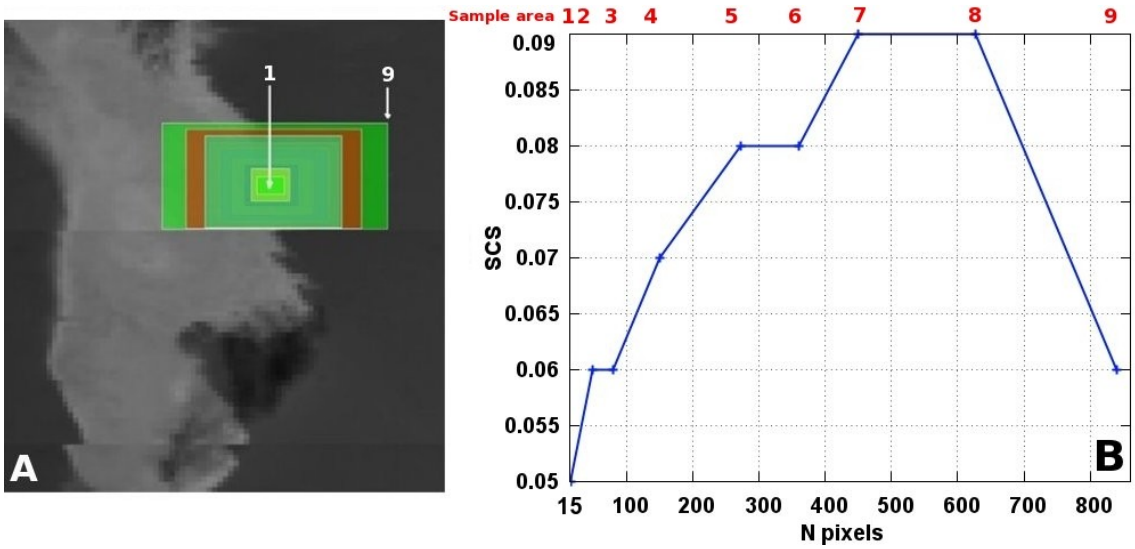

Figure 5.22. The Deep Horizon oil spill in the Gulf of Mexico, as it appears in the MODIS Aqua image on 25th April 2010 at 18:55 UTC in **(A)** a 250 m/pixel resolution single-band radiance image (λ_2=859 nm), over which different-sized sampling areas (1–9) were selected over the same region of the spill and **(B)** the impact of sampling area size (number of pixels) on the output values of the SCS classifier. Table 5.8 shows the results.

Table 5.8. The SCS results for the numbered sampling areas (1–9 from the smaller areas to the larger ones) displayed on Figure 5.22. TW=turbid water, WO=weathered oil, U=undetermined and σ=standard deviation.

Area No.	**N pixels**	**L_2 (W/m²/sr/µm)**		**L_1 (W/m²/sr/µm)**		**absolute (SCS)**	**Classification**
		Min.	**Max.**	**Min.**	**Max.**		
1	15	26.26	53.39	44.28	82.60	0.053	WO or TW
2	48	26.14	54.26	44.2	83.88	0.055	U
3	80	26.14	54.26	44.20	83.88	0.055	U
4	150	26.09	55.86	43.94	83.88	0.072	U
5	273	25.90	56.38	43.83	83.88	0.081	U
6	360	25.65	57.14	43.39	84.73	0.083	U
7	450	25.44	57.43	43.26	85.17	0.086	U
8	627	25.44	57.43	43.16	85.17	0.085	U
9	840	25.32	58.63	42.92	89.74	0.063	U
						σ=0.014 $\overline{SCS}$=0.07	

The mean SCS value that resulted from this experiment was 0.07±0.014 – a value which is within the accepted range of the same classification result (undetermined). This probably signifies a highly weathered oil (above the WO/TW classification shown for the smallest sampling area) for the remaining eight sampling areas. Furthermore, the classification was insensitive to the size of pixel numbers, which indicates the homogeneity (the non mixing of classes) of the selected areas.

5.4.4 Oil spill in lake Maracaibo, Venezuela – 18th January, 2003

In lake Maracaibo,Venezuela (Figure 5.23) scattered oil spills were visible outside the sun-glint area in MODIS Terra image on 18th January, 2003 at 12:35 UTC (Figure 5.24) .

Figure 5.23. Location map of oil spills in lake Maracaibo,Venezuela observed in MODIS Terra on 18th January, 2003 at 12:35 UTC.

The spill's image (Figure 5.24) was created using the radiometric transformation at 250 m/pixel resolution. The original contrast of the spill is positive due to it laying outside the sun-glint zone and was inverted by the transformation in the Figure.

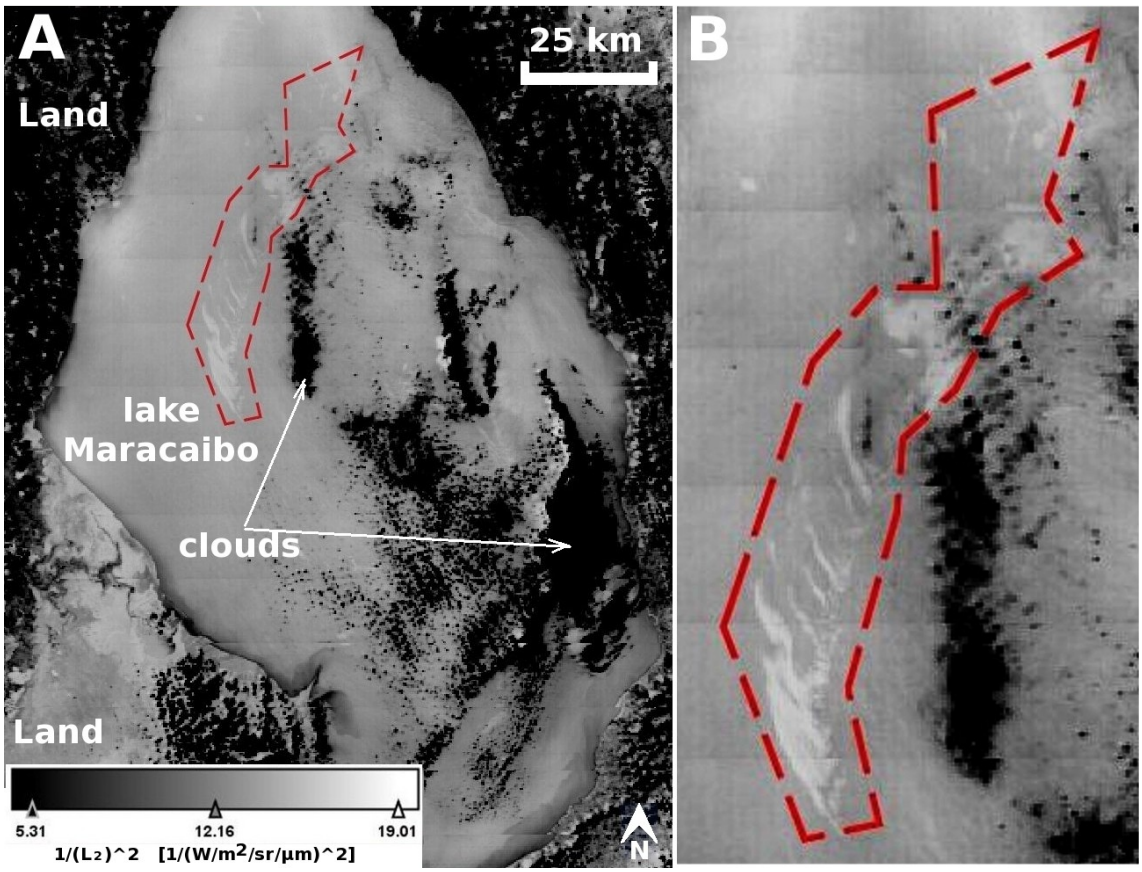

Figure 5.24. Oil spills in lake Maracaibo,Venezuela **(A)** observed in a MODIS Terra image (encircled by red markings) on 18th January, 2003 at 12:35 UTC using the radiometric transformation at 250 m/pixel resolution. Image is centred at position N9° 49′ 56.9" W71° 38′ 14.2" **(B)** A zoomed-in image of the spills taken from (A).

Two RGB colour composites were created to show the appearance of the spills in them: A 500 m/pixel resolution natural RGB colour composite corresponding to bands λ_1=645 (aggregated from the 250 m/pixel band group), λ_4=555 and λ_3=469 nm respectively (Figure 5.25A), and a 250 m/pixel resolution false RGB colour composite corresponding to bands λ_2=859, λ_1=645 and λ_1=645 nm respectively (Figure 5.25B). The bulk of spills seen in the natural and false colour composites appear darker than surrounding waters, due to their location outside the severe sun-glint area.

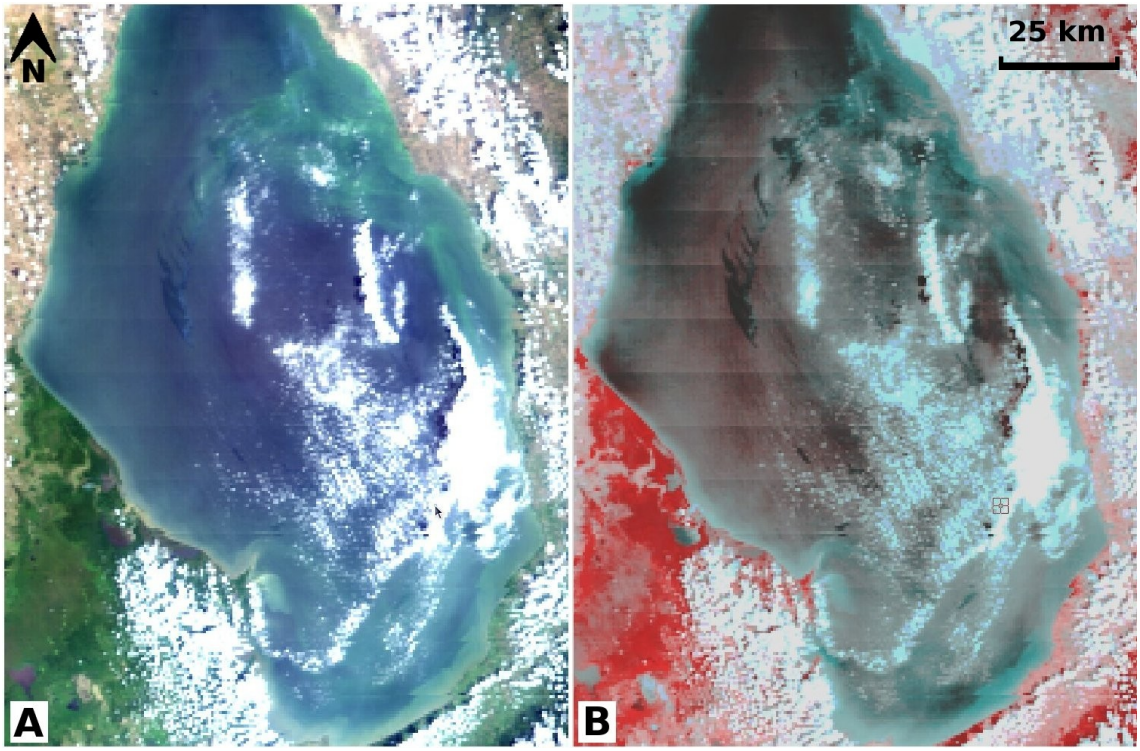

Figure 5.25. The oil spills in lake Maracaibo,Venezuela viewed in MODIS Terra on 18th January, 2003 at 12:35 UTC in **(A)** 500 m/pixel resolution natural RGB colour composite corresponding to bands λ_1=645 (aggregated from the 250 m/pixel band group), λ_4=555 and λ_3=469 nm respectively in; and in a **(B)** 250 m/pixel resolution false RGB colour composite corresponding to bands λ_2=859, λ_1=645 and λ_1=645 nm respectively. Both images are centred at position N9° 49′ 56.9" W71° 38′ 14.2".

An aerial view covering part of the spill is shown in Figure 5.26 showing streaks across its surface similar to those seen in the MODIS Terra images (Figure 5.25).

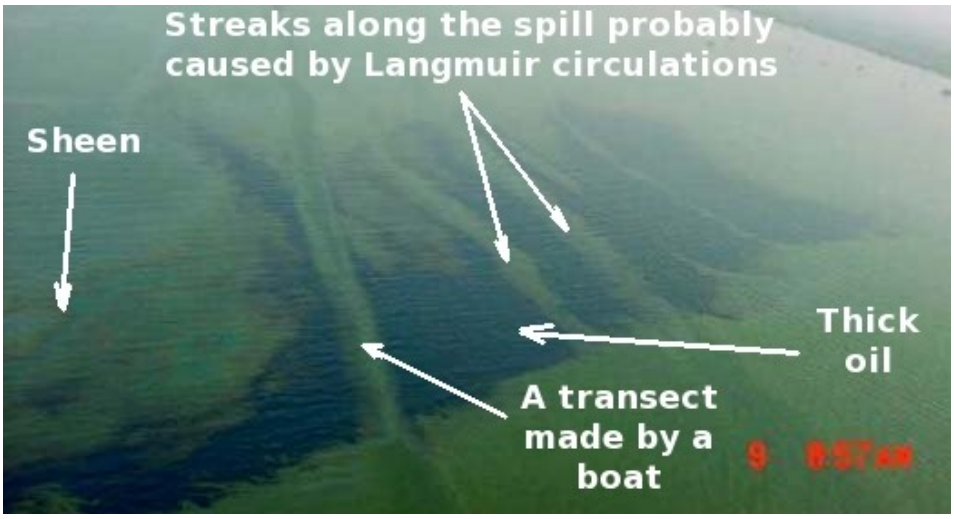

Figure 5.26. Part of the lake Maracaibo,Venezuela oil spill seen from the air (unknown scale and date) (Hu et al., 2003).

A 250 m/pixel resolution single NIR band radiance image (λ_2=859 nm) was created (shown in Figure 5.27), over which four sampling areas were selected covering different parts of the spill where the SCS classifier was applied. Table 5.9 shows the results of this classification process.

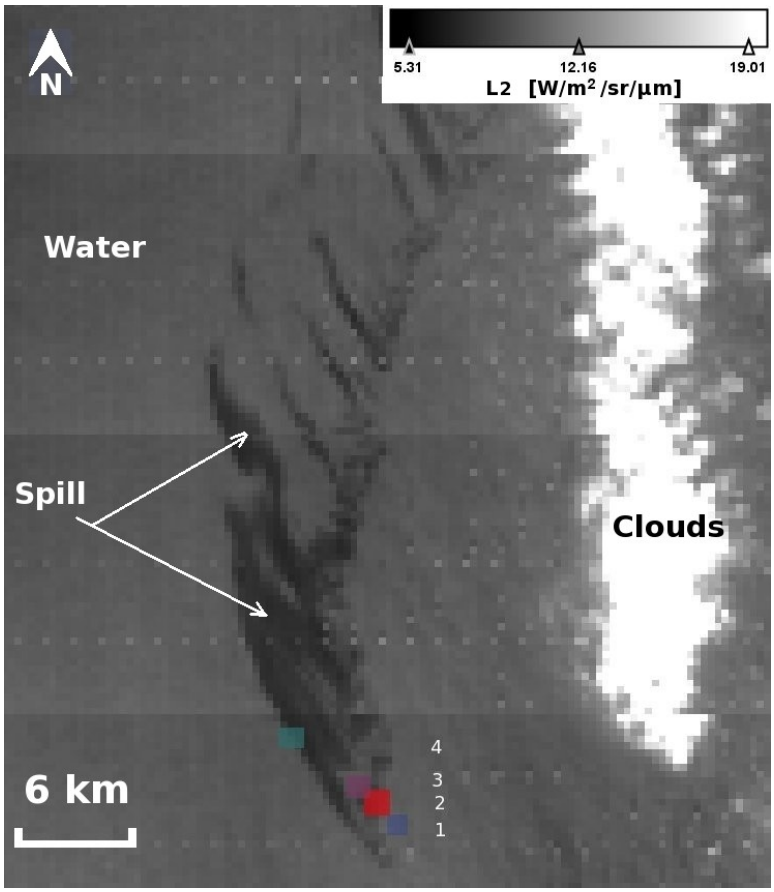

Figure 5.27. Part of the oil spills in lake Maracaibo,Venezuela seen in MODIS Terra on 18th January, 2003 at 12:35 UTC. The image is 250 m/pixel resolution single-band radiance image from (λ_2=859 nm), over which multiple sampling areas (1–4) were selected. The classification results are summarized in Table 5.9.

Table 5.9. The SCS results for the numbered sampling areas (1–4) displayed in Figure 5.27. MTO=medium thickness oil, PC=pure class and U=undetermined.

Area No.	N pixels	L_2 (W/m²/sr/µm)		L_1 (W/m²/sr/µm)		Absolute (SCS)	Classification
		Min.	Max.	Min.	Max.		
1	9	10.37	10.94	24.72	25.55	0.009	PC (water)
2	9	8.53	10.01	22.73	24.56	0.032	MTO
3	9	8.79	9.71	23.10	24.85	0.010	PC (oil)
4	9	7.32	9.89	20.92	23.86	0.065	U

5.5 The calibration of the SCS over oil spill look-alikes

The SCS classifier was calibrated over different oil spill look-alikes observed in the MODIS sensor. The map shown in Figure 5.28 identifies different MODIS swaths (passes) in which different oil spill look–alikes were observed and they included: two cases of surface algae, one of which was under the sun–glint, while the other was not. The third case is a combination of different cloud types, their shadows, as well as low wind–speed areas.

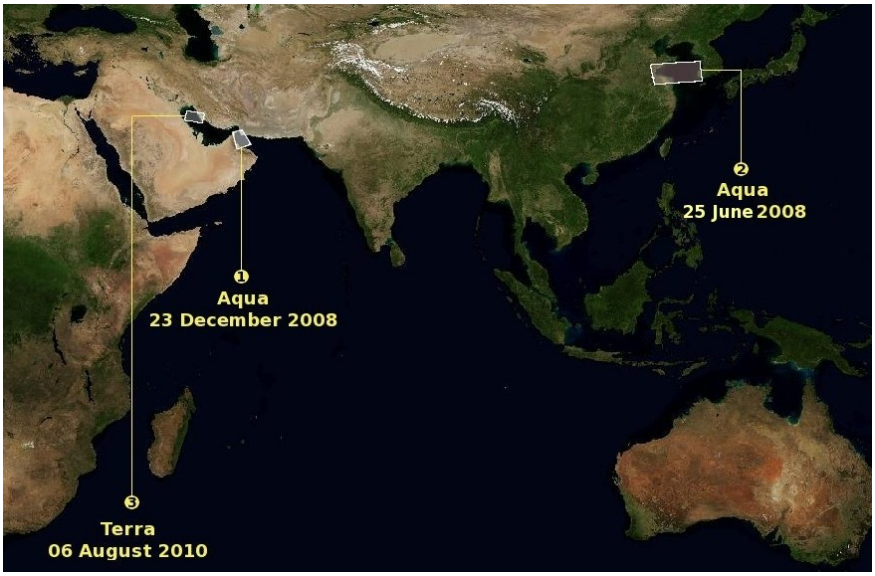

Figure 5.28. A map displaying the location of different MODIS swaths in which oil spill look–alikes were observed.

5.5.1 Surface floating algae (RSA)– 23rd December, 2008

A large algal bloom (species unspecified) was seen in MODIS Aqua on 23rd December, 2008 at 09:46 UTC out of the sun–glint zone in the Strait of Hormuz in the RSA. Figures 5.29A 5.29B respectively show two colour composites: a 500 m/pixel spatial natural RGB composite corresponding to bands λ_1=645 (aggregated from the 250 m/pixel band group), λ_4=555 and λ_3=469 nm respectively and a 250 m/pixel resolution false RGB composite corresponding to bands λ_2=859, λ_1=645 and λ_1=645 nm respectively. In the natural colour composite (Figure 5.29A), the surface blooms appear as dark brownish or blueish. In the false colour composite (Figure 5.29B) they appear reddish, due to the "red–edge" phenomena (high absorption in the red coupled with high reflectance in the NIR).

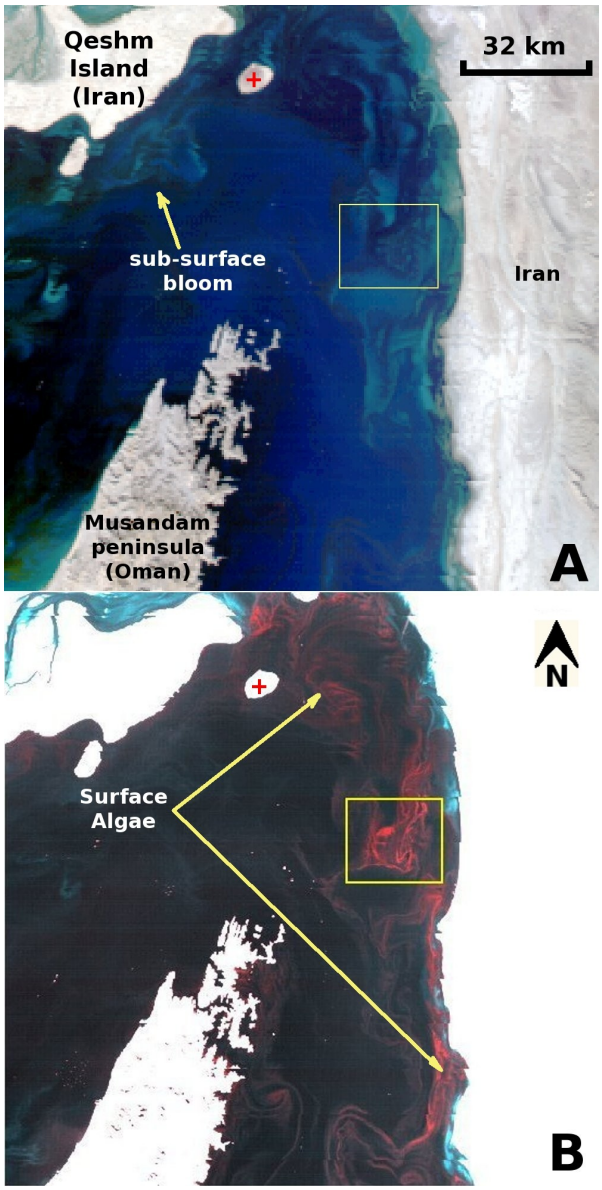

Figure 5.29. An algal bloom (species unspecified) in the Strait of Hormuz (RSA) observed out of the sun–glint zone in MODIS Aqua on 23rd December, 2008 at 09:46 UTC in two colour composites: **(A)** a 500 m/pixel resolution natural RGB composite corresponding to bands λ_1=645 (aggregated from the 250 m/pixel band group), λ_4=555 and λ_3=469 nm respectively and **(B)** a 250 m/pixel resolution RGB false composite corresponding to bands λ_2=859, λ_1=645 and λ_1=645 nm respectively. The study area is shown enclosed by the yellow box. The red + mark is positioned at N26° 51′ 27.5" E56° 21′ 25.2".

A 500 m/pixel resolution Chlor-a map (Figure 5.30A) of the bloom area shows high concentrations of surface and near–surface blooms with their pixels masked in black for failing to estimate their Chlor-a values. This occurs either because their structure is so dense as to not allow ocean–colour water leaving radiances to be estimated or because their Chlor-a values are so high as to be accepted as valid by the Chlor-a algorithm.

Figure 5.30B shows the spectral radiance plot of two different concentration points of the surface bloom (corresponding to two different values of SCS) as well as water, in relation to the 250 m/pixel band group.

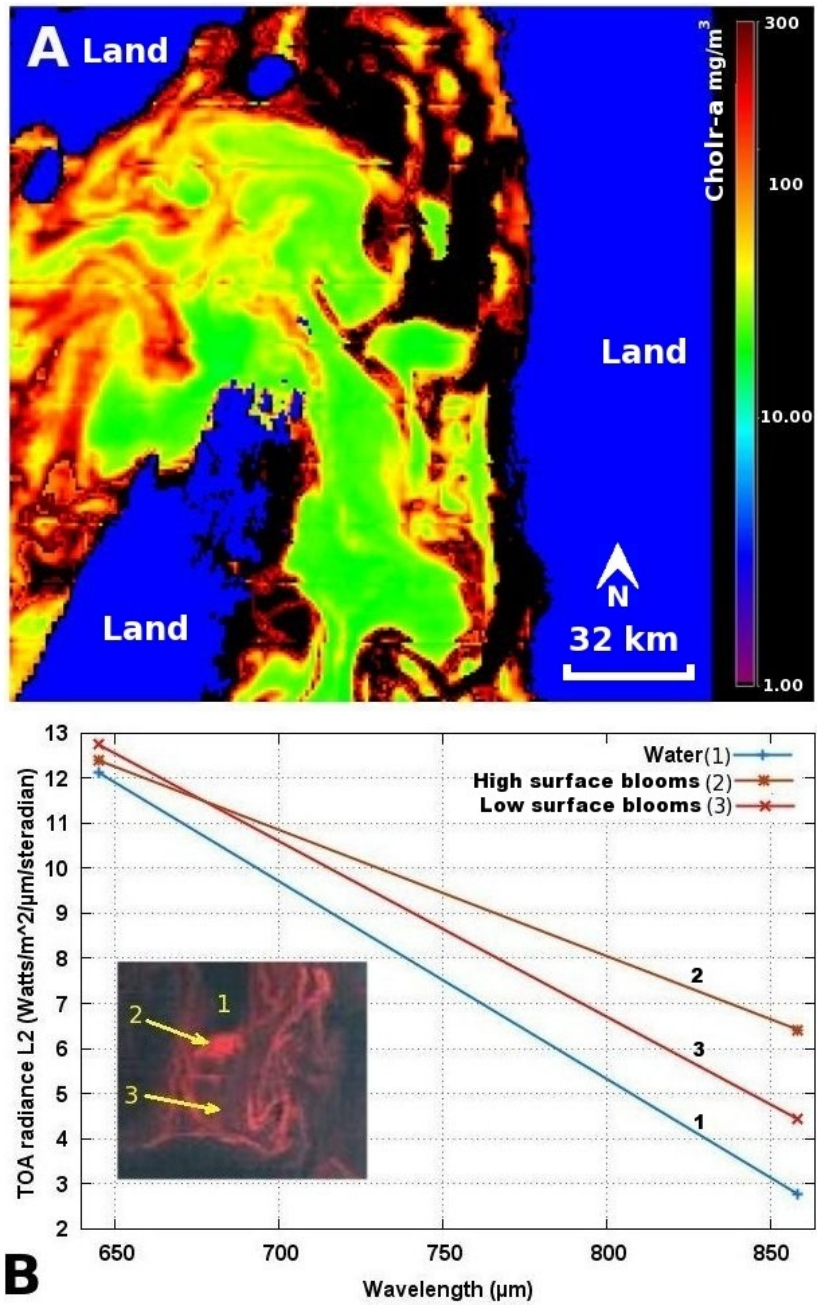

Figure 5.30. High concentration of surface blooms detected in the RSA by MODIS Aqua on 23rd December, 2008 at 09:46 UTC. **(A)** The bloom in a 500 m/pixel resolution MODIS Chlor-a map, where surface blooms are masked in black (failed Chlor-a pixels). Land is masked in blue. **(B)** The radiance–response spectral plot (250 m/pixel band group) for water (point 1) and two different concentrations of surface bloom (points 2 and 3 respectively). Refer to the inset image (zoomed–in image taken from Figure 5.29B) to identify the location of the points. The straight lines were shown for demonstration purposes and carry no regression significance.

A set of SCS sampling areas (1–8) were aligned across part of a mixed–class bloom (Figure 5.31A) as shown in the Figure 5.31B.

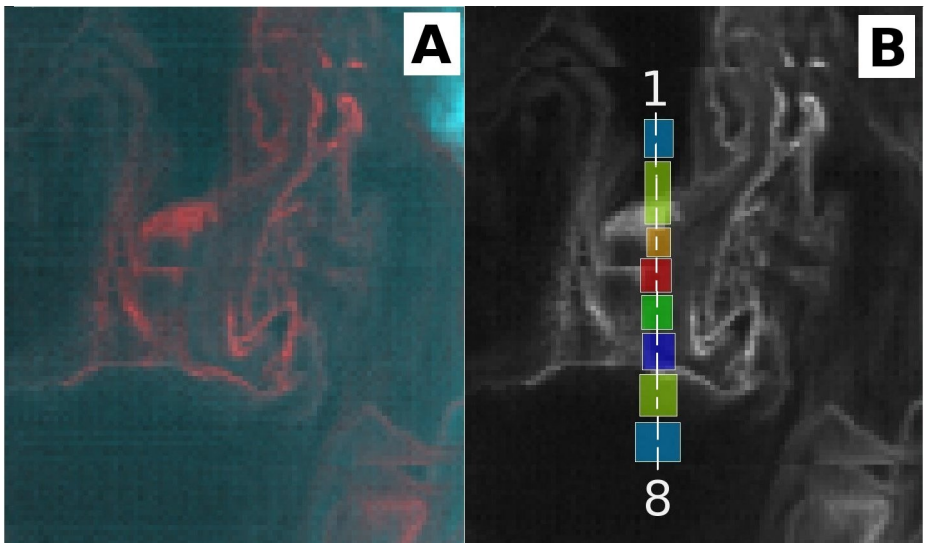

Figure 5.31. **(A)** A zoomed–in image of the bloom taken from the study area (enclosed by a yellow box in Figure 5.29). **(B)** shows a single NIR band radiance image (λ_2=859 nm), over which a series of sampling areas (1–8) were selected to apply the SCS classifier and a line crossing the middle of the areas from (1–8). The results are summarized in Table 5.10.

The SCS results (displayed in Table 5.10) were plotted against the corresponding area number (Figure 5.32A) and compared to a transect plot (Figure 5.32B) for a line crossing the middle of all sampling areas (Figure 5.31B).

Table 5.10. The SCS results for the numbered sampling areas (1–8) displayed on Figure 5.31. TW=turbid water, WO=weathered oil, SA=surface algae, PC=pure class and U=undetermined.

Area No.	**N pixels**	**L_2 (W/m^2/sr/µm)**		**L_1 (W/m^2/sr/µm)**		**absolute (SCS)**	**Classification**
		Max.	**Min.**	**Max.**	**Min.**		
1	38	2.85	2.67	12.55	11.83	0.001	PC (water)
2	55	6.76	2.72	12.88	12.18	0.30	SA
3	34	5.03	3.27	13.04	12.61	0.13	U
4	46	4.28	3.41	13.20	12.31	0.047	TW or WO
5	51	5.40	3.34	13.25	12.63	0.14	U
6	51	4.49	2.81	13.15	12.28	0.11	U
7	55	4.82	2.75	13.5	12.12	0.13	U
8	57	2.95	2.75	12.71	12.01	0.003	PC (water)

The resulting curve–profiles from the two plots are similar. High concentrations of near–surface blooms produce absolute SCS values greater than or equal to 0.20.

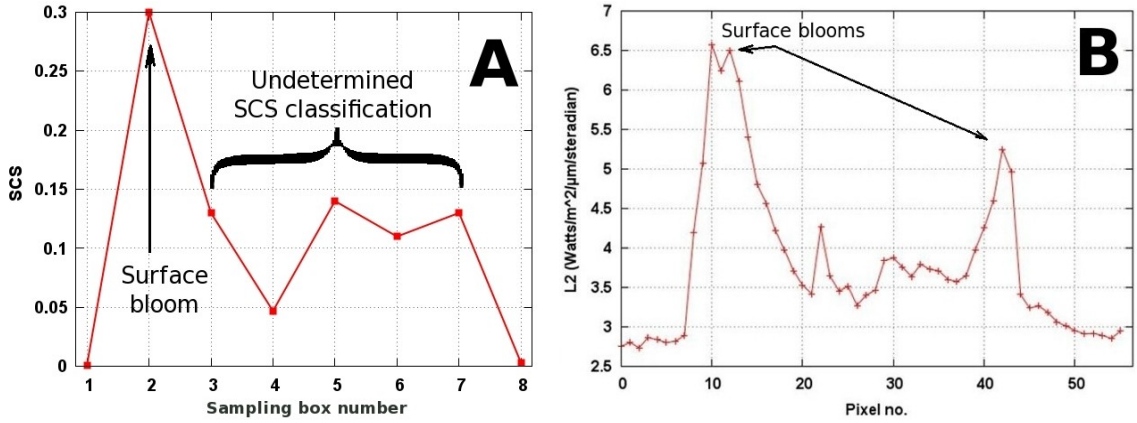

Figure 5.32. **(A)** The SCS values (shown in Table 5.10) were plotted against the number sampling area selected over the mixed–class blooms (Figure 5.31B). **(B)** A transect of the radiance response at (λ_2=859 nm) of a line drawn across the central part of all sampling areas. The profile of the resulting curves from the two plots are similar.

5.5.2 Surface floating algae (Yellow sea)– 25th June, 2008

An *Ulva prolifera* bloom was seen in the Yellow sea Qingdao, eastern China directly under the sun–glint in MODIS Terra on 25th June, 2008 at 12:00 UTC. The surface blooms appear (Figure 5.33) in a set of MODIS Terra radiance images (250 m/pixel resolution) processed from: the single red (λ_1=645 nm) band; NIR (λ_2=859 nm) band; and a false RGB colour composite corresponding to bands λ_2=859, λ_1=645 and λ_1=645 nm respectively. The surface blooms appear darker than water (negative contrast) under the red band (λ_1=645 nm) image (Figure 5.33A) due to high absorption of the red band. Whereas, under the NIR band (λ_2=859 nm) image (Figure 5.33B), the surface blooms appear brighter than water (positive contrast) due to high reflectance in the NIR band. The colour of the *Ulva prolifera* bloom (inset image in Figure 5.34A) appears greenish from the 500 m/pixel spatial resolution natural RGB colour composite corresponding to bands λ_1=645, λ_4=555 and λ_3=469 nm respectively shown in Figure 5.34A. A 250 m/pixel radiance spectral plot is seen in Figure 5.34B for water and surface bloom, from which it is possible to identify the high turbidity of the surrounding sea water due to high water–leaving radiances in the red. This is most likely attributed to the case 2 waters (turbid waters) of the Yellow sea, where suspended–sediment concentrations are 1 to 3 orders of magnitude higher than "typical" shelf depth waters in

most other parts of the world (Wells & Huh, 1984). With regard to the SCS relationship shown in Equation 5.1 and with reference to the minimum and maximum reflectance responses that correspond to the red–NIR bands in water and surface blooms, the non-absolute relationship can, thus, be re–formulated for this particular case as:

$$SCS = \left| \frac{[L_{NIR}]_{Algae}}{[L_R]_{Water}} - \frac{[L_{NIR}]_{Water}}{[L_R]_{Algae}} \right| \tag{5.7}$$

which for a non-absolute SCS value is expected to be negative at this particular point of the bloom.

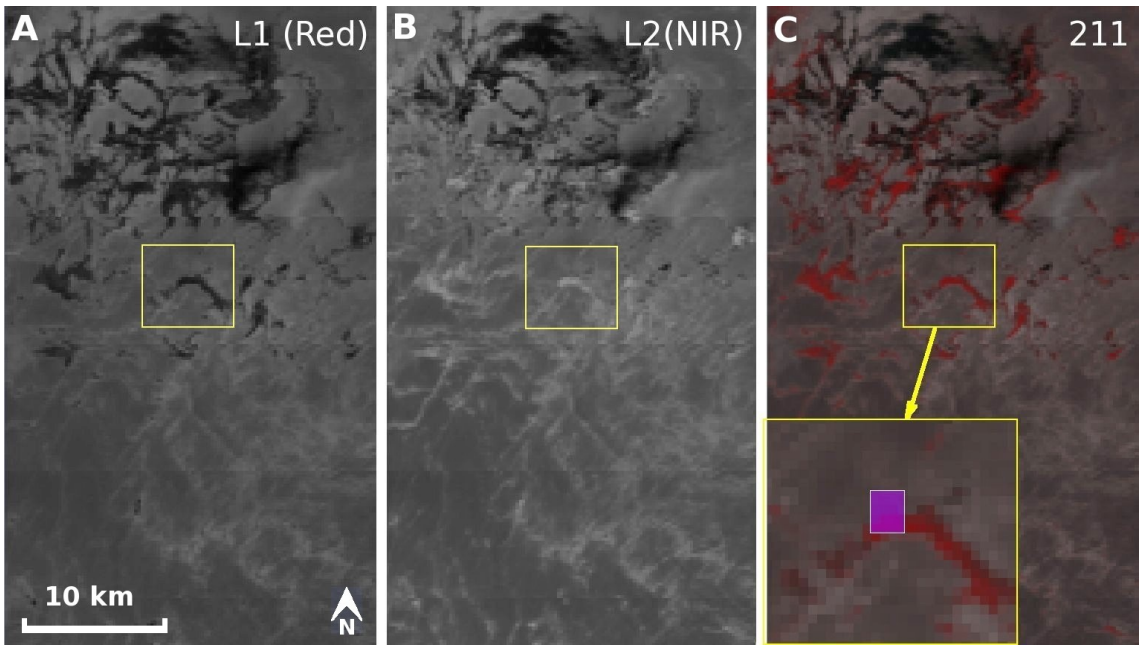

Figure 5.33. An *Ulva prolifera* bloom in the Yellow Sea visible in MODIS Terra on 25th June, 2008 at 12:00 UTC directly under the sun–glint seen in 250 m/pixel resolution radiance–processed images (L): **(A)** L1 (Red: λ_1=645 nm), where surface blooms appear darker than water (negative contrast); **(B)** L2 (NIR: λ_2=859 nm), where surface blooms appear brighter than water (positive contrast); and **(C)** a false RGB colour composite image corresponding to bands λ_2=859, λ_1=645 and λ_1=645 nm respectively. The false composite image (inset) shows a zoomed–in image of a selected area highlighting the reddish coloured bloom due to red–edge effect. Images are centred at position N35°43'38" E120°30'34".

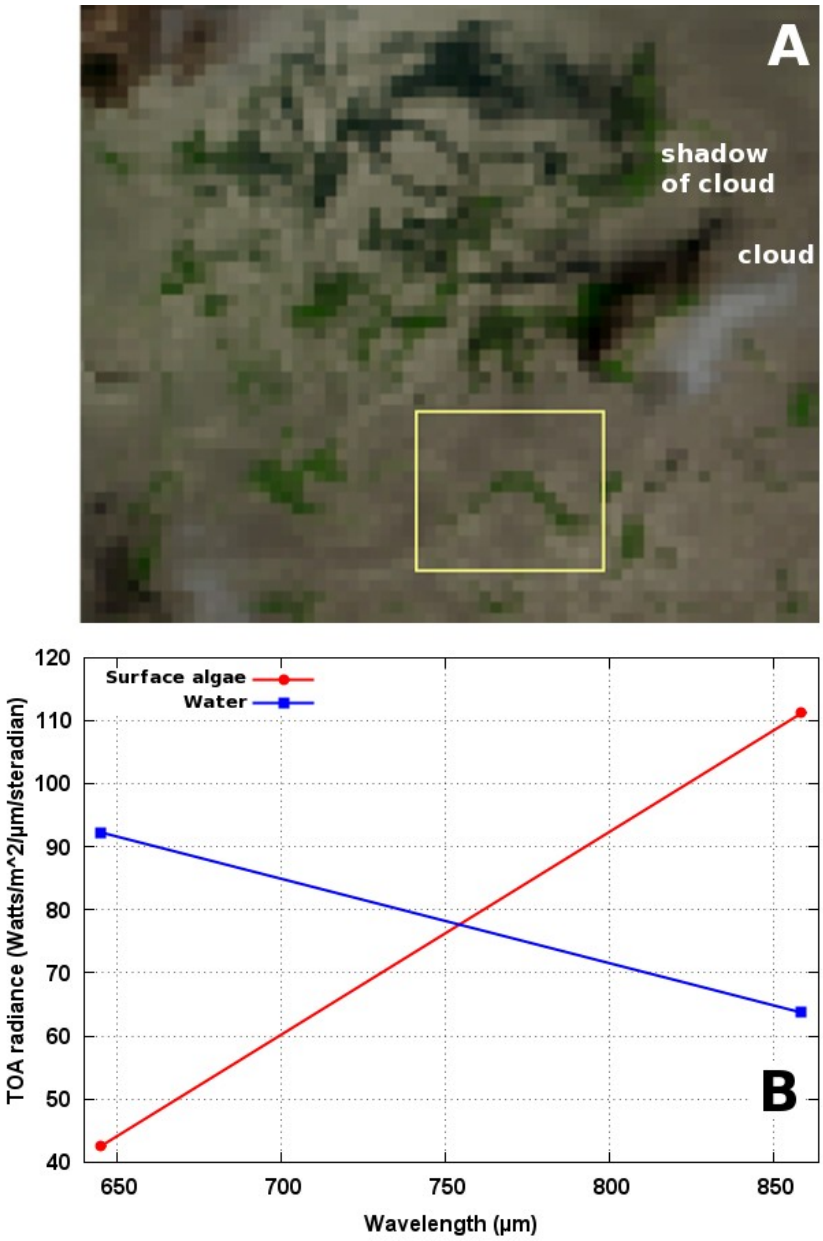

Figure 5.34. An *Ulva prolifera* bloom in the Yellow Sea observed in MODIS Terra on 25th June, 2008 at 12:00 UTC directly under the sun–glint in **(A)** the 500 m/pixel spatial resolution natural RGB colour composite corresponding to bands λ_1=645 (aggregated from the 250 m/pixel band group), λ_4=555 and λ_3=469 nm respectively. An area of the bloom was selected (enclosed by the yellow box). **(B)** A 250 m/pixel band group spectral plot of the radiance values of water and surface bloom. The straight lines in the spectral plot were added for demonstration purposes.

Therefore, five test areas of the bloom were selected, in addition to the sampling area chosen in the inset image of Figure 5.33C and marked as area 1 on Figure 5.35. From the results shown in Table 5.2, area 1 did produce a negative SCS value caused by the high sedimentation in the sea water (high water–leaving radiance in the red band).

However, the absolute SCS classification results for all five areas were consistent as having values greater than or equal to 0.20

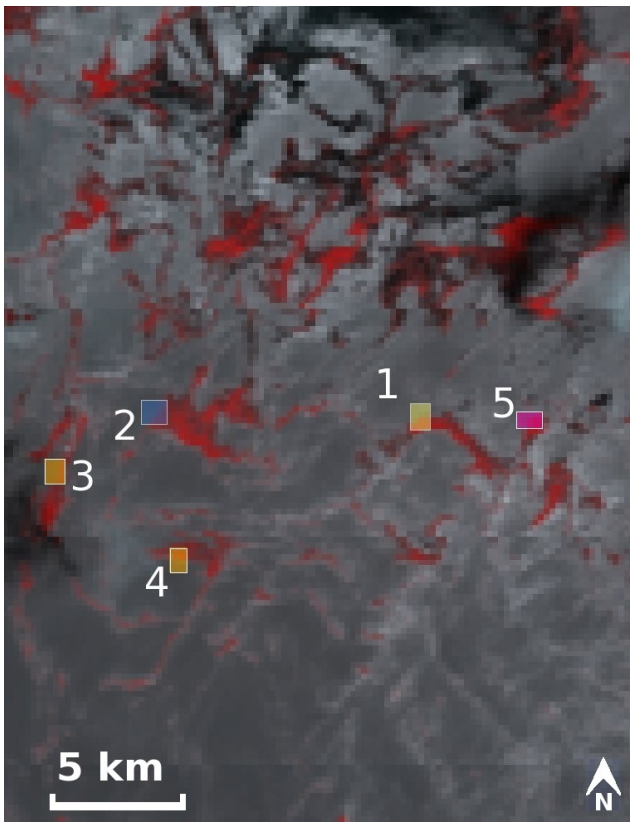

Figure 5.35. Surface blooms of the *Ulva prolifera* species in the Yellow Sea observed in MODIS Terra image on 25th June, 2008 at 12:00 UTC directly under the sun–glint. The image is a 250 m/pixel resolution false RGB colour composite corresponding to bands λ_2=859, λ_1=645 and λ_1=645 nm respectively, over which five different sampling areas were selected to apply the SCS classifier. Table 5.2 shows the results of the classification.

Table 5.11. The estimated SCS value for the selected sample area shown in Figure 5.35. Mean of the absolute SCS values is 0.30 with a standard deviation of 0.08.

Area number	**Total pixels**	**L_2 (W/m^2/sr/µm)**		**L_1 (W/m^2/sr/µm)**		**SCS**
		Max.	**Min.**	**Max.**	**Min.**	
1	17	111.15	60.52	93.54	42.58	0.19
2	15	92.38	52.14	80.22	55.54	0.21
3	12	99.48	48.93	80.82	51.56	0.28
4	25	99.48	46.94	80.82	51.56	0.32
5	14	115.20	62.38	99.68	40.48	0.39

5.5.3 Clouds, cloud–shadows and low–wind areas

Several oil spill look–alikes such as clouds, cloud–shadows, low wind speed patterns, as well as oil spills were classified by the SCS method. These features were observed under a sun–glint zone in MODIS Terra on 6th August, 2010 at 07:26 UTC inside the RSA (see the swath's location on the map in Figure 5.28). A set of 250 m/pixel resolution radiance–based (L) images were produced of the data: a single bands L1 (Red, λ_1=645 nm, Figure 5.36A); L2 (NIR, λ_2=859 nm Figure 5.36B); and a false RGB colour composite corresponding to bands λ_2=859, λ_1=645 and λ_1=645 nm respectively (Figure 5.36C).

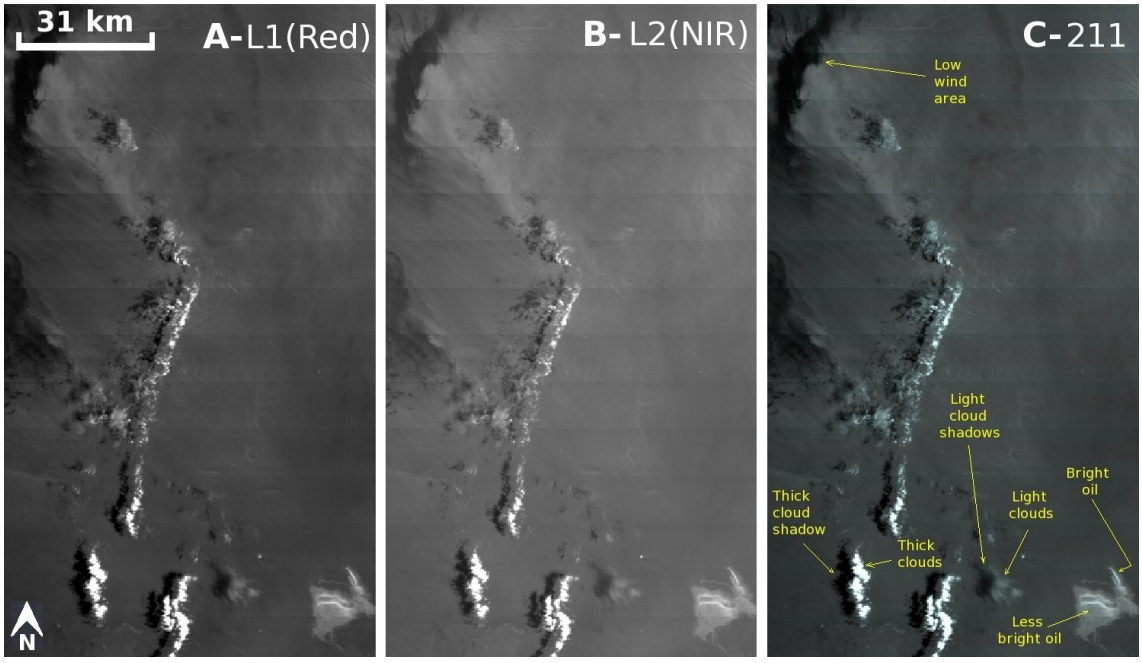

Figure 5.36. Clouds, cloud-shadows and low-wind patterns observed in a MODIS Terra on 6th August, 2010. The images are 250 m/pixel resolution representing **(A)** L1 (Red, λ_1=645 nm), **(B)** L2 (NIR, λ_2=859 nm) and **(C)** a false RGB colour composite corresponding to bands λ_2=859, λ_1=645 and λ_1=645 nm respectively. Images are centred at position N28°27'34" E50°10'15".

From the classification results shown in Table 5.11, the light clouds classification was very close to the classification of the reference water class. The classification output for thick clouds (highlighted in the Table), however, was similar to oil under sun–glint conditions. This is probably caused by the large radiance backscatter caused by the thick clouds in the red and NIR bands as oil would respond. Therefore, in such circumstances, alternative methods should be used in order to mask–out clouds and their shadows from the scene before applying the SCS classifier. The easiest and quickest

option to achieve this, is to do it interactively (manually) by a visual inspection.

Table 5.12. Estimated SCS values of selected oil spill look–alike features shown in Figure 5.36. LTO=light thickness oil, MTO=Medium thickness oil, WO=weathered oil, PC=pure class, Oil=thick oil and U=undetermined. Thick clouds were misclassified as oil. The shaded row(s) is for area(s) under the sun–glint.

Pattern name	Total pixels	L_2 (W/m^2/sr/µm)		L_1 (W/m^2/sr/µm)		SCS	Classification
		Max.	Min.	Max.	Min.		
Bright oil	13	71.84	38.78	111.42	62.23	0.022	LTO
Less bright oil	52	55.29	38.48	83.76	60.76	0.027	MTO
Low wind area	14	32.9	21.76	54.22	40.11	0.064	U
Light clouds	25	53.04	38.5	85.21	61.54	0.003	PC (water)
Light cloud shadow	52	38.43	24.64	61.54	43.99	0.064	U
Thick clouds	20	212.66	39.73	323.04	63.94	0.037	Oil
Thick cloud shadow	51	39.64	16.72	62.57	33.55	0.14	U

5.6 Estimating the uncertainties in the SCS

According to the uncertainties registered in the MODIS L1B files for each spectrum, the measured TOA radiances are acceptable to nominal value (5%). Therefore, to estimate the overall fractional error output in the SCS values, Equations 5.8 and 5.9 were used.

$$Z = \frac{A}{B} \; or \; AB \rightarrow \left(\frac{\Delta Z}{Z}\right)^2 = \left(\frac{\Delta A}{A}\right)^2 + \left(\frac{\Delta B}{B}\right)^2 \tag{5.8}$$

where Z is an arbitrary function resulting from the ratio or the product of arbitrary values A and B, with the corresponding uncertainties ΔZ, ΔA and ΔB respectively.

$$E = C \pm D \rightarrow \Delta E^2 = \Delta C^2 + \Delta D^2 \tag{5.9}$$

where E is an arbitrary function made up of the arbitrary values C and D either added or subtracted, whose corresponding uncertainties are ΔE, ΔC and ΔD respectively. Table 5.12 shows an illustrative example of how the uncertainty in the SCS output values were estimated.

Table 5.13. The estimated fractional error in the SCS values using Equations 5.8 and 5.9.

$max_2 \pm 5\%$	$max_1 \pm 5\%$	$min_2 \pm 5\%$	$min_1 \pm 5\%$	$(max_2/max_1) \pm \Delta Z_1$	$(min_2/min_1) \pm \Delta Z_2$	$SCS \pm \Delta E$
6.65	17.49	5.38	15.41	0.38±0.03	0.35±0.02	0.03±0.04

The final error calculated for the SCS value was comparable to the SCS values. This is inherently disadvantageous whenever subtraction involves two almost equal sized values, each of which measured independently (Squires, 2001). It was, therefore, decided to use instead the standard deviation value (σ) of each classification group as a more appropriate measure for uncertainty in SCS values.

5.7 The validation of the SCS

5.7.1 Over MERIS data

The Medium Resolution Imaging Spectrometer (MERIS) is a MODIS-like sensor (maximum resolution of 300 m/pixel at nadir) on-board the European satellite ENVISAT. MERIS uses 15 spectral bands over the 390–1040 nm range, four bands of which (see Table 5.13) to be used in the SCS classifier: NIR bands (λ_{13}=865 and λ_{14}=890 nm); the red bands (λ_6=620 and λ_7 =665 nm); and the blue (λ_2=442.5 nm) and green (λ_5=560 nm) bands that were also used to produce other RGB colour composites.

Table 5.14. MERIS bands used in the SCS classifier including those used for the RGB colour composites.

Band index	Band centre (nm)	Band width (nm)
2 (Blue)	442.5	10
5 (Green)	560	10
6 (Red)	620	10
7 (Red)	665	10
13 (NIR)	865	20
14 (NIR)	885	10

A relatively small unidentified oil spill (8.8 km^2) was found in the Adriatic Sea using the 300 m/pixel resolution visible bands of MERIS on 22nd August, 2003 at 09:20 UTC (swath shown in Figure 5.37A). Two RGB colour composites radiance images

were created to view the spill in: a false RGB composite corresponding to bands λ_{13}=865, λ_7=665 and λ_7=665 nm respectively (Figure 5.37B) and a natural RGB composite corresponding to bands λ_7=665, λ_5=560 and λ_2=442.5 nm respectively (Figure 5.37C).

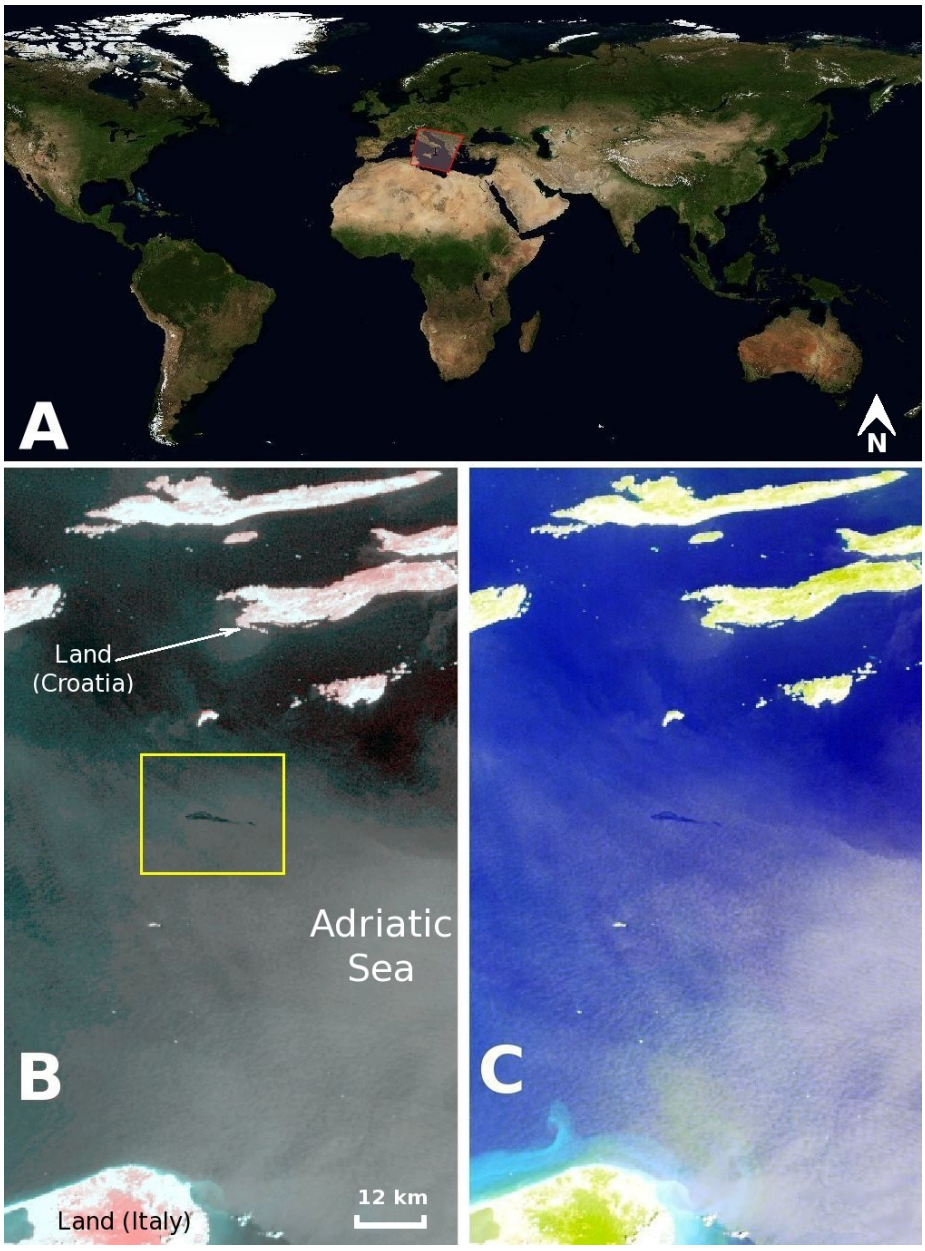

Figure 5.37. A relatively small unidentified oil spill (8.8 km^2) visible in ENVISAT MERIS L1B subset (300 m/pixel resolution) on 22nd August, 2003 at 09:20 UTC: **(A)** The location map of the spill in the Adriatic Sea. **(B)** A false RGB colour composite corresponding to bands λ_{13}=865, λ_7=665 and λ_7=665 nm respectively showing the spill highlighted by a yellow box (the image is centred at N42°33'56" E16°27'41") and **(C)** a natural RGB colour composite corresponding to bands λ_7=665, λ_5=560 and λ_2=442.5 nm respectively.

A single NIR band radiance image was produced (λ_{13}=865 nm) on which a sampling area (N=42 pixel) was selected over which the SCS algorithm was applied using the NIR and red bands outlined in Table 5.13; the results are shown in Table 5.14. The classification results for the investigated oil patch were consistent across all bands used (mean SCS value 0.040±0.003). This further demonstrate the stability of the SCS classification results even when applied using different spectral ranges and used over different spatial resolutions other than MODIS's, as it was the case in MERIS.

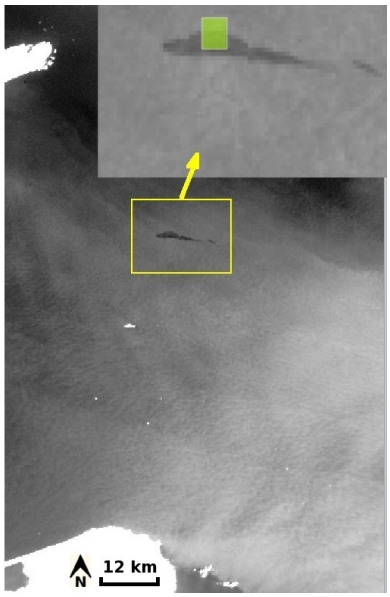

Figure 5.38. An oil spill in the Adriatic Sea seen on 22nd August, 2003 at 09:20 UTC in a single-band radiance image produced from MERIS band (λ_{13}=865 nm). The inset shows the sampling area (N=42 pixel) selected over the spill and water to test the SCS classifier. The results are shown in Table 5.14.

Table 5.15. The MERIS red and NIR channel (see Table 5.13) combinations used in testing the SCS method over the oil spill incident shown in Figure 5.38. Radiance values in (mW/m^2/sr/nm) and N pixels=42. The standard deviation is denoted by σ.

NIR	Red	L_2 (W/m^2/sr/µm)		L_1 (W/m^2/sr/µm)		SCS	Classification
		Max.	Min.	Max.	Min.		
λ_{13}	λ_6	3.39	2.68	13.58	12.68	0.038	Oil
λ_{13}	λ_7	3.39	2.68	10.53	9.63	0.044	Oil
λ_{14}	λ_6	3.13	2.45	13.58	12.68	0.037	Oil
λ_{14}	λ_7	3.13	2.45	10.53	9.63	0.042	Oil
						σ=0.003 $\overline{SCS}$=0.04	

The SCS algorithm was also tested in monitoring oil spills and surface algal blooms during the operation of ROPME's MODIS ground receiving station in 2007. During this period, more than 100 incidents were successfully detected and classified as oil spills using the SCS classifier (see Appendix A for a selection of incidents). *In situ* verification methods were used to achieve true positive identification of classified spills in addition to the use of SAR data. Figure 5.39 shows the location map of three examples of such cases, whose details are summarized in the following section.

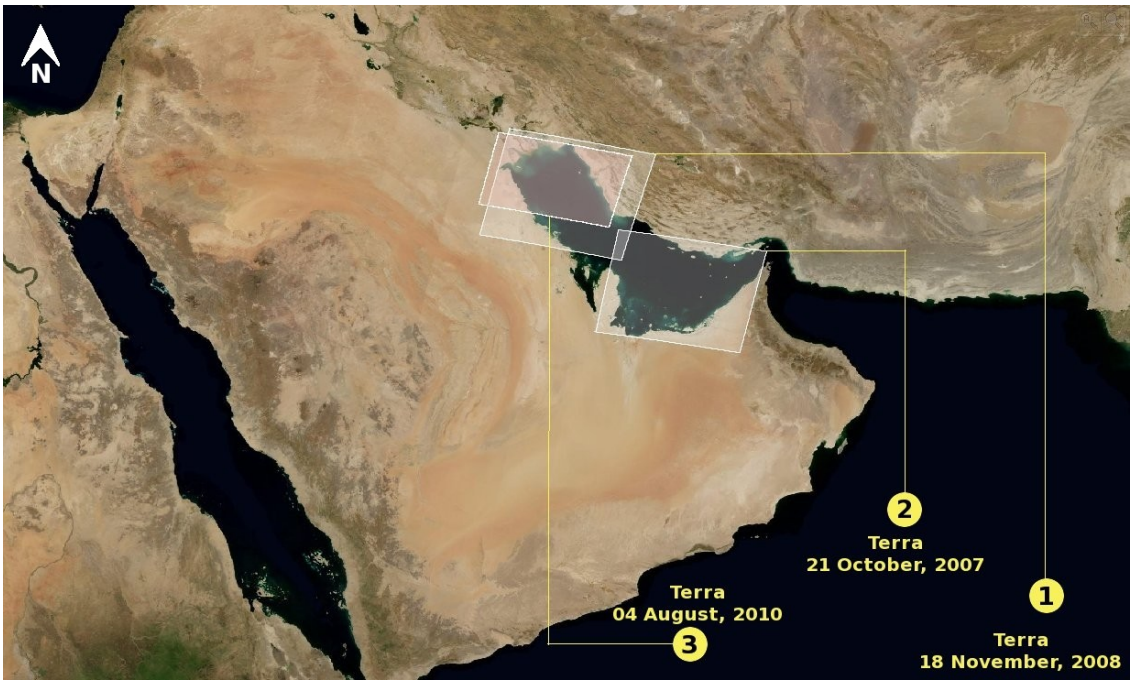

Figure 5.39. The MODIS swaths in which three spill incidents were identified first by the SCS method and were later verified as true positives by *insitu* methods.

5.7.2 Ardeshir (Aboozar) oilfield (Iran) – 18th November, 2008

An oil spill from the Iranian Ardeshire (Aboozar) oilfield (medium type oil, API°=26.9[38]) with an estimated length of 16 km was visible in MODIS Terra out of the sun–glint coverage area on 18th November, 2008 at 07:38 UTC. A 250 m/pixel resolution false RGB colour composite image of the spill corresponding to bands λ_2=859, λ_1=645 and λ_1=645 nm respectively is shown in Figure 5.40A. Figure 5.40B shows part of the spill from an aerial view provided by the Iranian environmental agency (timing unspecified), where the oil appears as a light reddish/brownish strip surrounded by a lighter sheen layer. The average wind speed estimated by the ASCAT

[38] According to ETC Spills Technology Databases, Oil Properties Database (http://www.etc-cte.ec.gc.ca/databases/OilProperties/)

instrument at 10 m above sea level was ~ 6 m/s.

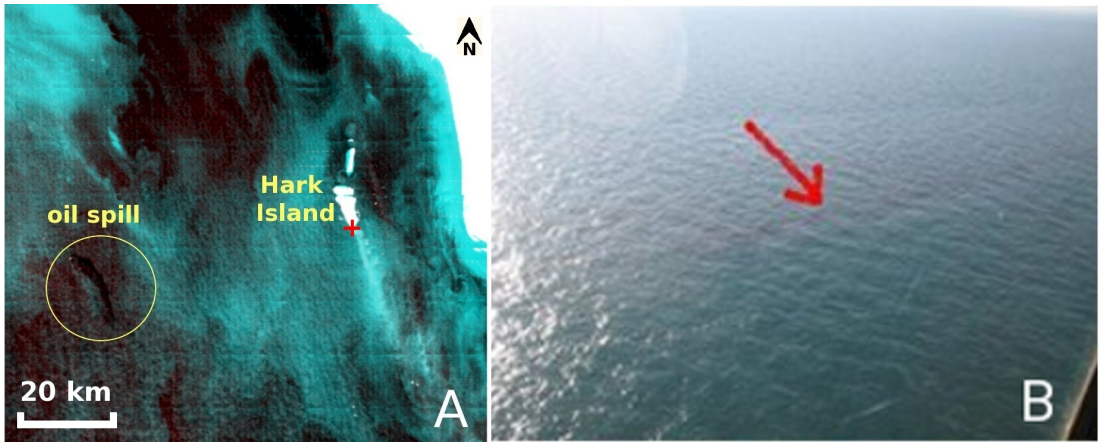

Figure 5.40. An oil spill from Ardeshir (Aboozar) oilfield, Iran observed by MODIS Terra on 18th November, 2008 at 07:38 UTC as it appears in **(A)** a 250 m/pixel resolution false RGB colour composite corresponding to bands λ_2=859, λ_1=645 and λ_1=645 nm respectively and in **(B)** an aerial view appearing as a brownish/reddish strip in the water (courtesy of the Iranian environmental agency). The red + mark is positioned at N29° 12' 21.2" E50° 19' 16.6".

Figure 5.41 shows a 250 m/pixel single–band image processed from (λ_2=859 nm) of the oil spill track, over which three SCS sampling areas (1–3) were selected to asses how the oil's concentration will vary as it disperses away from the source(s).

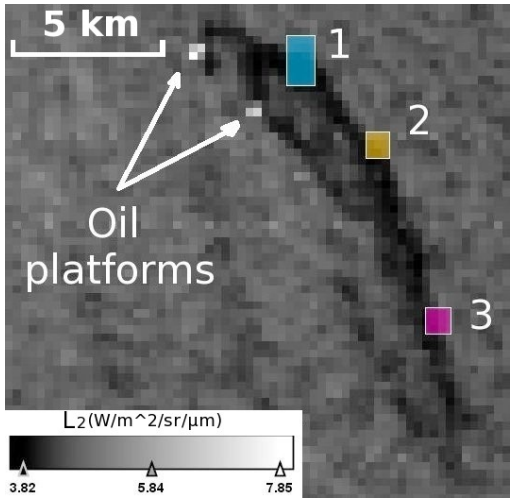

Figure 5.41. A 250 m/pixel resolution single NIR band image (λ_2=859 nm) zoomed–in from the spill image shown in Figure 5.40A. Three sampling areas were selected over the spill to perform the SCS classification whose results are shown in Table 5.15.

Table 5.16. The results of the SCS for the three areas (1–3) selected over the spill case shown in Figure 5.41. LTO=light thickness oil and Oil=thick oil.

Area number	N pixels	L_2 (W/m²/sr/µm)		L_1 (W/m²/sr/µm)		SCS±0.002	Classification
		Min.	Max.	Min.	Max.		
1	12	3.71	4.66	13.26	14.65	0.038	Oil
2	8	3.88	4.74	13.65	14.84	0.035	Oil
3	8	3.89	4.61	13.76	15.07	0.023	LTO

Because area 3 is furthest from the source(s) of the spill than areas 2 and 3, the SCS classified the oil's concentration as light thickness rather than thick oil, which was the classification given for the areas closest to the source of the spill. The result agrees with the expectations that the oil's thickness will get thinner as it moves further away from its original sources.

5.7.3 Jabal Ali port (Dubai, UAE) – 21st October, 2007

While performing the SCS calibration on a suspected patch (unreported) near Jabal Ali port in Dubai, UAE (covered in section 5.3.1 of this chapter and shown as number 6 on Figure 5.7), it was classified as oil (SCS=0.036±0.002). Figure 5.42 shows a 250 m/pixel resolution zoomed–in image of the spill produced using the radiometric transformation. A year later the United Arab Emirates (UAE) environmental sources did confirm the findings by declaring that there was a diesel leak from a moving a ship that caused the spill.

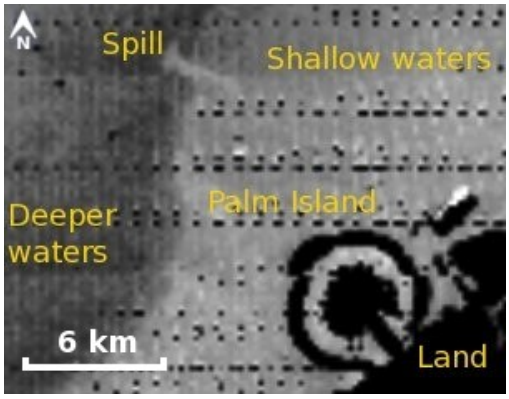

Figure 5.42. A small diesel spill that leaked from a ship in the port of Jabal Ali port in Dubai, UAE appearing in a 250 m/pixel resolution MODIS Terra image on 21st October, 2007 (marked as 6 on Figure 5.7) produced using the radiance transformation (the scanner lines are visible in the image due to high contrast stretching). The image is centred at position N25° 2' 16.6" E54° 57′ 10.3".

Figure 5.43 shows a single–band radiance image (λ_2=859) over which three sampling areas were selected to conduct the SCS classification and their results are shown in Table 5.16.

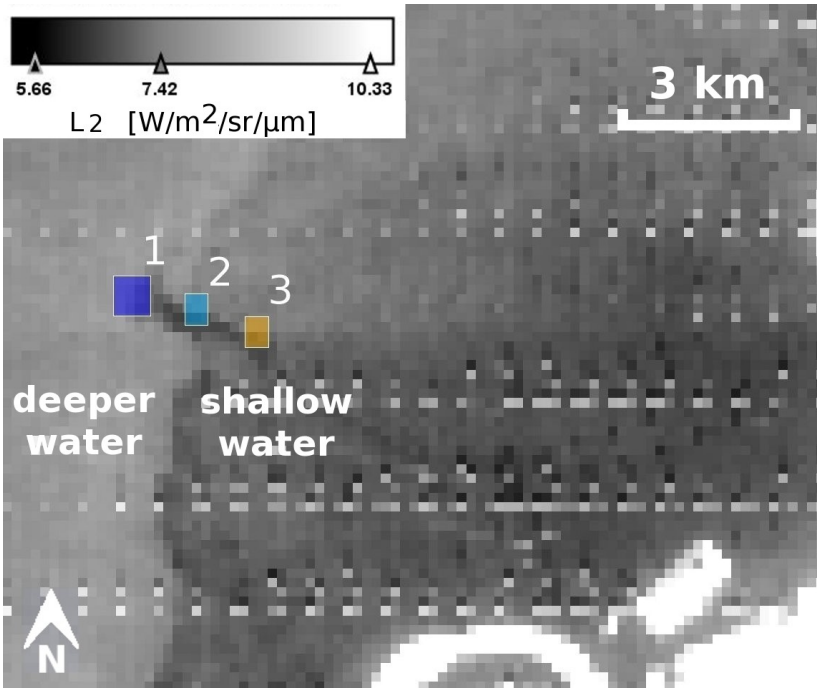

Figure 5.43. A 250 m/pixel resolution single NIR band radiance image (λ_2=859 nm) for the oil spill incident shown in Figure 5.42, over which three SCS sampling areas (1–3) were selected whose results are summarized in Table 5.16. The image is centred at position N25° 4' 0.076" E55° 0' 44.15".

Table 5.17. The results of the SCS for the areas selected over the spill case shown in Figure 5.43. LTO=light thickness oil and MTO=medium thickness oil.

Area number	Total pixels	L_2 (W/m²/sr/µm)		L_1 (W/m²/sr/µm)		SCS	Classification
		Min.	Max.	Min.	Max.		
1	10	7.079	8.042	19.19	20.37	0.026	MTO
2	7	6.49	7.40	18.22	19.61	0.021	LTO
3	7	6.60	7.41	18.77	19.51	0.028	MTO

5.7.4 Al Ahmadi loading terminal (Kuwait) – 4th August, 2010

On 2nd August, 2010 an oil spill (~ 63.30 km²) near Al Ahmadi oil terminal (Kuwait) occurred when heavy crude oil (18 °API) leaked from a loading terminal into the sea. The spill was visible in MODIS Terra on 4th August, 2010 at 07:38 UTC under a sun–glint area. Figure 5.44A shows the spill in a 500 m/pixel resolution natural RGB

colour composite corresponding to bands λ_1=645 (aggregated from the 250 m/pixel band group), λ_4=555 and λ_3=469 nm respectively, while Figure 5.44B shows it in 250 m/pixel resolution false RGB colour composite corresponding to bands λ_2=859, λ_1=645 and λ_1=645 nm respectively.

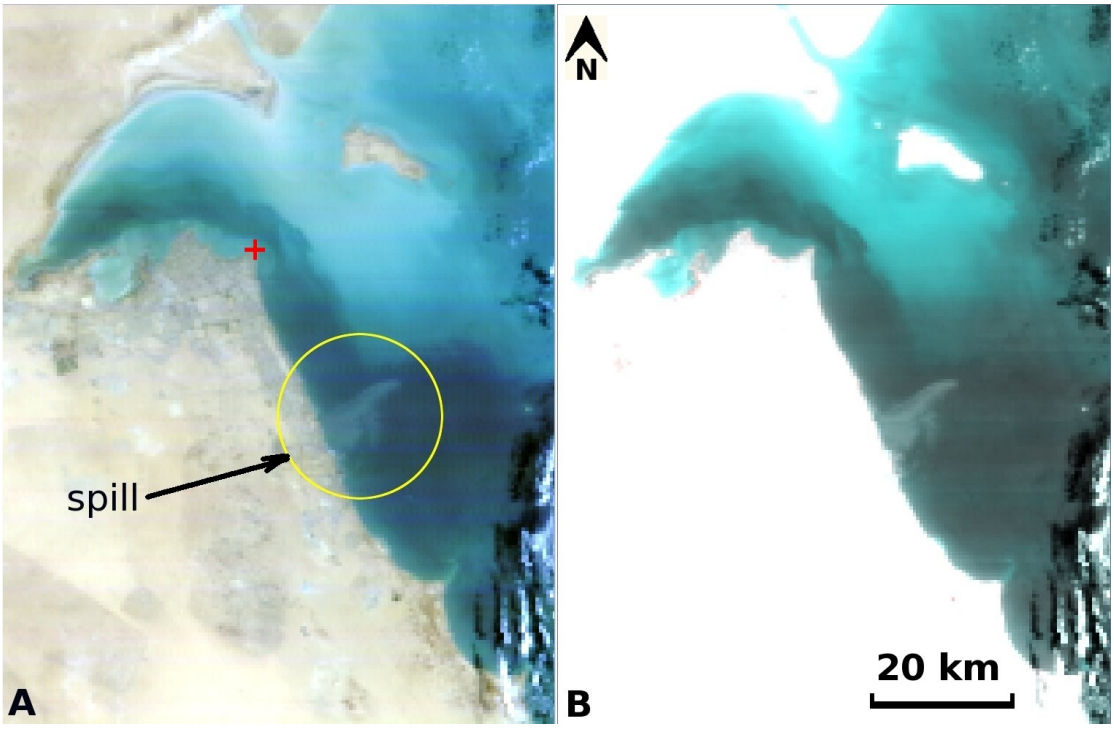

Figure 5.44. An oil spill near Al Ahmadi oil terminal (Kuwait) seen in MODIS Terra image on 4th August, 2010 at 07:38 UTC in the following 500 m/pixel resolution RGB colour composites: **(A)** natural composite corresponding to bands λ_1=645 (aggregated from the 250 m/pixel band group), λ_4=555 and λ_3=469 nm, and in a **(B)** false colour composite corresponding to bands λ_2=859, λ_1=645 and λ_1=645 nm respectively (aggregated from the 250 m/pixel band group). The red + marking is positioned at N29° 21' 0.47" E48° 6' 0.55".

The average wind speed estimated by the ASCAT instrument at 10 m above sea level was ~ 6 m/s. The SCS classification was applied to six different areas on the spill (see Figure 5.45). The thickness distribution projected by the results (Table 5.17) matched those expected; such that thicker oil is closer to the source and less thick oil is further away from it. Nevertheless, none of the classification results for thickness matched that of a thick oil, which was expected for the heavy oil–type involved in the spill. This can be attributed to the two–day delay in detecting the spill during which it was exposed to extremely hot weather conditions (common to Kuwait's weather during the summer periods) which reduced it's original viscosity.

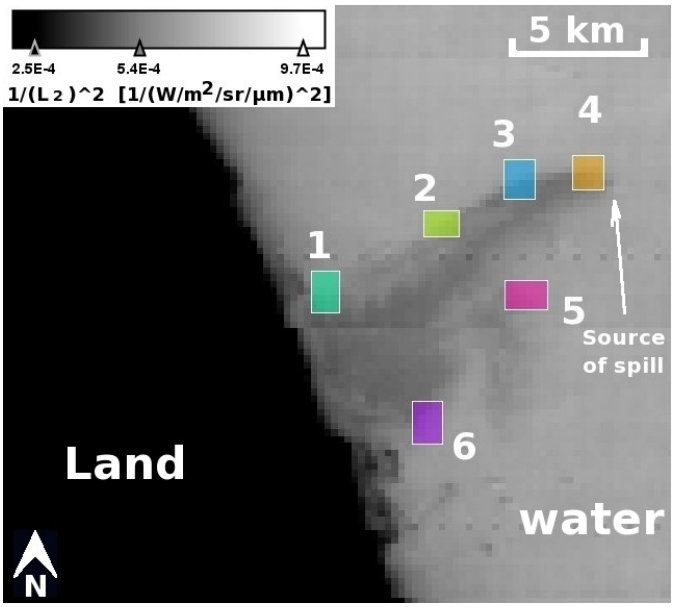

Figure 5.45. Oil spill near Al Ahmadi oil terminal (Kuwait) seen in a MODIS Terra image observed on 4th August, 2010 at 07:38 UTC in the following 500 m/pixel resolution image produced using the radiometric transformation over which (1–6) sampling areas were selected to perform the SCS classification. The results are shown in Table 5.17. The image is centred at position N29° 8' 52" E48° 10' 25".

Table 5.18. The SCS results for the numbered sampling areas displayed on Figure 5.45. LTO=light thickness oil and PC=pure class.

Area number	Total pixels	L_2 (W/m²/sr/µm)		L_1 (W/m²/sr/µm)		SCS	Classification
		Min.	Max.	Min.	Max.		
1	28	41.22	46.11	69.37	76.16	0.01	PC (sheen or water)
2	15	38.97	43.28	65.26	71.61	0.007	PC (sheen or water)
3	24	38.59	44.45	65.13	72.39	0.02	LTO
4	30	38.42	44.57	64.58	72.42	0.02	LTO
5	24	39.44	43.09	66.16	71.72	0.005	PC (sheen or water)
6	29	39.74	45.04	66.88	74.38	0.01	PC (sheen or water)

This argument is supported by the SST recorded around the spill area (SST ~ 30 °C) estimated from MODIS SST map shown in Figure 5.46A. The SST4 temperature map was also produced (Figure 5.46B), from which the spill appears well–delineated due to solar reflectance off its almost homogeneous layer, unlike the SST map, in which the spill's borders are hardly visible. The Chlor-a product could not be produced over the spill's area due to sun–glint interference.

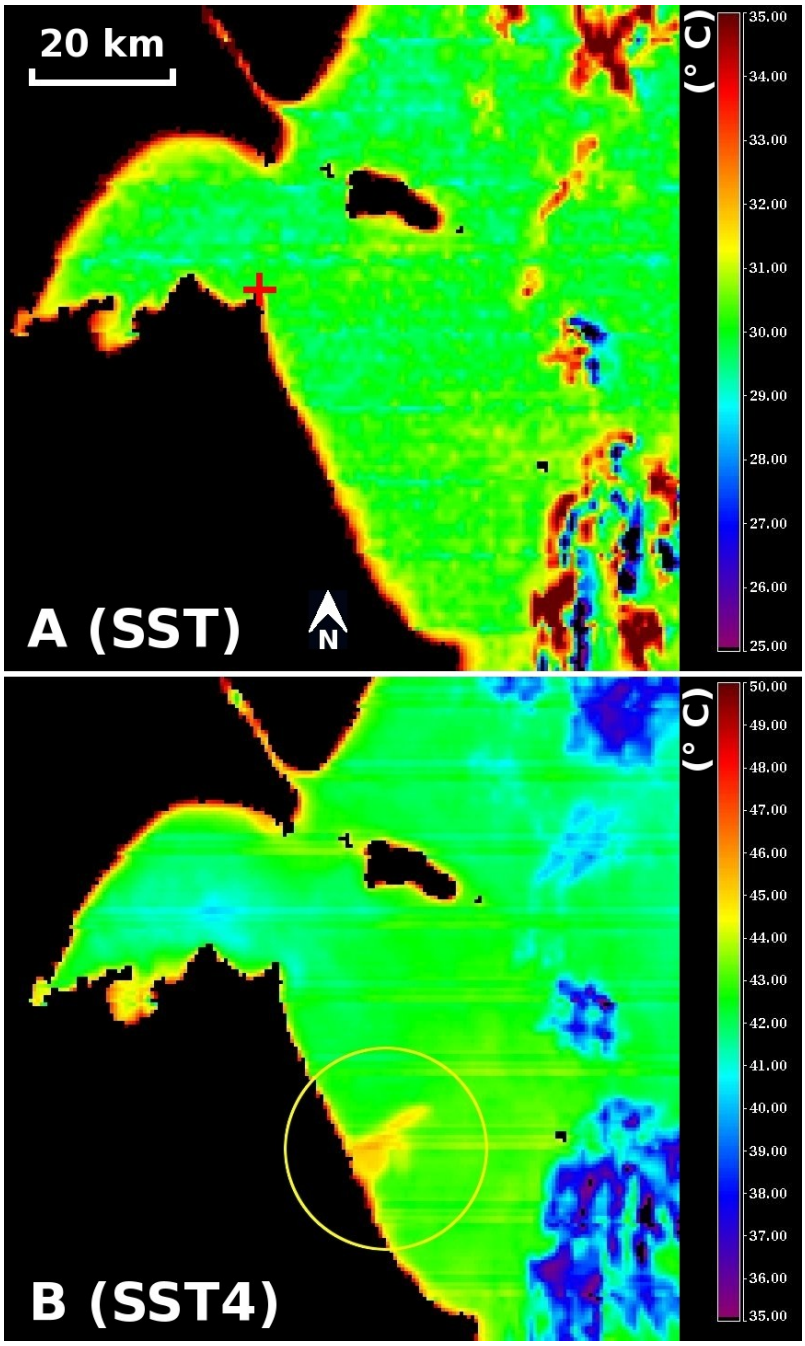

Figure 5.46. The 500 m/pixel resolution (interpolated from 1 km/ pixel resolution band group) MODIS Terra on 4th August, 2010 at 07:38 UTC. **(A)** SST (11–12 µm) and **(B)** SST4 (3.96–4.05 µm). The red + marking is positioned at N29° 21' 0.47" E48° 6' 0.55".

The spill was also observed in ENVISAT ASAR data (C–band, HH polarization, 1 km/pixel resolution) on 4th August, 2010 at 06:50 UTC as shown in Figure 5.47.

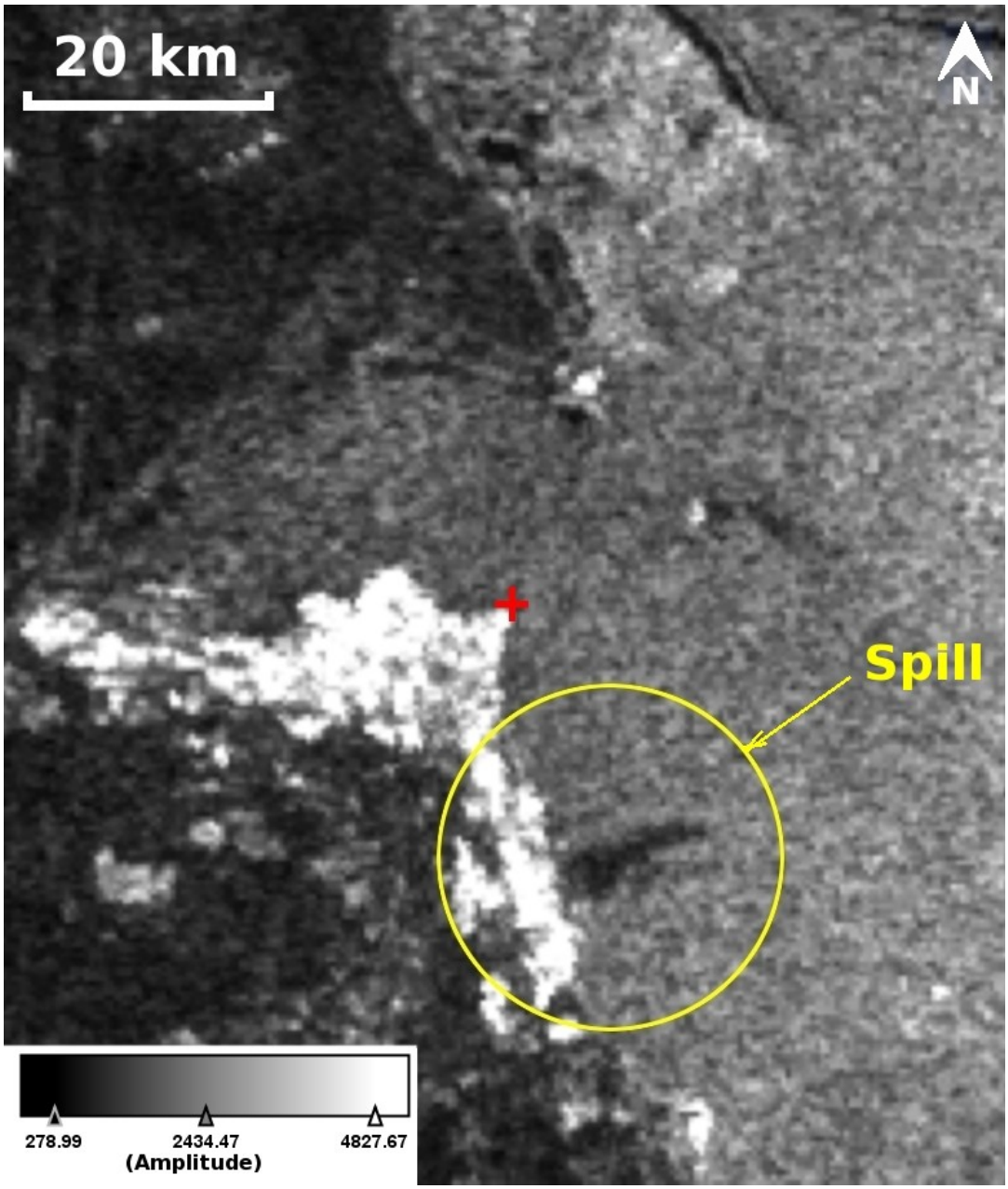

Figure 5.47. The oil spill near Al Ahmadi oil terminal (Kuwait) seen (circled) in ENVISAT ASAR image (C–band, HH polarization, 1 km/pixel resolution) observed on 4th August, 2010 at 06:50 UTC. The red + marking is positioned at N29° 21' 0.47" E48° 6' 0.55".

On 8th August, 2010, a visit was arranged to view the spill on–site as it had reached the shore line. Figure 5.48 shows the layers of sheen and weathered oil that were observed during the visit, including some of the cleaning equipment that was used at the time such as buoys.

Figure 5.48. *In situ* photos taken on 8th August, 2010 of the oil spill that occurred near Al Ahmadi oil terminal (Kuwait) observed by MODIS 4th August, 2010. The images show **(A)** sheen visible at the shoreline; **(B)** used oil–absorbent buoys; **(C)** weathered patches of oil surrounded by sheen; and **(D)** cleaned–up oil piled up on the sand beaches.

The empirical results produced by the SCS classifier were consistent over geographically and environmentally different datasets. This consistency was insensitive to atmospheric interference since oil spills were detected to within ±30° from nadir, thus minimizing the impact of path radiance. The contribution of Rayleigh scattering was minimal as well due to the spectrum's longer wavelengths (red and NIR bands) used in the SCS algorithm. Whenever analysis was carried out over clear sea water, the results obtained were consistent regardless of its geographic location. This demonstrates the efficiency of using the red and NIR bands in the SCS, which case I water is spectrally insensitive to. Hence, the classifier becomes highly dependent on the optical properties of the contrasted surface layer (oil or surface blooms) at the surface of clear water.

5.8 Summary

As a result of the calibration and validation work carried out in the previous sections and based on the preliminary classification table derived earlier (Table 5.2), a more precise and comprehensive classification table (Table 5.18) has been derived to categorize the different classes of oil thickness including surface blooms.

Table 5.19. A classification table based on the SCS calibration results for different oil spill thickness, including unpolluted sea water and surface floating blooms.

Mean SCS	Class	Remarks	Uncertainty ±
≤ 0.01	PC (Single class)		
0.02	LTO (Light thickness oil, sheen)	Sheen, according to the Bonn Agreement Aerial Surveillance Handbook, is a thin layer of oil whose thickness ranges between 0.04 μm and 0.3 μm (Carpenter, 2007).	0.002
0.03	MTO (Medium thickness oil)		0.002
0.04	Oil (Thick oil)		0.002
0.05	TW (Turbid water) or WO (weathered oil)	Suspended oil mixtures, such as weathered or dispersed oil, can scatter light in a similar manner to other suspended particles, and thus increase the water–leaving radiance in the red and NIR bands (Byfield, 1998).	0.003
0.10	U (Undetermined)	The undetermined class is common in many classes and requires further *in situ* investigation for determination.	0.020
≥ 0.20	SA (Surface blooms)		

The next chapter will discuss the details of an algorithm proposed specifically to classify one of the prime oil spill look-alike features – the surface floating blooms. This inverse strategy of detection aims to complement the results reached in this chapter by making use of MODIS's green and blue bands that belong to its 500 m band group, in conjunction to the aggregated red and NIR 250 m bands.

Chapter 6: The surface algae bloom index (SABI)

6.1 Introduction

As has been discussed earlier in chapter 3, there are several species of algae that exist in the RSA, that can sometimes mistakenly be classified as oil spills when being viewed by the MODIS and SAR sensors. This chapter will highlight examples of oil-spill look-alike incidents that were caused by such species, and investigate the spectral techniques that may be applied to discriminate them from oil spills. Most algae formations that occur in relatively high concentrations near to or at the water surface can be characterised by a "red-edge" effect similar to that of land vegetation. This phenomenon which is not observed in oil spills, occurs at the highest reflectance slope between the maximum absorption in the red and the maximum reflectance in the NIR (0.7 μm–1.0 μm), due to the presence of chlorophyll pigments (Tucker, 1979; Jackson et al., 1983). This characteristic has been successfully employed for quantifying land vegetation cover using the normalized difference vegetation index (NDVI) algorithm. Consequently, this chapter will explore the spectral characteristics of ocean-floating algae and examine the possibilities and limitations of employing the NDVI algorithm to distinguish such species. A further investigation will be followed to select the appropriate bands of MODIS that may be employed in an algorithm similar to the NDVI, but more specific to the marine environment termed surface algal bloom index (SABI). The parameters that are expected to affect the spectral properties of surface algal formations, and may impact their detectability in satellite data will also be examined. These include for instance, wind speed, sea surface temperature and sun-glint. Atmospheric phenomena such as clouds and dust will also be analysed. A number of MODIS standard biophysical products have been generated to provide a measure for some of these parameters. However, their production requires performing atmospheric correction, which depends on the black pixel assumption. That is zero (or at least negligible) radiance in the near-infrared (NIR) bands (λ_2=859 nm and λ_{15}=748 nm) over the ocean water due to strong water absorption in this region of the spectrum. This assumption, however, does not hold over floating algae, due to their high NIR reflectance, which causes an overestimation of the retrieved aerosol loading, and subsequently an underestimation of water-leaving radiances. Several studies, however,

have been conducted to improve the atmospheric correction, but until now no robust atmospheric correction algorithm specifically designed for floating algae has yet been developed (Hu, 2009).

A statistical analysis will be presented towards the end of the chapter to compare the accuracy of the SABI results to that of NDVI in order to understand the uncertainties involved and to improve the quality of interpretation. Whenever SAR data of surface blooms were available, they were compared with the same blooms observed in MODIS data. Pixel size differences between the two sensors were acknowledged while conducting this comparison.

Unless otherwise stated, the images used in this chapter were not geometrically-corrected in order to ensure that the analysis was performed on data in its raw format and not have it modified by the pixel interpolation resulting from the geo-referencing operation. Therefore, the spatial scales and geographic markings shown on the images should be viewed as approximations.

6.2 Definition of the SABI

Researchers like Kahru et a1 (1993) have examined the use of the normalized difference vegetation index (NDVI) on cyanobacterial blooms floating at the water surface. The NDVI (Equation 6.1) was proposed by Rouse et al. (1974) to measure land vegetation, by normalizing the output from −1 to +1 in order to partially account for the differences in illumination and surface slope;

$$NDVI = \frac{X_{NIR} - X_R}{X_{NIR} + X_R} \tag{6.1}$$

where X is the calibrated top-of-atmosphere (TOA) radiance (L_t)[39] or at the TOA reflectance (ρ_t) at the centred wavelength of the NIR and red (R) bandwidths. For the case of MODIS, the red and NIR bands are the 250 m/pixel spectral band group; λ_1=645 nm and λ_2=859 nm respectively.

More recent algorithms have been proposed specifically for the detection of high concentrations of chlorophyll and surface algae: the Maximum Chlorophyll Index (MCI) and the MODIS Floating Algae Index (FAI) proposed by Gower et al. (2005) and Hu (2009) respectively. Gower et al. based the MCI on the peak radiance near 709 nm quantified in The Medium Resolution Imaging Spectrometer (MERIS) data by the

[39] Calibrated TOA radiance is a L1B radiance with additional radiance and polarization calibrations (NASA OceanColor, 2010).

difference between the radiance measured at this wavelength and a baseline radiance linearly interpolated from measurements at 681 and 753 nm. Hu (2009), however, based his proposed FAI algorithm on MODIS bands by measuring the difference between reflectance at NIR band (λ_2=859 nm) and a linear baseline between the red band (λ_1=645 nm) and short-wave infra-red band (λ_5=1240).

The surface algal bloom index (SABI) is a four-band ratio-based algorithm proposed to measure the relative red-edge characteristic of floating algae in water:

$$SABI = \frac{X_{NIR} - X_R}{X_B + X_G} \equiv \frac{red\text{-}edge\ bands}{ocean\text{-}colour\ bands} \tag{6.2}$$

or

$$SABI = \frac{X_{NIR}}{X_B + X_G} - \frac{X_R}{X_B + X_G} \tag{6.3}$$

where the quantity of X has been defined earlier for Equation 6.1, using the centred wavelength of each bandwidth of the 500 m resolution MODIS band group: R (λ_1=645 nm) and NIR (λ_2=859 nm), which are both aggregated from the 250 m/pixel resolution MODIS band group; and bands B (λ_3=469 nm) and G (λ_4=555 nm).

The numerator in the SABI equation represents the red-edge term characterised by the maximum slope between the highest absorption in the red and the highest reflectance in the NIR. The denominator term, however, was introduced to reflect case I water properties (strong absorption in the NIR accompanied with varying responses in the blue and green bands that correspond with varying concentrations of phytoplankton in water). This was proposed, since it is unlikely for floating algae to exist in isolation from the surrounding water column species, and the conditions that causes their "inverted sedimentation" (Kahru et al., 1994). These conditions occur when algae loses its ability to remain in the water column and accumulate near the surface (Horstmann et al., 1986). The subtraction term between the red and NIR in the numerator and the summation term between the blue and green in the denominator, are collectively expected to make the SABI equation less sensitive to Rayleigh and aerosol scattering, which affect the blue, green and red bands in particular.

It is possible to choose MODIS spectral bands available within the 1 km spatial resolution band group instead of the bands available within 500 m resolution group to detect surface algae. However, due to the scarcity of these events and their moderate spatial distribution, priority dictates using the highest spatial resolution bands provided

by the sensor. Particularly in regions similar to the RSA, where algal species are mostly characterised as being filamentous (thread-like) rather than mat-forming species.

Because the SABI equation is a ratio, it has the advantage of cancelling out all spectrally independent signal variations such as those arising from changing irradiance levels that accompany different sun angles, clouds/shadow and all other multiplicative atmospheric conditions. This will not, however, account for any spectral dependencies that are caused by other additive atmospheric effects.

6.2.1 The SABI methodology

Atmospheric correction was not performed on the data used for the calibration or validation process, because the objective of this research, at this stage, was not to produce a biophysical parameter such as concentration (Wang & Shi, 2007; Metsamaa et al., 2006), but rather, to map the spatial distribution of these biological species and to identify their spectral properties that makes them distinguishable from oil spills. Furthermore, higher precision is required only to determine water-leaving radiances at wavelengths shorter than about 530 nm (Gower et al., 2008). Particularly since aerosol scattering is responsible for approximately 10–40% of the total radiance (Carder et al., 2002), and is not as strongly dependent on wavelength as Rayleigh scattering is (which is proportional to λ^{-4}). Therefore, a Rayleigh-corrected reflectance (rhos) was used after using SeaDAS to produce it (using Equation 6.4) for each band required by Equations 6.1 and 6.2.

$$rhos(\lambda) = \frac{\pi}{t(\lambda)t_0(\lambda)F_0(\lambda)\cos\theta}\left(\frac{L_t(\lambda)}{t_{oz}(\lambda)} - L_r(\lambda)\right) \tag{6.4}$$

where $L_t(\lambda)$ and $L_r(\lambda)$ are the calibrated TOA radiance and Rayleigh radiance respectively; $t(\lambda)$ and $t_0(\lambda)$ are the Rayleigh diffuse transmittance from surface to sensor and sun to surface respectively; $t_{oz}(\lambda)$ is the ozone transmittance at both directions; and F_0 is the solar irradiance.

SeaDAS was used to process the L1B data to produce L_t values including other bio-optical products for correlation purposes, such as the 500 m resolution Chlor-a, SST (interpolated from the 1 km thermal bands) and aerosol optical thickness at 869 nm (τ_{869}). The standard masks produced in SeaDAS such as cloud, failed Chlor-a, sun-glint and others were also used to test their behaviour over pixels of surface algae. The NDVI and SABI outputs derived from Rayleigh-corrected reflectances will be denoted by NDVI_r and SABI_r respectively, as opposed to their corresponding TOA radiance

quantities denoted by NDVI_t and SABI_t respectively.

In order to improve the efficiency of surface bloom detection, different red green blue (RGB) colour composite images were generated in 500 m/pixel resolution. Interactive colour stretching was also performed on these composites, whenever necessary, to enhance their contrast. The composites comprised of the natural RGB colour corresponding to bands λ_1=645 (aggregated from 250 m resolution band group), λ_4=555 and λ_3=469 nm respectively and a false RGB colour composite corresponding to the aggregated 250 m/pixel resolution bands λ_2=859, λ_1=645 and λ_1=645 nm respectively. The reason for producing the false colour composite was to identify the surface and near-surface blooms by highlighting their red-edge effect in making them appear reddish in colour similar to land vegetation. The reddish appearance is prompted by the red colour assigned to the NIR reflectance response, which is quite high in surface blooms and very low in the surroundings sea waters due to prevailing absorption.

6.3 The calibration of the SABI

Five MODIS datasets have been used in this thesis for calibrating the SABI algorithm, whose swaths are shown in Figure 6.1. Two of which are related to surface algal blooms (see Appendix C for a review of different bloom species discussed in this study) and the other three are oil spill related.

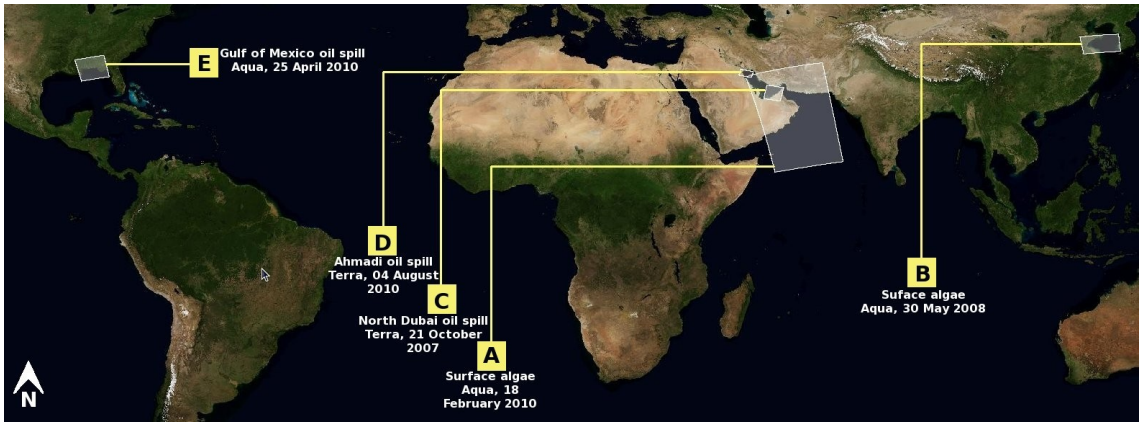

Figure 6.1. The location map of the different MODIS swaths, over which the SABI calibration was conducted. The datasets include two algal bloom events (A and B) and three oil spill incidents (C, D and E).

6.3.1 *Noctiluca miliaris*– RSA

Noctiluca miliaris (synonym *Noctiluca scintillans* Macartney) is a non-photosynthetic marine dinoflagellate (Bhimachar & George, 1950) that preys on phytoplankton to support its optimal growth (Lee & Hirayama, 1992; Kioeboe & Titelman, 1998). Figure 6.2 shows a bloom of the *N. miliaris* species appearing in a MODIS Aqua image on 18th February, 2010 at 09:10 UTC (swath shown in Figure 6.1A) as thin filaments that tend to aggregate by turbulent eddies at the surface to form large, slimy green patches across the Arabian Sea.

The image (Figure 6.2) was produced using a 250 m/pixel resolution natural RGB colour composite corresponding to the Rayleigh-corrected reflectance bands λ_1=645 , λ_4=555 and λ_3=469 nm respectively (λ_4 and λ_3 were oversampled from the 500 m/pixel resolution band group). This particular case of bloom was chosen for calibration due to its large spatial distribution which covered almost the entire Arabian Sea and included in the same frame a visible thick layer of dust, clouds and a moderate sun-glint area. The same bloom event was produced using a false RGB colour composite corresponding to the 250 m/pixel resolution Rayleigh-corrected reflectance bands λ_2=859, λ_1=645 and λ_1=645 nm respectively as shown in Figure 6.3.

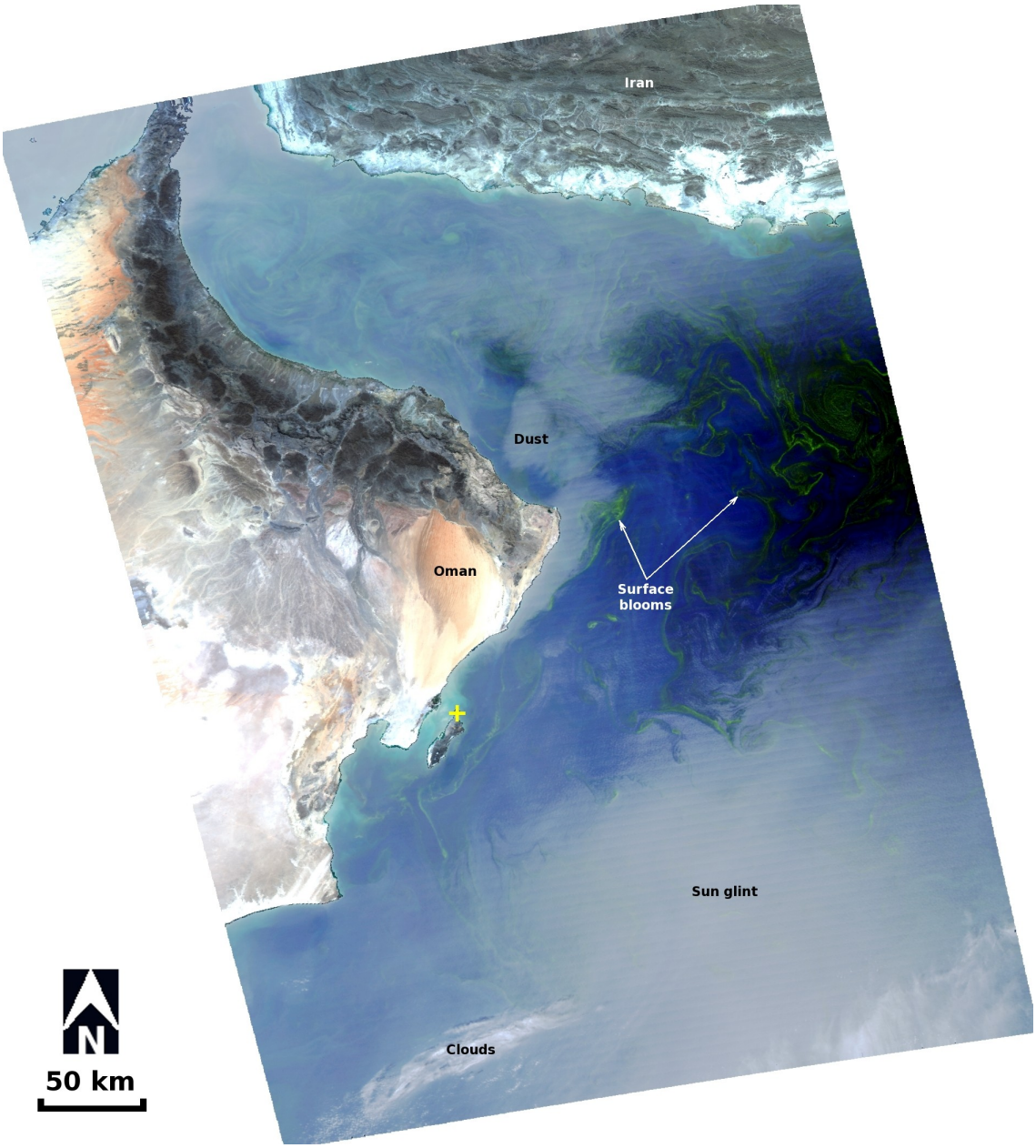

Figure 6.2. A *N. miliaris* bloom in the Arabian Sea observed in MODIS Aqua on 18th February, 2010 at 09:10 UTC. The 250 m/pixel resolution RGB colour composite image (geometrically-corrected) corresponding to the Rayleigh-corrected reflectance bands λ_1=645 , λ4=555 and λ3=469 nm respectively (λ3 and λ4 were oversampled from the 500 m/pixel resolution band group). The scene includes a visible layer of dust, clouds and a moderate sun-glint zone. Blooms appear as large greenish structural filaments. The yellow (+) mark is positioned at N20° 42' 29" E58° 53' 15".

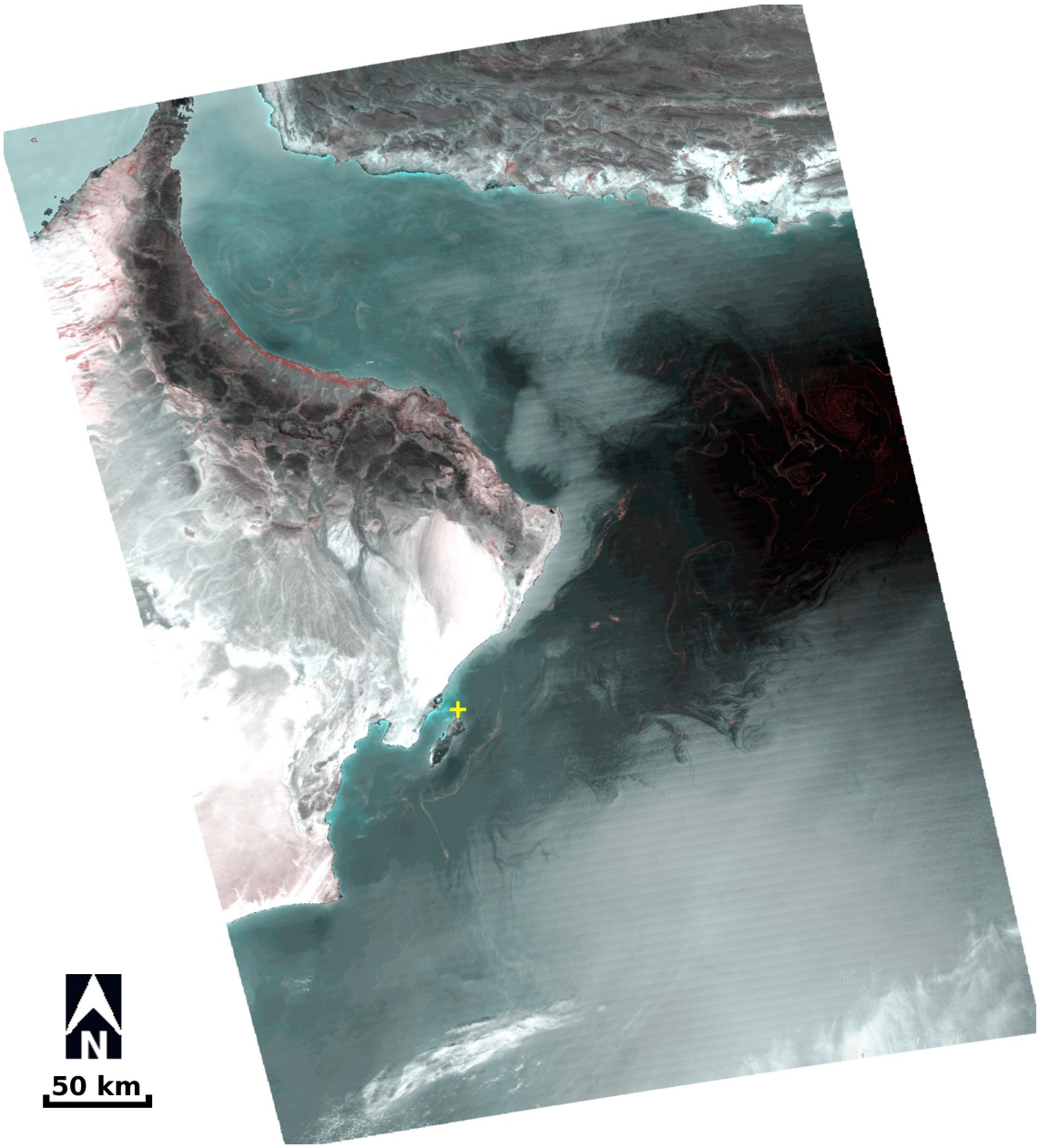

Figure 6.3. A *N. miliaris* bloom in the Arabian Sea observed in MODIS Aqua on 18th February, 2010 at 09:10 UTC. The 250 m/pixel resolution false RGB colour composite image (geometrically-corrected) corresponding to the Rayleigh-corrected reflectance bands λ_2=859, λ_1=645 and λ_1=645 nm respectively. Surface and near-surface blooms appear reddish in colour due to the red-edge effect. The scene includes a visible layer of dust, clouds and a moderate sun-glint zone. The yellow (+) mark is positioned at N20° 42' 29" E58° 53' 15".

The 500 m/pixel resolution MODIS standard Chlor-a product of the bloom was processed as shown in Figure 6.4, where the failed Chlor-a pixels were masked in blue. This failure occurs because water leaving radiance values at these pixels are negative (Robinson et al., 2000). When the calculated Chlor-a levels are outside the physical

limits (that is, greater than 640 mg/m^3), or very small values (less than 0.01 mg/m^3) (Robinson et al., 2000), then a warning flag is set instead to indicate their unreliability. The negative water leaving radiance values and/or the extreme upper limit of Chlor-a values may indicate the presence of surface or near-surface blooms.

Although the SST data for the surface bloom (shown in Figure 6.5) were masked in black due to a sharp sudden rise in temperature relative to the surrounding sea water temperatures, the temperature of sub-surface blooms were generally higher than surrounding bloom-free sea waters (by ~ 1 °C). This confirms the findings of Kahru et al. (1993) and Sato et al. (1998) who pointed out that SST "hot spots" can act as indicators for high concentrations of near-surface bioactivity. This phenomena is probably caused by the absorption of solar light by the *N. miliaris* species to be dissipated later as heat. The corresponding SABI_r and NDVI_r images of the same bloom event were also processed and are shown in Figures 6.6 and 6.7 respectively. Figure 6.7 also shows three lines crossing part of the dust plume (a to a'), part of the sun-glint (b to b') and surface algae (c to c'). The quality of output is almost identical between the two Figures, although the SABI_r appears less sensitive to coastal turbid waters than NDVI_r. This is largely attributed to the significant scattering caused by non-plankton particles and dissolved organic matter in the red and NIR regions rather than in the blue and green regions (Ruddick et al., 2001). Figures 6.8 and 6.9 show the corresponding SABI_t and NDVI_t images respectively. Colour stretching was interactively applied to all images in order to produce the best contrast between surface blooms and water.

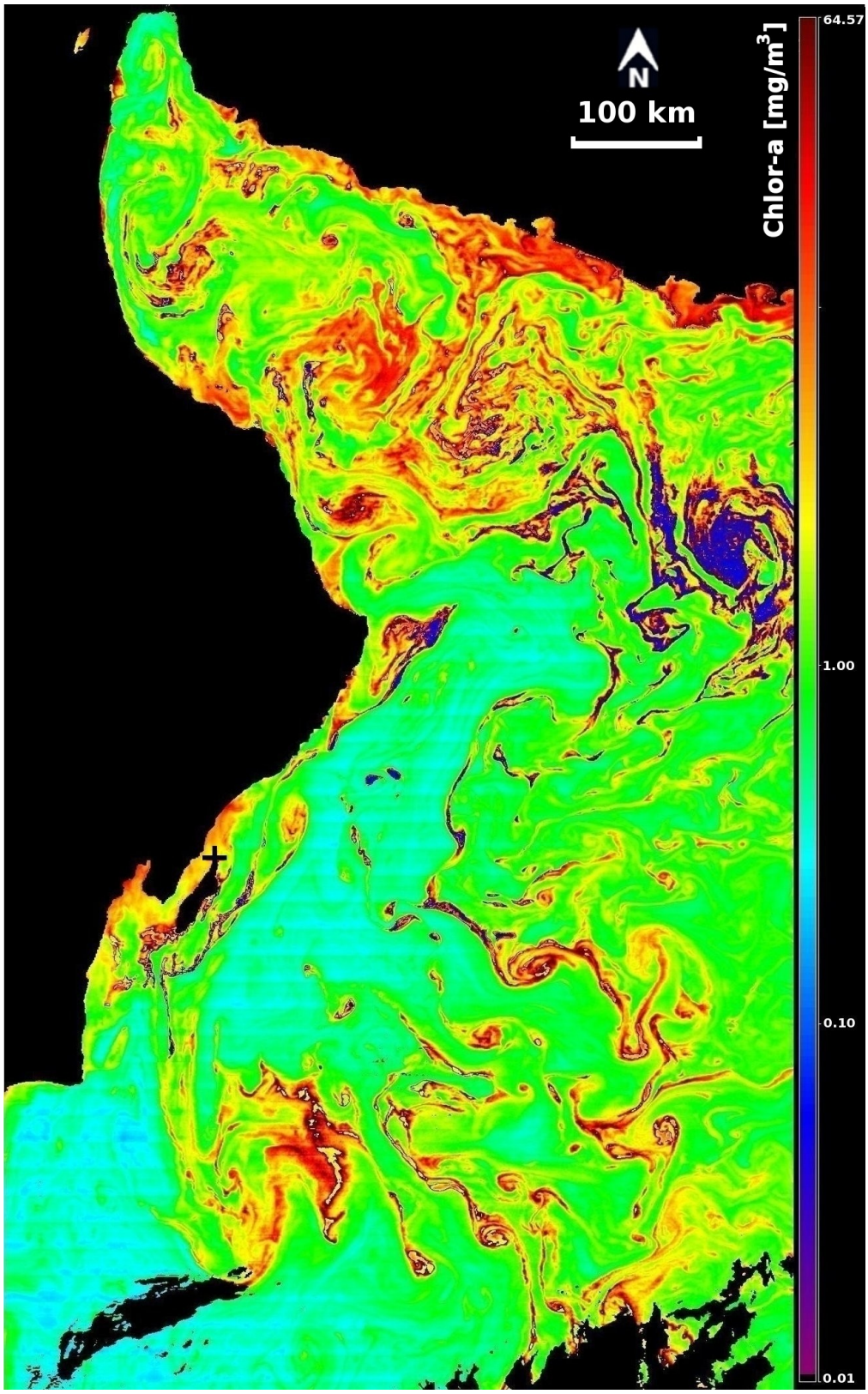

Figure 6.4. A 500 m/pixel resolution Chlor-a image of the *N. miliaris* bloom in the Arabian Sea observed in MODIS Aqua on 18th February, 2010 at 09:10 UTC. The blooms appear as large structural filaments. Failed Chlor-a pixels are masked in blue. Land, clouds and severe sun-glint zone are masked in black. The black (+) mark is positioned at N20° 42' 29" E58° 53' 15".

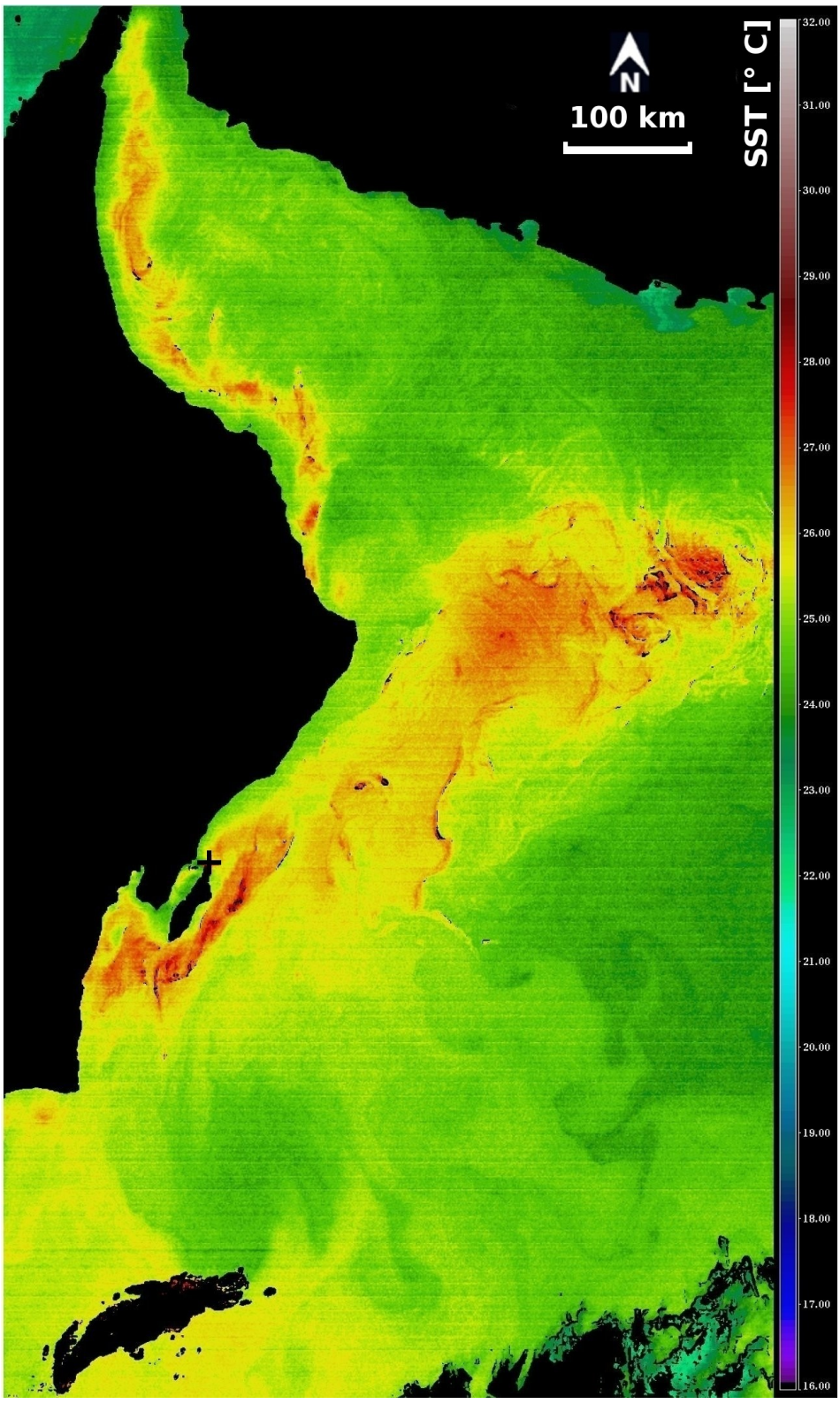

Figure 6.5. A 500 m/pixel resolution SST image (interpolated from the 1 km/pixel thermal bands) of the *N. miliaris* bloom in the Arabian Sea observed in MODIS Aqua on 18th February, 2010 at 09:10 UTC. Land, clouds and failed SST pixels are all masked in black. The SST appears less sensitive to the interference of light dust layers and sun-glint. High density blooms appear with relatively higher temperatures than surrounding sea waters. The black (+) mark is positioned at N20° 42' 29" E58° 53' 15".

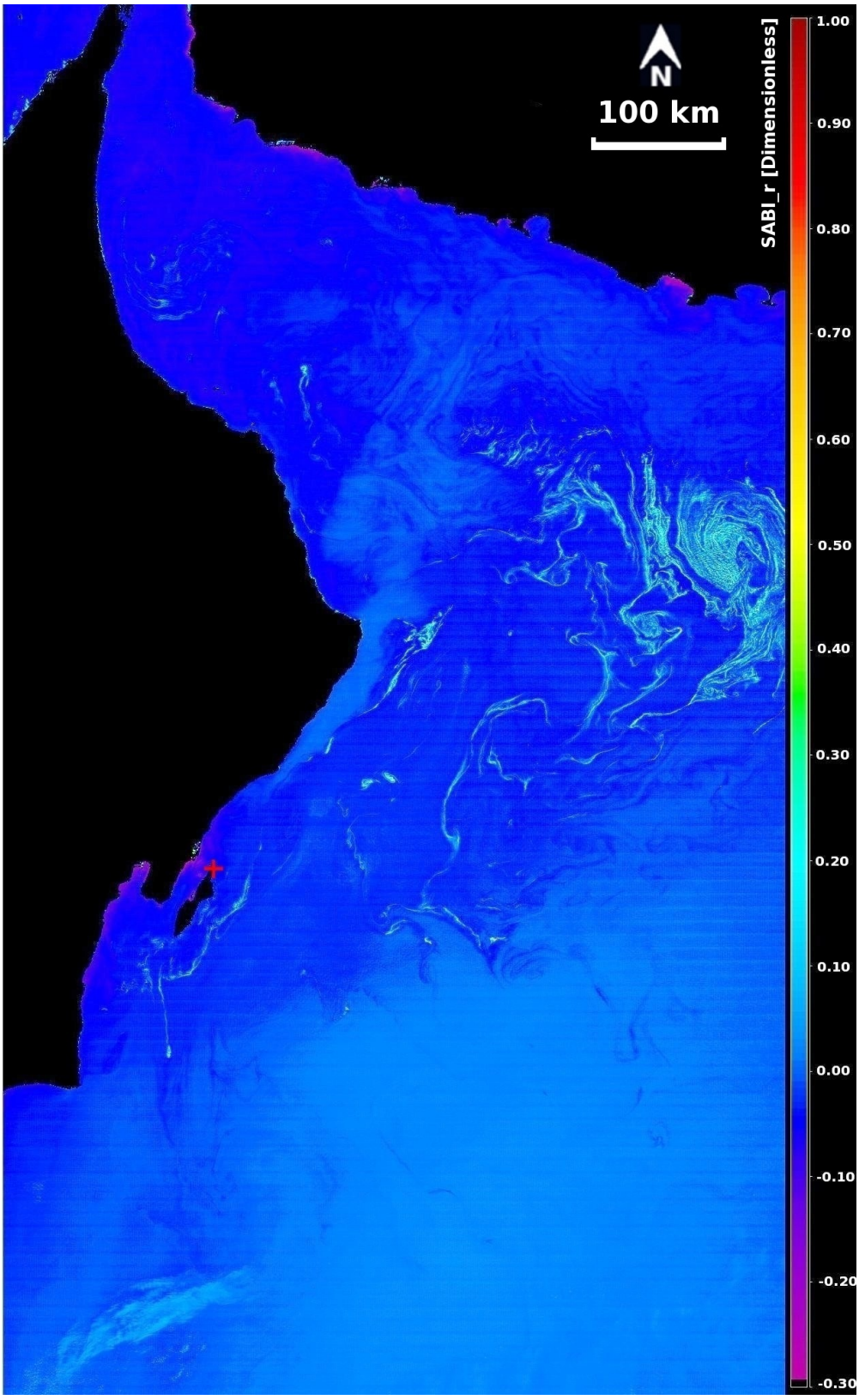

Figure 6.6. A 500 m/pixel resolution SABI_r (Rayleigh-corrected reflectance band) image of the *N. miliaris* bloom in the Arabian Sea observed in MODIS Aqua on 18th February, 2010 at 09:10 UTC. Land pixels are masked in black. Surface and near-surface blooms are well delineated in the water. Clouds, sun-glint and dust layer are all still visible. The red (+) mark is positioned at N20° 42' 29" E58° 53' 15".

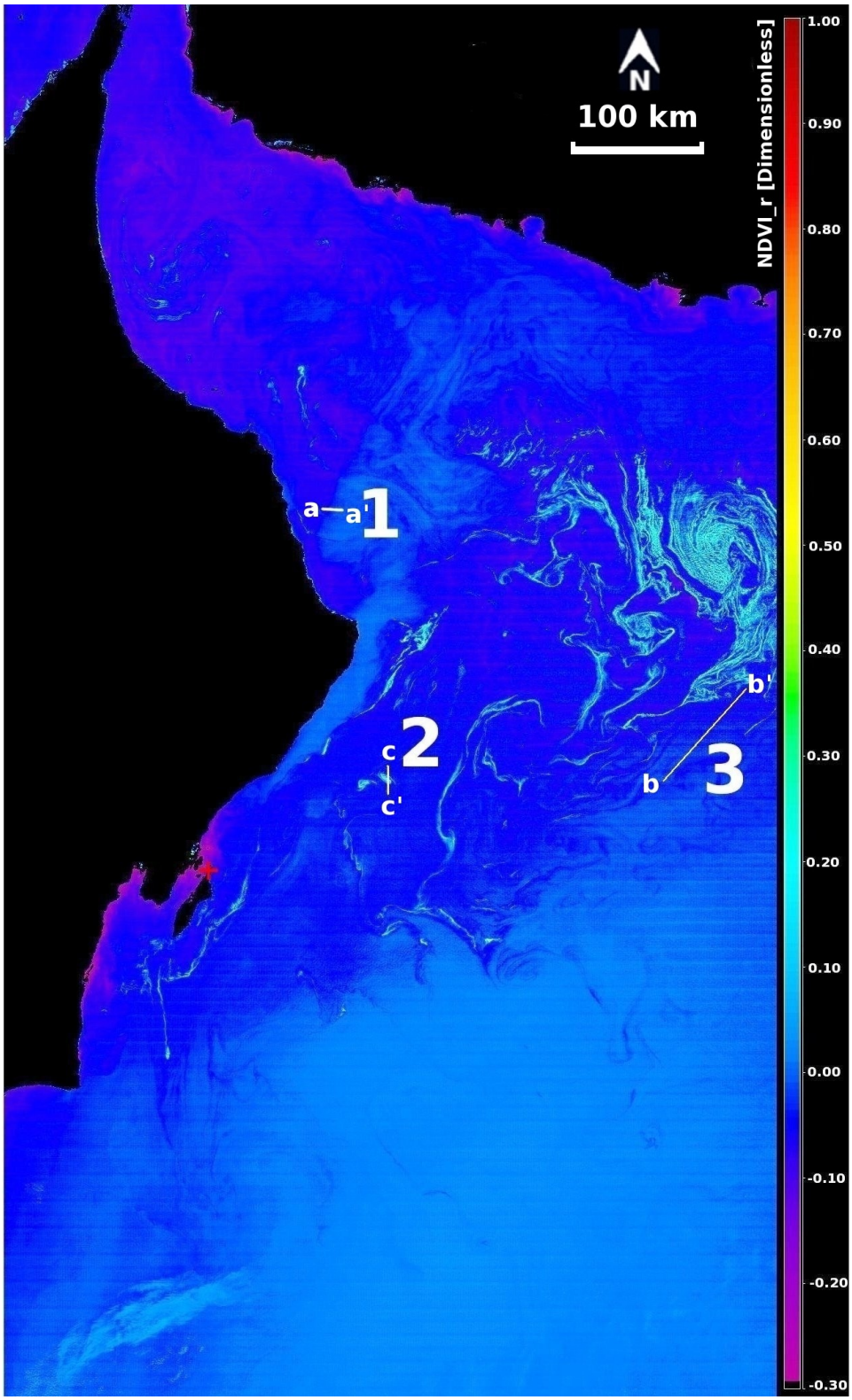

Figure 6.7. A 500 m/pixel resolution NDVI_r (Rayleigh-corrected reflectance band) image of the *N. miliaris* bloom in the Arabian Sea observed in MODIS Aqua on 18th February, 2010 at 09:10 UTC. Land pixels are masked in black. Surface and near-surface blooms are well delineated in the sea water. Clouds, sun-glint and dust layer are all still visible. Three line transects are selected over (1) dust plume; (2) surface algae; and (3) part of the sun-glint. The red (+) mark is positioned at N20° 42' 29" E58° 53' 15".

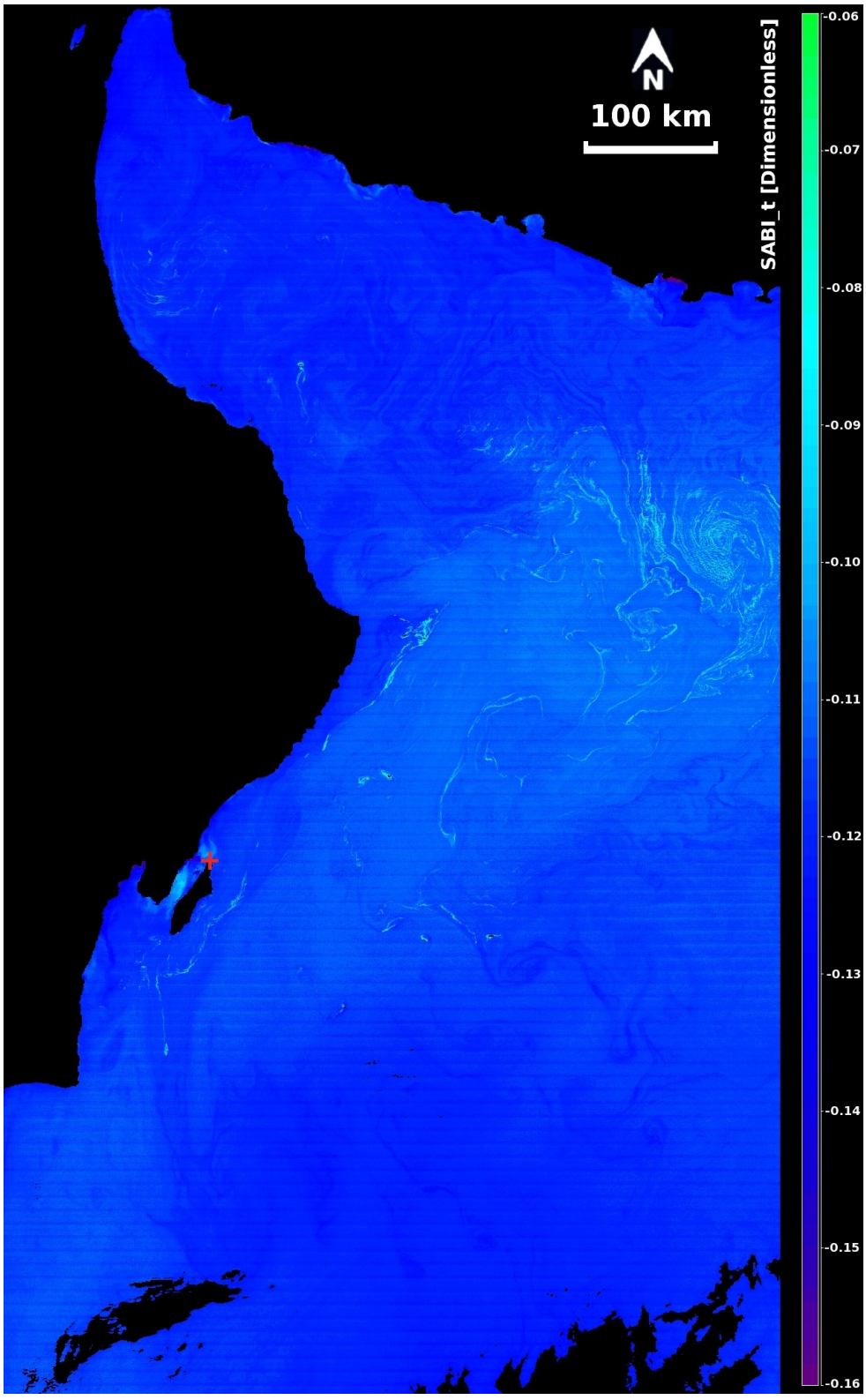

Figure 6.8. A 500 m/pixel resolution SABI_t (calibrated TOA radiance) image of the *N. miliaris* bloom in the Arabian Sea observed in MODIS Aqua on 18th February, 2010 at 09:10 UTC. SABI_t values greater than or equal to -0.10 clearly delineated surface and near-surface blooms, with class mixing occurring near shallow turbid sea waters. The thin dust layers, clouds and sun-glint zone are hardly visible. Land is masked in black. The red (+) mark is positioned at N20° 42' 29" E58° 53' 15".

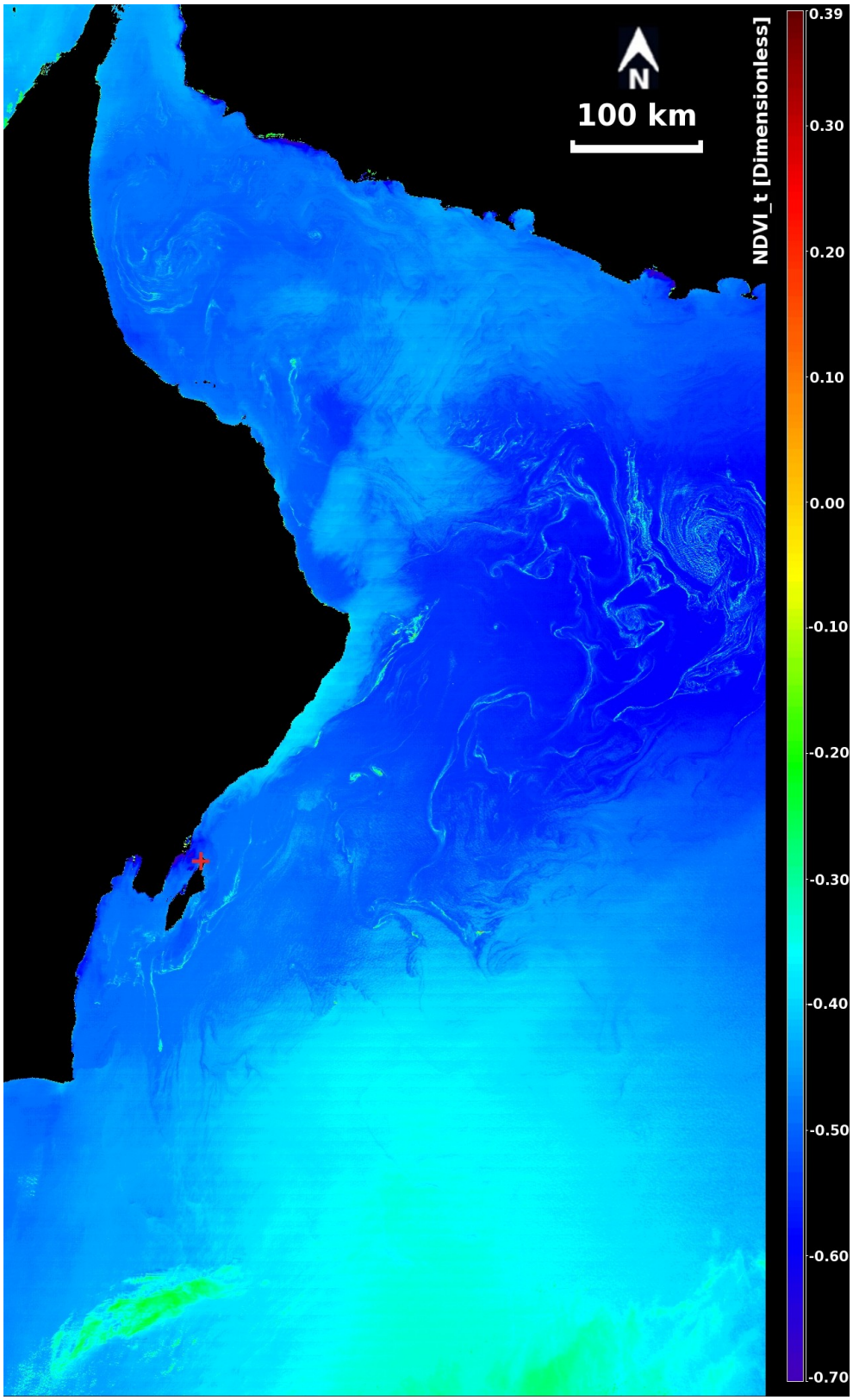

Figure 6.9. A 500 m/pixel resolution NDVI_t (calibrated TOA radiance) image of the *N. miliaris* bloom in the Arabian Sea observed in MODIS Aqua on 18th February, 2010 at 09:10 UTC. Dust layer, clouds and sun-glint zone are clearly visible. Land is masked in black. Surface and near-surface blooms clearly delineated in the sea water. The red (+) mark is positioned at N20° 42' 29" E58° 53' 15".

The transects of the lines crossing the dust plume, sun-glint and surface blooms (seen on Figure 6.7) are shown in Figures 6.10A, 6.10B and 6.10C respectively for SABI_r, NDVI_r, SABI_t and NDVI_t. The SABI_r and NDVI_r transect profiles are generally very similar over the dusty layer (Figure 6.10A), where both appear negative over less dense layers of dust (Taua_869 $\leq$ 0.18) and clear waters. These similarities are probably caused by the high absorption in the NIR coupled with high scattering in red. These values gradually start to approach zero as the dusty layer becomes denser (Taua_869 > 0.18) due to comparable scattering between the red and NIR bands in such dust concentrations. From the transects shown in Figures 6.10A and 6.10B, it is clear that SABI_t has demonstrated less sensitivity over dust and sun-glint regions than the NDVI_t due to its efficient "smoothing" effect due to high molecular scattering over these phenomenon particularly in the visible part of the spectrum (more in the blue and green bands than it is in the red). The contrast between surface blooms to clear sea waters is shown for SABI_t in Figure 6.10C, was the least in comparison to other relations. While SABI_r and NDVI_r (the Rayleigh-corrected reflectance relations) have demonstrated the maximum contrast between surface blooms and sea water. In Figure 6.10C, all transects did reveal a trend over the red-edge effect displayed by the surface and near-surface blooms, which correlated well with the failed pixels of Chlor-a. This is a good indicator that surface and near-surface blooms are the main reason for the failure of Chlor-a algorithm over such phenomenon. The SABI_t transect shown in Figure 6.10C, does support the findings that surface and near-surface blooms are always represented by SABI_t values greater than or equal to -0.10. These findings indicate the superiority of the SABI_t product over other products such as the NDVI_t in delineating surface blooms even when the scene is masked with sun-glint or with an aerosol layer (dust).

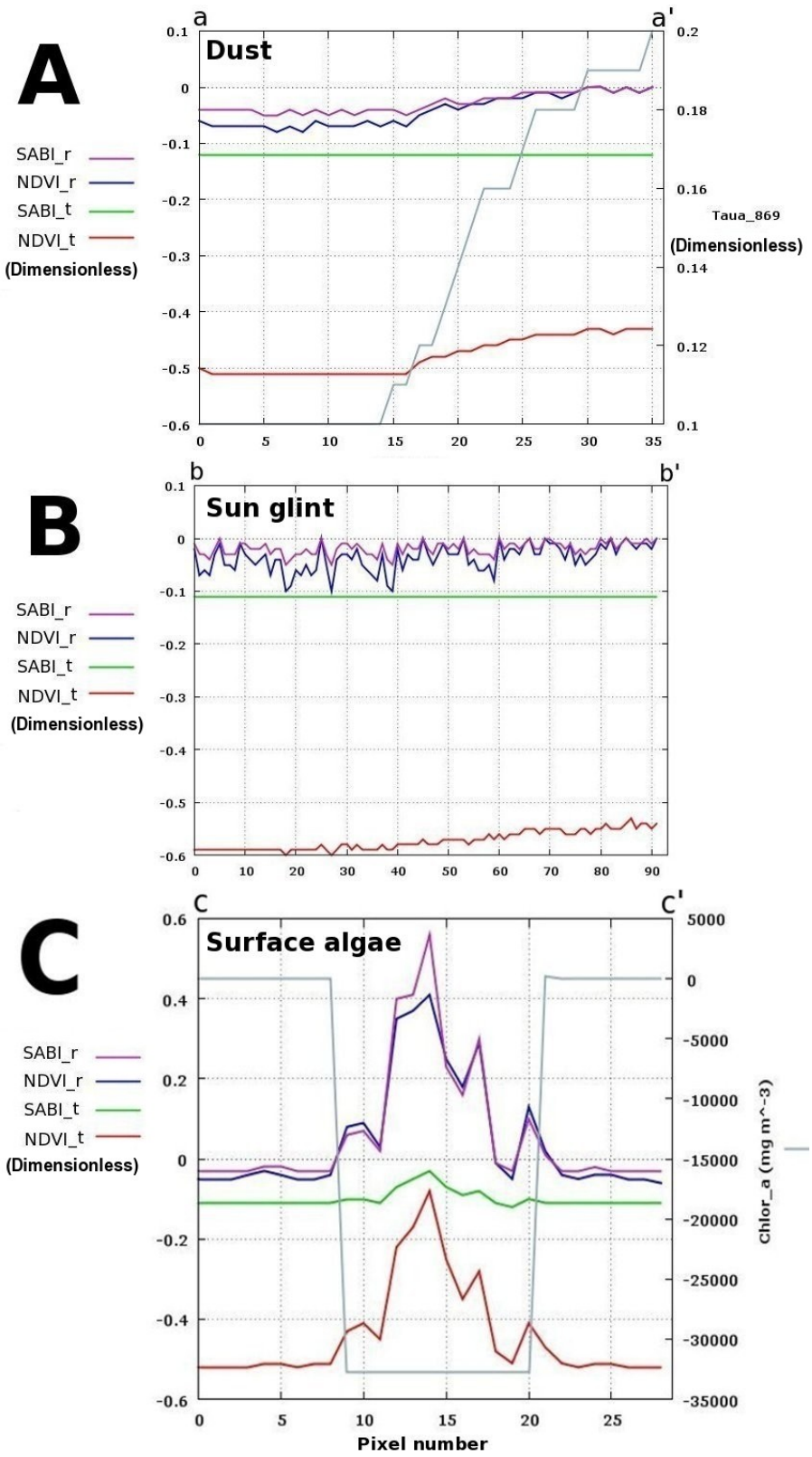

Figure 6.10. Three transects taken from the *N. miliaris* bloom scene in MODIS Aqua on 18th February, 2010 at 09:10 UTC that took place in the Arabian Sea shown in Figure 6.7. The transects show the impact of **(A)** dust layer, **(B)** sun-glint region and **(C)** surface blooms on SABI_r, NDVI_r, SABI_t and NDVI_t respectively.

A subset image of the bloom in Chlor-a taken from Figure 6.4 is shown in Figure 6.11A. This image was compared against the corresponding ENVISAT ASAR image (mode level 0, C-band, VV polarization) taken on 18th February, 2010 at 06:01 UTC (Figure 6.11B). The blooms in the ASAR image appear dark due to them dampening the sea water surface, similar to oil and low-wind speed areas.

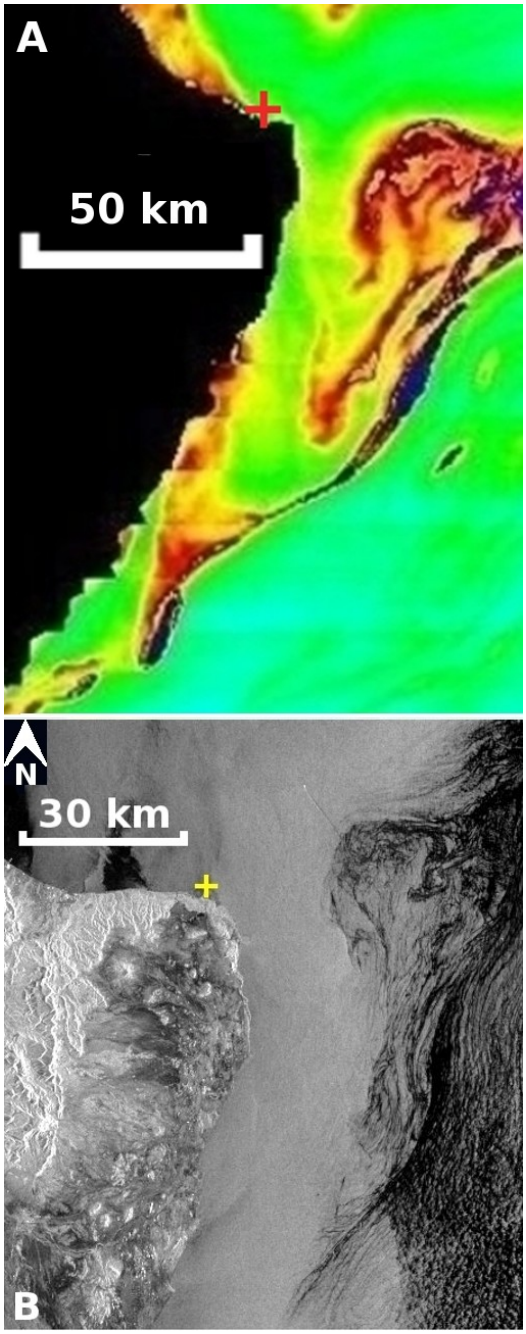

Figure 6.11. Part of the *N. miliaris* bloom in the Arabian Sea viewed in MODIS Aqua on 18th February, 2010 at 09:10 UTC in **(A)** a Chlor-a subset taken from Figure 6.4. **(B)** An ENVISAT ASAR image (image mode level 0, 150 m/pixel, C-band, VV polarization) 18th February, 2010 at 06:01 UTC, where part of bloom appears as a dark formation opposite the (+) mark positioned at N22° 32' 24 E59° 46' 24".

Over the bloom shown earlier as point 2 in Figure 6.11A, a sample area (224 pixels) was selected containing mixed classes of blooms including clear sea water (Figure 6.12B). After which a scatter plot was produced (Figure 6.13) to investigate whether a correlation exists between SABI_r and SABI_t over the classes included in that area. The plot does reveal a high correlation between the two variables (R^2=0.97), from which the -0.10 SABI_t value (the baseline value for surface floating bloom) corresponds to a SABI_r value equal to ~ 0.10.

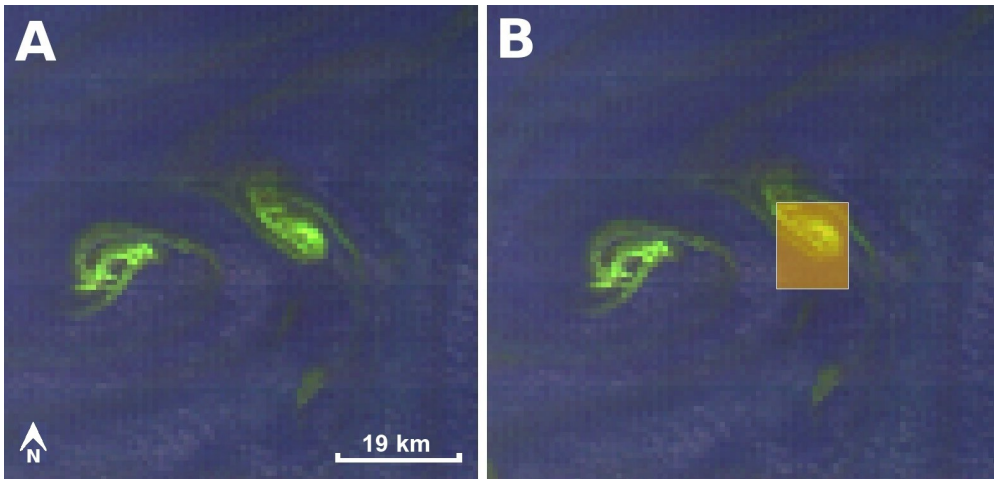

Figure 6.12. **(A)** A zoomed-in image of the *N. miliaris* bloom scene taken from the bloom shown as point 2 in Figure 6.11A. **(B)** An area selected (224 pixels) over the visible surface bloom inclusive of clear waters and sub-surface blooms. The scatter plot of this area is shown in Figure 6.13.

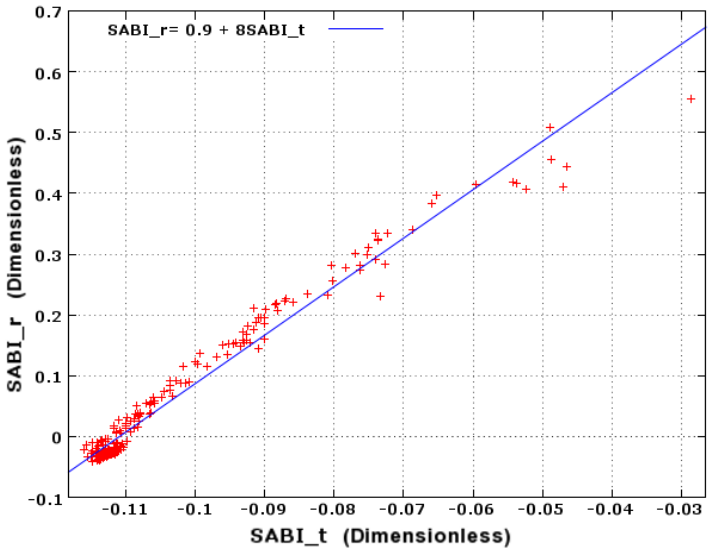

Figure 6.13. A scatter plot of SABI_r against SABI_t over a sampling area (224 pixels) shown in Figure 6.12B. The plot reveals a high correlation between the two variables (R^2=0.97). Also, the baseline value for surface blooms in SABI_t equal to -0.10 corresponds to a SABI_r value equal to ~ 0.10.

6.3.2 *Ulva prolifera* – Yellow Sea

Ulva prolifera is an unattached filamentous green macro-algae formerly known as *Enteromorpha prolifera* (Hayden et al., 2003). A surface bloom of the *Ulva prolifera* species was observed in MODIS Aqua on 30th May, 2008 at 05:36 UTC near the coastline of Qingdao overlooking the Yellow sea, China (swath shown in Figure 6.1B). A 500 m/pixel resolution false RGB colour composite image corresponding to the calibrated radiance bands λ_2=859, λ_1=645 and λ_1=645 nm respectively (λ_1 and λ_2 were aggregated from 250 m/pixel resolution band group) was produced (Figure 6.14). The surface and near-surface blooms appear reddish in colour in the Figure due to the red-edge effect.

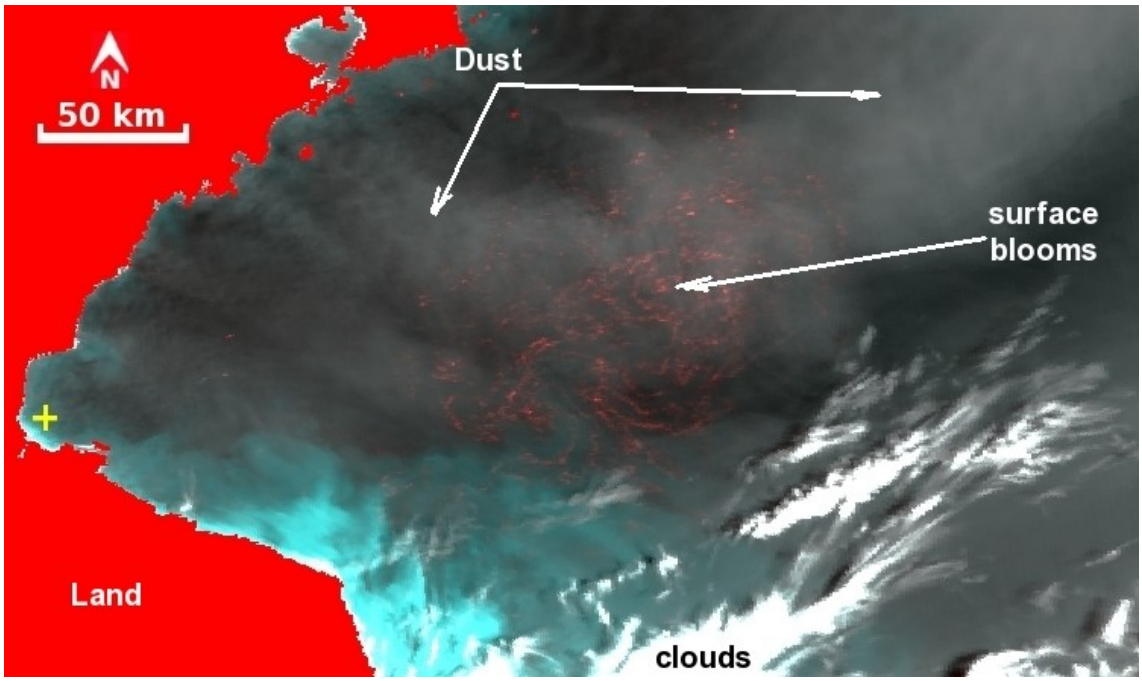

Figure 6.14. A geometrically-corrected MODIS Aqua image of an *Ulva prolifera* bloom in the Yellow Sea, China observed on 30th May, 2008 at 05:36 UTC. The image was constructed from the calibrated TOA radiance values using the 500 m/pixel resolution false RGB colour composite corresponding to bands λ_2=859, λ_1=645 and λ_1=645 nm respectively (aggregated from 250 m/pixel resolution band group). The yellow (+) mark is positioned at N34° 52' 15" E119° 16' 44".

A set of 500 m/pixel resolution images were processed (geometrically-corrected) from the calibrated radiometric data using the following the bands: blue (λ_3=469 nm), green band (λ_4=555 nm), red (λ_1=645 nm) and NIR (λ_2=859 nm) where λ_1 and λ_2 were both aggregated from the 250 m resolution band group. The reason for producing these image transformations is to highlight the spectral quality of the SABI relationship in delineating surface algae formations under different atmospheric conditions.

Figure 6.15A shows an image of the *Ulva prolifera* bloom constructed from the ratio of the radiometric response in the NIR band to the sum of the radiometric response in the blue and green bands. The surface blooms are well delineated due to the longer NIR signal reflected off the chlorophyll present in the surface algae to the sensor, with minimal losses due to the scattering of aerosols and dust particles. Figure 6.15B shows the same bloom event in an image constructed from a radiometric ratio in the red band to the sum of the radiometric response in the blue and green bands. The surface blooms area hardly visible in the Figure because the signal is scattered off the aerosol and dust layers which is strongest in the shorter visible bands. The SABI_t image shown in Figure 6.16A (the difference between Figure 6.15A and Figure 6.15B) smoothed out the atmospheric effects (aerosols and molecules). Figure 6.16B shows the *Ulva prolifera* bloom in the 500 m/pixel resolution natural RGB colour composite corresponding to the Rayleigh-corrected reflectance bands λ_1=645, λ_4=555 and λ_3=469 nm respectively, where a line (a to b) was selected across the bloom, water, aerosols and the clouds. The transect of this line is shown in Figure 6.17.

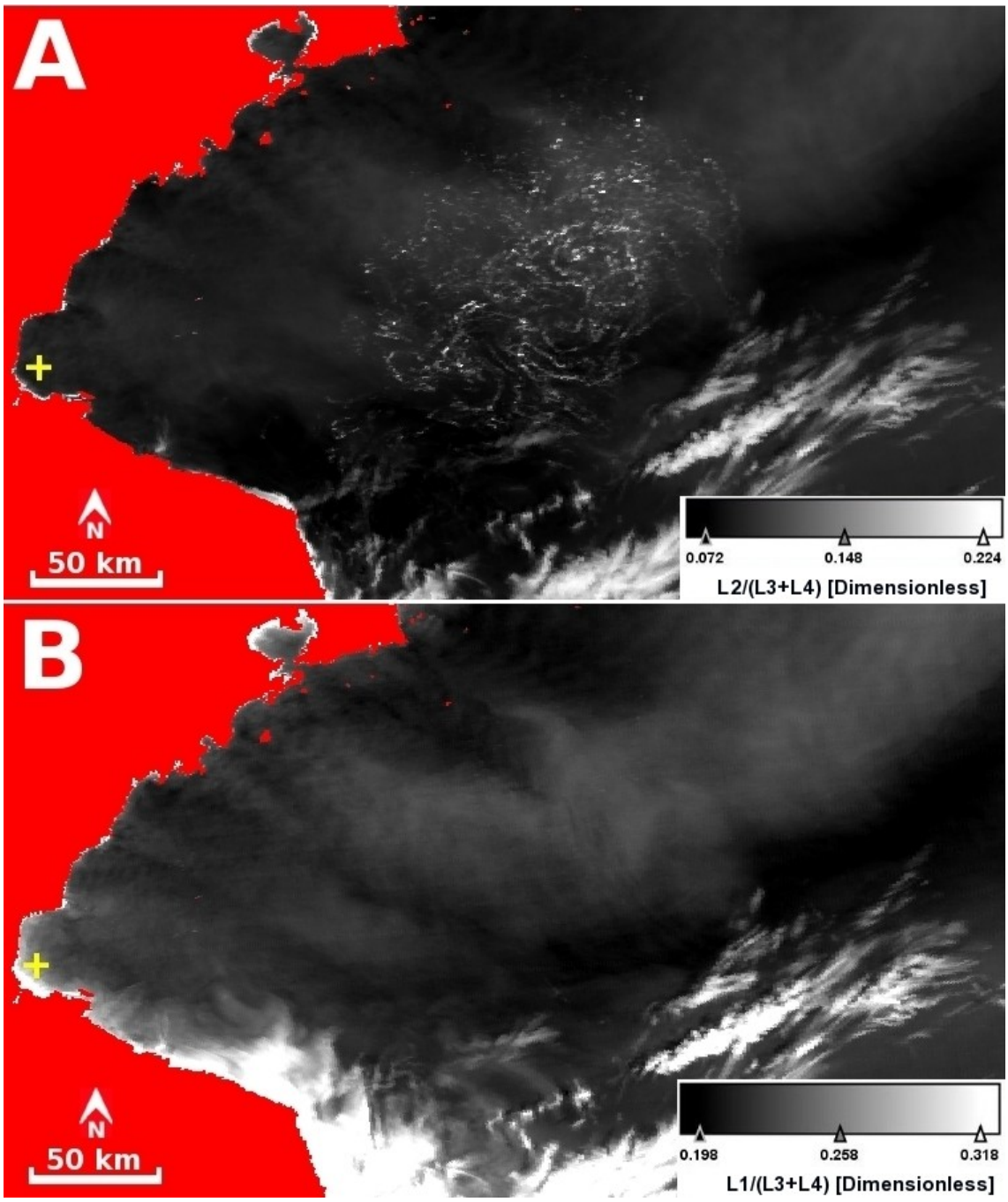

Figure 6.15. A geometrically-corrected 500 m/pixel resolution MODIS Aqua image of an *Ulva prolifera* bloom in the Yellow Sea observed on 30th May, 2008 at 05:36 UTC. The images were constructed from the calibrated TOA radiance (L) values using **(A)** the ratio of the λ_2=859 nm (aggregated from the 250 m resolution band group) to the sum of λ_3=469 nm and λ_4=555 nm (the surface blooms are well visible), and **(B)** the ratio of λ_1=645 nm (aggregated from the 250 m resolution band group) to the sum of λ_3=469 nm and λ_4=555 nm (The surface blooms are hardly visible due to sever scatter caused by dust layers in the short visible bands). Thick clouds are also visible in both scenes. The yellow (+) mark is positioned at N34° 52' 15" E119° 16' 44".

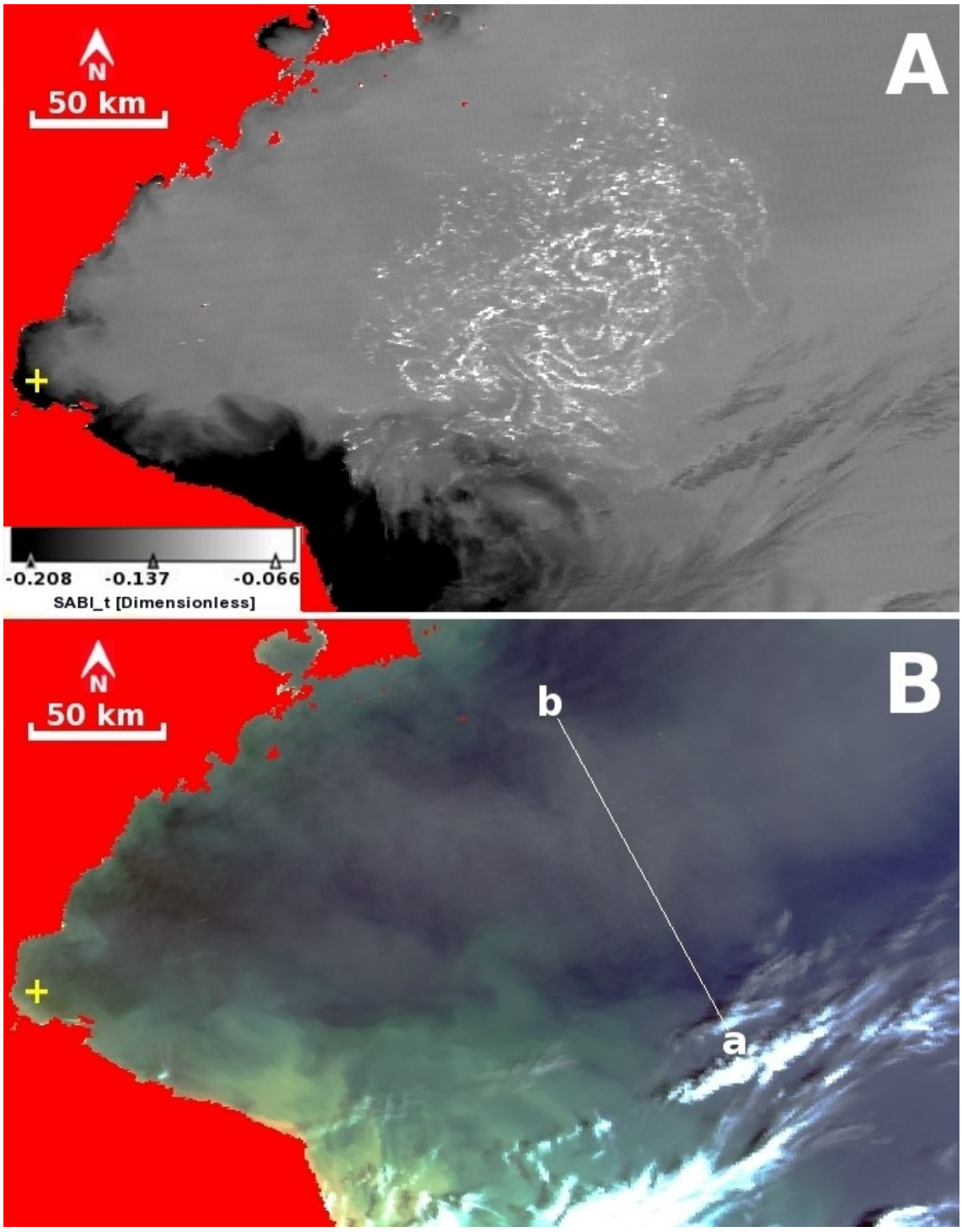

Figure 6.16. A geometrically-corrected 500 m/pixel resolution MODIS Aqua image of an *Ulva prolifera* bloom in the Yellow Sea observed on 30th May, 2008 at 05:36 UTC. The images were constructed from the calibrated TOA radiance values using **(A)** the SABI_t formula and **(B)** the natural RGB colour composite corresponding to the calibrated TOA radiance bands bands λ_1=645 (aggregated from the 250 m resolution band group), λ_4=555 and λ_3=469 nm respectively. A line (a to b) was drawn across the bloom, water, aerosols and the clouds, whose transect is shown in Figure 6.17. The yellow (+) mark is positioned at N34° 52' 15" E119° 16' 44".

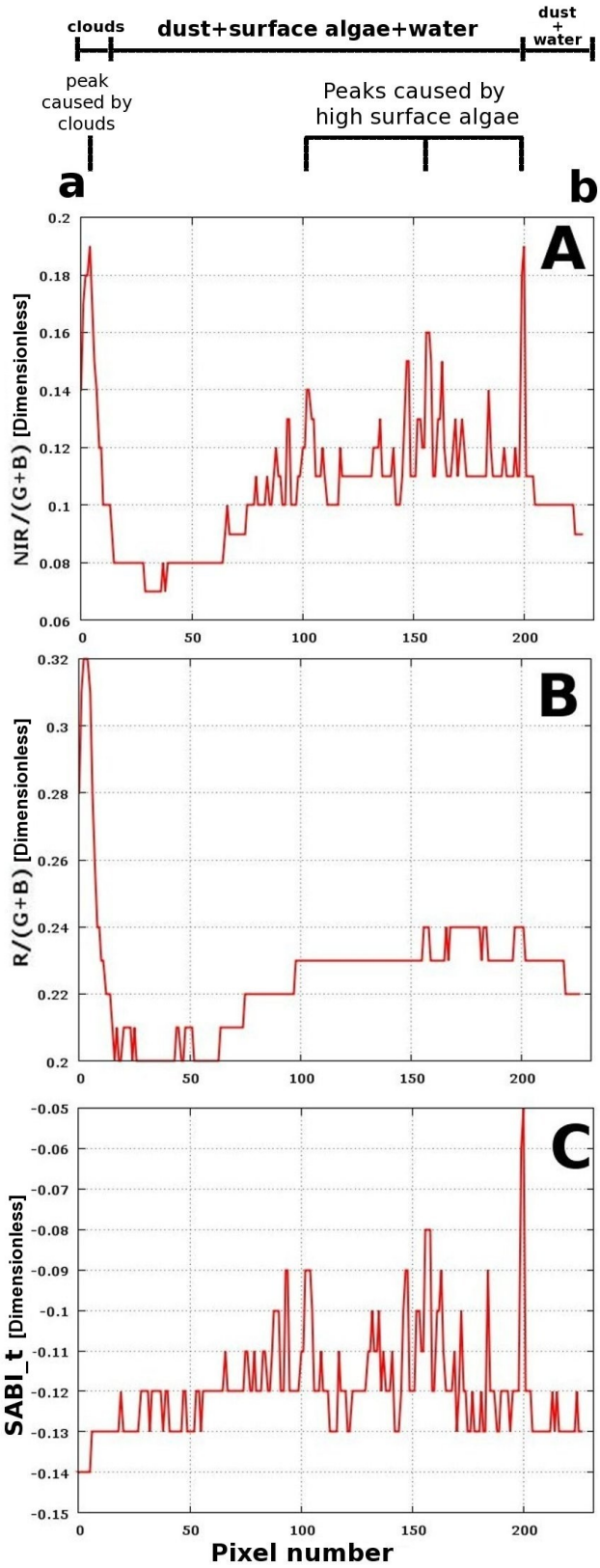

Figure 6.17. The transects of the line a to b (from Figure 6.16B) over clouds, dust, surface algae in (A) the ratio of the NIR (λ2=859 nm) band to the sum of the blue (λ3=469 nm) and green (λ4=555 nm) bands, (B) the ratio of the red (λ_1=645 nm) band to the sum of the blue (λ3=469 nm) and green (λ4=555 nm) bands and (C) is (A) minus (B).

6.3.3 Oil spill: Terra on 21st October, 2007 (off-glint conditions)

A reported oil spill was observed outside the sun-glint zone in MODIS Terra data on 21st October, 2007 at 07:02 UTC (swath shown in Figure 6.1C). A 500 m/pixel resolution natural RGB colour composite corresponding to bands λ_1=645 (aggregated from the 250 m resolution band group), λ_4=555, λ_3=469 nm respectively was constructed of the spill shown in Figure 6.18 (the same as in Figure 5.6B), over which other suspected spills were also highlighted (circled).

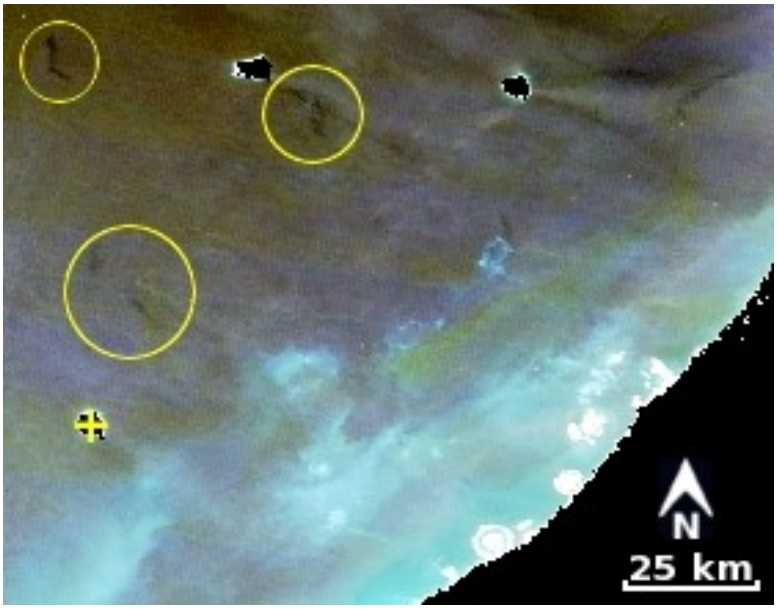

Figure 6.18. Out of sun-glint oil spill(s) (negative contrast) observed in a MODIS Terra image opposite Dubai, UAE on 21st October, 2007 at 07:02 UTC. The image is a 500 m/pixel resolution natural RGB colour composite produced from the Rayleigh-corrected reflectance data corresponding to bands λ_1=645 (aggregated from the 250 m resolution band group), λ_4=555, λ_3=469 nm respectively. Some of the spills are circled. The yellow (+) mark is positioned at N25° 13' 48" E54° 13'.

The average wind speed estimated by the QuikSCAT satellite at 10 m above sea level is 6±2 m/s near the suspected patches with an average SST of 32.40 °C estimated from MODIS SST product (not shown). The SABI_t and NDVI_t images were processed over the spill incident shown in Figures 6.19A and 6.19B respectively. The spills are clearly demarcated in the NDVI_t image unlike its corresponding SABI_t image, where the spills are hardly visible. The lack of visibility of the oil spills in the SABI_t could be attributed to the high Rayleigh scattering in the blue and green bands over the water and oil, more so than in the longer red and NIR bands, in addition to the lack of solar illumination from sun-glint. Hence, the overall SABI_t output becomes

smaller than the corresponding NDVI_t output. Thus, making the SABI_t a good discriminator between surface blooms and oil.

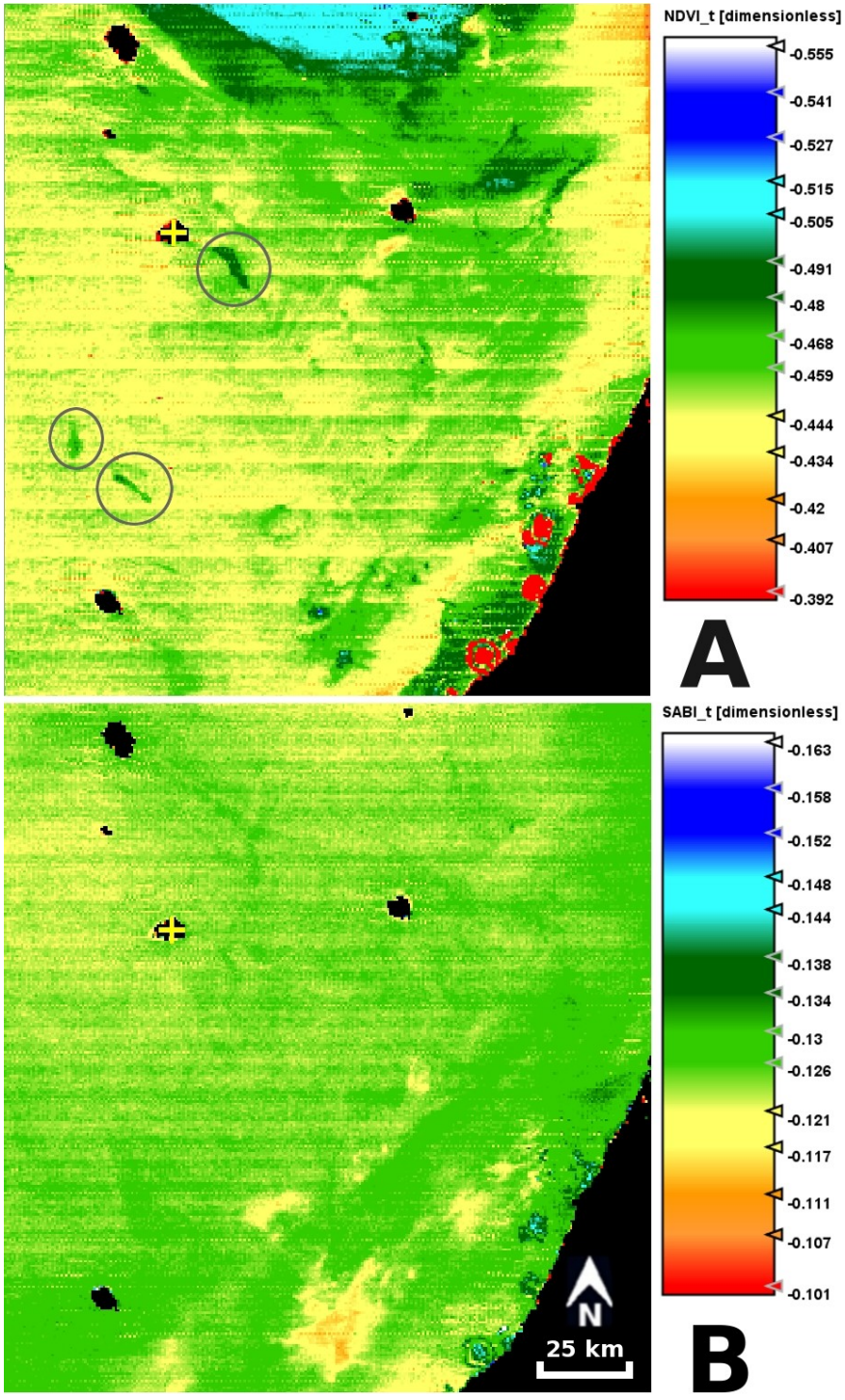

Figure 6.19. Out of the sun-glint oil spills (negative contrast) observed in MODIS Terra image opposite Dubai, UAE on 21st October, 2007 at 07:02 UTC. The 500 m/pixel resolution **(A)** NDVI_t and **(B)** SABI_t images. The spills (circled) are highly visible in the SABI_t as they are in the NDVI_t. The yellow + mark is positioned at N25° 54' 33" E54° 32' 16".

This is clearly supported by the spectral plot of the TOA calibrated radiances for oil and water shown in Figure 6.20A. Their plots are very similar in shape and strength. Figure 6.20B shows the corresponding spectral plot of oil and water in the Rayleigh-corrected TOA reflectance (rhos), which did reveal the minute spectral differences between oil and water after removing the influence of Rayleigh scattering. Both spectral plots, however, agreed on the negative contrast (darker than water) with which the oil appeared with in relation to sea water due to absence of sun-glint.

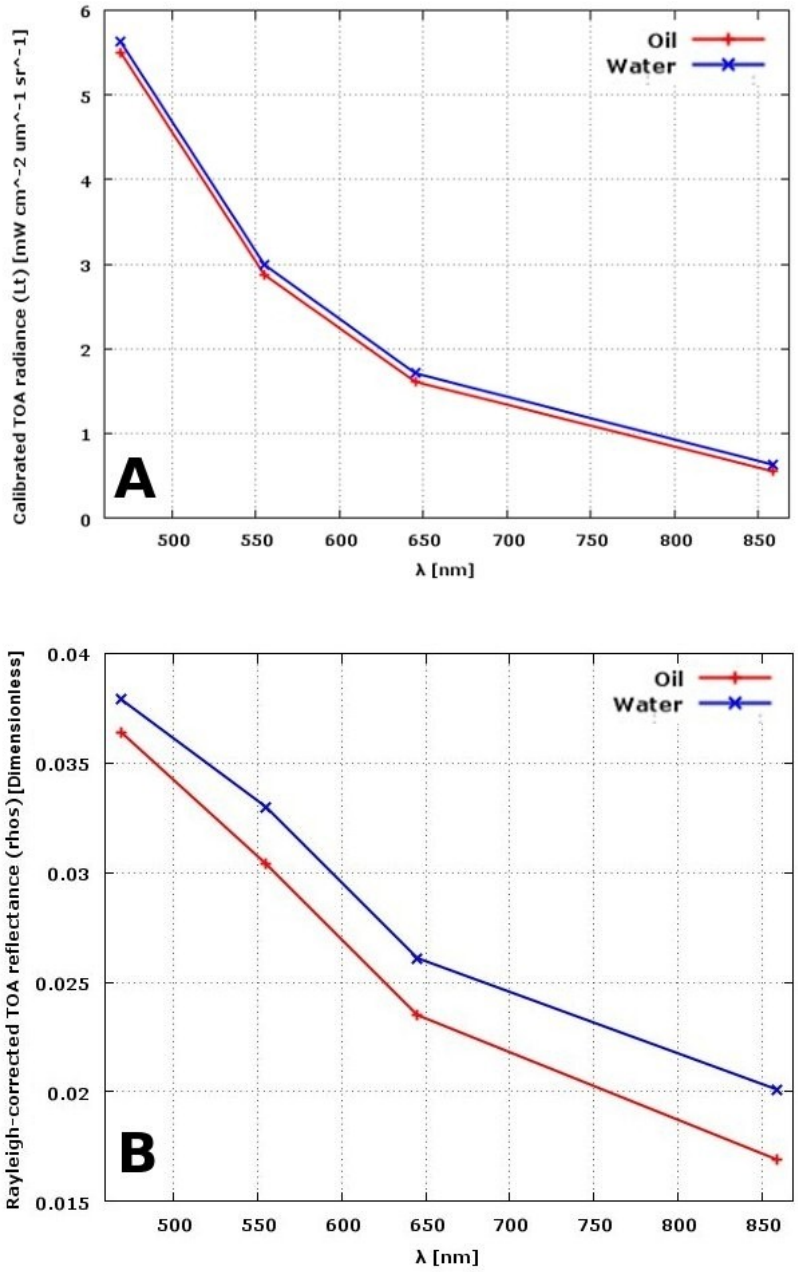

Figure 6.20. The spectral plots for clear sea water and oil at the oil spill incident observed in MODIS Terra opposite Dubai, UAE on 21st October, 2007 at 07:02 UTC in **(A)** the calibrated TOA radiances and in **(B)** the Rayleigh-corrected reflectance responses.

6.3.4 Oil spill: Terra on 4th August, 2010 (moderate in-glint conditions)

An oil spill caused by a heavy crude leak (~ 69 km^2) on 2nd August, 2010 near Al Ahmadi oil terminal, Kuwait was observed in MODIS Terra on 4th August, 2010 at 07:38 UTC (swath shown in Figure 6.1D). Figure 6.21A (the same as Figure 5.44A) shows the spill under a moderate sun-glint in a 500 m/pixel resolution natural RGB colour composite image corresponding to the Rayleigh-corrected reflectance bands λ_1=645 (aggregated from the 250 m resolution band group), λ_4=555 and λ_3=469 nm respectively. The average wind speed estimated by the Advanced Scatterometer (ASCAT) instrument 10 m above sea level was ~ 6 m/s around the spill area. The Figure also shows a zoomed-in image of a line (a to b) crossing the spill and oil-free waters (Figure 6.21B).

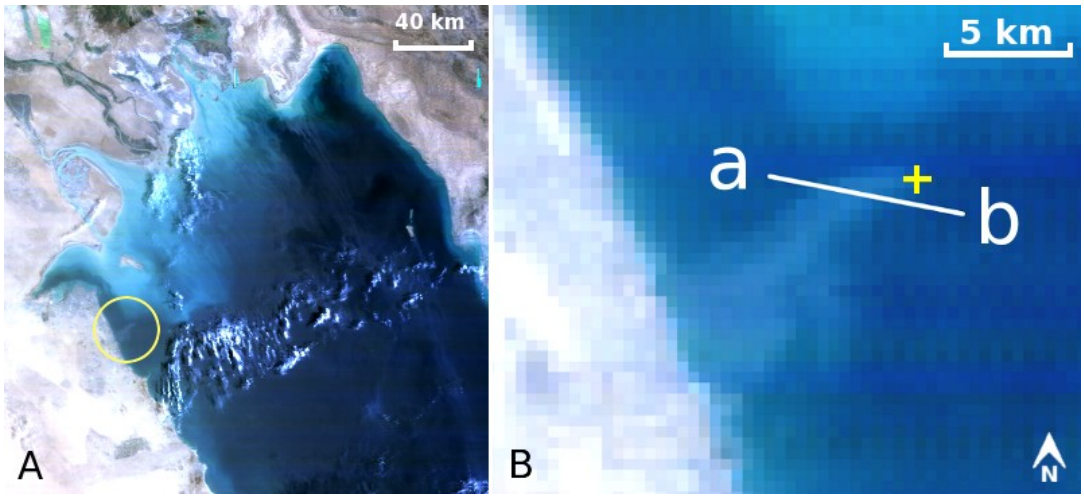

Figure 6.21. An oil spill occurred near Al Ahmadi terminal, Kuwait observed by MODIS Terra under the sun-glint zone on 4th August, 2010 at 07:38 UTC. **(A)** The positive-contrast spill appears circled in a geometrically-corrected image created from a 500 m/pixel resolution natural RGB colour composite corresponding to the Rayleigh-corrected reflectance bands λ_1=645 (aggregated from the 250 m resolution band group), λ_4=555 and λ_3=469 nm respectively. **(B)** The spill in a zoomed-in image with a line (a to b) crossing the spill and oil-free waters whose transect is shown in Figure 6.23. The yellow + mark is positioned at N29° 08' 36" E48° 17'3 8".

The NDVI_r, NDVI_t, SABI_r and SABI_t were processed over the spill. The NDVI_r (Figure 6.22A) and SABI_r images (Figure 6.22C) appear almost identical over the oil surface. Apart from the SABI_t (Figure 6.22D), all other responses have demonstrated a slight contrast difference between the oil-polluted and oil-free sea waters, which is virtually non existent in the SABI_t. This is likely caused by the smoothing that SABI_t does over the high Rayleigh scattering in the blue and green

bands.

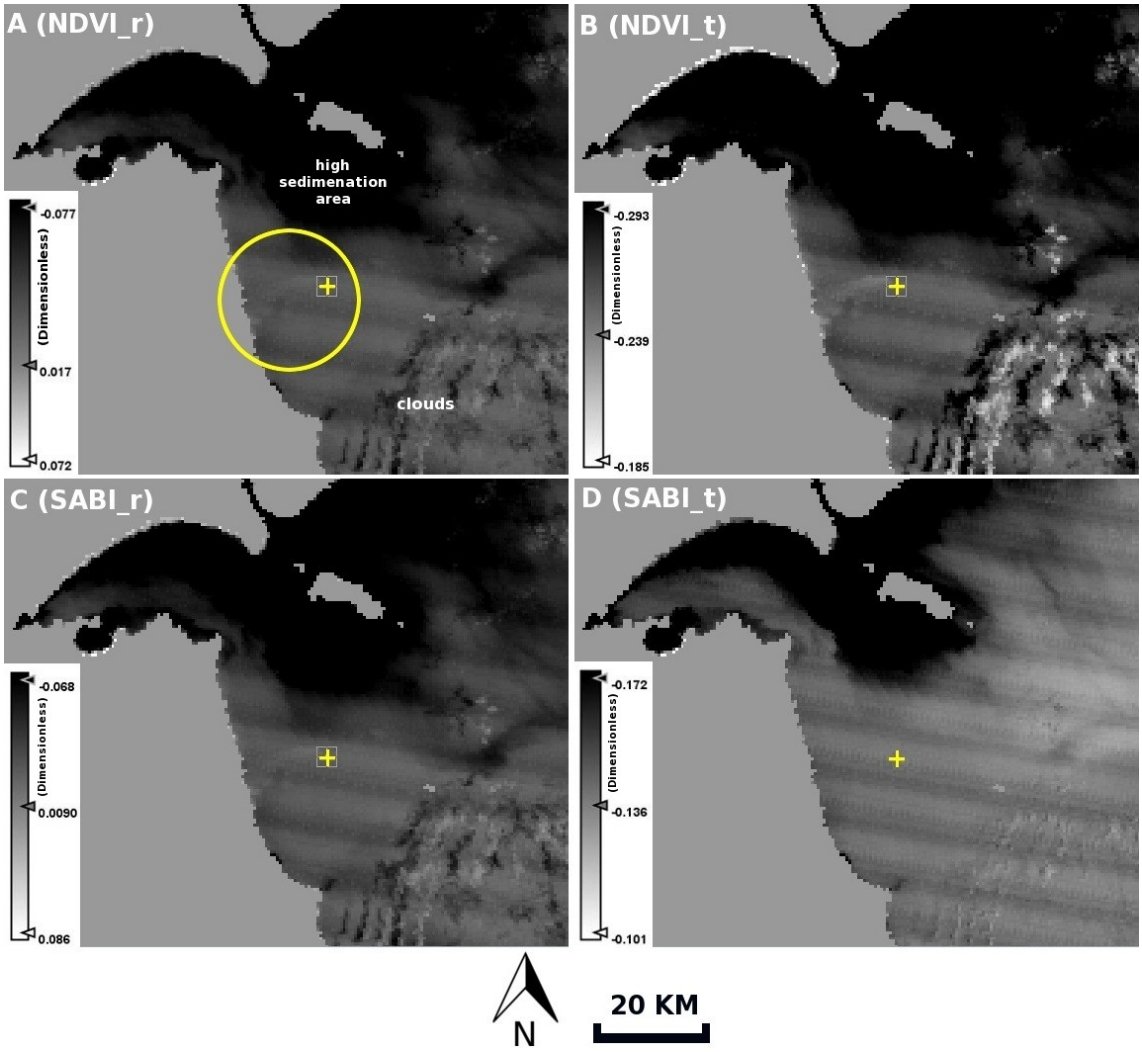

Figure 6.22. An oil spill near Al Ahmadi terminal, Kuwait observed by MODIS Terra image on 4th August, 2010 at 07:38 UTC in a geometrically-corrected 500 m/pixel resolution set of images: **(A)** NDVI_r, **(B)** NDVI_t, **(C)** SABI_r and **(D)** SABI_t. The spill is hardly visible in (D) unlike in the other images. Land is masked in grey. The yellow + mark is positioned at N29° 08' 36" E48° 17' 38".

The transects for the line a to b shown in Figure 6.21B are shown in Figure 6.23. A minor contrast difference (~ 1%) appears between the SABI_r and NDVI_r at the oil-water border, caused probably by the different concentrations of sheen on both sides of the spill.

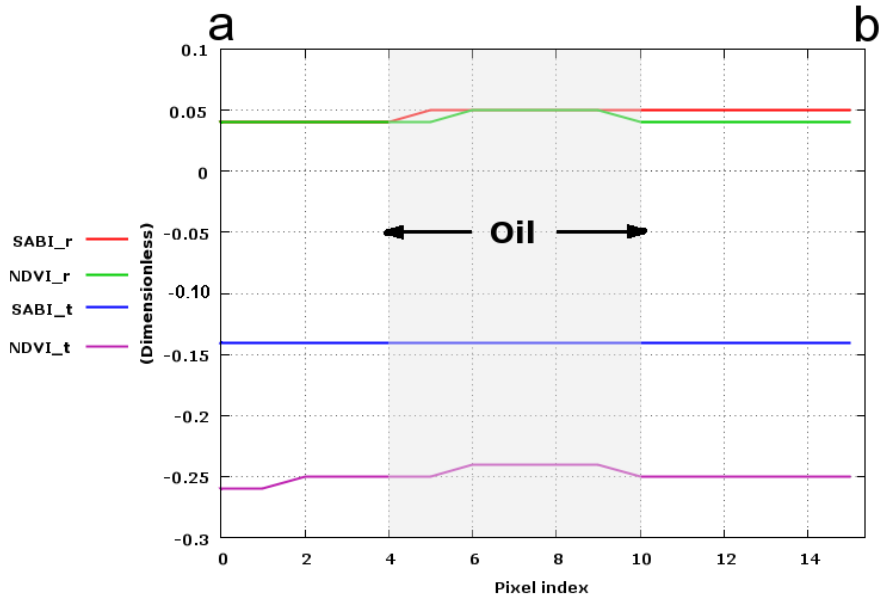

Figure 6.23. The SABI_r, NDVI_r, SABI_t and NDVI_t transects for the line (a to b) crossing the oil spill (Figure 6.21B) and clear waters. Approximately 1% contrast difference appears between the SABI_r and NDVI_r at the oil-water border due probably to different concentrations of sheen at both sides of the spill. Oil is represented by the shaded area. SABI_t appears less sensitive over oil and water.

6.3.5 Oil spill: Aqua on 25th April, 2010 (sever in-glint conditions)

The Gulf of Mexico Deepwater Horizon oil spill was visible in MODIS Aqua on 25th April, 2010 under severe sun-glint conditions (swath shown in Figure 6.1E). Figure 6.24 shows the spill in the SABI_t and NDVI_t images, in which the spill appears well-delineated due to a significant signal reflectance across all visible bands including NIR directly back to the sensor as a result of the spill's location in relation to the sun-glint. This effect made the spill's different textures and thicknesses (including the adjacent sheen layers) sharply defined. According to NOAA (2010), the wind speeds on that date ranged between 15-20 knot (7.7–10.3 m/s) with waves between 4-6 foot (1.2–1.8 m), contributing to the successful application of a dispersant by an aircraft.

A line (a to b) was selected across the spill and sea water over a 500 m/pixel resolution natural RGB colour composite corresponding to the Rayleigh-corrected reflectance in bands λ_1=645 (aggregated from the 250 m resolution band group) λ_4=555 and λ_3=469 nm respectively as shown Figure 6.25A (the same as in Figure 5.19B). The line is also shown across a 500 m/pixel resolution false RGB colour composite image corresponding to the Rayleigh-corrected reflectance in bands λ_2=859, λ_1=645 and λ_1=645 nm respectively (λ_1 and λ_2 aggregated from the 250 m resolution band group)

shown in Figure 6.25B.

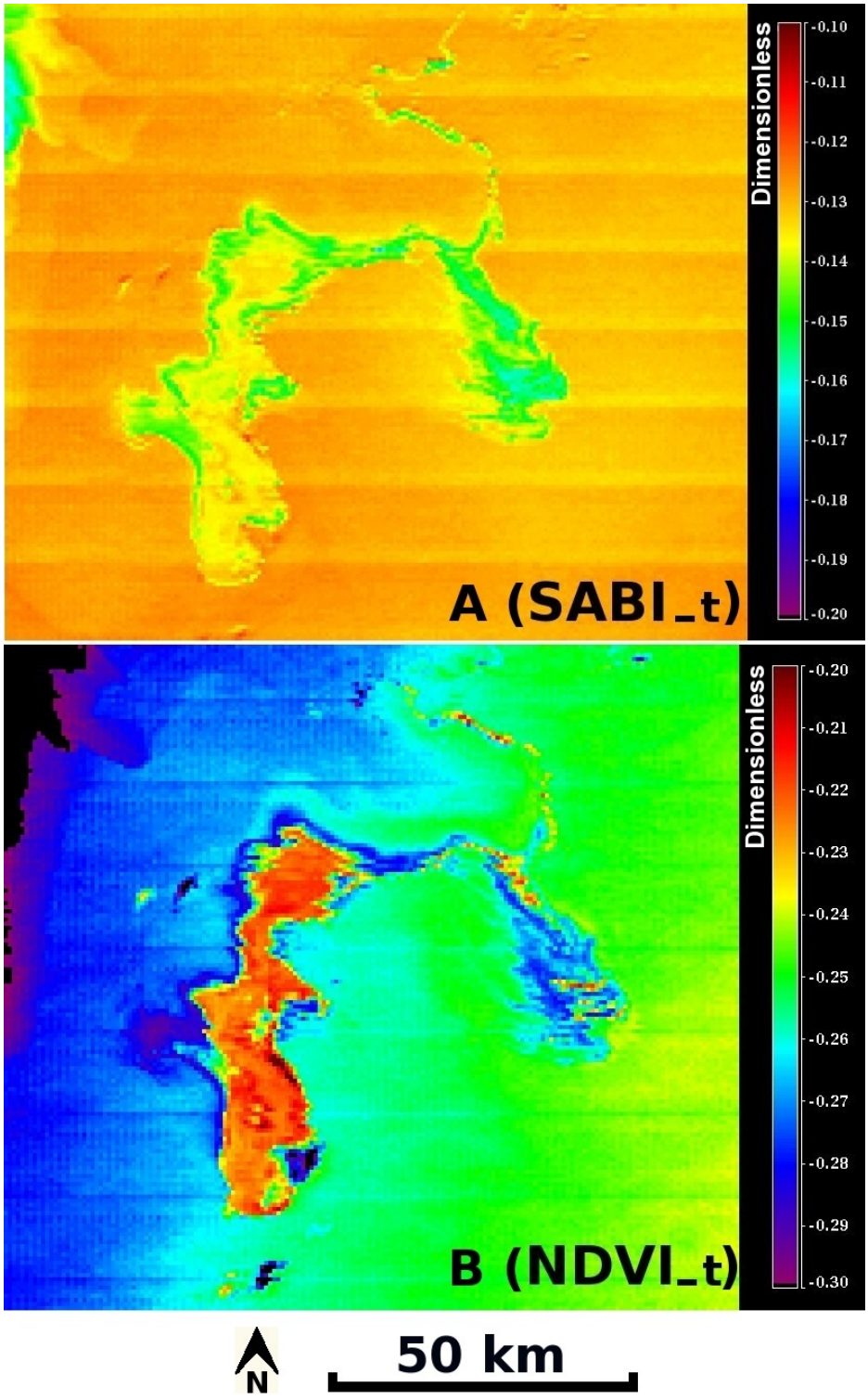

Figure 6.24. The **(A)** SABI_t and **(B)** NDVI_t images of the Gulf of Mexico Deepwater Horizon oil spill processed from MODIS Aqua, 25th April, 2010. The spill appears well-delineated in both images, as well as the different concentrations of oil, due to the spill falling directly under the sun-glint region,.

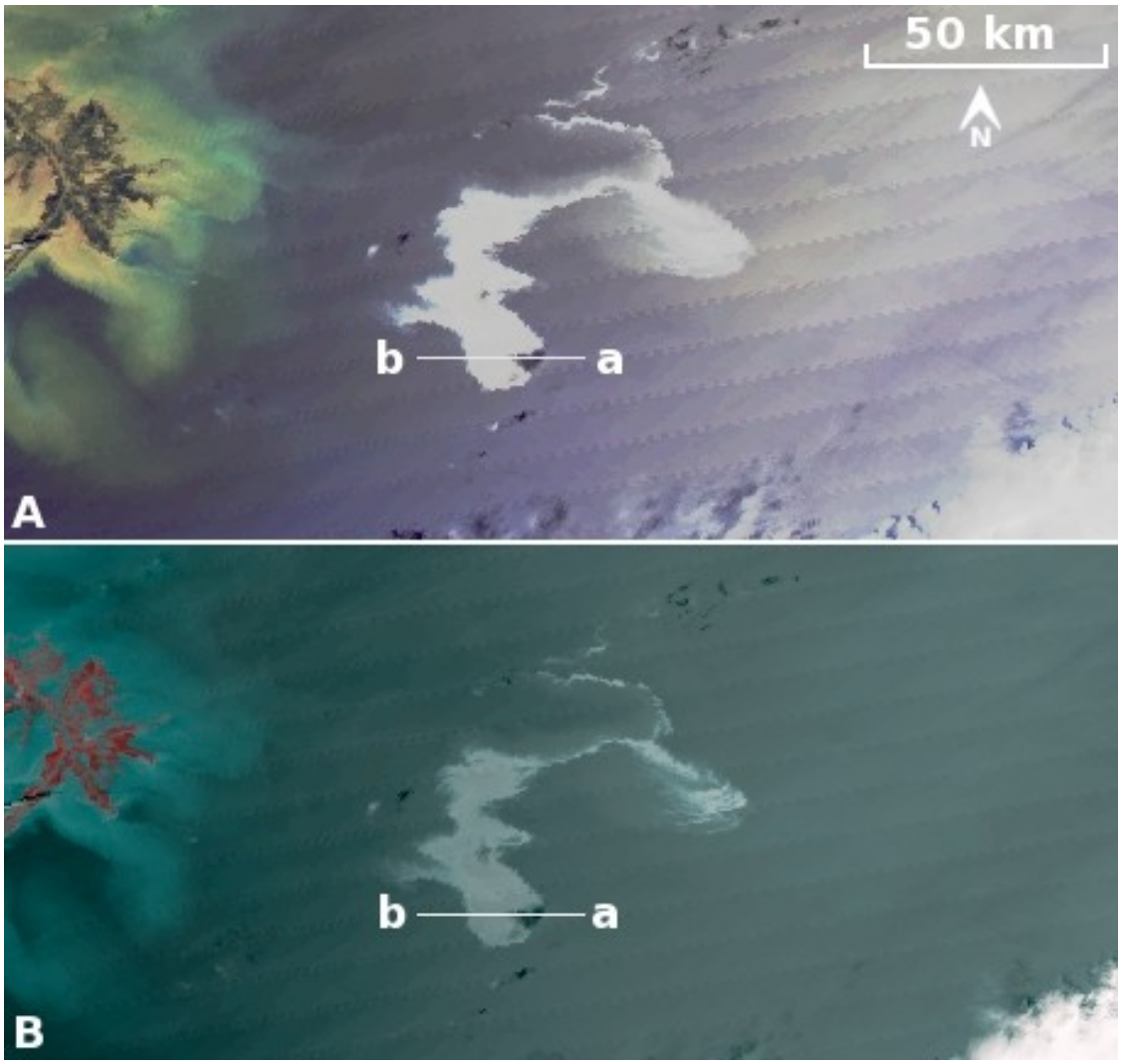

Figure 6.25. The Deepwater Horizon oil spill in the Gulf of Mexico observed in MODIS Aqua, 25th April, 2010 as it appears in a 500 m/pixel resolution images (λ_1 and λ_2 are both aggregated from 250 m/pixel resolution band group) made up from Rayleigh-corrected reflectance RGB colour composites: **(A)** natural composite corresponding to bands λ_1=645, λ_4=555 and λ_3=469 nm respectively and **(B)** false composite corresponding to bands λ_2=859, λ_1=645 and λ_1= 645 nm respectively. A line (a to b) was selected crossing part of the spill whose transects are shown in Figure 6.26B. The spill appears with a positive contrast due to it falling under the sun-glint.

The transect for the line a to b (a zoomed-in image shown in Figure 6.26A) was plotted in relation to SABI_t and NDVI_t (see Figure 6.26B). Although, both relations did reveal the different thickness details of the oil spill, SABI_t has demonstrated the least sensitivity, resulting in a much lower contrast between oil and water than NDVI_t. This contrast difference between the two indices is primarily attributed to the denominator, since they both share the same numerator.

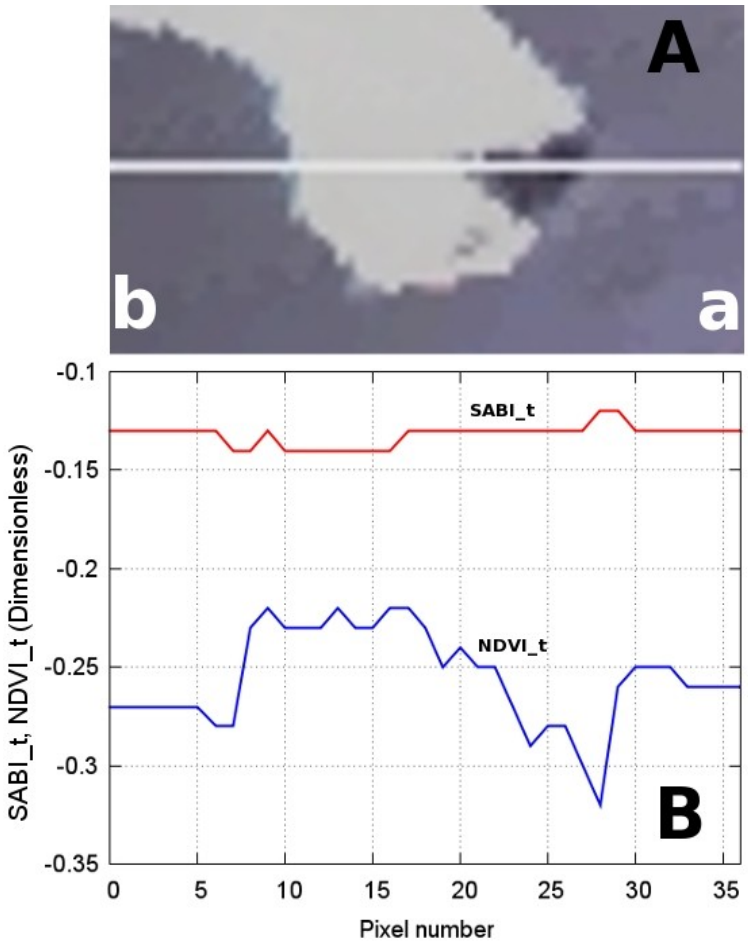

Figure 6.26. **(A)** A zoomed-in image of a line crossing part of the Deepwater Horizon oil spill from a to b taken from Figure 6.25. **(B)** The SABI_t and NDVI_t transects of the (a to b) line.

The calibration results show that the SABI_t product supersedes the NDVI_t in detecting a variety of surface biological species under different environmental conditions. Under the SABI_t, water-floating blooms were found to maintain a baseline value of -0.10. Below this value, oil spills among other things, are represented. This unique property allowed the SABI_t algorithm to act as a robust discriminator between surface floating blooms and oil. These results were further validated over different oil spills and bloom species including those detected outside the RSA using sensors other than MODIS.

The data produced from the calibrated TOA radiance values such as SABI_t and NDVI_t provided the best results when compared with those derived from the Rayleigh-corrected reflectance (SABI_r and NDVI_r). For this reason, the following validation section will be confined to using the SABI_t and NDVI_t data only.

6.4 The validation of the SABI

Figure 6.27 shows the location map of the different datasets used in the validation of the SABI_t algorithm in the thesis.

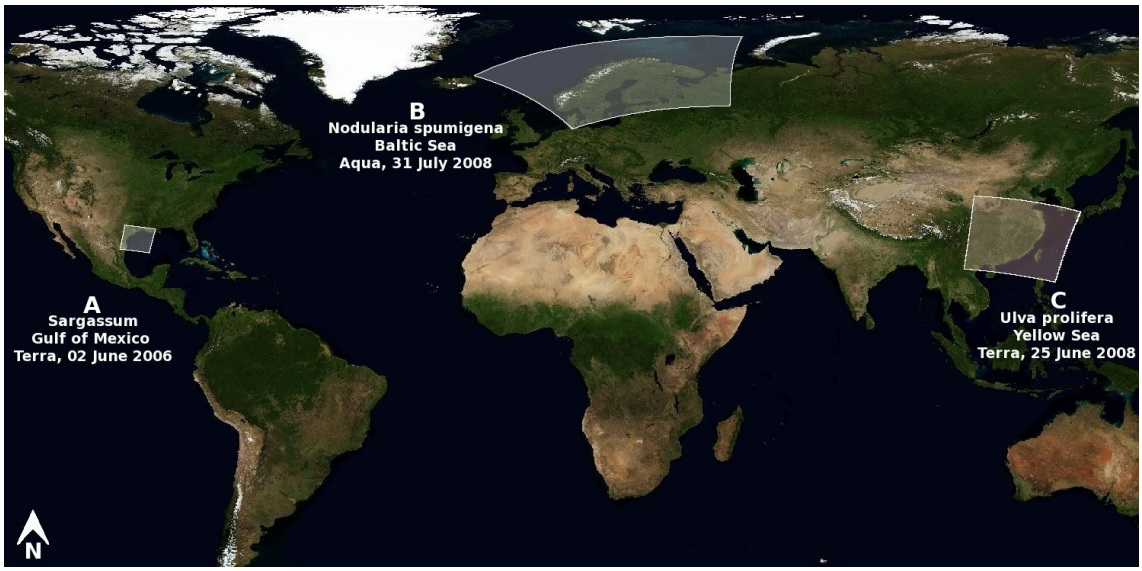

Figure 6.27. The different MODIS swaths, in which surface bloom incidents and oil spills were observed and subjected to the validation of SABI_t.

6.4.1 Sargassum– Gulf of Mexico

Sargassum is characterized as having elongated, narrow fronds and numerous spherical gas-filled bladders called vesicles that allow the plant to float freely (Littler et al., 1989). The colour of Sargassum can vary from yellow to brown to black (Hacker & Madin, 1991). Partly surface-exposed Sargassum patches were observed in the Gulf of Mexico by MODIS Terra on 2nd June, 2006 at 01:55 UTC under a moderate sun-glint (swath shown in Figure 6.27A). The mean wind speed derived from QuikScat was 4±2 m/s. Two sets of 500 m/pixel resolution colour composite images were produced (λ_1 and λ_2 are both aggregated from the 250 m resolution band group) from the Rayleigh-corrected reflectances: a false RGB composite corresponding to bands λ_2=859, λ_1=645 and λ_1=645 nm respectively (Figure 6.28A) and a natural RGB composite corresponding to bands λ_1=645 , λ_4=555 and λ_3=469 nm respectively (Figure 6.28B). In Figure 6.28A, the surface floating Sargassum appears reddish due to the red-edge mixed with sub-surface Sargassum and clouds in the same image. Figures 6.29A, 6.29B and 6.29C show the accumulations of Sargassum in a MODIS Chlor-a, NDVI_t and the SABI_t images respectively. Over the Chlor-a image (Figure 6.29A) three points

representing: (1) surface Sargassum, (2) clouds and (3) sub-surface bloom were selected to compare their responses.

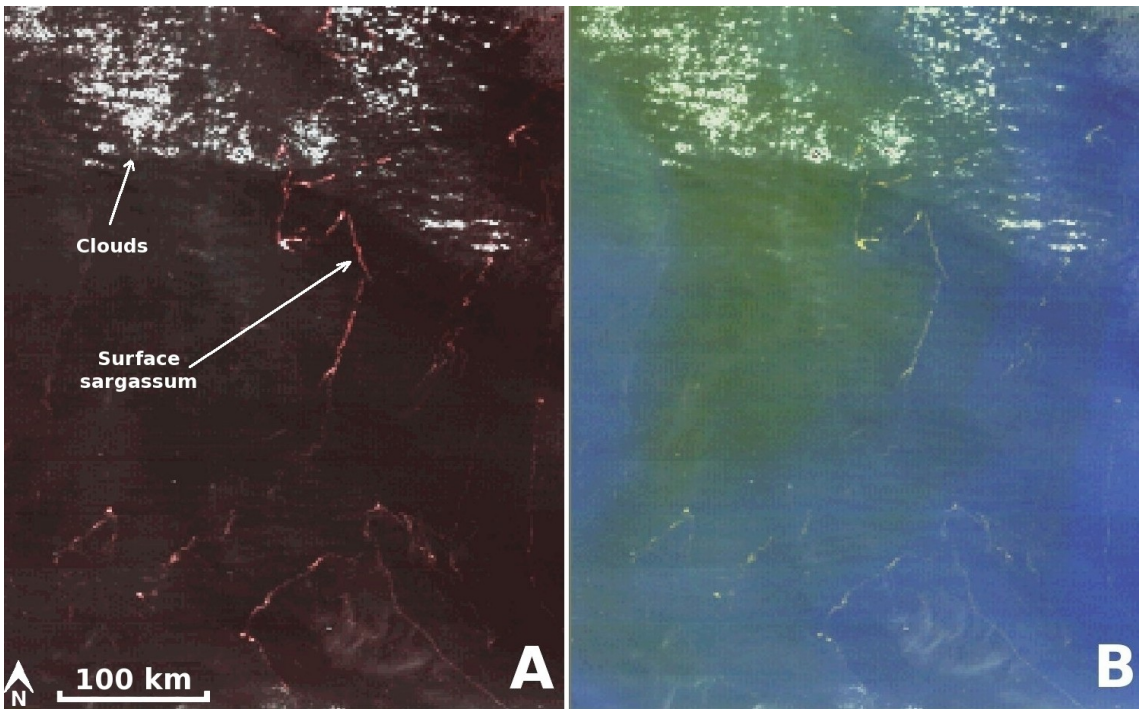

Figure 6.28. Sargassum in the Gulf of Mexico observed in MODIS Terra on 2nd June, 2006 at 01:55 UTC showing partly surface-exposed patches as they appear in a 500 m/pixel resolution images (λ_1 and λ_2 are both aggregated from 250 m/pixel resolution band group) made up from Rayleigh-corrected reflectance RGB colour composites: **(A)** False composite corresponding to bands λ_2=859, λ_1=645, and λ_1=645 nm respectively and **(B)** natural composite corresponding to bands λ_1=645, λ_4=555 and λ_3=469 nm respectively. Sargassum appears as filamentous or thread-like structures. The centre of the images is positioned at N28° 14' 29" E94° 01' 32".

The standard SeaDAS cloud mask classifies pixels as clouds if their Rayleigh-corrected TOA reflectance rhos (at λ_{16}=865) value is greater than 0.027 (2.7%) (Robinson et al., 2000). The cloud mask in Figure 6.29A, mistakenly flagged surface Sargassum at point 1. The clouds shown at point 2 in the same Figure, were correctly classified as clouds by the cloud mask. The NDVI_t mis-classified clouds as surface Sargassum (Figure 6.29B), unlike the SABI_t which did not mis-classify them as surface blooms (Figure 6.29C). SABI_t has, therefore, successfully demonstrated its superiority over NDVI_t in filtering out almost all cloud classes and not mixing them with surface floating Sargassum.

At surface Sargassum shown in point 3 (Figure 6.29A), the Chlor-a concentration was recorded low (0.11 mg/m^3) and did not fail as expected. This is because SABI_t

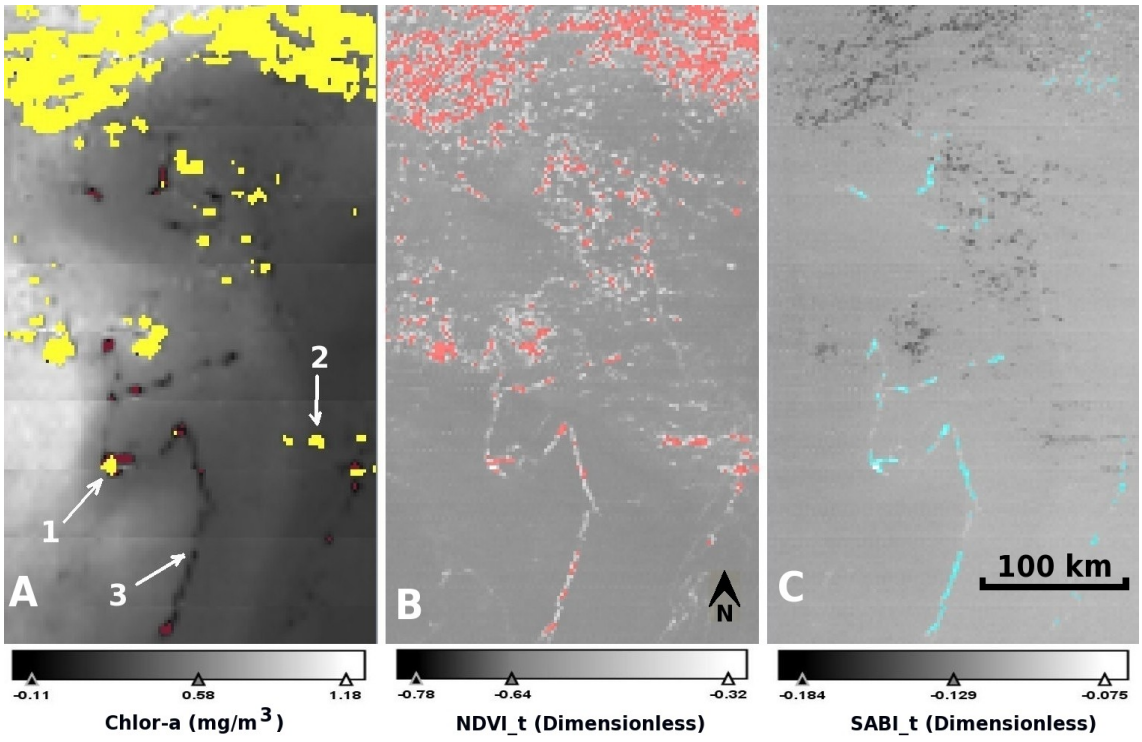

Figure 6.29. Sargassum in the Gulf of Mexico observed in MODIS Terra on 2nd June, 2006 at 01:55 UTC as it appears in the 500 m/pixel resolution: (A) Chlor-a, where the failed Chlor-a pixels are masked in red and clouds are masked in yellow; (B) NDVI_t, where the values between -0.4 and zero were masked in red; and in the (C) SABI_t, where the values greater than or equal to -0.10 are masked in blue. Three points selected on A representing: (1) surface Sargassum, (2) clouds and (3) near-surface Sargassum. The centre of images is positioned at N28° 34' 42" E93° 50' 20".

and NDVI_t are highly sensitive to significant differences between the red and NIR signals (thus high in surface and near-surface Sargassum). Unlike the Chlor-a algorithm which is highly sensitive to differences between the blue and green responses and thus insignificant in species such as Sargassum. These differences can be seen in the spectral plot shown in Figure 6.30 between water and surface Sargassum. Table 6.1 summarizes all these results.

Table 6.1 SABI_t, NDVI_t and Chlor-a values over selected points appearing in Figure 6.29.

Point No.	Description	SABI_t (dimensionless)	NDVI_t (dimensionless)	Chlor-a (mg/m^3)
1	Surface Sargassum	0.05	0.08	Non valid data
2	Thin clouds	– 0.12	– 0.32	Non valid data
3	Sub-surface Sargassum/bloom	– 0.09	– 0.35	0.11

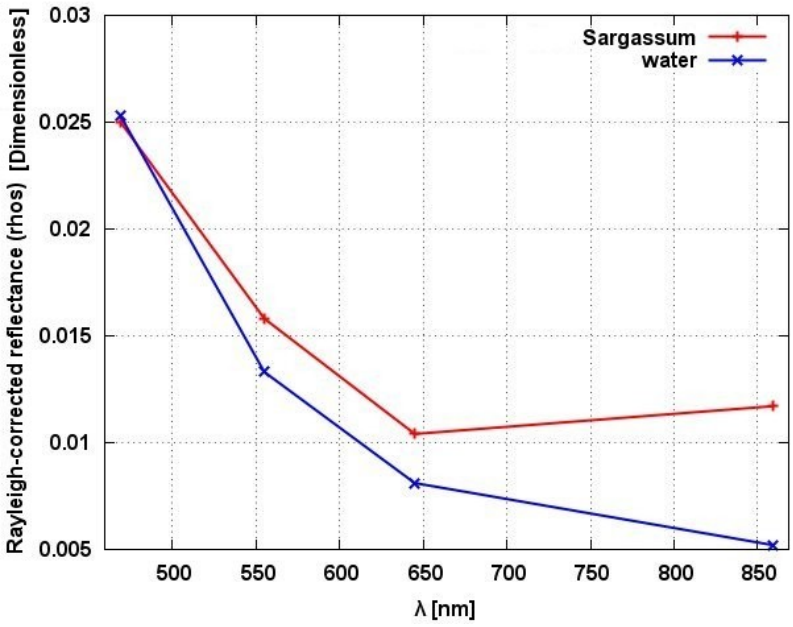

Figure 6.30. The spectral plot of near-surface Sargassum bloom (point 3) and adjacent water shown in Figure 6.29A in relation to the 500 m/pixel resolution Rayleigh-corrected reflectance (rhos) values.

The SST of the bloom (not shown) did not reveal significant temperature differences between Sargassum and the surrounding sea water except at point 1 (Figure 6.29A), where it was flagged as poor quality SST (invalid value). This, according to Franz (2006) occurs when the 3×3 pixel neighbourhood of point 1 is: (1) experiencing saturation or non-spatial uniformity reflectance in the red band (λ_{14}=678 nm); and (2) the SST retrieval was cold relative to the reference.

6.4.2 *Nodularia spumigena*– Baltic Sea

Nodularia spumigena is a hepatotoxic cyanobacterium (Kononen, 1992) that can colour the water green, blue-green or yellow. A bloom of the *N. spumigena* species was observed in the Baltic sea by MODIS Aqua on 31st July, 2008 at 10:55 UTC (swath shown in Figure 6.27B). A set of 500 m/pixel resolution colour composite images (λ_1 and λ_2 aggregated from the 250 m resolution band group) were produced from the Rayleigh-corrected reflectance values: RGB natural composite corresponding to bands λ_1=645, λ_4=555 and λ_3=469 nm respectively shown in Figure 6.31A and a false RGB composite corresponding to bands λ_2=859, λ_1=645 and λ_1=645 nm respectively shown in Figure 6.31B. The mean wind speed recorded by QuikScat at the time was 5±2 m/s.

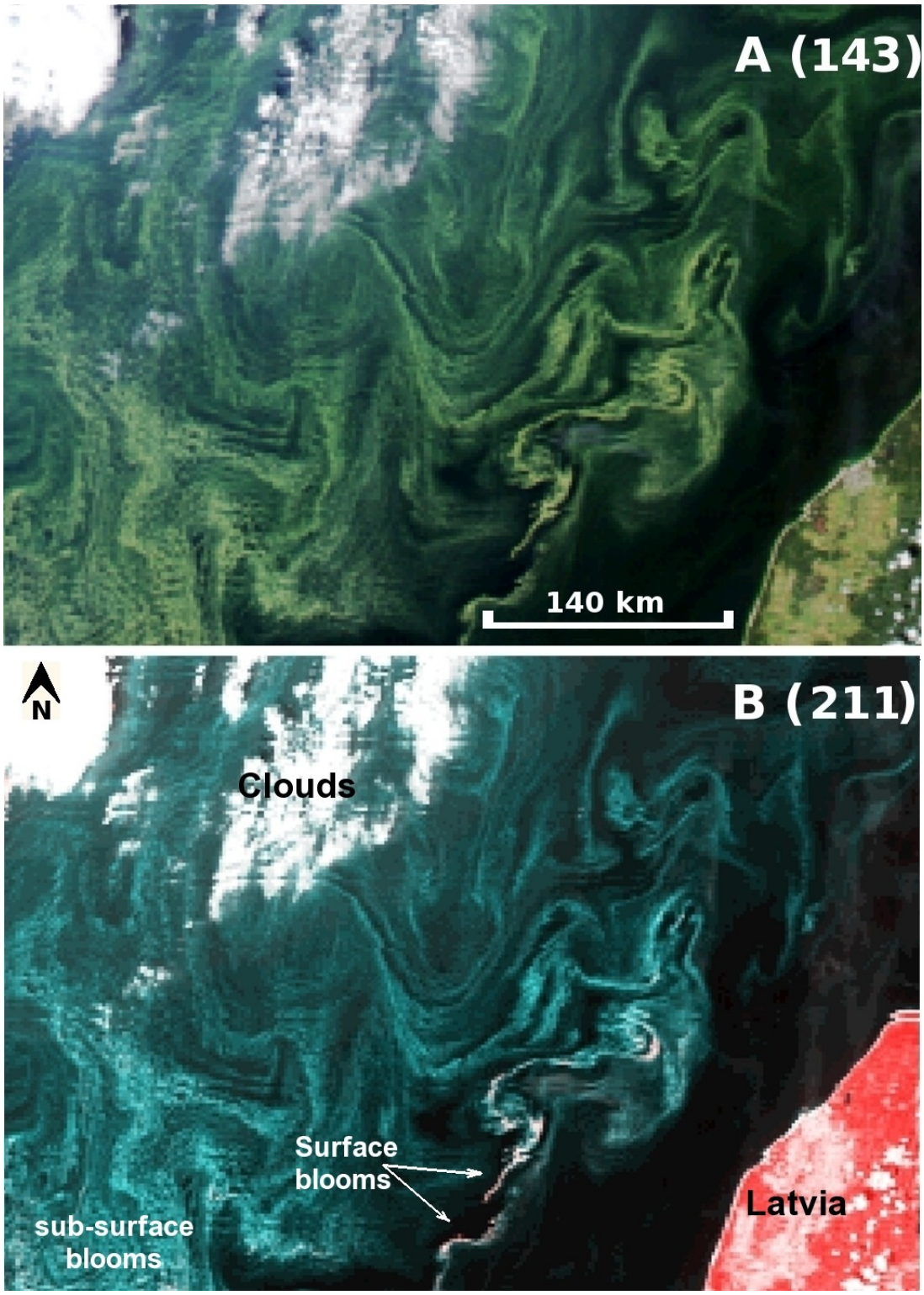

Figure 6.31. A bloom of the *N. spumigena* species observed in the Baltic Sea by MODIS Aqua on 31st July, 2008 at 10:55 UTC as it appears in the 500 m/pixel resolution images (λ_1 and λ_2 are both aggregated from 250 m/pixel resolution band group) made up from different Rayleigh-corrected reflectance RGB colour composite values: **(A)** Natural composite corresponding to bands λ_1=645, λ_4=555 and λ_3=469 nm respectively, and **(B)** False composite corresponding to bands λ_2=859, λ_1=645 and λ_1=645 nm respectively. The top-left corner of both images is positioned at N57° 25' 08" E18° 41' 12".

The SABI_t product of the bloom was processed (Figure 6.32) including a zoomed-in image of this bloom (Figure 6.33). The corresponding Chlor-a and SST colour images of the bloom area are shown in Figures 6.34 and 6.35 respectively. Failure to retrieve valid Chlor-a values from the standard MODIS product (Figure 6.34) occurs when water leaving radiances become negative for any of the bands used in Equation (4.12). This can happen when the bloom is floating close to or at the water surface, and thus violating the dark pixel assumption, which is a necessary prerequisite for standard atmospheric correction. Failure can also be caused by the presence of absorbing aerosols (non-maritime aerosols) such as soot and mineral dust levels (Werdell et al., 2007). Either of these will cause an overestimation or over-subtraction at all bands, with increasing severity for shorter wavelengths (that is the blue portion of the spectrum) (Wang, 2000). SABI_t values greater than or equal to -0.10 appeared reddish in the false RGB colour composite (Figure 6.31B), but did not correlate well with all of the failed Chlor-a pixels, since the failure is not only caused by the presence of surface blooms. The cloud mask used in the Chlor-a image (Figure 6.34) has falsely classified surface blooms as clouds. The temperature of the blooms was estimated from the SST data shown in Figure 6.35 to be 1–2 °C higher than surrounding sea waters due to *Noctiluca* dissipating absorbed solar energy as heat.

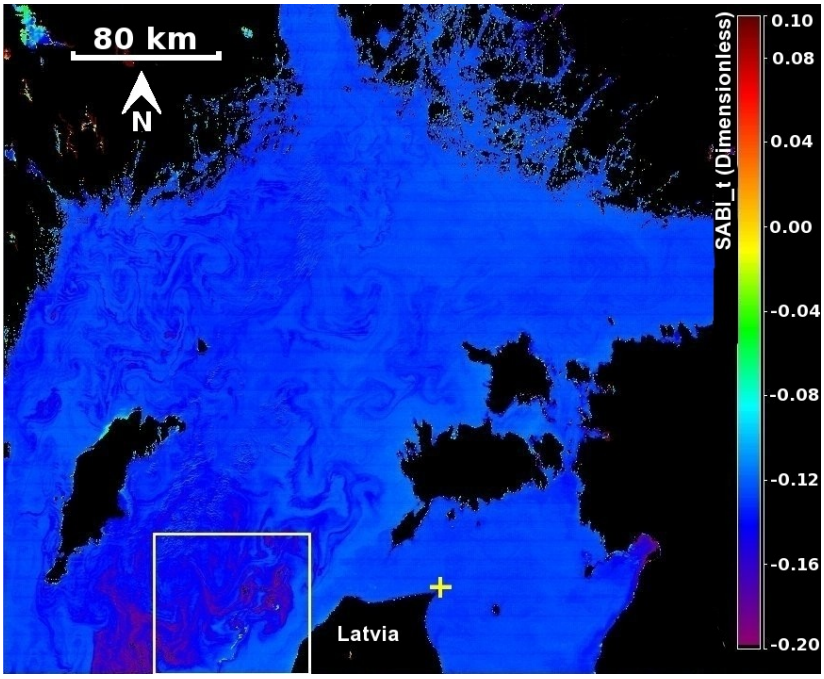

Figure 6.32. The SABI_t image of the *N. spumigena* bloom in the Baltic Sea observed in MODIS Aqua, 31st July, 2008 at 10:55 UTC . Sampled surface blooms are selected (enclosed by a box) whose zoomed-in image is shown in Figure 6.33. The yellow (+) mark is positioned at N57° 48' 12" E22° 38' 36".

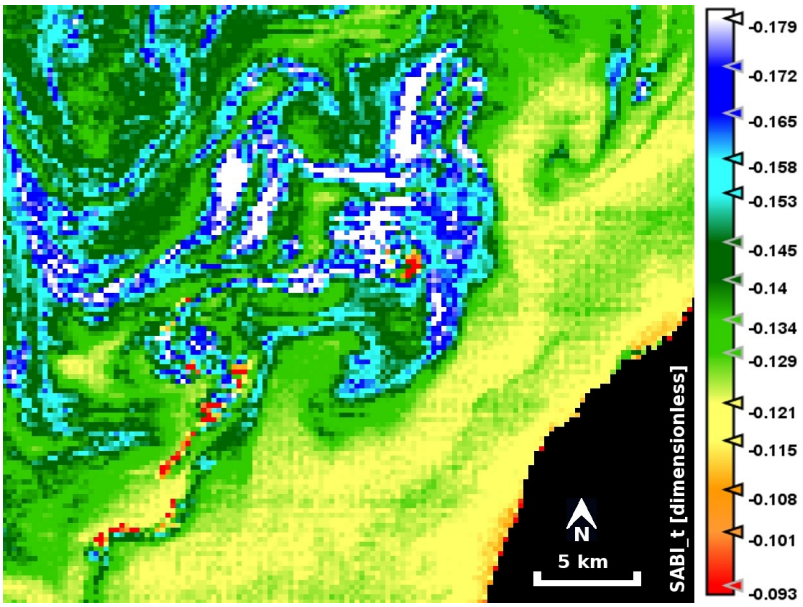

Figure 6.33. A zoomed-in SABI_t image of the *N. spumigena* bloom (taken from Figure 6.32) in the Baltic Sea observed in MODIS Aqua, 31st July, 2008 at 10:55 UTC. SABI_t values greater than or equal to -0.10 represent surface and near-surface blooms. The centre of the image is positioned at N57° 20' 21" E20° 32' 44".

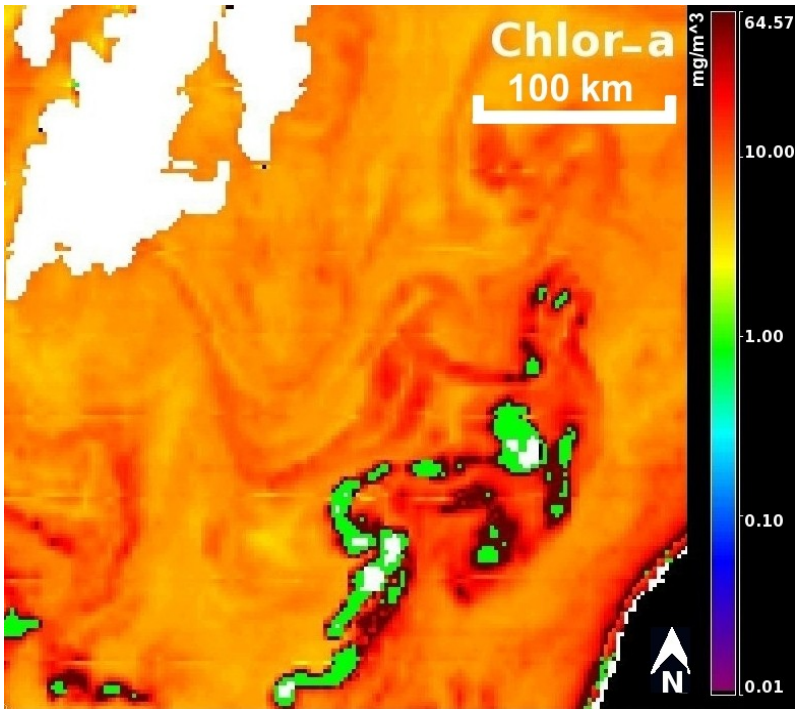

Figure 6.34. The N. spumigena bloom in the Baltic Sea observed in MODIS Aqua on 31st July, 2008 at 10:55 UTC as it appears in a Chlor-a map (clouds are masked in white while failed Chlor-a pixels are masked in green). Some surface blooms were misclassified as clouds. The centre of the image is positioned at N57° 32' 16" E20° 32' 06".

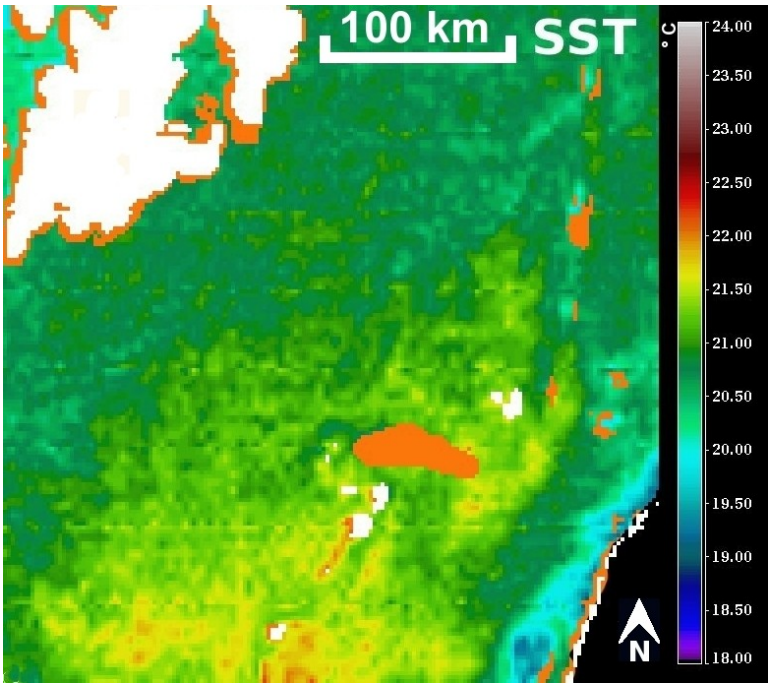

Figure 6.35. The *N. spumigena* bloom in the Baltic Sea observed in MODIS Aqua on 31st July, 2008 at 10:55 UTC as it appears in SST (clouds are masked in white and poor quality SST pixels are masked in orange). Surface and near-surface blooms have 3% higher SST than surrounding sea water temperatures. The centre of the image is positioned at N57° 32' 16" E20° 32' 06".

6.4.3 *Ulva prolifera*– Yellow Sea

A bloom of the *Ulva prolifera* species was observed in MODIS Terra on 25th June, 2008 at 12:00 UTC located near the coastline of Qingdao (eastern China) directly under a severe sun-glint (swath shown in Figure 6.27C). A set of 500 m/pixel resolution colour composite images (λ_1 and λ_2 aggregated from the 250 m resolution band group) were produced from the Rayleigh-corrected reflectance values: A natural RGB composite corresponding to bands λ_{11}=645 , λ_4=555 and λ_3=469 nm respectively (Figure 6.36A) and a false RGB composite corresponding to bands λ_2=859, λ_1=645 and λ_1=645 nm respectively (Figure 6.36B). Zoomed-in images of the surface bloom areas were selected from each RGB colour composite: The natural (Figure 6.36C) and false (Figure 6.36D) colour composites respectively. In all of these images adjacent low level clouds and their associated shadows are also visible. The wind speed data at the bloom event was not readily available at the time. It can be estimated as not exceeding 8 m/s, because at such speeds the surface aggregates are expected to disperse (Kahru et al., 1993; Mazur-Marzec & Plinski, 2009). The Chlor-a product was irretrievable due to severe sun-glint coverage over the area.

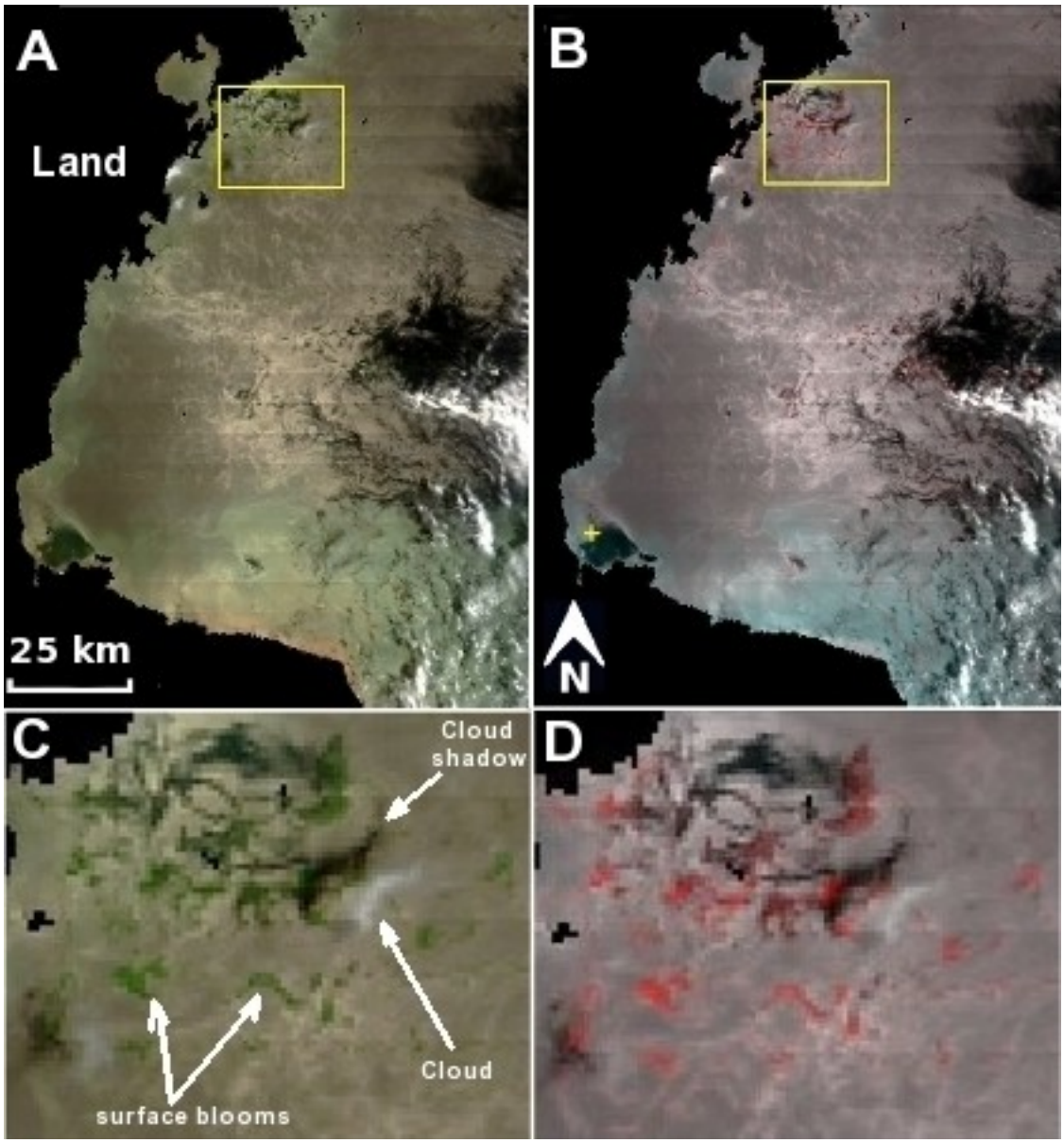

Figure 6.36. An *Ulva prolifer*a bloom in the Yellow Sea, China observed in MODIS Terra on 25th June, 2008 at 12:00 UTC directly under the sun-glint. The 500 m/pixel resolution images (λ_1 and λ_2 are both aggregated from 250 m/pixel resolution band group) are made up from different Rayleigh-corrected reflectance RGB colour composite values: **(A)** natural composite corresponding to bands λ_1=645, λ_4=555 and λ_3=469 nm respectively. **(B)** A false composite corresponding to bands λ_2=859, λ_1=645 and λ_1= 645 nm respectively. **(C)** A zoomed-in image of surface blooms selected from A. **(D)** A zoomed-in image of surface blooms selected from B. The yellow (+) mark is positioned at N34° 52' 15" E119° 16' 44".

The 500 m/pixel resolution SABI_t and NDVI_t images were produced for the surface bloom incident in Figures 6.37A and 6.37B respectively.

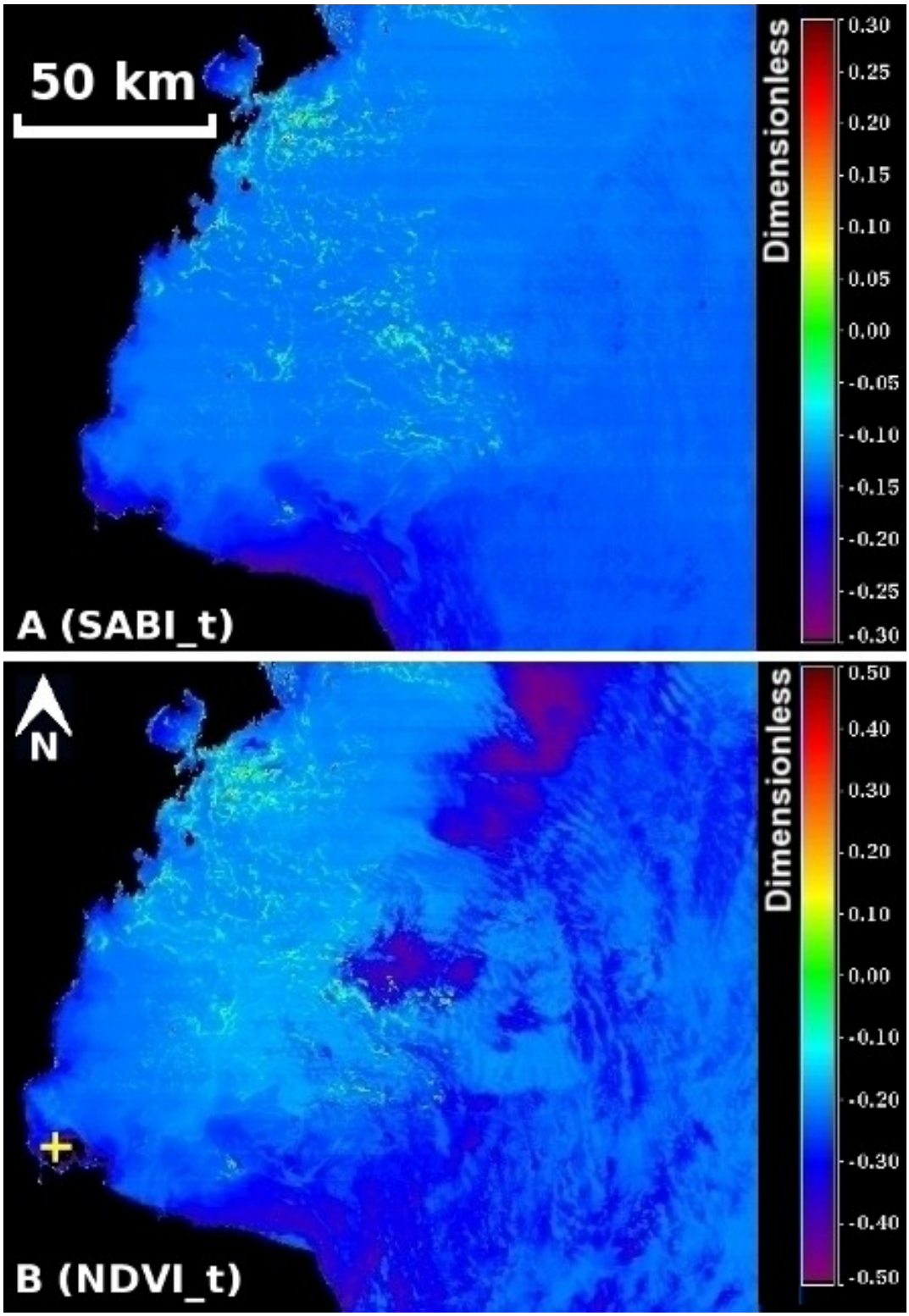

Figure 6.37. The *Ulva prolifera* bloom in the Yellow Sea, China observed by MODIS Terra on 25th June 2008 at 12:00 UTC directly under the sun-glint zone. A bloom is visible in the 500 m/pixel resolution images of the **(A)** SABI_t and **(B)** NDVI_t. The yellow (+) mark is positioned at N34°52'15" E119°16'44".

Despite the presence of a severe sun-glint coverage over the surface bloom areas, SABI_t (Figure 6.37A) produced better quality results than NDVI_t (Figure 6.37B) even with the presence of clouds, cloud shadows and different classes of water. The surface and near-surface blooms had a SABI_t index value equal to or greater than -0.10. The scales were adjusted to produce the best contrast results between the floating biological species and the background sea water for both maps.

6.5 The application of the SABI_t over Landsat data

The visible near infra-red (VNIR) bands available in the Landsat–4/TM were used as input into the SABI algorithm. Table 6.1 shows these band group and the corresponding MODIS 500 m band group.

Table 6.1. The Landsat–4/TM (30 m/pixel resolution) bands that were used in the SABI algorithm and the corresponding MODIS 500 m/pixel bands (λ_1 and λ_2 are aggregated from the 250 m band group).

Band Number	Landsat bands (µm)	Landsat bandwidth	MODIS bands (µm)	MODIS bandwidth
1	0.45–0.52	0.07	0.459 – 0.479	0.020
2	0.52–0.60	0.08	0.545 – 0.565	0.019
3	0.63–0.69	0.06	0.62 – 0.67*	0.05
4	0.76–0.90	0.14	0.841 – 0.876*	0.035

An unspecified filamentous–type of algal species was visible in Landsat–4/TM on 13th October, 1990 inside the RSA, Iran. A set of 30 m/pixel resolution RGB colour composites images were composed of the surface bloom: a natural colour composite (Figure 6.38A) corresponding to bands λ_3=660, λ_2=560 and λ_1= 485 nm respectively and a false RGB colour composite (Figure 6.38B) corresponding to bands λ_4=830, λ_3=660 and λ_3= 660 nm respectively. The SABI image of the bloom is shown in Figure 6.39, in which surface and near-surface blooms were flagged at SABI values greater than or equal to -0.10; a result consistent with that of MODIS (although 10% of the denser clouds were misclassified as surface blooms).

* Aggregated from the 250 m band group.

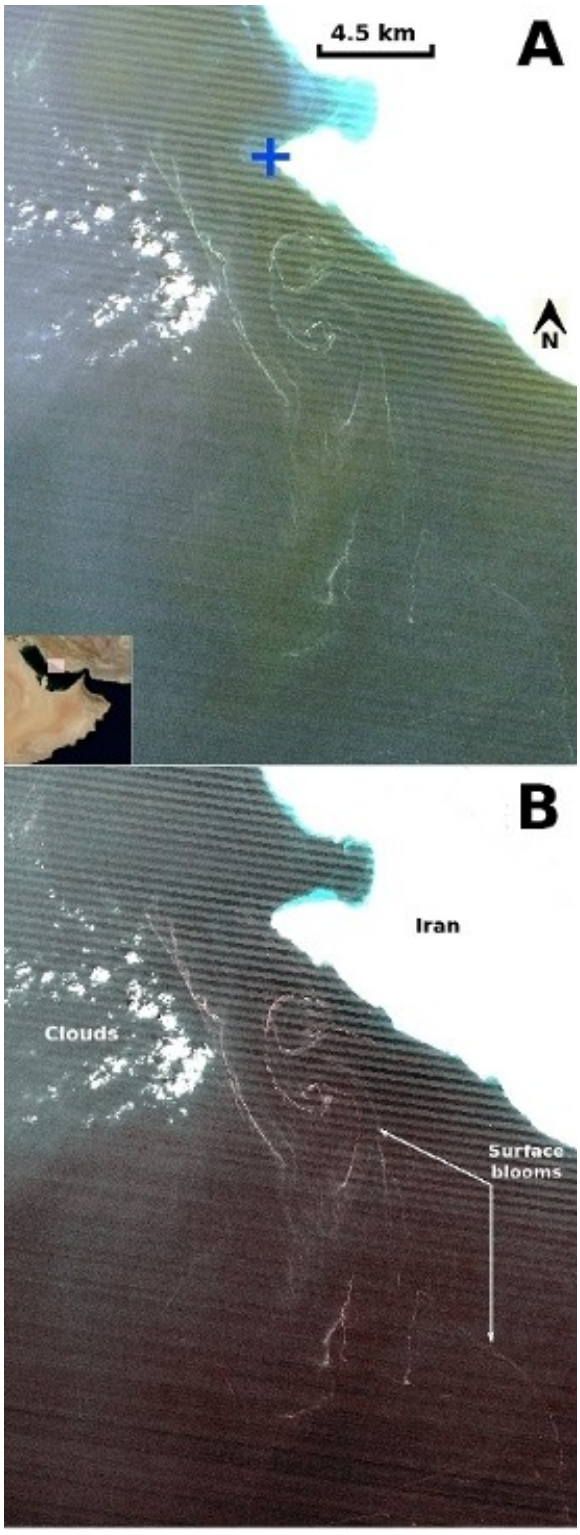

Figure 6.38. Unspecified filamentous-type species observed in Landsat–4/TM on 13th October, 1990 at 06:37 UTC inside the RSA, opposite Iran. The geometrically-corrected images are comprised of 30 m/pixel resolution RGB colour composites using single-band tiff formats: **(A)** natural composite corresponding to bands λ_3=660, λ_2=560 and λ_1= 485 nm respectively (satellite swath is shown inset); and **(B)** a false composite corresponding to bands λ_4=830, λ_3=660 and λ_3= 660 nm respectively. The blue (+) mark is positioned at N27°23'23" E52°34'38".

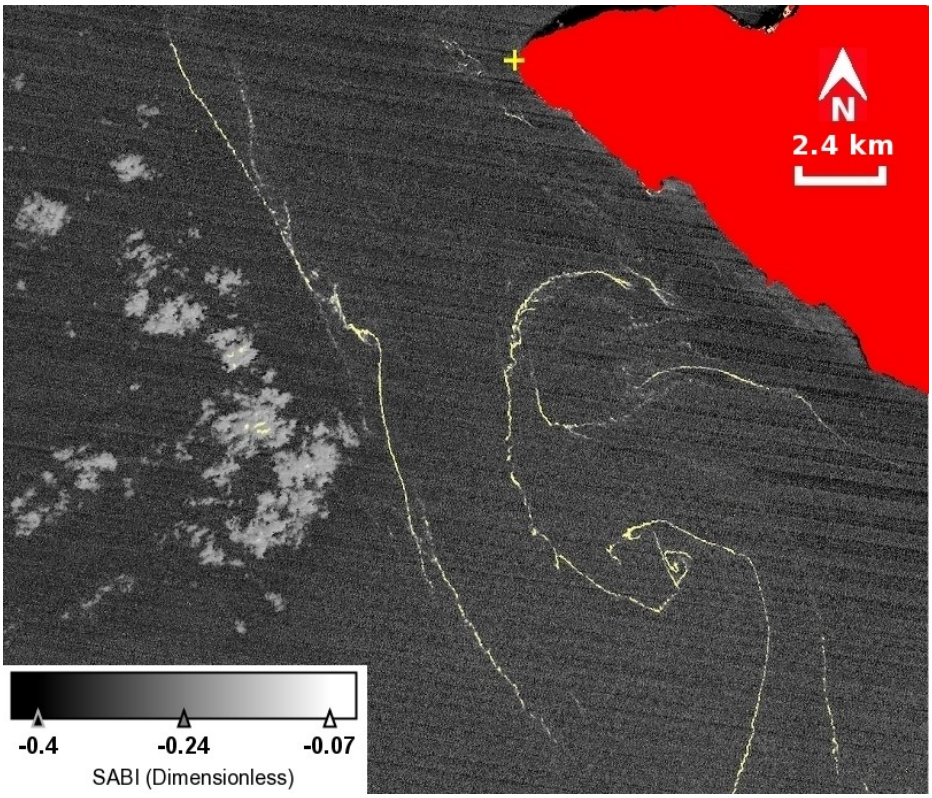

Figure 6.39. The 30 m/pixel SABI image (geometrically-corrected) of an unspecified filamentous-type species observed in Landsat–4/TM on 13th October, 1990 at 30 m resolution. SABI pixels greater than or equal to -0.1 were masked in yellow (10% of the clouds were misclassified). Land is masked in red. The yellow (+) mark is positioned at N27° 23' 23" E52° 34' 38".

6.6 The performance of the SABI_t and NDVI_t over oil spills

An oil spill in the Baltic Sea, Estonia was visible in the MODIS Aqua dataset on 31st July, 2008 at 10:55 UTC (swath shown in Figure 6.27B) under a moderate sun-glint. NDVI_t and SABI_t were processed for the oil spill incident as shown in Figures 6.40A and 6.40B respectively. The appearance of oil matches those results acquired for similar oil spills under moderate sun-glint during the calibration process. The mean aerosol optical thickness τ_{869} value estimated by SeaDAS over the area of interest was 0.07, which is not severe aerosol optical thickness. The SABI_t has demonstrated lower sensitivity over the oil layer and sea water than did the NDVI_t. This is caused by significant Rayleigh scattering over surface reflectance, particularly in the shorter part of the spectrum used in SABI_t. This is demonstrated in the spectral plot of the calibrated TOA radiance taken at two different sea water points and a third point on the oil shown in Figure 6.41, which are hardy indistinguishable from each other.

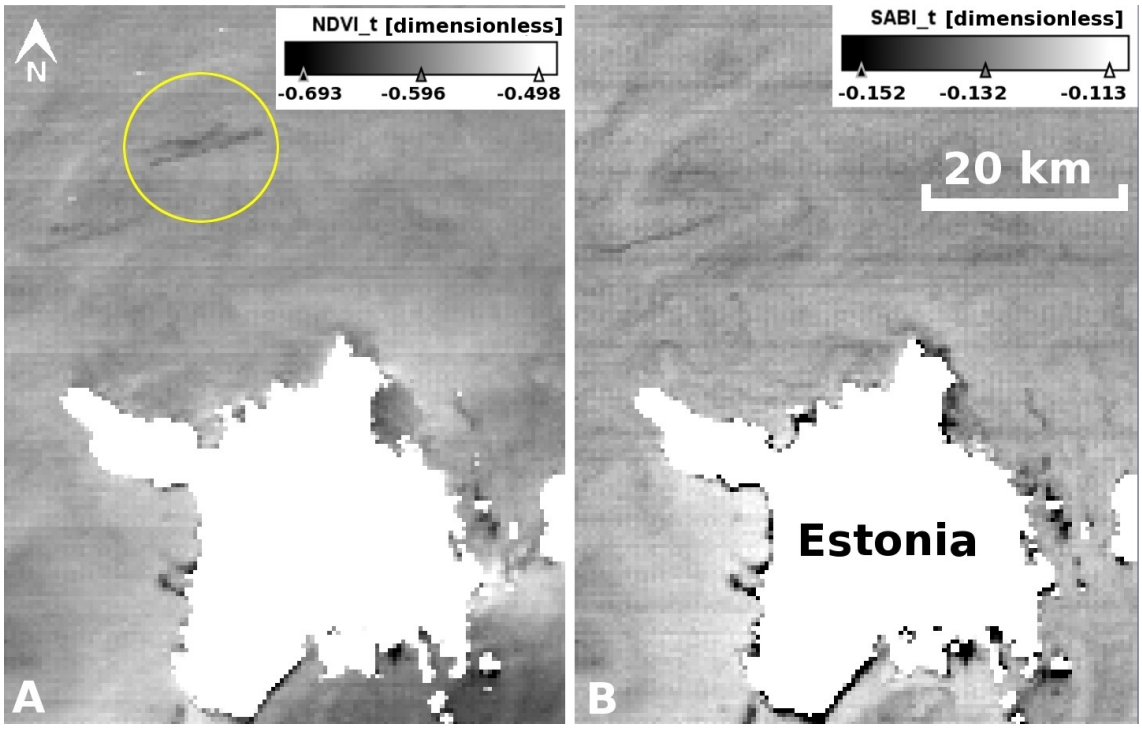

Figure 6.40. An oil spill (circled and centred at N59°14' 39", E22°10' 29") visible in the MODIS Aqua on 31st July, 2008 (swath shown in Figure 6.27B) located in the Baltic Sea, Estonia, under a moderate sun-glint area as it appears in (A) NDVI_t and (B) SABI_t. The spill is hardly visible under the SABI_t.

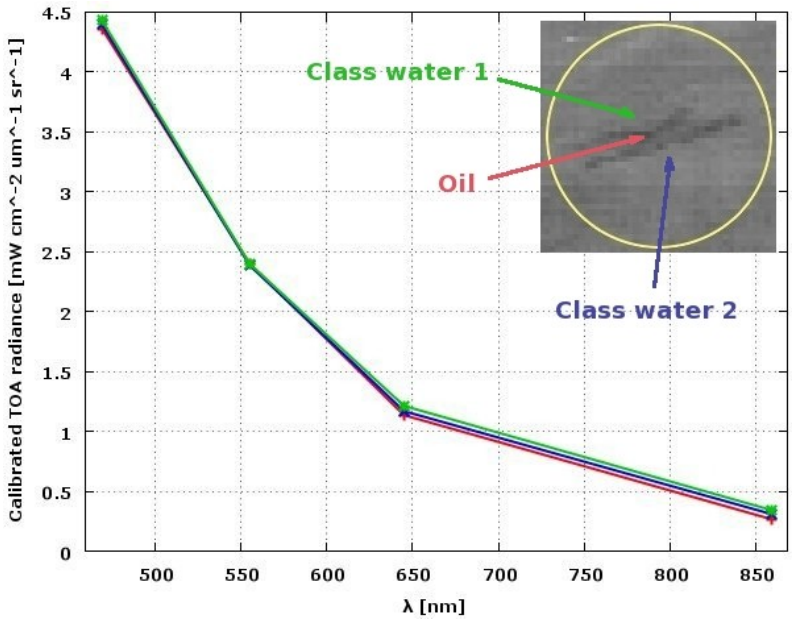

Figure 6.41. The spectral plot of two different classes of water including the oil spill in the calibrated TOA radiances. Inset taken from the spill shown in Figure 6.40.

Another spectral plot of the Rayleigh-corrected reflectance at the same three points (Figure 6.42), suggests that the oil spill is so thin that its spectral profile is very close to that of sea water.

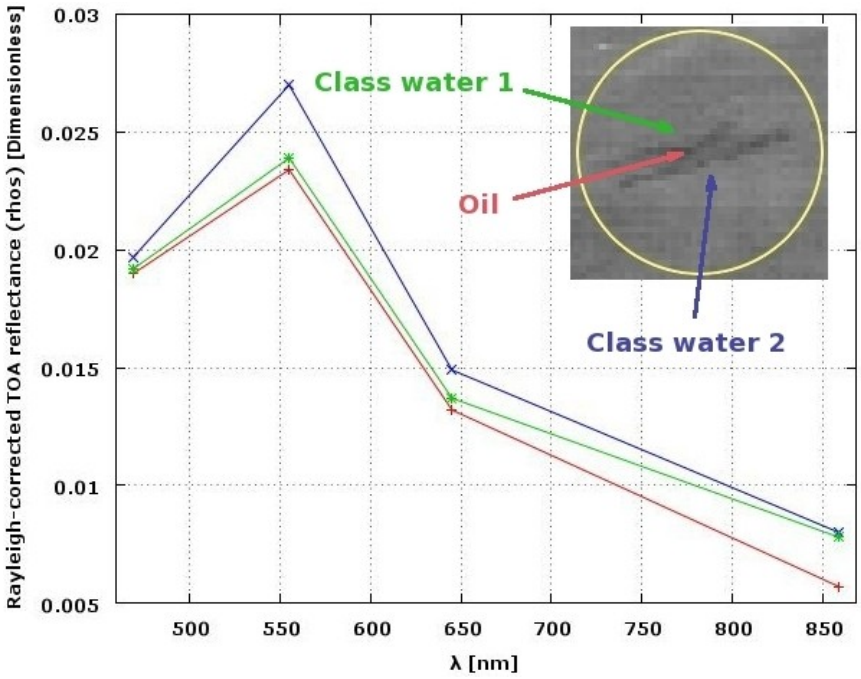

Figure 6.42. The spectral plot of two different classes of water including the oil spill in the Rayleigh-corrected reflectance. Inset taken from the oil spill shown in Figure 6.40.

6.7 Stability results between the SABI_t and NDVI_t

A sampling area (N pixels) was selected over an area containing sample end members of sea water with mixed classes of surface and sub-surface blooms for each of the four validation cases used in this study. From which, the SABI_t (N=606 pixels) and NDVI_t (N=824 pixels) results were respectively compared through a set of box plots[40] shown in Figure 6.43 for each case. The profile of the line passing through the mean SABI_t values clearly points to the stability of the SABI_t over the NDVI_t algorithm for the quantization of biological surface and near-surface blooms over a variety of global datasets at different atmospheric and sun-glint conditions as well as different surface bloom species. The extreme mean radiance value for the Yellow Sea case (Figure 6.43) could be attributed to the presence of the bloom directly under the sun-glint and to the high Chlor-a concentration that existed in the floating Ulva prolifera species. The distance from the maximum to the mean values (dmax) in all box plots

[40] Box plots are graphical exploratory data tool used to display five values from a set of data used: the extremes, the upper and lower hinges (quartiles), and the median (McGill et al., 1978).

seen in Figure 6.43, was larger than the distance from the minimum to the mean (dmin). This is caused by the abundance of the water class (dmin) over the mixed class blooms (dmax).

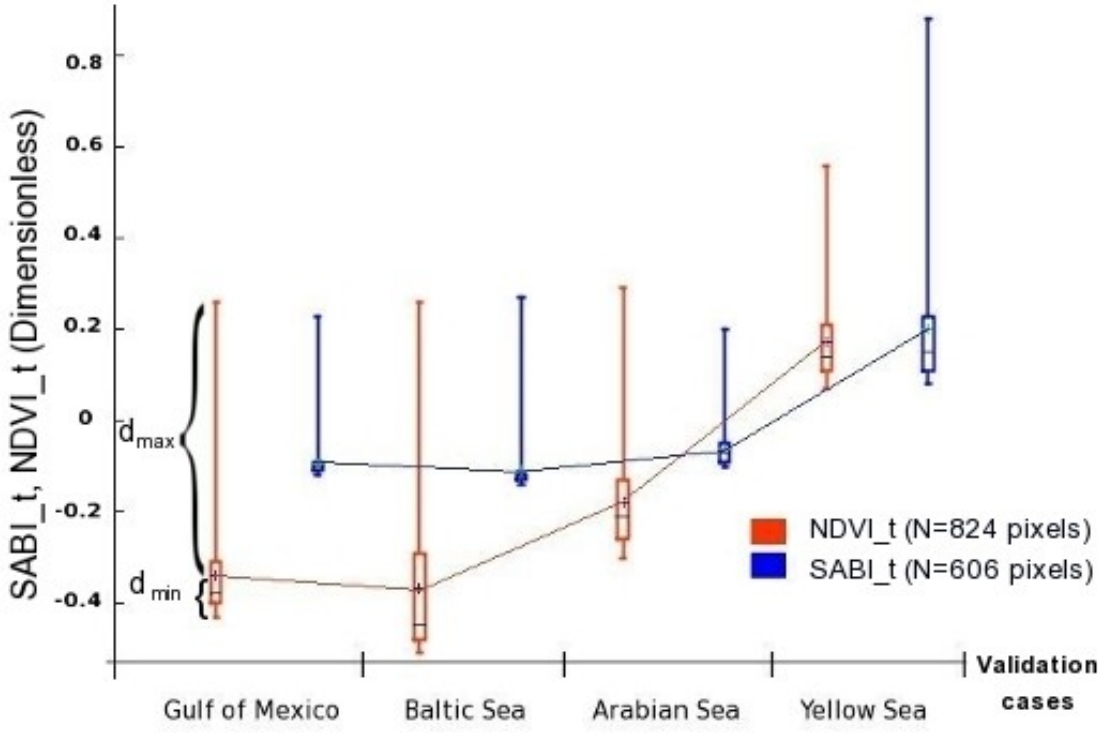

Figure 6.43. Box plots of NDVI_t and SABI_t taken from sampling areas (N=824 pixels) and (N=606 pixels) respectively containing mixed classes of blooms (surface and sub-surface) as well as water from each dataset used in the validation of this study. The profile of the line connecting the mean values from each box plot points to the stability of SABI_t over NDVI_t over different conditions and species.

6.8 Summary

The the SABI identifies the presence of surface floating blooms and discriminates them from oil using the bands available in MODIS's 500 and 250 m/pixel spatial resolution groups, according to the index table shown in Table 6.2 and the corresponding class names.

Table 6.2. The SABI_t classification table over surface blooms and oil

Classification	SABI_t range
Surface blooms	SABI_t ≥ -0.10
Oil	SABI_t < -0.1

The SABI_t images that were used in this chapter (calibration and validation) are shown in Figures from 6.44–6.47, over which SABI_t pixels greater than or equal to -0.10 were masked in yellow. This highlights the ability of SABI_t to detect different surface and near-surface bloom species under different cloud, aerosol and sun-glint conditions. This unique property is useful in discriminating surface and near-surface blooms from oil spills and identifying them as positive look-alikes.

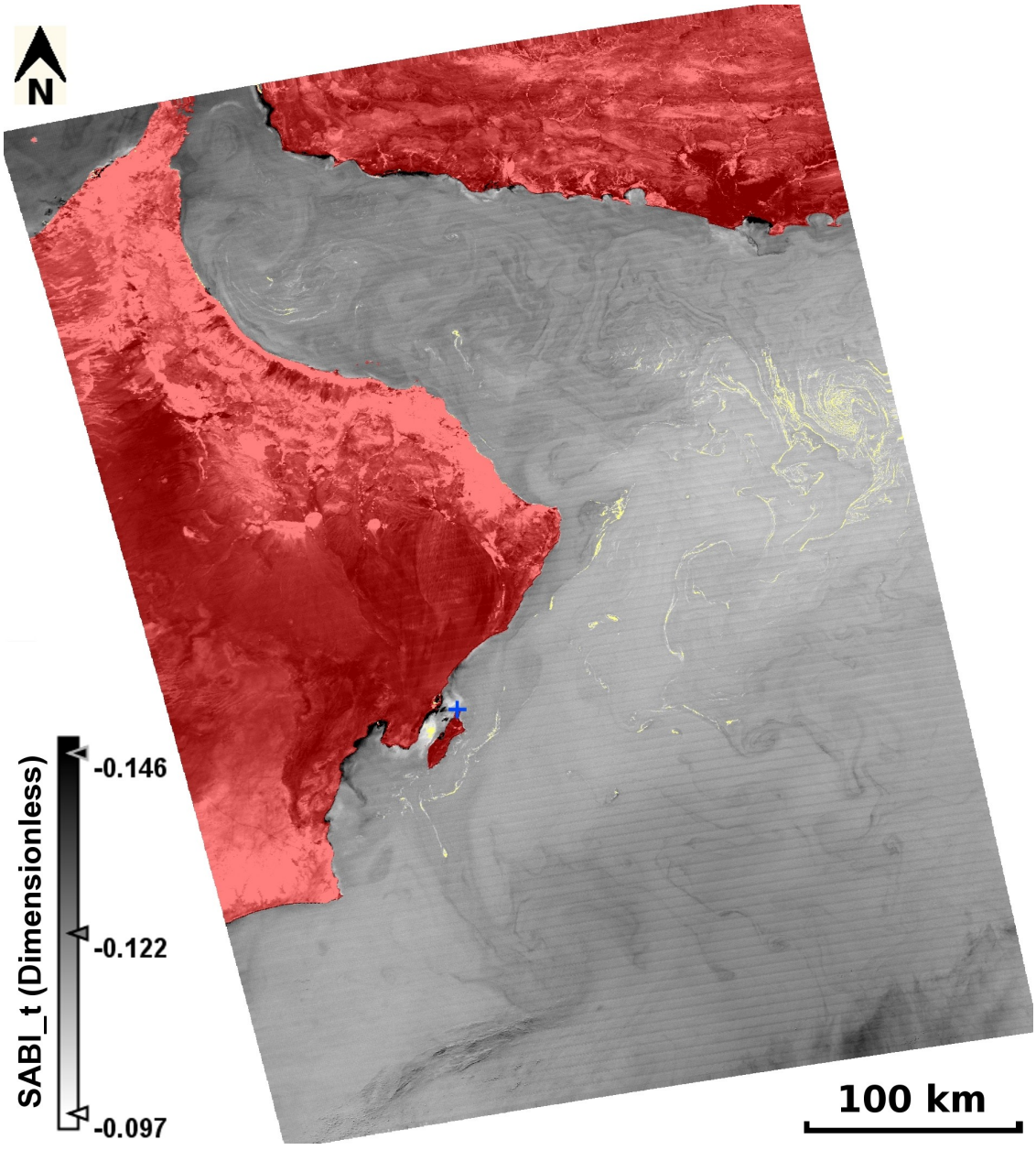

Figure 6.44. The 250 m/pixel resolution SABI_t (calibrated TOA radiance) geometrically-corrected image of the *N. miliaris* bloom in the Arabian Sea observed in MODIS Aqua on 18th February, 2010 at 09:10 UTC. The λ_3=469 and λ_4=555 nm were both oversampled from the 500 m resolution band group. SABI_t values greater than or equal to -0.10 masked the surface blooms in yellow. Land is masked in red. The blue (+) mark is positioned at N20° 42' 29" E58° 53' 15".

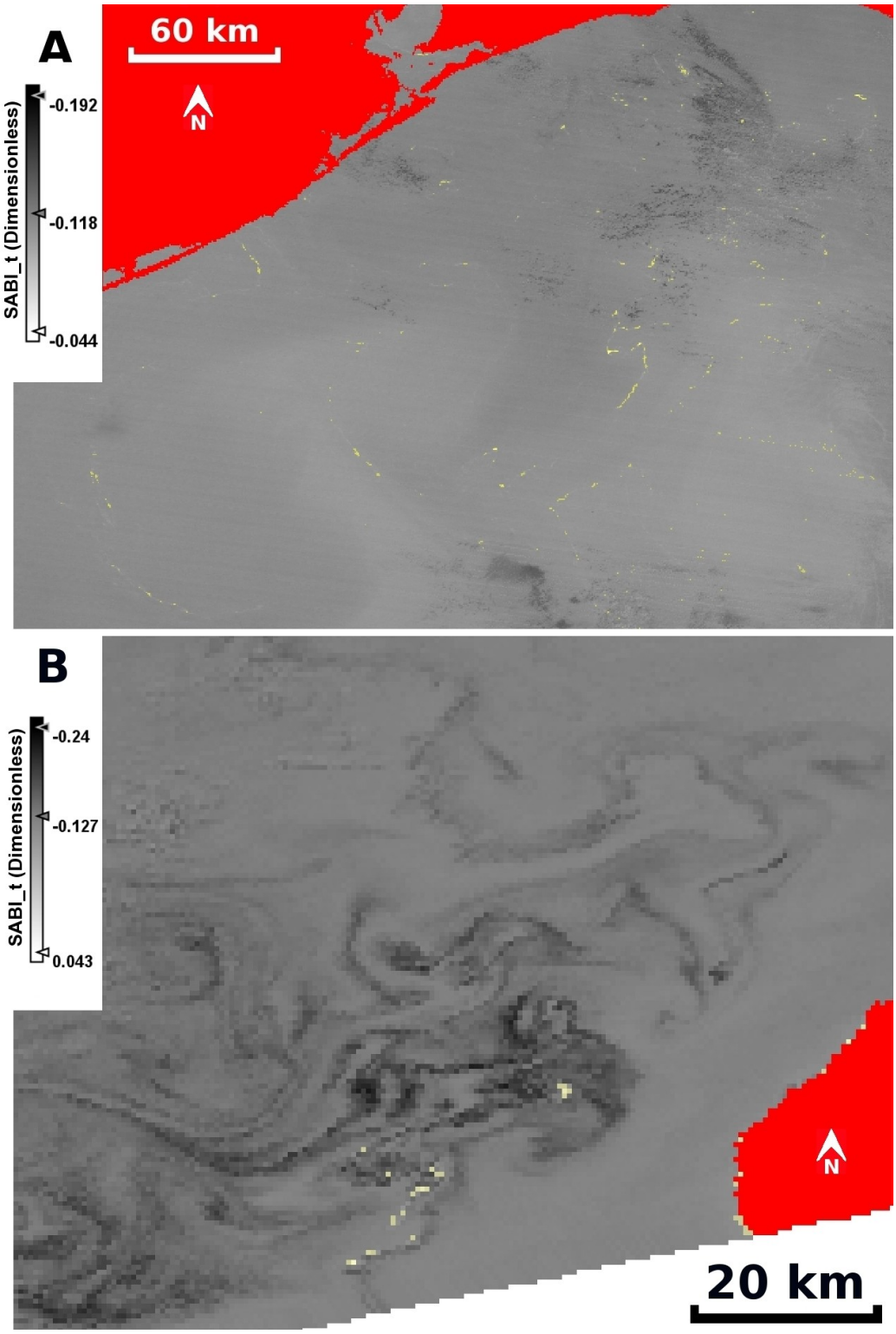

Figure 6.45. The 500 m/pixel resolution SABI_t (calibrated TOA radiance and geometrically-corrected) images of **(A)** Sargassum in the Gulf of Mexico observed in MODIS Terra, 2nd June, 2006 at 01:55 UTC. The image is centred at position N28° 19' 08" E94° 38' 15". **(B)** *N. spumigena* bloom in the Baltic Sea observed in MODIS Aqua on 31st July, 2008 at 10:55 UTC. The image is centred at position N57° 40' 26" E20° 41' 31". Surface and near-surface blooms were masked in yellow for SABI_t values greater than or equal to -0.10. Land is masked in red.

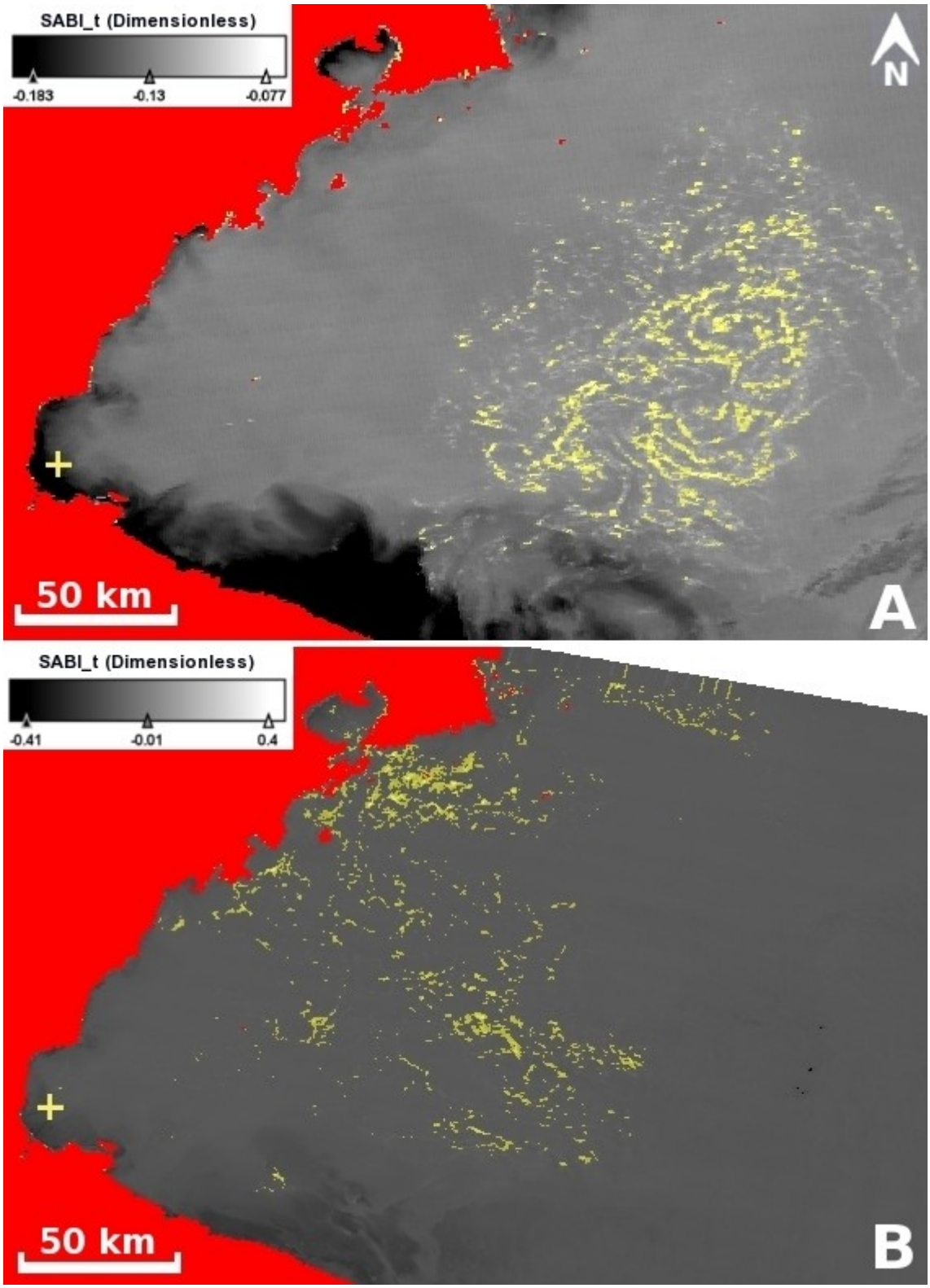

Figure 6.46. The 500 m/pixel resolution SABI_t (calibrated TOA radiance geometrically-corrected) images of the *Ulva prolifera* bloom in the Yellow Sea, China observed in MODIS **(A)** Aqua on 30th May, 2008 at 05:36 UTC and **(B)** Terra on 25th June at 12:00 UTC, 2008. Surface and near-surface blooms were masked in yellow for SABI_t values greater than or equal to -0.10. Land is masked in red. The yellow (+) mark is positioned at N34° 52' 15" E119° 16' 44".

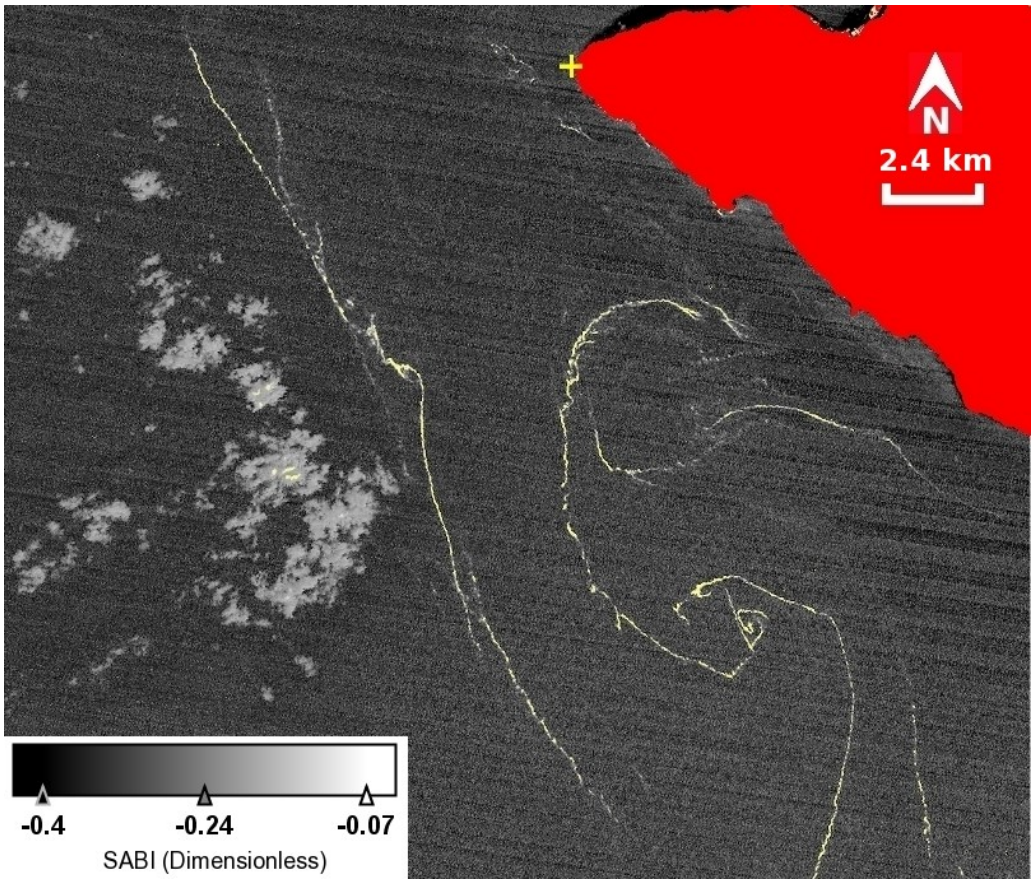

Figure 6.47. The 30 m/pixel SABI image (geometrically-corrected) of an unspecified filamentous-type species observed in the Landsat–4/TM on 13th October, 1990. SABI pixels greater than or equal to -0.1 were masked in yellow (10% of the clouds were misclassified). Land is masked in red. The yellow (+) mark is positioned at N27° 23' 23" E52° 34' 38".

The following chapter (Chapter 7) of this thesis will discuss the weaknesses and strengths of both the SCS and the SABI algorithms in the light of the results presented in chapters 5 and 6 respectively, and whether they can complement each other to further the goals of this research.

Chapter 7: Summary of results and discussion

7.1 Introduction

The objective of this thesis is to investigate and assess the conditions in which an optical satellite sensor such as the Moderate Resolution Imaging Spectroradiometer (MODIS) can quantitatively identify and discriminate oil spills from look–alikes in almost cloud–free regions such as those typified by ROPME[41] sea area (RSA). The oil spill data that are used for the calibration and validation process in this project were primarily acquired from within the regional sea defined as the RSA. The dataset included archived data of historically verified cases of oil spills including near–real–time (NRT) data. The NRT time data was received through the MODIS receiving station based in ROPME, Kuwait. As a result of this investigation, two methods were proposed to achieve its goal: The spectral contrast shift (SCS) and the surface algal bloom index (SABI). Due to the coarse resolution of MODIS it is characterized with (maximum resolution of 250 m/pixel at nadir), the research focussed its attention on using MODIS's highest spatial resolution bands and used other resolutions as supporting data.

The SCS (Equation 7.1) is a dimensionless index that classifies oil thickness using the maximum (max) and minimum (min) top–of–atmosphere (TOA) radiance values of MODIS's 250 m high resolution channels: the red (λ_1=645 nm) and NIR (λ_2=859 nm) in a selected area inclusive of two dominant classes, one of which should be oil–free water.

$$SCS = \left| \frac{[L_2]_{max}}{[L_1]_{max}} - \frac{[L_2]_{min}}{[L_1]_{min}} \right| \tag{7.1}$$

The SABI aims to inversely discriminate oil spills by identifying their most common look–alike phenomena, surface floating blooms. It uses the TOA radiance values that belong to the 500 m/pixel resolution channels at its centred–wavelengths: Red (λ_1=645 nm); NIR (λ_2=859 nm); blue (B: λ_3=469 nm) and green (G: λ_4=555 nm). Bands λ_1 and λ_2 are both aggregated from the 250 m/pixel resolution MODIS band group. The SABI (Equation 7.2) is a dimensionless quantity that exploits the "red edge" effect exhibited by surface chlorophyll–enriched blooms that might be mistakenly classified as oil spills.

[41] Regional Organization for the Protection of the Marine Environment (ROPME).

$$SABI = \frac{L_{NIR} - L_R}{L_B + L_G} = \frac{L_{NIR}}{L_B + L_G} - \frac{L_R}{L_B + L_G} \equiv A - B \quad (7.2)$$

Oil spill incidents that occurred outside the RSA, as well as those observed through non–MODIS data were also used in this study to test the methods' validity outside the RSA and to determine the reliability of the method under different environmental settings that might affect imaging quality. Amongst the factors investigated for their possible contribution to the overall accuracy of the methods were: sun–glint; aerosols and dust; oil properties such as thickness, oil spill look–alikes such as surface blooms. This chapter will discuss the theoretical concept that underpins each proposed method, in relation to the experimental outcome. This is followed by a comparative analysis of all three methods to assess their strengths and weaknesses in relation to oil spill classification and discrimination from look–alikes.

7.2 The SCS summary of results

This project has analysed different cases of oil spill incidents (Table 7.1) for the calibration and validation of the SCS classifier.

Table 7.1. Oil spill incidents used in the calibration and validation analysis of the SCS. (*) denotes MERIS data and X denotes undetermined. U=Unknown, H=Heavy, L=Light and M=Medium.

no	Date	Contrast	in-glint	Location	Viscosity type	Mean SCS	Area (pixels)
1	16/07/08	negative	no	RSA	U	0.03	84
2	02/06/10	positive	yes	RSA	U	0.04	43
3	01/08/06	positive	yes	Mediterranean Sea	H	0.04	20
4	04/09/05	negative	no	Gulf of Cagliari	U	0.08	15
5	25/04/10	positive	yes	Gulf of Mexico	L	0.05	48
6	18/01/03	positive	yes	Lake Maracaibo	H	0.03	9
7	22/08/03	negative	no	Adriatic Sea	U	0.04	42
8	18/11/08	negative	no	RSA	M	0.04	8
9	21/10/07	negative	no	RSA	L	0.02	7
10	04/08/10	positive	yes	RSA	H	0.03	24

As a result of calibration and validation work discussed chapter 5 and based on the preliminary classification table derived earlier (Table 5.2), a more precise table (Table 7.2 reproduced from Table 5.19) is derived to categorize the different classes of oil thickness including surface blooms.

Table 7.2. A classification table derived based on the average SCS output values representing different thickness of oil spills, including to unpolluted water and surface floating blooms.

Mean SCS	**Classification category**	**Remarks**	**Uncertainty ±**
≤ 0.01	PC=Pure class		0.004
0.02	LTO (Light thickness oil, sheen)		0.002
0.03	MTO (Medium thickness oil)		0.002
0.04	Oil (Thick oil)		0.002
0.05	TW (Turbid water) or WO (weathered oil)		0.003
0.10	U (Undetermined)	Further analysis is needed	0.02
≥ 0.20	SA (Surface bloom)		0.07

The maximum radiance values in the NIR (L_{2max}) were plotted against the maximum radiance values in the red (L_{1max}) and the same was done for the corresponding minimum values (Figures 7.1–7.3) for all oil spill cases covered in this study, who shared the same SCS classification value (Tables 7.3–7.8).

Table 7.3. Oil spills used in the study whose mean absolute SCS classification less than or equal to 0.01. The mean standard deviation (σ) for all results was 0.004 (dimensionless). Shaded rows refer to oil spills observed under the sun–glint (positive contrast). Radiance values (L) are in $W/m^2/sr/\mu m$.

No	Date	L_{2MIN}	L_{2MAX}	L_{1MIN}	L_{1MAX}	L_{2MAX}/L_{1MAX}	L_{2MIN}/L_{1MIN}	SCS±0.004
1	25/04/10	51.45	53.32	80.76	83.41	0.649	0.647	0.002
2	25/04/10	52.73	54.10	80.99	82.86	0.653	0.651	0.002
3	25/04/10	26.28	26.85	44.59	45.42	0.591	0.589	0.002
4	04/08/10	39.44	43.09	66.16	71.72	0.601	0.596	0.005
5	04/08/10	38.97	43.28	65.26	71.61	0.604	0.597	0.007
6	18/01/03	10.37	10.94	24.72	25.55	0.428	0.419	0.009
7	18/01/03	8.79	9.71	23.10	24.85	0.391	0.381	0.010
8	21/10/07	6.45	7.18	17.33	18.80	0.382	0.372	0.010
9	04/08/10	41.22	46.11	69.37	76.16	0.605	0.594	0.011
10	04/08/10	39.74	45.04	66.88	74.38	0.606	0.594	0.012
11	25/05/05	46.74	72.08	74.19	112.22	0.642	0.630	0.012
12	04/09/05	7.53	7.94	18.42	18.86	0.421	0.409	0.012

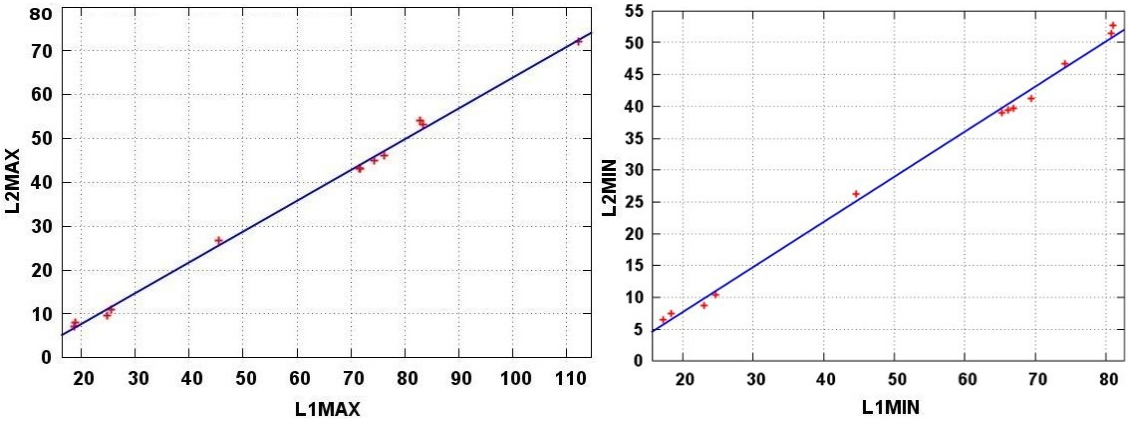

Figure 7.1. Scatter plot of L_{2max} against L_{1max} and L_{2}min against L_{1min} (see Table 7.3) for the different oil spills cases (different dates and locations) whose mean SCS value is less than or equal to 0.01.

Table 7.4. Oil spills used in the study whose mean absolute SCS classification is (0.015–0.025). The mean standard deviation (σ) for all results was 0.002 (dimensionless). Shaded rows refer to oil spills observed under the sun–glint (positive contrast). Radiance values (L) are in W/m²/sr/µm.

No	Date	L_{2MIN}	L_{2MAX}	L_{1MIN}	L_{1MAX}	L_{2MAX}/L_{1MAX}	L_{2MIN}/L_{1MIN}	SCS±0.002
1	01/08/06	22.53	33.74	38.62	56.17	0.600	0.583	0.017
2	01/08/06	21.53	25.31	37.2	42.40	0.597	0.579	0.018
3	04/08/10	38.59	44.45	65.13	72.39	0.614	0.593	0.021
4	04/08/10	38.42	44.57	64.58	72.42	0.615	0.595	0.020
5	21/10/07	6.49	7.40	18.22	19.61	0.377	0.356	0.021
6	21/10/07	5.94	6.77	16.46	17.70	0.382	0.361	0.021
7	01/08/06	21.10	29.74	36.65	49.69	0.599	0.576	0.023
8	18/11/08	3.89	4.61	13.76	15.07	0.306	0.283	0.023
9	21/10/07	6.09	6.98	16.8	18.06	0.386	0.363	0.023

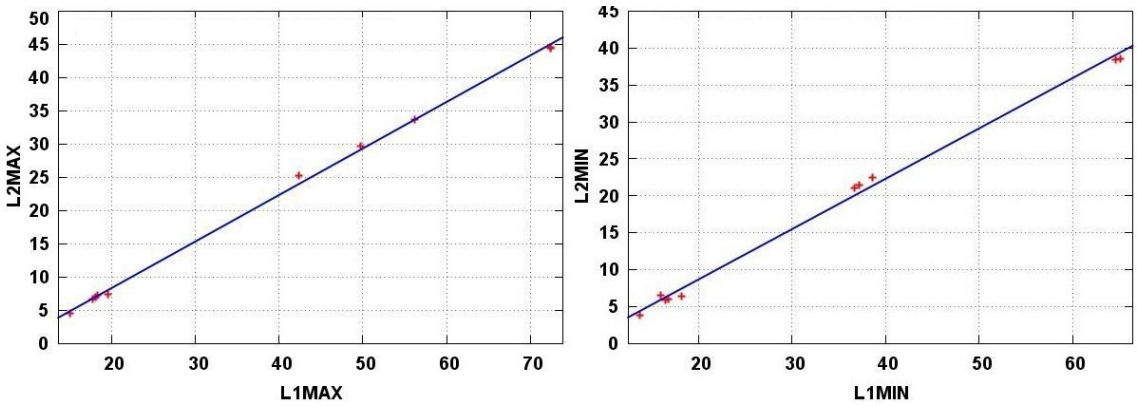

Figure 7.2. Scatter plot of L2max against L1max and L2min against L1min (see Table 7.4) for the different oil spills cases (different dates and locations) whose mean SCS value is 0.01–0.02.

Table 7.5. Oil spills used in the study whose absolute SCS classification (0.025–0.035). The mean standard deviation (σ) for all results was 0.002 (dimensionless). Shaded rows refer to oil spills observed under under the sun–glint (positive contrast). Radiance values (L) are in W/m²/sr/µm.

No	Date	L_{2MIN}	L_{2MAX}	L_{1MIN}	L_{1MAX}	L_{2MAX}/L_{1MAX}	L_{2MIN}/L_{1MIN}	SCS±0.002
1	21/10/07	7.08	8.04	19.19	20.37	0.395	0.369	0.026
2	25/05/05	51.79	80.60	79.78	118.97	0.677	0.649	0.028
3	25/05/05	54.90	100.69	87.51	153.57	0.656	0.627	0.029
4	21/10/07	6.60	7.41	18.77	19.51	0.380	0.352	0.028
5	16/07/08	7.34	8.86	19.30	21.42	0.414	0.380	0.034
6	21/10/07	5.38	6.65	15.41	17.49	0.380	0.349	0.031
7	18/01/03	8.53	10.01	22.73	24.56	0.408	0.375	0.033

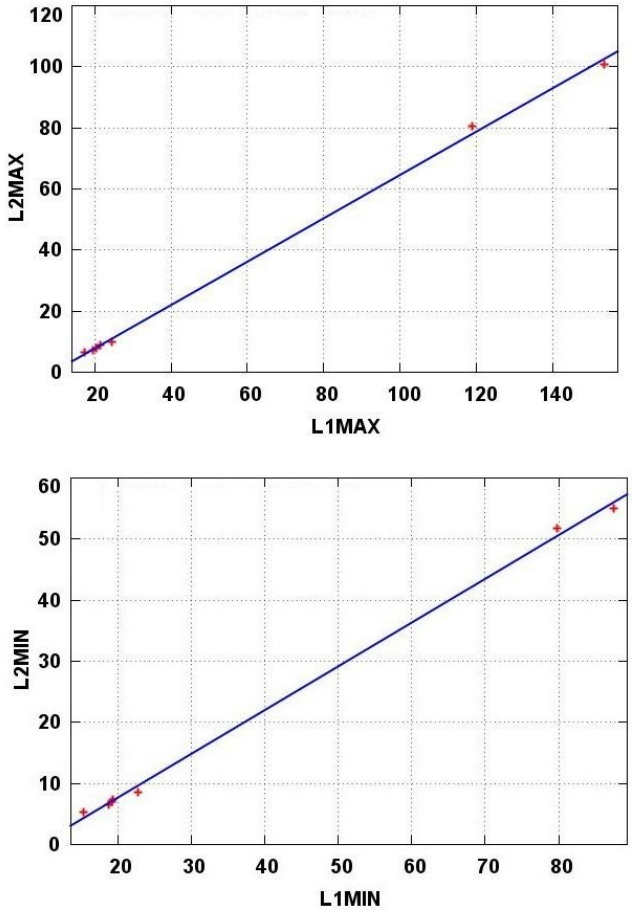

Figure 7.3. Scatter plot of L_{2max} against L_{1max} and L_{2min} against L_{1min} (see Table 7.5) for the different oil spills cases (different dates and locations) whose mean SCS value is 0.02–0.03. Radiance values (L) are in W/m^2/sr/µm.

Table 7.6. Oil spills used in the study whose absolute SCS classification (0.035–0.045). The mean standard deviation (σ) for all results was 0.002 (dimensionless). Shaded rows refer to oil spills observed under under the sun–glint (positive contrast). Radiance values (L) are in W/m^2/sr/µm.

No	Date	L_{2MIN}	L_{2MAX}	L_{1MIN}	L_{1MAX}	L_{2MAX}/L_{1MAX}	L_{2MIN}/L_{1MIN}	SCS±0.002
1	01/08/06	20.24	34.31	35.94	57.40	0.598	0.563	0.035
2	21/10/07	5.43	6.57	15.86	17.41	0.377	0.342	0.035
3	18/11/08	3.88	4.74	13.65	14.84	0.319	0.284	0.035
4	02/06/10	38.89	63.30	65.06	99.71	0.635	0.598	0.037
5	01/08/06	20.54	27.25	36.34	45.36	0.601	0.565	0.036
6	21/10/07	6.56	8.00	18.33	20.29	0.394	0.358	0.036
7	25/05/05	50.94	78.49	78.81	114.69	0.684	0.646	0.038
8	25/05/05	37.09	59.80	61.70	93.59	0.639	0.601	0.038
9	04/09/05	6.33	7.83	17.02	19.02	0.412	0.372	0.040
10	18/11/08	3.71	4.66	13.26	14.65	0.318	0.280	0.038
11	21/10/07	5.93	7.28	16.75	18.51	0.393	0.354	0.039

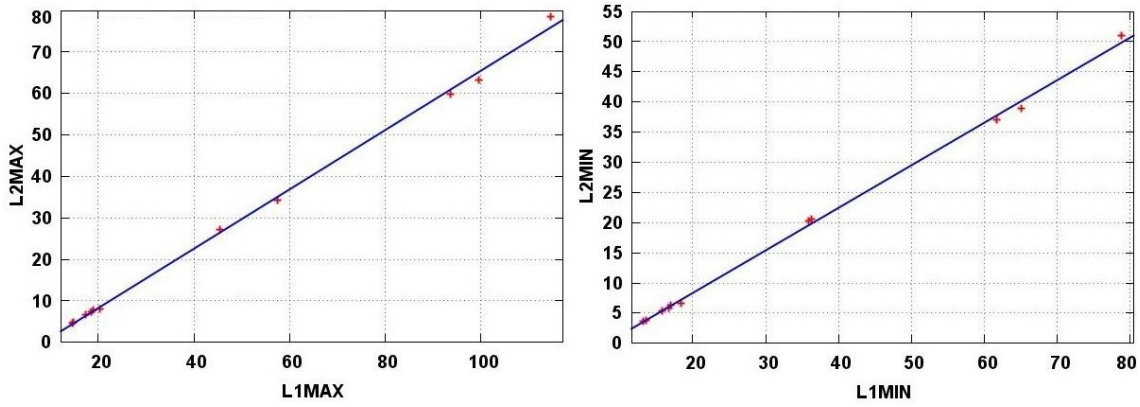

Figure 7.4. Scatter plot of L2max against L1max and L2min against L1min (see Table 7.6) for the different oil spills cases (different dates and locations) whose mean SCS value is 0.03–0.04. Radiance values (L) are in W/m2/sr/µm.

Table 7.7. Oil spills used in the study whose absolute SCS classification (0.045–0.055). The mean standard deviation (σ) for all results was 0.004 (dimensionless). Shaded rows refer to oil spills observed under under the sun–glint (positive contrast). Radiance values (L) are in W/m^2/sr/µm.

No	Date	L_{2MIN}	L_{2MAX}	L_{1MIN}	L_{1MAX}	L_{2MAX}/L_{1MAX}	L_{2MIN}/L_{1MIN}	SCS±0.004
1	21/10/07	6.57	8.11	18.33	20.06	0.404	0.358	0.046
2	25/04/10	26.46	53.45	44.82	83.51	0.640	0.590	0.050
3	25/04/10	26.26	53.39	44.28	82.6	0.646	0.593	0.053

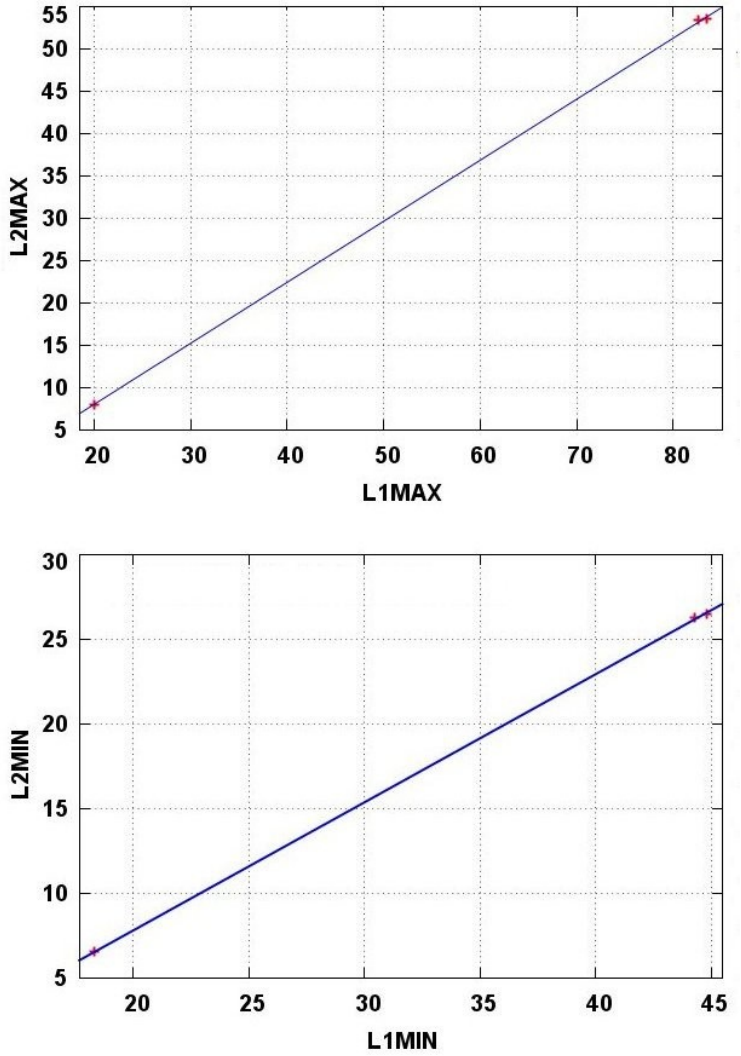

Figure 7.5. Scatter plot of L2max against L1max and L2min against L1min (see Table 7.7) for the different oil spills cases (different dates and locations) whose mean SCS value is 0.04–0.05. Radiance values (L) are in W/m^2/sr/µm.

Table 7.8. Oil spills used in the study whose absolute SCS classification (0.055–0.15). The mean standard deviation (σ) for all results was 0.02 (dimensionless). Shaded rows refer to oil spills observed under under the sun–glint (positive contrast). Radiance values (L) are in W/m²/sr/µm.

No	Date	L_{2MIN}	L_{2MAX}	L_{1MIN}	L_{1MAX}	L_{2MAX}/L_{1MAX}	L_{2MIN}/L_{1MIN}	SCS±0.02
1	25/04/10	25.44	57.43	43.26	85.17	0.674	0.588	0.086
2	25/04/10	12.52	30.63	25.01	50.38	0.608	0.501	0.107
3	25/05/05	49.63	151.94	78.55	277.44	0.548	0.632	0.084
4	25/04/10	26.14	54.26	44.2	83.88	0.647	0.591	0.056
5	25/04/10	25.32	58.63	42.92	89.74	0.653	0.590	0.063
6	18/01/03	7.32	9.89	20.92	23.86	0.415	0.350	0.065
7	01/08/06	21.72	41.87	37.57	64.7	0.647	0.578	0.069
8	25/04/10	26.09	55.86	43.94	83.88	0.666	0.594	0.072
9	04/09/05	6.44	9.42	17.73	21.31	0.442	0.363	0.079
10	25/05/05	12.35	20.84	26.87	38.67	0.539	0.460	0.079
11	25/04/10	25.9	56.38	43.83	83.88	0.672	0.591	0.081
12	25/04/10	25.65	57.14	43.39	84.73	0.674	0.591	0.083
13	25/04/10	25.44	57.43	43.16	85.17	0.674	0.589	0.085

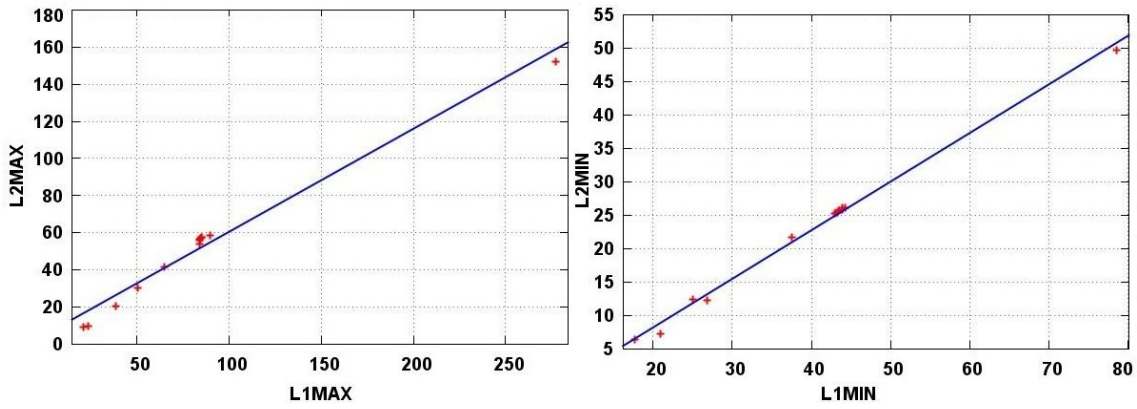

Figure 7.6. Scatter plot of L2max against L1max and L2min against L1min for the different oil spills cases (different dates and locations) whose mean SCS value is 0.05–0.10 and values are shown in (Table 7.8). Radiance values (L) are in W/m2/sr/µm.

The scatter plots in Figures 7.1 to 8.6 affirm the linear correlation that exists between maximum and minimum radiance responses in the red and NIR bands for different oil types of equal thicknessess, even if they are observed under different illumination conditions.

7.3 The SABI summary of results

The case studies covered in this project were of different biological species taken from different global locations including the RSA and under different sun–glint conditions (Table 7.9).

Table 7.9. The details of the different surface bloom species over which the SABI and the NDVI indices were tested.

No	Date	Sensor	Bloom under sun–glint	Type of species	Geographic location
1	18/02/2010	MODIS	no	*Noctiluca miliaris*	Outer RSA
2	30/05/2008 25/06/2008	MODIS	yes	*Ulva prolifera*	Yellow sea, China
3	02/06/2006	MODIS	yes	Sargassum	Gulf of Mexico, USA
4	31/07/2008	MODIS	no	*Nodularia spumigena*	Baltic Sea
5	13/10/1990	Landsat-4/TM	no	Undetermined	Inner RSA

The SABI_t relationship was broken down into two terms A and B (Equation 7.2) to demonstrate the effectiveness of SABI_t in suppressing the effects of clouds, sun–glint and dust in the detection of surface blooms. The term A (representative of the NIR radiance signal from surface blooms) is strong enough to be visible through a relatively high layer of dust (Figure 7.7A, the same as Figure 6.15A). Particularly, since molecular scattering in the longer NIR band is almost negligible in relation to the shorter visible blue and green bands. This is in conjunction with the high NIR absorption caused by the surrounding waters coupled with the high water–leaving radiances in the visible blue and green bands. Water–surface blooms, due to chlorophyll, will also have a higher absorption in the red band (represented by B in Equation 7.2) relative to the combination of atmospheric scattering and high water–leaving radiance in the blue and green bands (Figure 7.7B, the same as Figure 6.15B). The high signal response from the thick clouds and sun–glint in both the A and B terms, almost cancel out to produce the

SABI_t relationship (Figure 7.7C, the same as Figure 6.16A). A line (a to b) was selected across the bloom, water, aerosols and the clouds as shown in the 500 m/pixel resolution natural RGB colour composite (Figure 7.7D, the same as Figure 6.16B) corresponding to the Rayleigh-corrected reflectance bands λ_1=645, λ_4=555 and λ_3=469 nm respectively.

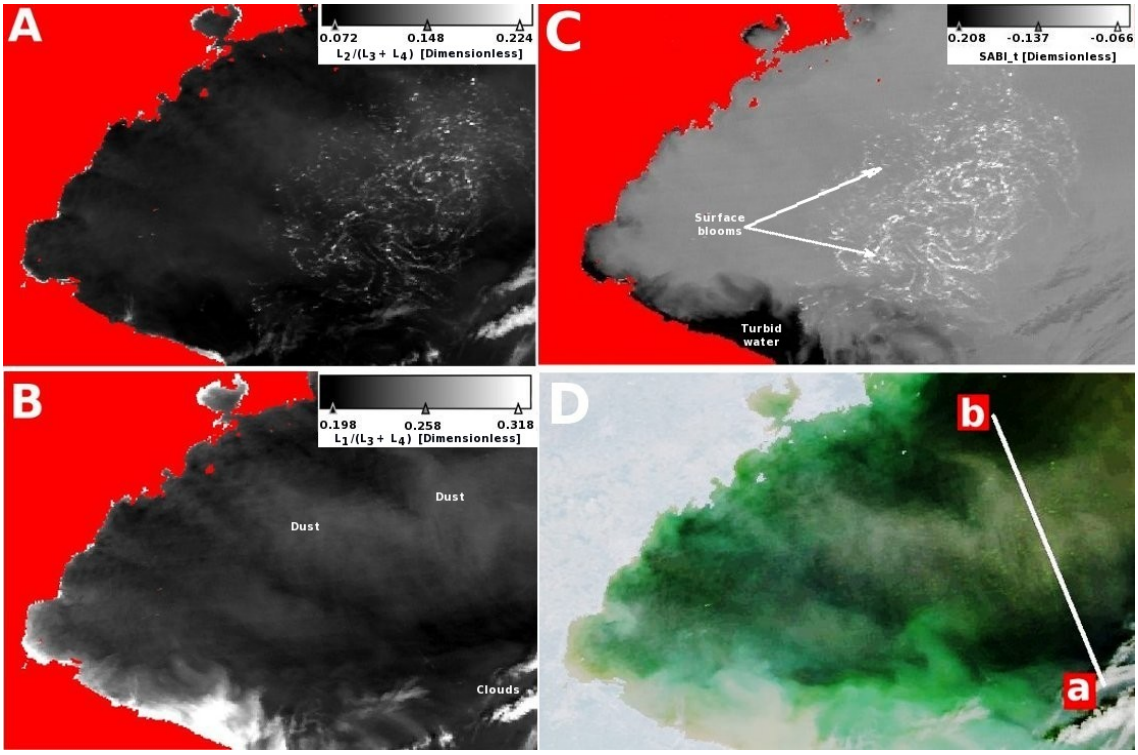

Figure 7.7. A geometrically–corrected 500 m/pixel resolution MODIS Aqua image of the *Ulva prolifera* bloom in the Yellow Sea (30th May, 2008 at 05:36 UTC), constructed from the calibrated TOA radiance values (L) using the following band ratios **(A)** λ_2=859 nm (aggregated from the 250 m resolution band group) divided by the sum of λ_3=469 nm and λ_4=555 nm. **(B)** λ_1=645 nm (aggregated from the 250 m resolution band group) divided by the sum of λ_3=469 nm and λ_4=555 nm (dust layer scatter the visible bands and surface blooms hardly visible). Thick clouds are also visible in both scenes. **(C)** the SABI_t (difference between A and B). **(D)** The natural RGB colour composite corresponding to the Rayleigh–corrected reflectance corresponding to bands λ_1=645 (aggregated from the 250 m resolution band group), λ_4=555 and λ_3=469 nm respectively, over which a line (a to b) was selected across the bloom, water, aerosols and the clouds. The transect of the line is shown in Figure 7.8.

This is summarised in the transect shown in Figure 7.8 (the same as Figure 6.17) for the line a–b shown in Figure 7.7D.

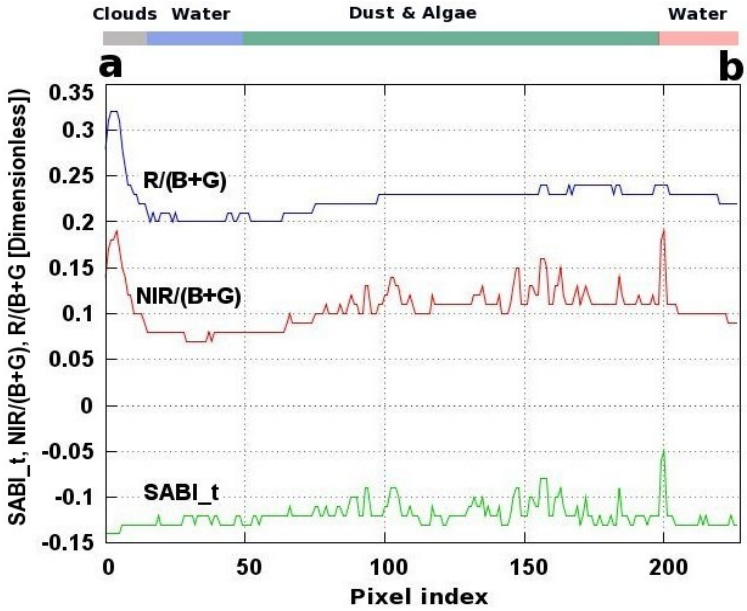

Figure 7.8. The transects of the line (a to b) shown in Figure 7.2D selected over clouds; water; dust, surface blooms; and water are: **R/(B+G)** which is the ratio of the red (λ_1=645 nm) band to the sum of the blue (λ_3=469 nm) and green (λ_4=555 nm) bands. The **NIR/(B+G)** is the ratio of the NIR (λ_2=859 nm) band to the sum of the same blue and green bands. The **SABI_t** is [NIR/(B+G)] – [R/(B+G)].

SABI_t was tested over surface blooms observed in Landsat–4/TM using its bands that corresponded with MODIS's 500 m resolution band group (see Table 7.10). The results of the test were consistent with those generated from MODIS data, in classifying surface blooms as having SABI_t values greater than or equal to – 0.10. 10% of the dense high altitude clouds observed in the dataset, were misclassified as surface blooms by SABI_t. This was probably caused by high scattering occurring across all four bands used in the SABI_t algorithm and its large bandwidths compared to MODIS's.

Table 7.10. Landsat–4/TM (30 m resolution) band group that were used as input in the SABI algorithm and the corresponding MODIS 500 m band group.

Band Number	Landsat TM bands (µm)	Landsat bandwidth (µm)	MODIS bands (µm)	MODIS bandwidth (µm)
1	0.45–0.52	0.07	0.459 – 0.479	0.020
2	0.52–0.60	0.08	0.545 – 0.565	0.019
3	0.63–0.69	0.06	0.62 – 0.67	0.05
4	0.76–0.90	0.14	0.841 – 0.876	0.035

7.4 Discussion

Many of the marine scientists and environmentalist question the efficiency of a satellite ocean colour sensor such as MODIS at being able to detect and classify oil spills. Their doubts are largely based upon the sensors lack of visibility during the night and in the presence of thick clouds. However, in almost cloud-free regions such as those found in ROPME, MODIS has been proven- through this research, to be an ideal candidate for the detection of oil spills, particularly since it is equipped with a number of qualities that make up for some of its shortcomings. For example, its data is received freely by satellite ground stations; it has a reasonable spectral resolutions (36 channels) which are distributed across three moderate spatial resolutions (1000, 500 and 250 m); it has a short revisiting time (1–2 days) - due to being on-board two satellites; as well as having a wide range field of view (±55°).

This research has focussed its analysis on the band groups that belong to MODIS's highest spatial resolution (that is, 250 and 500 m close to nadir) shown in Table 7.11 (adopted from Table 1.1). The reason for this is because the RSA covers an area equal to approximately 240,000 km^2 (Linden et al., 1990), with an average oil spill size of few 100's km^2, which is considerably small in comparison to MODIS's moderate spatial resolution.

Table 7.11. MODIS's spectral bandwidths that were used in the development of the SCS and SABI relationships.

Band	Bandwidth (nm)
1	620 - 670
2	841 - 876
3	459 - 479
4	545 - 565

For these reasons the SCS was developed using the red (λ_1=645 nm) and NIR (λ_2=859 nm) bands embedded within MODIS's 250 m highest spatial resolution band group. Also, the usefulness of using these bands when discriminating between oil and water were asserted by earlier studies such as those carried out Rong-Rong Li et al. (2003), Miller & McKee (2004), Mati Kahru et al. (2004) and Chust & Sagarminaga (2006).

The SCS classifier is an edge–type classifier that quantifies how the radiance contrast of an investigated class (such as oil) varies or shifts in the red and NIR bands in relation to the corresponding radiances of the adjacent clear sea water. Over pure and

homogeneous class (that is, a zero contrast with its surrounding sea water), the SCS classifier will yield a zero value as in the case of pure oil or sea water. These spectral variations correspond to the different scattering (reflectance) and absorption properties that each class respond to in the red and NIR bands of MODIS's 250 m band group.

Being a new type of classifier, the SCS does share the Parallelepiped classification method in its use of extreme values and the Spectral Angle Mapper method its insensitivity to illumination. Therefore, the results are independent from the spill's position to the sun-glint (that is, independent from whether the contrast is positive or negative in relation to clear sea water).

The reason for using the extreme radiance red and NIR responses instead, for example, of using the average response values is to avoid the need to perform complex and lengthy calculations in order to define the classes, which is a prerequisite for working out the averages. The classifier was also found to provide reliable and consistent empirical results, without the need to estimate these averages. Such efficiency renders the SCS classifier advantageous for field operations' use by acting as an early warning trigger for the detection of oil spills and surface blooms.

During this research, oil spills were found to maintain their contrast (positive or negative) against sea water in either the red or NIR bands. This, in effect, means that each of the ratio terms used in the SCS relationship (Equation 7.1) can represent the contrast of a single class; that is either sea water or oil. Surface blooms, however, due to their high reflectance in the NIR and varying absorption properties in the red band, will not always maintain the same contrast in the red band (depending on the type of species being detected). For example, blooms due to the *Ulva prolifera* species seen in the Yellow sea Qingdao, eastern China (section 5.9.2) appear darker than the surrounding water (negative contrast) in the red band due to higher absorption in this band. Whereas in the case of Sargassum (section 6.3.3), the surface species maintain a positive contrast with respect to the surrounding clear water in the red band.

The SCS relationship uses the at-sensor radiance values (that is, TOA radiances) in the red and NIR bands and not the at-water surface reflectance values which are produced after performing atmospheric correction. This is because MODIS's standard method selected for performing the atmospheric correction is called the “dark pixel” method. It assumes ocean water to be optically black (case I waters) by having a zero water–leaving radiance in the NIR (Gordon & Clark, 1981). Despite this, the empirical results produced from the SCS classifier were consistent even when conducted over

geographically and environmentally different datasets and appeared insensitive to the atmosphere. This is because oil spills were visible in MODIS's images when observed within ±30° from nadir positions, and hence the impact of path radiance was reduced. As for the contribution of Rayleigh scattering, it is expected to be minimal since the SCS algorithm uses the longer wavelengths of the spectrum (that is, the red and NIR bands). Furthermore, choosing clear sea water as a reference class in the SCS also contributes to the efficiency of the algorithm because its spectral response is independent in the red and NIR bands. Therefore, the classifier becomes highly sensitive to the optical properties of the contrasted surface layer (oil or otherwise) in relation to the clear-water reference class.

Currently, the classification involves a manual visual inspection carried out over a radiometric grey-scale image in the NIR to decided where and how to designate the sampling areas. The investigation starts with finding the patterns that appear either with a negative or positive contrast at the water surface while masking out land, clouds and cloud-shadows. After that, a relatively small area (size between 20–60 pixels) is selected inclusive of two pure classes, one of which is the adjacent clear sea water. The size of the selected area is critical to ensure that both classes are pure and experiencing the same atmospheric and illumination conditions. The impurity of classes (class-mixing) may bias the overall classification result in favour of the predominate contrasted class. Artefacts visible in the image such as scanner lines, error detection pixels, sharp noisy pixels and “bow–tie” pixels are avoided so as not to bias the overall classification output. Because the TOA radiance data is used in the analysis of the SCS, the bow–tie effect (overlap of MODIS scanner lines due to its large field–of–view covering part of the earth's curvature) will be visible at the edges of MODIS images. However, since all oil spills are visible within a confined region close to nadir (within ±30°), the bow-tie effect is by default non-existing.

Although this research is aimed primarily at investigating the MODIS's sensor as a case study, it did nevertheless, use data produced by other optical sensors such as MERIS. When the SCS classifier was tested on MERIS data (see chapter 5) using its red bands (λ_6=620 and λ_7=665 nm) and NIR bands (λ_{13}=865 and λ_{14}=890 nm), it produced results consistent with those from MODIS. This indicates the validity of the algorithm when used over data produced by sensors whose spectrum includes similar red and NIR bandwidths as MODIS.

The classification table introduced by the SCS in Table 7.2 labelled turbid water and weathered oil as one class attached to the mean SCS value of 0.05. It is possible that both phenomena can give the same response, since according to Byfield (1998), the scattering of suspended oil mixtures such as weathered or dispersed oil is similar to non–oil based suspended particles in water (turbid water) in the red and NIR bands. The research was also not able to provide an adequate definition for the mean classification value of 0.10, and labelled it as an undetermined class. It is worth noting, however, that most of the observed patterns that were classified with this classification fell under the sun-glint (Table 7.8) and had their classification laying between the classifications of TW/WO and surface bloom (mean SCS=0.20). This may, therefore, be indicative of a classification that quantifies a sub-surface type of turbidity that is higher than the TW/WO class but less than a surface bloom classification. In order to accurately verify this type of class a more precise *in situ* examination is needed.

A certain category of high altitude clouds was sometimes misclassified as oil when measured next to clear sea water. For this reason, it is necessary to manually mask out clouds and their shadows from the scene in order to avoid such misclassification.

The classification results produced by the SCS classifier could not always be readily validated by *in situ* means. However, it was possible to infer the validation from some of the distinct shapes of oil spills and the position of the analysis on the spill. For instance, a single spill may have several classifications of thickness depending on where the classifier is applied. Therefore, the classification outcome did conform with expectations that the spill's thickness furthest from the source of the spill should be lighter than it is nearer to the source. The SCS classification results have also agreed with the common spill's shape shown in Figure 7.9 (produced earlier in Figure 5.18B), where the relatively narrow areas of thick oil (point 2) moving downwind leading edge, surrounded by oil sheen (points 1 and 3) trailing off in the upwind direction. The SCS classifier produced a value of 0.04 at point 2 and values 0.012 and 0.005 at points marked 1 and 3 respectively – matching what was expected from such spill's shape.

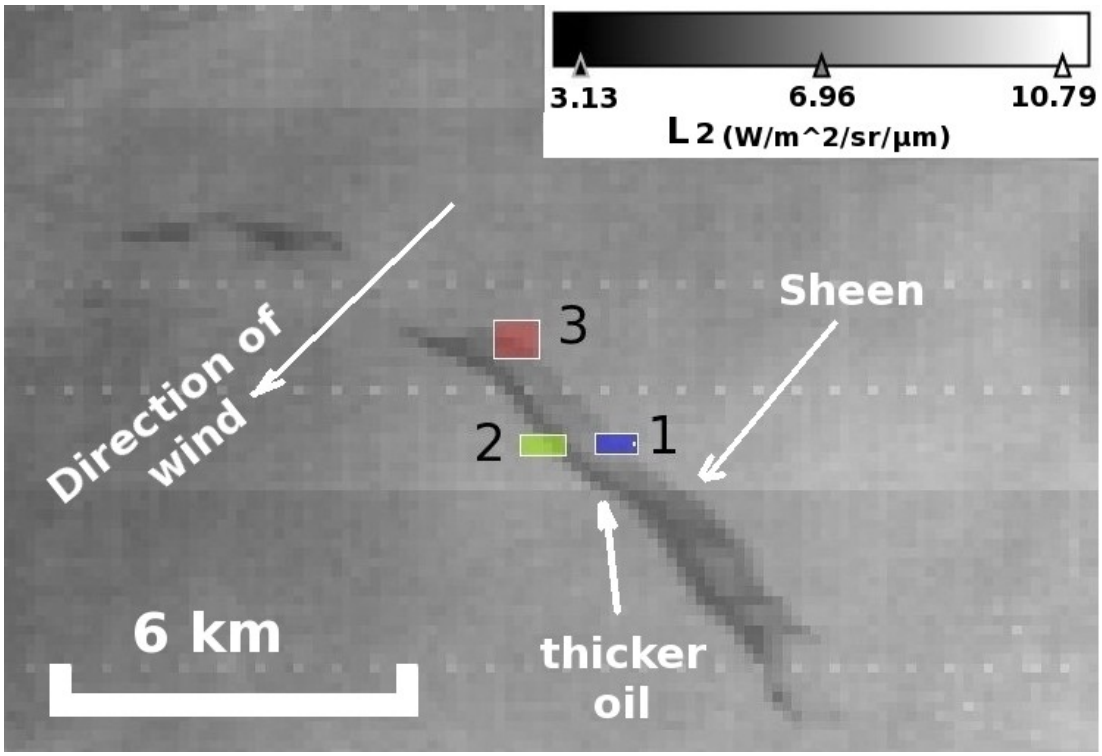

Figure 7.9. An old spill observed in MODIS Terra on 4th September, 2005 around the south-eastern coast of the Gulf of Cagliari (Sardinia-Italy). The spill appears in a single NIR band radiance image (λ_2=859 nm) over which the SCS sampling areas are shown.

The SABI method is a four–band formula (Equation 7.2) whose main objective is to delineate and identify chlorophyll–enriched species that float at the water surface that may falsely be classified as oil spills. Thus, the SABI does not directly identify oil spills viewable in MODIS, but rather ascertain their non–existence by identifying their prime look–alike –surface floating blooms. This look-alike property that dense surface blooms are characterised with is clearly visible in the SAR data, where such blooms appear as dark aggregates at the water surface similar to the appearance of oil. This appearance is caused by the dampening that these blooms exert on the gravitational sea waves (Bragg waves) that causes the microwaves to be scattered out of the sensor's view.

In this research, an RGB colour combination is used to identify these biological surface blooms. This colour composite assigns the red colour to the radiometric data in the NIR channel and the green and blue colours to the red channel data. Due to the high reflectance in NIR that these species exhibit, the surface blooms appear reddish in colour relative to the dark background colour of the water. However, obscurity can sometimes occur due to sever nearby sun-glint conditions and/or the presence of substantial layers of aerosols (dust) over the blooms.

Researchers such as Kahru et al (1993) have already examined the use of the NDVI, which is a valuable quantitative vegetation monitoring tool over land, on surface-floating cyanobacterial blooms. This is one of the reasons why the NDVI was chosen to be compared to the performance of the SABI in this study. Secondly, because both relationships exploit the "red edge" phenomenon in their numerators. Other researchers have developed specific new techniques to delineate and quantify bloom structures floating at the water surface. Gower et al. (2005), for example, proposed the MCI using the peak radiance near 709 nm in MERIS to detect high concentrations of chlorophyll and surface algae. Hu (2009) on the other hand, recently proposed the FAI algorithm that uses MODIS's short-wave infra-red band (λ_5=1240 nm) combined with red and NIR bands.

As in the case of the SCS, it is not feasible to use atmospherically–corrected data over surface–water species due to the high NIR reflectance that violated the "dark pixel" assumption, leading to an over–estimation of the aerosol load. For this reason, this study compared the performance of the SABI and NDVI over water using the calibrated TOA radiances (SABI_t and NDVI_t) and the Rayleigh–corrected reflectances (SABI_r and NDVI_r). Since both algorithms shared the same numerator (that is, representative of red-edge), the denominator in each index becomes the main determining factor for any significant differences that may exist between the two indices. The denominator of the SABI was suggested to reflect the properties of water. That are strong absorption in the NIR and varying absorption/scattering levels in the blue (λ_3=469 nm) and green (λ_4=555 nm) bands in response to the varying concentrations of phytoplankton in water.

The results from the SABI_r were slightly better than those obtained from the NDVI_r but very similar. The contrast of the SABI_t over surface blooms was 25% less than the corresponding NDVI_t and 16% less than SABI_r. Nevertheless, the SABI_t had outperformed all other indices (SABI_r, NDVI_r and NDVI_t) in being less sensitive over varying levels of dust, clouds, cloud-shadows and sun–glint illumination. This is because the radiometric weight carried out by its numerator is independent from that of its denominator, since each applies a different set of bands to the other, unlike in the case of the NDVI. Therefore, the SABI_t relationship effectively averages (smooths) out the noisy responses it receives from the blue and green bands caused by these high scattering sources allowing only the high red-edge signal from surface blooms. Also, because of the presence of the blue and green bands in the SABI_t high

concentrations of sub-surface blooms will be spatially mapped by the algorithm in relation to low or zero concentration of sub-surface blooms. Registering this information is particularly useful in interlinking the two phenomena (sub and at surface blooms), firstly since it is unlikely, in most cases, for the surface blooms to exist in isolation from its sub–surface species. Secondly, The mapped tracks of both bloom types act as tracers for surface currents associated with the eddies, and finally the blooms' spatial distribution may help in identifying the type of species involved and probably help in understanding their life cycle.

The SABI_t was found to classify 95% of surface blooms, showing values greater than or equal to -0.10±0.02 (the SABI_t baseline value for surface blooms), which corresponds to a SABI_r value of 0.10±0.2. Misclassification may occur over high altitude thick clouds and over highly turbid sea water due to significant scattering in the red and/or NIR bands, particularly in highly turbid coastal waters.

Under the SABI_t product and outside the glint region, the appearance of oil spills is hardly distinguishable from the background water (zero contrast), since the red-edge term (the radiometric difference between the red and NIR bands) is negligible over both the water and oil. Under the glint area, however, oil spills will become well delineated because radiance becomes saturated over the spill's surface area across all bands used in the SABI's algorithm. In either case, oil spills will always have values less than the SABI_t baseline value of -0.10±0.02.

The MODIS Chlor-a product masks out surface floating blooms either because their Chlor-a output readings are unrealistically high or because they are considered optically opaque “scum” that masks out all water–leaving radiances. Under severe sun–glint conditions, however, the Chlor-a product cannot be processed due to the large interference from the sun's specular reflection. In such circumstances, the SABI_t relationship, can provide a robust alternative to map surface blooms and to discriminate them from oil spills without the need to perform any complicated atmospheric correction operations.

The MODIS 500 m/pixel resolution SST (interpolated from the 1 km/pixel resolution longer thermal bands 11–12 μm) and Chlor-a maps were also processed over the possible oil spill areas to investigate whether it can be delineated in either maps. In all of the investigated oil spill incidents carried out in this research, none of them revealed credible thermal differences from the surrounding water, except in the case of the Gulf of Mexico oil spill due to its massive size. This was probably attributed to

MODIS's coarse spatial resolution in relation to the size of investigated spills, in conjunction with its limited sensitivity in the thermal infra–red channels that prevented it from detecting the minute thermal differences between oil and water. Also none of the spills were masked as invalid Chlor-a pixels in the corresponding Chlor-a maps. This might have occured due to the optical properties of the oil itself combined with its relatively small thickness that made it transparent to the blue and green water–leaving radiances used in the Chlor-a algorithm (unlike its opaque look–alike surface blooms), in addition to the coarse spatial resolution of the sensor. Similarly, waters densely populated with large spatial distributions of sub-surface blooms (high Chlor-a concentrations) appeared with approximately 1–2 °C higher temperature than the surrounding bloom-free waters in MODIS's SST products. The data gained from SST4 maps are only valid during night time observations. However, when SST4 data are used during the day and close to the sun-glint region (approximately ±20°-30° from the central glint area) over oil spills and and surface blooms, the different textural details in these pattern become highlighted due to different sun-glint reflections off their varying thickness layers. This proves the usefulness of the SST4 maps in highlighting the textural details of surface-floating patterns within sun-glint regions.

The detection process of oil spills in MODIS data involved using a combined application of both methods discussed above. Data processing started with the production of a grey–scale image using the radiometric transformation in the NIR band of the 250 m/pixel resolution band group (Equation 4.22). The purpose of this transformation is to highlight the suspected patterns that appear at the water–surface close to offshore oilfields and shipping routes, by inverting their contrast with water. Prior known patterns such as clouds, cloud-shadows, tankers, offshore platforms and land are excluded from the manual marking of possible oil spill targets. The SCS analysis is again manually performed on the suspected patterns using the detailed description discussed earlier. According to the SCS classifier, a true positive oil spill should have its SCS classification value lie between the accepted range of 0.02–0.04. A GIS map is then used to identify the nearest oil-related installations/tankers that may have contributed to spill(s) detected. SCS values greater than or equal to 0.20 classify surface blooms, after which, the false RGB colour composite corresponding to bands λ_2=859, λ_1=645 and λ_1=645 nm respectively is then analysed. In this colour composite, surface blooms should appear as distinct reddish spatial patches floating at the water surface. In which case, the SABI_t is then produced from the level2 ocean colour

product that includes the calibrated TOA radiance values in the red, NIR, green and blue bands (the red and NIR bands are aggregated from the 250m band group). The reason for analysing the SABI_t product is to acquire clearer visibility over the blooms in dusty and glint-covered areas and to confirm these findings by delineating them at SABI_t values greater than or equal to -0.10. MODIS's standard products such SST, Chlor-a and SST4 were then analysed to provide useful complementary data in order to improve the quality of the decision making process on oil spills. In the event ASAR data becomes available and found to coinciding with that of MODIS imagery, synergy between the two sensors becomes a very powerful tool in classifying oil spills, even when their spatial resolutions do not match. Finally, field *in situ* data when received, can either confirm or negate the classification results. Figure 7.10 summarises the different stages discussed in the classification and validation procedure of oil spills.

Throughout this study, the wind speed recorded over the analysed data was found to be within an approximate range of 3–10 m/s, which generally agrees with the observations made by Hühnerfuss et al. (1978). Wind speeds above the maximum value quoted in this range, will cause the oil slicks and their look-alikes (such as surface blooms) to be disintegrated, thus rendering them non-viewable in MODIS imagery.

While investigating the shapes of some of the large oil spills observed by MODIS, it became apparent that it is possible to apply shape-based techniques that are normally applied over the SAR data to extract the dark features associated with oil spills on MODIS data. In optical sensors, however, oil spills can appear with a positive contrast as well as with negative contrast relative to sea water. This variability in contrast depends on the properties of the bidirectional reflectance distribution function that governs the sun-target-sensor configuration. Shi et al. (2007), for example, demonstrated how it is possible to automatically extract oil spills viewed in MODIS data by using the fuzzy C–means cluster algorithm. The spill's size viewable in satellite ocean colour sensors is critical in determining their suitability for applying the shape methods over them, for they must be large enough relative to the spatial resolution of the sensor to be detected. Appendix C proposes a preliminary method to classify the viscosity of relatively large oil spills and to discriminate them from look-alikes based on their edge and texture properties. This method (termed the oil spread index–OSI) is in need of further development in order to produce more reliable results.

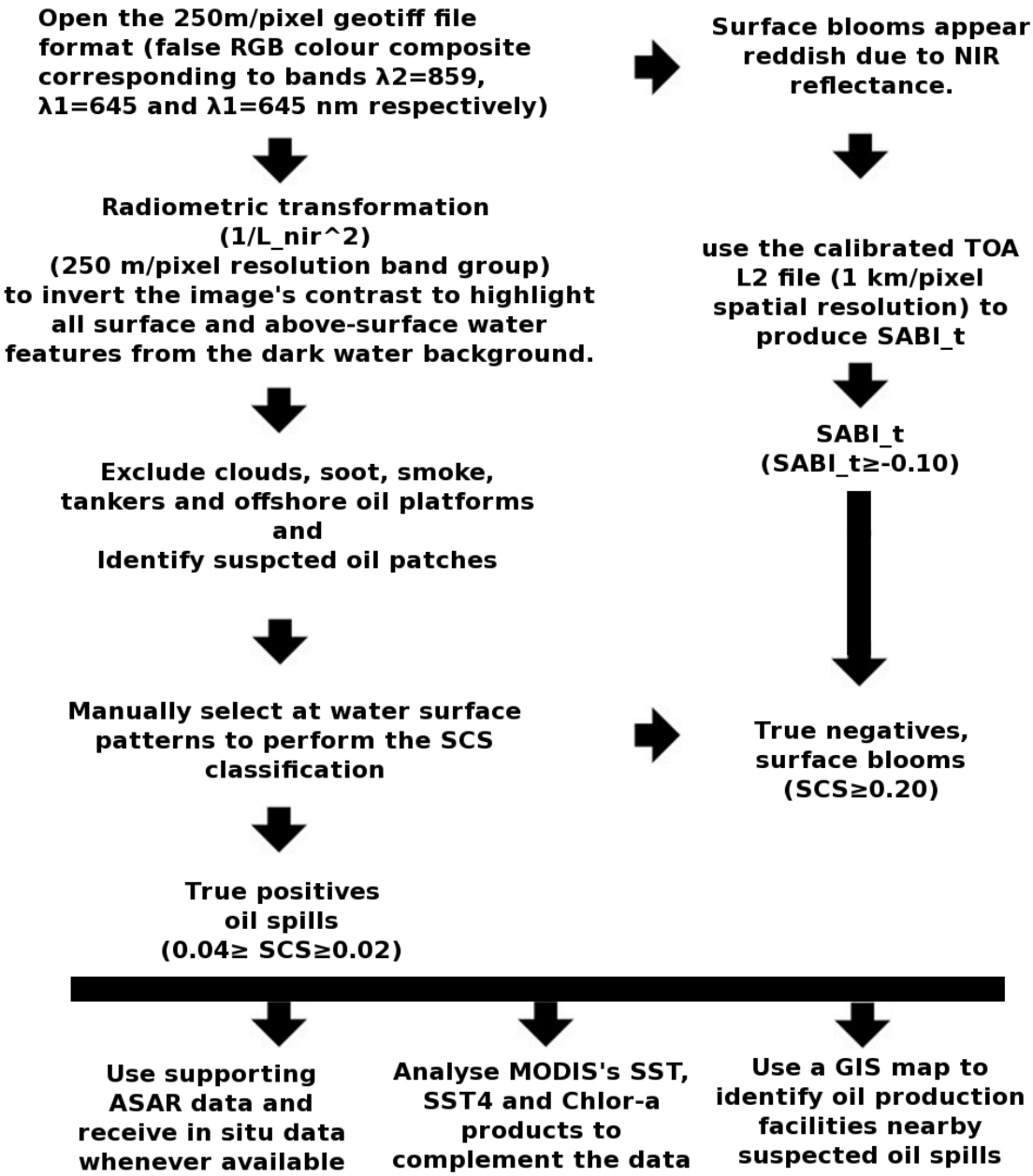

Figure 7.10. A flow chart outlining the different stages used in the classification and validation procedure performed on of oil spills observed in MODIS imagery.

The two methods discussed were applied over two oil spill incidents, one of which was the Deepwater Horizon oil platform accident in the Gulf of Mexico and the other was near the oil terminal within the RSA, Kuwait (Table 7.12). Both spills produced consistent results to what has already been presented earlier.

Table 7.12. The oil spill incidents over which the SCS and the SABI_t detection methods were applied to. MTO=Medium thickness oil, LTO=Light thickness oil (sheen) and L2M= Light–Medium.

No	Date	Location	Oil viscosity type	Mean SCS±0.002	SABI
1	25/04/10	Gulf of Mexico	Light	0.03 (MTO)	< -0.10
3	04/08/10	RSA	Heavy	0.02 (LTO)	< -0.10

7.5 Recommendations and future work

- Currently, the SCS method uses the red and NIR bands because they belong to MODIS's highest spatial resolution spectral group and for their ability to discriminate oil spills, as was proved already by previous studies. Nevertheless, further research is required to assess the suitability of other bands than the red and NIR as spectral inputs into the SCS classifier. Today, the availability of several multi and hyper spectral sensors (including MODIS's spectral channels) covering a variety of spatial resolutions, bandwidths and bit quantizations, may provide a multitude of valid alternatives for implementation in the SCS. These additional spectral bands may also provide further discriminatory information useful for extending the applicability of the SCS classifier over different species in different habitats. Therefore, it is possible to transcend the functionality of the SCS beyond marine habitat to include, for example, vegetation or desertification cover overland, provided that a reference class is designated.

- The classification concept introduced by the SCS classifier has the potential to broaden its applicability to other research fields beside physical oceanography. For example, it can be used in chemistry or biology when separating, for instance, the constituents of different-contrasted dye mixtures from each other.

- It is recommended to develop either fully or semi automatic solutions, as opposed to the fully interactive methods currently being used in the SCS classifier. Such techniques would be advantageous for improving the efficiency of classification particularly over large-sized satellite datasets. This can be performed by suggesting the use of a window, of pixel size (n×n), that moves (slides) over an image and calculates the SCS over each segment it covers. This

process is repeated until the moving window covers the whole image. The classification is carried out on the image after masking out the undesirable visible objects such as land, clouds and cloud-shadows. The results, after which, will be compared to the predefined SCS index table and a new classified image will be generated based on the assignment of classes from each sampling window.

- It is recommended to validate the results of the SABI algorithm against other surface bloom species, other than the ones covered in this thesis like for example close-to-surface coral reefs. The diversity of species can include those that have: a broad spatial distribution at the water surface; ones that have varying types and concentrations of chlorophyll pigments; and those whose buoyancy level varies at the water surface. The reliability of the SABI results should also be examined in relation to the data produced by other standard ocean colour products such as the fluorescence line height (FLH) and photosynthetically active radiation (PAR). FLH is a relative measure of the amount of radiance leaving the sea surface which is presumably a result of chlorophyll fluorescence emission (Abbott & Letelier, 1999), while PAR measures the quantum energy flux from the Sun in the spectral range 400-700 nm (Frouin et al., 2001) .

- Further work is required to examine the applicability and validity of the methods developed in this thesis to datasets produced from other types of sensors other than satellite such as airborne and hand-held devices. These devices are distinct from satellite sensors due to their higher spatial resolutions and negligible atmospheric load.

Chapter 8: Conclusions

8.1 Introduction

The study evaluated the effectiveness and reliability of an ocean–colour sensor – such as MODIS (the Moderate Resolution Imaging Spectroradiometer) at discriminating oil spills from look–alikes in almost cloud–free conditions. Satellite imagery of spills were investigated relative to different conditions in which they were observed, such as: the their position to a sun–glint; their size relative to MODIS's spatial and spectral resolutions; sea surface temperature; wind speed and aerosol load. As a result of this research, two robust new methods have been developed: The spectral contrast shift (SCS) and the surface algal bloom index (SABI). As a result of this research, a set of conclusions have been reached regarding its outcome.

8.1.1 The MODIS sensor

- MODIS is an effective sensor for detecting oil spills over areas characterised with 80–90% cloud–free conditions such as those found in the RSA.
- MODIS has proved its efficiency in detecting oil spills: Its data is freely available through its direct–broadcast mode, it has adequate spatial resolutions (250 and 500 m/pixel), sufficient spectral resolutions, a short temporal resolution (available on–board two satellites with 1–2 days revisiting times), and a wide field of view.
- MODIS's standard bio–geophysical products such as sea surface temperature (SST4 and SST) and chlorophyll-a (Chlor-a) have proven their usefulness in providing valuable complementary information for the identification process of oil spills.
- The wind speed results from this research agree with the range cited in the literature of 3–12 m/s as the optimal sea state conditions for observing oil spills and surface floating blooms in MODIS, beyond which patterns will be undetectable.

8.1.2 The spectral contrast shift (SCS)

- The SCS is a robust new method proposed to identify oil spills and classify their thickness by using MODIS extreme (maximum and minimum) top–of–atmosphere radiance (TOA) values in the 250 m/pixel resolution bands: the red (λ_1=645 nm) and the NIR (λ_2 =859 nm) measured over a relatively small area selected to encompass part of an unknown class and part of the surrounding clear sea water.
- The SCS classifier has revealed consistent and highly sensitive results independent of sun glint illuminations and sensor type. Oil spills will have SCS values lying within the range (0.02–0.04±0.002) corresponding to different thickness of oil. The SCS also classifies surface floating blooms as having SCS values greater than or equal to 0.20.
- The SCS classifier occasionally misclassified particular categories of clouds and cloud shadows as oil spills due to their shared spectral properties in the red and NIR bands. Therefore, clouds should be masked out first from the images using MODIS standard cloud mask or interactively by an operator,

8.1.3 The surface algal bloom index (SABI)

- The proposed surface algal bloom index (SABI) successfully discriminated chlorophyll–enriched species that float at the water surface from oil spills, without the need to perform complex corrections for atmosphere and sun glint effects. SABI uses a ratio between the difference of radiometric responses in the red (λ_1=645 nm) and the NIR (λ_2=859 nm), aggregated from the 250 m resolution band group, to the sum of the radiometric responses in the blue (λ_3=469 nm) and green (λ_4=555 nm) bands of MODIS's 500 m/pixel resolution spectral group.
- The high water–leaving radiance in the blue and green bands coupled with high water absorption in the NIR is exploited by the SABI method to delineate high concentrations of sub–surface blooms.
- The SABI values greater than or equal to -0.10 classifies 95% of surface blooms with a misclassification of 5% due to very shallow turbid waters and thick clouds. This baseline value corresponds to 0.10 in the Rayleigh–corrected reflectance relationship of the SABI.

- Oil spills visible in the SABI will always have values lower than the SABI baseline value for surface blooms, which makes it a good discriminator between the two.
- The SABI algorithm outperformed the normalized difference vegetation index (NDVI) for the detection surface floating blooms in being less sensitive to varying levels of dust, clouds and sun glint. This is attributed to the sum of the blue and green bands in the SABI algorithm that smooths out the amplified noise caused by such factors.

References

Abbott, M.R. & Letelier, R.M. (1999). *Algorithm Theoretical Basis Document Chlorophyll Fluorescence (MODIS Product Number 20)*. [Online]. Available from: http://modis.gsfc.nasa.gov/data/atbd/atbd_mod22.pdf.

Abdali, F. & Al-Yakoob, S. (1994). Environmental dimensions of the Gulf War: potential health impacts. *The Gulf War and the environment*. p. 85.

Abed, I. & Hellyer, P. (2001). *United Arab Emirates, a new perspective*. Trident Press Ltd.

Ackerman, S.A., Strabala, K.I., Menzel, W.P., Frey, R.A., Moeller, C.C. & Gumley, L.E. (1998). Discriminating clear sky from clouds with MODIS. *Journal of Geophysical Research*. 103. pp. 32141-32158.

Ackleson, S.G., Pitts, D.E., Sullivan, K.D. & Reynolds, R.M. (1992). Astronaut observations of the Persian (Arabian) Gulf during STS-45. *Geocarto International*. 7 (4). p. 59.

Al-Awadhi, F. (1999). The Year of the Ocean and its crucial importance to the Gulf* 1. *Desalination*. 123 (2-3). pp. 127–133.

Alawadi, F., Amos, C., Byfield, V. & Petrov, P. (2008). The application of hyperspectral image techniques on MODIS data for the detection of oil spills in the RSA. In: *Proceedings of SPIE*. 2008, Cardiff, Wales, United Kingdom, pp. 71100Q-71100Q-12.

Al-Ghunaim, I., Abuzar, M. & Al-Qurnas, F.S. (1992). Delineation and monitoring of oil spill in the Arabian Gulf by using Landsat Thematic Mapper(TM) data. In: *the 1 st Thematic Conference on Remote Sensing for Marine and Coastal Environments, New Orleans, LA, USA, 06/15-17/92*. 1992, pp. 1151–1160.

Al-Hinai, K.G., Khan, M.A., Dabbagh, A.E. & Bader, T.A. (1993). Analysis of Landsat Thematic Mapper Data for Mapping Oil Slick Concentrations-Arabian Gulf Oil Spill 1991. *The Arabian Journal for Science and Engineering*. 18 (2). pp. 85–93.

Ali, M.Y. & Riley, J.P. (1986). The distribution of halomethanes in the coastal waters of Kuwait. *Marine Pollution Bulletin*. 17 (9). pp. 409–414.

Alpers, W. & Hühnerfuss, H. (1989). The Damping of Ocean Waves by Surface Films: A New Look at an Old Problem. *J. Geophys. Res*. 94. pp. 6251–6265.

Al-Rabeh, A.H., Cekirge, H.M. & Gunay, N. (1989). A stochastic simulation model of oil spill fate and transport. *Applied Mathematical Modelling*. 13 (6). pp. 322–329.

Al-Yamani, F., Bishop, J., Ramadhan, E., Al-Husaini, M. & Al-Ghadban, A.N. (2004). *Oceanographic atlas of Kuwait's waters*. Kuwait: Kuwait Institute for Scientific Research.

Al-Yamani, F.Y., Bishop, J.M., Al-Rifaie, K. & Ismail, W. (2007). The effects of the river diversion, Mesopotamian Marsh drainage and restoration, and river damming on the marine environment of the northwestern Arabian Gulf. *Aquatic Ecosystem Health & Management*. 10. pp. 277-289(13).

American Society for Testing and Materials (1993). *Annual book of ASTM standards*. Philadelphia, Pennsylvania, USA.: American Society for Testing and Materials.

Anderson, D.M. (1997). Turning back the harmful red tide. *Nature*. 388 (6642). pp. 513–14.

Antoine, D. & Morel, A. (1998). Relative Importance of Multiple Scattering by Air Molecules and Aerosols in Forming the Atmospheric Path Radiance in the Visible and Near-Infrared Parts of the Spectrum. *Applied Optics*. 37 (12). pp. 2245-2259.

Baker, J.M. & Dicks, B. (1982). The environmental effects of pollution from the Gulf oil industry. In: *IUCN/MEPA report for the Expert Meeting of the Gulf Co-ordinating Council to review environmental issues*. 1982.

Banse, K. (1987). Seasonality of phytoplankton chlorophyll in the central and northern Arabian Sea. *Deep Sea Research Part A. Oceanographic Research Papers*. 34 (5-6). pp. 713–723.

Barth, H.J. (2002). *The 1991 Gulf War Oil Spill-Its ecological effects and recovery rates of intertidal ecosystems at the Saudi Arabian Gulf coast - results of a 10-year monitoring period*.

Basart, S., Pérez, C., Cuevas, E., Baldasano, J.M. & Gobbi, G.P. (2009). Aerosol characterization in Northern Africa, Northeastern Atlantic, Mediterranean Basin and Middle East from direct-sun AERONET observations. *Atmospheric Chemistry & Physics*. 9. pp. 8265–8282.

Bento, R.C. (2009). *Proposed management plan for the Rul Al-Faqeet marine protected area, Fujaira, UAE.*

Beydoun, Z.R. (1991). *Arabian plate hydrocarbon geology and potential*. Tulsa, OK (United States); American Association of Petroleum Geologists.

Bhimachar, B. & George, P. (1950). Abrupt set-backs in the fisheries of the malabar and kanara coasts and “red water” phenomenon as their probable cause. In: *Plant Sciences*. 1 June 1950, pp. 339-350.

Böhm, E., Morrison, J.M., Manghnani, V., Kim, H.S. & Flagg, C.N. (1999). The Ras al Hadd Jet: Remotely sensed and acoustic Doppler current profiler observations in 1994-1995. *Deep Sea Research Part II: Topical Studies in Oceanography*. 46 (8-9). pp. 1531–1549.

Boyd, J.N., Kucklick, J.H., Scholz, D., Walker, A.H., Pond, R. & Bostrom, A. (2001). Effects of oil and chemically dispersed oil in the environment. *Prepared by Scientific and Environmental Associates, Inc., Cape Charles, VA. Prepared for American Petroleum Institute: Washington, DC*. 49.

BP (2009). *BP Statistical Review of World Energy June 2009*. [Online]. British Petroleum. Available from: http://www.bp.com/liveassets/bp_internet/globalbp/globalbp_uk_english/reports_and_publications/statistical_energy_review_2008/STAGING/local_assets/2009_downloads/statistical_review_of_world_energy_full_report_2009.pdf.

Brekke, C. & Solberg, A.H. (2005). Oil spill detection by satellite remote sensing. *Remote Sensing of Environment*. 95 (1). pp. 1–13.

Brown, C. & Fingas, M. (2005). A review of current global oil spill surveillance, monitoring and remote sensing capabilities. In: *Proc. 28th Arctic and Marine Oil Spill Program (AMOP) Tech. Seminar*. 2005, pp. 7–9.

Brown, O.B. & Minnett, P.J. (1999). MODIS infrared sea surface temperature algorithm-Algorithm Theoretical Basis Document. *Products: MOD28. ATBD Reference Number: ATBD-MOD-25*.

Brown, R.A. (1980). Longitudinal instabilities and secondary flows in the planetary boundary layer: A review. *Reviews of Geophysics*. 18 (3). pp. 683–697.

Buckmaster, J. (1973). Viscous-gravity spreading of an oil slick. *Journal of Fluid Mechanics*. 59 (3). pp. 481–491.

Bulgarelli, B. & Tarchi, D. (2006). *Exploratory use of MODIS in oil-spill monitoring*. In: 2006, Joint Research Centre - Institute for the Protection and Security of the Citizen, pp. 49-60.

Byfield, V. (1998). *Optical remote sensing of oil in the marine environment*. University of Southampton, School of Ocean and Earth Science.

Carder, K.L., Cattrall, C. & Chen, F.R. (2002). *MODIS Clear Water Epsilons Algorithm Theoretical Basis Document ATBD 21*. [Online]. Available from: http://modis.gsfc.nasa.gov/data/atbd/atbd_mod21.pdf.

Carder, K.L., Chen, F.R., Lee, Z., Hawes, S. & Cannizzaro, J.P. (2003). *MODIS Ocean Science Team Algorithm Theoretical Basis Document, ATBD 19: Case 2 chlorophyll-a, v7*. University of South Florida, College of Marine Science, St Petersburg.

Carder, K.L., Gregg, W.W., Costello, D.K., Haddad, K. & Prospero, J.M. (1991). Determination of Saharan dust radiance and chlorophyll from CZCS imagery. *Journal of Geophysical Research*. 96. pp. 5369-5378.

Cekirge, H.M., Koch, M., Long, C., Giammona, C.P., Binkley, K., Engelhardt, R. & Jamail, R. (1995). State-of-the-art techniques in oil spill modeling. In: *Proceedings of the 1995 International Oil Spill Conference*. 1995, pp. 67–72.

Centre of Documentation, Research and Experimentation on Accidental Water Pollution (2006). *Aerial observation of oil pollution at sea-operational guide*. France: Cedre.

Centre of Documentation, Research and Experimentation on Accidental Water Pollution (2007). *Use and analyse of satellite SAR images for oil spills detection*. France.

Chao, S., Kao, T.W. & Al-Hajri, K.R. (1992). A numerical investigation of circulation in the Arabian Gulf. *Journal of Geophysical Research*. 97. p. 11.

Chust, G. & Sagarminaga, Y. (2006). The multi-angle view of MISR detects oil slicks under sun glitter conditions. *Remote Sensing of Environment*. 107 (1-2). pp. 232–239.

Clark Jr, R.C. & Symons, L.C. (1993). Mt Mitchell oceanographic expedition in the Gulf. *Marine Pollution Bulletin*. 27. pp. 31–34.

Clemente-Colón, P. & Yan, X.H. (2000). Low-backscatter ocean features in synthetic aperture radar imagery. *Johns Hopkins APL Technical Digest*. 21 (1). pp. 116–121.

Concawe (1998). *Heavy fuel oils*. product dossier no. 98/109. CONCAWE's Petroleum Products and Health Management Groups, Brussels.

Condley, C.J. (1991). The application of spaceborne synthetic aperture radar in the maritime environment. *NASA STI/Recon Technical Report N*. 94. p. 20596.

Cosnefroy, H., Leroy, M. & Briottet, X. (1996). Selection and characterization of Saharan and Arabian desert sites for the calibration of optical satellite sensors. *Remote Sensing of Environment*. 58 (1). pp. 101 - 114.

Cox, C. & Munk, W. (1956). Slopes of the sea surface deduced from photographs of the sun glitter. *Bulletin of the Scripps Institute of Oceanography*. 6. pp. 401-488.

Cox, C. & Munk, W. (1954). Statistics of the sea surface derived from sun glitter. *J. Mar. Res*. 13 (2). pp. 198–227.

Crombie, D.D. (1955). *Doppler Spectrum of Sea Echo at 13.56 Mc./s.*

Cross, A.M. (1992). Monitoring marine oil pollution using AVHRR data: observations off the coast of Kuwait and Saudi Arabia during January 1991. *International Journal of Remote Sensing*. 13 (4). pp. 781–788.

Cullen, H.M., Demenocal, P.B., Hemming, S., Hemming, G., Brown, F.H., Guilderson, T. & Sirocko, F. (2000). *Climate Change and the Collapse of the Akkadian Empire: Evidence From the Deep Sea.*

Das, V.K., Gouveia, A.D. & Varma, K.K. (1980). Circulation and water characteristics on isanosteric surfaces in the northern Arabian Sea. *Indian Journal of Marine Sciences*. 9. pp. 156–165.

Data provided by the European Space Agency (2010). *Galathea 3 EMU Radar look at ocean features and oil spills - Background*. [Online]. 2010. Radar look at ocean features and oil spills - Background. Available from: http://galathea3.emu.dk/satelliteeye/casestudies/radar1/back_uk.html. [Accessed 5 January 2011].

Delille, D. & Delille, B. (2000). Field observations on the variability of crude oil impact on indigenous hydrocarbon-degrading bacteria from sub-Antarctic intertidal sediments. *Marine Environmental Research*. 49 (5). pp. 403 - 417.

Demin, B.T., Yermakov, S.A., Pelinovskkiy, Y., Talipova, T.G. & Sheremet'yeva, A. (1985). Study of the elastic properties of sea surface-active films. *Izvestiia*. 21 (4). p. 312.

Deschamps, P.Y., Herman, M. & Tanre, D. (1983). Modeling of the atmospheric effects and its application to the remote sensing of ocean color. *Applied Optics*. 22 (23). pp. 3751-3758.

Desnos, Y.L., Closa, J., Rosich, B., Bellini, A., Laur, H. & Meisl, P. (2007). *Asar Ground Processor Verification And Wave Validation*.

Dessì, F., Melis, M.T., Naitzaa, L. & Marini, A. (2008). MODIS data processing for coastal and marine environment monitoring: A study on anomaly detection and evolution in gulf of cagliari (sardinia-italy). *ISPRS*. XXXVII (Part B8. Commission VIII, WG VIII/6.).

Dietz, R.S. & Lafond, E.C. (1950). Natural Slicks on the Ocean. *Journal of Marine Research*. 39. pp. 69-76.

D. Noerdlinger, P. (2010). *NASA Newsroom*. [Online]. 2010. Available from: http://newsroom.gsfc.nasa.gov/sdptoolkit/leaputc.html. [Accessed 13 June 2010].

Dongzhi, Z. & Peifu, C. (2000). The Research of Visual Light Wave-band Feature Spectrum of Sea-surface Oil Spill. *Remote Sensing Technology and Application*. 15 (3). pp. 160–164.

Duing, W. (1970). *The monsoon regime of the currents in the Indian Ocean*. 1st Ed. Honolulu: East-West Center Press (Honolulu).

El-Fadel, M., El Sayegh, Y., Abou Ibrahim, A., Jamali, D. & El-Fadl, K. (2002). The Euphrates-Tigris basin: a case study in surface water conflict resolution. *Journal of Natural Resources & Life Sciences Education*. 31. pp. 99-110.

Elliott, A.J. (1986). Shear diffusion and the spread of oil in the surface layers of the North Sea. *Ocean Dynamics*. 39 (3). pp. 113–137.

Elliott, A.J., Hurford, N. & Penn, C.J. (1986). Shear diffusion and the spreading of oil slicks. *Marine Pollution Bulletin*. 17 (7). pp. 308–313.

Elshorbagy, W. (2005). *Overview of Marine Pollution in the Arabian Gulf with Emphasis on Pollutant Transport Modeling*. In: 2005, Dubai, UAE: UAE University.

Emery, K.O. (1956). *Sediments and water of Persian Gulf*.

Esaias, W.E., Abbott, M.R., Barton, I., Brown, O.B., Campbell, J.W., Carder, K.L., Clark, D.K., Evans, R.H., Hoge, F.E., Gordon, H.R. & others (1998). An Overview of MODIS Capabilities for Ocean Science Observations. *IEEE Geoscience and Remote Sensing Society*. 36 (4). pp. 1250-1265.

Espedal, H. (1999). Detection of oil spill and natural film in the marine environment by spaceborne SAR. *IEEE 1999 International Geoscience and Remote Sensing Symposium, 1999. IGARSS'99 Proceedings*. 3. pp. 1478-1480.

Facey, R. (2008). Pollution from sea based sources. *Protecting the Gulf's Marine Ecosystems from Pollution*. pp. 163–189.

Fannelop, T.K. & Waldman, G.D. (1972). Dynamics of oil slicks. *AIAA Journal*. 10. pp. 506–510.

Fay, J.A. (1971). *Physical Processes in the Spread of Oil on a Water Surface.* In: 1971, Washington, DC: American Petroleum Institute, pp. 463-467.

Fay, J.A. (1969). The spread of oil slicks on a calm sea. *Oil in the sea*. ((D. P. Hoult)). pp. 53-63.

Fett, R.W. & Bohan, W.A. (1983). *Navy tactical applications guide. Volume 5, Part 1: Indian Ocean (Red Sea/Persian Gulf) weather analysis and forecast applications*. Monterey, CA.

Fingas, M.F. & Brown, C.E. (1997). Review of oil spill remote sensing. *Spill Science & Technology Bulletin*. 4 (4). pp. 199–208.

Fingas, M.F., Brown, C.E. & Mullin, J.V. (1998). *The visibility limits of oil on water and remote sensing thickness detection limits*. In: 1998, (Environmental Research Institute of Michigan, pp. 411–418.

Fiscella, B., Giancaspro, A., Nirchio, F., Pavese, P. & Trivero, P. (1994). Oil spill monitoring in the Mediterranean Sea using ERS SAR data. *ESA Earth Observation Quarterly*. 440.

Floodgate, G.D. (1995). Some environmental aspects of marine hydrocarbon bacteriology. *Aquatic Microbial Ecology*. 9 (1). pp. 3–11.

Fortner, B. (1998). HDF: the hierarchical data format. *Dr. Dobb's journal*. 23 (5). pp. 42–48.

Franklin, L.A. & Forster, R.M. (1997). The changing irradiance environment: consequences for marine macrophyte physiology, productivity and ecology. *European Journal of Phycology*. 32 (3). p. 207.

Franz, B.A. (2006). *Implementation of SST Processing within the OBPG*. [Online]. 2006. Implementation of SST Processing within the OBPG. Available from: http://oceancolor.gsfc.nasa.gov/DOCS/modis_sst/. [Accessed 4 April 2010].

Franz, B. (2007). *MODIS Ocean Data Processing, presentation at the MODIS Remote Sensing Workshop*.

Friehe, C.A., Shaw, W.J., Rogers, D.P., Davidson, K.L., Large, W.G., Stage, S.A., Crescenti, G.H., Khalsa, S.J.S., Greenhut, G.K. & Li, F. (1991). Air-sea fluxes and surface layer turbulence around a sea surface temperature front. *Journal of Geophysical Research*. 96 (C5). pp. 8593–8609.

Frouin, R., Franz, B. & Wang, M. (2001). *Algorithm to estimate PAR from SeaWiFS data Version 1.2-Documentation*. [Online]. Available from: http://disc.sci.gsfc.nasa.gov/UARS/oceancolor/PDFs/seawifs_par_algorithm.pdf .

Gade, M., Alpers, W., Huehnerfuss, H., Masuko, H. & Kobayashi, T. (1998a). Imaging of biogenic and anthropogenic ocean surface films by the multifrequency/multipolarization SIR-C/X-SAR. *Journal of Geophysical Research*. 103 (C9). pp. 18–851.

Gade, M., Alpers, W., Hühnerfuss, H., Wismann, V.R. & Lange, P.A. (1998b). On the reduction of the radar backscatter by oceanic surface films: Scatterometer measurements and their theoretical interpretation. *Remote Sensing of Environment*. 66 (1). pp. 52–70.

Garver, S.A., Siegel, D.A. & Mitchell, B.G. (1994). Variability in Near-Surface Particulate Absorption Spectra: What Can a Satellite Ocean Color Imager See? *Limnology and Oceanography*. 39 (6). pp. 1349-1367.

Gillot, A., Aston, G.H.R., Bananzinga, P., le Gal la Salle, Y. & Mason, M.J. (1988). Field guide to the application of dispersants to oil spills. *Available from the National Technical Information Service, Springfield VA 22161, as PB 89-115984. Price codes: E 04 in paper copy, A 01 in microfiche. Report*. (2/88).

Glover, N.W. (2007). *Abu Dhabi National Oil Company Strategy for Enhancement of Oil Spill Response Capability*. In: 2007, Japan: Petroleum Association of Japan (PAJ), p. 13.

Goddard, C.C. & Jupp, B.P. (2001). The radionuclide content of seaweeds and seagrasses around the coast of Oman and the United Arab Emirates. *Marine pollution bulletin*. 42 (12). pp. 1411–1416.

Golob, R. & Bruss, E. (1984). *Statistical analysis of oil pollution in the Kuwait Action Plan Region and the implications of selected world-wide oil spills to the region*. Geneva: United Nations Environmental Program Regional Seas reports and studies.

Goodman, R.H. (1989). Application of the technology in the remote sensing of oil slicks. In: *Lodge*. John Wiley & Sons Ltd.

Gordon, H.R., Brown, J.W. & Evans, R.H. (1988a). Exact Rayleigh scattering calculations for use with the Nimbus-7 Coastal Zone Color Scanner. *Applied Optics*. 27 (5). pp. 862-871.

Gordon, H.R., Brown, O.B., Evans, R.H., Brown, J.W., Smith, R.C., Baker, K.S. & Clark, D.K. (1988b). A semianalytic radiance model of ocean color. *Journal of*

Geophysical Research. 93. pp. 10909-10924.

Gordon, H.R. & Clark, D.K. (1981). Clear water radiances for atmospheric correction of coastal zone color scanner imagery. *Applied Optics*. 20 (24). pp. 4175-4180.

Gordon, H.R. & Wang, M. (1994a). Influence of oceanic whitecaps on atmospheric correction of ocean-color sensors. *Applied Optics*. 33 (33). pp. 7754-7763.

Gordon, H.R. & Wang, M. (1994b). Retrieval of water-leaving radiance and aerosol optical thickness over the oceans with SeaWiFS: a preliminary algorithm. *Applied Optics*. 33 (3). pp. 443-452.

Gordon, H.R., Clark, D.K., Brown, J.W., Brown, O.B., Evans, R.H. & Broenkow, W.W. (1983). Phytoplankton pigment concentrations in the Middle Atlantic Bight: comparison of ship determinations and CZCS estimates. *Appl. Opt*. 22. pp. 20–36.

Gordon, H.R. & Voss, K. (1999). *MODIS Normalized Water-leaving Radiance Algorithm Theoretical Basis Document (MOD 18) Version 4*. [Online]. NASA. Available from: http://modis.gsfc.nasa.gov/data/atbd/atbd_mod17.pdf.

Gould Jr., R.W., Arnone, R.A. & Martinolich, P.M. (1999). Spectral Dependence of the Scattering Coefficient in Case 1 and Case 2 Waters. *Applied Optics*. 38 (12). pp. 2377-2383.

Government of Fujairah (2008). *Fujairah Statistics Yearbook 2008*. Statistics and Planning Department Government of Fujairah.

Gower, J., King, S., Borstad, G. & Brown, L. (2005). Detection of intense plankton blooms using the 709 nm band of the MERIS - imaging spectrometer. *International Journal of Remote Sensing*. 26 (9). p. 2005.

Gower, J.F.R., King, S.A., Borstad, G.A. & Brown, L. (2008). The importance of a band at 709 nm for interpreting water-leaving spectral radiance. *Canadian Journal of Remote Sensing*. 34 (3). pp. 287-295.

Gregg, W.W. & Carder, K.L. (1990). A Simple Spectral Solar Irradiance Model for Cloudless Maritime Atmospheres. *Limnology and Oceanography*. 35 (8). pp. 1657-1675.

Group, T.W. (1988). The WAM model-a third generation ocean wave prediction model. *Journal of Physical Oceanography*. 18 (12). pp. 1775–1810.

Grüner, K., Reuter, R. & Smid, H. (1991). A new sensor system for airborne measurements of maritime pollution and of hydrographic parameters. *GeoJournal*. 24 (1). pp. 103-117.

Guenther, B., Barnes, W., Knight, E., Barker, J., Harnden, J., Weber, R., Roberto, M., Godden, G., Montgomery, H. & Abel, P. (1995). *MODIS Calibration: A Brief Review of the Strategy for the At-Launch Calibration Approach*. 1995.

Guinard, N.W. (1971). *The remote sensing of oil slicks*. In: 1971, Ann Arbor: Environmental Research Institute of Michigan, pp. 1005-1011.

Hacker, S.D. & Madin, L.P. (1991). Why habitat architecture and color are important to shrimps living in pelagic Sargassum: Use of camouflage and plant-part mimicry. *Marine ecology progress series. Oldendorf*. 70 (2). pp. 143–155.

Hackett, B., Breivik, Ø. & Wettre, C. (2006). Forecasting the Drift of Objects and Substances in the Ocean. In: E. P. Chassignet & J. Verron (eds.). *Ocean Weather Forecasting*. Springer Netherlands, pp. 507-523.

Hassan, E.M. & Gerges, M.A. (1994). Implications of climate change in the ROPME [Regional Organization for the Protection of the Marine Environment] region: an overview. *UNEP Regional Seas Reports and Studies (UNEP)*.

Hatten, G., Salo, C., Merrow, C. & Parker, K. (1999). *MODIS Operations Concept Document, Version 2.1 MCST Document*.

Hayden, H., Blomster, J., Maggs, C., Silva, P., Stanhope, M. & Waaland, R. (2003). Linnaeus was right all along: Ulva and Enteromorpha are not distinct genera. *European Journal of Phycology*. 38 (3). pp. 277-294.

Hayes, M.O., Hoff, R., Michel, J., Scholz, D. & Shigenaka, G. (1992). *Introduction to coastal habitats and biological resources for oil-spill response*. Seattle, WA (United States): National Oceanic and Atmospheric Administration.

Hennings, I., Matthews, J. & Metzner, M. (1994). Sun glitter radiance and radar cross-section modulations of the sea bed. *Journal of Geophysical Research*. 99 (C8). p. 16.

Hess, M., Koepke, P. & Schult, I. (1998). Optical Properties of Aerosols and Clouds: The Software Package OPAC. *Bulletin of the American Meteorological Society*. 79. pp. 831-844.

Hidy, G.M. & Plate, E.J. (1966). Wind action on water standing in a laboratory channel. *Journal of Fluid Mechanics*. 26. pp. 651–687.

Holben, B.N., Eck, T.F., Slutsker, I., Tanré, D., Buis, J.P., Setzer, A., Vermote, E., Reagan, J.A., Kaufman, Y.J., Nakajima, T. & others (1998). Multi-band automatic sun and sky scanning radiometer system for measurements of aerosols. *Rem. Sens. Environ*. 66. pp. 1–16.

Holt, B. (2004). SAR imaging of the ocean surface. *Synthetic aperture radar marine user's manual*. pp. 25–81.

Hooker, S.B., Esaias, W.E., Feldman, G.C., Gregg, W.W. & MacClain, C.R. (1992). *An overview of SeaWiFS and ocean color*. NASA.

Hoots, F.R. & Roehrich, R.L. (1988). Spacetrack Report No. 3–Models for Propagation of NORAD Element Sets. *Project Spacetrack Reports, Peterson*.

Horstmann, H., Piepen, H.V.D. & Barrot, K.W. (1986). Influence of river water on the southeastern Baltic Sea as observed by NIMBUS 7/CZCS imagery. *Ambio*. pp. 286-289.

Hoult, D.P. (1972). Oil spreading on the sea. *Annual Review of Fluid Mechanics*. 4 (1). pp. 341–368.

Hubert, W.E., Hull, A.N., Morford, D.R. & Englebretson, R.E. (1983). *Forecasters handbook for the Middle East/Arabian Sea*. Monterey Calif: Oean data systems inc.

Hu, C., Muller-Karger, F.E., Taylor, C., Myhre, D., Murch, B., Odriozola, A.L. & Godoy, G. (2003). MODIS detects oil spills in Lake Maracaibo, Venezuela. *Eos AGU Trans*. 84 (33). pp. 313–319.

Hu, C. (2009). A novel ocean color index to detect floating algae in the global oceans. *Remote Sensing of Environment*. 113 (10). pp. 2118-2129.

Hu, C., Li, X., Pichel, W.G. & Muller-Karger, F.E. (2009). Detection of natural oil slicks in the NW Gulf of Mexico using MODIS imagery. *Geophysical Research Letters*. 36. p. 5 PP.

Hughes, P. (1956). A determination of the relation between wind and sea-surface drift. *Quarterly Journal of the Royal Meteorological Society*. 82. pp. 494–502.

Hughes, P. & Hunter, J.R. (1979). *Physical oceanography and numerical modelling of the Kuwait Action Plan Region*. Paris: UNESCO.

Hühnerfuss, H., Alpers, W. & Jones, W.L. (1978). Measurements at 13. 9 GHz of the radar backscattering cross section of the North Sea covered with an artificial surface film. *Radio Science*. 13. pp. 979–983.

Hulst, H.C.V.D. (1981). *Light scattering by small particles*. Courier Dover Publications.

Hunter, J.R. (1985). A review of the residual circulation and mixing processes in the Kap region, with reference to applicable modelling techniques. *Oceanography Modeling of the Kuwait Action Plan (KAP) Region*. pp. 37–45.

Hunter, J.R. (1986). The physical oceanography of the Arabian Gulf: a review and theoretical interpretation of previous observations. In: *The First Arabian Gulf Conference on Environmental and Pollution*. 1986, pp. 1–23.

Hunter, J.R. (1982). The physical oceanography of the Arabian Gulfs: a review and theoretical interpretation of previous observations. In: *Marine Environment and Pollution*. 1982, Kuwait, pp. 1-23.

Hurford, N. (1989). Review of Remote Sensing Technology. In: *The Remote sensing of oil slicks: proceedings of an international meeting organized by the Institute of Petroleum and held in London in May 1988*. 1989, p. 7.

Husain, T. (1995). Kuwaiti oil fires: Regional environmental perspectives. *Pergamon, Oxford (UK)*. 1. p. 292.

Ibrahim, S.A. (2004). Environmental impact of seawater desalination plants. *Environmental Monitoring and Assessment*. 16 (1). pp. 75–84.

IDA (2006). *Worldwide Desalination Plant Inventory*. International Desalination Association.

ITOPF (1986). *Fate of Marine Oil Spills*. London: The International Tanker Owners Pollution Federation Limited.

Jackson, R., Slater, P. & Pinter Jr., P. (1983). Discrimination of growth and water stress in wheat by various vegetation indices through clear and turbid atmospheres. *Remote Sensing of Environment*. 13 (3). pp. 187-208.

Jha, M.N., Levy, J. & Gao, Y. (2008). Advances in Remote Sensing for Oil Spill Disaster Management: State-of-the-Art Sensors Technology for Oil Spill Surveillance. *Sensors*. 8. pp. 236–255.

Johansen, Ø. (2000). DeepBlow-a Lagrangian Plume Model for Deep Water Blowouts. *SINTEF Report STF66 F*. 6 (2). pp. 103-111.

Jones, D.A. (1986). *A field guide to the sea shores of Kuwait and the Arabian Gulf*. University of Kuwait.

Jones, D.A. (1985). The biological characteristics of the marine habitats found within the ROPME Sea Area. In: *Proceedings of the Symposium on Regional Marine Pollution Monitoring and Research Programmes, Al-Ain*. 1985, pp. 71-89.

Jones, D.A., Watt, I. & Woodhouse, T.D. (1994). Surveys and management of the intertidal habitat. *Establishment of a Marine Habitat and Wildlife Sanctuary for the Gulf Region. Final Report for Phase II*. pp. 374–405.

Jordan, R.E. & Payne, J.R. (1980). *Fate and Weathering of Petroleum Spills in the Marine Environment: A Literature Review and Synopsis*. USA: Ann Arbor Science Publishers, Inc.,Ann Arbor, MI.

Junge, C.E. (1963). *Air chemistry and radioactivity*. International geophysics 4. New York, USA: Academic Press.

Kaempf, J. & Sadrinasab, M. (2006). The circulation of the Persian Gulf: a numerical study. *Ocean Science*. 2 (1). pp. 27–41.

Kahru, M., Horstmann, U. & Rud, O. (1994). Satellite detection of increased cyanobacteria blooms in the Baltic Sea: Natural fluctuation or ecosystem change? *Ambio. Stockholm*. 33 (8). pp. 469–472.

Kahru, M., Leppänen, J.M. & Rud, O. (1993). Cyanobacterial blooms cause heating of the sea surface. *Marine Ecology-Progress Series*. 101. pp. 1–1.

Kahru, M., Mitchell, B.G., Diaz, A. & Miura, M. (2004). MODIS Detects a Devastating Algal Bloom in Paracas Bay, Peru. *Eos*. 85 (45). p. 465.

Karathanassi, V., Topouzelis, K., Pavlakis, P. & Rokos, D. (2006). An object-oriented methodology to detect oil spills. *International Journal of Remote Sensing*. 27. pp. 5235–5251.

Karpicz, R., Dementjev, A., Kuprionis, Z., Pakalnis, S., Westphal, R., Reuter, R. & Gulbinas, V. (2005). Laser fluorosensor for oil spot detection. *Lithuanian Journal of Physics*. 45 (3). pp. 213–218.

Karpouzli, E. & Malthus, T. (2007). *Passive Remote Sensing of Oil Slicks: Areview of the State-of-the-Art*.

Kaufman, Y.J. & Tanré, D. (1998). *Algorithm for remote sensing of tropospheric aerosol from MODIS*. Goddard Space Flight Center: NASA MODIS Algorithm Theoretical Basis Document.

Kay, S., Hedley, J.D. & Lavender, S. (2009). Sun Glint Correction of High and Low Spatial Resolution Images of Aquatic Scenes: a Review of Methods for Visible and Near-Infrared Wavelengths. *Remote Sensing*. 1 (4). pp. 697-730.

Khattak, S., Vaughan, R. & Cracknell, A. (1991). Sunglint and its observation in AVHRR data. *Remote Sensing of Environment*. 37 (2). pp. 101-116.

Khordagui, H. (2002). Power and desalination plants. *The Gulf Ecosystem: Health and Sustainability*. pp. 173–191.

Killops, S.D. & Killops, V.J. (1993). *Introduction to organic geochemistry*. Harlow, Essex, England and New York: Longman Scientific & Technical.

King, M.D., Byrne, D.M., Herman, B.M. & Reagan, J.A. (1978). Aerosol size distributions obtained by inversion of spectral optical depth measurements. *Journal of Atmospheric Sciences*. 35. pp. 2153-2167.

Kioeboe, T. & Titelman, J. (1998). Feeding, prey selection and prey encounter mechanisms in the heterotrophic dinoflagellate Noctiluca scintillans. *Journal of Plankton Research*. 20 (8). pp. 1615–1636.

Kirk, J.T. (1994). *Light and photosynthesis in aquatic ecosystems*. 2nd Ed. Cambridge University Press.

Koleske, J.V. (1995). *Paint and coating testing manual: Fourteenth edition of the Gardner-Sward handbook*. Gardner-Sward handbook. Philadelphia, PA: ASTM International.

Kononen, K. (1992). *Dynamics of the toxic cyanobacterial blooms in the Baltic Sea*.

Kostianoy, A.G., Lebedev, S.A., Litovchenko, K.T., Stanichny, S.V. & Pichuzhkina, O.E. (2004). Satellite remote sensing of oil spill pollution in the southeastern Baltic Sea. *Gayana (Concepción)*. 68. pp. 327–2332.

Król, T., Stelmaszewski, A. & Freda, W. (2006). Variability in the optical properties of a crude oil- seawater emulsion. *Oceanologia*. 48. pp. 203–211.

Kruse, F.A., Lefkoff, A.B., Boardman, J.W., Heidebrecht, K.B., Shapiro, A.T., Barloon, P.J. & Goetz, A.F.H. (1993). *The spectral image processing system (SIPS)-interactive visualization and analysis of imaging spectrometer data*. In: 1 August 1993, pp. 192-201.

Kubat, M., Holte, R.C. & Matwin, S. (1998). Machine Learning for the Detection of Oil Spills in Satellite Radar Images. *Machine Learning*. 30. pp. 195-215.

Kwarteng, A.Y., Singhroy, V., Saint-Jean, R. & Al-Ajmi, D. (1997). Radarsat SAR Data Assessment of the Oil Lakes in the Greater Burgan Oil Field, Kuwait. In: *proceedings of International Symposium: Geomatics in the Era of Radarsat, Ottawa, Canada*. 1997.

Langmuir, I. (1938). Surface motion of water induced by wind. *Science*. 87 (2250). pp. 119–123.

Lardner, R.W., Belen, M.S. & Cekirge, H.M. (1982). Finite difference model for tidal flows in the Arabian Gulf. *Computers & Mathematics with Applications*. 8 (6). pp. 425-444.

Lattemann, S. & Höpner, T. (2008). Environmental impact and impact assessment of seawater desalination. *Desalination*. 220 (1-3). pp. 1-15.

Law, R.J. (1981). Hydrocarbon concentrations in water and sediments from UK marine waters, determined by fluorescence spectroscopy. *Marine Pollution Bulletin*. 12 (5). pp. 153-157.

Lee, J.K. & Hirayama, K. (1992). Effects of salinity, food level and temperature on the population growth of Noctiluca scintillans (Macartney). *Bulletin of the Faculty of Fisheries-Nagasaki University (Japan)*. 71. pp. 163-168.

Lehr, W.J. & Simecek-Beatty, D. (2000). The Relation of Langmuir Circulation Processes to the Standard Oil Spill Spreading, Dispersion, and Transport Algorithms. *Spill Science & Technology Bulletin*. 6 (3). pp. 247–253.

Lentz, S.A., Felleman, F. & Advocates, O. (2003). *Oil Spill Prevention: A Proactive Approach*. In: 2003, Washington, DC: American Petroleum Institute, p. 25.

Linden, O., Abdulraheem, M.Y., Gerges, M.A., Alam, I., Behbehani, M., Borhan, M.A. & Al-Kassab, L.F. (1990). *State of the marine environment in the ROPME Sea Area.* UNEE Nairobi, Kenya: UNEP Regional Seas Reports and Studies.

Literathy, P., Khan, N.Y. & Linden, O. (2002). Oil and petroleum industry. *The Gulf ecosystem: health and sustainability*. p. 127.

Littler, D.S., Littler, M.M., Bucher, K.E. & Norris, J.N. (1989). *Marine plants of the Caribbean*. Smithsonian Institution Press.

Liu, A.K., Wu, S.Y., Tseng, W.Y. & Pichel, W.G. (2000). Wavelet analysis of SAR images for coastal monitoring. *Canadian journal of remote sensing*. 26 (6). pp. 494–500.

Liu, M., Westphal, D.L., Walker, A.L., Holt, T.R., Richardson, K.A. & Miller, S.D. (2007). COAMPS Real-Time Dust Storm Forecasting during Operation Iraqi Freedom. *Weather and Forecasting*. 22. p. 192.

Lunel, T., Davies, L., Shimwell, S., Byfield, V., Boxall, S. & Gurney, C. (1997). *Review of aerial/satellite remote sensing carried out at the Sea empress incident*. In: 1997, Copenhagen, Denmark, pp. 731–732.

MacDonald, I.R., Guinasso, N.L., Ackleson, S.G., Amos, J.F., Duckworth, R., Sassen, R. & Brooks, J.M. (1993). Natural oil slicks in the Gulf of Mexico visible from space. *Journal of Geophysical Research*. 98. pp. 16351-16364.

Madhupratap, M., Kumar, S.P., Bhattathiri, P.M.A., Kumar, M.D., Raghukumar, S., Nair, K.K.C. & Ramaiah, N. (1996). *Mechanism of the biological response to winter cooling in the northeastern Arabian Sea*.

Marmorino, G.O., Smith, G.B., Toporkov, J.V., Sletten, M.A., Perkovic, D. & Frasier, S.J. (2008). Evolution of ocean slicks under a rising wind. *Journal of Geophysical Research*. 113 (C4). p. C04030.

Matthews, J. (2005). Stereo observation of lakes and coastal zones using ASTER imagery. *Remote Sensing of Environment*. 99 (1-2). pp. 16-30.

Matthews, J.P., Wismann, V.R. & Lwiz, K. (1997). The observation of the surface roughness characteristics of the Rhine plume frontal boundaries by simultaneous airborne thematic mapper and multifrequency helicopter-borne radar scatterometer. *International Journal of Remote Sensing*. 18. pp. 2021-2033.

Mazur-Marzec, H. & Plinski, M. (2009). Do toxic cyanobacteria blooms pose a threat to the Baltic ecosystem? *Oceanologia*. 51 (3). pp. 293–319.

McClain, C.R., Evans, R.H., Brown, J.W. & Darzi, M. (1995). SeaWiFS quality control masks and flags: initial algorithms and implementation strategy. *Vol*. 28. pp. 3–7.

McGill, R., Tukey, J. & Larsen, W. (1978). Variations of Box Plots. *The American Statistician*. 32 (1). pp. 12-16.

Melsheimer, C. & Keong, K.L. (2001). Sun glitter in Spot images and the visibility of oceanic phenomena. In: *Paper presented at the 22nd Asian Conference on Remote Sensing*. 2001, p. 9.

Melshelmer, C., Alpers, W. & Gade, M. (1996). Investigation of multifrequency/multipolarization radar signaturesof rain cells, derived from SIR-C/X-SAR data. In: *Remote Sensing for a Sustainable Future*. 1996, Lincoln, NE , USA, pp. 1370 - 1372.

MEMAC (2008). *Biennial report 2006-2008*. Bahrain: Marine Emergency Mutual Aid Centre (MEMAC).

Mészáros, E. (1981). *Atmospheric chemistry: fundamental aspects*. Elsevier.

Metsamaa, L., Kutser, T. & Stroembeck, N. (2006). Recognising cyanobacterial blooms based on their optical signature: a modelling study. *Boreal Environment Research*. 11 (6). pp. 493–506.

Michel, J. (1992). Oil behavior and toxicity. In: *Introduction to coastal habitats and biological resources for spill response*. Report HMRAD, p. 10.

Mielke, J.E. (1990). Oil in the ocean: the short-and long-term impacts of a spill. In: *Cong research service report for Congress, July*. 1990, p. 1990.

Miller, R.L. & McKee, B.A. (2004). Using MODIS Terra 250 m imagery to map concentrations of total suspended matter in coastal waters. *Remote Sensing of Environment*. 93 (1-2). pp. 259–266.

Miller, S.D. (2003). A consolidated technique for enhancing desert dust storms with MODIS. *Geophysical Research Letters*. 30. p. 4.

MODIS Cloud Mask Team,, K., Ackerman, S., Strabala, K... & Menzel, P. (2006). *Discriminating clear-sky from cloud with MODIS algorithm theoretical basis document (mod35)*.

Najafi, H.S. (1997). *Modelling tides in the Persian Gulf using dynamic nesting*. PhD. University of Adelaide, Dept. of Applied Mathematics.

NASA (2010). *MODIS Website - Components of MODIS*. [Online]. 2010. Available from: http://modis.gsfc.nasa.gov/about/specifications.php. [Accessed 11 May 2010].

NASA Johnson Space Center (1991). *Image Science & Analysis Laboratory,* [Online]. 1991. Available from: http://eol.jsc.nasa.gov.

NASA OBPG (2010). *NASA Oceancolour Level-3 prodcuts*. [Online]. 2010. Available from: http://oceancolor.gsfc.nasa.gov/cgi/l3. [Accessed 6 December 2010].

NASA OceanColor (2010). *Ocean Color Reprocessing 2009*. [Online]. 2010. Available from: http://oceancolor.gsfc.nasa.gov/REPROCESSING/R2009/modisa_calibration/. [Accessed 9 January 2011].

Nishihama, M., Wolfe, R., Solomon, D., Patt, F., Blanchette, J., Fleig, A. & Masuoka, E. (1997). MODIS level 1A earth location: algorithm theoretical basis document version 3.0. *SDST-092, MODIS Science Data Support Team*. p. 147.

NOAA (2002). *Trajectory Analysis Handbook*. [Online]. NOAA Hazardous Material Response Division. Available from: http://response.restoration.noaa.gov/book_shelf/939_trajanalysis.pdf.

NOAA Magazine Online (2010). *NOAA Magazine Online (Story 91)*. [Online]. 2010. NOAA Magazine Online (Story 91). Available from: http://www.magazine.noaa.gov/stories/mag91.htm. [Accessed 26 April 2010].

NOAA Web Update (2010). *DeepH2Oweb_25Apr.doc*. [Online]. 2010. Available from: http://www.incidentnews.gov/attachments/8220/526199/DeepH2Oweb_25Apr.doc. [Accessed 22 July 2010].

Norse, E.A. & Amos, J. (2010). *Impacts, Perception, and Policy Implications of the Deepwater Horizon Oil and Gas Disaster*. p. 16.

North, P., Grey, W., Heckel, A., Brockmann, C., Consult, B., Regner, P. & ESRIN, E. (2009). *MERIS/AATSR Synergy Algorithms for Cloud Screening, Aerosol Retrieval and Atmospheric Correction*. p. 44.

OBPG (2010a). *OceanColor FTP Directory Page*. [Online]. 2010a. Available from: http://oceancolor.gsfc.nasa.gov/ftp.html. [Accessed 15 June 2010].

OBPG (2010b). *SeaDAS Ancillary Data Info*. [Online]. 2010b. Available from: http://oceancolor.gsfc.nasa.gov/seadas/doc/toplevel/anc_info.html. [Accessed 13 June 2010].

O'Brien, J.A. (1971). Wind tunnel experiments on oil slick transport. *Journal of Hydraulic Research*. 9 (2). pp. 197–215.

OceanColor (2010). *OceanColor Formats*. [Online]. 2010. Available from: http://oceancolor.gsfc.nasa.gov/DOCS/ocformats.html#3. [Accessed 30 May 2010].

Oostdam, B.L. (1980). Oil pollution in the Persian Gulf and approaches, 1978. *Marine Pollution Bulletin*. 11 (5). pp. 138–144.

Osadchy, V.Y., Shifrin, K.S. & Gurevich, I.Y. (1994). Remote sensing and measurement of the thickness of oil films on the sea surface using reflectivity contrast. In: J. S. Jaffe (ed.). *Ocean Optics XII*. 26 October 1994, Bergen, Norway: SPIE, pp. 747-758.

Otremba, Z. (1999). Selected results of light field modeling above the sea surface covered by thin oil film. *Computer Simulation and Boundary field problems, Environmental Simulations*. 41. pp. 5-13.

Otremba, Z. & Król, T. (2001). Light attenuation parameters of polydisperse oil-in-water emulsion. *Optica Applicata*. 31 (3). pp. 599–609.

Otremba, Z. & Piskozub, J. (2001). Modelling of the optical contrast of an oil film on a sea surface. *Opt. Express*. 9 (8). pp. 411–416.

Owens, E.H. & Teal, A.R. (1990). Shoreline clean-up following the "Exxon Valdez" oil spill-field data collection within the SCAT program. In: *Proceedings of the 13th Arctic and Marine Oil Spill Program (AMOP) Technical Seminar*. 1990, pp. 411–421.

Paerl, H.W. & Ustach, J.F. (1982). Blue-green algal scums: an explanation for their occurrence during freshwater blooms. *Limnology and Oceanography*. 27 (2). pp. 212–217.

Pavia, R. & Payton, D. (1983). An approach to observing oil at sea. In: *Proceedings of the 1983 Oil Spill Conference, 28 February–3 March*. 1983, pp. 345–349.

Payne, J.R. (1994). Section 4.0. Use of oil spill weathering data in toxicity studies for chemically and naturally dispersed oil slicks. In: *Proceedings of the First Meeting of the Chemical Response to Oil Spills: Ecological Effects Research Forum. Marine Spill Response Corporation, Washington, DC. MSRC Technical Report Series*. 1994, pp. 94–017.

Perrone, T.J. (1979). *Winter Shamal in the Persian Gulf.* Monterey California: Naval environmental prediction research facility.

PML (2010). *DSRS: MODIS downlink packet format*. [Online]. 2010. Available from: http://www.sat.dundee.ac.uk/modisformat.html#ccsds. [Accessed 28 May 2010].

Price, A.R.G. & Sheppard, C.R.C. (1991). The Gulf: Past, present and possible future states. *Marine Pollution Bulletin*. 22 (5). pp. 222–227.

Privett, D.W. (1959). *Monthly charts of evaporation from the Northern Indian Ocean (including the Red Sea and the Persian Gulf): QJR Met*. Soc.

Prospero, J.M., Ginoux, P., Torres, O., Nicholson, S.E. & Gill, T.E. (2002). Environmental characterization of global sources of atmospheric soil dust identified with the Nimbus 7 Total Ozone Mapping Spectrometer (TOMS) absorbing aerosol product. *Rev. Geophys*. 40 (1). p. 1002.

Purser, B.H. & Seibold, E. (1973). The principal environmental factors influencing Holocene sedimentation and diagenesis in the Persian Gulf. *The Persian Gulf: New York, Springer-Verlag*. pp. 1–9.

Pye, K. (1991). Aeolian Dust and Dust Deposits. *Encyclopedia of earth system science*. p. 35.

Qasim, S.Z. (1982). Oceanography of the northern Arabian Sea. *Deep Sea Research Part A. Oceanographic Research Papers*. 29 (9). pp. 1041–1068.

Radwan, S.S., Al-Hasan, R.H., Al-Awadhi, H., Salamah, S. & Abdullah, H.M. (1999). Higher oil biodegradation potential at the Arabian Gulf coast than in the water body. *Marine Biology*. 135 (4). pp. 741-745.

Rakha, K., Al-Salem, K. & Neelamani, S. (2007). Hydrodynamic Atlas for the Arabian Gulf. *J Coast Res*. 50. pp. 550–554.

Randall, J.E. & Hoover, J.P. (1995). *Coastal fishes of Oman*. University of Hawaii Press.

Rand, R.S., Satterwhite, M.B., Davis, D.A., Anderson, J.E. & VA, A.T.E.C.F.B. (1992). *Methods of monitoring the Persian Gulf oil spill using digital and hardcopy multiband data*. Fort Belvoir, VA, USA: Army Topographic Engineering Center.

Rao, D.V., Al-Hassan, J.M., Al-Yamani, F., Al-Rafaie, K., Ismail, W., Nageswara Rao, C.V. & Al-Hassan, A. (2003). Elusive red tides in Kuwait coastal waters. *Harmful Algae News*. 24. pp. 10–13.

Rao, S. & Al-Yamani, F. (1998). Phytoplankton ecology in the waters between Shatt Al-Arab and Straits of Hormuz, Arabian Gulf: A review. *Plankton Biology and Ecology*. 45 (2). pp. 101–116.

Readman, J.W., Bartocci, J., Tolosa, I., Fowler, S.W., Oregioni, B. & Abdulraheem, M.Y. (1996). Recovery of the coastal marine environment in the Gulf following the 1991 war-related oil spills. *Marine Pollution Bulletin*. 32 (6). pp. 493–498.

Reynolds, R.M. (2002a). Meteorology and climate. *The Gulf Ecosystem: Health and Sustainability*. pp. 41–52.

Reynolds, R.M. (2002b). Oceanography. *The Gulf Ecosystem: Health and Sustainability, Backhuys Publishers, Leiden*. pp. 53–64.

Reynolds, R.M. (1993). Physical oceanography of the Gulf, strait of Hormuz, and the gulf of Oman- results from the Mt Mitchell expedition. *Marine Pollution Bulletin*. 27. pp. 35–59.

Rezai, H., Wilson, S., Claereboudt, M. & Riegl, B. (2004). Coral reef status in the ROPME Sea Area: Arabian/Persian Gulf, Gulf of Oman and Arabian sea. In: *Status of Coral Reefs of the World: 2004*. 2004, Queensland, Australia: Australian Institute of Marine Science,, pp. 155-170.

Richards, J.A. (1993). *Remote sensing digital image analysis: An introduction*. 2nd Ed. New York: Springer-Verlag.

Robinson, I.S. (2004). *Measuring the oceans from space: the principles and methods of satellite oceanography*. Springer/Praxis.

Robinson, I.S. & Mitchelson, E.G. (1983). Satellite Observations of Ocean Colour [and Discussion]. *Philosophical Transactions of the Royal Society of London. Series A, Mathematical and Physical Sciences*. 309 (1508). pp. 415–432.

Robinson, I.S., Wells, N.C. & Charnock, H. (1984). The sea surface thermal boundary layer and its relevance to the measurement of sea surface temperature by airborne and spaceborne radiometers. *International journal of remote sensing*. 5. pp. 19–45.

Robinson, W.D., Schmidt, G.M., McClain, C.R. & Werdell, P.J. (2000). Changes made in the operational SeaWiFS processing. *SeaWiFS postlaunch calibration and validation analyses, Part*. 2. pp. 1999–206892.

Rochford, D.J. (1964). Salinity maxima in the upper 1000 metres of the north Indian Ocean. *Australian Journal of Marine and Freshwater Research*. 15. pp. 1–24.

Rodrigue, J.P. (2004). Straits, passages and chokepoints: a maritime geostrategy of petroleum distribution. *Les Cahiers de Geographie du Quebec*. 48 (135). pp. 357–374.

Rong-Rong Li, Kaufman, Y., Bo-Cai Gao & Davis, C. (2003). Remote sensing of suspended sediments and shallow coastal waters. *IEEE Transactions on Geoscience and Remote Sensing*. 41 (3). pp. 559-566.

ROPME (2003). *State of the Marine Environment Report (SOMER)*. Kuwait: ROPME.

Rouse, J.W., Haas, R.H., Schell, J.A., Deering, D.W. & Harlan, J.C. (1974). Monitoring the vernal advancement and retrogradation (green wave effect) of natural vegetation. *NASA/GSFC Type III Final Report, Greenbelt, Md*. 371.

Ruddick, K.G., Gons, H.J., Rijkeboer, M. & Tilstone, G. (2001). Optical Remote Sensing of Chlorophyll a in Case 2 Waters by Use of an Adaptive Two-Band Algorithm with Optimal Error Properties. *Applied Optics*. 40 (21). pp. 3575-3585.

Sadiq, M. & McCain, J.C. (1993). *The Gulf War aftermath*. Springer.

Salem, F. & Kafatos, M. (2001). Hyperspectral image analysis for oil spill mitigation. In: *Paper presented at the 22nd Asian Conference on Remote Sensing*. 2001, p. 9.

Salem, F., Kafatos, M., El-Ghazawi, T., Gomez, R. & Yang, R. (2002). Hyperspectral Image Analysis for Oil Spill Detection. In: *Proceedings: JPL AVIRIS Workshop 2002*. 2002, Pasadena: Jet Propulsion Laboratory., p. 323.

Salisbury, J.W., D'Aria, D.M. & Sabins Jr, F.F. (1993). Thermal infrared remote sensing of crude oil slicks. *Remote Sensing of Environment*. 45 (2). pp. 225–231.

Salomonson, V.V., Barnes, W.L., Maymon, P.W., Montgomery, H.E. & Ostrow, H. (1989). MODIS: advanced facility instrument for studies of the Earth as asystem. *IEEE Transactions on Geoscience and Remote Sensing*. 27 (2). pp. 145–153.

Samberg, A. (2005). Advanced oil pollution detection using an airborne hyperspectral lidar technology. In: *Proceedings of SPIE*. 2005, p. 308.

Sato, M.S., Suzuki, M. & Hayashi, H. (1998). The Density of a Homogeneous Population of Cells Controls Resetting of the Program for Swarmer Formation in the Unicellular Marine MicroorganismNoctiluca scintillans. *Experimental Cell Research*. 245 (2). pp. 290-293.

Sauer, T.C., Michel, J., Hayes, M.O. & Aurand, D.V. (1998). Hydrocarbon characterization and weathering of oiled intertidal sediments along the Saudi Arabian Coast two years after the Gulf War oil spill. *Environment International*. 24 (1-2). pp. 43-60.

Scholz, D., Kucklick, J., Pond, R., Walker, A., Bostrom, A. & Fischbeck, P. (1999). *Fate of Spilled Oil in Maue Waters: Where Does It Go?* (4691). p. 57.

Schott, J.R., Kuo, S.D., Brown, S.D. & Raqueno, R.V. (1997). Prediction of observed image spectra using synthetic image generation models. In: M. R. Descour & S.

S. Shen (eds.). *Imaging Spectrometry III*. 31 October 1997, San Diego, CA, USA: SPIE, pp. 81-93.

Sellner, K.G. (1997). Physiology, ecology, and toxic properties of marine cyanobacteria blooms. *Limnology and Oceanography*. 42 (5). pp. 1089–1104.

Sengupta, R., Fondekar, S. & Alagarsamy, R. (1993). State of oil pollution in the northern Arabian Sea after the 1991 Gulf oil spill. *Marine Pollution Bulletin*. 27. pp. 85-91.

Shaban, A., Ghoneim, E., Hamzé, M. & El-Baz, F. (2007). A post-conflict assessment to interpret the distribution of oil spill off-shore Lebanon using remote sensing. *Lebanese Science Journal*. 8 (2). p. 75.

Sheppard, C., Price, A. & Roberts, C. (1992). *Marine ecology of the Arabian region: patterns and processes in extreme tropical environments*. Academic Pr.

Sheppard, C.R. (1993). Physical environment of the Gulf relevant to marine pollution: An overview. *Marine Pollution Bulletin*. 27. pp. 3–8.

Shettle, E.P. & Fenn, R.W. (1979). *Models for the aerosols of the lower atmosphere and the effects of humidity variations on their optical properties*.

Shetye, S.R., Gouveia, A.D. & Shenoi, S.S. (1994). Circulation and water masses of the Arabian Sea. *Journal of Earth System Science*. 103 (2). pp. 107–123.

Shi, L., Zhang, X., Seielstad, G., Zhao, C. & He, M. (2007). *Oil Spill Detection by MODIS Images using Fuzzy Cluster and Texture Feature Extraction*. In: 6 2007, Aberdeen, Scotland, UK, pp. 1-5.

Siegel, D.A., Wang, M., Maritorena, S. & Robinson, W. (2000). Atmospheric Correction of Satellite Ocean Color Imagery: The Black Pixel Assumption. *Applied Optics*. 39 (21). pp. 3582-3591.

Small, J. & Martin, J. (2002). The generation of non-linear internal waves in the Gulf of Oman. *Continental Shelf Research*. 22 (8). pp. 1153-1182.

Smith, C.L. (1974). Determination of the leeway of oil slicks. *United States Coast Guard Report CG-D-60-75*.

Smith, J.A. (2002). Observations of Langmuir Circulation From FLIP. In: *AGU Fall Meeting Abstracts*. 2002, p. 0215.

Smith, J. (1968). *'Torrey Canyon' pollution and marine life. report by the Plymouth Laboratory of the Marine Biological Association of the United Kingdom*. London, UK: Cambridge University Press.

Solberg, A.S. (2005). Automatic detection and estimating confidence for oil spill detection in SAR images. In: *Proceedings of the International Society for Photogrammetry and Remote Sensing 2005*. 2005, p. 6.

Sorkhoh, N., Al-Hasan, R., Radwan, S. & Hopner, T. (1992). Self-cleaning of the Gulf. *Nature*. 359 (6391). p. 109.

Spaulding, M.L. (1988). A state-of-the-art review of oil spill trajectory and fate modeling*. *Oil and Chemical Pollution*. 4 (1). pp. 39–55.

Squires, G.L. (2001). *Practical physics*. Cambridge University Press.

Stolzenbach, K.D., Madsen, O.S., Adams, E.E., Pollack, A.M. & Copper, C.K. (1977). *Review and evaluation of basic techniques for predicting the behavior of surface oil slicks*. Massachusetts Institute of Technology, Cambridge, MA.

Strabala, K.I., Gumley, L.E., Rink, T.D., Huang, H. & Dengel, R. (2003). *MODIS direct broadcast products and applications*. In: 1 April 2003, SPIE, pp. 402-412.

Stramma, L., Cornillon, P., Weller, R.A., Price, J.F. & Briscoe, M.G. (1986). Large Diurnal Sea Surface Temperature Variability: Satellite and In Situ Measurements. *Journal of Physical Oceanography*. 16. pp. 827-837.

Stringer, W.J., Dean, K.G., Guritz, R.M., Garbeil, H.M., Groves, J.E. & Ahlnaes, K. (1992). Detection of petroleum spilled from the MV Exxon Valdez. *International Journal of Remote Sensing*. 13 (5). pp. 799–824.

Stumpf, R.P., Arnone, R.A., Gould, R.W., Martinolich, P.M. & Ransibrahmanakul, V. (2003). A partially coupled ocean-atmosphere model for retrieval of water-leaving radiance from SeaWiFS in coastal waters. *NASA Tech. Memo*. 206892. pp. 51–59.

Sugden, W. (1963). The hydrography of the Persian Gulf and its significance in respect to evaporative deposition. *American Journal of Science*. 261. pp. 741–755.

Su, W., Charlock, T.P. & Rutledge, K. (2002). Observations of reflectance distribution around sunglint from a coastal ocean platform. *Applied optics*. 41 (35). pp. 7369–7383.

Svejkovsky, J. & Muskat, J. (2006). *Real-time detection of oil slick thickness patterns with a portable multispectral sensor*. U.S. Department of the Interior Minerals Management Service.

Sverdrup, H.U., Johnson, M.W. & Fleming, R.H. (1942). *The oceans, their physics, chemistry, and general biology*. Prentice-Hall, Inc.

Swift, S.A. & Bower, A.S. (2003). Formation and circulation of dense water in the Persian/Arabian Gulf. *J. Geophys. Res*. 108 (1). p. 3004.

Toller, G.N., Isaacman, A., Kuyper, J. & Salomonson, V. (2003). *MODIS Level 1B product user's guide*. Greenbelt, MD 20771: NASA/Gooddard Space Flight Center.

Trieschmann, O., Hunsänger, T. & Barjenbruch, U.B. (2001). A multiple remote sensor system for the aerial surveillance of the North Sea and Baltic Sea. In: *Presented at the Fifth International Airborne Remote Sensing Conference*. 2001, p. 20.

Trivero, P., Fiscella, B., Gomez, F. & Pavese, P. (1998). SAR detection and characterization of sea surface slicks. *International Journal of Remote Sensing*. 19 (3). pp. 543–548.

True, W.R. (1999). Worldwide gas processing continues to expand, shift balance. *Oil and Gas Journal*. 97 (24). pp. 41-46.

Tseng, W.Y. & Chiu, L.S. (1994). AVHRR observations of Persian Gulf oil spills. In: *Surface and Atmospheric Remote Sensing: Technologies, Data Analysis and Interpretation*. 1994, pp. 779– 782.

Tsukihara, T. (1995). Weathering experiment on spilled crude oils using a circulating water channel. In: *Proceedings: prevention, behavior, control, cleanup*. 1995, p. 435.

Tucker, C.J. (1979). Red and photographic infrared linear combinations for monitoring vegetation. *Remote Sensing of Environment*. 8 (2). pp. 127-150.

Tudhope, A.W., Lea, D.W., Shimmield, G.B., Chilcott, C.P. & Head, S. (1996). Monsoon climate and Arabian Sea coastal upwelling recorded in massive corals from southern Oman. *Palaios*. 11 (4). pp. 347–361.

UNEP (1983). *Action Plan for the protection of the marine environment and the coastal areas of Bahrain, Iran, Iraq, Kuwait, Oman, Qatar, Saudi Arabia and the United Arab Emirate.* UNEP Regional Seas Reports and Studie. UNEP.

Valenzuela, G.R. (1978). Theories for the interaction of electromagnetic and oceanic waves—A review. *Boundary-Layer Meteorology*. 13 (1). pp. 61–85.

Visible Earth (2010). *Space Radar Image of North Sea, Germany*. [Online]. 23 October 2010. Available from: http://visibleearth.nasa.gov/view_rec.php?id=416. [Accessed 23 October 2010].

Walters, K.R. & Sjoberg, W.F. (1990). *The Persian Gulf Region-A Climatological Study*. Air force environmental technical applications center.

Wang, M. (2000). The SeaWiFS atmospheric correction algorithm updates. *SeaWiFS postlaunch calibration and validation analyses, Part*. 1. pp. 2000–206892.

Wang, M. & Bailey, S.W. (2000). *Correction of the Sunglint Contamination on the SeaWiFS Aerosol Optical Thickness Retrievals*. p. 6.

Wang, M. & Shi, W. (2007). The NIR-SWIR combined atmospheric correction approach for MODIS ocean color data processing. *Optics Express*. 15 (24). pp. 15722-15733.

WCMC (1991). *Gulf war environmental information service impact on the land and atmosphere*. London: World Conservation Monitoring Centre.

Wells, J. & Huh, O. (1984). Fall-Season Patterns of Turbidity and Sediment Transport in the Korea Strait and Southeastern Yellow Sea. In: *Ocean Hydrodynamics of*

the Japan and East China Seas. Elsevier, pp. 387-397.

Werdell, P.J., Franz, B.A., Bailey, S.W., Harding Jr, L.W. & Feldman, G.C. (2007). Approach for the long-term spatial and temporal evaluation of ocean color satellite data products in a coastal environment. In: *Proc. SPIE 6680*. 2007, San Diego, CA, USA: International society for optics and photonics.

Wheeler, R.B. (1978). *The fate of petroleum in the marine environment*. Houston, TX: Exxon Production Research Co.

Wolfe, R.E., Nishihama, M., Fleig, A.J., Kuyper, J.A., Roy, D.P., Storey, J.C. & Patt, F.S. (2002). Achieving sub-pixel geolocation accuracy in support of MODIS land science. *Remote Sensing of Environment*. 83 (1-2). pp. 31-49.

Wright, J.L. (1974). *A hydrographic and acoustic survey of the Persian Gulf*. MSc. Naval Postgraduate School.

Xiong, X., Salomonson, V.V., Kuyper, J., Tan, L., Chiang, K., Sun, J. & Barnes, W.L. (2005). *Status of the MODIS Level 1B Algorithms and Calibration Tables*. In: 2005, pp. 2231–2234.

Xiong, X. & Barnes, W. (2006). An overview of MODIS radiometric calibration and characterization. *Advances in Atmospheric Sciences*. 23 (1). pp. 69-79.

Yender, R., Michel, J. & Lord, C. (2002). *Managing seafood safety after an oil spill*. Hazardous Materials Response Division, Office of Response and Restoration, National Oceanic and Atmospheric Administration.

Yoshida, J., Matsuyama, M., Senjyu, T., Ishimaru, T., Morinaga, T., Arakawa, H., Kamatani, A., Maeda, M., Otsuki, A., Hashimoto, S., Kasuga, I., Koike, Y., Mine, Y., Kurita, Y., Kitazawa, A., Noda, A., Hayashi, T., Miyazaki, T. & Takahashi, K. (1998). Hydrography in the RSA during the RT/V Umitaka-Maru Cruises. *Offshore Environment of the ROPME Sea Area after the War-related Oil Spills*. pp. 1–22.

Zarba, M., Mohammad, O., Anderlini, V., Literathy, P. & Shubo, F. (1985). Petroleum residues in surface sediments of Kuwait. *Marine pollution bulletin*. 16 (5). pp. 209–211.

Zhang, Y. (2000). Analysis of oil film spectrum and monitoring oil spilled by remote sensing. *Marine environmental science/Haiyang Huanjing Kexue. Dalian*. 19 (3). pp. 5–10.

Zheng, Q., Yan, X.H., Huang, N.E., Klemas, V. & Pan, J. (1997). The effects of water temperature on radar scattering from the water surface: An X-band laboratory study. *The Global atmosphere and ocean system*. 5 (3). pp. 273–294.

Appendices

A: Gulf of Mexico oil spill observed in different satellite images

Some of the different satellite based remote sensing images of the Deepwater Horizon oil spill that have occurred in the Gulf of Mexico on 22th April, 2010:

24th April, 2010

- The Phased Array type L-band Synthetic Aperture Radar (PALSAR) instrument on-board the Advanced Land Observing Satellite (ALOS)

25th April, 2010

- MODIS sensor on-board the Aqua satellite
- SPOT 5 satellite
- The Advanced Land Imager (ALI) on the Earth Observing-1 (EO-1) satellite
- The Medium Resolution Imaging Spectrometer (MERIS) instrument on-board the ENVISAT satellite
- TerraSAR-X satellite

26th April, 2010

- QuickBird satellite
- Advanced Synthetic Aperture Radar (ASAR) instrument on-board the ENVISAT satellite
- RADARSAT-1 satellite

27th April, 2010

- The WorldView-2 satellite

29th April, 2010

- GeoEye-1 satellite

30th April, 2010

- Constellation of small Satellites for the Mediterranean basin Observation (COSMO-SkyMed)

1st May, 2010

- Landsat 7 Enhanced Thematic Mapper Plus (ETM+) satellite
- Multi-angle Imaging SpectroRadiometer (MISR) instrument on the Terra satellite
- The Advanced Spaceborne Thermal Emission and Reflection Radiometer (ASTER) instrument on the Terra satellite

4th May, 2010

- The International Space Station (ISS) Expedition 23 m

Figure A.1. The Phased Array type L-band Synthetic Aperture Radar (PALSAR) image of the Gulf of Mexico oil spill on taken on 24th April, 2010 at 16:25 UTC. Observation mode is FBS (original resolution 100 m/pixel) at an off-nadir angle of 28.8°, path 482 and in a descending direction[1]. The use of the L-band leads to a reduction in the contrast of the spill, but shape detection is still possible.

[1] http://www.palsar.ersdac.or.jp/e/collection/-topic-image/

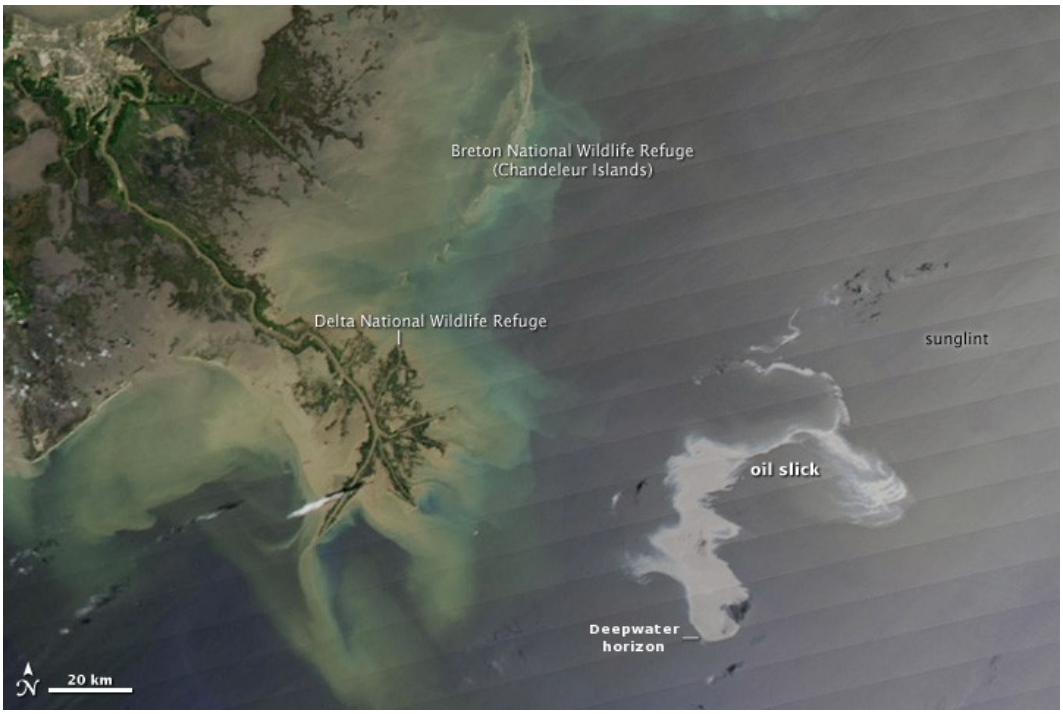

Figure A.2. A 250 m/pixel resolution MODIS Aqua image of the Deepwater Horizon oil spill in the Gulf of Mexico (positioned at latitude N28° 44.20′ and longitude W88° 23.23′) on 25th April, 2010 in natural RGB colour composite corresponding to bands λ_1=645, λ_4=555, λ_3=469 nm (λ_4 and λ_3 oversampled from the 500 m/pixel band group). The spill appears brighter than water because of its position within the sun glint area © NASA[2].

[2] http://www.flickr.com/photos/gsfc/4557390157/

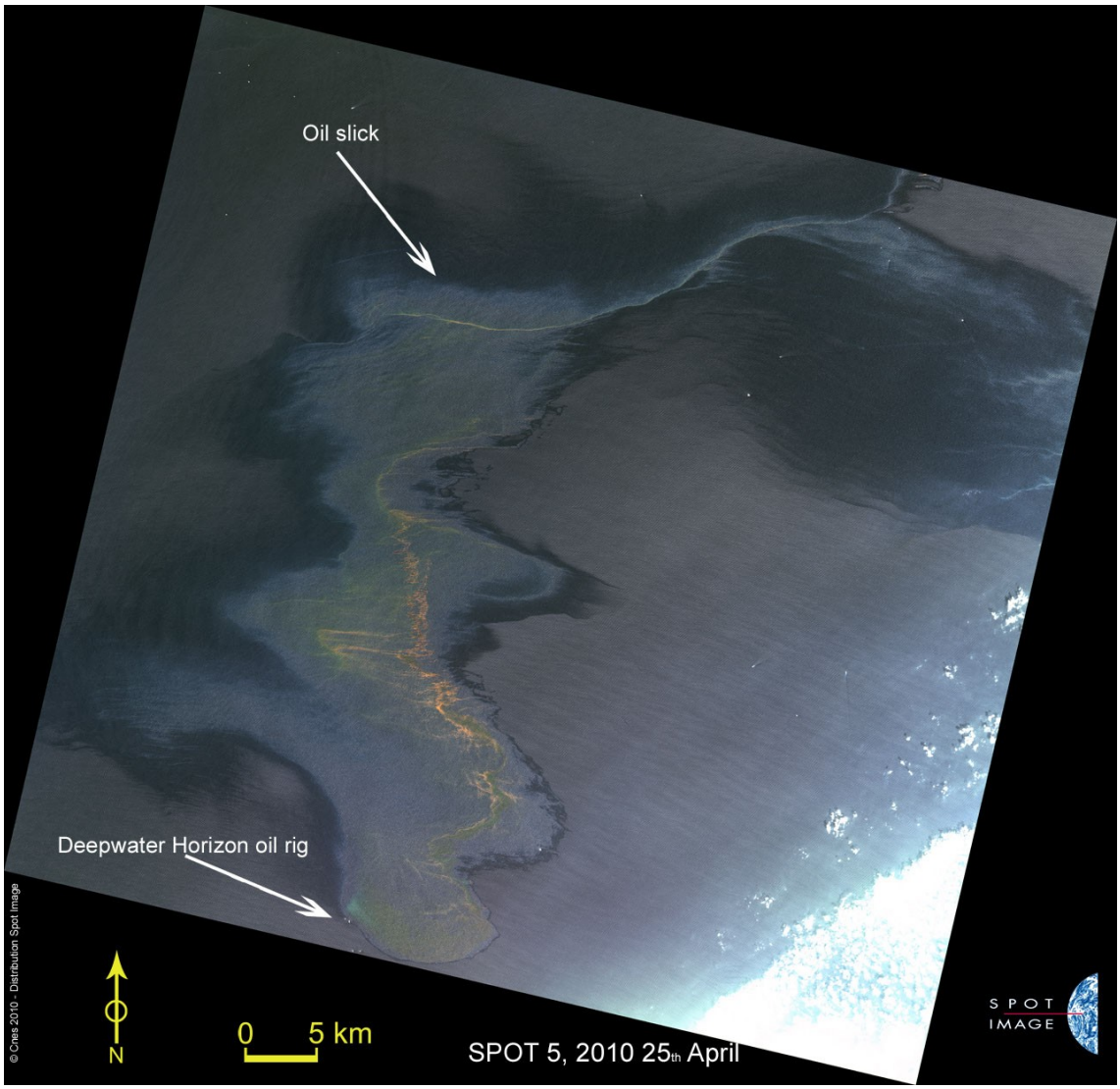

Figure A.3. The oil spill from the Deepwater Horizon oil rig (positioned at latitude N28° 44.20′ and longitude W88° 23.23′) in the Gulf of Mexico appearing in SPOT 5 on 25th April, 2010 at 16:31 UTC in 10 m/pixel resolution with an unspecified RGB colour composite © Centre National d'Etudes Spatiales (CNES)[3].

[3] http://www.spot.com/web/SICORP/3198-oil-spill-in-the-gulf-of-mexico-spot-5-mobilized.php

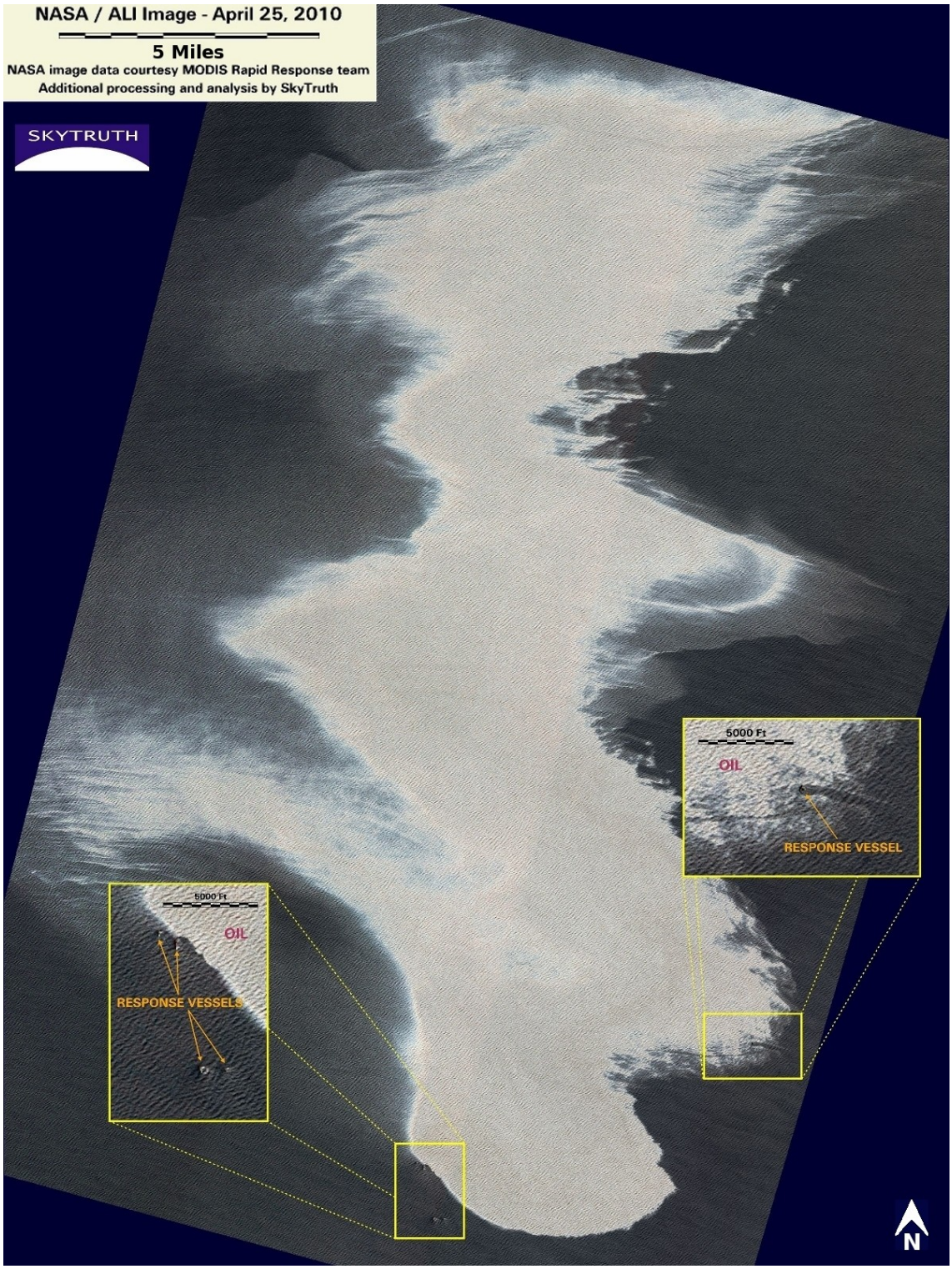

Figure A.4. A high resolution image (30 m/pixel, unspecified RGB colour composite) of the Deepwater Horizon oil spill in the Gulf of Mexico produced by the Advanced Land Imager (ALI) on NASA's Earth Observing-1 (EO-1) satellite on 25th April, 2010[4]. Image is centred at the position N28°55'23" W88°22'15".

[4] http://www.flickr.com/photos/skytruth/4557813199/in/set-72157623909364472/

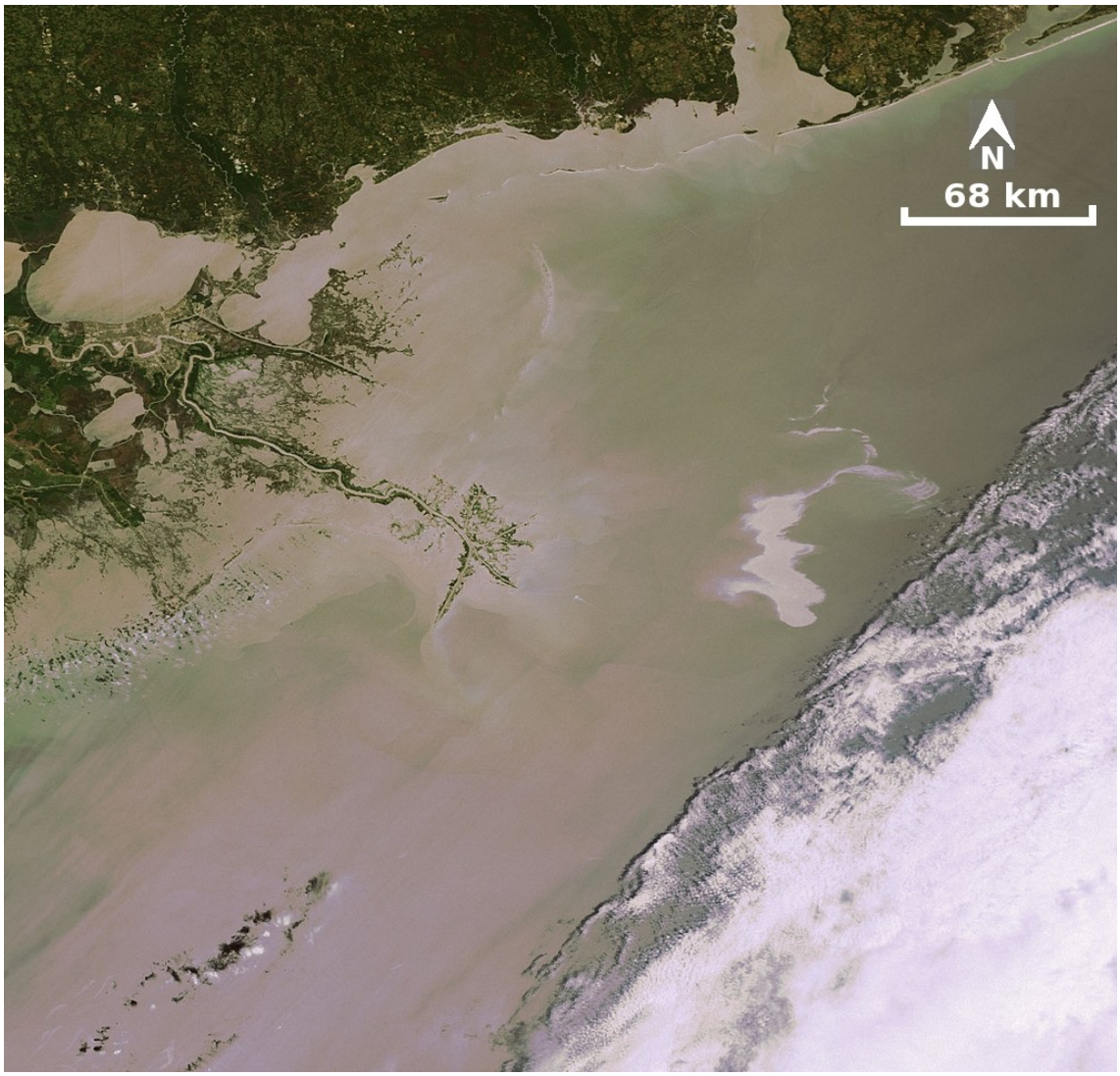

Figure A.5. The Deepwater Horizon oil spill appears in a natural RGB colour image acquired by the Medium Resolution Imaging Spectrometer (MERIS) instrument (300 m/pixel resolution) on-board the ENVISAT satellite on 25th April, 2010. The spill is visible as a white whirl on the right. Image is centred at the position N29° W89° © European Space Agency (ESA)[5].

[5] http://earth.eo.esa.int/cgi-bin/satimgsql.pl?show_url=2042&startframe=0

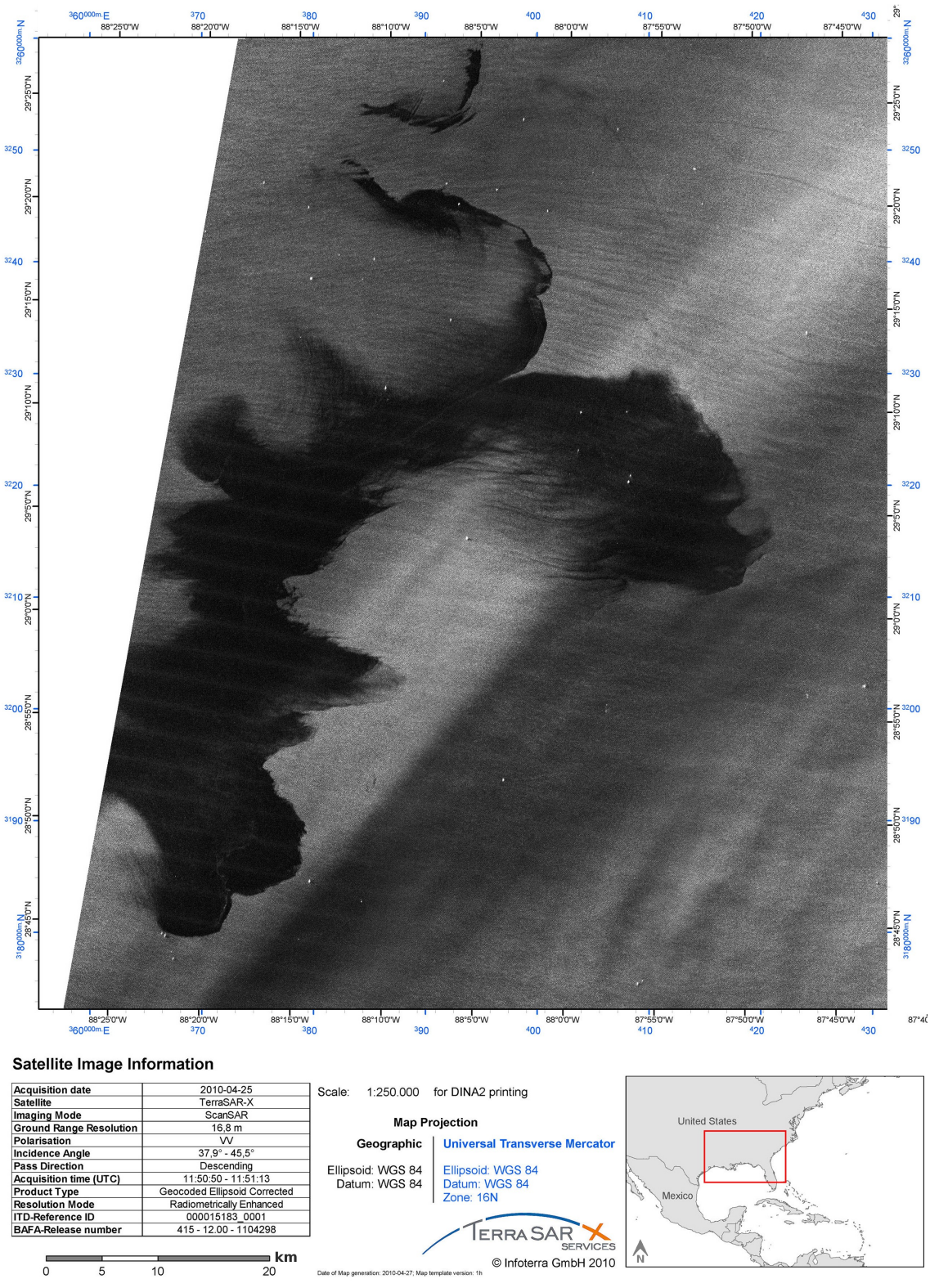

Figure A.6. The Deepwater Horizon oil spill that have occurred in the Gulf of Mexico as it appears in TerraSAR-X (X-band) image acquired on 25th April, 2010. Image is centred at the position N28°58'36" W88°06'09" © Infoterra[6].

[6] http://www.scanex.ru/en/news/News_Preview.asp?id=n11722249

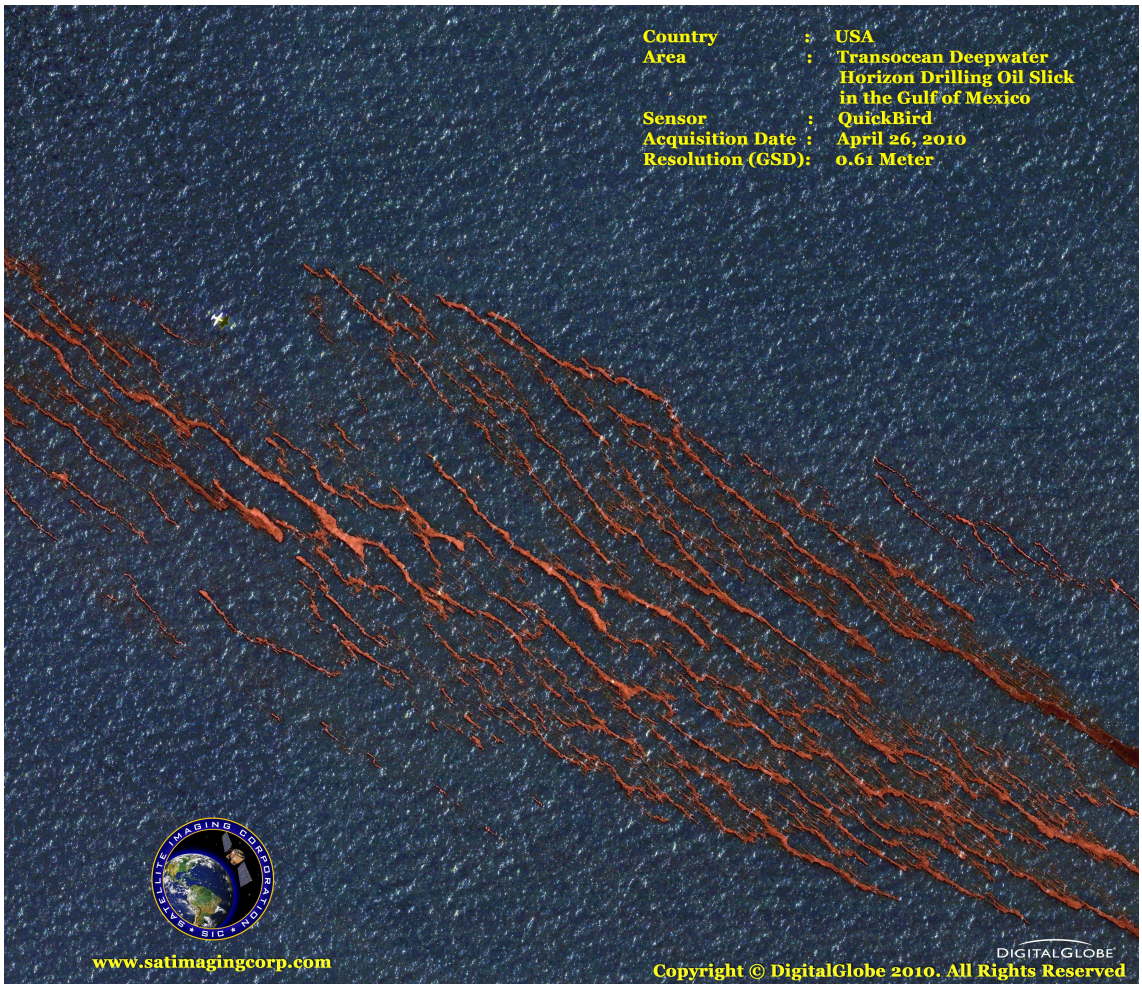

Figure A.7. A natural RGB colour image of the Deepwater Horizon oil spill in the Gulf of Mexico and associated clean up in QuickBird satellite corresponding to bands red (630–690 nm), green (520–600 nm) and blue (450–520 nm). The image was taken on 26th April, 2010 © DigitalGlobe[7].

[7] http://www.satimagingcorp.com/gallery/quickbird-gulf-of-mexico-oil-slick.html

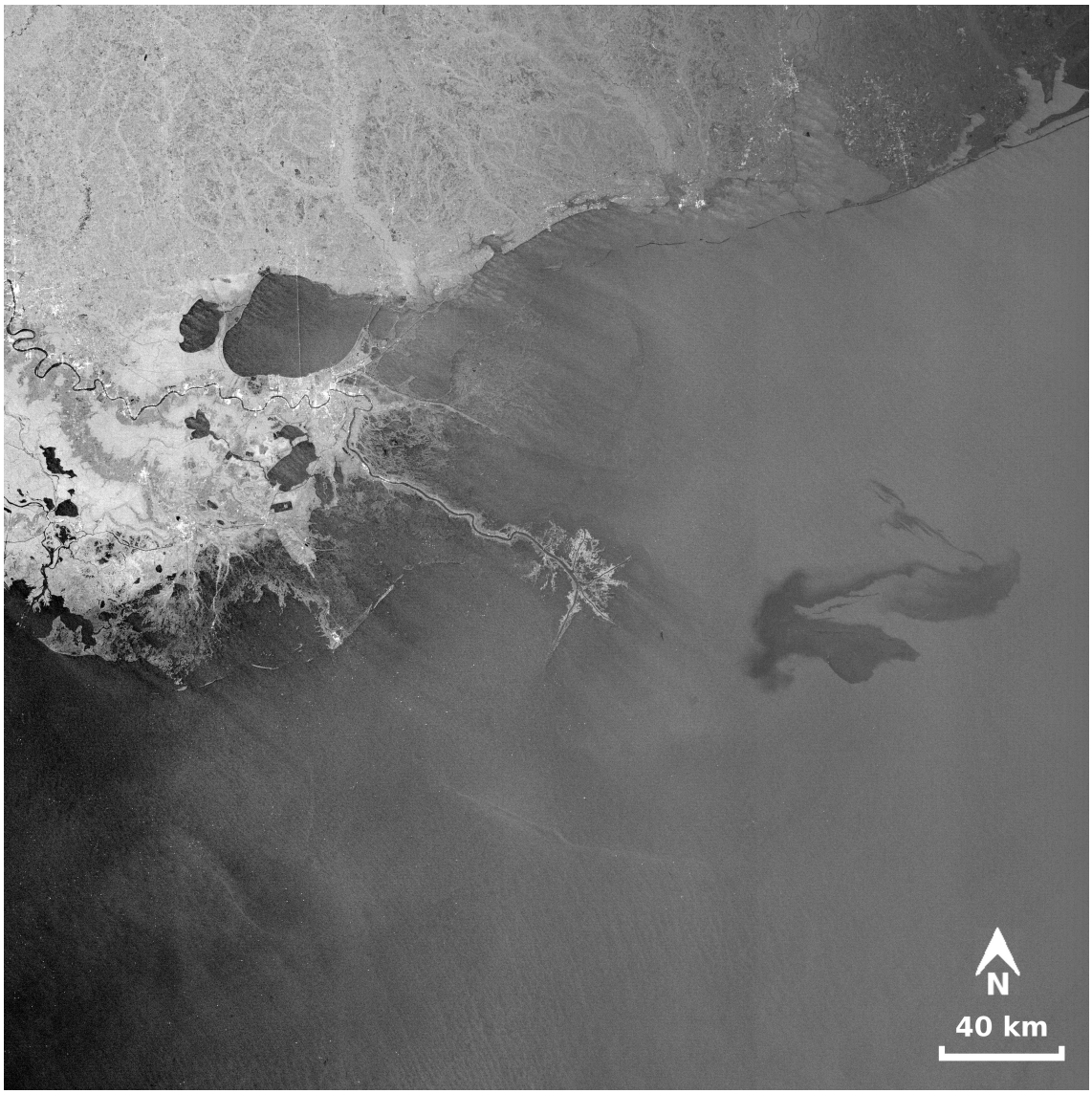

Figure A.8. An ENVISAT Advanced Synthetic Aperture Radar (ASAR) Wide Swath image (150 m/pixel resolution, C-band) image acquired on 26th April, 2010 of the Gulf of Mexico oil spill. Centre of image coordinates are at: N29° W89° © ESA[8].

[8] http://earth.eo.esa.int/cgi-bin/satimgsql.pl?show_url=2033&startframe=0

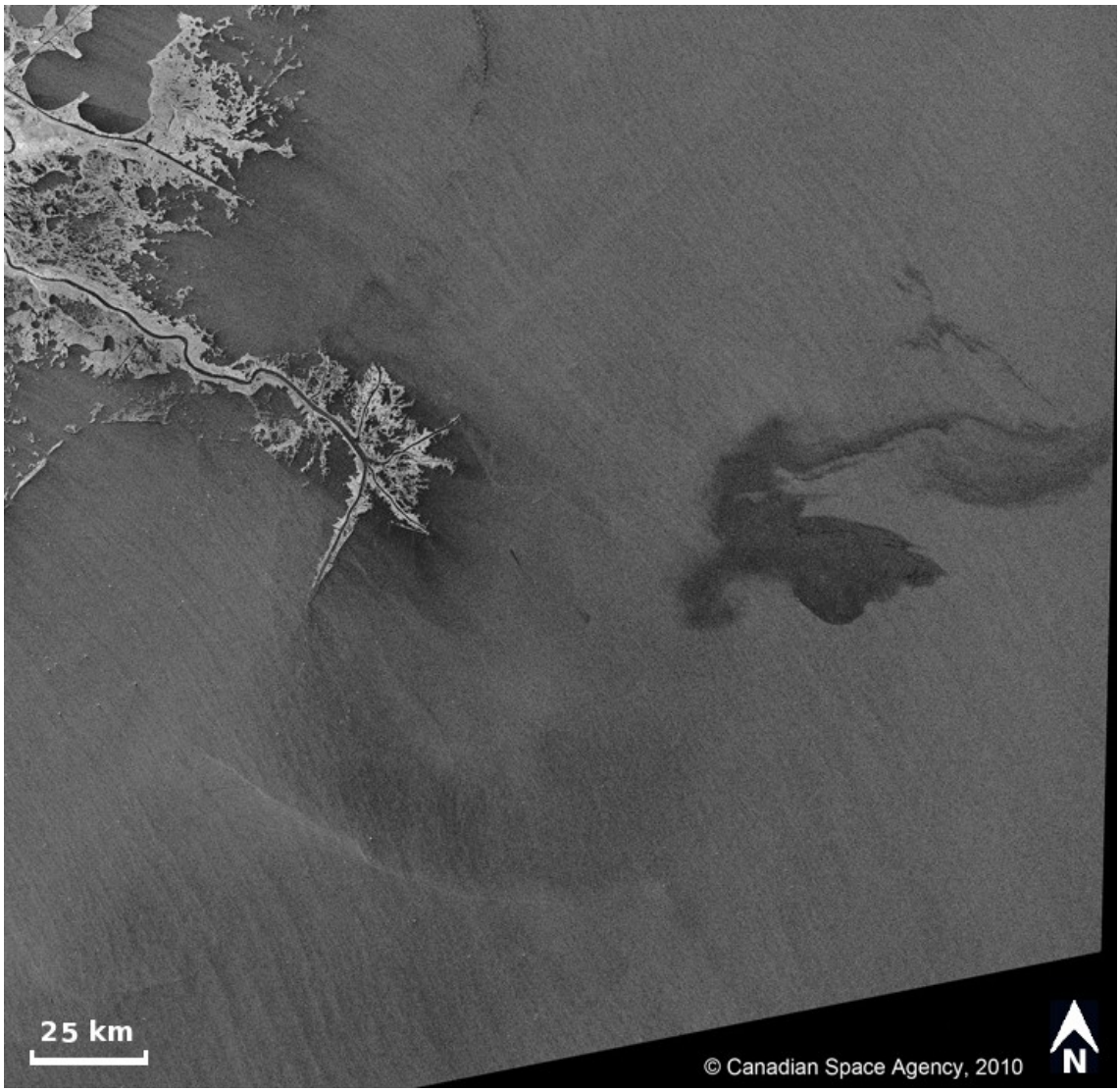

Figure A.9. The Gulf of Mexico oil spill visible in a RADARSAT-1 image produced using the ScanSAR Narrow A Beam mode (50 m/pixel resolution, C-band) taken on 26th April, 2010 at 11:59 UTC. The image is centred at the position N29°04'24" W88°48'18" © Canadian Space Agency (CSA)[9].

[9] http://www.disasterscharter.org/web/charter/activation_details?p_r_p_1415474252_assetId=ACT-308

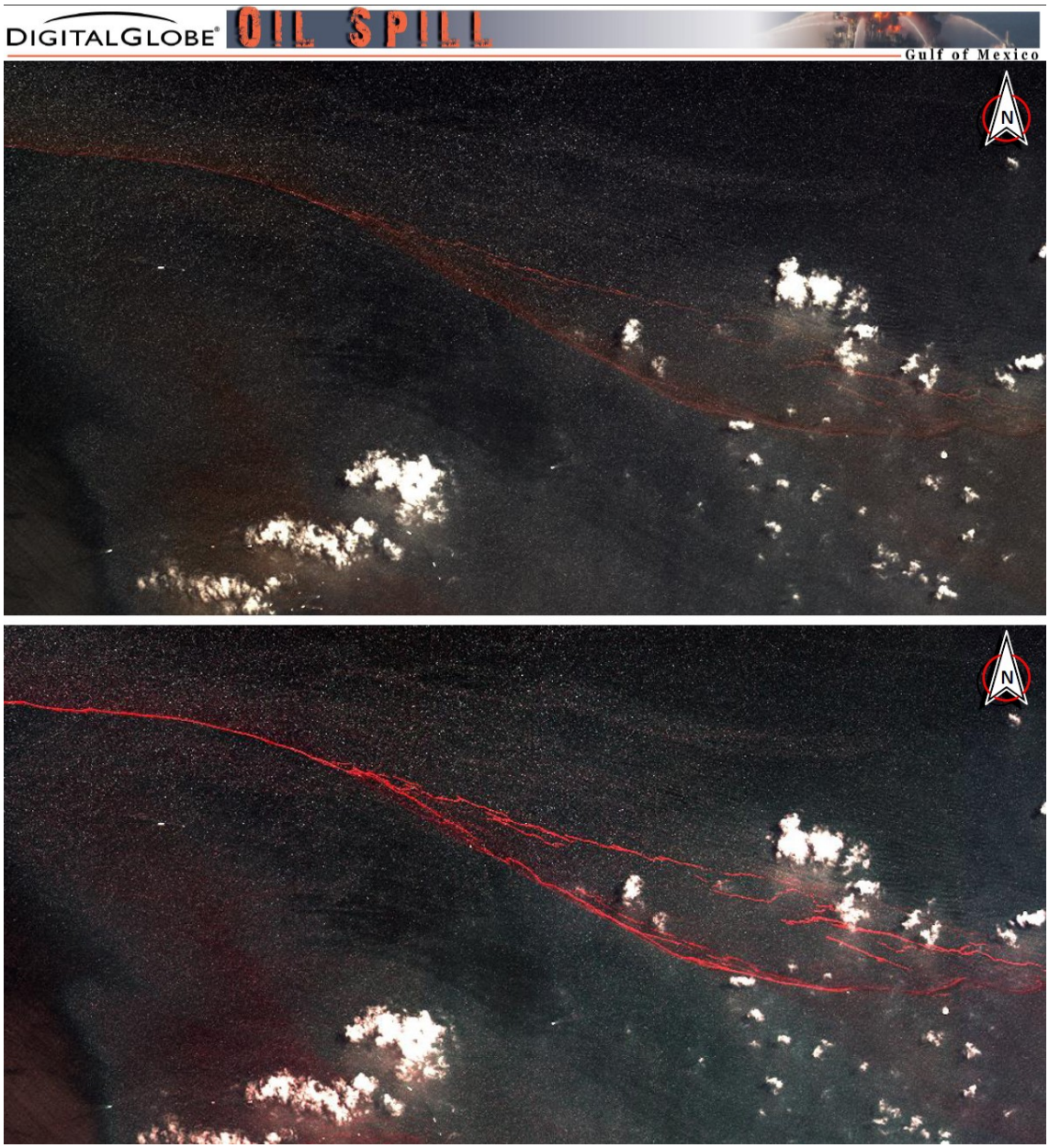

Figure A.10. The Gulf of Mexico oil spill in the WorldView-2 satellite (1.84 m pixel/resolution) acquired on 27th April, 2010. The spectral bands used in the creation of the images are: Coastal Band (λ_1=400–450 nm), Blue (λ_2=450–510), Green (λ_3=510–580), Red (λ_4=630–690) and Near-IR1 (λ_5=770–895), Yellow Band (λ_6=585–625 nm), Red Edge Band (λ_7=705–745 nm), Near-IR2 Band (λ_8=860–1040 nm). The different RGB colour composites correspond to bands (Top) λ_5 λ_3 λ_2 And (Bottom) λ_8 λ_2 λ_1. In both images the oil appears as long red streaks and clouds appear scattered around in white colour © DigitalGlobe[10].

[10] http://www.scanex.ru/en/news/News_Preview.asp?id=n11722249

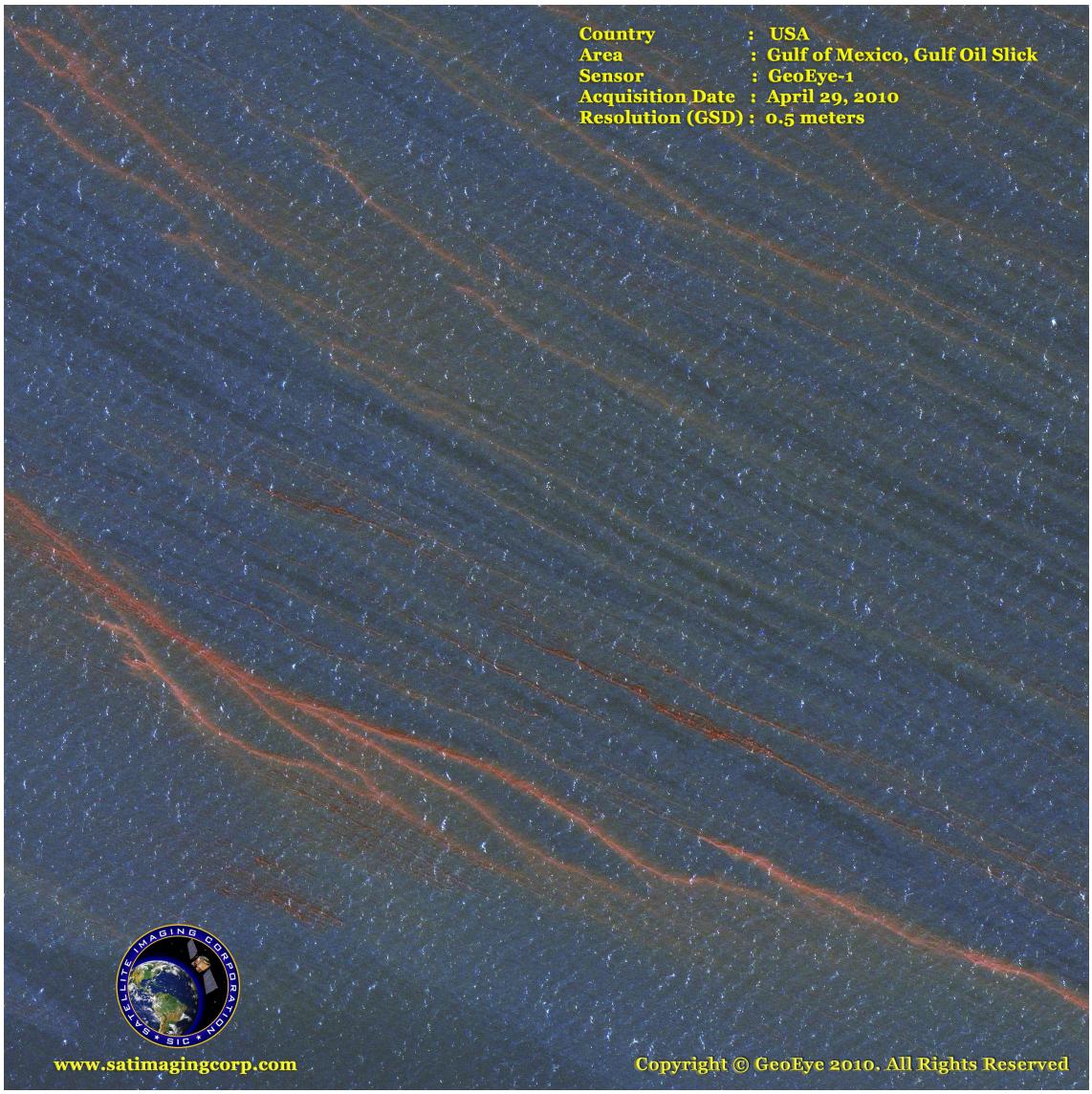

Figure A.11. The Gulf of Mexico oil spill that was caused by an explosion on-board the offshore drilling rig Deepwater Horizon as it is seen in GeoEye-1 satellite on 29th April, 2010 in the natural RGB colour composite corresponding to bands red (655–690 nm), green (510–580 nm) and blue (450–510 nm). The oil appears as long red/orange streaks with white speckle appearing at the water surface due to reflections from the water waves and/or white-caps © DigitalGlobe[11].

[11] http://www.satimagingcorp.com/gallery/geoeye-1-gulf-mexico-oil-slick.html

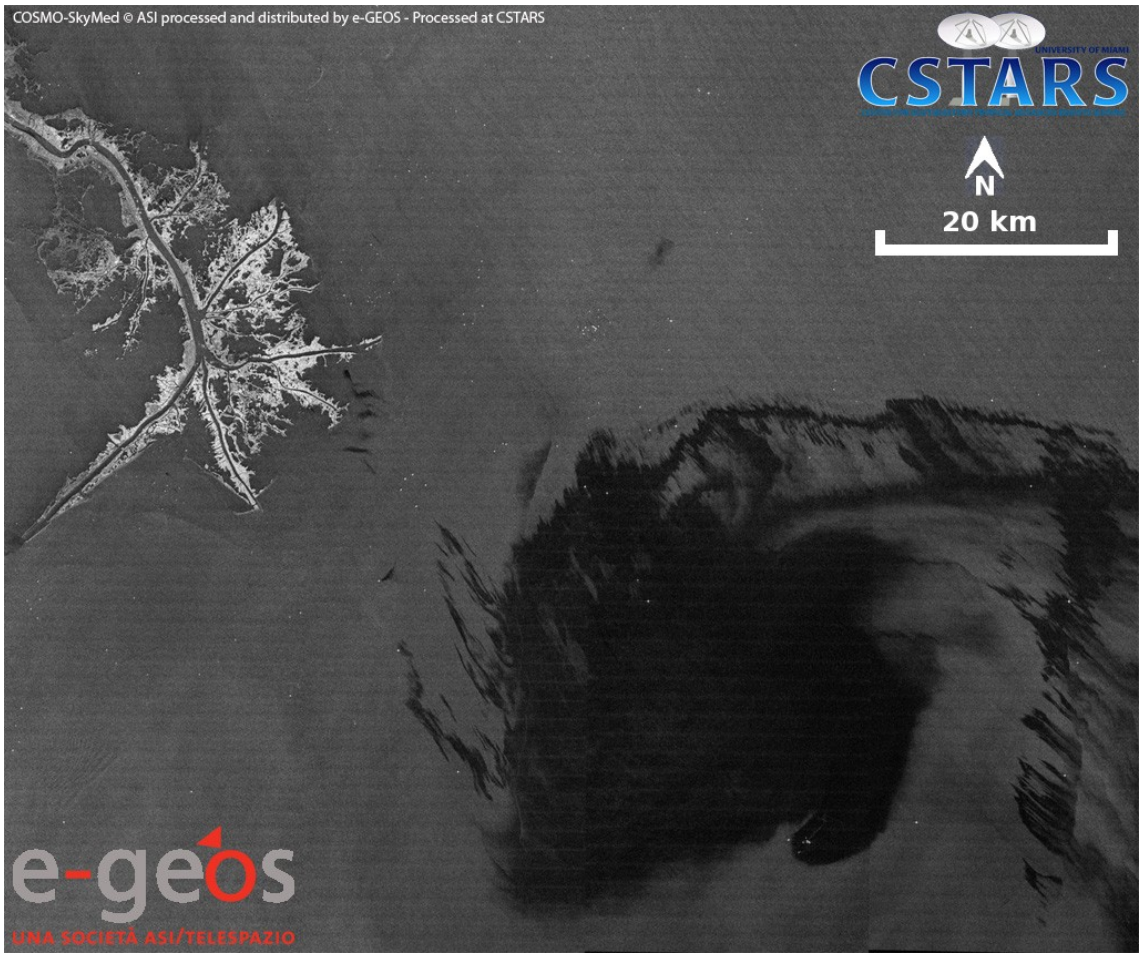

Figure A.12. An image of the Deepwater Horizon oil spill in the Gulf of Mexico acquired a SAR image (ScanSAR mode with 50 m/pixel resolution, polarization HH, X-band) by the Constellation of small Satellites for the Mediterranean basin Observation (COSMO-SkyMed) on 30th April, 2010 at 23:51 UTC. The image is centred at the position N29°03'26" W88°42'31" © CSTARS[12].

[12] http://www.rsmas.miami.edu/oilspill/timeline/scientific-perspective/

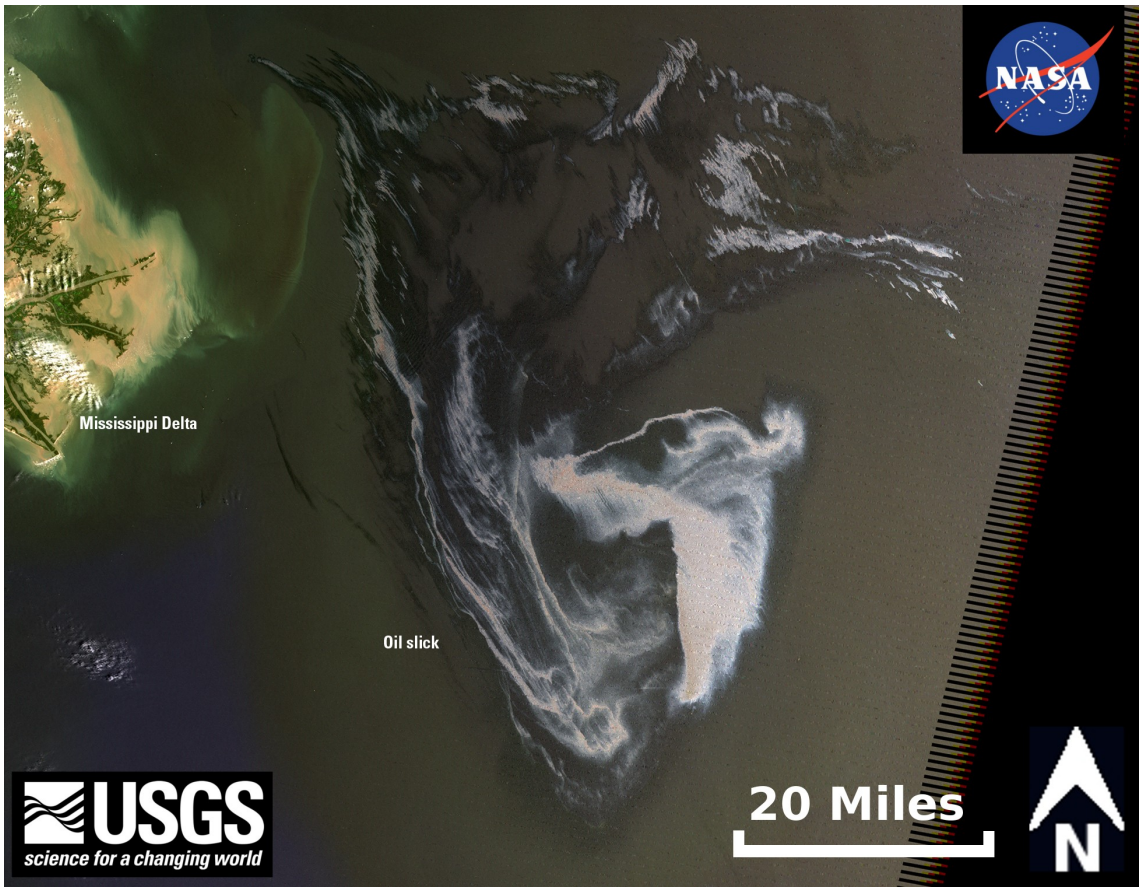

Figure A.13. A 30 m/pixel resolution Lansat 7 ETM+ natural colour image acquired by the U.S. Geological Survey (USGS) on 1st May, 2010 showing the extent of the Deepwater Horizon oil spill in the Gulf of Mexico[13]. The image is centred at the position N29°09'14" W88°38'39" © USGS.

[13] http://www.flickr.com/photos/usgeologicalsurvey/4703144374/sizes/o/in/photostream/

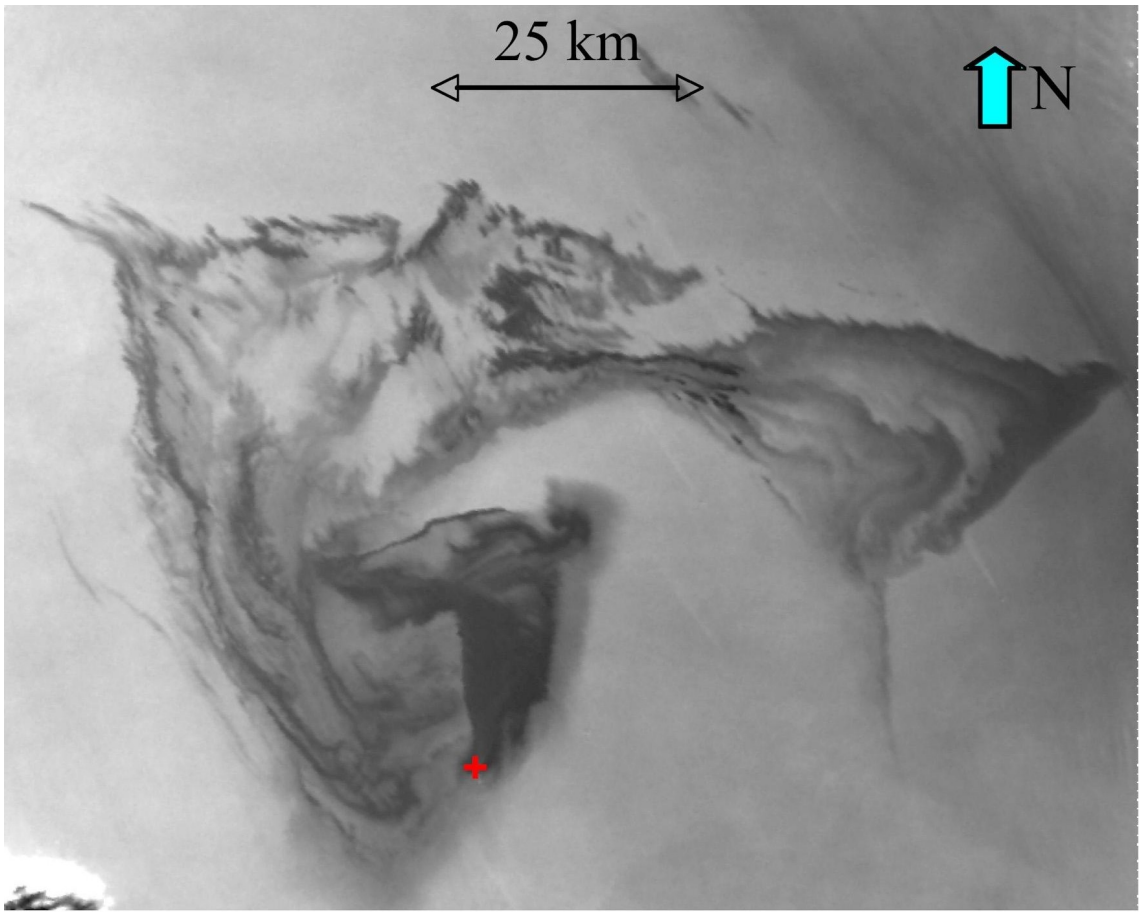

Figure A.14. The Gulf of Mexico Oil Slick in the Multi-angle Imaging SpectroRadiometer (MISR) instrument on the Terra satellite acquired on 1st May, 2010 at 16:44 UTC. The red symbol indicates the approximate position of the Deepwater Horizon platform (marked + in red positioned at latitude N28° 44.20′ and longitude W88° 23.23′). The image is a multi-angle composite image of the oil spill (275 m resolution from nadir), showing the ratio between the reflectances of the 26.1° aftward viewing (Aa) camera and the 26.1° forward viewing (Af) camera. The Af camera sees the reflection of sunlight from the oil more strongly than the Aa camera, so this ratio makes the oil slick appear dark grey. The uncontaminated water appears much lighter. This composite image reveals finer detail of the oil on the surface than can be seen from the nadir-viewing camera alone. Darker regions indicate higher concentrations of oil on the surface. This image also shows more clearly the large concentration of oil emanating from the source. Careful examination of the image also reveals thin streaks running from northwest to southeast that terminate at a point. These correspond to boats that are assisting with the clean-up effort © NASA/GSFC/LaRC/JPL, MISR Team[14].

[14] http://www.nasa.gov/topics/earth/features/oilspill/pia-13099.html

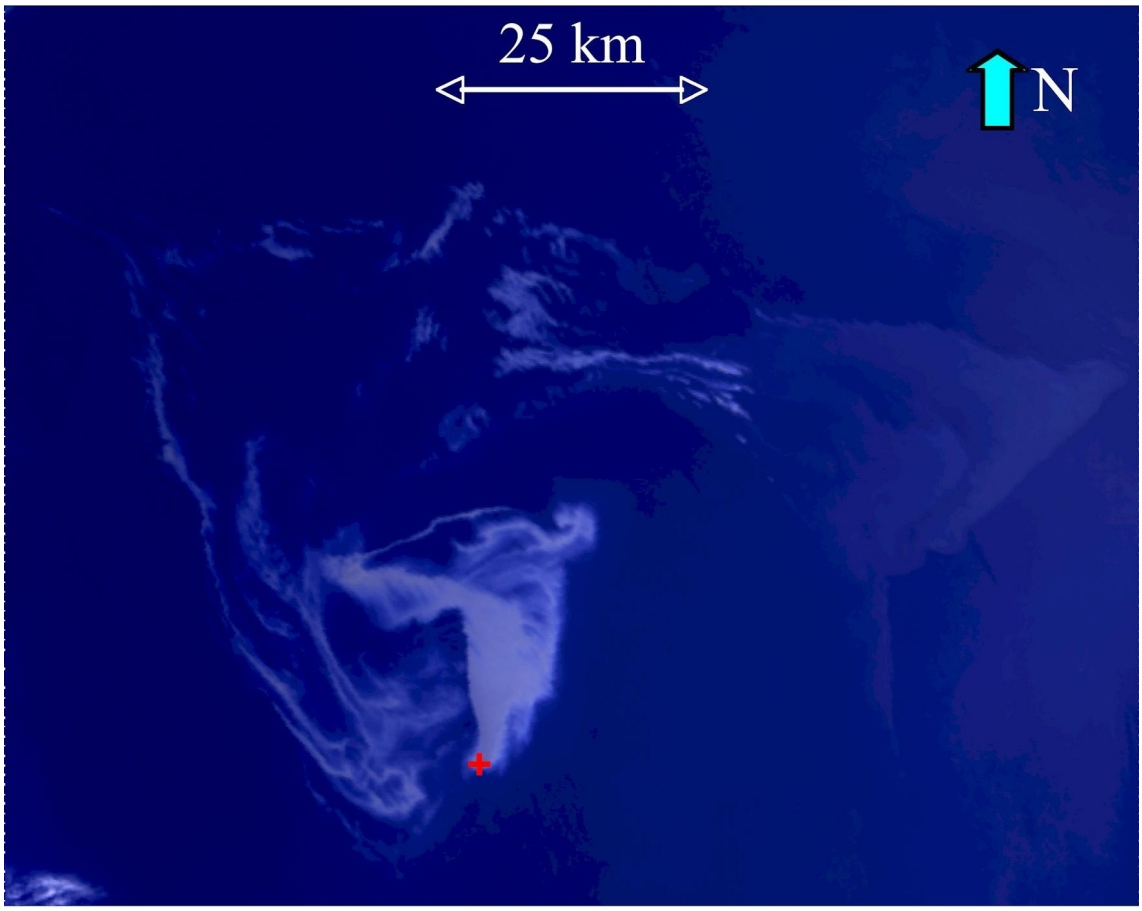

Figure A.15. The Gulf of Mexico Oil Slick in the Multi-angle Imaging SpectroRadiometer (MISR) instrument on the Terra satellite acquired on 1st May, 2010 at 16:44 UTC. The red symbol indicates the approximate position of the Deepwater Horizon platform (marked + in red positioned at latitude N28° 44.20′ and longitude W88° 23.23′). The image is an enhanced "true colour" view (unspecified RGB colour composite) of the oil slick at 275 m (resolution from MISR's nadir (downward)-viewing camera. This change in the reflection of sunlight makes the oil slick appear lighter blue on the darker blue waters. Some clouds are visible in the extreme lower left corner of the image © NASA/GSFC/LaRC/JPL, MISR Team[15].

[15] http://www.nasa.gov/topics/earth/features/oilspill/pia-13099.html

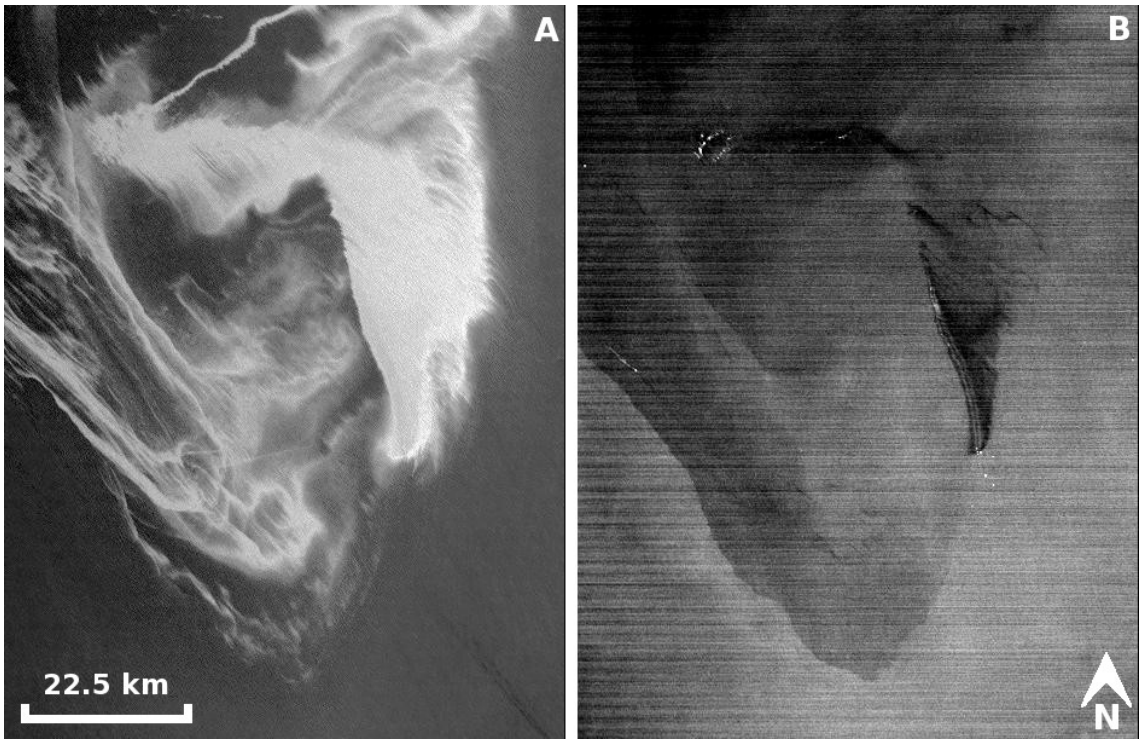

Figure A.16. The Advanced Spaceborne Thermal Emission and Reflection Radiometer (ASTER) instrument on NASA's Terra spacecraft captured this pair of images of the Deepwater Horizon oil spill in the Gulf of Mexico on 1st May, 2010. This ASTER image is located at N29.0° latitude, W88.3° longitude. No land is visible in the image. **(A)** Acquired in the visible part of the spectrum, the varying shades of white reflect different thicknesses of oil. The source of the oil spill is visible as the bright white area in the bottom centre of the image. The thickest part of the oil spill extends vertically from it, appearing somewhat like the ash plume of an erupting volcano. The wispy patterns of the oil spill reflect the transport of the oil by waves and currents. (B) A thermal picture of the same area, with the coldest surfaces appearing dark, and the warmest appearing white. Only the thickest parts of the oil slick are colder than the ocean water temperature. In the upper left, bright spots are fires where attempts have been made to burn the slick. Large dark-light patterns are ocean currents that concentrate and disperse the oil plume © NASA/GSFC/METI/ERSDAC/JAROS, and U.S./Japan ASTER Science Team[16].

[16] http://photojournal.jpl.nasa.gov/catalog/PIA13091

Figure A.17. An image of the oil spill that occurred in the Deepwater Horizon oil rig in Gulf of Mexico taken on 4th May, 2010 at 22:33 UTC by a crew member of the International Space Station (ISS) of the Expedition 23 mission. The view in this image is towards the west; the ISS was located over the eastern edge of the Gulf of Mexico when the image was taken. The Mississippi River Delta and nearby Louisiana coast (image top) appear dark in the sun-glint that illuminates most of the image. Sun-glint is caused by sunlight reflecting off the water surface—much like a mirror—directly back towards the astronaut observer on the Space Station. The sun-glint improves the identification of the oil spill. Oil on the water smooths the surface texture, and the mirror-like reflection of the sun accentuates the difference between the smooth, oil-covered water (dark to light grey) and the rougher water of the reflective ocean surface (coloured silver to white). Wind and water currents patterns have modified the oil spill's original shape into streamers and elongated masses. Other features visible in the image include a solid field of low cloud cover at the lower left corner of the image. V-shaped ship or boat wakes are visible in the large image. Wave patterns at image lower right are most likely caused by tidal effects. The image is centred at the position N29.4° latitude and W88.2° longitude[17].

[17] http://eol.jsc.nasa.gov/sseop/EFS/photoinfo.pl?PHOTO=ISS023-E-32397

B: Description of biological species used in the thesis

A brief description of the biological species that were investigated in this thesis, particularly in relation to the surface algal bloom index (SABI) algorithm that was discussed chapter 6. The species include: (1) *Noctiluca scintillans* (synonym *Noctiluca miliaris*); (2) *Nodularia spumigena;* (3) *Enteromorpha prolifera (Ulva prolifera*); (4) *Trichodesmium;* and (5) Sargassum.

1- Noctiluca scintillans

Noctiluca scintillans (also published as *Noctiluca miliaris*) is a free-living non-parasitic marine-dwelling species of dinoflagellate that exhibits bioluminescence. The bioluminescent characteristic of *N. scintillan*s is produced by a luciferin-luciferase system located in thousands of spherically shaped organelles, or "micro-sources", located throughout the cytoplasm of this single-celled protist (see Figure B.1).

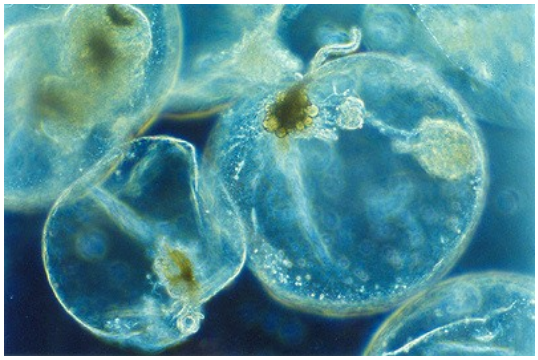

Figure B.1. microscopic image of *N. scintillans*[18].

Non-luminescent populations within the genus *Noctiluca* lack these micro-sources. *N. scintillans* is a heterotrophic (non-photosynthetic) organism that engulfs its food (phagotrophic) which primarily consists of plankton, including diatoms and other dinoflagellates, as well as fish eggs and bacteria. Diatoms are often found in the vacuoles (internal membrane-bound storage compartments) within these single-celled creatures.

N. scintillans can be found widely distributed throughout the world, often along the coast, in estuary, and shallow areas of the continental shelf that receive plenty of light which promotes the growth of the phytoplankton that make up a large portion of *N. scintillans's* diet (see Figure B.2).

[18] http://de.academic.ru/dic.nsf/dewiki/938719

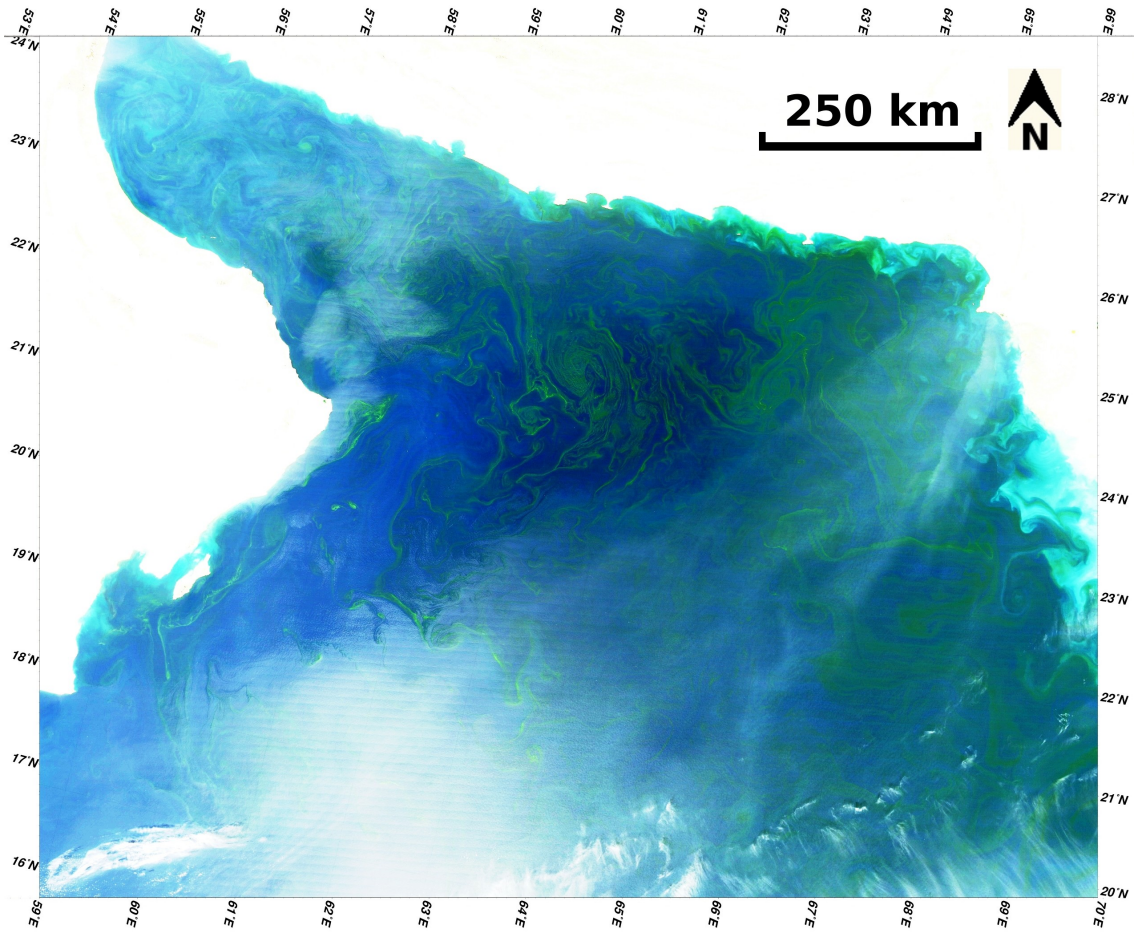

Figure B.2. A natural RGB colour composite image of *N. scintillans* bloom in the Arabian Sea seen in MODIS Aqua on 18th February, 2010 at 09:15 UTC. The composite corresponds to bands λ_1=645, λ_4=555 and λ_3=469 nm respectively at 250 m/pixel resolution (λ_4 and λ_3 are collocated from the 500 m resolution band group). The scene includes a visible layer of dust, clouds and moderate sun glint zone. Land is masked in white and blooms appear as large greenish structural filaments. Contrast stretching was performed to highlight the blooms © Image courtesy of NASA Earthobservatory[19].

High concentrations of their plankton food source that likely result from environmental conditions such as well-mixed nutrient-rich waters and seasonal circulation factors are implicated in population blooms of *N. scintillans*, known as "red tides". Swimmers may report being illuminated by a ghostly glow-in-the-dark plankton - a floating bloom of algae which fires up into a fluorescent sparkle when disturbed. Runoff from agricultural pollution may contribute to the severity of these blooms. However this is not required to cause explosive growth of *N. scintillans*.

Not all blooms associated with *N. scintillans* are red. The colour of *N. scintillans* is in part derived from the pigments of organisms inside the vacuoles of *N. scintillans*. For

[19] http://earthobservatory.nasa.gov/IOTD/view.php?id=43050

instance, green tides result from *N. scintillans* populations that contain green-pigmented prasinophytes (green plant algae, *Subphylum Chlorophyta*) that are living in their vacuoles. The species itself does not appear to be toxic, but as they feed voraciously on phytoplankton high levels of ammonia accumulate in these organisms which is then excreted by *N. scintillans* into the surrounding area which may add to the neurotoxic chemicals being produced by other dinoflagellates, such as *Alexandrium spp.* or *Gonyaulax spp.*, that do result in the death of other aquatic life in the area[20].

2- Sargassum

Species of this genus of algae may grow to a length of several metres. They are generally brown (see Figure B.3) or dark green in colour and consist of a holdfast, a stipe, and a frond.

Figure B.3. Pelagic brown algae in the genus *Sargassum*. The berry-like structures are gas-filled bladders known as pneumatocysts, which provide buoyancy to the plant. © Image courtesy of H. Scott Meister, SCDNR[21].

Oogonia and *antheridia* occur in conceptacles embedded in receptacles on special branches. Some species have berrylike gas-filled bladders which help keep the fronds afloat to promote photosynthesis. Many have a rough sticky texture, which together with a robust but flexible body, helps it to withstand strong water currents. The thick masses of Sargassum provide an environment for a distinctive and specialised group of

[20] http://en.wikipedia.org/wiki/Noctiluca_scintillans#cite_note-0

[21] http://oceanexplorer.noaa.gov/explorations/04etta/logs/aug25/media/sargassum.html

marine animals and plants, many of which are not found elsewhere.

Sargassum is commonly found in the beach drift near Sargassum beds where they are also known as gulfweed (see Figure B.4), a term also used to include all seaweed species washed up on shore. They are found throughout tropical areas of the world and are often the most obvious macrophyte in near-shore areas where Sargassum beds often occur near coral reefs. The plants grow sub-tidally and attach to coral, rocks or shells in moderately exposed or sheltered rocky or pebble areas. In some cases (e.g., the Sargasso Sea) there are large populations of floating Sargassum[22].

Figure B.4. Mats of floating sargassum in the Gulf of Mexico on 31st August, 2010. © Image courtesy of Sea Turtle Conservancy[23].

3- *Trichodesmium*

Trichodesmium is a marine cyanobacterium found worldwide in surface waters of tropical and subtropical oceans (see Figure B.5).

[22] http://en.wikipedia.org/wiki/Sargassum

[23] http://www.conserveturtles.org/seaturtleblog/index.php?number=45

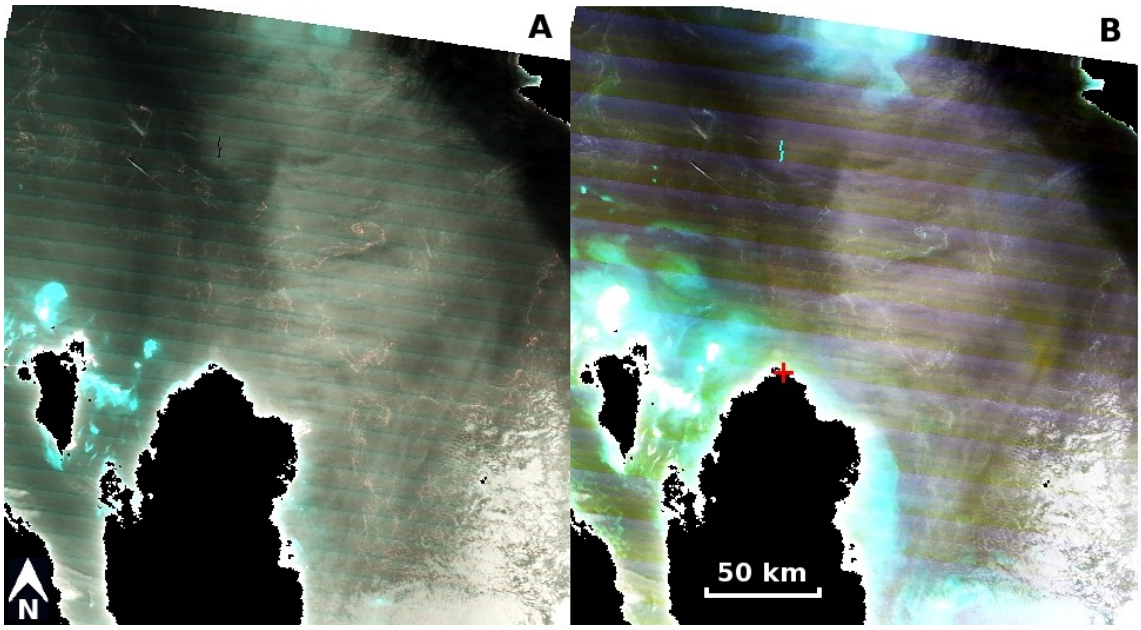

Figure B.5. MODIS Terra image taken on 24th April, 2009 at 07:09 UTC. The reddish patches are representing floating blooms in the middle of ROPME sea area. Land is masked in black. The red mark (+) is positioned at the location N26° 9' 58" E51° 15' 43". © ROPME MODIS receiving station.

Sailors sometimes refer to *Trichodesmium* as sea sawdust because it forms colonies that can be quite large (up to 1 cm) and visible to the naked eye. Small blooms resemble sawdust floating on the water surface; larger blooms can look like oil slicks or slightly foamy pollution and can be so far-reaching that they are visible from space. *Trichodesmium* migrates up and down in the water column, so the amount seen on the surface of the water may vary with time of day. *Trichodesmium* blooms occur offshore in oligotrophic waters, but they can occasionally reach near-shore areas when currents and winds push an established offshore bloom to inshore areas. These blooms are not related to coastal nutrient sources or pollution. Most or all of the phosphorus that *Trichodesmium* requires for nutrition is taken up directly from the water, and most of the nitrogen it requires is derived from nitrogen gas (N_2) dissolved in the water. High-biomass *Trichodesmium* blooms in the Gulf of Mexico tend to occur between May and September, a time of high storm activity in the. Dust storms from Sahara Desert in Africa contains high concentrations of iron. Nitrogenous, the specialized enzyme *Trichodesmium* uses to convert N_2 to a more usable form, has a high iron requirement. The iron-rich Saharan dust is blown into the atmosphere, transported across the Atlantic Ocean by wind currents. In general, *Trichodesmium* is not a good food source for zooplankton or fish; it is actively grazed on by only a few specialized zooplankton.

Figure B.6. *In situ* pictures of the *Trichodesmium erythraeum* species taken on 24th April, 2009 from a boat © Image courtesy of the ministry of environment Qatar.

Trichodesmium blooms have a unique "sweet" smell when they decay, and large blooms can turn the water red or pink when stressed cells leach out water-soluble accessory pigments (called *phycoerythrins*). At various times in their development, *Trichodesmium* blooms can also appear brown (healthy bloom), green (blooms in initial decay state after accessory pigments have leached out, making the chlorophyll a visible in cells), or white (after chlorophyll a decays)[24].

4- *Enteromorpha prolifera (Ulva prolifera)*

Enteromorpha prolifera (Müller) also knows as *Ulva prolifera* is a filamentous green alga (fronds to 1m), branched, monosiphonous, and benthic macroalga (see Figure B.7) has hollow thalli with longitudinal rows of quadrangular to polygonal cells. Cells contain starch grains, large parietal chloroplasts, and vacuoles that reach up to 40% of cell volume.

[24] http://research.myfwc.com/features/view_article.asp?id=22896

Figure B.7. Algae at the Olympic sailing venue, Qingdao on 30th June, 2008 where workers set up a bridge to transport the algae © Image courtesy of the Guardian newspaper[25].

E. prolifera is typically a marine species, known in North America from the coasts, inland salt springs, and western salt lakes. It is known from various waters, generally brackish or salty, in Asia, Europe, and Central America. This edible crop species comprises different strains that are known to survive, grow, and reproduce in very low salinity (0.1–1‰), brackish, salty, or briny waters. *E. prolifera* has been recorded from a wide range of water temperatures but many strains prefer temperatures around 15–25 °C and reach an upper critical limit at 30–34 °C. It grows well in eutrophic conditions, in which it sometimes can become a dominant benthic species. It can sometimes be limited by phosphorus. Scottish experiments indicate that dense mats of *E. prolifera* in intertidal sandflats could have detrimental effects for species depending on planktonic larval recruitment[26].

5- *Nodularia spumigena*

Nodularia spumigena is a genus of filamentous, planktonic, photosynthetic, diazotrophic, nitrogen-fixing cyanobacteria, or blue-green algae. They occur mainly in brackish or salinic waters and can occasionally form heavy algal blooms that are harmful to humans[27] (see Figure B.8).

[25] http://www.guardian.co.uk/world/gallery/2008/jun/30/pollution.olympicgames2008?picture=335366705#/?picture=335366724&index=1

[26] http://nas.er.usgs.gov/queries/FactSheet.aspx?speciesID=2714

[27] http://en.wikipedia.org/wiki/Nodularia

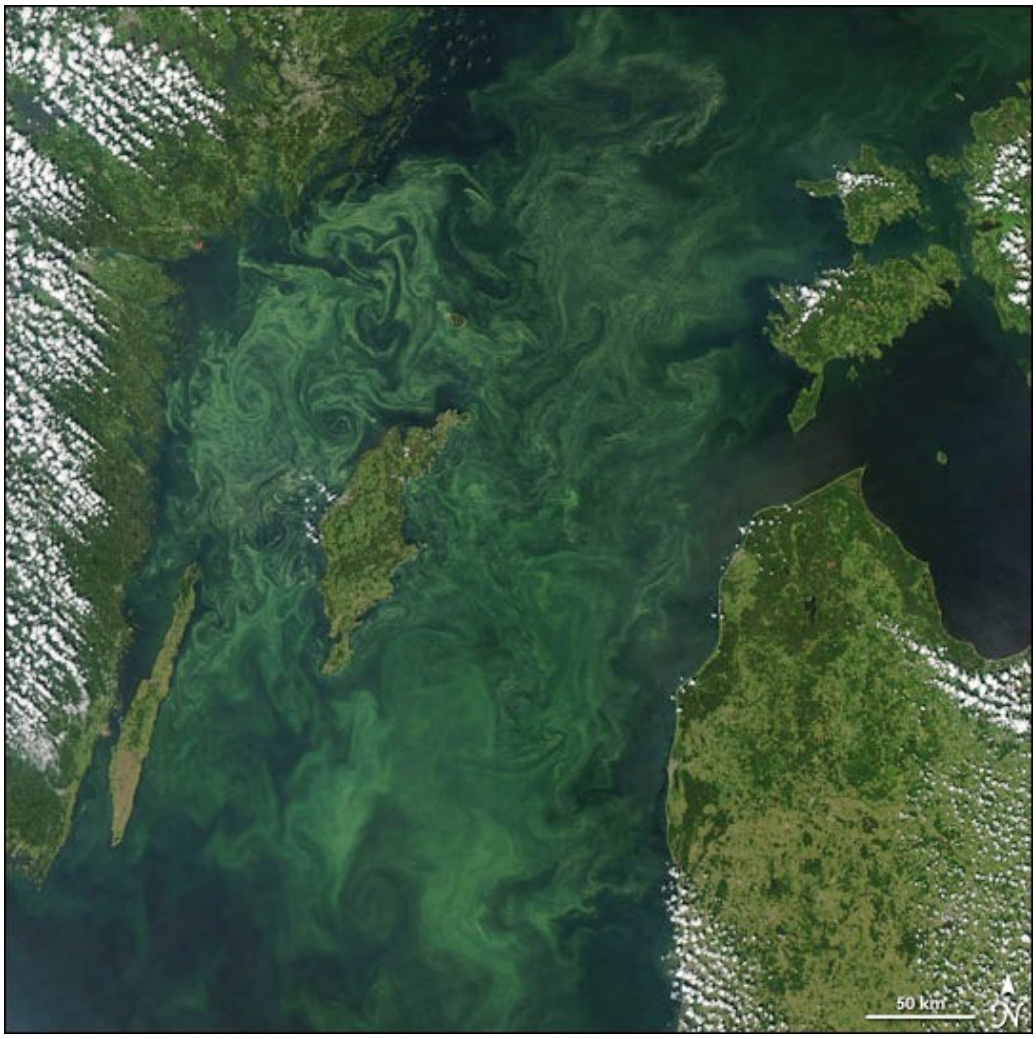

Figure B.8. A 1 km/pixel resolution natural RGB colour composite MODIS Aqua image acquired on 5th July, 2005 showing the deep green swirls of the summer bloom around the Swedish island of Gotland. The summer bloom is usually caused by blue-green algae growing on the surface of the water. The algae thrive when ocean waters are warm and winds are calm. Strong winds would churn the ocean, stirring the plants down into the water's depths. Though these blooms occur naturally, human activity can increase the number of widespread blooms. Agricultural and industrial run-off pour fertilizers into the sea, providing the additional nutrients that algae need to form large, dense blooms © Image courtesy of NASA Earthobservatory[28].

Nodularia is one of the dominating species during the extensive cyanobacterial blooms in the Baltic Sea, which are one of the largest in the world. It is also found in Lake Alexandrina, in the south-east of southern Australia. It is commonly found near the surface of the water because is has a high tolerance of ultraviolet radiation[29]. They have increased in both frequency and magnitude in the Baltic Sea in recent decades, and

[28] http://earthobservatory.nasa.gov/NaturalHazards/view.php?id=15125

[29] http://microbewiki.kenyon.edu/index.php/Nodularia_Spumigena.

researchers are divided on the cause. Some put it down to eutrophication – an excess of nutrients in the water – caused by human emissions of nitrogen and phosphorus over the past 150 years. Others have studied the Baltic Sea's bottom sediment and argue that this is a natural phenomenon that has been ongoing for more than 7,000 years and is due instead to climate variations. *N. spumigena* (see Figure B.9) normally dominates for as long as the surface water is warm and still[30].

Figure B.9. An electron micro-photographs of the *Nodularia spumigena* species from the Gotland sea, Sweden. The photographs were taken by R. Bahlo, S. Busch and R courtesy of Hansen from the © Leibniz Institute for Baltic Sea Research[31].

[30] http://www.physorg.com/news/2010-12-eutrophication-toxic-cyanobacteria.html.

[31] http://www.io-warnemuende.de/gallery-of-baltic-microalgae.html.

C: The oil spread index (OSI)

A new method is being proposed that uses shape and texture analysis to identify oil spills from optical satellite data. The new method, termed the oil spread index (OSI), aims to interactively discriminate between relatively large oil spills and look-alikes observed in MODIS data. Oil spills that fulfil the following conditions are compatible with the OSI model:

1. The spill must be large (covers an area not less than 10×20 pixels of MODIS's 250 m/pixel resolution data) to provide enough spatial distribution to conduct this analysis;
2. the spreading of the spill should be solely influenced by its inertial and inter-facial forces; and
3. the oil is assumed to have undergone negligible changes to its viscosity due to weathering factors.

Spills that do not match these criteria are incompatible with the OSI analysis. Oil spills that violate condition (2), may include those that originate from a moving object which creates a distinctive linear-shaped spill. If, however, the source of the spill is stationary, then the OSI analysis may be carried out at a distance from the point of release to emphasise inertial and surface tension forces. Also, to satisfy this condition, the OSI method must confine its investigation to offshore spills, in order to avoid the additional forces that may affect the spreading of near-shore oil spills. These added effects include river discharge; baroclinic currents; tidal currents; and stokes drift. As for criterion (3), its violation can include old spills that have been dispersed and broken down into “feathered” streaks (see Figure C.1A for an example) due to natural weathering conditions such as strong wind and sea currents (Langmuir currents), or artificially dispersed due to treatment with a dispersant. The shape of the spill shown in Figure C.1B was caused by winds pushing the heavy components of the mineral oil film to the downwind side (dark line in the image), so the "feathered" side is always located upwind. When an investigated patch is positively classified as an oil spill according to the OSI model, it is then possible to estimate the viscosity group that the oil belongs to.

The experimental procedure proposed by the OSI technique will be applied to MODIS data over the RSA and elsewhere. To complement this validation process, corresponding SAR data, whenever it is feasible, will be used too. The work presented in this chapter will complement the spectral methods described earlier for oil spill

discrimination, in order to improve the accuracy of identification.

Due to MODIS's coarse spatial resolution (maximum 250 m/pixel at nadir), the shape and texture analysis was confined to relatively large oil spills, covering an area not less than 10 ×20 pixels (not less than ~ 12 km^2). Therefore, a spill that may appear with enough sharp details in the SAR data, may not appear as sharp when viewed in the corresponding MODIS data, due to its large pixel size averaging.

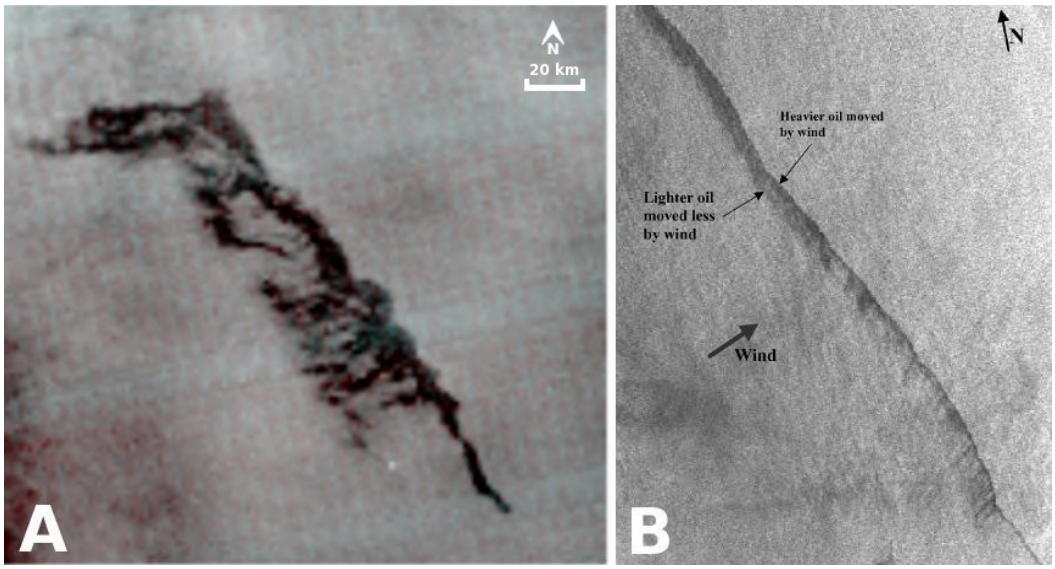

Figure C.1. **(A)** An ageing oil spill (~ 119 km^2) appearing in a 250 m/pixel spatial resolution MODIS Aqua image at false RGB colour composite corresponding to bands λ_2=859, λ_1=645 and λ_1=645 nm respectively seen in the Arabian Sea on 28th April, 2010 at 09:27 UTC (centre point is at N24° 36' 37" E58° 39" 58"). **(B)** A section of an ERS-2 (C-band, VV) SAR image (scale and location unknown) taken over the Indian Ocean on 6th April, 1999 at 04:58 UTC showing a "feathered" structure of an oil trail. The wind direction arrow in the image was obtained from the modelled surface wind field provided by the European Centre for Medium-range Weather Forecasts (ECMWF) ©ESA.

Introduction

The OSI methodology can be summarised in the following three steps: firstly delineating the suspected spill patterns using an edge enhancement filter on a grey scale image (produced for example from a single band of MODIS's 250 m/pixel band group); followed by an analysis of the spill edge features, and texture distribution relative to the surrounding water texture; and finally, estimating its relative viscosity type using the OSI algorithm, once it has been classified as oil. An additional contrast stretching may be needed in order to highlight the granularity level of the inspected patch.

The Sobel operator measures (in 2-D spatial direction) the approximate absolute gradient magnitude on an image to emphasizes the regions of high spatial frequency that correspond to edges. Its larger convolution kernel (3×3) smooths the input image to a greater extent and so makes the operator less sensitive to noise. The operator also generally produces considerably higher output values for similar edges, compared with the other edge detection filters. It is an isotropic operator such that it applies equally well in all directions in an image, with no particular sensitivity or bias towards one particular set of directions (*e.g.* compass directions)[32]. After applying the Sobel filter on an investigated pattern, the edge gradient of the pattern's border will be assessed in terms of: (a) the uniformity of its border's width (mean border width); (b) its continuity; and (c) the granularity of the patch's surface structure relative to its surroundings.
Therefore, relatively fresh oil spills (detected within the first ~ 12-24 hours from the time of their occurrence), will have a relatively homogeneous border-width free from sharp points or geometric discontinuities (defined in Figure C.2) apart from their apparent point source.

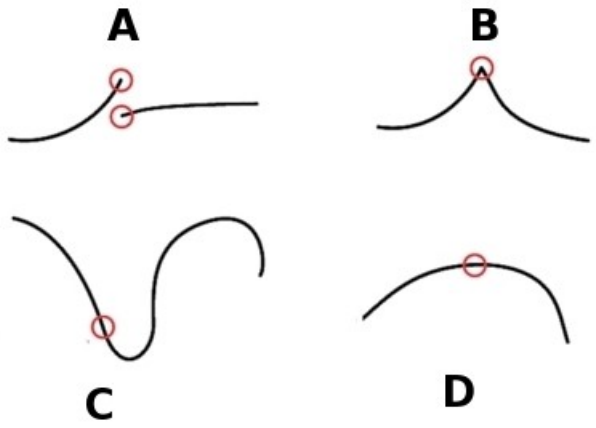

Figure C.2. Different types of continuity to demonstrate the OSI-shape compatibility criteria. **(A)** Discontinuity (incompatible with the OSI); **(B)** zero curvature level (due to the angle), but continuous (incompatible with the OSI); **(C)** inflection point curvature: first derivative is a constant but not zero, second derivative changes signs at the point (compatible with the OSI); and **(D)** curvature: first derivative is zero, second derivative can be either positive or negative (compatible with the OSI).

According to the OSI definition, a relatively fresh oil spill would have its borders characterised with a uniform mean width after applying the Sobel filter on it. Figure C.3 demonstrates this example for a spill detected in RADARSAT on 22nd March, 2007.

[32] http://homepages.inf.ed.ac.uk/rbf/HIPR2/sobel.htm

Two lines were drawn across the border gradient at points 1 and 2 (Figure C.3A), whose transects are shown to be almost identical in the plot shown in Figure C.3B.

After applying the Sobel filter, the texture of the spill's surface area would generally appear less noisy to that of the surrounding water. This is probably caused by the dampening exerted by the viscous oil at the water surface and the suppression of capillary waves. Such features are enhanced considerably when the spill is viewed by MODIS under a sun-glint zone.

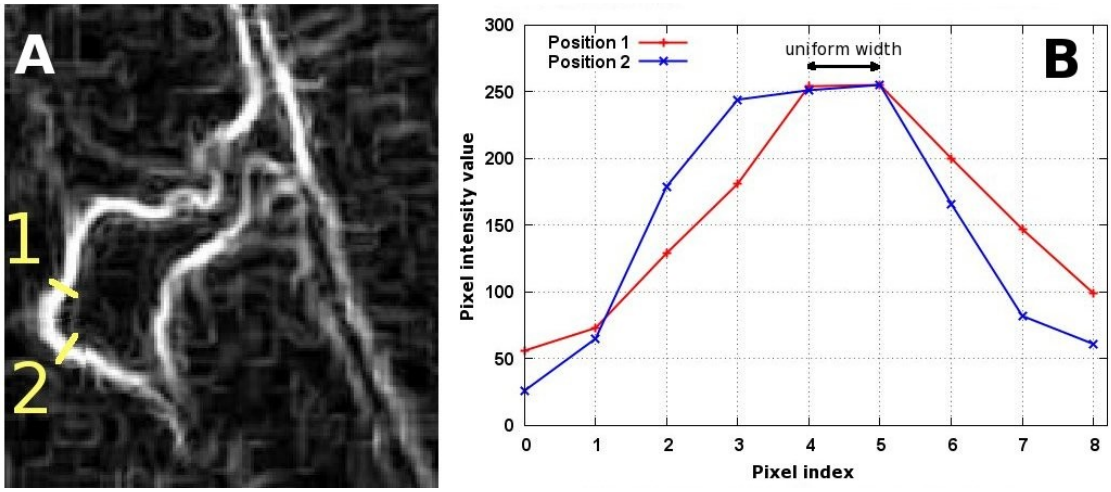

Figure C.3. **(A)** A RADARSAT image on 22nd March, 2007 (scale and location unknown), showing an oil spill after applying the Sobel filter with two lines drawn across its border at points 1 and 2. **(B)** shows the transects at these two points with an almost equal width at the spill's border.

In summary, according to the criteria set by the OSI model: an offshore oil spill involving a heavy crude oil, at moderate wind speeds between 2-3 m/s and 12-15 m/s, would appear with a smoothly curved, continuous and equal-width boundary, whose surface area would be characterised with having a less granular texture than the surrounding sea water. Failing to possess any of these conditions may, on the other hand, indicate several options: the original viscosity of the oil has changed due to natural or artificial weathering (sprayed with a dispersant); or that the oil type involved in the spill was of a light viscous type (that is, its viscosity is close to that of sea water); or it is of low concentration or thickness sufficient enough to be classified as sheen; or it could be attributed to an oil spill look-alike.

Theoretical background

Crude oils are generally divided into light, medium and heavy, on the basis of their °API[33] gravity measurements. When an investigated pattern is classified as an oil spill (according to the shape and texture prerequisites set by the OSI) it is then possible to estimate the oil's viscosity group (η). This is done by approximating the spill shape with a series of successive circles, whose dimension should increase as the spill disperses away from its presumed point source. If, for example, two circles are to be drawn inside the spill's inner surface area, each with radii r_1 and r_2 respectively where $r_1 \neq r_2$ (signifying a lateral spread) and both are measured in pixels. In reference to Figure C.4A, the following should be considered whilst drawing the circles: (1) The circle should cover the maximum possible area of the spill's area to the extent that it acts as a tangent for at least two points of the inner border of the spill; and, (2) the next adjacent circle (radius r_2) should be drawn in contact with the first circle (radius r_1) at a tangent point. The sum of the circles' diameters will represent that part of the spill's length (as shown in Figure C.4B).

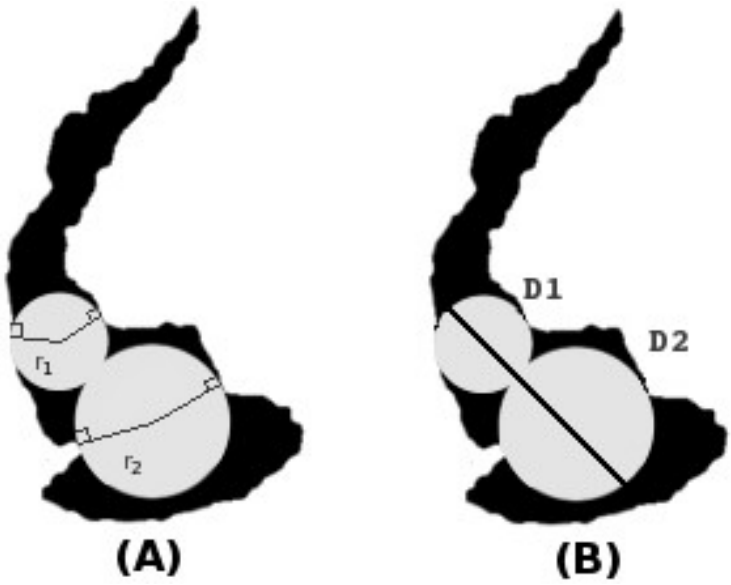

Figure C.4. Demonstrating the methodology of the OSI: **(A)** draw two circles over the spill's area each with radius r_1 and r_2 respectively ($r_1 \neq r_2$ and radii are measured in pixels). **(B)** The sum of the two circles' diameters D1 and D2 respectively, is approximately equal to the spill's length for the part that is covered by the circles.

[33] American Petroleum Institute gravity (°API) a scale for quantifying an inverse relationship with specific gravity. The Specific gravity of an oil is its density in relation to pure water. It determines whether or not the oil will float.

The OSI and viscosity (η) can then be evaluated using Equations C.1 and C.2 respectively:

$$OSI = \sin(\frac{\theta}{2}) = \frac{D_{i+1} - D_i}{D_{i+1} + D_i} \equiv \frac{measure\ of\ lateral\ spread}{part\ of\ the\ spill\ length} \quad \text{(C.1)}$$

where D_i and D_{i+1} are the diameters of the two consecutive circles i and i+1 respectively. The sum $(D_{i+1}+D_i)$ represents the length part of the spill that is covered by the two consecutive circles. The angle θ is a measure of the lateral spread and is defined as shown in Figure C.5.

$$\eta \propto \frac{1}{OSI} \quad \text{(C.2)}$$

$\sin(\delta 1)=(r1-r2)/(r1+r2)$

$\sin(\delta 2)=(r1-r2)/(r1+r2)$

$\sin(\frac{\theta}{2})=(r1-r2)/(r1+r2)$ where $\delta 1=\delta 2=\delta$ and $2\delta=\theta$

or

$\sin(\frac{\theta}{2})=(D1-D2)/(D1+D2)$

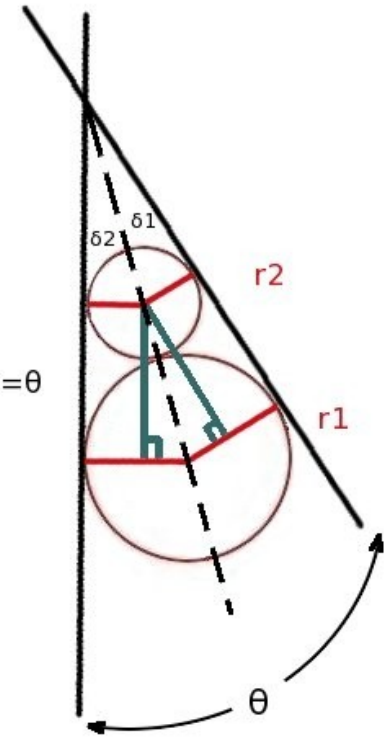

Figure C.5. A schematic diagram showing two consecutive circles each with radius r1 (diameter D1) and r2 (diameter D2) drawn over part of the spill area. The lateral spread of the spill is represented by sin(θ/2).

If two spills S1 and S2 (shown schematically in Figure C.6) of different oil types each with a viscosity group η1 and η2 respectively both experiencing similar environmental conditions, then the lateral spread of S1 becomes greater than that of S2 (OSI1 > OSI2) and hence, η1< η2.

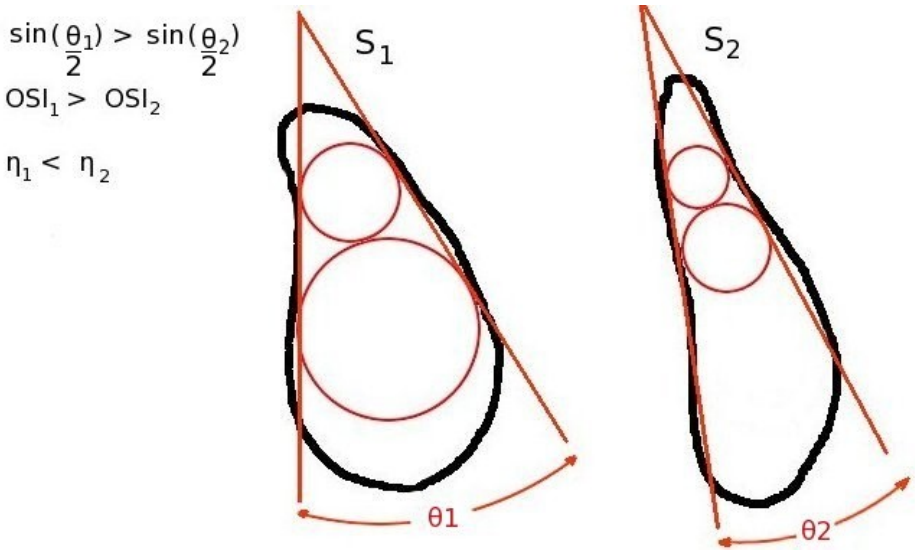

Figure C.6. Two spills S_1 and S_2 involving two different oil types of viscosity η_1 and η_2 respectively. If both spills are experiencing similar environmental conditions, then the lateral spread of S_1 will become greater than that of S_2 ($OSI_1 > OSI_2$) and hence, $\eta_1 < \eta_2$.

Linear-shaped spills (that is, spills lacking lateral spread) are not compatible with the shape conditions proposed by the OSI criteria because their size may not be large enough to apply the method and the circles drawn will be equal in size (see Figures C.7A and C.7B), yielding a zero dispersion rate according to the OSI formula.

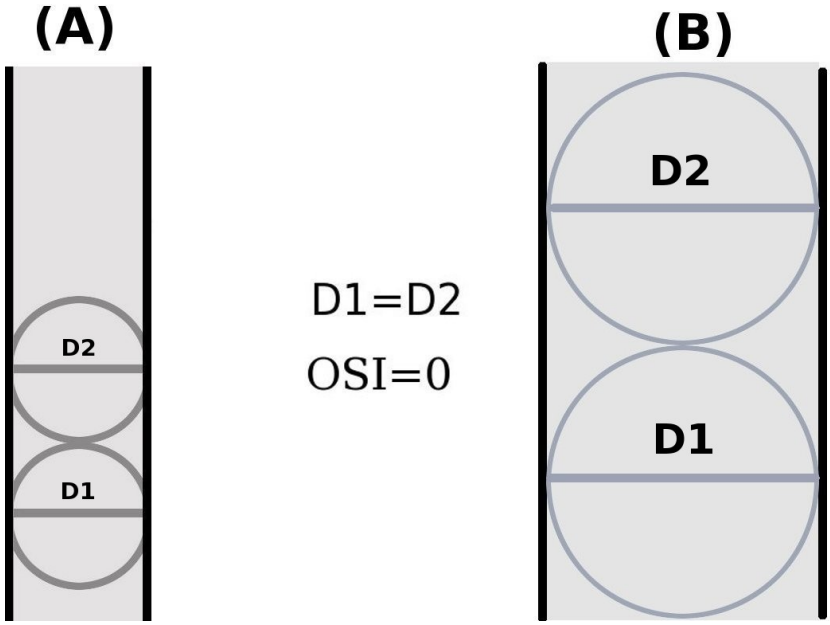

Figure C.7. A schematic diagram showing two linear-shaped spills: **(A)** Thin and **(B)** wide. Such spills are incompatible with the OSI criterion because their equal-sized circles leads to a zero OSI value (no lateral spread).

Examples of usage

The OSI theory was tested over two different categories of oil spill look-alikes such as biological surface bloom such as algae and low wind patterns. The map shown in Figure C.8 identifies the satellite swaths over which theses examples were carried out.

Figure C.8. The different MODIS swaths (except B) in which different oil spills and oil spill look-alikes were used in the examples of the implemention of the OSI.

1.0 Oil spill look-alikes

A surface floating bloom of cyanobacteria (*Trichodesmium erythraeum*) was detected on 19th April, 2009 in MODIS Aqua (swath location shown in Figure C.8C) and in ENVISAT ASAR (C-band, HH polarization, 1 km/pixel resolution), observed at different times (see Appendix C for a review of the different bloom species discussed in this thesis). The floating filaments of bloom observed in MODIS Aqua at 10:06 UTC are shown in Figure C.9A as being reddish structures floating at the sea water surface. The image was produced from the 250 m/pixel false RGB colour composite corresponding to bands λ_2=859, λ_1=645 and λ_1=645 nm respectively. The corresponding ASAR image was taken at 18:35 UTC showing the same bloom (Figure C.9B) as having completely dark formations. Low-wind areas also appear dark in the image and with virtually no existing texture patterns, even after changing the level of contrast. This dark feature is due to a reduction in sea surface roughness (dampening of capillary sea waves) caused either by surface blooms (similar to oil) or by a diminishing range of wind speeds and ultimately causing solar illumination to be reflected off its mirror-like surface away from the sensor and hence appear dark in satellite images. Spectrally,

however, surface biological blooms can appear different in MODIS when compared to ASAR images (compare Figures C.10A and C.10B), but texturally they appear very similar in terms of their irregular and discontinuous shape after applying the Sobel filter.

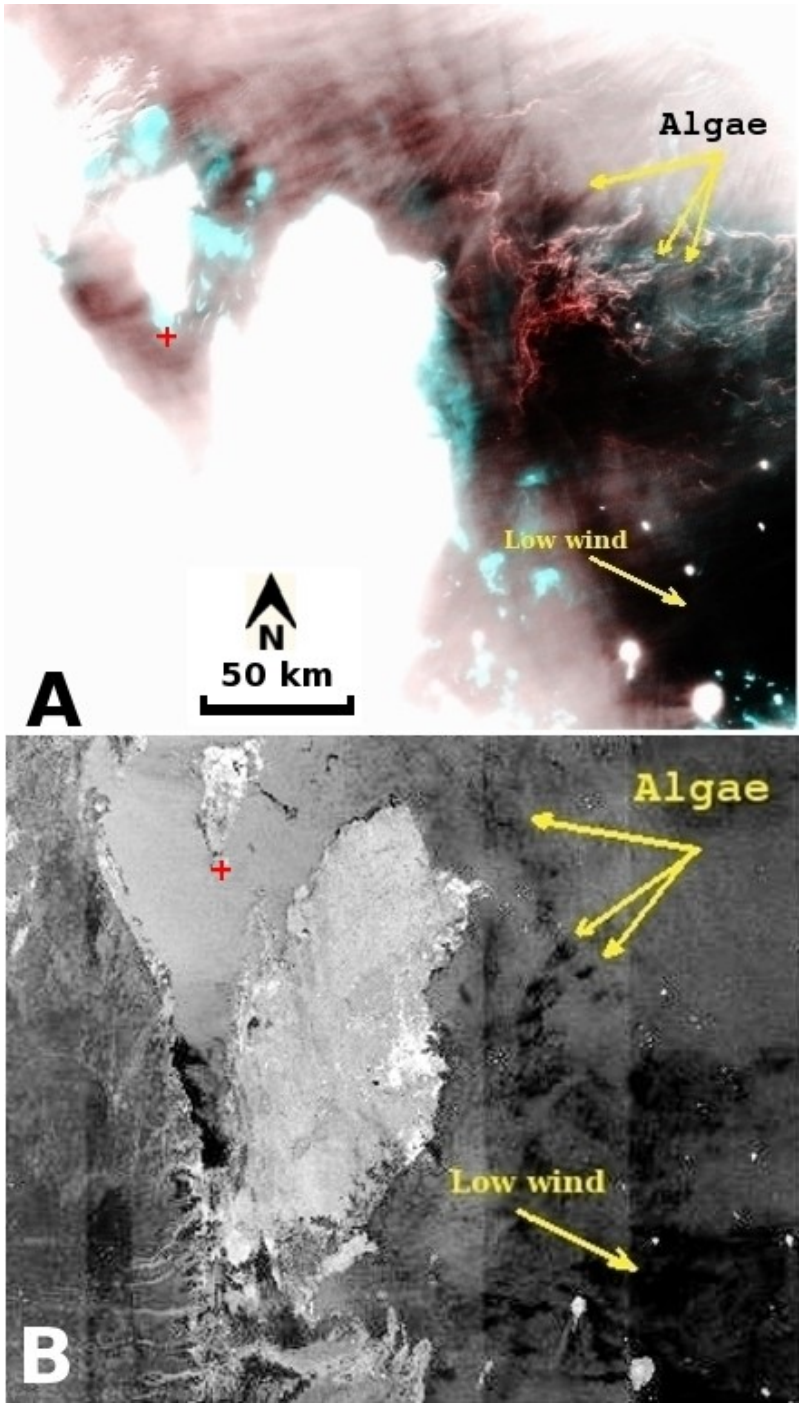

Figure C.9. A surface bloom of *Trichodesmium erythraeum* on 19th April, 2009 observed in **(A)** MODIS Aqua at 10:06 UTC (average SST 22.5° C) as it appears in a 250 m/pixel resolution false RGB colour composite corresponding to bands λ_2=859, λ_1=645 and λ_1=645 nm respectively and in **(B)** ENVISAT ASAR (C-band, HH polarization, 1 km/pixel resolution) image at 18:35 UTC © ESA. The red + mark is positioned at N25° 48' 13.9" E50° 33' 9.6".

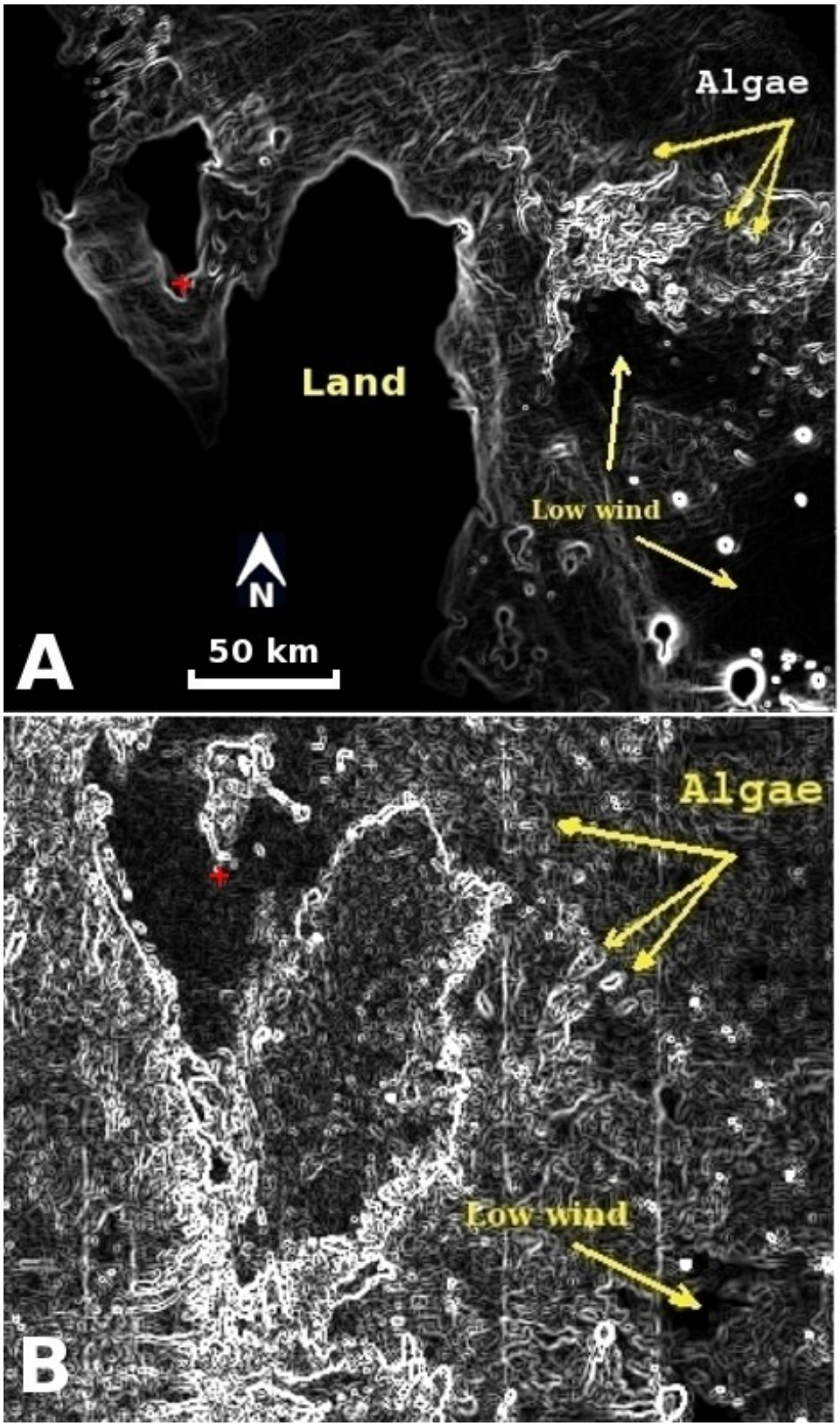

Figure C.10. The surface bloom of *Trichodesmium erythraeum* on 19th April, 2009 shown in Figure C.9 after applying the Sobel filter on **(A)** MODIS Aqua and **(B)** ENVISAT ASAR (C-band, HH polarization, 1 km/pixel resolution) image © ESA. In both images, the blooms' texture appears irregular, and with broken borders. The red + mark is positioned at N25° 48' 13.9" E50° 33' 9.6".

However, after applying the Sobel filter over the low wind patterns visible in both sensor images, their border structures appear either with or without multiple discontinuities, but texturally will always appear dark due to lack of surface waves. To the inexperienced observer, the shape of such blooms may mistakenly be classified as oil due to their shared floating mechanism.

2.0 Oil spills

2.1 Gulf of Mexico oil spill

On 22nd April, 2010 an oil spill caused by a leak 1524 m below the water surface from the Deepwater Horizon oil rig in the Gulf of Mexico was captured by the RADARSAT-2 satellite (ScanSAR narrow, VV polarization) on 23th April, 2010 (see Appendix B to view the spill under different satellite sensors). The image is shown in Figure C.11A, where it is estimated to cover an area of about 1000 km^2. The OSI methodology was applied to the spill by applying the Sobel filter to the image (see in Figure C.11B), after which circles were drawn across its surface to estimate the viscosity group of the observed oil (see in Figure C.11C).

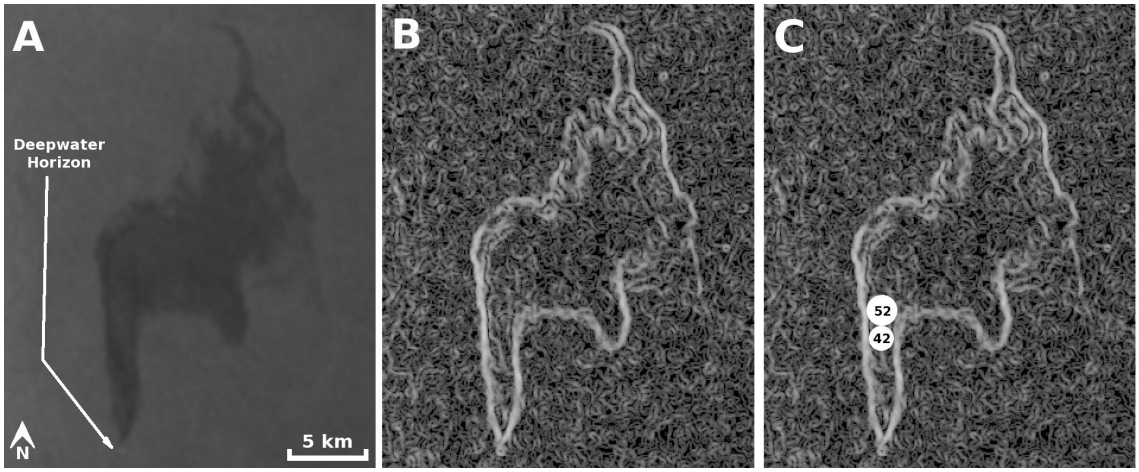

Figure C.11. **(A)** The Gulf of Mexico Deepwater Horizon oil spill (SG=0.85) in RADARSAT-2 (scanSAR narrow, VV polarization) on 23rd April, 2010 at 23:49 UTC, **(B)** after applying the Sobel filter), and **(C)** after applying the OSI (0.11) method © Macdonald Dettwiler and Associates Ltd (MDA). The Deepwater Horizon oil rig is located at position N28° 44.20′ W88° 23.23′.

The computed OSI value was 0.11 classifying the oil's viscosity as being light to medium viscous-type oil matching the original viscosity of the leaking oil (light sweet crude oil with SG=0.850). The mean wind speed and SST values estimated by NOAA[34] during the spill was 7 m/s and 22.5 °C (see Figure C.12) respectively.

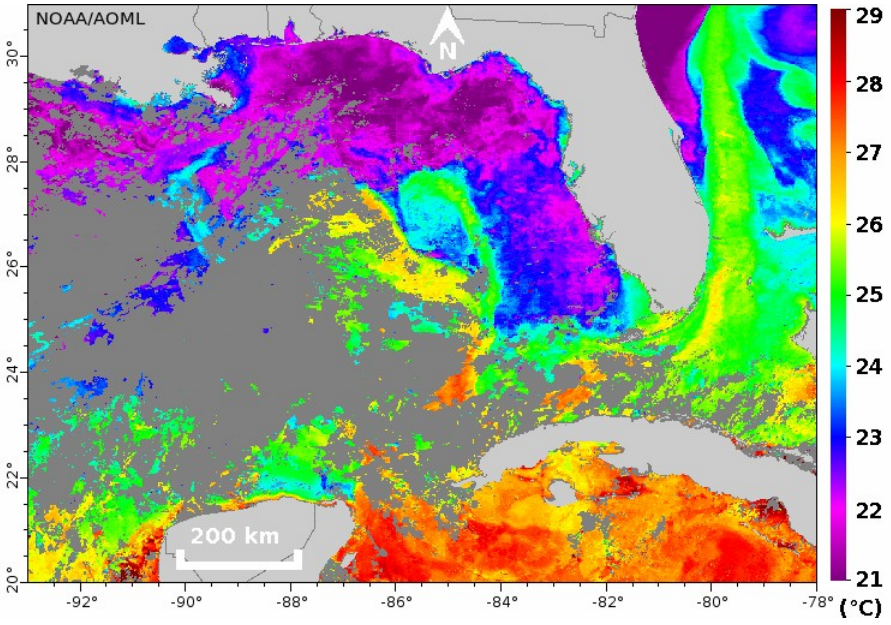

Figure C.12. Advanced Very High Resolution Radiometer (AVHRR) SST fields (resolution at nadir 1.09 km) on 23rd April, 2010 for the Gulf of Mexico area. The SST value around the location of the oil rig (located at N28° 44.20′ W88° 23.23′) is 22.5 °C. Data courtesy of CoastalWatch, carib. And GoM Regional Node[35].

By 25th April 2010, the size of the Deepwater Horizon oil spill had reached approximately the size of 1500 km^2 and the weather conditions had allowed it to be visible in MODIS Aqua and SPOT 5 shown in Figures C.13A and C.13B respectively.

[34] http://www.sciencedirect.com/science/article/B6V7X-3SX6XM8-6/2/c8e9003fce5dacd9a320ca2061571631

[35] http://www.aoml.noaa.gov/phod/dhos/sst.php

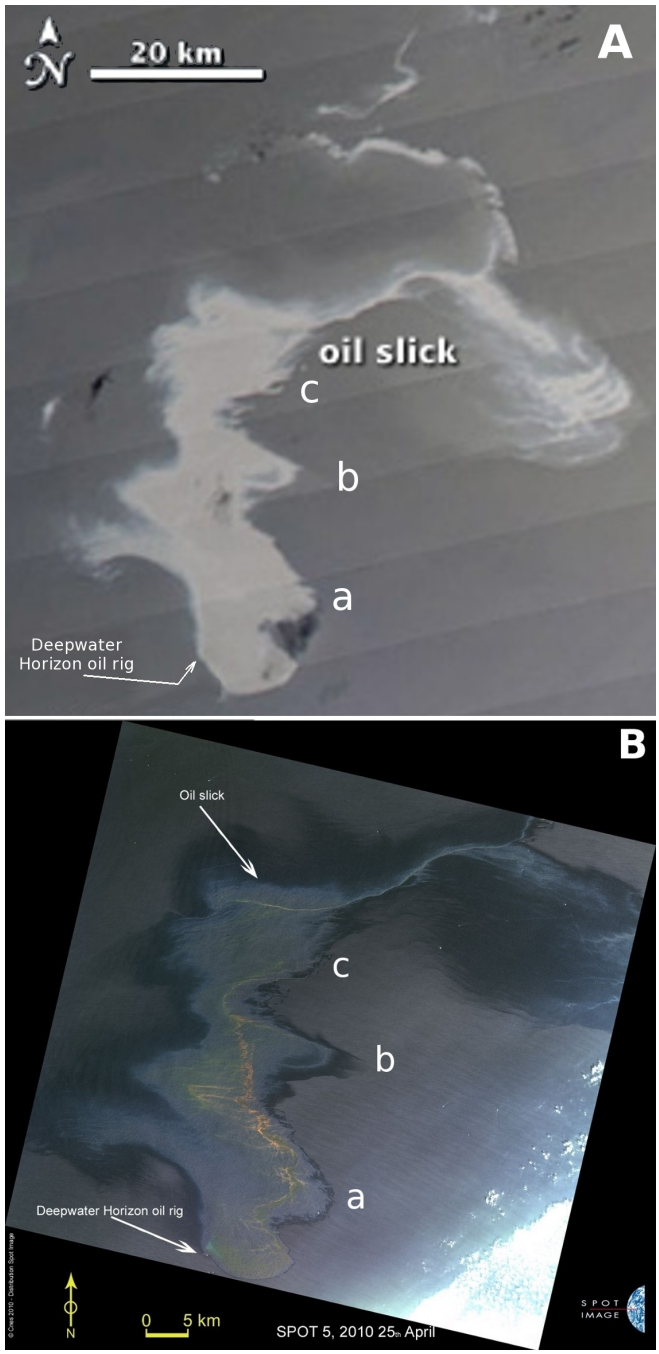

Figure C.13. The Gulf of Mexico oil spill on 25th April, 2010 **(A)** at 18:55 UTC in the 250 m/pixel MODIS Aqua in natural RGB colour composite corresponding to bands λ_1=645, λ_4=555 and λ_3=469 nm respectively (λ_4 and λ_3 oversampled from the 500 m/pixel band group). Data from NASA, MODIS Rapid Response (B) SPOT 5 image (unknown RGB colour composite) at 10 m/pixel resolution captured on the same day at 16:31 UTC. Points a, b and c are shown on both images respectively. The Deepwater Horizon oil rig is located at the position N28° 44.20′ W88° 23.23′.

The MODIS image (Figure C.13A) is a 250 m/pixel resolution natural RGB colour composite corresponding to bands λ_1=645, λ_4=555 and λ_3=469 nm respectively (λ_4 and

λ_3 oversampled from the 500 m/pixel band group). The SPOT 5 image (Figure C.13B) is in 10 m/pixel resolution with an unspecified RGB colour composite. The oil slick in these images is likely to include areas of thicker oil surrounded by areas of relatively thin surface films. The SPOT 5 image in particular indicates a relatively thick oil layer in the centre of the slick. The central strip of red in this image is the thickest area. The darker edges are thinner oil - probably sheen. The spill's contrast under the MODIS image appears positive over the whole area, including the fringes, due to sun-glint effect, but the thicker areas appear with a relatively brighter contrast. The presence of sun-glint over the spill area also prevented the production of MODIS SST and Chlor-a maps.

NOAA[36] estimated the wind speed to be 15–20 knots (7.7–10.3 m/s) and wave heights of 4–6 foot (1.2–1.8 m). The SST estimated for the surrounding sea water was 22.7 °C (see Figure C.14).

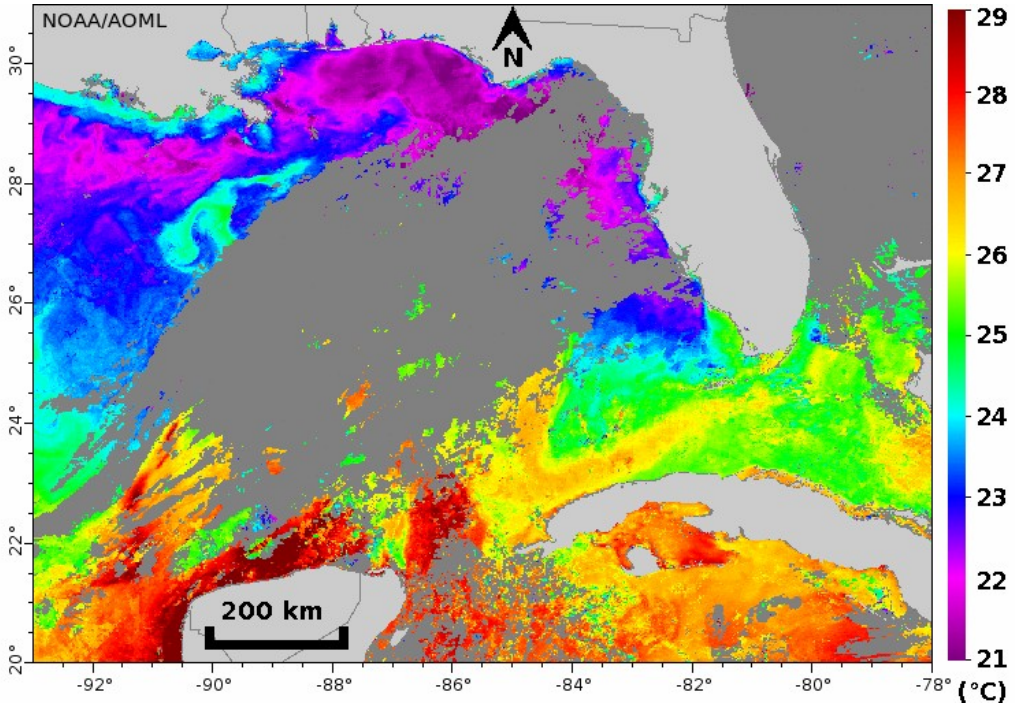

Figure C.14. AVHRR SST fields (resolution at nadir 1.09 km) on 25th April, 2010. The SST value around the location of the oil rig (positioned at N28° 44.20′ W88° 23.23′) is 22.7 °C. Data courtesy of CoastalWatch, carib. And GoM Regional Node[37].

The Sobel-filter was applied to Figures C.13A and C.13B followed by the application of the OSI as shown in Figures C.15A and C.15B respectively. The spill did exhibit

[36] http://www.sciencedirect.com/science/article/B6V7X-3SX6XM8-6/2/c8e9003fce5dacd9a320ca2061571631

[37] http://www.aoml.noaa.gov/phod/dhos/sst.php

discontinuities and lack of uniformity in its gradient border which are features different to the ones proposed by the OSI for fresh oil spills. This can be attributed to the extreme weathering conditions that the oil was exposed to, particularly since it had been leaking for three days (the leak started on 20th April, 2010) in addition to the fact that parts of the spill had been sprayed with a dispersant. Nevertheless, the OSI estimate was carried out and it was found to be equal to 0.18.

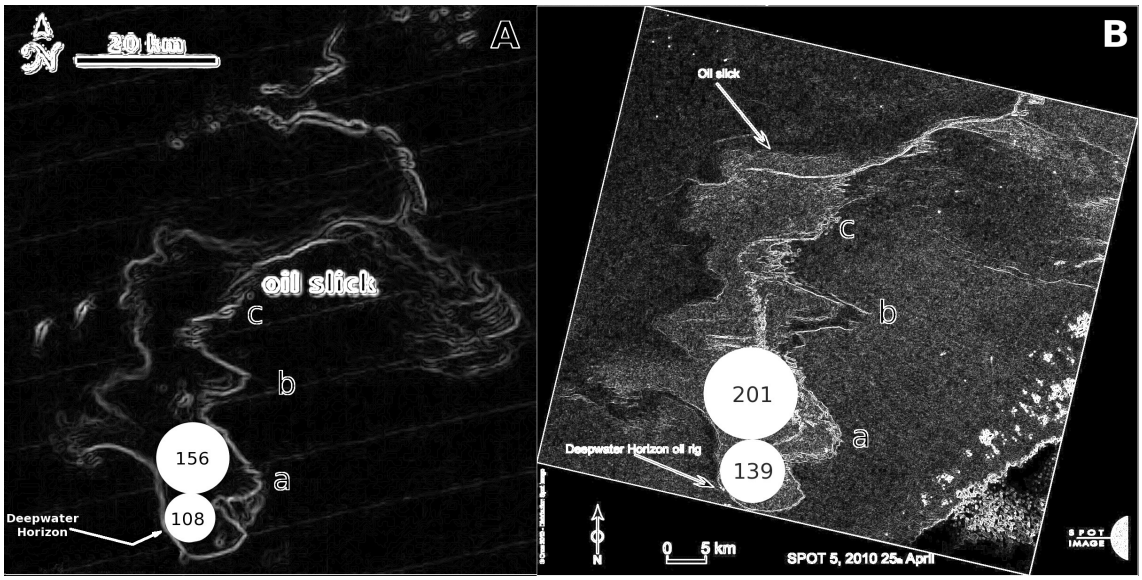

Figure C.15. The Gulf of Mexico Deepwater Horizon oil spill on the 25th April, 2010 after converting the original image shown in Figure C.13 into a grey scale image and applying the Sobel filter, followed by the OSI estimation procedure on **(A)** MODIS Aqua image and **(B)** SPOT 5. The resulting OSI value was consistent between the two data sets and equal to 0.18.

2.2 Al Ahmadi terminal oil spill, Kuwait

On 4th August, 2010 an oil spill (size ~ 69 km^2) was detected by MODIS Terra at 07:38 UTC near Al Ahmadi oil terminal (Kuwait). The image shown in Figure C.16A shows the spill (circled) at 250 m/pixel spatial resolution false RGB colour composite corresponding to bands λ_2=859, λ_1=645 and λ_1=645 nm respectively. The spill was also visible in ENVISAT ASAR data (C-band, HH polarization, 1 km/pixel spatial resolution) at 06:50 UTC shown (circled) in Figure C.16B. According to the terminal officials, the spill occurred when heavy crude oil (18 °API, SG=0.95) started leaking from an offshore loading terminal on 2nd August, 2010, two days prior to its detection in MODIS Terra. The average wind speed estimated at the time of the spill by the Advanced Scatterometer (ASCAT) instrument 10 m above sea level was ~ 6 m/s.

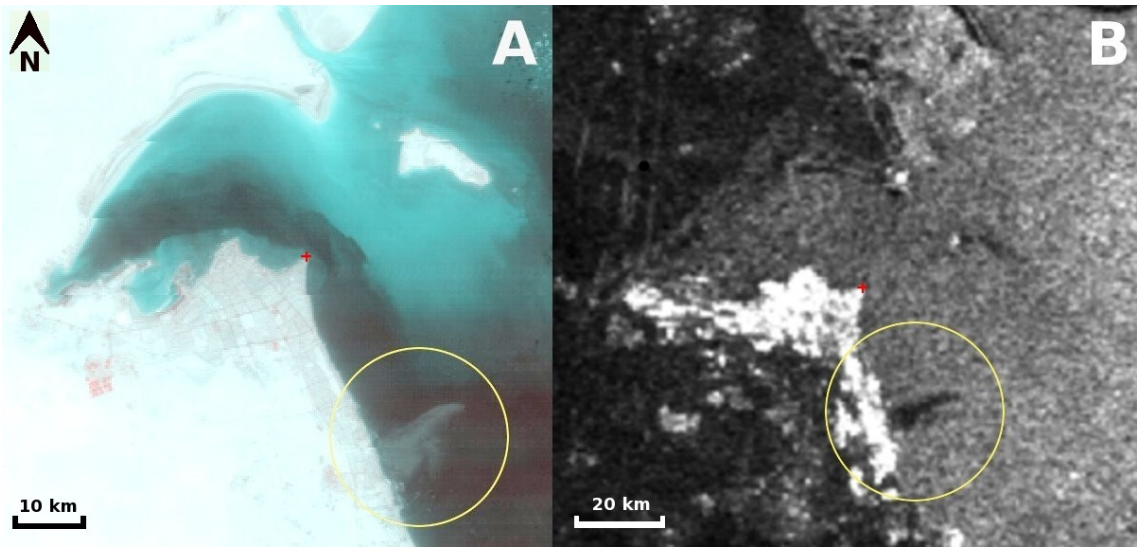

Figure C.16. Oil spill (18 °API, SG=0.95) near Al Ahmadi oil terminal (Kuwait) shown in **(A)** a 250 m/pixel spatial resolution MODIS Terra image on 4th August, 2010 at 07:38 UTC as it appears in a false RGB colour composite corresponding to bands λ_2=859, λ_1=645 and λ_1=645 nm respectively and in **(B)** ENVISAT ASAR (C-band, HH polarization, 1 km/pixel resolution) at 06:50 UTC of the same day © ESA. The red + marking is located at N29° 21' 2.9" E48° 5' 57.4".

The implementation of the OSI method on the MODIS Terra image (shown in Figure C.17) and ENVISAT data (shown in Figure C.18) have produced values equal to 0.22 and 0.23 respectively. The original viscosity of the oil may have changed due to the prevailing warm weather conditions at the time of the spill which the oil was exposed to for two days prior to its detection by MODIS.

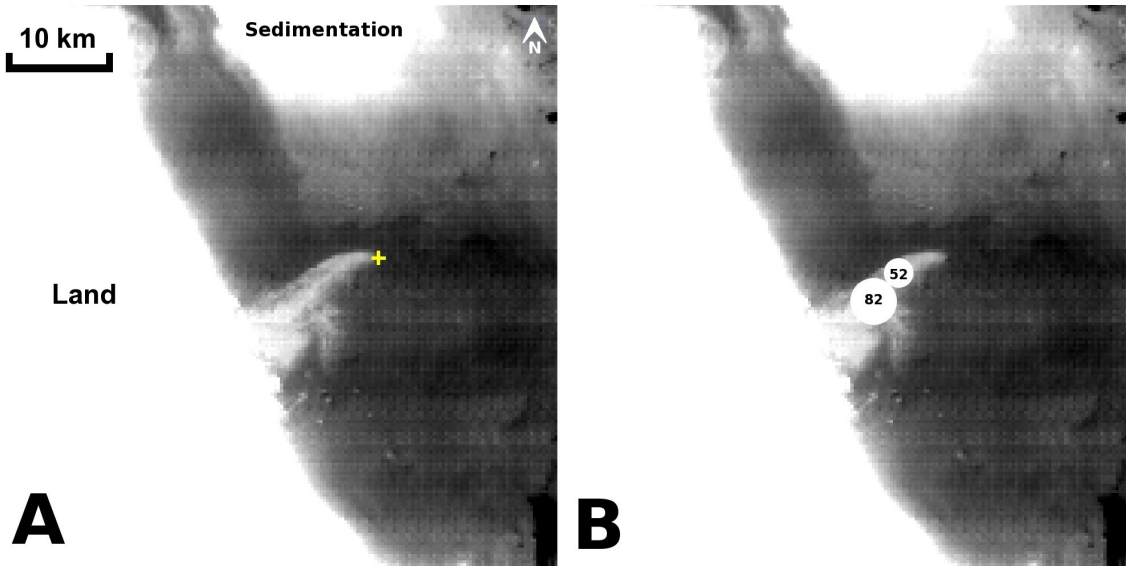

Figure C.17. The same spill incident shown in Figure C.16A, as it appears in the grey scale MODIS Terra image produced from a single band (λ_l=645 nm) **(A)** before applying the OSI method and **(B)** after applying the method. The resulting OSI value came to 0.22. The yellow + marking is located at 29° 08' 36" 48° 17' 18".

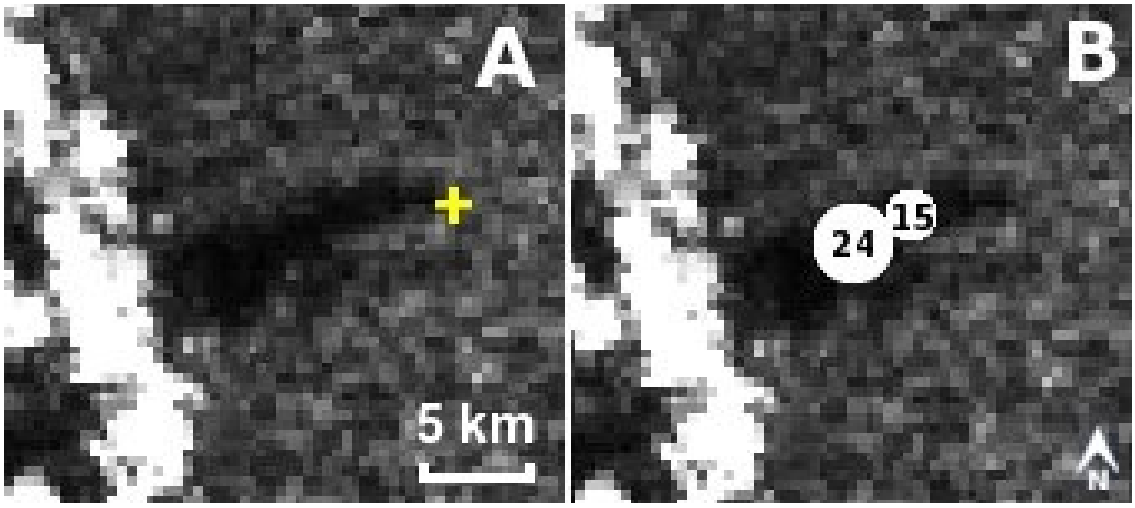

Figure C.18. The oil spill that occurred near Al Ahmadi terminal (shown in Figure C.16B) is visible in ENVISAT ASAR image data (C-band, HH polarization, 1 km/pixel resolution) on 4th August, 2010 at 06:50 UTC **(A)** before applying the OSI method and (B) after applying the method which estimated an OSI value of 0.23 (greater than 0.02, the base-line index for a light to medium viscosity group) © ESA. The yellow + marking is located at 29° 08' 36" 48° 17' 18".